





# DISSERTATION

Synthese und Charakterisierung neuer und funktionalisierter MOFs  
basierend auf Elementen der 13. Gruppe und deren spezielle  
optische Eigenschaften

Zur Erlangung des Doktorgrades  
der Mathematisch-Naturwissenschaftlichen Fakultät der  
Christian-Albrechts-Universität zu Kiel

vorgelegt von  
Martin Krüger

Kiel, im September 2017



Erster Gutachter:

Prof. Dr. Norbert Stock

Zweiter Gutachter:

Prof. Dr. Christian Näther

Tag der mündlichen Prüfung:

29.11.2017



*Meinen Eltern und Freunden*





## Synthese und Charakterisierung neuer und funktionalisierter MOFs basierend auf Elementen der 13. Gruppe und deren spezielle optische Eigenschaften

Diese Arbeit beschäftigt sich zum einen mit der Synthese und Charakterisierung neuer Metall-Organischer Gerüstverbindungen basierend auf den trivalenten Kationen  $\text{Al}^{3+}$ ,  $\text{Ga}^{3+}$  und  $\text{In}^{3+}$  und zum anderen mit der gezielten Herstellung von MOFs die den optischen Effekt der Frequenzverdopplung aufweisen. Dafür wurden sowohl neue Verbindungen synthetisiert, als auch neue Funktionalisierungen bekannter Gerüststrukturen hergestellt. Zur Entdeckung und Syntheseoptimierung wurde auf Hochdurchsatzmethoden zurückgegriffen. In dieser Arbeit dienten die Linker 1,2,4,5-Tetrakis(4-carboxyphenyl)benzol ( $\text{H}_4\text{TCPB}$ ), 4,4'-Benzophenondicarbonsäure ( $\text{H}_2\text{BPDC}$ ) und 4,4'-Oxydibenzoesäure ( $\text{H}_2\text{ODB}$ ) zur Synthese neuer Al-MOFs. Unter Verwendung von  $\text{H}_4\text{TCPB}$  konnte CAU-9  $[\text{Al}_2(\text{OH})_2(\text{TCPB})] \cdot 2\text{DMF}$  erhalten werden. Die thermisch hoch stabile Verbindung ist isoretikulär zu MIL-118B und Al-PMOF. Mit  $\text{H}_2\text{BPDC}$  konnte die Verbindung CAU-21-BPDC  $[\text{Al}(\text{OH})(\text{BPDC})]$  hergestellt werden, deren Kristallstruktur aus Röntgen-Einkristalldaten gelöst und verfeinert werden konnte. Diese Verbindung ist pseudopolymorph zu CAU-8-BPDC, dessen Kristallstruktur ebenfalls aus Röntgen-Einkristalldaten bestimmt wurde. Bei der Verwendung der zur  $\text{H}_2\text{BPDC}$  geometrisch sehr ähnlichen Dicarbonsäure  $\text{H}_2\text{ODB}$  konnten ebenfalls Verbindungen mit CAU-8- ( $\text{CAU-8-ODB}$ ,  $[\text{Al}(\text{OH})(\text{ODB})]$ ) und CAU-21- ( $\text{CAU-21-ODB}$ ,  $[\text{Al}(\text{OH})(\text{ODB})]$ ) Struktur erhalten werden. Diese sind ebenfalls Pseudopolymorphe, aber auch isoretikulär zu ihren -BPDC-Derivaten. CAU-21 ist aus oktanuclearen Ringen eckenverknüpfter  $\text{AlO}_6$  Polyeder aufgebaut, die in einer **bcu** Packung angeordnet sind. Jede anorganische Baueinheit ist durch jeweils zwei Linkermoleküle mit jeder der benachbarten acht Baueinheiten verbrückt, sodass eindimensionale Poren mit variablen Durchmesser entstehen. Für den zweiten Teil der Arbeit, indem MOFs hergestellt wurden die den optischen Effekt der Frequenzverdopplung aufweisen, wurden 5-Fluoroisophthalsäure ( $\text{H}_2\text{mBDC-5F}$ ), Isophthalsäure ( $\text{H}_2\text{mBDC}$ ), 4,4',4''-s-Triazin-2,4,6-triyl-tribenzoesäure ( $\text{H}_3\text{TATB}$ ), 2-Aminoterephthalsäure ( $\text{H}_2\text{BDC-NH}_2$ ), 2-Nitroterephthalsäure ( $\text{H}_2\text{BDC-NO}_2$ ) und 2-Amino-5-nitroterephthalsäure ( $\text{H}_2\text{BDC-NH}_2/\text{NO}_2$ ) verwendet. Mit  $\text{H}_2\text{mBDC-5F}$ ,  $\text{H}_2\text{mBDC}$  und  $\text{H}_3\text{TATB}$  konnte eine weitere funktionalisierte Variante des Al-MOFs CAU-10 ( $\text{CAU-10-H/F}_x$ ,  $[\text{Al}(\text{OH})(\text{mBDC})_{1-x}(\text{mBDC-5F})_x]$   $x = 0.11; 0.28; 0.44$ ) im Mixed-Linker Verfahren sowie eine Variante basierend auf ein größeres Linkermolekül

(CAU-10-HTATB, [Al(OH)(TATB)]) erhalten werden. Die Sorptionseigenschaften konnten durch Größe und Funktionalisierung des Linkers maßgeblich beeinflusst werden, jedoch war ein Nachweis eines SHG Effektes nicht möglich. Unter Verwendung der monofunktionalisierten Terephthalsäuren H<sub>2</sub>BDC-NH<sub>2</sub> und H<sub>2</sub>BDC-NO<sub>2</sub> konnten funktionalisierte In-MOFs mit **qtz** Topologie erhalten werden ([In(BDC-NH<sub>2</sub>)(BDC-NH<sub>2</sub>)]). Bei der Synthese des In-MOFs mit H<sub>2</sub>BDC-NO<sub>2</sub> wurde eine *in situ* Reduktion des Linkermoleküls zur unfunktionalisierten und aminofunktionalisierten Terephthalsäure beobachtet. Weiterhin wurde unter Verwendung von H<sub>2</sub>BDC-NH<sub>2</sub>/NO<sub>2</sub> ein kubischer In-MOF erhalten (DMA<sub>2</sub>[In<sub>3</sub>(O)(BDC-NH<sub>2</sub>NO<sub>2</sub>)<sub>4.5</sub>]), dessen Kristallmorphologie vom Volumenverhältnis der verwendeten Lösungsmittel abhängt. Die synthetisierten In-MOFs mit **qtz** Topologie sind aufgrund ihrer Struktur potentielle Kandidaten für nicht linear optisch aktive Materialien. Mit dem bifunktionalisierten Linker, welcher das Donor-Akzeptor Muster von *p*-Nitroanilin (PNA) aufweist, wurden ebenfalls Al-, Ga- und In-Derivate des MIL-53 hergestellt. Hier sollte versucht werden, die zentrosymmetrische und daher optisch nicht aktive Struktur des PNA durch den Einbau in einen MOF aufzubrechen und so eine optisch aktive Verbindung zu erhalten. Es konnten MIL-53 Derivate unter Verwendung des Linkers H<sub>2</sub>BDC-NH<sub>2</sub>/NO<sub>2</sub> hergestellt werden ([M(OH)(BDC-NH<sub>2</sub>/NO<sub>2</sub>)] M = Al, Ga, In), die je nach Synthesemethode unterschiedlich stark optisch aktiv waren.

## Synthesis and characterization of new and functionalized MOFs based on group 13 elements and their special optical properties

This thesis deals on the one hand with the synthesis and characterization of new metal-organic frameworks based on the trivalent cations  $\text{Al}^{3+}$ ,  $\text{Ga}^{3+}$  and  $\text{In}^{3+}$  and on the other hand with the targeted synthesis of MOFs exhibiting second harmonic generation (SHG) activity as a special optical effect. Aiming at this target new compounds, as well as new functionalizations of hitherto known frameworks were synthesized. For discovery and optimization of the synthesis conditions high-throughput methods were employed. In this work the linker molecules 1,2,4,5-tetrakis(4-carboxyphenyl)benzene ( $\text{H}_4\text{TCPB}$ ), 4,4'-benzophenonedicarboxylic acid ( $\text{H}_2\text{BPDC}$ ) and 4,4'-oxydibenzoic acid ( $\text{H}_2\text{ODB}$ ) were used for the synthesis of new Al-MOFs. Employing  $\text{H}_4\text{TCPB}$  the MOF  $[\text{Al}_2(\text{OH})_2(\text{TCPB})] \cdot 2\text{DMF}$  (CAU-9) was obtained, a highly stable compound with a structure isorecticular to the ones of MIL-118B and Al-PMOF. The use of  $\text{H}_2\text{BPDC}$  led to the formation of CAU-21-BPDC  $[\text{Al}(\text{OH})(\text{BPDC})]$ , a pseudo polymorph to CAU-8-BPDC. Their structures were determined using single crystal XRD data. If  $\text{H}_2\text{ODB}$ , a geometrically very similar linker molecule compared to  $\text{H}_2\text{BPDC}$ , is employed, CAU-8-type (CAU-8-ODB,  $[\text{Al}(\text{OH})(\text{ODB})]$ ) and CAU-21-type (CAU-21-ODB,  $[\text{Al}(\text{OH})(\text{ODB})]$ ) structures were obtained. These are also pseudo polymorphic structures as well as isorecticular to their -BPDC derivatives. The structure of CAU-21 is built up by octanuclear rings of corner-sharing  $\text{AlO}_6$  polyhedra arranged in a **bcu** packing. Each IBU is linked via two linker molecules to each of the eight adjacent IBUs. Thus, one dimensional modulated pores are formed. In the second part of this work, dealing with the synthesis of MOFs showing SHG activity, 5-fluoroisophthalic acid ( $\text{H}_2m\text{BDC-5F}$ ), isophthalic acid ( $\text{H}_2m\text{BDC}$ ), 4,4',4''-s-triazine-2,4,6-triyl-tribenzoic acid ( $\text{H}_3\text{TATB}$ ), 2-aminoterephthalic acid ( $\text{H}_2\text{BDC-NH}_2$ ), 2-nitroterephthalic acid ( $\text{H}_2\text{BDC-NO}_2$ ) and 2-amino-5-nitroterephthalic acid ( $\text{H}_2\text{BDC-NH}_2/\text{NO}_2$ ) were used. Employing  $\text{H}_2m\text{BDC-5F}$  and  $\text{H}_2m\text{BDC}$  in the mixed linker approach an additional functionalization of the Al-MOF CAU-10 (CAU-10-H/ $F_x$ ,  $[\text{Al}(\text{OH})(m\text{BDC})_{1-x}(m\text{BDC-5F})_x]$   $x = 0.11, 0.28, 0.44$ ) as well as a derivative based on the extended linker molecule  $\text{H}_3\text{TATB}$  (CAU-10-HTATB,  $[\text{Al}(\text{OH})(\text{TATB})]$ ) were obtained. The sorption properties could be altered decisively, but an SHG effect could not be observed. The use of the mono functionalized terephthalic acids  $\text{H}_2\text{BDC-NH}_2$  and  $\text{H}_2\text{BDC-NO}_2$  led to the formation of In-MOFs with **qtz** topology ( $[\text{In}(\text{BDC-NH}_3)(\text{BDC-NH}_2)]$ ). An *in situ* reduction of  $\text{H}_2\text{BDC-NO}_2$  resulting in unfunctionalized and amino functionalized terephthalate molecules

was observed during synthesis of the In-MOF. Employing the bifunctionalized linker H<sub>2</sub>BDC-NH<sub>2</sub>/NO<sub>2</sub> a cubic In-MOF (DMA<sub>2</sub>[In<sub>3</sub>(O)(BDC-NH<sub>2</sub>NO<sub>2</sub>)<sub>4.5</sub>]) was obtained. Its crystal morphology depends on the volume ratio of the solvents used in the synthesis. Because of their structural properties the In-MOFs with **qtz** topology turned out to be potential candidates as nonlinear optic (NLO) materials. The bifunctionalized linker H<sub>2</sub>BDC-NH<sub>2</sub>/NO<sub>2</sub>, which is mimicking the donor-acceptor motif of *p*-nitroanniline (PNA), also served as a linker molecule for the synthesis of Al-, Ga- and In- derivatives of MIL-53. By its incorporation into this MOF structure the centrosymmetric alignment of the PNA molecule should be transferred into a polar, optically active material. The use of H<sub>2</sub>BDC-NH<sub>2</sub>/NO<sub>2</sub> led to the formation of MIL-53 derivatives ([M(OH)(BDC-NH<sub>2</sub>/NO<sub>2</sub>)] M = Al, Ga, In), exhibiting different SHG activities depending on the synthesis conditions employed.

# DANKSAGUNG

Mein Dank gilt an erster Stelle natürlich an Professor Stock für die Betreuung dieser Arbeit und die Chance seit dem Bachelor quasi durchgängig in seinem Arbeitskreis tätig sein zu können. Dabei hatte er immer ein offenes Ohr für Probleme und auch die Geduld diese gemeinsam anzugehen.

Ebenso viel Dank gebührt Dr. Helge Reinsch, der meine wissenschaftliche Laufbahn ebenso begleitet hat. Danke Helge, dass du immer mit Rat und Tat zur Seite standst! Keine Frage blieb unbeantwortet und keine Struktur ungelöst. Auch meinen weiteren Struktur-Göttern, Dr. Andrew Kentaro Inge und Martin Albat, möchte ich für alles danken, womit sie sich beschäftigt haben.

Meinen speziellen Dank gilt der alten Riege des AK Stock, die einem immer wieder auf die richtige Bahn gelenkt haben, bis man auf eigenen Füßen stehen konnte. Das gilt speziell für Dr. Nele Reimer und Dr. Felicitas Niekil, die selbst nach ihrem Abschied immer wieder nachgefragt und für den richtigen Ansporn gesorgt haben.

Aber auch den Menschen, die heimlich, still und leise im Hintergrund arbeiten, ohne die aber jegliches Forschen unmöglich ist, möchte ich hiermit meinen Dank aussprechen. Dazu gehören die spektroskopische Abteilung der anorganischen und die NMR Abteilung der organischen Chemie, Frau Jess für die vielen TG- und Einkristallmessungen, der Werkstatt und nicht zu vergessen Britta Bahn, der Engel des AK Stock. Britta, danke, dass du dich immer um alles gekümmert hast, ob es nun Kleinigkeiten waren oder großer Arbeitsaufwand dahinter steckte. Ich werde unsere morgendlichen Tee-Kränzchen vermissen, indem auch mal private Sachen zur Sprache kamen.

Vielen Dank auch an alle Bachelor und Praktikanten für die Unterstützung. Ich hoffe ich konnte genauso viel zurück geben. Auch an die Azubis möchte ich meinen Dank richten. Durch die Abnahme vieler Kleinigkeiten haben sie die einem die Arbeit etwas erleichtert.

Der wichtigste Dank geht jedoch an meine Familie und Freunde für alle Unterstützung, die sie geleistet haben. Ohne euch wäre nichts von alledem möglich gewesen!



# INHALTSVERZEICHNIS

## I. Allgemeiner Teil

<b>1. Einleitung</b>	<b>1</b>
<b>2. Präparative Methoden</b>	<b>4</b>
2.1 Solvothermalsynthese .....	4
2.2 Hochdurchsatzmethoden .....	6
<b>3. Charakterisierungsmethoden</b>	<b>8</b>
3.1 Röntgenbeugung.....	10
3.2 Grundlagen Röntgenpulverbeugung .....	12
3.2.1 Indizierung und Zellverfeinerung .....	13
3.2.2 Strukturlösung und Strukturverfeinerung.....	14

## II. Kumulativer Hauptteil

<b>4. Synthese und Charakterisierung neuer und funktionalisierter MOFs basierend auf Elementen der 13. Gruppe und deren spezielle optische Eigenschaften</b>	<b>17</b>
4.1 Einführung in die Nichtlineare Optik (NLO) und optische Frequenzverdopplung (SHG – Second Harmonic Generation) .....	18
4.2 Voraussetzungen und Anwendung nichtlinear optischer und SHG-aktiver Materialien .....	21
4.3 Experimentelle Bestimmung des Nichtlinearen Effektivitäts-Koeffizienten $\langle d_{eff} \rangle$ ..	23
4.4 Second Harmonic Generation in MOFs .....	25
4.4.1 NLO-MOFs basierend auf chiralen Linkermolekülen.....	26

4.4.2 Oktupolare MOFs mit NLO-Funktionalität .....	28
4.4.3 NLO-aktive MOFs mit Quarz-Topologie.....	29
4.5 Optische Aktivität in MIL-53 und CAU-10.....	31
4.6 Synthese und Charakterisierung neuer Al-MOFs basierend auf Di- und Tetracarbonsäuren .....	34
4.6.1 [Al <sub>2</sub> (OH) <sub>2</sub> (TCPB)] – An Al-MOF based on a tetratopic linker molecule....	34
4.6.2 Polymorphous Al-MOFs Based on V Shaped Linker Molecules: Synthesis, Properties, and in Situ Investigation of Their Crystallization .....	47
4.7 Strategien zur Synthese von MOFs mit speziellen optischen Eigenschaften .....	61
4.7.1 Effect of partial linker fluorination and linker extension on structure and properties of the Al-MOF CAU-10 .....	61
4.7.2 Investigation of the Effect of polar Functional Groups on the Crystal Structures of Indium MOFs.....	72
4.7.3 Emergence of nonlinear optical activity by incorporation of a linker carrying the <i>p</i> -nitroaniline motif in MIL-53 frameworks.....	82
<b>5. Zusammenfassung</b>	<b>97</b>
<b>6. Ausblick</b>	<b>108</b>
<b>7. Literaturverzeichnis</b>	<b>110</b>
<b>III. Anhang</b>	<b>114</b>
<b>Liste der Publikationen und Beiträge</b>	<b>VIII</b>
<b>Curriculum Vitae</b>	<b>X</b>
<b>Eidesstattliche Erklärung</b>	<b>XI</b>





**TEIL I**

**ALLGEMEINER TEIL**



# 1 Einleitung

Das Gebiet der porösen Materialien hat sich sowohl in der akademischen als auch in der industriellen Forschung als bedeutend etabliert. Klassische Anwendungen liegen im Bereich von Gastrennung und -speicherung, Katalyse und Ionenaustausch, da die teils sehr hohen inneren Oberflächen mit den Gastmolekülen unterschiedlich wechselwirken können.<sup>[1]</sup> Eine grobe Einteilung poröser Materialien erfolgt nach der Porengröße, die das Material aufweist. Ein nanoporöses Material besitzt demnach Poren mit einer maximalen Größe von 100 nm. Ein solcher Stoff kann dann noch einmal als mikroporös (0.2 - 2 nm), mesoporös (2 - 50 nm) oder makroporös (50 - 1000 nm) klassifiziert werden.<sup>[2]</sup> Bei porösen Materialien ist in Hinblick auf eine potentielle Anwendung eine enge Porenradienverteilung entscheidend. Zu den wichtigsten Vertretern dieser Stoffklasse gehören die Zeolithe, die sowohl natürlich vorkommen, als auch synthetisch hergestellt werden können. Mit ihrer hohen thermischen Stabilität und der regelmäßigen Porenstruktur eignen sich diese Alumosilicate, die aus  $\text{SiO}_4$ - und  $\text{AlO}_4$ -Tetraedern aufgebaut sind, als Molekularsiebe und Trocknungsmittel im industriellen Bereich. Durch Austausch von  $\text{Si}^{4+}$  durch  $\text{Al}^{3+}$  können negative Gerüstladungen entstehen, die eine Anwendung als Ionentauscher und als katalytisch aktives Material ermöglichen.<sup>[3]</sup>

Die Herausforderungen durch die immer komplexer werdenden Anwendungsfelder machten die Entwicklung einer neuen Klasse von porösen Materialien erforderlich. Diese neue Materialklasse der Metall-Organischen Gerüstverbindungen (MOFs – Metal-Organic Frameworks) zeichnet sich durch den modularen Aufbau aus anorganischer Baueinheit (IBU – Inorganic Building Unit) und verbrückenden organischen Linkermolekülen aus.<sup>[4]</sup> Durch diesen Aufbau ist es theoretisch möglich, Verbindungen mit definierten Porengrößen und individuellen Poreneigenschaften herzustellen, die auf eine gezielte Anwendung optimiert sind. Anorganische Baueinheiten bestehen meist aus Metall-Sauerstoff-Clustern, die isoliert oder als komplexere kondensierte Baueinheiten vorliegen. Linkermoleküle benötigen mindestens zwei koordinative Gruppen um am Aufbau eines Netzwerkes, welches bei MOFs meist dreidimensional ist, beteiligt zu sein. Hierfür werden häufig aromatische Polycarbonsäuren<sup>[5]</sup> verwendet, aber auch Phosphonsäuren,<sup>[6]</sup> Sulfonsäuren<sup>[7]</sup> oder deprotonierbare heterocyclische stickstoffhaltige Aromate<sup>[8]</sup> sind möglich. Durch die

Kombination vieler möglicher IBUs mit der sehr hohen Anzahl an organischen Linkermolekülen entsteht eine theoretische Strukturvielfalt, die nur in der Präparation der Edukte und Produkte ihre Grenzen findet. Ebenso ist es möglich für bestimmte Anwendungsszenarien funktionalisierte Linker zu verwenden, die die Poreneigenschaften unter Erhalt des Netzwerkes verändern. Die Einführung von Sulfonsäuregruppen in das Gerüst ermöglicht es beispielsweise die Protonenleitfähigkeit des entstandenen MOFs zu beeinflussen.<sup>[9]</sup> Auch katalytische Reaktionen an den funktionellen Gruppen sind denkbar. Nicht nur durch den Einsatz funktionalisierter Linker werden die Porengrößen und -eigenschaften variiert, auch durch die Verwendung längerer oder kürzerer Moleküle lassen sich die Kapazitäten und Affinitäten zu bestimmten Gastmolekülen maßgeblich beeinflussen. Dies hat Einfluss auf die Sorptionseigenschaften des MOFs. Der Austausch der IBU mit einer geometrisch identischen eines anderen Metalls kann sowohl die elektronischen Eigenschaften des MOFs beeinflussen, als auch chemische Reaktion an den Metallzentren ermöglichen. Das gezielte Ersetzen von einzelnen anorganischen und organischen Baueinheiten durch geometrisch identische unter Erhalt der Topologie wird als Prinzip der isoretikulären Synthese bezeichnet.<sup>[10-11]</sup>

Die thermischen Eigenschaften von Metall-Organischen Gerüstverbindungen im Vergleich zu den bereits erwähnten Zeolithen unterscheiden sich stark. Aufgrund der in MOFs vorhandenen organischen Komponente nimmt die thermische Stabilität im Vergleich zu Zeolithen stark ab. Es wurde gezeigt, dass MOFs, die auf  $\text{Al}^{3+}$  und Polycarboxylationen basieren, im Vergleich zu anderen Vertretern der Klasse eine hohe thermische Stabilität aufweisen.<sup>[12]</sup> Weiterhin sind die geringe Toxizität und kommerzielle Verfügbarkeit an Aluminiumsalzen positive Faktoren in Hinblick auf eventuelle industrielle Anwendungen von Al-MOFs.<sup>[13]</sup> Probleme hierbei sind die teilweise hohen Preise für organische Linkermoleküle als auch die relativ drastischen Reaktionsbedingungen. Hier werden in der akademischen Forschung noch zumeist solvothermale Reaktionsbedingungen mit gesundheitsgefährdenden organischen Lösungsmitteln verwendet. Aber auch dort wurden in letzter Zeit Fortschritte erzielt, sodass sich einige MOFs in wässrigen Lösungen oder in als unbedenklich zählenden Lösungsmittelgemischen nahe des Siedepunktes synthetisiert werden können.<sup>[14-15]</sup> Durch die umfangreiche wässrige Chemie des Aluminiums sind die Reaktionen dabei aber empfindlich auf kleine Änderungen der Synthesebedingungen. Auf der anderen Seite bietet Aluminium als ein Vertreter der Elemente der 13. Gruppe eine sehr variable Strukturchemie, was das Entstehen von zahlreichen anorganischen Baueinheiten zur Folge hat.<sup>[16-17]</sup> Diese

umfangreiche Chemie wird für Gallium und Indium, auch Elemente der 13. Gruppe, ebenfalls beobachtet, sodass sich geometrisch identische IBUs bilden können. Da Al-MOFs in der Regel als mikrokristalline Pulver entstehen,<sup>[18]</sup> erfolgt die Strukturbestimmung in den wenigsten Fällen mittels Einkristall-Röntgenbeugung,<sup>[19]</sup> sondern aus Röntgenpulverbeugungsdaten<sup>[20]</sup> oder Mikrodiffraktion an einer Synchrotronquelle.<sup>[21]</sup> Hier kann es hilfreich sein, dass isoretikuläre Verbindungen basierend auf  $\text{Ga}^{3+}$  oder  $\text{In}^{3+}$  als Einkristalle anfallen, die durch Einkristall-Röntgenbeugung charakterisiert werden können.

Da sich auch bei einer isoretikulären Synthese die Syntheseparameter stark ändern können und für die Entdeckung neuer MOFs ebenfalls ein großer Parameterraum untersucht werden muss, wird ein Werkzeug benötigt um schnell und effektiv viele Reaktionen durchzuführen. Hierfür haben sich Hochdurchsatzmethoden etabliert.<sup>[18]</sup> Damit ist es möglich Reaktionen parallel in miniaturisierten Reaktoren durchzuführen und durch teilweise Automatisierung einzelner Synthese- und Charakterisierungsschritte schnell und kostengünstig Syntheseparameter zu optimieren oder neue Verbindungen zu entdecken. Da selbst eine kleine Veränderung der Syntheseparameter bei sonst unveränderten Edukten zu neuen Produkten führen kann, ist eine weitgehende Automatisierung der Synthese für die Reproduzierbarkeit der Ergebnisse von Vorteil.<sup>[22]</sup>

Diese Arbeit beschäftigt sich im ersten Teil mit der Synthese neuer und isoretikulärer MOFs basierend auf trivalenten Kationen. Dafür wurde das System  $\text{M}^{3+}$  / Linker / Wasser / DMF ( $\text{M} = \text{Al}^{3+}, \text{Ga}^{3+}, \text{In}^{3+}, \text{Cr}^{3+}$ ) eingehend untersucht und erhaltene Produkte umfassend charakterisiert. Der zweite Teil widmet sich der gezielten Herstellung von MOFs mit potentiellen nichtlinearen optischen Eigenschaften. Dafür wurden verschiedene funktionalisierte Linkermoleküle hergestellt und einige entstandene Verbindungen in Kooperation mit Arbeitsgruppen in Leuven und Namur auf ihre optische Aktivität untersucht. Für die Entdeckung aller Verbindungen und deren Syntheseoptimierungen wurden Hochdurchsatzmethoden verwendet.

## 2 Präparative Methoden

### 2.1 Solvothermalsynthese

Als Solvothermalsynthesen werden allgemein solche Reaktionen bezeichnet, die in einem geschlossenen Gefäß unter autogenem Druck oberhalb des Siedepunktes mindestens eines der verwendeten Lösungsmittel stattfinden.<sup>[23]</sup> Sie haben sich als die wichtigste Synthesemethode in der Darstellung von MOFs herausgestellt, denn sie bieten den Vorteil, dass auch metastabile Produkte erhalten werden können. Auch wenn über dem Siedepunkt mindestens eines Lösungsmittels gearbeitet wird, werden im Vergleich zu keramischen Festkörpermethoden relativ niedrige Reaktionstemperaturen und kürzere Reaktionszeiten verwendet.<sup>[24]</sup> Trotzdem kann bei einer Füllmenge von 10-20% und Temperaturen von 100-170 °C bereits ein Druck von 5-40 bar in den Reaktoren erreicht werden.<sup>[25]</sup> Unter diesen Bedingungen verändern sich die Eigenschaften der eingesetzten Lösungsmittel. Speziell bei Wasser steigt das Ionenprodukt, während Viskosität und Dielektrizitätskonstante abnehmen. Dabei dient das Wasser als Druckübertragungsmedium und als Lösungsmittel, in dem schwer lösliche Stoffe als Komplexe in Lösung gehen.<sup>[25]</sup> Des Weiteren ist es möglich, durch die Zugabe von Mineralisatoren wie Flusssäure oder Alkalimetallhydroxiden selbst Stoffe zu lösen, die unter Normalbedingungen unlöslich sind. Im Allgemeinen muss die Mindestlöslichkeit von 2-5% überschritten werden.<sup>[25]</sup> Weiterhin lassen sich mittels Solvothermalsynthesen Verbindungen mit Elementen in schwierig einstellbaren Oxidationsstufen herstellen. Hierfür ist die Synthese von hochreinem, ferromagnetischen CrO<sub>2</sub> ein Beispiel, welches in Magnetspeicherbändern Verwendung findet.<sup>[24-25]</sup>

Einzug in die moderne Festkörperforschung fand die Solvothermalsynthese nach dem zweiten Weltkrieg. Zu dieser Zeit stieg die Nachfrage nach industriell hergestellten Quarz-Kristallen, welche z.B. als Schwingquarz in elektrischen Uhren Anwendung finden, rapide an. Heute wird die Solvothermalsynthese unter anderem für die Herstellung von Einkristallen, sowie Edelsteinen und zur Aufreinigung von Erzen bei der Metallherstellung verwendet. Bei den meisten genannten Anwendungen wird Wasser als Lösungsmittel verwendet. Wird ausschließlich Wasser als Lösungsmittel gewählt, wird von einer Hydrothermalsynthese gesprochen. Smaragde entstehen beispielsweise unter hydrothermalen Bedingungen bei 500 – 600 °C und 1 kbar Druck.

Besondere Bedeutung hat die Solvothermalsynthese bei der Herstellung von Metall-Organischen Gerüstverbindungen. MOFs werden allgemein als kinetisch stabile Produkte betrachtet, die durch die Verwendung von keramischen Methoden nicht zugänglich wären. Keramische Methoden würden in den meisten Fällen zu einer Zersetzung der organischen Komponente führen und eingesetzte Metallsalze würden zu dichten Metalloxiden reagieren. Bei der Solvothermalsynthese hingegen können die Produkte aus Lösung kristallisieren und so kann die Bildung dichter, thermisch stabiler Verbindungen meist verhindert werden. Außerdem sorgt die Synthese nahe oder über dem Siedepunkt des Lösungsmittels für eine höhere Löslichkeit der organischen Komponente, die unter milderer Bedingungen möglicherweise unlöslich wäre. Zu beachten ist allerdings, dass es auch zu einer Reaktionsbeteiligung des verwendeten Lösungsmittels kommen kann. Bei dem Einsatz von Wasser können Hydroxidionen in die Struktur eingebaut werden. N,N-Dimethylformamid kann zu Ameisensäure und Dimethylamin hydrolysiert werden, welche die Synthese beeinflussen können. Aber auch Reaktionen des Lösungsmittels direkt mit der organischen Komponente sind möglich. So wurde die Methylierung von Aminoterephthalationen bei der Verwendung von Methanol als Lösungsmittel beobachtet. Auch die Reaktivität der Metallsalze während der Solvothermalsynthese muss beachtet werden. Metall-Nitrate und -Perchlorate wirken oxidierend und auch eine Änderung der Oxidationsstufe der Metallionen ist möglich. Daher sind exakte Vorhersagen über die Bildung etwaiger Reaktionsprodukte fast unmöglich.

In dieser Arbeit wurden Reaktoren verwendet, die aus Stahlautoklaven und Einsätzen aus Teflon bestehen (Abbildung 2.1.1) um den extremen Reaktionsbedingungen während der Solvothermalsynthese zu widerstehen.



**Abb. 2.1.1** Stahlautoklav (links) mit Teflonreaktor mit einem Füllvolumen von ca. 30 mL.



## 2.2 Hochdurchsatzmethoden

In Hinblick auf den Einfluss der vielen chemischen und physikalischen Parameter auf die Produktbildung während einer Synthese unter solvothermalen Bedingungen, ist ein effizientes Mittel zur Untersuchung großer Parameterräume nötig. Hier haben sich die Hochdurchsatzmethoden als hilfreiches Werkzeug etabliert. Mit deren Hilfe lassen sich komplexe Parameterräume um ein Vielfaches schneller und effizienter untersuchen, als es bei konventionellen Methoden der Fall ist. Dies ist vor allem bei neuen, noch nicht untersuchten chemischen Systemen vorteilhaft, wenn zuvor keine Aussage über mögliche Reaktionsprodukte getroffen werden kann. Hochdurchsatzmethoden basieren auf den Prinzipien der Miniaturisierung, Parallelisierung und Automatisierung. Das bedeutet, dass unter geringem Edukteinsatz viele Einzelreaktionen gleichzeitig durchgeführt werden. Dabei sollten so viele Arbeitsschritte wie möglich automatisiert erfolgen.<sup>[26]</sup>

Die Abfolge der Arbeitsschritte, die durchlaufen werden, gliedert sich in verschiedene Abschnitte (Abbildung 2.2.1). Nach einer ausführlichen Syntheseplanung erfolgt die Dosierung der Edukte in den Hochdurchsatzreaktor. Dies kann durch Verwendung eines Pipettierroboters teilautomatisiert durchgeführt werden. Anschließend wird der als Multiklav bezeichnete Reaktor verschlossen und einem definiertem Temperatur-Zeit-Programm unterworfen. Die Produkte werden durch eine spezielle Filtriervorrichtung isoliert und im Anschluss mittels Röntgenpulverbeugung vollautomatisiert charakterisiert. Durch Evaluation der erhaltenen Daten werden Informationen für anschließende Experimente gesammelt, auf deren Grundlage neue Synthesen geplant werden.

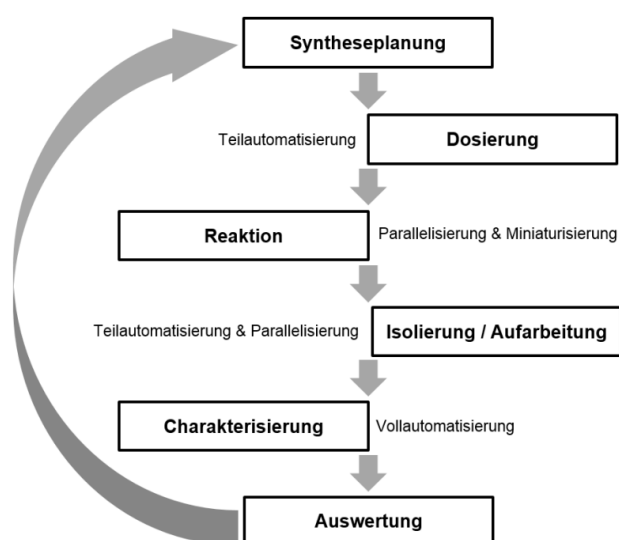


**Abb. 2.2.1** Arbeitsablauf einer Hochdurchsatzuntersuchung.<sup>[27]</sup>

Die Hochdurchsatzmethodik bietet zahlreiche Vorteile gegenüber konventioneller Reaktionsführung. Die Verwendung kleiner Reaktoren führt zur Herabsetzung des Chemikalienverbrauchs, was eine systematische Untersuchung auch mit schwer zugänglichen oder teuren Edukten ermöglicht. Durch die Parallelisierung und Automatisierung ist eine hohe Zeitersparnis und Reproduzierbarkeit der Ergebnisse möglich.<sup>[28]</sup> Allerdings lässt sich nicht jede Reaktion problemlos auf größere Volumina aufskalieren. Auch ist die Gefahr der Redundanz der erhaltenen Daten bei unsorgsamer Syntheseplanung gegeben.

Die in dieser Arbeit durchgeführten solvothermalen Hochdurchsatzreaktionen wurden sowohl in 24er- als auch in 48er-Stahlmultiklaven unter konventionellem Heizen durchgeführt (Abbildung 2.2.2). In den Reaktoren finden 24 bzw. 48 Tefloneinsätze Platz, welche ein maximales Füllvolumen von 2 mL bzw. 200  $\mu$ L besitzen. Diese werden mit Teflonfolie abgedeckt und mit Hilfe von zwei Stahlplatten unter Druck fest verschlossen.

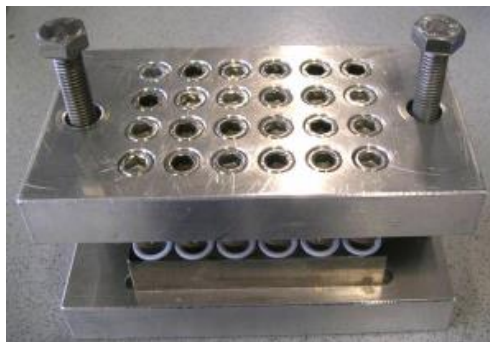


**Abb. 2.2.2** Stahlmultiklav mit 24 Tefloneinsätzen für die konventionelle Ofensynthese.

### 3 Charakterisierungsmethoden

Zur Charakterisierung der erhaltenen Verbindungen wurden unterschiedlichste Methoden eingesetzt. Die verwendeten Geräte zum Durchführungen der Messungen sind in Tabelle 3.1 aufgelistet. Zusätzliche *in-situ* Röntgenbeugungsexperimente wurden an der Beamline F3 des Beschleunigerrings DORIS des Deutschen Elektron Synchrotrons (DESY) in Hamburg durchgeführt. Diese dienen der Suche nach Intermediaten und der Untersuchung von Phasenumwandlungsprozessen. Innerhalb einer Kooperation mit der KU Leuven (Belgien) wurde die SHG Mikroskopie eingesetzt und die Frequenzverdopplung von monochromatischem Licht an nicht-zentrosymmetrischen Strukturen gemessen. Die mit Abstand wichtigste Methode zur Charakterisierung und Strukturaufklärung der hergestellten Verbindungen ist die Röntgenpulverdiffraktometrie. Daher soll im Folgenden näher auf das Grundprinzip dieser Methode und die notwendigen Schritte zur Bestimmung einer Kristallstruktur eingegangen werden. Die Verarbeitung der bei der Charakterisierung erhobenen Daten wurde mit Hilfe verschiedener Computerprogramme durchgeführt. Dafür wurden häufig mehrere Programme kombiniert um optimale Ergebnisse zu erhalten. Die verwendeten Programme sind in Tabelle 3.2 aufgeführt.

**Tab. 3.1** Übersicht über die in dieser Arbeit am häufigsten verwendeten Charakterisierungsmethoden.

<b>Methode</b>	<b>Gerät</b>	<b>Anmerkung</b>
Pulverdiffraktometrie	STOE StadiP Kombi	CuK $\alpha_1$ -Strahlung und MoK $\alpha$ -Strahlung, Transmissionsgeometrie, Image Plate und MYTHEN Detektor, xy-Probenstisch
	STOE StadiP	CuK $\alpha_1$ -Strahlung, Transmissionsgeometrie, MYTHEN Detektor
Einkristalldiffraktometrie	Bruker D8 Venture	MoK $\alpha$ -Strahlung, PHOTON 100 CMOS Detektor
IR-Spektroskopie	ALPHA-FT-IR A220/D-01	ATR-Einheit
Thermogravimetrische Analyse / Differentielle Thermoanalyse	NETZSCH STA 409 CD	Messung in Al <sub>2</sub> O <sub>3</sub> -Tiegeln in Luft, Heizrate von 4 K/min
CHNS-Elementaranalyse	Eurovektor EuroEA	He-Trägergas, Verbrennung in O <sub>2</sub> bei 1010 °C
Volumetrische Gassorption	BEL JAPAN INC. Belsorp <sub>max</sub>	Messungen von N <sub>2</sub> , H <sub>2</sub> , CO <sub>2</sub> und H <sub>2</sub> O bis 1 bar
NMR-Spektroskopie	Bruker Avance 200	Spektroskopie in Lösung
Rasterelektronenmikroskopie	Philips ESEM-XL 30	EDX-Detektor

**Tab. 3.2** Übersicht über die in dieser Arbeit verwendeten Computerprogramme.

Methode	Programm	Anmerkung
Pulverdiffraktometrie	STOE WinXPOW <sup>[29]</sup>	Messung und Auswertung
Indizierung	TOPAS Academic <sup>[30]</sup>	modifizierter DICVOL-Algorithmus
	EXPO 2009 <sup>[31]</sup>	
Zellparameterverfeinerung	TOPAS Academic <sup>[30]</sup>	Pawley-Methode
Visualisierung von Strukturen	Diamond 3.1 <sup>[32]</sup>	
Kraftfeldrechnungen	Materials Studio 4.1 <sup>[33]</sup>	
Strukturlösung	F.O.X. <sup>[34]</sup>	Realraummethode
	SHELXS <sup>[35]</sup>	direkte Methoden (Einkristalldaten)
	X-RED und X-SHAPE <sup>[36]</sup>	Absorptionskorrektur
Strukturverfeinerung	TOPAS Academic <sup>[30]</sup>	Rietveld-Methode (Pulverdaten)
	SHELXL <sup>[35]</sup>	direkte Methoden (Einkristalldaten)
Informationen aus Struktur	Platon <sup>[37-39]</sup>	Bestimmung theo. Porenvolumina
Topologiebestimmung	TOPOSPro <sup>[40]</sup>	
	Systre <sup>[41]</sup> (Gavrog) <sup>[42]</sup>	

### 3.1 Röntgenbeugung

Kristalle sind 3-D-translationsperiodische, homogene Festkörper. Sie bestehen also aus sich wiederholenden Einheiten, die als Elementarzellen bezeichnet werden. Die Elementarzellen definieren sich über die Zellparameter, d.h. über die Zelllängen  $a$ ,  $b$ ,  $c$  und -winkel  $\alpha$ ,  $\beta$ ,  $\gamma$ . In den Elementarzellen befinden sich Atome. Weiterhin können Netzebenen aufgespannt werden, deren Orientierungen durch die Miller Indizes ( $hkl$ ) angegeben werden. Parallele Netzebenen werden als Schar bezeichnet. Einzelne Ebenen in dieser Schar haben den Abstand  $d$ , der sich im Å-Bereich befindet. Für Beugungsexperimente an Kristallen muss also auf Röntgenstrahlung zurückgegriffen werden. Diese wird an der Elektronenhülle der Atome

gebeugt. Der Strahlengang zweier Röntgenstrahlen in einem Kristall mit zwei parallelen Netzebenen ist in Abbildung 3.1 dargestellt.

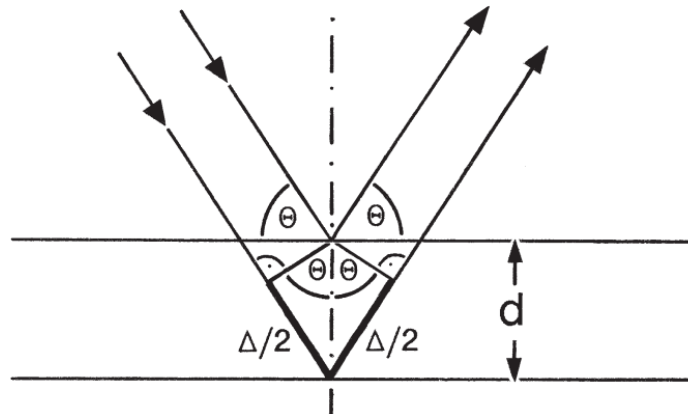


**Abb. 3.1** Beugung an zwei Netzebenen zur Erklärung der Bragg-Gleichung.<sup>[43]</sup>

Aus Abbildung 3.1 ist zu erkennen, dass die Röntgenstrahlen bei ihrem Weg durch den Kristall einen Gangunterschied  $\Delta$  besitzen. Durch den Gangunterschied kommt es zu Interferenzerscheinungen. Nur bei konstruktiver Interferenz kann im Beugungsbild ein Reflex erkannt werden. Das bedeutet, dass der Gangunterschied ein ganzzahliges Vielfaches  $n$  der Wellenlänge  $\lambda$  sein muss. Aus trigonometrischen Beziehungen ergibt sich für  $\Delta$  die Länge  $2d \cdot \sin\theta$ . Daraus lässt sich die Bragg-Gleichung (Gleichung 3.1.1) ableiten, die den Zusammenhang zwischen der Wellenlänge  $\lambda$ , dem Beugungswinkel  $\theta$  und dem Netzebenenabstand  $d$  herstellt.

$$n\lambda = 2d \sin\theta \quad (3.1.1)$$

Die Reflexe im Beugungsbild weisen unterschiedliche Intensitäten auf. Die Intensitäten korrelieren mit dem Betragsquadrat des Strukturfaktors (Gleichung 3.1.2).

$$I_{hkl} \propto |F_{hkl}|^2 \quad (3.1.2)$$

Der Strukturfaktor  $F_{hkl}$  definiert sich über die Strukturfaktorgleichung, die die Intensität der gemessenen Reflexe einer Netzebene ( $hkl$ ) mit der Anordnung der Atome ( $x, y, z$ ) in der Elementarzelle verknüpft (Gleichung 3.1.3).<sup>[43]</sup>

$$F_{hkl} = \sum_n f_n \{ \cos 2\pi(hx_n + ky_n + lz_n) + i \sin 2\pi(hx_n + ky_n + lz_n) \} \quad (3.1.3)$$

Der Parameter  $f_n$  ist hierbei der Atomformfaktor, der die Abhängigkeit der Streukraft von der Atomsorte und vom Beugungswinkel  $\theta$  beschreibt. Aus Beugungsexperimenten sind nur die

absoluten Werte der Strukturamplituden (Intensitäten) der einzelnen Reflexe zugänglich. Da sich eine elektromagnetische Welle aber durch die Wellenlänge, die Ausbreitungsrichtung, die Amplitude und durch die Phase definiert, gehen die Informationen über die Phase bei der Röntgenbeugung an Kristallen verloren. Dies wird als Phasenproblem bezeichnet, welches für die Bestimmung einer Struktur gelöst werden muss. Dafür stehen mathematische Methoden wie die Patterson-Methode<sup>[44]</sup> oder direkte Methoden<sup>[45]</sup> zur Verfügung.<sup>[46]</sup>

## 3.2 Grundlagen der Röntgenpulverbeugung

Bei der Röntgenbeugung an einzelnen Einkristallen werden diskrete Maxima in den Beugungsbildern beobachtet. Pulver bestehen jedoch aus einer Vielzahl mikrokristalliner Kristallite, die unterschiedlich im Raum orientiert sind. Jeder Kristall verursacht eigene Reflexe, sodass im Beugungsbild keine diskreten Maxima mehr beobachtet werden können, sondern diese zu Ringen verschmelzen. Diese Ringe werden als Debye-Scherrer-Ringe bezeichnet. Dabei kann es zur Überlagerung einzelner Ringe kommen, wodurch der zu erhaltene Informationsgehalt stark verringert werden kann. Greifen bei der Beugung noch Textureffekte der vermessenen Probe, d.h. durch Vorzugsorientierung der Kristallite können einzelne Reflexe nicht beobachtet werden, kann sich der Informationsgehalt noch weiter reduzieren. Ein Schnitt durch die Debye-Scherrer-Ringe ist dabei das eigentliche Pulverdiffraktogramm, welches erhalten wird (Abbildung 3.2).

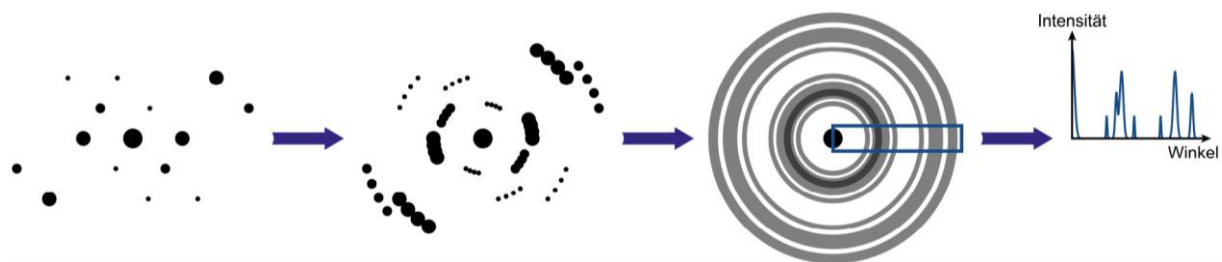


**Abb. 3.1** Überlagerung der diskreten Maxima bei Einkristallbeugung zu Debye-Scherrer-Ringen bei der Röntgenpulverbeugung. Ein Röntgenpulverdiffraktogramm ist dabei ein Schnitt durch diese Ringe.<sup>[47]</sup>

Hier werden Informationsgehalte aus drei Raumdimensionen auf eine Dimension reduziert. Trotzdem ist es möglich, den verloren gegangenen Informationsgehalt wiederherzustellen und Strukturen aus Röntgenpulverdaten zu ermitteln. Entscheidend hierfür ist die Qualität des gemessenen Pulverdiffraktograms, denn aus der Lage der Reflexe, deren Anzahl, Intensität und Halbwertsbreite können wichtige Informationen über den Netzebenenabstand, Symmetrie, die Anordnung der Atome und die Kristallitgröße gewonnen

werden. Nachfolgend sollen die einzelnen Schritte einer Strukturlösung aus Pulverdaten erläutert werden.

#### 3.2.1 Indizierung und Zellverfeinerung

Der erste Schritt zur Lösung einer unbekanntem Struktur ist die Indizierung des gemessenen Pulverdiffraktogramms. Dies bedeutet, dass den  $d$ -Werten des Diffraktogramms die korrespondierenden  $hkl$ -Werte der Netzebenen zugeordnet werden. Hierfür wird die quadratische Bragg-Gleichung verwendet, welche von der Art der Elementarzelle abhängig ist. Für eine kubische Elementarzelle mit  $a = b = c$  und  $\alpha = \beta = \gamma = 90^\circ$  ergibt sich die Gleichung zu:

$$\frac{1}{d^2} = \frac{h^2 + k^2 + l^2}{a^2} \quad (3.2.1.1)$$

Der Parameter  $\frac{1}{a^2}$  muss dabei ganzzahlige Vielfache von  $\frac{1}{d^2}$  annehmen, da die Miller-Indizes  $h$ ,  $k$  und  $l$  auch nur ganzzahlige Werte annehmen dürfen. Idealerweise lässt sich  $a$  also aus nur zwei Reflexen bestimmen. Werden keine durch Gleichung 3.2.1 nicht erlaubten zusätzlichen Reflexe gefunden, ist das Pulverdiffraktogramm kubisch indiziert. Durch Zentrierung und translatorische Symmetrieelemente in der Elementarzelle kann es zu zusätzlichen systematischen Auslöschungen kommen. Dies bedeutet, dass im Kristallsystem erlaubte Reflexe nicht beobachtet werden, da sie ausgelöscht sind.

Aufgrund der Komplexität der quadratischen Bragg-Gleichung bei symmetrieärmeren Kristallsystemen und die zu beachtenden systematischen Auslöschungen bei höheren Symmetrien werden Computerprogramme zur Indizierung von Pulverdiffraktogrammen verwendet. Diese ordnen durch mathematische Algorithmen den indizierten Reflexen eine oder mehrere mögliche Zellen zu. Außerdem werden durch die Programme mögliche Raumgruppen aufgrund der vorliegenden Auslöschungsbedingungen und der Zellmetrik vorgeschlagen.

Nachdem eine mögliche Elementarzelle gefunden wurde, ist es nötig deren Parameter für die spätere Strukturlösung zu verfeinern. Außerdem werden bei diesem Schritt die integralen Intensitäten erhalten, die Rückschlüsse auf die Lage der Atome in der Elementarzelle liefern. Ein genaues Anpassen der Reflexform ist ebenfalls unerlässlich für das Erhalten der Intensität und der exakten Position der Reflexe. Auf Basis der kleinsten Fehlerquadrate werden die Zellparameter iterativ verändert, bis das Quadrat der Differenz von errechneten zum gemessenen Diffraktogramm ein Minimum erreicht. Hierfür wird eine



peak-shape-Funktion verwendet, die die instrumentelle Verbreiterung (Lage und Geometrie der Quelle), die Streuung der Wellenlänge (quellenabhängige Verbreiterungsfunktion der Wellenlänge), den Probenfehler (Linienverbreiterung durch dynamische Streuung, Kristallitgröße, stress und strain) und die Untergrundfunktion simuliert. Die Pawley- und LeBail-Methode verfolgen diesen Ansatz.

Die Qualität der Anpassung kann sowohl optisch über den Vergleich des gemessenen und des berechneten Diffraktogramms als auch über verschiedene Gütekriterien beurteilt werden. Gebräuchliche Gütefaktoren sind der  $R_{wp}$ -Wert und der GoF (Goodness of Fit):<sup>[43]</sup>

$$R_{wp} = \sqrt{\left[ \frac{\sum \omega_i (I_{i,obs} - I_{i,clac})^2}{\sum \omega_i (I_{i,obs})^2} \right]} \quad \text{GoF} = \sqrt{\frac{\sum \omega_i (I_{i,obs} - I_{i,clac})^2}{n-p}} \quad (3.2.1.2 \text{ und } 3.2.1.3)$$

Dabei ist  $\omega_i$  ein Gewichtungsfaktor, der die Messgenauigkeit der Intensität angibt ( $\omega_i = \text{Zählrate} \cdot \text{Messzeit}$ ),  $I_{i,obs}$  und  $I_{i,clac}$  die gemessenen und berechneten Intensitäten am Punkt  $i$ ,  $n$  die Anzahl der gemessenen Punkte und  $p$  die Anzahl der verfeinerten Parameter. Im Idealfall strebt  $R_{wp}$  gegen Null und der GoF gegen Eins.<sup>[46]</sup>

### 3.2.2 Strukturlösung und Strukturverfeinerung

Sind durch Indizierung des Pulverdiffraktogramms die Zellparameter und daraus mögliche Raumgruppen basierend auf den Auslöschungsbedingungen erhalten worden, ist der nächste Schritt das Erstellen eines Strukturmodells. Über Gleichung 3.2.2.1 könnte theoretisch jedem Punkt im Kristall die Elektronendichte zugewiesen werden. Diese wird dabei aus der Fouriertransformation des Beugungsbildes erhalten und steht mit den Strukturfaktoren im direkten Zusammenhang:

$$\rho_{xyz} = \frac{1}{V} \sum_{hkl} F_{hkl} \cdot e^{-i2\pi(hx+kx+lz)} \quad (3.2.2.1)$$

Da aber nur Reflexintensitäten bestimmt werden können und durch das Phasenproblem eine direkte Zuweisung der Intensitäten zu den Strukturfaktoren nicht möglich ist, muss ein Umweg gegangen werden. Dazu werden z.B. direkte Methoden<sup>[45]</sup> oder Realraummethoden verwendet. Direkte Methoden basieren darauf, dass Phasen bestimmter Reflexgruppen, den Reflextripletts, mit einer gewissen Wahrscheinlichkeit voneinander ableitbar sind. Auch das Problem der Reflexüberlappung bei der Röntgenpulverbeugung durch Überlagerung von Reflexen mit ähnlichen  $d$ -Werten erschwert die Zuordnung der korrespondierenden Netzebenen.

Realraummethoden umgehen das Phasenproblem indem sie aus den erhaltenen kristallographischen Daten und der möglichst exakten Summenformel eine zufällige Kristallstruktur berechnen. Da das gemessene Pulverdiffraktogramm als Zielvorgabe dient, werden keine Intensitäten der einzelnen Reflexe benötigt. Die Struktur wird schrittweise global optimiert und die Lage der Atome zufällig geändert. Bei jedem Schritt wird ein theoretisches Diffraktogramm berechnet, welches mit dem experimentellen verglichen wird. Dies erfolgt so lange bis die Abweichung zwischen den Diffraktogrammen minimal ist. Da die Methode hohen Rechenaufwand erfordert, bietet es sich an Strukturfragmente für die Optimierung vorzugeben. Dies können bei MOFs Linkermoleküle sowie anorganische Baueinheiten sein, die als rigid bodies behandelt werden.<sup>[48]</sup>

Mit fortschreitender Technisierung lassen sich Strukturmodelle mit Hilfe von Kraftfeldmethoden berechnen. Hierzu ist der modulare Aufbau von MOFs von Vorteil. Als Basis dienen isoretikuläre Verbindungen, die durch Austausch einzelner Komponenten wie Linkermoleküle oder anorganische Baueinheiten modifiziert werden. Weiterhin werden die aus der Indizierung erhaltenen kristallographischen Daten zum Anpassen der Elementarzelle benutzt. Anschließend wird die bearbeitete Struktur geometrisch optimiert. Häufig werden DFT- (Dichte-Funktional-Theorie) oder UFF- (Universal Force Field – implementiert in Programmen wie Materials Studio<sup>[33]</sup>) Methoden verwendet um eine energieminierte Struktur zu erhalten.

Das durch die verschiedenen erwähnten Methoden erhaltene Strukturmodell muss an die experimentell gewonnenen Messdaten angepasst werden. Erst wenn das theoretische Modell mit ausreichender Übereinstimmung angepasst wurde, kann die Strukturbestimmung als abgeschlossen angesehen werden. Die hierfür am häufigsten verwendete Methode ist die nach Hugo Rietveld. Auch hier werden die Gitterparameter und das Reflexprofil verfeinert, doch zusätzlich erfolgt eine Verfeinerung der Atompositionen in der Elementarzelle, der Besetzungsfaktoren und der Auslenkungsparameter. Damit ist die Methode umfangreicher als die nach Pawley oder LeBail. Neben den bekannten Gütefaktoren,  $R_{wp}$  und GoF, wird bei der Rietveld-Verfeinerung noch der  $R_{Bragg}$ -Wert eingeführt (Gleichung 3.2.2.2). Dieser ist ein Maß für die Übereinstimmung der an jedem Messpunkt ermittelten experimentellen und theoretisch berechneten Intensitäten.

$$R_{Bragg} = \frac{\sum |I_{obs} - I_{calc}|}{\sum I_{obs}} \quad (3.2.2.2)$$



# **TEIL II**

## **KUMULATIVER HAUPTTEIL**



## **4 Synthese und Charakterisierung neuer und funktionalisierter MOFs basierend auf Elementen der 13. Gruppe und deren spezielle optische Eigenschaften**

In dieser Arbeit geht es zum einen um die Synthese und Charakterisierung neuer Al-MOFs basierend auf Di- und Tetracarbonsäuren, wobei sowohl isoretikuläre Verbindungen zu bekannten Gerüststrukturen als auch neue poröse Al-MOFs hergestellt werden sollten. Zum anderen sollten durch funktionalisierte Linkermoleküle und durch sinnvolle Wahl des verwendeten Metallsalzes bzw. MOF-Gerüsts gezielt Verbindungen synthetisiert werden, die nichtlineare optische Eigenschaften (NLO) aufweisen. Das Gebiet der nichtlinearen Optik ist schon länger bekannt und wurde an nichtporösen keramischen Materialien auch eingehend untersucht. Obwohl auch viele potentielle Vertreter im Bereich der Metall-Organischen Gerüstverbindungen zu finden sind, blieb diese Materialklasse bei den Untersuchungen bisher oft außen vor. Zweck dieser Materialien ist es, die Frequenz des eingestrahnten Lichtes zu verdoppeln. Hier werden jedoch keine Ausbeuten von 100% erreicht, da ein Großteil des eingestrahnten Lichtes unverändert wieder aus dem Material austritt. Ziel ist es, Materialien zu entwickeln, die die Ausbeute an frequenzverdoppelten Lichtes erhöhen.

Im Folgenden soll daher zunächst auf die theoretischen Grundlagen der optischen Frequenzverdopplung eingegangen, die Messmethode erläutert und mögliche Anwendungen solcher Materialien aufgezeigt werden. In einem zweiten Abschnitt sollen Metall-Organische Gerüstverbindungen vorgestellt werden, an denen bereits dahingehend Untersuchungen durchgeführt wurden.

#### 4.1 Einführung in die nichtlineare Optik (NLO) und optische Frequenzverdopplung (SHG – Second Harmonic Generation)

Wechselwirkt Materie mit einer elektromagnetischen Welle, regt das elektrische Feld der Strahlung (Fundamentale) die elektrischen Ladungen der Materie (Atomkerne und Elektronenhülle) zu einer periodischen Verschiebung an. Die Verschiebung der Elektronenhüllen der Atome um die Ruhelage führt zu einem oszillierenden Dipolmoment und somit zur Polarisierung. Jeder oszillierende Dipol emittiert eine Welle, die die gleiche Frequenz und Geschwindigkeit wie die Fundamentale besitzt. Bei isotropen Materialien besitzt die emittierte Welle eine Sinusform. Bei anisotropen Materialien ist diese Sinusform nur bei geringer Anregung des Dipolmomentes gegeben. Hier hängt die Polarisierbarkeit  $P$  linear von der elektrischen Feldstärke  $E$  ab, was in einer linearen Kennlinie resultiert (Gleichung 4.1.1).<sup>[49]</sup>

$$P(t) = \varepsilon_0 \chi^{(1)} E(t) \quad (4.1.1)$$

Der Proportionalitätsfaktor  $\chi^{(1)}$  ist hier die Suszeptibilität 1. Ordnung und  $\varepsilon_0$  die Permittivität des freien Raumes ausgedrückt durch die Dielektrizitätskonstante des Vakuums. Bei hohen Anregungen von anisotropen Materialien durch starke elektrischer Felder besitzt die durch den oszillierenden Dipol erzeugte Polarisationswelle keine Sinusform, da die Auslenkung der Elektronen nicht mehr zur Feldstärke der Fundamentalen proportional ist (Abb. 4.1.1). In diesem nichtlinearen Fall verallgemeinert sich Gleichung 4.1.1 zu einer Potenzreihe der elektrischen Feldstärke (Gleichung 4.1.2):<sup>[49]</sup>

$$\begin{aligned} P(t) &= \varepsilon_0 [\chi^{(1)} E(t) + \chi^{(2)} E^2(t) + \chi^{(3)} E^3(t) + \dots] \\ &= P^{(1)}(t) + P^{(2)}(t) + P^{(3)}(t) + \dots \end{aligned} \quad (4.1.2)$$

Diese Potenzreihe beinhaltet die Suszeptibilitäten der 2. und 3. Ordnung  $\chi^{(2)}$  und  $\chi^{(3)}$ . Der zweite Term repräsentiert die Nichtlinearität zweiter Ordnung, der dritte Term die Nichtlinearität dritter Ordnung, usw.. Die Koeffizienten der Suszeptibilität nehmen mit zunehmender Ordnung stark ab. Typisch sind Werte von:<sup>[49]</sup>  $\chi^{(1)} \approx 1$ ,  $\chi^{(2)} \approx 10^{-12}$  m/V und  $\chi^{(3)} \approx 10^{-21}$  m<sup>2</sup>/V<sup>2</sup>. Besteht die Feldstärke  $E$  aus einer reinen Sinuswelle  $E = E_0 \sin \omega t$ , und werden nur die linearen und quadratischen Glieder von Gleichung 4.1.2 betrachtet, ergibt sich die Polarisation zu:<sup>[50]</sup>

$$P = \varepsilon_0 (\chi E_0 \cdot \sin \omega t + \chi' \cdot E_0^2 \cdot \sin^2 \omega t) \quad (4.1.3)$$

oder umgestellt zu:

$$P = \frac{\varepsilon_0}{2} \chi' E_0^2 + \varepsilon_0 \chi E_0 \cdot \sin \omega t - \frac{\varepsilon_0}{2} \chi' E_0^2 \cos 2\omega t \quad (4.1.4)$$

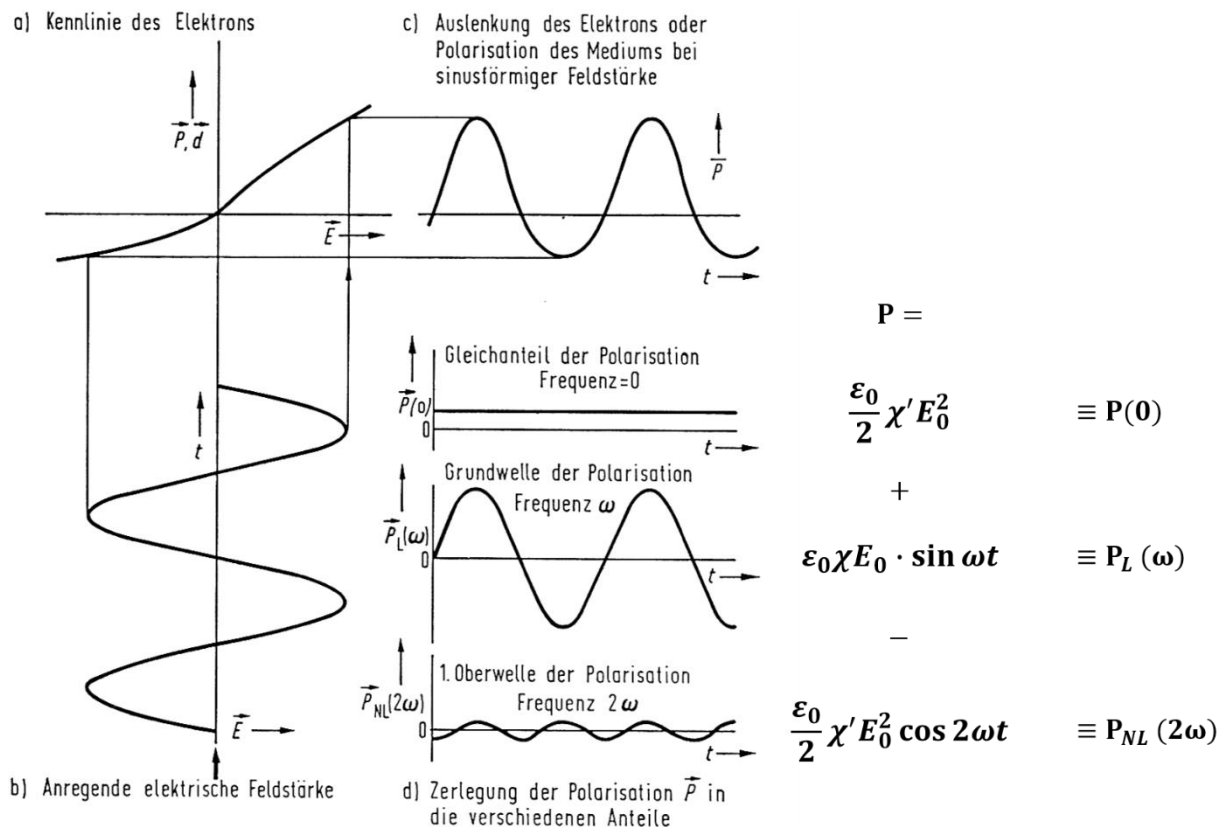


**Abb. 4.1.1** Bei starker Auslenkung des Dipols zur Ruhelage in anisotropen Materialien ist diese nicht mehr proportional zur Feldstärke, was sich in einer nicht-linearen Kennlinie äußert (a). Durch die Anregung durch eine sinusförmige elektrische Feldstärke  $E$  (b) entsteht eine Polarisation  $P$ , die nicht mehr sinusförmig ist (c). Die nicht-sinusförmige Polarisation  $P$  besteht aus einem Gleichanteil  $P(0)$  sowie sinusförmigen Polarisationen der Frequenzen  $\omega$  und  $2\omega$  (nach Ref.<sup>[50]</sup>).

Die Polarisation enthält außer der Grundwelle  $P_L(\omega)$  einen Gleichanteil  $P(0)$  und einen Anteil mit der doppelten Frequenz  $P_{NL}(2\omega)$  (vgl. Abb. 4.1.1). Bei Kristallen mit Inversionssymmetrie ist auch die Kennlinie symmetrisch. So entstehen Polarisationen, in denen die Anteile der geraden Harmonischen destruktiv interferieren.<sup>[50]</sup>

In einem Medium werden beim Durchlaufen der Fundamentalen an verschiedenen Stellen SHG-Wellen erzeugt. Da in Medien Dispersion herrscht, hat jede Welle eine frequenzabhängige Phasengeschwindigkeit. Diese ist abhängig vom Brechungsindex und der Kristalldomäne. Dadurch entsteht zwischen unterschiedlichen SHG-Wellen eine Phasenverschiebung, die in der Regel zur destruktiven Interferenz der erzeugten Harmonischen führen kann (Abbildung 4.1.2).



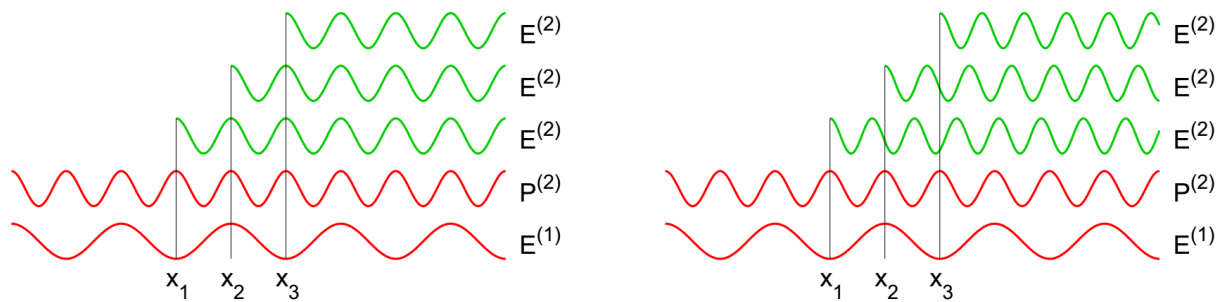


**Abb. 4.1.2** Fundamentale  $E^{(1)}$ , induzierte quadratische Polarisation  $P^{(2)}$  und zweite Harmonische  $E^{(2)}$  erzeugt an den Punkten  $x_1$ ,  $x_2$  und  $x_3$  in einem NLO-Material für zwei verschiedene Fälle. Links: zweite Harmonische mit der gleichen Geschwindigkeit wie die Fundamentale. Rechts: Normalfall mit verschiedenen Geschwindigkeiten, die zu einem sukzessiven Phasenversatz (Missmatch) der zweiten Harmonischen  $E^{(2)}$  führt.<sup>[51]</sup>

Nur wenn die Bedingung der Phasenanpassung erfüllt ist, kann eine Harmonische effektiv erzeugt werden. Das ist dann der Fall, wenn der Brechungsindex für Fundamentale und SHG-Welle gleich ist. Dies ist eine Bedingung, die nur in anisotropen Materialien bei einer bestimmten Einstrahlung des Lichtes relativ zur optischen Achse erfüllt sein kann. Hierzu wird der Einstrahlwinkel so gewählt, dass die Feldstärke  $E$  senkrecht zur optischen Achse steht. So wird neben der linearen Polarisation  $P_L(\omega)$  eine nicht-lineare Polarisation  $P_{NL}(2\omega)$  erzeugt, die parallel zur optischen Achse gerichtet ist. Diese Polarisation erzeugt einen Lichtstrahl, der ebenfalls parallel zur optischen Achse polarisiert ist und die Frequenz  $2\omega$  aufweist.<sup>[50]</sup>

Um Materialien hinsichtlich ihrer SHG-Aktivität vergleichen zu können, werden die nicht-linearen Effektivitätskoeffizienten  $\langle d_{eff} \rangle$  bestimmt. Diese Koeffizienten sind abhängig von der Struktur und Symmetrie der verwendeten Materialien ( $\chi^{(2)}$ ) und unterscheiden sich je nach Position des Kristalls relativ zur Fundamentale. Sie lassen sich theoretisch berechnen, jedoch weisen die verwendeten Kristalle Defekte auf, weshalb die Effektivität eines jeden Referenzkristalls im gewählten Setup bestimmt werden muss. Für die exakte Bestimmung von  $\langle d_{eff} \rangle$  werden die Effekte ausgenutzt, die zuvor in diesem Kapitel beschrieben wurden. Die vermessenen Kristalle der SHG-aktiven Materialien werden dann als Referenz zur Bestimmung der SHG-Aktivität von unbekanntem Stoffen verwendet, deren Effektivwert in Relation zur verwendeten Referenz angegeben wird.

## 4.2 Voraussetzungen und Anwendung nichtlinear optischer und SHG-aktiver Materialien

NLO- oder SHG-aktive Materialien müssen bestimmte Voraussetzungen erfüllen, um eine spätere Anwendung zu ermöglichen. Stoffe müssen chemisch und thermisch stabil sein, d.h. dass auch keine Phasenübergänge stattfinden dürfen, die die nicht-zentrosymmetrische Struktur aufheben. Weiterhin muss beachtet werden, dass das Material weder das einfallende, noch das emittierte Licht zu stark absorbieren darf. Die Absorption von Licht führt zur Erhitzung des Materials, was dieses zerstören könnte. Die Eignung von Materialien kann also auch von der Wellenlänge des verwendeten Lasers abhängig sein. Die wohl wichtigste Eigenschaft ist aber die Effektivität der Umwandlung von eingestrahlttem zu frequenzverdoppeltem Licht, angegeben als Nichtlinearer Effektivitäts-Koeffizient  $\langle d_{eff} \rangle$ . Klassische Materialien, die in der nichtlinearen Optik Anwendung finden, sind in Abbildung 4.2.1 aufgeführt, deren kristallographische Parameter sind in Tabelle 4.2.1 aufgelistet.

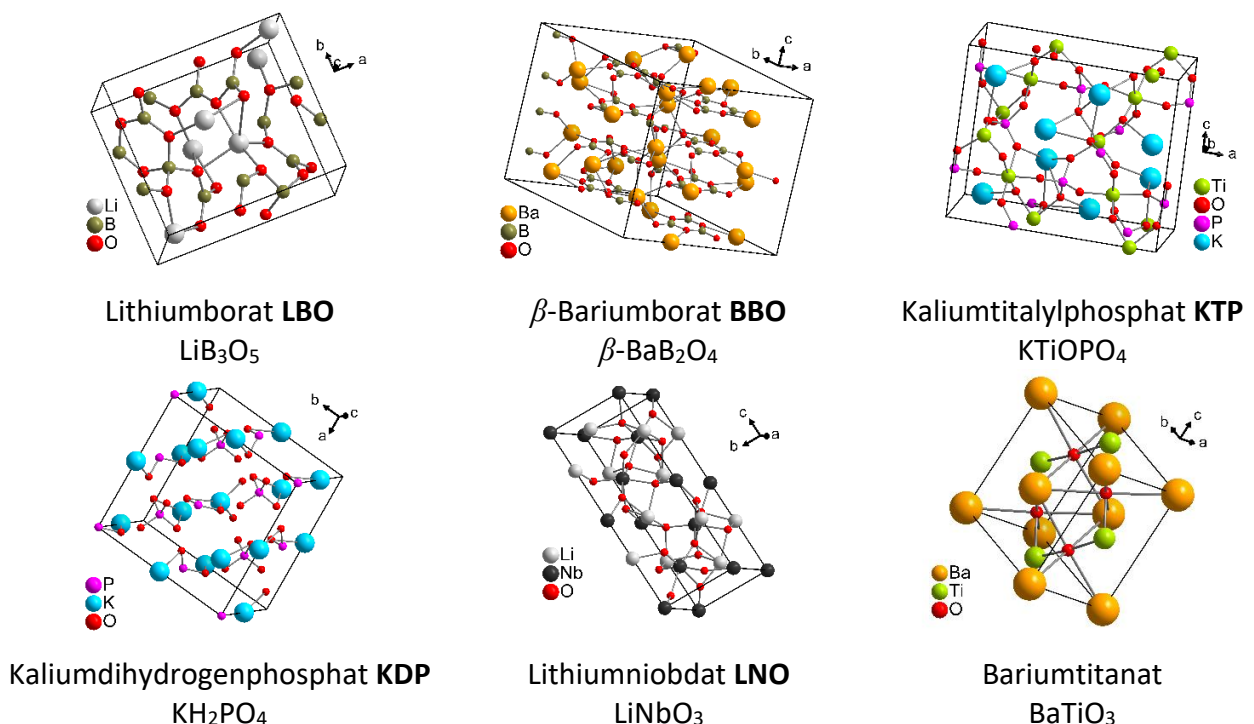


Abb. 4.2.1 Darstellung der klassischen NLO-Materialien.<sup>[52-57]</sup>

**Tab. 4.2.1** Kristallographische Parameter der klassischen NLO-Materialien.

	<b>LiB<sub>3</sub>O<sub>5</sub></b> <sup>[52]</sup>	<b><math>\beta</math>-BaB<sub>2</sub>O<sub>4</sub></b> <sup>[53]</sup>	<b>KTiOPO<sub>4</sub></b> <sup>[54]</sup>	<b>KH<sub>2</sub>PO<sub>4</sub></b> <sup>[55]</sup>	<b>LiNbO<sub>3</sub></b> <sup>[56]</sup>	<b>BaTiO<sub>3</sub></b> <sup>[57]</sup>
Raumgruppe	<i>Pna</i> 2 <sub>1</sub>	<i>R</i> 3	<i>Pna</i> 2 <sub>1</sub>	<i>Fdd</i> 2	<i>R</i> 3 <i>c</i>	<i>Amm</i> 2
<i>a</i> / Å	8.4440	12.532	12.7982(9)	10.4670	5.148(3)	4.0094
<i>b</i> / Å	7.3780	12.532	6.3937(7)	10.5330	5.148(3)	5.6214
<i>c</i> / Å	5.1460	12.717	10.5853(9)	6.926	13.863(3)	5.6386
$\alpha$ / °	90	90	90	90	90	90
$\beta$ / °	90	90	90	90	90	90
$\gamma$ / °	90	120	90	90	120	90

Die klassischen Materialien haben aber auch Nachteile wie langsame elektrooptische Antwortzeiten, geringe optische Qualität und aufwendige Herstellung. Organische oder teilweise organische Verbindungen hingegen können eine höhere SHG-Aktivität durch ein ausgedehntes  $\pi$ -Elektronensystem aufweisen.<sup>[58]</sup> Außerdem sprechen geringe Herstellungskosten, kurze Antwortzeiten des optischen Systems und eine hohe optische Belastbarkeit, bevor Schaden am Material entsteht, für sie.

Für gewöhnlich werden SHG-Materialien in der Laser-Industrie eingesetzt. So kann beispielsweise grünes Licht mit einer Wellenlänge von 532 nm aus einer infraroten Nd:YAG Quelle mit 1064 nm generiert werden. Dafür werden KDP-Kristalle vor die Lichtquelle platziert und ebenfalls ein Infrarotfilter montiert, der das intensive nicht frequenzverdoppelte Licht herausfiltert. Grüne Laserpointer, wie sie aus Hörsälen bekannt sind, funktionieren auf die gleiche Weise, nur dass auf den teuren Infrarotfilter verzichtet wird.<sup>[58]</sup> Weiterhin werden NLO-Materialien in der Optoelektronik eingesetzt. Geräte wie Optical Parametric Amplifiers (OPA) oder Optical Parametric Oscillators (OPO) nutzen den Effekt der Frequenzverdopplung und werden in der Laserspektroskopie eingesetzt. Zukünftig werden NLO-Materialien in optischen Computern Anwendung finden und fortschrittliche optische Kommunikationssysteme und Informationsübertragung ermöglichen. Nicht zuletzt werden diese Materialien heute schon in der hochauflösenden optischen Mikroskopie verwendet.<sup>[58]</sup>

### 4.3 Experimentelle Bestimmung des Nichtlinearen Effektivitäts-Koeffizienten $\langle d_{eff} \rangle$ .

Die experimentelle Bestimmung des Nichtlinearen Effektivitäts-Koeffizienten  $\langle d_{eff} \rangle$  erfolgte in dieser Arbeit in abgewandelter Form nach einem bereits veröffentlichten Verfahren.<sup>[59-60]</sup> Zuerst wird eine generelle SHG-Aktivität des Materials festgestellt und dann anhand eines Referenzmaterials der exakte Wert von  $\langle d_{eff} \rangle$  bestimmt. Der Aufbau der beiden Setups ist nahezu identisch. Bei beiden wird ein Laser mit einer Output-Wellenlänge von 800 nm verwendet. Zur Bestimmung der generellen SHG-Aktivität und der Polarisation der Probe wird ein Mikroskop eingesetzt, indem sich das einfallende Licht auf die Probe fokussieren lässt. Außerdem kann hier die Polarisationsrichtung des Lichtes um 360° gedreht werden. Zur Bestimmung von  $\langle d_{eff} \rangle$  wird ein Weitfeldmikroskop verwendet, mit dem nicht auf kleine Bereiche der Probe fokussiert wird, sondern die gesamte Probe mit Licht bestrahlt wird. Zur Analyse des SHG-Lichtes sind beide Mikroskope mit einem Detektor für Licht der Wellenlänge von 400 nm ausgestattet. Eine schematische Darstellung der beiden Setups ist in Abbildung 4.3.1 gezeigt.

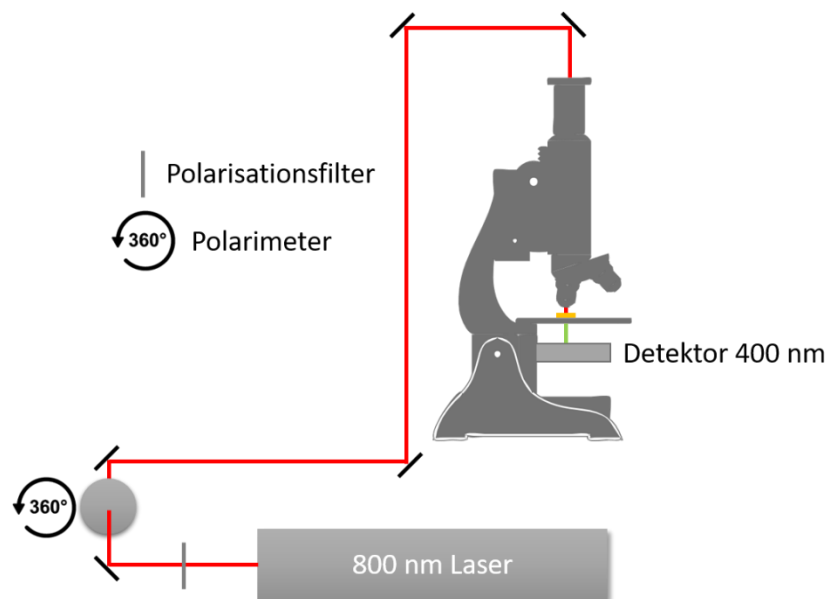


**Abb. 4.3.1** Schematische Darstellung des Setups zur Bestimmung der SHG-Aktivität und des Nichtlinearen Effektivitäts-Koeffizienten. Der Strahlengang des Lasers ist in Rot gezeigt. Beim Durchstrahlen der Probe (gelb) wird frequenzverdoppeltes Licht (grün) detektiert.

Eine Aussage über die SHG-Aktivität liefert ein Vergleich des optischen Bildes mit dem SHG Bild der gleichen Probe an identischen Positionen (Abbildung 4.3.2).

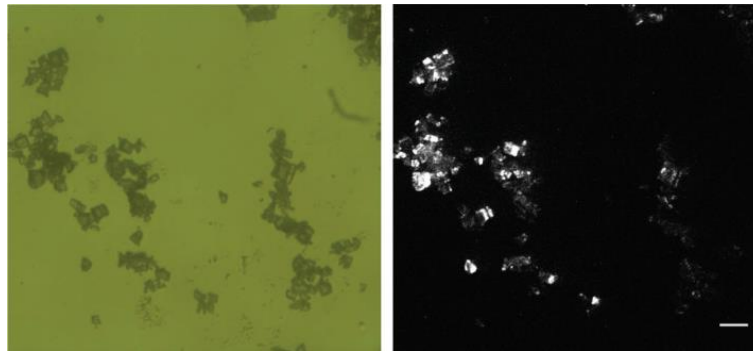


**Abb. 4.3.2** Ein Vergleich zwischen optischen Bild (links) und SHG Bild (rechts) von MIL-53(Fe), welches unter Zusatz von HF hergestellt wurde. Die Kristalle liefern ein frequenzverdoppeltes Signal, daher ist eine SHG-Aktivität klar zu erkennen.<sup>[61]</sup>

Mit dem ersten Setup ist es auch möglich die Polarisationsrichtung der zu vermessenden Probe (Kristalle) zu bestimmen. Außerdem ist erkennbar ob die Kristalle Domänen unterschiedlicher Polarität aufweisen. Dazu wird die Ebene des linear polarisierten Lichtes gedreht und winkelabhängig Bilder aufgenommen. Nach der Analyse der Bilder durch eine Software, die die Lichtintensität der Pixel extrapoliert, lässt sich die Polarisierung der Kristalle farblich kennzeichnen. Ist die Farbe einheitlich, weist der Kristall keine Domänen unterschiedlicher Polarität auf (Abbildung 4.3.3).

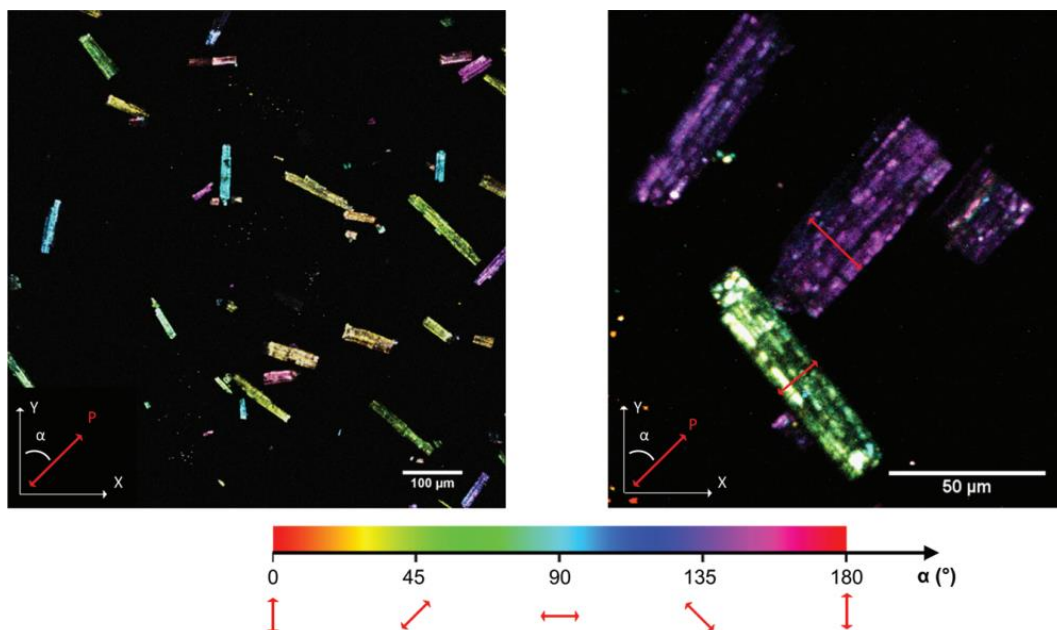


**Abb. 4.3.3** Polarisationsbild von MIL-53(Fe), welches unter Zusatz von HF hergestellt wurde. Die unterschiedliche Position der Kristalle liefert verschiedene Polarisationsrichtungen, die an der Farbskala ermittelt werden können (links). Auch eine gleichmäßige Polarisierung der Kristalle ohne die Präsenz von Domänen ist zu erkennen (rechts).<sup>[61]</sup>

Für die Ermittlung des Nichtlinearen Effektivitäts-Koeffizienten  $\langle d_{eff} \rangle$  werden Bilder bei definierter Belichtungszeit aufgenommen. Die Intensität des erhaltenen Signals wird ebenfalls mit einer Software aus den aufgenommenen Bildern erhalten. Zuerst wird ein Referenzmaterial vermessen, dessen SHG-Eigenschaften bekannt sind. Für diese Arbeit wurden BBO Kristalle mit einer Dicke von 100  $\mu\text{m}$  Dicke verwendet. Für die SHG-Intensität des Referenzmaterials ergibt sich

$$I_{2\omega,BBO} = A \frac{d_{00e}^2 L^2 I_{\omega,BBO}^2}{n_{\theta,2\omega,BBO} n_{\theta,\omega,BBO}^2} \quad (4.3.1)$$

mit dem Nichtlinearen Effektivitäts-Koeffizienten  $d_{00e}$  von BBO, der Dicke des BBO-Kristalls  $L$ , der Intensität des Laserlichtes  $I_{\omega}$ , dem Brechungsindex bei der Frequenz des SHG-Lichtes  $n_{\theta,2\omega,BBO}$  und dem Brechungsindex bei der Frequenz des Laser-Lichtes  $n_{\theta,\omega,BBO}^2$ . Anschließend wird die SHG-Intensität der zu vermessenden Probe bestimmt. Diese ergibt sich aus

$$I_{2\omega,x} = A \frac{\langle d_{eff} \rangle^2 r^2 I_{\omega,x}^2}{n_{2\omega,x} n_{\omega,x}^2} \quad (4.3.2)$$

mit den korrespondierenden Werten auf die zu vermessende Probe bezogen. Umstellen der Gleichungen zum Faktor  $A$ , der alle Variablen beschreibt, die bei Probe und Referenz identisch sind und Gleichsetzen ergibt für den Nichtlinearen Effektivitäts-Koeffizienten  $\langle d_{eff} \rangle$

$$\langle d_{eff} \rangle = \sqrt{\frac{I_{2\omega,x}}{I_{2\omega,BBO}} \cdot d_{00e}^2 \cdot \frac{L^2}{r^2} \cdot \frac{I_{\omega,BBO}^2}{I_{\omega,x}^2} \cdot \frac{n_{2\omega,x} n_{\omega,x}^2}{n_{\theta,2\omega,BBO} n_{\theta,\omega,BBO}^2}} \quad (4.3.3)$$

Zur exakten Bestimmung von  $\langle d_{eff} \rangle$  werden mehrere Kristallite der Probe vermessen und der Wert über die Anzahl der untersuchten Kristallite gemittelt.

#### 4.4 Second Harmonic Generation in MOFs

Metall-Organische Gerüstverbindungen kombinieren die Vorteile organischer Verbindungen hinsichtlich SHG mit den physikalischen Eigenschaften der klassischen NLO-Materialien. Durch ihre strukturelle Vielfalt können gezielt Verbindungen hergestellt werden, die den SHG-Effekt aufweisen. Dies geschieht durch die Verwendung verschiedener Linkermoleküle mit den passenden anorganischen Knotenpunkten. Weiterhin sind die chemischen Strukturen und Zusammensetzungen von MOFs individuell anpassbar, was eine Feineinstellung der NLO-Eigenschaften ermöglicht.<sup>[58]</sup> Ziel ist es eine Ladungstrennung und damit eine Polarisation in das Gerüst einzuführen. Dazu muss ein Donor-Akzeptor-System vorhanden sein, was durch geeignete funktionelle Gruppen erreicht wird. Es sind mehrere

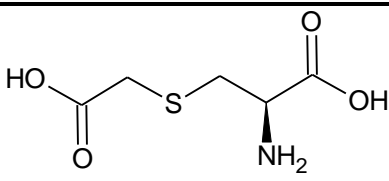
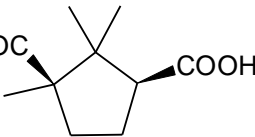
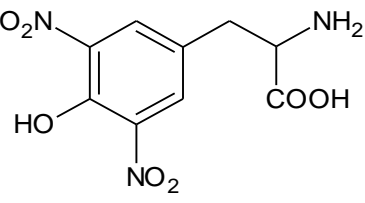
Strategien zur Synthese von nicht-zentrosymmetrischen Verbindungen mit SHG-Aktivität denkbar. Eine sichere Methode ist der Einbau von chiralen organischen Liganden in das MOF-Gerüst.<sup>[62]</sup> Auch die Verwendung von unsymmetrischen Linkern kann die Bildung von zentrosymmetrischen Strukturen verhindern. Oktupolare, oder Gerüste mit Quarz-Topologie weisen sehr oft SHG-Aktivität auf.<sup>[58]</sup> Für die Anwendung von Metall-Organischen Gerüstverbindungen als NLO-Materialien ist es wichtig, dass sie im SHG-Frequenzbereich transparent sind, sodass die optischen Verluste möglichst gering bleiben. Daher werden meist  $d^{10}$  Metallionen wie  $Zn^{2+}$  oder  $Cd^{2+}$  verwendet, um d-d Übergänge im sichtbaren Bereich zu verhindern. Diese bauen zudem tetrahedrische oder pseudotetrahedrische Knotenpunkte mit Carboxylaten auf, aus denen azentrische Verbindungen resultieren können. Da die meisten optisch aktiven Metall-Organischen Gerüstverbindungen diese Ionen enthalten, wird im Folgenden hauptsächlich auf solche Verbindungen eingegangen. Auch  $Mn^{2+}$  als  $d^5$  Ionen eignen sich für den Einsatz in der MOF-Synthese, da die gebildeten Verbindungen meist nur leicht rosa sind und so einen geringen Verlust im optischen Spektrum aufweisen.<sup>[58]</sup> Hauptgruppen-Metallionen wie  $Mg^{2+}$ ,  $Pb^{2+}$  und  $In^{3+}$  sind ebenfalls für die Synthese von optisch aktiven Materialien eingesetzt worden, jedoch zeigten diese Verbindungen eine moderate Aktivität.<sup>[63-65]</sup> Im Folgenden sollen SHG-aktive Verbindungen und Synthesestrategien vorgestellt werden.

#### 4.4.1 NLO-MOFs basierend auf chiralen Linkermolekülen

Im Prinzip sind alle chiralen MOFs SHG-aktiv, auch wenn sie nicht notwendigerweise eine hohe Ausbeute an frequenzverdoppeltem Licht erzeugen. Für die Synthese können sowohl aromatische als auch aliphatische organische Moleküle verwendet werden. Metall-Organischen Gerüstverbindungen, die auf chiralen aliphatischen Linkermolekülen basieren, zeigen im Vergleich zu den aromatischen Verbindungen eine geringere SHG-Aktivität.<sup>[66]</sup> Unter Verwendung eines Cystein-Derivats konnten mit  $Zn^{2+}$  und  $Cd^{2+}$  zwei isoretikuläre Verbindungen,  $[Zn(H_2O)(SCMC)]_n$  und  $\{[Cd(H_2O)(SCMC)] \cdot 2H_2O\}_n$ ,<sup>[67]</sup> hergestellt werden ( $H_2SCMC = S$ -Carboxymethyl-L-Cystein). Die Kristallstrukturen bestehen aus zweidimensionalen Schichten, die untereinander durch Wasserstoffbrückenbindungen zu einem 3D Netzwerk verbrückt sind. Außerdem konnte unter Verwendung des Linkers ein Mn-MOF  $[Mn(H_2O)(SCMC)]$ <sup>[68]</sup> hergestellt werden, der aber nur eine geringe SHG-Aktivität aufweist. Natürlich vorkommende chirale Linkermoleküle wie D-Camphersäure wurden

ebenfalls eingesetzt um chirale oder nicht-zentrosymmetrische Verbindungen zu erhalten.<sup>[69]</sup> Durch die Verwendung des aromatischen Linkers 3,5-Dinitrotyrosin ( $H_2dnty$ ) zur Synthese des Mn-MOFs  $[Mn(Hdnty)_2]$ <sup>[70]</sup> konnte nicht nur gezeigt werden, dass aromatische chirale Linkermoleküle den SHG-Effekt verstärken. Auch der Einbau eines schwach SHG-aktiven organischen Moleküls in eine Gerüststruktur führte zur Steigerung der Ausbeute des SHG-Signals. Auch ein Nd-MOF  $[Nd(Hdnty)_2(NO_3)(H_2O)_5] \cdot 3H_2O$  konnte mit diesem Linker erhalten werden.<sup>[70]</sup> Eine Übersicht über die vorgestellten Verbindungen ist in Tabelle 4.4.1.1 gezeigt.

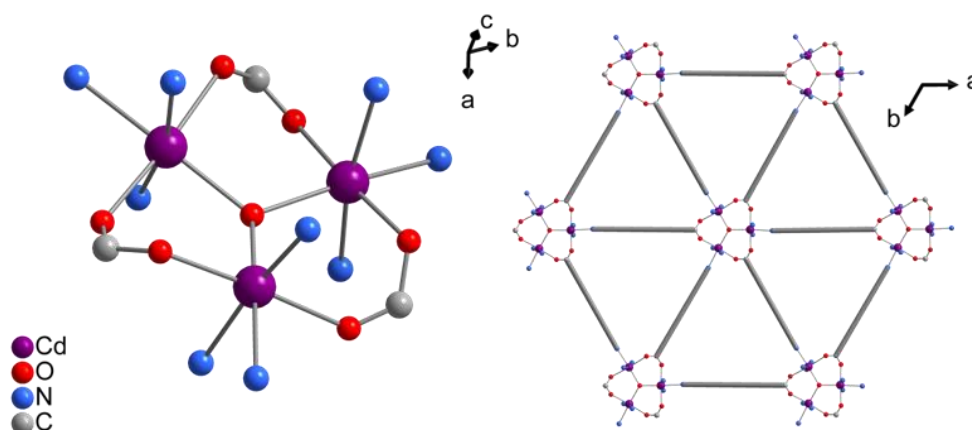
**Tab. 4.4.1.1** Übersicht über die vorgestellten NLO-Verbindungen basierend auf chiralen Linkermolekülen.

Verbindung	Linker	Raumgruppe	Ref.
$[Zn(H_2O)(SCMC)]_n$		$P2_1$	[67]
$\{[Cd(H_2O)(SCMC)] \cdot 2H_2O\}_n$		$P2_12_12_1$	[67]
$[Mn(H_2O)(SCMC)]$	S-Carboxymethyl-L-Cystein, $H_2SCMC$	$P2_1$	[68]
$\{[Zn(1,2-bimb)(D-ca)] \cdot 2H_2O\}_n$		$P2_1/n$	[69]
$[Zn(1,3-bimb)(D-ca)]_n$		$Pna2_1$	[69]
$[Cd(1,3-bimb)(D-ca)]_n$	D-Campfersäure, $H_2D-ca$	$Pna2_1$	[69]
	1,n-Bis(imidazol-1-ylmethyl)-benzol n=1,2; 1,n-bimb		
$[Mn(Hdnty)_2]$		$P2_12_12_1$	[70]
$[Nd(Hdnty)_2(NO_3)(H_2O)_5] \cdot 3H_2O$		$P2_1$	[70]
	3,5-Dinitrotyrosin, $H_2dnty$		



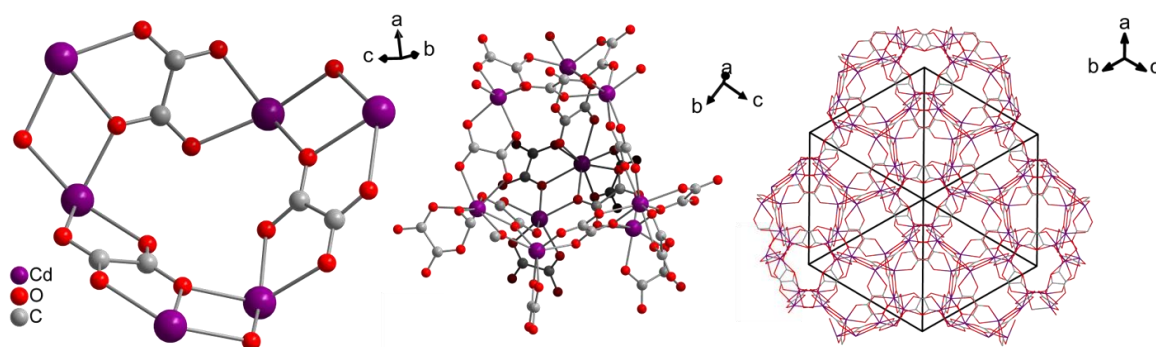
#### 4.4.2 Oktupolare MOFs mit NLO-Funktionalität

Oktupolare MOFs weisen eine  $C_3$  Drehachse auf. Sie besitzen eine höhere Transparenz, was die Ausbeute an SHG-Signal erhöht.<sup>[66]</sup> Trotz dieser Vorteile sind solche Strukturen selten. Eine SHG-aktive Verbindung wurde unter Verwendung von  $Cd^{2+}$  und Ethyl-4-[2-(4-pyridyl)ethenyl]benzoesäure (HL) hergestellt ( $[Cd_3(\mu_3-OH)_3L_6(py)_6](ClO_4)_2$ ,  $py = \text{Pyridin}$ ), die trinucleare Cd-Baueinheiten (IBUs) aufweist, welche wiederum zu sechs benachbarte IBUs durch die Linker verknüpft sind. So wird eine 2D Schichtstruktur aufgebaut (Abbildung 4.4.2.1).<sup>[71]</sup>



**Abb. 4.4.2.1** Trinuclearer Cluster von  $[Cd_3(\mu_3-OH)_3L_6(py)_6](ClO_4)_2$  (links) und Ausschnitt der Schichten, die gebildet werden (rechts). Eine dreizählige Drehachse ist klar erkennbar.<sup>[71]</sup>

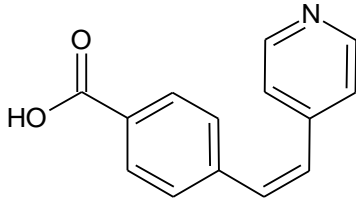
Ein poröser Cd-MOF,  $(H_2NMe_2)_2[Cd_3(C_2O_4)_4] \cdot MeOH \cdot 2H_2O$ , mit einem 3D Koordinationsnetzwerk wird mit Hilfe von Oxalaten aufgebaut. Dieser besteht aus  $[Cd_6(C_2O_4)_8]^{4-}$ -Clustern, die zwei Paare von gleichseitigen Dreiecken bilden, deren Zentrum auf einer  $C_3$ -Achse liegt. Flächenverknüpfung der  $Cd_3$ -Dreiecke führt zu  $Cd_9$ -Käfigen, welche wiederum so gepackt sind, dass ein oktopolares 3D-Netzwerk entsteht (Abbildung 4.4.2.2).<sup>[72]</sup>



**Abb. 4.4.2.2** Schematische Ansicht des  $[Cd_6(C_2O_4)_8]^{4-}$  Clusters (links), der zu einem  $Cd_9$ -Käfig verknüpft wird (mittig). Das oktopolare 3D Netzwerk ist rechts gezeigt.<sup>[72]</sup>

Das offene anionische Gerüst weist eine hohe Ionenaustauschkapazität für  $\text{NH}_4^+$ ,  $\text{Na}^+$  und  $\text{K}^+$  auf. Durch Austausch der Kationen kann die NLO-Aktivität variiert werden. Eine Übersicht über die vorgestellten Verbindungen ist in Tabelle 4.4.2.1 gezeigt.

**Tab. 4.4.2.1** Übersicht über die vorgestellten oktopolaren MOFs mit NLO-Aktivität

Verbindung	Linker	Raumgruppe	Ref.
$[\text{Cd}_3(\mu_3\text{-OH})_3\text{L}_6(\text{py})_6](\text{ClO}_4)_2$	 <p>Ethyl-4-[2-(4-pyridyl)ethenyl]-benzesäure, HL</p>	<i>R32</i>	[71]
$[(\text{H}_2\text{NMe}_2)_2\text{Cd}_3(\text{C}_2\text{O}_4)_4]$	Oxalsäure	<i>I-43d</i>	[72]

#### 4.4.3 NLO-aktive MOFs mit Quarz-Topologie

Tetraedrisch verknüpfte Netzwerke haben sich als topologisches Motiv mit einer starken Tendenz zur Bildung nicht-zentrosymmetrischer Strukturen herausgestellt. Die einfachste Art, die Symmetrie zu durchbrechen veranschaulicht die Struktur von  $\alpha$ -Quarz. Hier beträgt der Winkel der Si-O-Si-Bindung  $144^\circ$ , weshalb eine Zentrosymmetrie verhindert wird. Die erste Adaption in MOFs wurde mit Hilfe von Zink und 4-Cyanopyridin, die *in situ* zur Isonikotinsäure (Hinic) hydrolysiert wurde, durchgeführt. Mit dem azentrischen Linker wurde eine dreifach interpenitrierte Quarzstruktur,  $[\text{Zn}(\text{inic})_2]$ , erhalten, die eine schwache SHG-Aktivität aufweist (Abbildung 4.4.3.1).<sup>[73]</sup>

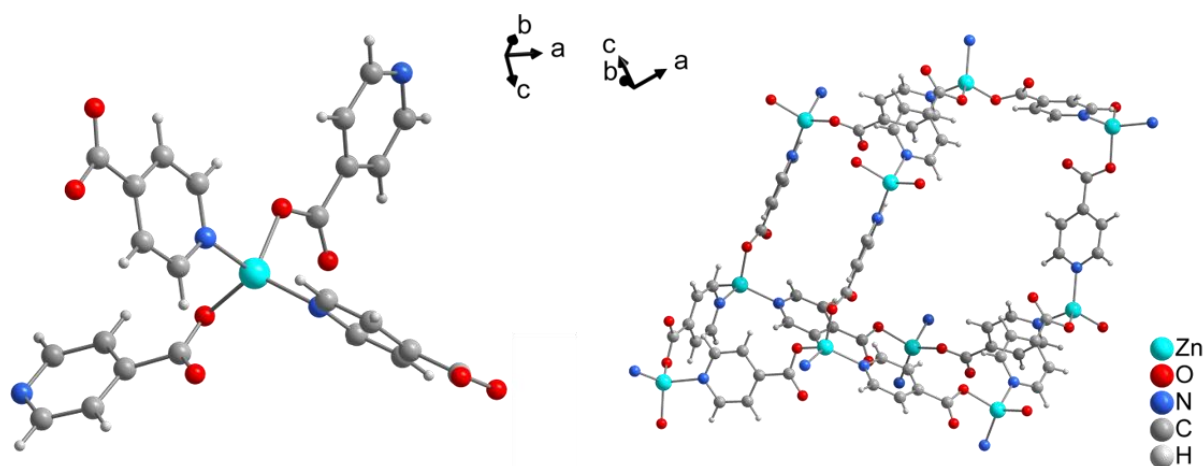


**Abb. 4.4.3.1** Tetraedrische Verknüpfung des Zn<sup>2+</sup>-Ions in [Zn(inic)<sub>2</sub>] (links) führt zum Aufbau eines 3D Quarz-Netzwerkes (rechts). Nur ein Käfig ist der Übersicht halber gezeigt.<sup>[73]</sup>

Dieses Prinzip wurde weiter ausgebaut und längere azentrische Linkermoleküle eingesetzt, was in höher interpenetrierten Netzwerken resultierte. Dabei konnte gezeigt werden, dass sich die SHG-Aktivität mit steigender Länge des verwendeten Linkers verstärkte.<sup>[74-75]</sup>

Da Indium eine Koordinationszahl von acht einnehmen kann, ist die Synthese von als Tetraederzentren wirkenden [In(-COO)<sub>4</sub>]-Clustern möglich. Ein MOF mit der Zusammensetzung (Hpy)<sub>2</sub>[In<sub>2</sub>(μ-OH)<sub>2</sub>(BTC)<sub>2</sub>], der diese InO<sub>8</sub>-Tetraederzentren besitzt, konnte mit Hilfe von In<sup>3+</sup> und Trimesinsäure (H<sub>3</sub>BTC) hergestellt werden. Dieser baut eine komplexe Struktur auf, die aus nicht-geschlossenen Ringen, welche entlang der *a*-Achse miteinander verbrückt sind, auf (Abbildung 4.4.3.2).<sup>[64]</sup> Dieser MOF besitzt zwar keine Quarz-Topologie, soll hier aber als Vertreter von p-Block-Elementen, die Tetraederzentren aufbauen, erwähnt werden.

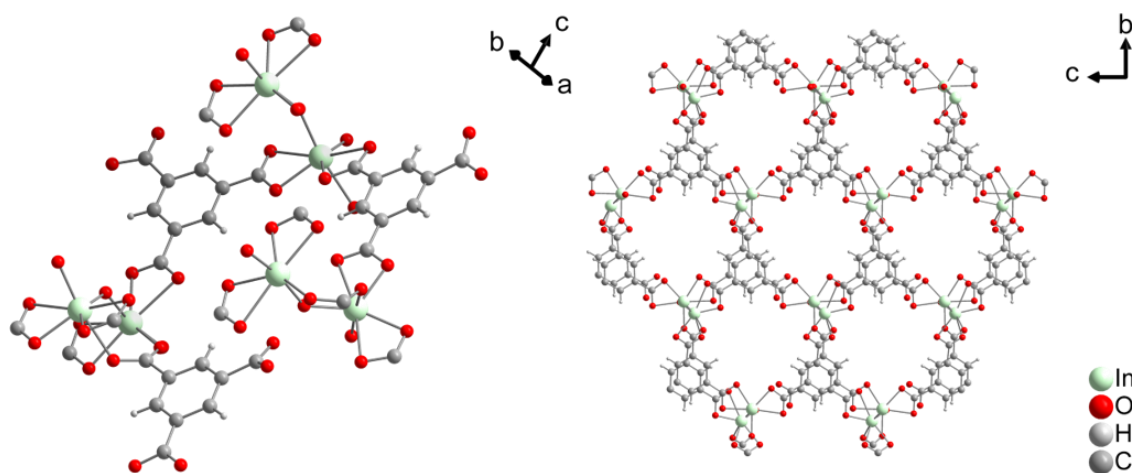


**Abb. 4.4.3.1** InO<sub>8</sub>-Polyeder bilden durch die Verknüpfung mit Trimesationen Ringe (links), die Schichten aufbauen, die durch weitere InO<sub>8</sub>-Oktaeder miteinander verbrückt sind (rechts).<sup>[64]</sup>

Eine Übersicht über die vorgestellten Verbindungen ist in Tabelle 4.4.3.1 gezeigt.

**Tab. 4.4.3.1** Übersicht über die vorgestellten oktopolaren MOFs mit NLO-Aktivität

Verbindung	Linker	Raumgruppe	Ref.
[Zn(inic) <sub>2</sub> ]	Isonikotinsäure, H <sub>in</sub> ic	<i>P</i> 2 <sub>1</sub> 2 <sub>1</sub> 2 <sub>1</sub>	[73]
(Hpy) <sub>2</sub> [In <sub>2</sub> (μ-OH) <sub>2</sub> (BTC) <sub>2</sub> ]	Trimesinsäure, H <sub>3</sub> BTC	<i>P</i> 2 <sub>1</sub>	[64]

#### 4.5 Optische Aktivität in MIL-53 und CAU-10

MIL-53 (MIL = Matériaux de l'Institute Lavoisier) ist der erste und daher am intensivsten untersuchte Al-MOF.<sup>[5]</sup> Er ist aufgebaut aus Ketten eckenverknüpfter AlO<sub>6</sub>-Oktaeder, die über Terephthalationen zu einem dreidimensionalen Netzwerk mit rautenförmigen Kanälen verknüpft werden. Der MOF kann ebenfalls mit Metallionen wie Fe<sup>3+</sup><sup>[76]</sup>, V<sup>3+</sup><sup>[77]</sup>, Sc<sup>3+</sup><sup>[78]</sup>, Cr<sup>3+</sup><sup>[79]</sup>, Ga<sup>3+</sup><sup>[80]</sup> und In<sup>3+</sup><sup>[81]</sup> und einer Reihe funktionalisierter Terephthalationen erhalten werden.<sup>[82-87]</sup> Die besondere Eigenschaft von MIL-53 ist dessen strukturelle Flexibilität. Je nach Art der in den Poren befindlichen Gastmoleküle oder in Abhängigkeit der Temperatur kann sich das Gerüst zusammenziehen oder ausdehnen. Dieses wurde sich zu Nutze gemacht und die SHG-Aktivität der *vnp*- (very narrow pore) und *lp*- (large pore) der Form von MIL-53(Al)-NH<sub>2</sub> [Al(OH)BDC-NH<sub>2</sub>] bestimmt. Erstere weist durch ihre azentrische Struktur SHG-Aktivität auf, die zweite nicht (Abbildung 4.5.1).<sup>[88]</sup>

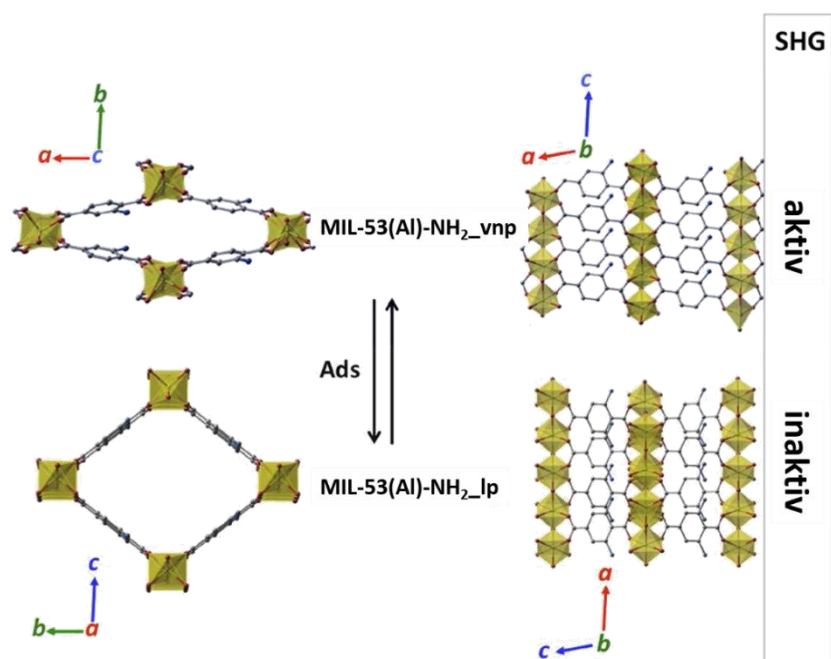


**Abb. 4.5.1** Die strukturelle Flexibilität von MIL-53(Al)-NH<sub>2</sub> führt zu einer reversiblen SHG-Aktivität. (nach Ref. <sup>[88]</sup>)

Da die Phasenumwandlung von MIL-53(Al)-NH<sub>2</sub> reversibel ist, ist es möglich die SHG-Aktivität gezielt zu schalten. Außerdem ist der Signal-Kontrast zwischen inaktiver und aktiver Form in diesem Material besonders hoch, da vergleichbare andere schaltbare Materialien auch in ihrer inaktiven Form SHG-Signal emittieren. Die beschriebenen Effekte konnten für unfunktionalisiertes MIL-53(Al) nicht beobachtet werden. Weiterhin konnte durch Zusatz von HF bei der Synthese von MIL-53(Fe) ebenfalls eine Verbindung mit optischer Aktivität erhalten werden (siehe Kapitel 4.3).<sup>[61]</sup>

Als CAU-10-X [Al(OH)(*m*BDC-X)] wird eine Reihe funktionalisierter Al-MOFs bezeichnet. Die Struktur von CAU-10 ist aufgebaut aus helikalen Ketten aus *cis*-eckenverknüpften AlO<sub>6</sub>-Oktaedern, verknüpft durch Isophthalationen zu einem dreidimensionalen Netzwerk. Die Isophthalationen können unterschiedlich funktionalisiert sein (Abbildung 4.5.2).<sup>[9, 20, 89]</sup> In CAU-10 wurde der SHG-Effekt ausgenutzt, um die Punktgruppen der verschiedenen funktionalisierten CAU-10-Derivate bestimmen zu können. So konnte zwischen zentrosymmetrisch und azentrisch kristallisierenden Verbindungen unterschieden werden, was die Bestimmung und Verfeinerung der Struktur aus Pulverdaten vereinfachte.<sup>[20]</sup>

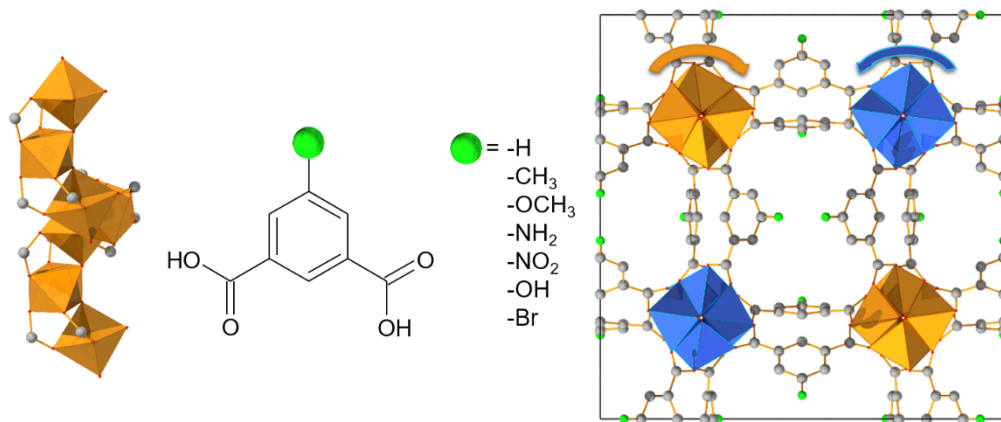


**Abb. 4.5.2** IBU von CAU-10, aufgebaut aus *cis*-eckenverknüpften AlO<sub>6</sub>-Oktaedern (rechts), mögliche Funktionalisierungen der als Linker verwendeten Isophthalsäure (mittig) und dreidimensionales Netzwerk von CAU-10.<sup>[9, 20, 89]</sup>

Eine Übersicht über SHG-Aktivität der einzelnen CAU-10-Derivate und den Raumgruppen, in denen sie kristallisieren, ist in Tabelle 4.5.1 gezeigt.

**Tab. 4.5.1** Raumgruppen und SHG-Aktivität der bekannten CAU-10-Derivate.

CAU-10-Material	Raumgruppe	SHG-Aktivität	Ref.	CAU-10-Material	Raumgruppe	SHG-Aktivität	Ref.
-H	$I4_1$	ja	[20]	-H/Br	$I4_1$	N/A	[89]
-Br	$I4_1/amd$	N/A	[89]	-H/CH <sub>3</sub>	n.A.	N/A	[89]
-CH <sub>3</sub>	$I4_1/amd^*$	nein*	[20]	-NO <sub>2</sub> /NH <sub>2</sub>	$P4_1$	N/A	[89]
	$P4_1$	ja		-OH/SO <sub>3</sub> H	$P4$	N/A	[90]
-OCH <sub>3</sub>	$I4_1/a$	nein	[20]	-H/SO <sub>3</sub> H	$I4_1$	N/A	[90]
-NH <sub>2</sub>	$P-4n2$	nein	[20]	-NO <sub>2</sub> /SO <sub>3</sub> H	$P4_1$	N/A	[90]
-NO <sub>2</sub>	$P4_1$	ja	[20]				
-OH	$P4$	ja	[20]				

\* aktivierte Probe N/A: nicht untersucht

In dieser Arbeit wurde hinsichtlich der Synthese von SHG-aktiven Metall-Organischen Gerüstverbindungen folgende Linkermoleküle eingesetzt: 5-Fluorisophthalsäure (H<sub>2</sub>mBDC-5F), 2-Aminoterephthalsäure (H<sub>2</sub>BDC-NH<sub>2</sub>), 2-Nitroterephthalsäure (H<sub>2</sub>BDC-NO<sub>2</sub>) und 2-Amino-5-nitroterephthalsäure (H<sub>2</sub>BDC-NH<sub>2</sub>/NO<sub>2</sub>). Zunächst wurde die Auswirkung der partiellen Fluorfunktionalisierung von CAU-10 [Al(OH)(mBDC-X)] mittels 5-Fluorisophthalsäure auf die Sorptionseigenschaften und die SHG-Aktivität untersucht. Anschließend wurden gezielt In-MOFs mit Quarz-Struktur hergestellt, die eine potentielle SHG-Aktivität aufweisen sollten. Weiterhin wurde der Einfluss der 2-Amino-5-nitroterephthalsäure auf die Kristallstruktur von MIL-53(Al) untersucht. Durch das ausgeprägte Donor-Akzeptor-System des H<sub>2</sub>BDC-NH<sub>2</sub>/NO<sub>2</sub> sollte eine Polarisierung des MOFs durch Ausrichtung der Linkermoleküle erreicht werden. Durch weitere Syntheseveruche mit Al<sup>3+</sup>, Ga<sup>3+</sup> und In<sup>3+</sup> in anderen Lösungsmitteln sollte die Ausrichtung der Linker verstärkt und so die SHG-Aktivität erhöht werden.

Zusätzlich wurden neue und isoretikuläre Al-MOFs auf Basis von Tetra- und gewinkelten Dicarbonsäuren hergestellt und auf deren Eigenschaften hin untersucht werden. Im Folgenden sind zunächst diese Ergebnisse dargestellt, bevor sich dem eingangs erläuterten Thema der optischen Aktivität gewidmet wird.

## 4.6 Synthese und Charakterisierung neuer Al-MOFs basierend auf Di- und Tetracarbonsäuren

### 4.6.1 $[\text{Al}_2(\text{OH})_2(\text{TCPB})]$ – An Al-MOF based on a tetratopic linker molecule

Der folgende Artikel wurde im Jahre 2015 in der Fachzeitschrift *Microporous and Mesoporous Materials*, ELSEVIER GmbH veröffentlicht. Der Wiederabdruck erfolgte mit freundlicher Genehmigung der ELSEVIER GmbH. Reproduced with permission from:

M. Krüger, R. Siegel, A. Dreischarf, H. Reinsch, J. Senker, N. Stock, *Micropor. Mesopor. Mat.*, **2015**, 216, 27-35. DOI: 10.1016/j.micromeso.2015.04.023.

In diesem Artikel geht es um die gezielte Herstellung einer zu MIL-118B<sup>[91]</sup>  $[\text{Al}_2(\text{OH})_2(\text{BTEC})]$  (BTEC<sup>4-</sup> = 1,2,4,5-Benzoltetracarboxylat) und zum Al-PMOF<sup>[92]</sup>  $[\text{Al}_2(\text{OH})_2(\text{TCPP})]$  (TCPP<sup>4-</sup> = meso-tetra(4-carboxylato-phenyl)porphyrin) isoretikulären Verbindung. Mit 1,2,4,5-tetrakis-(4-carboxyphenyl)-benzol ( $\text{H}_4\text{TCPB}$ ), einem im Vergleich zu  $\text{H}_4\text{BTEC}$  um vier Phenylringe verlängerten Linkermolekül, konnte ein neuer Al-MOF,  $[\text{Al}_2(\text{OH})_2(\text{TCPB})]\cdot 2\text{DMF}$  (CAU-9as), hergestellt werden. Zur Entdeckung und Syntheseoptimierung wurden Hochdurchsatzmethoden verwendet. Thermische Aktivierung bei 150 °C unter verringertem Druck führte zur Entfernung der Gastmoleküle (CAU-9act). CAU-9act enthält eine Verunreinigung an Böhmit, welche für die weiteren Charakterisierungsschritte berücksichtigt wurde. Stickstoff-Sorptionsmessungen ergaben eine Typ I Isotherme und eine scheinbare spezifische Oberfläche nach BET von 1118 m<sup>2</sup>/g und ein Mikroporenvolumen von 0.45 cm<sup>3</sup>/g. Temperaturabhängige Röntgenpulvermessungen zeigten eine thermische Stabilität von CAU-9 bis 480 °C und eine Veränderung der Zellparameter. Weiterhin wurde die Verbindung mittels <sup>27</sup>Al-, <sup>1</sup>H- und <sup>13</sup>C-NMR Festkörperspektroskopie untersucht. Die Kristallstruktur von CAU-9act konnte mittels Rietveld-Methoden verfeinert werden. Die Verbindung kristallisiert in der orthorhombischen Raumgruppe *Cmmm* ( $a = 31.562(4)$ ;  $b = 6.642(7)$ ;  $c = 10.6612(7)$  Å) und enthält Ketten, bestehend aus *trans*-eckenverknüpften  $\text{AlO}_6$ -Oktaedern, die durch die TCPB<sup>4-</sup>-Ionen miteinander verbrückt sind. Jedes TCPB<sup>4-</sup>-Ion verknüpft vier anorganische Baueinheiten, sodass zwei unterschiedlich große rautenförmige eindimensionale Poren entstehen, wovon die größeren untereinander über Fenster von 4 x 3.2 Å Größe miteinander verbunden sind.

Zusätzlich zu der in der Veröffentlichung vorgestellten Verbindung konnten isoretikuläre MOFs basierend auf  $\text{Ga}^{3+}$ ,  $\text{In}^{3+}$  und  $\text{Cr}^{3+}$  hergestellt werden. Die Entdeckung der Verbindungen und deren Syntheseoptimierungen gelang ebenfalls mittels Hochdurchsatzmethoden. Eine Indizierung der Pulverdiffraktogramme von Ga- und Cr-CAU-9 ergab eine orthorhombische Zelle mit C-Zentrierung. Mittels Pawley-Methoden ließen sich die Gitterparameter in der Raumgruppe *Cmmm* erfolgreich verfeinern. Für In-CAU-9 konnte Pawley-Verfeinerung in der monoklinen Raumgruppe *P2/m* durchgeführt werden. Die Strukturmodelle, die auf Basis von Al-CAU-9 erhalten wurden, konnten nicht durch Rietveld-Methoden bestätigt werden.

Für Ga-CAU-9,  $[\text{Ga}_2(\text{OH})_2(\text{TCPB})] \cdot 1.2\text{H}_2\text{O} \cdot 2.63\text{DMF}$ , wurde eine orthorhombische Elementarzelle mit den Zellparametern  $a = 21.861(2)$ ;  $b = 6.714(3)$  und  $c = 15.844(2)$  Å gefunden und verfeinert. Thermogravimetrische Messungen zeigten eine Stabilität des Gerüsts bis ca. 300 °C und ebenfalls durchgeführte  $\text{N}_2$ -Sorptionsmessungen ergaben eine Typ I Isotherme, was auf das Vorliegen einer mikroporöse Verbindung hindeutet. Die Auswertung der Isotherme nach BET ergab eine scheinbare spezifische Oberfläche nach BET von 510  $\text{m}^2/\text{g}$  und ein Mikroporenvolumen von 0.22  $\text{cm}^3/\text{g}$ .

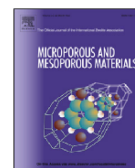
Die Indizierung des Pulverdiffraktogramms von In-CAU-9,  $[\text{In}_2(\text{OH})_2(\text{TCPB})] \cdot 3\text{DMF}$ , ergab eine monokline Elementarzelle mit den Zellparametern  $a = 11.637(1)$ ;  $b = 15.725(2)$ ;  $c = 7.204(1)$  Å und  $\beta = 80.97(2)^\circ$ . In thermogravimetrischen Messungen konnte eine Stabilität bis ca. 400 °C festgestellt werden. In  $\text{N}_2$ -Sorptionsmessungen konnte eine Typ I Isotherme erhalten werden, deren Auswertung nach BET eine scheinbare spezifische Oberfläche nach BET von 487  $\text{m}^2/\text{g}$  und ein Mikroporenvolumen von 0.21  $\text{cm}^3/\text{g}$  ergab.

Thermogravimetrische Messungen und Elementaranalysen zeigten, dass Cr-CAU-9,  $[\text{Cr}_2(\text{OH})_2(\text{TCPB})] \cdot 1.4\text{H}_2\text{O} \cdot 1.9\text{DMF} \cdot 2.9\text{Cr}_2\text{O}_3$ , Verunreinigungen von  $\text{Cr}_2\text{O}_3$  enthält, deren Bildung während der Syntheseoptimierung nicht unterbunden werden konnte. Bei ersterer Messung konnte ebenfalls eine thermische Stabilität bis ca. 350 °C festgestellt werden. Eine Indizierung des Pulverdiffraktogramms ergab eine orthorhombische Elementarzelle mit C-Zentrierung. Mittels Pawley-Methoden ließ sich die Zelle in der Raumgruppe *Cmmm* ( $a = 21.654(6)$ ;  $b = 6.829(3)$ ;  $c = 15.844(6)$  Å) verfeinern. Weiterhin wurde eine postsynthetische Modifizierung des MOFs durch Nitrierung des Linkers nach Bernt et al.<sup>[93]</sup> durchgeführt. Bei dem Versuch nahm die Kristallinität der Verbindung ab, die Gerüststruktur blieb jedoch erhalten.  $^1\text{H}$ -NMR-Spektren des Reaktionsproduktes, lassen eine Nitrierung von



Cr-CAU-9 vermuten, jedoch ist auch eine Oxidation des zentralen aromatischen Ringes des TCPB<sup>4-</sup> zum Benzochinon möglich. Dies konnte noch nicht abschließend geklärt werden.

Zusätzliche Informationen zur Veröffentlichung und zu den isoretikulären Ga-, In- und Cr-Verbindungen befinden sich im Angang.



## [Al<sub>2</sub>(OH)<sub>2</sub>(TCPB)] – An Al-MOF based on a tetratopic linker molecule



Martin Krüger<sup>a</sup>, Renée Siegel<sup>c</sup>, Anna Dreischarf<sup>a</sup>, Helge Reinsch<sup>b</sup>, Jürgen Senker<sup>c</sup>, Norbert Stock<sup>a,\*</sup>

<sup>a</sup> Institut für Anorganische Chemie, Christian Albrechts Universität zu Kiel, Kiel, Germany

<sup>b</sup> Centre for Materials Science and Nanotechnology Chemistry, University of Oslo, Oslo, Norway

<sup>c</sup> Department of Inorganic Chemistry 3, Universität Bayreuth, Bayreuth, Germany

### ARTICLE INFO

#### Article history:

Received 5 January 2015

Received in revised form

1 April 2015

Accepted 14 April 2015

Available online 22 April 2015

#### Keywords:

High-throughput methods

Metal-organic frameworks

Solvothermal synthesis

Microporous materials

Solid state NMR spectroscopy

### ABSTRACT

High-throughput methods were employed in the discovery and synthesis optimization of the new microcrystalline metal-organic framework (MOF) [Al<sub>2</sub>(OH)<sub>2</sub>(TCPB)] · 2 DMF (denoted CAU-9as), which contains the tetratopic linker ion 1,2,4,5-tetrakis-(4-carboxylatophenyl)-benzene (TCPB<sup>4-</sup>). The compound is obtained under solvothermal reaction conditions and activation at 150 °C leads to the removal of the guest molecules (CAU-9act). Detailed characterization was carried out by FT-IR and NMR spectroscopy, thermogravimetric analysis, gas sorption measurements and X-ray powder diffraction. CAU-9act crystallizes in an orthorhombic unit cell (space group *Cmmm*) with the cell parameters: *a* = 31.562(4), *b* = 6.642(7), *c* = 10.6612(7) Å. Modeling by force field calculations in combination with Rietveld refinement was used to determine the structure of CAU-9. The content of the asymmetric unit was corroborated based on NMR crystallographic strategies evaluating high-resolution <sup>1</sup>H, <sup>13</sup>C and <sup>27</sup>Al MAS NMR spectra. The structure of CAU-9 is isoreticular to the one of MIL-118B [Al<sub>2</sub>(OH)<sub>2</sub>(BTEC)] (BTEC = 1,2,4,5-benzenetetracarboxylate) and Al-PMOF [Al<sub>2</sub>(OH)<sub>2</sub>(TCPP)] (TCPP = meso-tetra(4-carboxylato-phenyl)porphyrin). According to the temperature dependent PXRD measurements and the thermogravimetric analysis, it is stable up to 480 °C in air. The nitrogen sorption measurement at 77 K has given a Brunauer–Emmett–Teller (BET) surface area of 1118 m<sup>2</sup> g<sup>-1</sup> and a micropore volume of 0.45 cm<sup>3</sup> g<sup>-1</sup>. In contrast to MIL-118 no rearrangement of the carboxylate groups from a mono- to bidentate coordination mode was observed upon activation.

© 2015 Elsevier Inc. All rights reserved.

### 1. Introduction

In the past few years the development of new metal organic frameworks (MOFs) has been in the focus of many investigations [1]. Often new linker molecules are employed in the search of compounds with unprecedented topologies [2]. Alternatively, functionalized linker molecules are used in order to tune the pore size and the pore surface chemistry, for example, for applications in catalysis or gas separation or to be able to carry out post synthetic modification reactions [3–5]. An important aspect of MOF chemistry is the modular synthesis concept allowing for a straightforward access of isoreticular MOF structures [6–10]. Using existing, well-known topologies, the size of the linker molecule is varied while retaining its principal shape resulting in an adaption of pore sizes [10–15]. As a result of the large linker molecules often

interpenetration is observed as shown for example in the IRMOF series [6]. This can be prevented through the choice of appropriate inorganic building units (IBUs) such as one-dimensional IBUs [9].

Carboxylate-based Al-MOFs have been of special interest due to their chemical and thermal stability, which is only surpassed by corresponding Cr- and Zr-MOFs [16,17]. An extraordinary advantage of aluminum is the fact that the salts are non-toxic and hence easy to handle and commercially available at low-cost. Therefore, aluminum based MOFs are of interest for industrial use [18]. A challenge in the investigation of Al-MOFs is the rich solution chemistry of Al<sup>3+</sup> which can lead to a variety of IBUs ranging from isolated Al<sup>3+</sup> ions, that are exclusively connected by carboxylate groups [16], to trimeric building units [19–21], rings of edge- and corner sharing AlO<sub>6</sub> polyhedra [11,12,22], chains of *trans*- or *cis*-corner sharing AlO<sub>6</sub> polyhedra [23–27], chains of edge sharing AlO<sub>6</sub> polyhedra [28] or very complex inorganic building units of corner-sharing Al<sub>13</sub>-oxo clusters [29]. An in depth study on the use of pyromellitic acid (1,2,4,5-benzenetetracarboxylic acid, H<sub>4</sub>BTEC) has been carried out by Loiseau et al. which lead to a variety of new Al-

\* Corresponding author.

E-mail address: [stock@ac.uni-kiel.de](mailto:stock@ac.uni-kiel.de) (N. Stock).

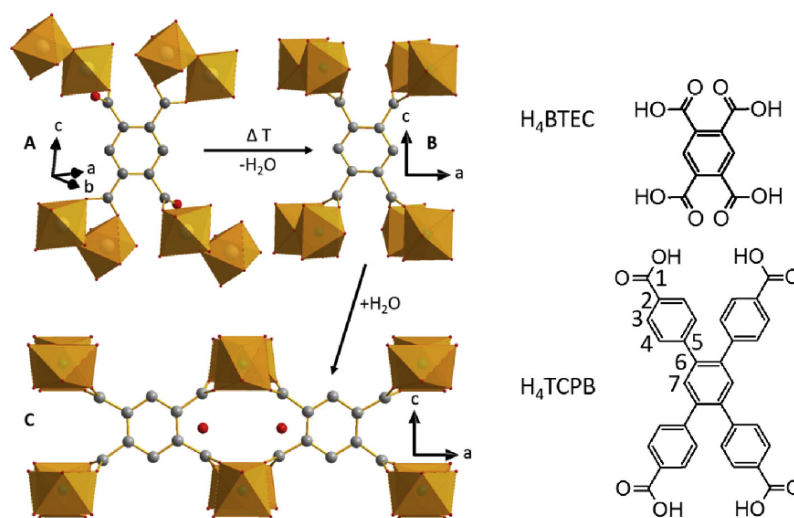


**Fig. 1.** Representation of the different forms of MIL-118 (left). Thermal treatment of as synthesized MIL-118A (A) leads to MIL-118B (B), which adsorbs water under ambient conditions forming MIL-118C (C) [30]. Carbon atoms are colored grey, oxygen red and the  $\text{AlO}_6$  polyhedra are orange. On the right side the extension of the  $\text{H}_4\text{BTEC}$  linker as it is used in the synthesis of MIL-118 to  $\text{H}_4\text{TCPB}$  which served as linker molecule in this investigation is shown. In addition labeling of the magnetically inequivalent carbon atoms is presented for a molecule with *mmm* symmetry. (For interpretation of the references to color in this figure legend, the reader is referred to the web version of this article.)

MOFs [28,30,31]. In particular a high-throughput investigation was carried out and the exact fields of formation were established. The pH of the reaction mixture was found to be the main variable on the product formation [31].

One Al-MOF obtained using  $\text{H}_4\text{BTEC}$  and undergoing irreversible structural changes upon heating is the MIL-118 series  $[\text{Al}_2(\text{OH})_2(\text{BTEC})]$  [30]. The structure of the as synthesized compound MIL-118A  $[\text{Al}_2(\text{OH})_2(\text{H}_2\text{O})_2(\text{BTEC})]$  exhibits a distinct structural feature, i.e. the carboxylate ions coordinate in a bidentate and a monodentate mode. Upon thermal treatment coordinated water molecules are removed and the free coordination site is occupied by the previously monodentate carboxylate group (MIL-118B  $[\text{Al}_2(\text{OH})_2(\text{BTEC})]$ ). Upon rehydration of MIL-118B under ambient conditions only water molecules are adsorbed in the pores and MIL-118C  $[\text{Al}_2(\text{OH})_2(\text{BTEC})] \cdot 3\text{H}_2\text{O}$  is formed (Fig. 1).

Here we present the results of our work on using an extended version of the  $\text{H}_4\text{BTEC}$  linker molecule, i.e.  $\text{H}_4\text{TCPB}$  (Fig. 1) in the synthesis of Al-MOFs, which was envisioned to lead to a structure isorecticular to MIL-118.

## 2. Experimental section

### 2.1. General

The chemicals used for the synthesis of CAU-9 are commercially available and were used without further purification. Discovery and synthesis optimization of this compound were carried out employing our 48-high-throughput reactor system for solvothermal high-throughput reactions [32–34]. The high-throughput PXRD measurements were performed in transmission geometry using a STOE HT diffractometer equipped with a *xy*-stage and an IPDS system ( $\text{Cu K}\alpha_1$  radiation). Collection of high-resolution powder diffraction data was possible on a STOE Stadi-P powder diffractometer equipped with a MYTHEN1K detector system ( $\text{Cu K}\alpha_1$  radiation). Temperature dependent high-resolution powder diffraction data was recorded on a STOE StadiP-Combi diffractometer using  $\text{Cu K}\alpha_1$  radiation and equipped with a MYTHEN1K detector. These measurements were carried out under air in a 0.5 mm quartz capillary in

a range of 3–45° 2 $\theta$  with a measuring time of 85 min for each temperature step. MIR spectra were recorded on an ATI Matheson Genesis spectrometer equipped with an ATR unit in the spectral range of 400–4000  $\text{cm}^{-1}$ . The thermogravimetric analyses were performed using a NETSCH STA 409 CD analyzer. The samples were heated in  $\text{Al}_2\text{O}_3$  crucibles at a rate of 4  $\text{K min}^{-1}$  under a flow of air (75  $\text{mL min}^{-1}$ ). The TG data were corrected for buoyancy and current effects. Sorption experiments were carried out using a Belsorp-max instrument (BEL JAPAN INC.). Before the sorption experiments, the samples were activated at 150 °C under vacuum ( $10^{-2}$  kPa) over night. For setting up a structural model Accelrys Materials Studio 4.1 was used [35]. Rietveld refinement of this structural model was carried out with TOPAS Academic v4.1 [36]. Theoretical micropore volumes were calculated using the calc solv feature implemented in PLATON [37]. A probe molecule with a diameter of 2.6 Å was used. Parametric Pawley refinements were performed using Powder3D Parametric [38].

### 2.2. Solid-state nuclear magnetic resonance

All solid-state NMR experiments were acquired on a Bruker Avance-III HD operating at a  $B_0$  field of 14.1 T.  $^1\text{H}$  (600.15 MHz) high-resolution spectra were acquired after a 90° pulse of 1.4  $\mu\text{s}$  with a spinning speed of 62.5 kHz using a commercial 1.3 mm MAS double resonance probe (Bruker).  $^{13}\text{C}$  (150.9 MHz) MAS spectra were obtained with a ramped cross-polarization (CP) experiment where the nutation frequency  $\nu_{\text{nut}}$  on the proton channel was varied linearly by 30%. The samples were spun at 20 kHz in 3.2 mm MAS triple resonance probe (Bruker). The corresponding  $\nu_{\text{nut}}$  on the  $^{13}\text{C}$  channel and the contact time were adjusted to 70 kHz and 3.0 ms, respectively. Proton broadband decoupling with spinal-64 was applied during acquisition. Both the  $^1\text{H}$  and  $^{13}\text{C}$  spectra are referenced with respect to TMS (tetramethylsilane) using the secondary standard adamantane. Finally, the  $^{27}\text{Al}$  (156.4 MHz) 1D experiments were acquired after a 3° flip angle of 0.5  $\mu\text{s}$  with a spinning speed of 40 kHz (1.9 mm probe). The reference was set using a solution of  $\text{AlCl}_3$  adjusted to pH of one with hydrochloric acid. The  $^1\text{H}$ – $^{27}\text{Al}$  2D spectrum was acquired at a spinning rate of

62.5 kHz using the *D*-HMQC technique with a SR4 recoupling of 256  $\mu\text{s}$  [39]. And the  $^{27}\text{Al}$  STMAS spectrum was acquired with a spinning rate of 40 kHz using the DQF-STMAS-split-t1 pulse sequence [40]. The  $^{27}\text{Al}$  1D NMR spectra were simulated using the program SIMPSON [41].

### 2.3. Preparation

High-throughput investigations under solvothermal reaction conditions were carried out by employing our 48 high-throughput reactor system equipped with Teflon reactors of 0.25 mL each [32–34]. Using this setup the reaction temperature (120–200 °C), the reaction time (12–18 h) the molar ratio of  $\text{Al}^{3+}$ : $\text{H}_4\text{TCPB}$  (between 1:2 and 8:2, one unit corresponds to the amount of 4.48  $\mu\text{mol}$ ) and the volume ratio DMF (*N,N*-dimethylformamide): $\text{H}_2\text{O}$  (between 0:150  $\mu\text{L}$  and 150:0  $\mu\text{L}$ ), the overall concentration, the effect of additives (2M NaOH, 2M  $\text{HNO}_3$ , benzoic acid, pyridine, methanol, ethanol, THF) and other solvents (pyridine, methanol, ethanol, THF) were investigated (Table S1).

The synthesis optimization led to the following optimized synthesis procedure: To a mixture of  $\text{Al}(\text{NO}_3)_3 \cdot 9\text{H}_2\text{O}$  (24.6  $\mu\text{mol}$ , 12.7 mg, Merck) and 1,2,4,5-Tetrakis(4-carboxyphenyl)benzene ( $\text{H}_4\text{TCPB}$ , 8.96  $\mu\text{mol}$ , 5.0 mg, Sigma Aldrich) 100  $\mu\text{L}$  of *N,N*-dimethylformamide (1.30 mmol, Grüsing) and 50  $\mu\text{L}$  of deionized water (2.78 mmol) were added. The reactor was sealed carefully and heated at 150 °C for 18 h. The reactor was cooled down within 12 h to room temperature. The product was filtered off, washed with water (CAU-9as) and subsequently activated at 150 °C at  $10^{-2}$  kPa for 16 h (CAU-9act). Elemental analysis in combination with the results of the thermogravimetric measurements revealed that CAU-9as has the composition of  $[\text{Al}_2(\text{OH})_2(\text{TCPB})] \cdot 2 \text{DMF}$  and contains small amounts of X-ray amorphous  $\text{AlO}(\text{OH})$  (8.5 wt-%). Although many synthesis parameters were investigated a remaining impurity of  $\text{AlO}(\text{OH})$  was detected, which could not be removed. This side product was taken into account for the characterization.

### 2.4. Molecular simulations

All calculations were carried out using the program Materials Studio 4.1 [35] following the procedure previously described [10,16]. The lattice parameters were fixed to the experimental values and energy minimization calculations were carried out using the universal force field (UFF) as implemented in the Forcite module in Materials Studio 4.1 [35]. In order to get reasonable force field parameters for the calculations the values for  $\text{Fe}^{2+}$  ions had to be used for the  $\text{Al}^{3+}$  ions. This is because the UFF only contains values for aluminum in a tetrahedral coordination environment [16]. This approach has previously shown to lead to a suitable structural starting model, which can be used in the subsequent Rietveld refinement with TOPAS Academic 4.1 [36].

For setting up a structural model of CAU-9 the structure of MIL-118B, which crystallizes in the orthorhombic space group *Pbam* was used and the  $\text{H}_4\text{BTEC}$  linker molecule was extended to  $\text{H}_4\text{TCPB}$  through insertion of phenyl rings. The structure prediction resulted in a model with the space group symmetry *P1*. The subsequent Rietveld refinement did not, however, lead to a satisfying agreement between observed and calculated intensities. Starting from the structure of the recently reported Al-PMOF [42], which exhibits the same topology as MIL-118B but crystallizes in the higher symmetric orthorhombic space group *Cmmm*, a model which lead to an appropriate refinement was obtained. The porphyrine ring was replaced by a benzene ring and the lattice parameters were determined from the position of the first three reflections 200, 001 and 201.

## 3. Results and discussion

### 3.1. Discovery and synthesis optimization

High-throughput methods employing our home build 48 reactor system [32–34] were used in the investigation of the system  $\text{Al}^{3+}/\text{H}_4\text{TCPB}/\text{H}_2\text{O}/\text{DMF}/\text{additive}$ . In contrast to the synthesis of MIL-118 which was carried out in water a temperature of 210 °C [30], we chose to use DMF as a solvent to improve the solubility of the linker molecule, which allows us to work at a lower reaction temperature of 150 °C. In the first high-throughput reaction the molar ratio  $\text{Al}:\text{H}_4\text{TCPB}$  was varied from 1:2 to 8:2 and the volume ratio  $\text{H}_2\text{O}:\text{DMF}$  was kept at 50:100  $\mu\text{L}$  (Fig. 2). The detailed synthesis conditions and a selection of corresponding PXRD patterns are shown in Table S1 and Fig. S1, respectively.

Already in the first investigations highly crystalline products could be obtained (Fig. S1). The crystallinity of the samples was assessed by considering the signal to noise ratio and peak width of the measured PXRD patterns. Nevertheless, further investigations (app. 130 reactions) studying the reaction temperature e.g. at lower and higher temperatures (120 °C, 130 °C and 200 °C) and the reaction time (between 12 and 24 h) were carried out but did not lead to an improvement of the crystallinity. The influence of the volume ratio of  $\text{H}_2\text{O}:\text{DMF}$  was scanned from 0:150 to 150:0  $\mu\text{L}$  and the use of ethanol instead of DMF led to a strong decrease of the crystallinity of the samples. Addition of 2M NaOH solution in the range of 10–150  $\mu\text{L}$  or 2M  $\text{HNO}_3$  solution in the range of 5–30  $\mu\text{L}$  also lead to a decrease of crystallinity. Although many reactions were carried out, the formation of X-ray amorphous  $\text{Al}(\text{OH})_3$  or  $\text{AlO}(\text{OH})$  could not be prevented. In the PXRD patterns of the activated compound (Fig. S2) one reflection is observed that can be assigned to boehmite ( $\text{AlO}(\text{OH})$ ). The presence of the latter was successfully confirmed by  $^{27}\text{Al}$  MAS NMR spectroscopy.

Synthesis optimization led to following optimum molar ratio of the starting materials:  $\text{Al}^{3+}:\text{H}_4\text{TCPB}:\text{DMF}:\text{H}_2\text{O} = 5.5:2:145:310$ . A reaction temperature of 150 °C and a reaction time of 18 h with cooling down for 12 h was found to be optimal.

### 3.2. Crystal structure

The PXRD pattern of CAU-9act could not be directly indexed. Nevertheless, taking the structure of Al-PMOF into account a suitable structural model was set up [42]. The quadratic Bragg equation was used to determine the starting cell parameters from the position of the first three reflections in the powder pattern.

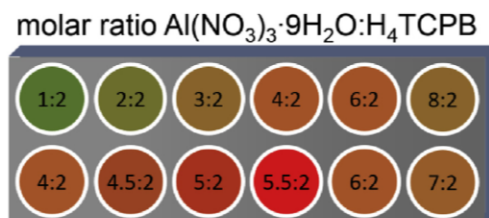
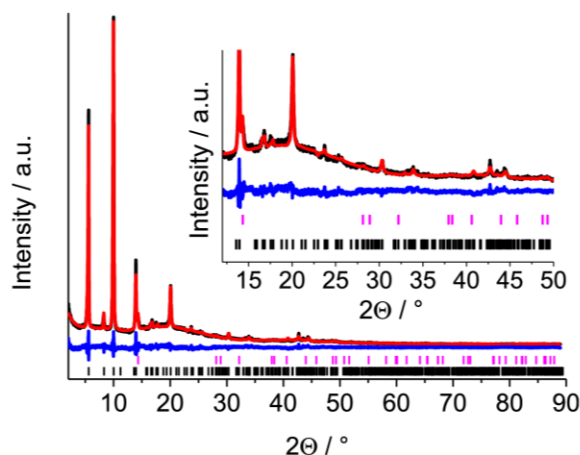


Fig. 2. Results of the high-throughput investigation of the first screening investigations of the system  $\text{Al}^{3+}/\text{H}_4\text{TCPB}/\text{DMF}/\text{H}_2\text{O}/\text{additive}$ . The value of 1 corresponds to 4.48  $\mu\text{mol}$  of starting material. To demonstrate the reproducibility of the synthesis some reactions were carried out twice using the same molar ratios. The increasing crystallinity is shown by the change of the color. Green color indicates less, red color shows higher crystallinity. Samples with the highest crystallinity could be obtained at a molar ratio  $\text{Al}^{3+}:\text{H}_4\text{TCPB}$  of 5.5:2 and a volume ratio  $\text{H}_2\text{O}:\text{DMF}$  of 50:100  $\mu\text{L}$ . (For interpretation of the references to color in this figure legend, the reader is referred to the web version of this article.)



**Fig. 3.** Rietveld plot for the refinement of activated CAU-9 ( $\lambda = 1.5406 \text{ \AA}$ ). For the refinement the impurity of boehmite was taken into account. The observed intensities are shown in black, the calculated intensities in red. The blue line is the difference plot, vertical bars mark the Bragg reflection positions. The ticks for CAU-9act are shown in black, those for boehmite are shown in pink. (For interpretation of the references to color in this figure legend, the reader is referred to the web version of this article.)

These parameters were used for setting up a structural model employing force field calculations and by appropriately modifying the linker molecules. The structural model of CAU-9 was successfully refined using the Rietveld method using TOPAS Academic v4.1 (Fig. 3, Table 1) [36]. The cif-file and a table with selected bond lengths are reported in the supporting information (Table S2).

The asymmetric unit of CAU-9act is shown in Fig. S3 and contains one  $\text{Al}^{3+}$  ion, one oxygen atom corresponding to the  $\mu\text{-OH}$  group and a linker molecule on a special position (*mmm* symmetry). The structure of CAU-9act contains chain-type inorganic building units composed of *trans* corner-sharing  $\text{AlO}_6$  polyhedra, which are the IBUs predominantly observed in Al-MOFs synthesized in the presence of water. The octahedra are slightly distorted ( $\text{Al-O1/O2}$  bond lengths: 1.86(2) and 1.94(1)  $\text{\AA}$ ,  $\text{O1-Al1-O2} = 83.9(5)^\circ$ ). These numbers agree well with values previously reported for different Al-MOFs [23,28,30,31]. Each carboxylate group bridges two adjacent  $\text{Al}^{3+}$  ions (Fig. 4, upper left), and thus each  $\text{TCPB}^{4-}$  linker molecule connects four of IBUs. Fig. S4 shows the connection of one  $\text{TCPB}^{4-}$  ion to four different IBUs. The resulting framework possesses two different kinds of one dimensional elliptical pores ( $5 \times 9 \text{ \AA}$  and  $4.5 \times 10.4 \text{ \AA}$ , van der Waals radii subtracted), which are running along [010] (Fig. 4, upper right). These pores are connected by small windows (3  $\text{\AA}$  in diameter) in the [001] and [110] direction (Fig. 4, bottom right and left, respectively).

**Table 1**  
Results of the Rietveld refinement of CAU-9.

Spacegroup	<i>Cmmm</i>
<i>a</i>	31.562(4) $\text{\AA}$
<i>b</i>	6.642(7) $\text{\AA}$
<i>c</i>	10.6612(7) $\text{\AA}$
GOF	1.54
$R_{\text{Bragg}}$	0.68%
$R_{\text{WP}}$	5.28%
Wavelength	$\text{Cu K}\alpha_1$
Atoms	10
Restraints	15

### 3.3. Thermal stability

Temperature dependent X-ray powder diffraction was carried out in air to investigate the structural changes upon thermal treatment (Fig. 5 and Fig. S5). Therefore a sample of CAU-9as in a capillary (0.5 mm) was heated up to 250  $^\circ\text{C}$  in steps of 15  $^\circ\text{C}$  steps and from 250  $^\circ\text{C}$  to 500  $^\circ\text{C}$  in steps of 25  $^\circ\text{C}$ . CAU-9 is stable up to approximately 480  $^\circ\text{C}$ . Pronounced changes of the relative intensities are observed which are due to the loss of the occluded solvent molecules. Only very small shifts of the reflections are found which demonstrates the rigidity of the framework.

The temperature dependent PXRD data was also employed in parametric Pawley refinements in the space group *Cmmm* using the software Powder3D parametric (Fig. 5 left) [38]. Only small changes in the lattice parameters are noticeable. This corresponds to the slightly decreasing length of the *c*-axis (10.8271(6) to 10.5121(4)  $\text{\AA}$ ). Also a shrinking of the length of the *b*-axis is observed (6.606(2) to 6.574(2)  $\text{\AA}$ ). This decrease is caused by the removal of the guest molecules. At higher temperatures the thermal expansion leads to an increase of the *b*-axis to 6.623(5)  $\text{\AA}$ .

To quantify the mass of guest molecules incorporated, thermogravimetric investigations were performed under air with a heating rate of 4 K/min for CAU-9as and CAU-9act (Fig. 6). The results obtained correspond well to that of the temperature dependent PXRD measurements. The weight loss above 480  $^\circ\text{C}$  can be attributed to the decomposition of the framework. Quantitative evaluation of the data obtained by elemental analysis and thermogravimetric measurements shows that X-ray amorphous  $\text{Al}(\text{OH})_3$  or  $\text{AlO}(\text{OH})$  or mixtures thereof must be present in CAU-9as. The presence of impurities containing  $\text{AlO}_6$  polyhedra was also confirmed by NMR spectroscopy. For the calculations it was assumed that the weight loss above 480  $^\circ\text{C}$  is only due to the decomposition of the framework, i.e. the oxidation of the linker molecule, and that  $\text{Al}_2\text{O}_3$  was formed as the final product. PXRD measurements of the final residue only showed the presence of an X-ray amorphous product. Taking the molar ratio of  $\text{Al}:\text{TCPB}^{4-} = 2:1$  in CAU-9 into account the mass difference was assigned to boehmite ( $\text{AlO}(\text{OH})$ ). Because of the presence of nitrogen in the elemental analysis of CAU-9as the first step in the TG curve is assigned to the removal of DMF molecules. A relatively good agreement of calculated and observed values for the thermogravimetric and elemental analyses is obtained for the formula  $([\text{Al}_2(\text{OH})_2(\text{TCPB})] \cdot 2 \text{ DMF})$  (CAU-9as) and  $([\text{Al}_2(\text{OH})_2(\text{TCPB})])$  (CAU-9act) taking into account the presence of approximately 0.85 equivalents of boehmite ( $\text{AlO}(\text{OH})$ ), which corresponds to 8.5 wt-% in the reaction product (Table 2). The first weight loss observed between 170 and 300  $^\circ\text{C}$  for CAU-9as amounts to 18.1% and corresponds well to the loss of two solvent molecules (calc. 17.2%). The activated sample CAU-9act exhibits almost no weight change up to 300  $^\circ\text{C}$ . Upon storage under ambient conditions no water molecules were adsorbed and hence the hydrophobic character of the compound is confirmed. Above 300  $^\circ\text{C}$  only a small weight change up to the decomposition temperature is observed. This could be due to small amounts of residual solvent molecules and the dehydration of boehmite ( $\text{AlO}(\text{OH})$ ) [43]. The results of the thermogravimetric and elemental analyses are summarized in Table 2.

### 3.4. IR- and NMR-Spectroscopy

The IR spectra of CAU-9as and CAU-9act in comparison with the one of  $\text{H}_4\text{TCPB}$  are shown in Fig. S6 and Fig. 7. Main vibrations discussed in the manuscript are labeled with asterisks. Bands of small intensity (Fig. S6) appear at 3702  $\text{cm}^{-1}$  in the spectra of the title compound. These are due to the presence of the

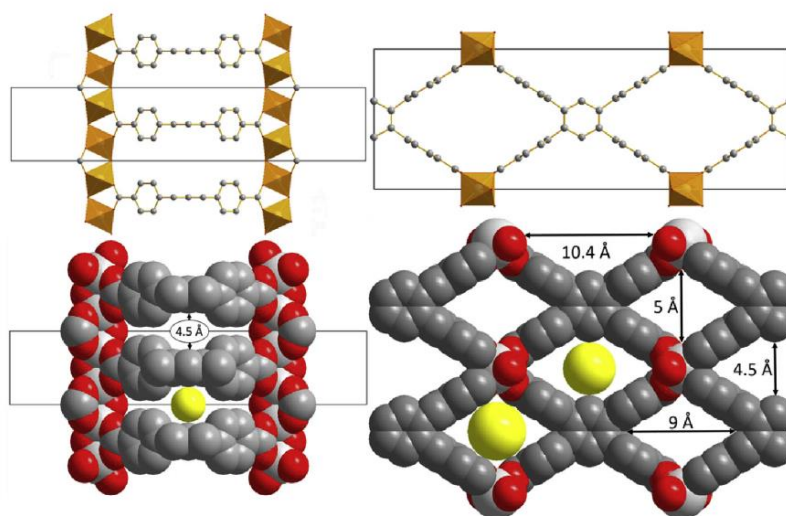


**Fig. 4.** Crystal structure of CAU-9act. Chains of *trans* corner-sharing  $\text{AlO}_6$  polyhedra are connected by the  $\text{TCPB}^{4-}$  linker molecule, here shown along [001] (upper left) and along [010] (upper right) in ball-and-stick model. The corresponding space filling models with the pore diameters obtained by taking the van der Waals radii into account are shown on the bottom left and right, respectively.  $\text{AlO}_6$  polyhedra are presented in orange, Al atoms in light grey, oxygen in red and carbon atoms are dark grey. (For interpretation of the references to color in this figure legend, the reader is referred to the web version of this article.)

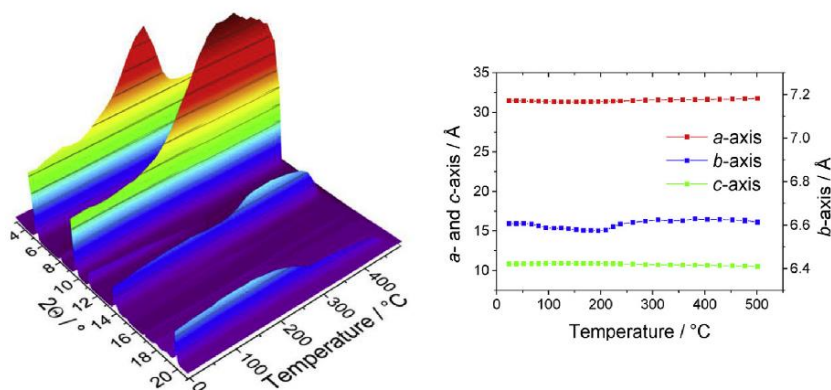


**Fig. 5.** Results of the temperature dependent PXRD measurements of CAU-9as (left). On the right the results of the parametric Pawley refinement are shown. Top, middle and bottom line correspond to the *a*-, *b*- and *c*-axis, respectively. Standard deviations, although included, are too small to be recognizable.

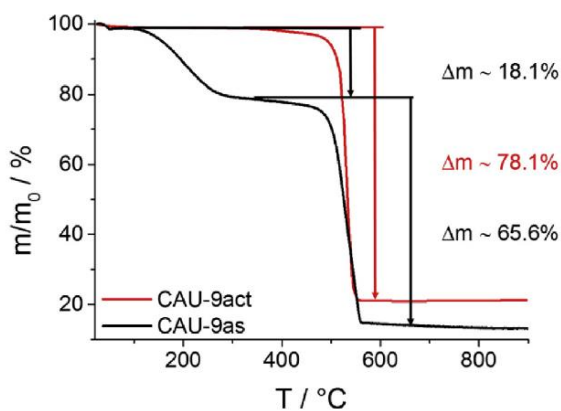


**Fig. 6.** Results of the thermogravimetric measurements of the CAU-9as and CAU-9act. The weight losses are marked in the graphs.

$\mu$ -OH-groups in the inorganic building unit. Changes are mainly observed for the bands corresponding to the CO vibrations of the carboxylic acid group. The C=O stretching vibration located at  $1680\text{ cm}^{-1}$  in the spectrum for  $\text{H}_4\text{TCPB}$ . Due to the coordination to the  $\text{Al}^{3+}$  ions a band at  $1608\text{ cm}^{-1}$  is observed that can be assigned to the asymmetric stretching vibration [24,44]. The band at  $1680\text{ cm}^{-1}$  in the spectrum of CAU-9as is due C=O stretching vibration of the DMF molecules occluded inside the channels. This vibration nearly disappears upon activation of the sample. The symmetric stretching vibration of the coordinating carboxylate groups is located at  $1416\text{ cm}^{-1}$ . At  $1556$  and  $1519\text{ cm}^{-1}$  the ring-stretching vibrations are observed, whereas C–H out of plane deformation vibrations of the aromatic ring absorb at  $854$  (1,2,4,5-substituted aromatic ring) and  $771\text{ cm}^{-1}$  (1,4-substituted aromatic ring). The latter bands are characteristic for the substitution pattern and are observed in all three IR-spectra [14]. An OH deformation vibration is located at  $970\text{ cm}^{-1}$  which corresponds to  $\mu$ -OH groups bridging the  $\text{Al}^{3+}$  ions [45].

**Table 2**

Results of the thermogravimetric and the elemental analyses. The measured values are compared with the theoretical ones.

Molecular formula	Elemental analysis [%]			Thermogravimetric analysis weight loss [%]			
	C	H	N	Step 1 100–300 °C	Step 2 480–600 °C	Step 3 >600 °C	
CAU-9act with 8.5 wt-% boehmite [Al <sub>2</sub> (OH) <sub>2</sub> (TCPB)]	Meas.	53.8	2.9	0.3	0	78.1	21.9
	Calc.	56.6	3.0	0	0	77.8	20.8
CAU-9as with 8.5wt-% boehmite [Al <sub>2</sub> (OH) <sub>2</sub> (TCPB)] · 2 DMF	Meas.	56.9	4.7	3.7	18.1	65.6	16.3
	Calc.	57.6	4.2	1.7	17.2	65.4	17.4

The <sup>27</sup>Al MAS spectra of both the as-synthesized and activated sample (Fig. 8) indicate the presence of an AlO<sub>6</sub>-containing impurity (−10 to +20 ppm signal deconvoluted into two signals). In CAU-9act the signal corresponds to around 27 at-% (7.7 wt-%) of the total intensity of the <sup>27</sup>Al spectrum. This is in agreement with the 8.5 wt-% of boehmite (AlO(OH)) impurity proposed from the TG data. As expected from the crystallographic structure, the <sup>27</sup>Al-NMR spectrum of CAU-9 exhibits a single resonance with the typical shape of a second-order quadrupolar interaction (0 to −50 ppm). The quadrupolar coupling constant (C<sub>Q</sub>) of the activated sample (C<sub>Q</sub> = 8.8 MHz) is smaller than the one of the as-synthesized sample (C<sub>Q</sub> = 10.3 MHz). The larger C<sub>Q</sub> for the latter is probably due to an increased distortion of the AlO<sub>6</sub> octahedra in the framework caused by the presence of two DMF molecules per formula unit.

As seen from the deconvolution of the <sup>27</sup>Al spectra depicted in Fig. 8, for both samples, the resonances for boehmite and CAU-9 exhibit some broadening coming from a distribution of the isotropic chemical shift and of the quadrupolar coupling constant. Indeed, the STMAS spectrum of the activated sample (Fig. 9) shows that the right “horn” slowly moves towards lower chemical shift values, while the left “horn” shift stays constant. This increases the splitting between the two horns resulting in a larger C<sub>Q</sub> while the asymmetry parameter η is around zero for all F2 slices. At the same time the position of the left horn remains constant which implies that the trend of the isotropic chemical shift is compensating for the small increase of the second-order quadrupolar shift.

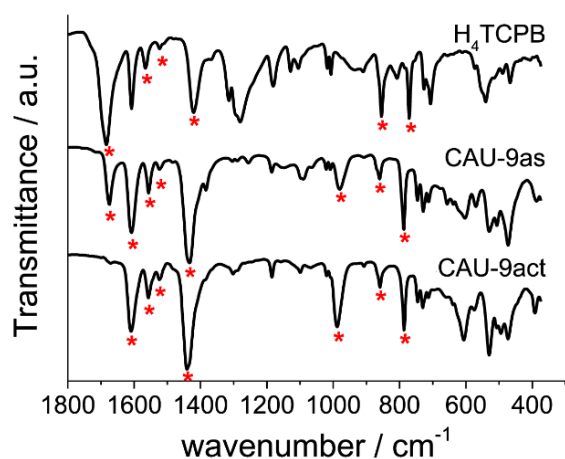


**Fig. 7.** IR spectra from 350–1800 cm<sup>−1</sup> of H<sub>4</sub>TCPB, CAU-9as and CAU-9act. The full spectra are shown in Fig. S6. Main vibrations which are discussed in the manuscript are labeled with an asterisk.

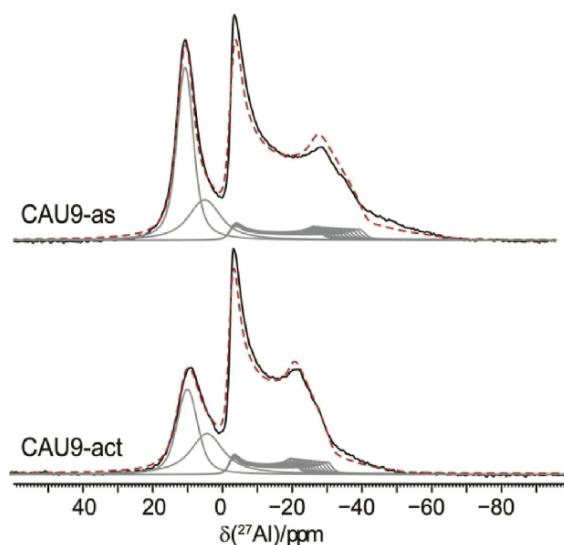


**Fig. 8.** <sup>27</sup>Al MAS spectra of CAU-9as (top) and CAU-9act (bottom) together with the deconvolution (sub-spectra in grey and sum in dashed red lines) taking into account the isotropic chemical shift and a second-order quadrupolar broadening. For both C<sub>Q</sub> is distributed over a range of roughly 2 MHz. (For interpretation of the references to color in this figure legend, the reader is referred to the web version of this article.)

The <sup>27</sup>Al 1D spectra of both samples were simulated by summing 11–12 sub-spectra of equally spaced C<sub>Q</sub> and isotropic shift. For the CAU-9act and CAU-9as samples the C<sub>Q</sub> was varied from 7.8 to 9.8 MHz and from 9.2 to 11.4 MHz, respectively, and the isotropic shift from 1.9 to 5.1 ppm and from 2.7 to 6.9 ppm, respectively. Only in this way the simulated spectra match the experimental ones confirming the presence of distribution of roughly 2 MHz. This distribution is assigned to local distortions and small rearrangements of the framework.

The <sup>1</sup>H NMR spectra (Fig. 10, right) of CAU-9act and CAU-9as exhibit three and four well resolved resonances. The <sup>1</sup>H signal of the methyl groups of the DMF molecules are clearly visible at 1.4 ppm. In contrast the signal of the protons attached to the sp<sup>2</sup> C-atom cannot be clearly assigned. Based on the results of the integration, the signal is hidden by the very intensive peak at 6.8 ppm which is assigned to the aromatic protons H4/H7 (Figs. 1 and 10). Analyzing the relative intensities leads to 2.2 DMF molecules per formula unit which matches well to the results of the TG data. In the <sup>1</sup>H–<sup>27</sup>Al HETCOR spectrum (Fig. 10, left) two cross peaks at 2.5 ppm/5.5 ppm and 2.5 ppm/(−30–0 ppm) are observed. While the former originates from AlO(OH) (boehmite) the latter is attributed to CAU-9act. Compared to the <sup>27</sup>Al 1D spectrum of CAU-9act the <sup>27</sup>Al resonance of boehmite is highfield shifted indicating that an additional proton free impurity probably Al<sub>2</sub>O<sub>3</sub> is also present in small amounts. Interestingly, the proton shift of the OH groups in CAU-9act and boehmite is identical within the limit of the experimental accuracy. For the as-synthesized material the incorporation of DMF molecules leads to a downfield shift of about 2.1 ppm–4.65 ppm for the μ–OH resonances which is due to hydrogen bond interactions between μ–OH and DMF. Such chemical shifts are similar to the ones previously observed in the case of MIL-53 [39]. The two remaining peaks at 6.8 and 7.8 ppm are assigned to the aromatic protons H4/H7 and H3, respectively (Fig. 1).

Finally, the <sup>13</sup>C spectra (Fig. 11 and Fig. S7) show five resonances which can be unequivocally assigned to the different carbon atoms

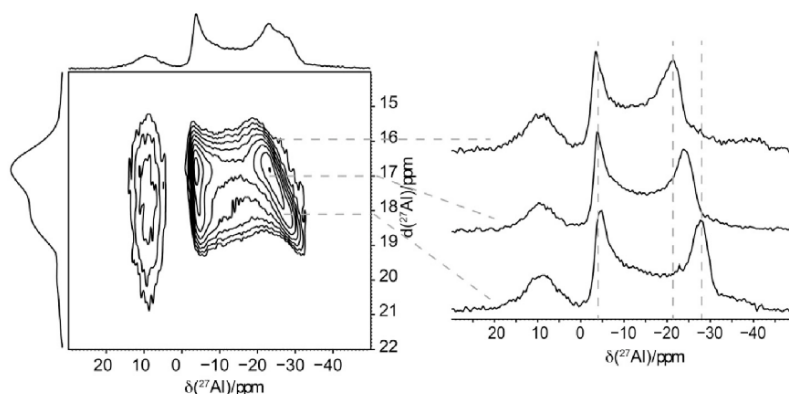


Fig. 9.  $^{27}\text{Al}$  STMAS spectrum of CAU-9act (left) with slices along F2 to demonstrate the continuous change of  $C_Q$  while the asymmetry  $\eta$  remains constant with a value close to zero.

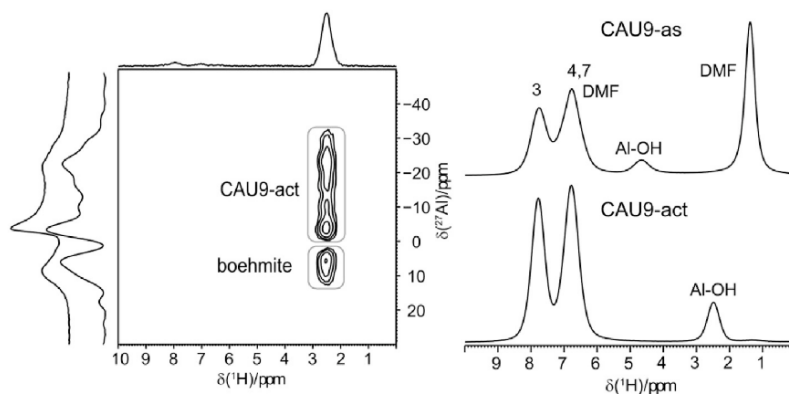


Fig. 10.  $^1\text{H}$ - $^{27}\text{Al}$  D-HMQC HETCOR spectrum of CAU-9act (left) showing the correlation of the proton resonance at 2.5 ppm and the  $^{27}\text{Al}$  resonance of both boehmite and CAU-9act. On top and to the left the F2 and F1 projections are displayed. For a better comparison also the  $^{27}\text{Al}$  1D spectrum for CAU-9act was added next to the F1 projection.  $^1\text{H}$  high-resolution MAS spectra (right) of CAU-9act (bottom) and CAU-9as (top) with together with an assignment of the resonances.

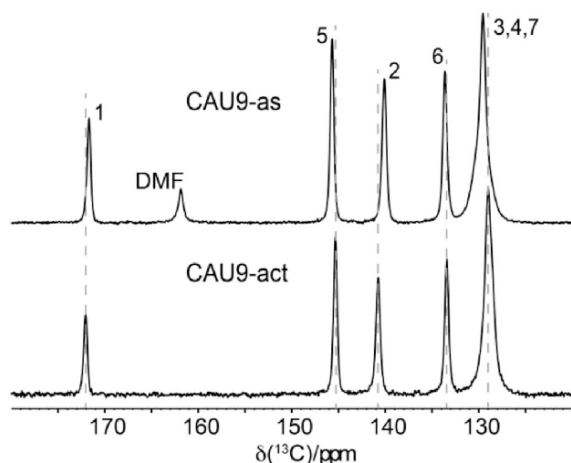


Fig. 11.  $^{13}\text{C}$  CP MAS spectra CAU-9act (bottom) and CAU-9as (top). The dashed vertical lines are guides for the eye.

of the TCPB linker and three additional resonances for the as-synthesized sample which are assigned to DMF at 29.8, 34.7 and 161.9 ppm. A close comparison of both  $^{13}\text{C}$  spectra shows small chemical shift differences between the two samples. The biggest shift differences of 0.5 and 0.7 ppm are observed for the C atom of the carboxylate group ( $\sim 171$  ppm) and the connected ipso-carbon atom ( $\sim 140$  ppm). Both are close to the inorganic building unit which will be effected most by the presence or absence of DMF molecules. Thus, those chemical shift differences confirm the rearrangement of the framework when DMF is removed. This observation is in accordance with the results of the temperature-dependent PXRD measurements.

$^{27}\text{Al}$ ,  $^1\text{H}$ , and  $^{13}\text{C}$  NMR spectra present noticeable differences between the as-synthesized and activated CAU-9 material. These changes in the spectra are attributed to a rearrangement of the CAU-9 framework after DMF is removed upon activation. However, unlike MIL-118, no rearrangement of the carboxylate groups from a mono- to bidentate coordination mode was observed.

### 3.5. Adsorption

Prior to all measurements CAU-9as was activated over night at  $150^\circ\text{C}$  and  $10^{-2}$  kPa. The  $\text{N}_2$ -sorption measurement at 77 K resulted



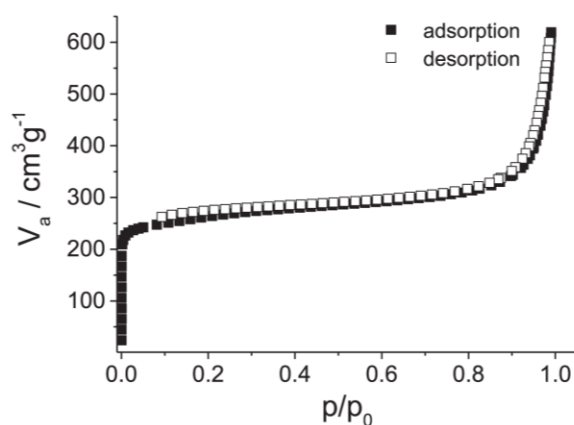


Fig. 12.  $N_2$ -sorption isotherms at 77 K. This isotherm was obtained for the sample containing X-ray amorphous  $Al(OH)_3$ .

in a Type I isotherm which is typical for microporous materials (Fig. 12) [46]. CAU-9as contains X-ray amorphous  $Al(OH)_3$  and  $Al(OH)_3$  impurities and therefore the values of the specific surface area and the micropore volume were corrected after the measurement taking the impurity as boehmite ( $Al(OH)_3$ ) into account. To determine the appropriate linear region for the BET analysis a Rouquerol-plot was calculated [46,47].

CAU-9 exhibits a weight corrected apparent specific surface area of  $1118 \text{ m}^2/\text{g}$  ( $1023 \text{ m}^2/\text{g}$  without correction) and a micropore volume of  $0.45 \text{ cm}^3/\text{g}$  ( $0.41 \text{ cm}^3/\text{g}$  without correction), the latter was calculated from the amount of adsorbed nitrogen at  $p/p_0 = 0.18$ . This value corresponds reasonably well to the solvent accessible volume calculated from the crystal structure using PLATON ( $0.55 \text{ cm}^3/\text{g}$ ), which uses a random probe molecule (water) with a diameter of  $2.6 \text{ \AA}$  [37]. Because of the small distance between the linker molecules ( $3.1 \text{ \AA}$ , Fig. 4) PLATON adds these pores when calculating the theoretical micropore volume. In sorption measurements these pores will probably not be accessible due to the kinetic diameter of the nitrogen molecule of  $3.64 \text{ \AA}$  [7].

To confirm the hydrophobic properties of CAU-9 water sorption experiments at 298 K were carried out (Fig. S9). A type III isotherm with two, not well-defined steps ( $p/p_0 = 0.4\text{--}0.6$  and  $0.6\text{--}1.0$ ) and a total uptake of  $0.23 \text{ g}\cdot\text{g}^{-1}$  is observed. CAU-9 exhibits a low affinity towards water which is proven by the low uptake in the water sorption isotherm at low pressures. The water uptake is smaller than the one reported for MIL-53 ( $0.3 \text{ g}\cdot\text{g}^{-1}$  [13]) or MIL-100/101(Cr) ( $1.43 \text{ g}\cdot\text{g}^{-1}$  and  $0.67 \text{ g}\cdot\text{g}^{-1}$ , respectively [13]).

#### 4. Conclusion

A new Al-MOF, noted CAU-9, was successfully synthesized and characterized. CAU-9 was discovered investigating the system  $Al^{3+}/H_4\text{TCPB}/\text{DMF}/H_2O/\text{additive}$ . A molar ratio of  $Al^{3+}:H_4\text{TCPB}:\text{DMF}:H_2O = 5.5:2:145:310$ , a reaction temperature of  $150 \text{ }^\circ\text{C}$  and a reaction time of 18 h with cooling down for 12 h was found to be optimal. An impurity could be found which was characterized as boehmite ( $Al(OH)_3$ ) in the activated compound. This impurity was taken into account for further characterization. Molecular simulations were carried out to obtain a structural model for the subsequent Rietveld refinement. The new MOF exhibits the same topology as observed for MIL-118B [30] or Al-PMOF [42]. CAU-9 is thermally highly stable up to  $480 \text{ }^\circ\text{C}$  substantiated by thermogravimetric and temperature dependent PXRD measurements.

Although an impurity of boehmite is present, the compound exhibits a BET-surface area and a micropore volume of  $1118 \text{ m}^2/\text{g}$  and  $0.45 \text{ cm}^3/\text{g}$ , respectively. The differences in the  $^{27}\text{Al}$ ,  $^1\text{H}$  and  $^{13}\text{C}$  solid-state NMR spectra between the as-synthesized and activated CAU-9 demonstrate a rearrangement of the framework upon removal of DMF molecules. In contrast to MIL-118 this does not lead to the formation of new bonds.

#### Acknowledgments

The authors acknowledge the Deutsche Forschungsgemeinschaft (SPP1362, SE 1417/3-2, STO 643/5-2) for funding. For the temperature dependent PXRD measurements we would like to thank Dr. rer. nat. Sasha Correll from STOE & Cie GmbH, Darmstadt. We also acknowledge the very helpful remarks of reviewer 1.

#### Appendix A. Supplementary data

Supplementary data related to this article can be found at <http://dx.doi.org/10.1016/j.micromeso.2015.04.023>.

#### References

- [1] Q.-L. Zhu, Q. Xu, Chem. Soc. Rev. 43 (2014) 5468–5512.
- [2] M.T. Wharmby, M. Snoyek, T. Rhauderwiek, K. Ritter, N. Stock, Cryst. Growth Des. 14 (2014) 5310–5317.
- [3] A. Corma, H. Garcia, F.X. Llabres i Xamena, Chem. Rev. 110 (2010) 4606–4655.
- [4] L.E. Kreno, K. Leong, O.K. Farha, M. Allendorf, R.P. Van Duyne, J.T. Hupp, Chem. Rev. 112 (2011) 1105–1125.
- [5] J.-R. Li, J. Sculley, H.-C. Zhou, Chem. Rev. 112 (2011) 869–932.
- [6] M. Eddaoudi, J. Kim, N. Rosi, D. Vodak, J. Wachter, M. O’Keeffe, O.M. Yaghi, Science 295 (2002) 469–472.
- [7] C.R. Reid, I.P. O’Koy, K.M. Thomas, Langmuir 14 (1998) 2415–2425.
- [8] N.C. Burtch, H. Jasuja, K.S. Walton, Chem. Rev. 114 (2014) 10575–10612.
- [9] N.L. Rosi, J. Kim, M. Eddaoudi, B. Chen, M. O’Keeffe, O.M. Yaghi, J. Am. Chem. Soc. 127 (2005) 1504–1518.
- [10] I. Senkowska, F. Hoffmann, M. Fröba, J. Getzschmann, W. Böhlmann, S. Kaskel, Micropor. Mesopor. Mat. 122 (2009) 93–98.
- [11] H. Reinsch, M. Feyand, T. Ahnfeldt, N. Stock, Dalton Trans. 41 (2012) 4164–4171.
- [12] F. Gándara, H. Furukawa, S. Lee, O.M. Yaghi, J. Am. Chem. Soc. 136 (2014) 5271–5274.
- [13] S.K. Henninger, F. Jeremias, H. Kummer, C. Janiak, Eur. J. Inorg. Chem. 2012 (2012) 2625–2634.
- [14] N. Reimer, B. Gil, B. Marszalek, N. Stock, CrystEngComm 14 (2012) 4119–4125.
- [15] Y. Wu, V.K. Peterson, E. Luks, T.A. Darwish, C.J. Kepert, Angew. Chem. 126 (2014) 5275–5278.
- [16] H. Reinsch, M. Krüger, J. Wack, J. Senker, F. Salles, G. Maurin, N. Stock, Micropor. Mesopor. Mat. 157 (2012) 50–55.
- [17] H. Reinsch, N. Stock, Micropor. Mesopor. Mat. 171 (2013) 156–165.
- [18] M. Gaab, N. Trukhan, S. Maurer, R. Gummaraju, U. Müller, Micropor. Mesopor. Mat. 157 (2012) 131–136.
- [19] C. Volkringer, D. Popov, T. Loiseau, G. Férey, M. Burghammer, C. Riekel, M. Haouas, F. Taulelle, Chem. Mater. 21 (2009) 5695–5697.
- [20] M. Haouas, C. Volkringer, T. Loiseau, G. Férey, F. Taulelle, Chem. Mater. 24 (2012) 2462–2471.
- [21] T. Wittmann, R. Siegel, N. Reimer, W. Milius, N. Stock, J. Senker, Chem. Eur. J. 21 (2015) 314–323.
- [22] T. Ahnfeldt, N. Guillou, D. Gunzelmann, I. Margiolaki, T. Loiseau, G. Férey, J. Senker, N. Stock, Angew. Chem. 121 (2009) 5265–5268.
- [23] T. Loiseau, C. Serre, C. Huguenard, G. Fink, F. Taulelle, M. Henry, T. Bataille, G. Férey, Chem. Eur. J. 10 (2004) 1373–1382.
- [24] S. Biswas, T. Ahnfeldt, N. Stock, Inorg. Chem. 50 (2011) 9518–9526.
- [25] T. Loiseau, L. Lecroq, C. Volkringer, J. Marrot, G. Férey, M. Haouas, F. Taulelle, S. Bourrelly, P.L. Llewellyn, M. Latroche, J. Am. Chem. Soc. 128 (2006) 10223–10230.
- [26] H. Reinsch, M.A. van der Veen, B. Gil, B. Marszalek, T. Verbiest, D. de Vos, N. Stock, Chem. Mater. 25 (2012) 17–26.
- [27] H. Reinsch, S. Waitschat, N. Stock, Dalton Trans. 42 (2013) 4840–4847.
- [28] C. Volkringer, T. Loiseau, M. Haouas, F. Taulelle, D. Popov, M. Burghammer, C. Riekel, C. Zlotea, F. Cuevas, M. Latroche, D. Phanon, C. Knöfel, P.L. Llewellyn, G. Férey, Chem. Mater. 21 (2009) 5783–5791.
- [29] H. Reinsch, B. Marszalek, J. Wack, J. Senker, B. Gil, N. Stock, Chem. Commun. 48 (2012) 9486–9488.
- [30] C. Volkringer, T. Loiseau, N. Guillou, G. Férey, M. Haouas, F. Taulelle, N. Audebrand, I. Margiolaki, D. Popov, M. Burghammer, C. Riekel, Cryst. Growth Des. 9 (2009) 2927–2936.

## 4 Synthese und Charakterisierung neuer und funktionalisierter MOFs basierend auf den Elementen der 13. Gruppe und deren spezielle optische Eigenschaften

---

- [31] C. Volkringer, T. Loiseau, N. Guillou, G. Férey, M. Haouas, F. Taulelle, E. Elkaim, N. Stock, *Inorg. Chem.* 49 (2010) 9852–9862.
- [32] S. Bauer, N. Stock, *Chem. Unserer Zeit* 41 (2007) 390–398.
- [33] N. Stock, *Chem. Ing. Tech.* 82 (2010) 1039–1047.
- [34] N. Stock, *Micropor. Mesopor. Mat.* 129 (2010) 287–295.
- [35] *Materials Studio v4.1*, Accelrys Software Inc.
- [36] A. Coelho, *Topas Academic 4.1*.
- [37] A.L. Spek, *PLATON, a Multipurpose Crystallographic Tool*, Utrecht University, Utrecht, The Netherlands, 2010.
- [38] R.E.D.P. Rajiv, M. Jansen, *Powder 3D Parametric*, 2010.
- [39] J. Wack, R. Siegel, T. Ahnfeldt, N. Stock, L. Mafra, J. Senker, *J. Phys. Chem. C* 117 (2013) 19991–20001.
- [40] R. Siegel, J. Rocha, L. Mafra, *Chem. Phys. Lett.* 470 (2009) 337–341.
- [41] M. Bak, J.T. Rasmussen, N.C. Nielsen, *J. Magn. Reson.* 147 (2000) 296–330.
- [42] A. Fateeva, P.A. Chater, C.P. Ireland, A.A. Tahir, Y.Z. Khimyak, P.V. Wiper, J.R. Darwent, M.J. Rosseinsky, *Angew. Chem.* 124 (2012) 7558–7562.
- [43] S. Ram, T.B. Singh, L.C. Pathak, *Phys. Status Solidi A* 165 (1998) 151–164.
- [44] H. Reinsch, M. Krüger, J. Marrot, N. Stock, *Inorg. Chem.* 52 (2013) 1854–1859.
- [45] J.M. Salazar, G. Weber, J.M. Simon, I. Bezverkhy, J.P. Bellat, *J. Chem. Phys.* 142 (2015) 124702.
- [46] K.S.W. Sing, D.H. Everett, R.A.W. Haul, L. Moscou, R.A. Pierotti, J. Rouquerol, T. Siemieniowska, *Pure Appl. Chem.* 57 (1985) 603–619.
- [47] J. Moellmer, E.B. Celer, R. Luebke, A.J. Cairns, R. Staudt, M. Eddaoudi, M. Thommes, *Micropor. Mesopor. Mat.* 129 (2010) 345–353.



#### 4.6.2 Polymorphous Al-MOFs Based on V Shaped Linker Molecules: Synthesis, Properties, and in Situ Investigation of Their Crystallization

Der folgende Artikel wurde im Jahre 2017 in der Fachzeitschrift *Inorganic Chemistry*, ACS veröffentlicht. Der Wiederabdruck erfolgte mit freundlicher Genehmigung der ACS. Reproduced with permission from:

M. Krüger, A. K. Inge, H. Reinsch, Y.-H. Li, M. Wahiduzzaman, C.-H. Lin, S.-L. Wang, G. Maurin, N. Stock, *Inorg. Chem.*, **2017**, *56*, 5851-5862. DOI: 10.1021/acs.inorgchem.7b00202.

Bei der Untersuchung des Systems  $\text{Al}^{3+}/4,4'$ -Benzophenondicarbonsäure ( $\text{H}_2\text{BPDC}$ )/DMF/ $\text{H}_2\text{O}$  mittels Hochdurchsatz- und *in situ*-Methoden konnte eine neue Verbindung der Zusammensetzung  $[\text{Al}(\text{OH})(\text{BPDC})]$  (CAU-21-BPDC) erhalten werden. Die Kristallstruktur konnte mit Hilfe von Einkristallröntgenbeugungsdaten bestimmt werden. CAU-21-BPDC kristallisiert in der tetragonalen Raumgruppe  $I422$  mit den Zellparametern  $a = b = 17.2528(7)$ ,  $c = 23.864(1)$  Å und ist aus oktanuclearen Ringen aus *cis*-eckenverknüpften  $\text{AlO}_6$ -Oktaedern aufgebaut, die die anorganischen Baueinheit formen. Die IBUs sind kubisch innen zentriert gepackt und je zwei IBUs sind durch zwei  $\text{BPDC}^{2-}$ -Ionen miteinander verbrückt. So entstehen eindimensionale, zugängliche Poren, die einen variablen Durchmesser von 3.6 – 6.5 Å aufweisen. Zusätzlich werden nicht zugängliche Poren durch die Verknüpfung der IBUs mit den  $\text{BPDC}^{2-}$ -Ionen ausgebildet. Das CAU-21-BPDC-Netzwerk ist polymorph zu dem von CAU-8-BPDC.<sup>[19]</sup> Wird 4,4'-Benzophenondicarbonsäure durch die geometrisch sehr ähnliche 4,4'-Oxydibenzoessäure ( $\text{H}_2\text{ODB}$ ) in der Synthese ersetzt, können Verbindungen, die zu CAU-8-BPDC und CAU-21-BPDC isoretikulär sind, erhalten werden. Weiterhin wurde ein Koordinationspolymer,  $[\text{Al}(\text{OH})(\text{HODB})_2]$ , synthetisiert und strukturell charakterisiert. Die beiden Al-MOFs basierend auf  $\text{H}_2\text{ODB}$  sind ebenfalls polymorph. Die Struktur von CAU-8-ODB konnte erfolgreich mit Hilfe von Röntgenpulverbeugungsdaten verfeinert werden, während für CAU-21-BPDC nur die Zellparameter erhalten und verfeinert werden konnten. Die Struktur wurde durch DFT-Rechnungen bestätigt. Die Verbindungen des CAU-8 Strukturtyps sind unter Luft bis ca. 350 °C stabil und porös gegenüber  $\text{N}_2$  und  $\text{CO}_2$ . Die MOFs mit CAU-21-Struktur sind bis 300 °C stabil, adsorbieren aber nur  $\text{CO}_2$ . Zusätzliche Informationen zu der Veröffentlichung befinden sich im Gangang.

## Polymorphous Al-MOFs Based on V-Shaped Linker Molecules: Synthesis, Properties, and in Situ Investigation of Their Crystallization

Martin Krüger,<sup>†</sup> A. Ken Inge,<sup>‡</sup> Helge Reinsch,<sup>†</sup> Yuan-Han Li,<sup>§</sup> Mohammad Wahiduzzaman,<sup>||</sup> Chia-Her Lin,<sup>⊥</sup> Sue-Lein Wang,<sup>§</sup> Guillaume Maurin,<sup>||</sup> and Norbert Stock<sup>\*,†</sup>

<sup>†</sup>Institut für Anorganische Chemie, Christian-Albrechts-Universität, Max-Eyth-Straße 2, 24118 Kiel, Germany

<sup>‡</sup>Berzelii Center EXSELENT on Porous Materials and Department of Materials and Environmental Chemistry, Stockholm University, Stockholm S-106 91, Sweden

<sup>§</sup>Department of Chemistry, National Tsing Hua University, Hsinchu 300, Taiwan

<sup>||</sup>Institut Charles Gerhardt Montpellier, UMR-5253 Université Montpellier CNRS ENSCM, Place E. Bataillon 34095, Montpellier cedex 05, France

<sup>⊥</sup>Department of Chemistry, Chung-Yuan Christian University, 200 Chung Pei Road, Chung-Li 32023, Taiwan

### Supporting Information

**ABSTRACT:** The in situ and systematic high-throughput investigation of the system  $\text{Al}^{3+}$ /4,4'-benzophenonedicarboxylic acid ( $\text{H}_2\text{BPDC}$ )/DMF/ $\text{H}_2\text{O}$  in the presence of various additives was carried out, and a new Al-MOF of composition  $[\text{Al}(\text{OH})(\text{BPDC})]$ , denoted as CAU-21-BPDC, was obtained. Its crystal structure was determined from single-crystal X-ray diffraction data (space group  $I422$ ,  $a = b = 17.2528(7)$  Å,  $c = 23.864(1)$  Å). The structure is built up by octanuclear rings of cis corner-sharing  $\text{AlO}_6$  polyhedra forming the inorganic building unit (IBU). These  $\{\text{Al}_8\text{O}_8\}$  IBUs are arranged in a **bcu** packing and connected via  $\text{BPDC}^{2-}$  ions in a way that each IBU is linked via two linker molecules to each of the eight adjacent IBUs. Thus, accessible, one-dimensional modulated pores with a diameter between 3.6 and 6.5 Å are formed. In addition, tetrahedral cavities are formed by the  $\text{BPDC}^{2-}$  linker molecules. The framework of CAU-21-BPDC is polymorphous with that of CAU-8-BPDC, which contains one-dimensional chains of trans corner-sharing  $\text{AlO}_6$  polyhedra connected by  $\text{BPDC}^{2-}$  ions. Replacing  $\text{H}_2\text{BPDC}$  by 4,4'-oxydibenzoic acid ( $\text{H}_2\text{ODB}$ ), which contains an oxygen atom between the phenyl rings instead of a keto group, leads to the synthesis of Al-MOFs isorecticular with CAU-8-BPDC and CAU-21-BPDC. In addition, a coordination polymer,  $[\text{Al}(\text{HODB})_2(\text{OH})]$ , was discovered and structurally characterized. The structure of CAU-8-ODB was refined from powder X-ray diffraction data, while a Pawley refinement was carried out for CAU-21-ODB to determine the lattice parameters and confirm phase purity. The structure of CAU-21-ODB was confirmed using density functional theory (DFT) calculations. A thorough characterization shows that the CAU-8 and CAU-21-type structures are stable up to 350 and 300 °C in air, respectively, almost independent of the linker molecules incorporated. The former MOFs are porous toward  $\text{N}_2$  and  $\text{CO}_2$ , while the latter only adsorb  $\text{CO}_2$ .



### INTRODUCTION

In the past few years a large number of porous metal–organic frameworks (MOFs) based on trivalent aluminum cations have been reported.<sup>1–3</sup> The increasing interest in these compounds is due to their high thermal and chemical stability.<sup>4</sup> Furthermore,  $\text{Al}^{3+}$  salts are commercially available, which makes the synthesized MOF materials interesting for industrial applications.<sup>5</sup> The high stability allows postsynthetic modification (PSM) to introduce versatile functional groups to the MOF framework.<sup>6–10</sup> The use of prefunctionalized linker molecules is an alternative way to vary the chemical and physical properties of the pore walls in order to tune the

sorption behavior and to allow for PSM.<sup>11–14</sup> From a chemist's point of view the use of aluminum for MOF synthesis is interesting and quite challenging at the same time, due to its rich aqueous solution chemistry.<sup>15,16</sup> The diversity of inorganic building units (IBUs) in Al-MOFs<sup>1–3,17,18</sup> leads in combination with the virtually limitless possible organic linker molecules to various framework structures.<sup>19</sup> In Al-MOFs, solely octahedral coordination of the  $\text{Al}^{3+}$  cations has been identified,<sup>20</sup> and with the exception of CAU-4<sup>21</sup> only IBUs containing corner- and/or

Received: February 28, 2017

edge-sharing  $\text{AlO}_6$  polyhedra have been reported. The structural diversity of these IBUs ranges from isolated  $\text{AlO}_6$  octahedra<sup>21</sup> to 1D building units<sup>11–13,22–31</sup> and ringlike IBUs<sup>20,32–34</sup> to even more complex structures.<sup>18,34–37</sup> During the past few years, we have systematically studied the influence of the ligand size, shape, and flexibility on the structure of Al-MOFs.<sup>1,2</sup> In the course of the investigation of the system  $\text{Al}^{3+}/4,4'$ -benzophenonedicarboxylic acid ( $\text{H}_2\text{BPDC}$ )/water/DMF the new Al-MOF CAU-8-BPDC ( $[\text{Al}(\text{OH})(\text{BPDC})]$ ) was discovered and fully characterized.<sup>23</sup> In addition a second crystalline phase was observed that was difficult to obtain as a phase-pure compound.

Al-MOFs are usually obtained under solvothermal reaction conditions, and their crystallization can be studied by time-resolved X-ray diffraction.<sup>38–48</sup> These investigations render information regarding crystallization kinetics<sup>40</sup> or the formation of crystalline intermediate phases or additional byproducts. Hence, in situ studies can help to get insights into the crystallization process and they can even be used to establish a possible reaction path.<sup>49</sup>

In this contribution, we report the results of the in situ studies of the crystallization of CAU-8-BPDC and the phase-pure synthesis of the hitherto unknown polymorphic second phase in the system  $\text{Al}^{3+}/4,4'$ -benzophenonedicarboxylic acid ( $\text{H}_2\text{BPDC}$ )/water/DMF, as well as the isorecticular compounds that are formed when  $\text{H}_2\text{BPDC}$  is replaced by 4,4'-oxydibenzoic acid ( $\text{H}_2\text{ODB}$ ). All new compounds were thoroughly characterized by powder X-ray diffraction (PXRD) combined with density functional theory (DFT) calculations, thermogravimetric analysis, elemental analysis, and  $^1\text{H-NMR}$  and IR spectroscopy as well as gas sorption measurements.

## EXPERIMENTAL SECTION

**Materials and Methods.** The chemicals used in the syntheses are commercially available and were used without further purification. Organic linker molecules were purchased from TCI Europe NV. Discovery and synthesis optimization were carried out employing our 24-high-throughput (HT) reactor system for solvothermal reactions.<sup>50–54</sup> This reactor system contains custom-made Teflon reaction vessels with a maximum volume of 2 mL. For scale-up syntheses, 30 mL Teflon-lined steel autoclaves were used. In situ and ex situ investigations were carried out in 5 mL Schott Duran glass reactors with vigorous stirring. The high-throughput PXRD measurements were performed in transmission geometry using a STOE HT diffractometer equipped with an  $xy$  stage and an image plate detector system ( $\text{Cu K}\alpha_1$  radiation). Collection of high-resolution PXRD data was possible on a STOE Stadi-P powder diffractometer equipped with a MYTHEN1K detector system ( $\text{Cu K}\alpha_1$  radiation). Temperature-dependent high-resolution powder diffraction data were recorded on a STOE StadiP diffractometer using  $\text{Cu K}\alpha_1$  radiation and equipped with a MYTHEN1K detector. These measurements were carried out in air in 0.5 mm quartz capillaries in the range of  $2\text{--}44^\circ 2\theta$ . Single-crystal X-ray diffraction data were collected on a Bruker D8 Venture instrument equipped with a PHOTON 100 CMOS detector using  $\text{Mo K}\alpha$  radiation (CAU-21-BPDC) and on a Bruker APEX DUO diffractometer equipped with  $\text{Cu K}\alpha_1$  radiation ( $[\text{Al}(\text{HODB})_2(\text{OH})]$ ).  $^1\text{H-NMR}$  spectroscopy was carried out on a Bruker DRX 500 spectrometer at 200 MHz. IR spectra were recorded on an ATI Matheson Genesis spectrometer equipped with an ATR unit in the spectral range of  $400\text{--}4000\text{ cm}^{-1}$ . Thermogravimetric analyses were performed using a NETZSCH STA 409 CD analyzer. The samples were heated in  $\text{Al}_2\text{O}_3$  crucibles at a rate of  $4\text{ K min}^{-1}$  in a flow of air ( $75\text{ mL min}^{-1}$ ). The TG data were corrected for buoyancy and current effects. A HEKAtech Euro EA Elemental Analyzer was used for elemental analysis. Sorption experiments were carried out using a Belsorp-max instrument (BEL JAPAN INC.) and a Micromeritics

ASAP2020 system. Before the sorption experiments, the samples were activated at  $200^\circ\text{C}$  under reduced pressure ( $10^{-2}\text{ kPa}$ ) for 48 h.

**HT Experiments To Afford CAU-21-BPDC (1).** High-throughput investigations under solvothermal reaction conditions were carried out for the system  $\text{Al}^{3+}/4,4'$ -benzophenonedicarboxylic acid ( $\text{H}_2\text{BPDC}$ )/water/DMF by employing our 24-high-throughput reactor system equipped with Teflon reactors with a volume of 2 mL.<sup>52–54</sup> Using this setup the reaction temperature ( $110\text{--}150^\circ\text{C}$ ), the reaction time ( $12\text{--}24\text{ h}$ ), the  $\text{Al}^{3+}:\text{H}_2\text{BPDC}$  molar ratio (between 4:3 and 7:8; one unit corresponds to the amount of  $37\text{ }\mu\text{mol}$ ), the DMF ( $N,N$ -dimethylformamide): $\text{H}_2\text{O}$  volume ratio (between 100:400  $\mu\text{L}$  and 400:100  $\mu\text{L}$ ), and the effect of additives ( $10\text{--}15\text{ mg}$  benzoic acid) were investigated (Table S1 in the Supporting Information). Phase-pure CAU-21-BPDC can only be obtained as microcrystalline powders.

**Optimized Reaction Conditions and Scale-Up Synthesis for CAU-21-BPDC (1).** The HT synthesis optimization led to the following optimized synthesis procedure: to a mixture of  $129.6\text{ }\mu\text{L}$  of 2 M  $\text{Al}(\text{NO}_3)_3\cdot 9\text{H}_2\text{O}$  in  $\text{H}_2\text{O}$  ( $259\text{ }\mu\text{mol}$ ), 70 mg 4,4'-benzophenonedicarboxylic acid ( $\text{H}_2\text{BPDC}$ ,  $259\text{ }\mu\text{mol}$ ), and 10 mg benzoic acid ( $\text{HBA}$ ,  $82\text{ }\mu\text{mol}$ ) were added 300  $\mu\text{L}$  of  $N,N$ -dimethylformamide (3.86 mmol) and 70.4  $\mu\text{L}$  of deionized water (5.36 mmol). The reactor was sealed and heated to  $110^\circ\text{C}$  within 6 h, held at this temperature for 24 h, and then cooled to room temperature within 72 h. The product was filtered off, washed with  $N,N$ -dimethylformamide at  $65^\circ\text{C}$  for 3 h, filtered again, and subsequently activated at  $200^\circ\text{C}$  at  $10^{-2}\text{ kPa}$  for 48 h. The additional washing step in DMF is necessary because the raw product contains recrystallized linker molecules.

Larger amounts of CAU-21-BPDC can be obtained using 648.2  $\mu\text{L}$  of 2 M  $\text{Al}(\text{NO}_3)_3\cdot 9\text{H}_2\text{O}$  in  $\text{H}_2\text{O}$  (1.3 mmol), 350 mg of 4,4'-benzophenonedicarboxylic acid ( $\text{H}_2\text{BPDC}$ , 1.3 mmol), 50 mg of benzoic acid (410  $\mu\text{mol}$ ), 1.5 mL of  $N,N$ -dimethylformamide (19.3 mmol), and 352  $\mu\text{L}$  of deionized water (26.8 mmol) in a 30 mL Teflon lined steel autoclave. The temperature program and the additional washing and activation steps are the same as in the optimized synthesis conditions of CAU-21-BPDC (yield: 0.27 g, 66% based on  $\text{H}_2\text{BPDC}$ ).

**Synthesis of Single Crystals of CAU-21-BPDC (1).** Single crystals of CAU-21-BPDC suitable in size for a structure determination could be obtained during the HT optimization experiments from a 2 mL reactor (Figure 1). This synthesis batch also contained recrystallized linker molecules and crystals of CAU-8-BPDC. In this experiment 64.8  $\mu\text{L}$  of 2 M  $\text{Al}(\text{NO}_3)_3\cdot 9\text{H}_2\text{O}$  in  $\text{H}_2\text{O}$  (185  $\mu\text{mol}$ ), 50 mg of  $\text{H}_2\text{BPDC}$  (185  $\mu\text{mol}$ ), 250  $\mu\text{L}$  of DMF, and 185.2  $\mu\text{L}$  of  $\text{H}_2\text{O}$  were heated in an HT reactor up to  $145^\circ\text{C}$  over 1 h, held at this temperature for 12 h, and cooled to room temperature over 1 h.

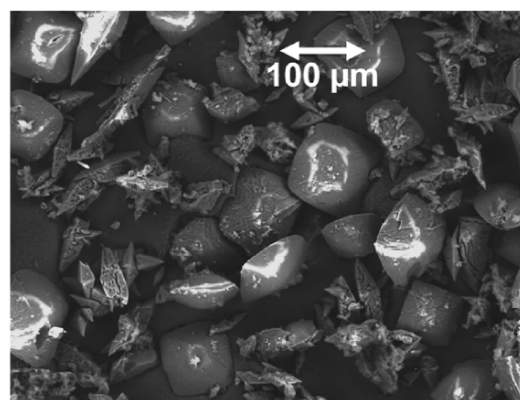


**Figure 1.** SEM micrograph of the crystals of CAU-21-BPDC obtained as a phase mixture with CAU-8-BPDC. Larger crystals of CAU-21-BPDC (approximately  $100\text{ }\mu\text{m}$ ) are visible along with smaller crystals of CAU-8-BPDC and recrystallized linker molecules.<sup>23</sup>

B

DOI: 10.1021/acs.inorgchem.7b00202  
Inorg. Chem. XXXX, XXX, XXX–XXX

Table 1. Summary of the Important Crystallographic Parameters of the Structure Determination and Refinement of the Title Compounds<sup>a</sup>

	CAU-8-BPDC	CAU-8-ODB	CAU-21-BPDC	CAU-21-ODB	
				DFT calculations	Pawley refinement of PXRD data
structure determination	single-crystal data	powder data	single-crystal data	DFT calculations	Pawley refinement of PXRD data
formula	AlC <sub>15</sub> H <sub>8</sub> O <sub>6</sub>	AlC <sub>14</sub> H <sub>8</sub> O <sub>6</sub>	AlC <sub>15</sub> H <sub>8</sub> O <sub>6</sub>	AlC <sub>14</sub> H <sub>8</sub> O <sub>6</sub>	
Z	16	16	16	16	
cryst syst	tetragonal	tetragonal	tetragonal	tetragonal	tetragonal
a (Å)	12.984(2)	13.1035(7)	17.2528(7)	16.6220	16.583(6)
b (Å)	12.984(2)	13.1035(7)	17.2528(7)	16.6220	16.583(6)
c (Å)	52.301(10)	51.757(4)	23.864(1)	23.5280	23.52(1)
V (Å <sup>3</sup> )	8818(3)	8886(1)	7103.4(7)	6500.57	6467(6)
space group	I4 <sub>1</sub> /a	I4 <sub>1</sub> /a	I422	I422	
solution method	direct methods SHELXS <sup>57</sup>	least-squares Rietveld <sup>56</sup>	direct methods SHELXS <sup>57</sup>	DFT calculations	
2θ range (deg)	1.6–25.0	4–70	2.4–26.4		2–90
R <sub>wp</sub> (%)		5.81			4.49
R <sub>Bragg</sub> (%)		1.19			
GOF	0.899	2.46	1.065		1.99
total and unique data, R <sub>int</sub>	30871, 3851, 0.123		24969, 3655, 0.136		
obsd data (I > 2σ(I))	1916		2338		
R1, wR2	0.089, 0.242		0.078, 0.172		
Δe min/max (e/Å <sup>3</sup> )	–0.31, 0.59		–0.29, 0.44		
calcd density (g/cm <sup>3</sup> )	0.941	0.921	1.164	1.223	
torsion angle between rings (deg)	58	60	64	72	
angle between rings (deg)	120	116	121	117	

<sup>a</sup>The Pawley refinement of CAU-21-ODB is displayed in Figure S4 in the Supporting Information.

#### HT Experiments To Afford CAU-8-ODB and CAU-21-ODB.

For the system Al<sup>3+</sup>/4,4'-oxydibenzoic acid (H<sub>2</sub>ODB)/water/DMF, high-throughput investigations under solvothermal reaction conditions were carried out by employing our 24-high-throughput reactor system.<sup>52–54</sup> The variation of the reaction temperature (125–170 °C), the Al<sup>3+</sup>:H<sub>2</sub>ODB molar ratio (between 0.3:0.8 and 7:5; one unit corresponds to the amount of 39 μmol), the DMF (N,N-dimethylformamide):H<sub>2</sub>O (volume ratio between 400:100 μL and 1000:0 μL), and the Al<sup>3+</sup> source (Al(NO<sub>3</sub>)<sub>3</sub>·9H<sub>2</sub>O, Al<sub>2</sub>(SO<sub>4</sub>)<sub>3</sub>·18H<sub>2</sub>O, and AlCl<sub>3</sub>·6H<sub>2</sub>O) were investigated (Table S2 in the Supporting Information). Phase-pure products of CAU-8-ODB and CAU-21-ODB can only be obtained as microcrystalline powders.

**Optimized Reaction Conditions for CAU-8-ODB (2).** The following synthesis conditions are the optimized ones for CAU-8-ODB: a reaction mixture of 107.7 mg of 4,4'-oxydibenzoic acid (H<sub>2</sub>ODB, 0.25 mmol), 53.3 mg of Al(NO<sub>3</sub>)<sub>3</sub>·9H<sub>2</sub>O (0.25 mmol), and 6.0 mL of DMF was heated at 120 °C in a 23 mL Teflon-lined digestion bomb for 2 days followed by slow cooling at 6 °C h<sup>-1</sup> to room temperature. A pale yellow powder of **2** was filtered off, washed with N,N-dimethylformamide at 85 °C overnight, filtered again, and subsequently activated at 200 °C at 10<sup>-2</sup> kPa for 16 h (yield: 20 mg, 25% based on H<sub>2</sub>ODB).

**Optimized Reaction Conditions and Scale-Up Synthesis for CAU-21-ODB (3).** The HT synthesis optimization led to the following optimized synthesis procedure: to a mixture of 22.4 mg of AlCl<sub>3</sub>·6H<sub>2</sub>O (93 μmol) and 24 mg of 4,4'-oxydibenzoic acid (H<sub>2</sub>ODB, 93 μmol), and 400 μL of N,N-dimethylformamide (5.15 mmol) was added 100 μL of deionized water (5.55 mmol). The reactor was sealed carefully and heated to 170 °C within 1 h, held at this temperature for 12 h, and finally cooled to room temperature within 1 h. The product was filtered off, washed with N,N-dimethylformamide at 65 °C for 3 h, filtered again, and subsequently activated at 200 °C at 10<sup>-2</sup> kPa for 48 h. The additional washing step in DMF is necessary because the raw filtered product contains recrystallized linker molecules.

Larger amounts of CAU-21-ODB can be obtained using 336 mg of AlCl<sub>3</sub>·6H<sub>2</sub>O (1.4 mmol), 360 mg of 4,4'-oxydibenzoic acid (H<sub>2</sub>ODB,

1.4 mmol), 6 mL of N,N-dimethylformamide (77 mmol), and 1.5 mL of deionized water (83 mmol) in a 30 mL Teflon-lined steel autoclave. The temperature program and the additional washing and activation steps are the same as in the optimized synthesis conditions of CAU-21-ODB (yield: 92 mg, 23% based on H<sub>2</sub>ODB).

**Solvothermal Synthesis of [Al(HODB)<sub>2</sub>(OH)] (4).** A reaction mixture of 4,4'-oxydibenzoic acid (H<sub>2</sub>ODB, 0.2582 g, 0.1 mmol), aluminum chloride (AlCl<sub>3</sub>, 0.1334 g, 0.1 mmol), and H<sub>2</sub>O (5.0 mL) was heated at 120 °C for 2 days, followed by slow cooling at 6 °C h<sup>-1</sup> to room temperature. The colorless and small crystals of [Al-(HODB)<sub>2</sub>(OH)] were filtered off, washed with H<sub>2</sub>O and ethanol, and dried under ambient conditions.

**Structure Determination.** The crystal structure of CAU-21-BPDC was solved and refined using single-crystal X-ray diffraction data. Hydrogen atoms were added using a riding model. Due to the positional disorder of guest species, residual electron density in the pores was accounted for using the reverse Fourier transform routine SQUEEZE.<sup>55</sup> For the isorecticular compounds of CAU-8-BPDC and CAU-21-BPDC based on ODB<sup>2-</sup> the structural models were obtained as follows. The cell parameters were obtained by indexing laboratory high-resolution PXRD data using TOPAS-Academic.<sup>56</sup> The isorecticular structures of CAU-8-BPDC and CAU-21-BPDC served as starting models for CAU-8-ODB and CAU-21-ODB, where the BPDC<sup>2-</sup> was substituted by ODB<sup>2-</sup> (ligand replacement strategy). The geometries were subsequently optimized at the density functional theory (DFT) level, retaining the indexed cell parameters obtained from experimental PXRD data (see details of the computations below). The resulting model of CAU-8-ODB was used as a starting point for further Rietveld refinement with TOPAS-Academic 4.1.<sup>56</sup> This led to a satisfied structure model of the solid, as evidenced by the Rietveld plots (Figure S15 in the Supporting Information). For this refinement, the two aromatic C<sub>7</sub> subunits of the linker molecules were treated as rigid bodies while all other atoms were freely refined. Residual electron density in the channels was attributed to the presence of water molecules, represented by oxygen atoms. To account for asymmetric peak broadening and preferred orientation, a

C

DOI: 10.1021/acs.inorgchem.7b00202  
Inorg. Chem. XXXX, XXX, XXX–XXX

fourth-order spherical harmonics correction was used. Rietveld refinement of the structural model for CAU-21-ODB was not possible due to overly high unallocated electron density in the pores. However, we found that simulated PXRD patterns of the DFT geometry optimized structures with experimental cell parameters show excellent agreement with experimentally observed PXRD patterns (Figures S1–S3 and Tables S3 and S4 in the Supporting Information).

In order to obtain truly minimum energy conformers, all of the structure models were further fully optimized at the DFT level, with both atomic positions and unit cell parameters allowed to relax. We determined that the cell parameters of both CAU-8-ODB and CAU-21-ODB minimum energy structures remain very similar to the experimental values. Detailed information about the crystal data of CAU-21-BPDC and the results of the refinement of CAU-8-ODB as well as the calculated crystal data of CAU-21-ODB are summarized in Table 1. For comparative purposes crystal data for CAU-8-BPDC are also given. Bond lengths are provided in Tables S5–S7 in the Supporting Information.

Detailed information on the crystal structure solution and refinement of  $[\text{Al}(\text{HOD})_2(\text{OH})]$  can be found in the Supporting Information.

**Computation Details.** The periodic DFT calculations were performed using the Quickstep module<sup>58</sup> of the CP2K program<sup>59,60</sup> employing the Gaussian plane wave (GPW) formalism. The general gradient approximation (GGA) to the exchange–correlation functional according to Perdew–Burke–Ernzerhof (PBE)<sup>61</sup> was used in combination with Grimme’s DFT-D3 semiempirical dispersion corrections.<sup>62,63</sup> Triple- $\zeta$  plus valence polarized Gaussian-type basis sets (TZVP-MOLOPT) were considered for all atoms, except for the Al metal centers, where double- $\zeta$  plus valence polarization functions (DZVP-MOLOPT) were employed.<sup>64</sup> The interaction between core electrons and valence shells of the atoms were described by the pseudopotentials derived by Goedecker, Teter, and Hutter (GTH).<sup>65–67</sup> The auxiliary plane wave basis sets were truncated at 400 Ry.

**Pore Size Distribution (PSD).** The geometric methodology reported by Gelb and Gubbins<sup>68</sup> was used to calculate the pore size distributions (PSD) of the minimum energy structures, as depicted in Figure S5 in the Supporting Information. In these calculations, the van der Waals parameters of the framework atoms were adopted from universal force field (UFF).<sup>69</sup>

**In Situ Crystallization Experiments.** EDXRD experiments were carried out at HASYLAB, beamline F3 at DESY, Hamburg, Germany. The white beam synchrotron radiation (4–55 keV) was detected by a liquid nitrogen cooled germanium semiconductor detector system. The detector angle was set to approximately  $1.9^\circ$ . The best results were obtained by collimating the beam to  $0.2 \times 0.2 \text{ mm}^2$ . To heat the samples, a custom-made reactor system heated by an external thermostat (JULABO) was used. The reaction temperature of the reaction mixture was achieved within 2 min.<sup>70</sup> The energy dispersive measurements were performed, and the obtained spectra were recalculated to the  $2\theta$  range (for  $\lambda = 1.5406 \text{ \AA}$ ) using STA-12<sup>71</sup> as a standard. The experiments were carried out in 5 mL Schott Duran glass reactors. The combined reactants of 740  $\mu\text{L}$  of 0.5 M  $\text{Al}_2(\text{SO}_4)_3 \cdot 18\text{H}_2\text{O}$  in  $\text{H}_2\text{O}$  (370  $\mu\text{mol}$ ), 200 mg of  $\text{H}_2\text{BPDC}$  (740  $\mu\text{mol}$ ), 1200  $\mu\text{L}$  of *N,N*-dimethylformamide (15.5 mmol), and 60  $\mu\text{L}$  of deionized water (3.33 mmol) were homogenized by shaking, and the reaction vessel was immediately transferred to the in situ reactor system. The reaction was carried out at 140, 150, and 153  $^\circ\text{C}$  with vigorous stirring.

## RESULTS AND DISCUSSION

In a previous study of the system  $\text{Al}^{3+}/\text{H}_2\text{BPDC}/\text{DMF}/\text{water}$ , two different products were obtained. One of the compounds, CAU-8-BPDC ( $[\text{Al}(\text{OH})\text{BPDC}]$ ),<sup>23</sup> could be obtained as a phase-pure product and was therefore thoroughly characterized. The other product did not show any porosity toward nitrogen. Due to the complexity of the system, CAU-8-BPDC was difficult to isolate as a phase-pure product. Impurities of recrystallized linker molecules and the second compound,

denoted now as CAU-21-BPDC ( $[\text{Al}(\text{OH})\text{BPDC}]$ , 1), were present in most syntheses using nonoptimized synthesis conditions. Because of this complex crystallization behavior an in situ time-resolved PXRD investigation was carried out at DESY, Hamburg, Germany.

### In Situ Time-Resolved X-ray Diffraction Investigation.

The crystallization of CAU-8-BPDC was investigated at 140, 150, and 153  $^\circ\text{C}$ . Figure S8 in the Supporting Information and Figure 2 show the PXRD patterns as a function of reaction

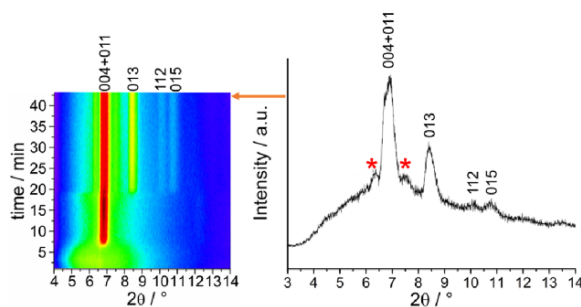


**Figure 2.** Results of the in situ time-resolved X-ray diffraction investigation of CAU-8-BPDC at 153  $^\circ\text{C}$ . Reflections of CAU-8-BPDC are marked with their  $hkl$  indices; additional reflections originating from CAU-21-BPDC are marked with red asterisks. In the top view picture (left), first the formation of a crystalline intermediate is observed, which transforms to CAU-8-BPDC (visible by appearance of the 013, 112, and 015 reflections). The strongest reflection of the intermediate and the 004 and 011 reflections of CAU-8-BPDC are located in the signal around  $6.8^\circ 2\theta$ . On the right side is given the PXRD pattern taken at 45 min, showing the additional peaks of CAU-21-BPDC, marked with red asterisks.

time. The evaluation of the measurements is shown in Figure S9 in the Supporting Information, and a summary of the crystallization behavior of the compounds is presented in Figure 3.

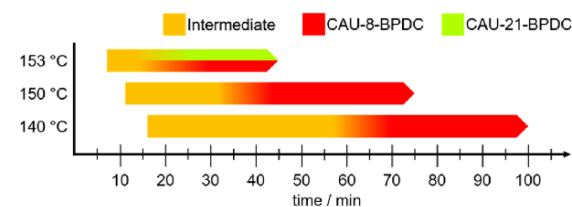


**Figure 3.** Comparison of the formation times of the intermediate, CAU-8-BPDC, and CAU-21-BPDC phases.

At 140  $^\circ\text{C}$ , a crystalline intermediate is formed after 16 min, which transforms completely into CAU-8-BPDC during the following 46 min. Full crystallization of CAU-8-BPDC at this temperature is observed after 100 min (Figure S8A in the Supporting Information). At 150  $^\circ\text{C}$ , the formation of the crystalline intermediate starts after 12 min and the transformation into CAU-8-BPDC takes 23 min. The time of full crystallization of CAU-8-BPDC is shortened to 75 min (Figure S8B). Increasing the temperature further leads not only to even shorter reaction times but also to the formation of CAU-21-BPDC. At 153  $^\circ\text{C}$  the formation of the crystalline intermediate starts after 7 min, and after an additional 10 min CAU-8-BPDC and CAU-21-BPDC are formed. This transformation is



completed after 45 min. Referring to the results of the in situ PXRD investigation, we focused our attention on the phase-pure synthesis of the intermediate and CAU-21-BPDC phases.

The intermediate phase was also obtained by quenching of the reaction mixtures (Figures S6 and S7 in the Supporting Information), but we were not able to index the PXRD pattern. Therefore, subsequent investigations focused on the new Al-MOF CAU-21-BPDC (**1**).

**HT Investigation of CAU-21-BPDC.** CAU-21-BPDC was discovered during the systematic investigation of the system  $\text{Al}^{3+}/\text{H}_2\text{BPDC}/\text{DMF}/\text{water}$  under solvothermal reaction conditions. The first occurrence was already previously reported, where **1** was denoted as a "non-porous byproduct".<sup>23</sup> Further detailed HT investigations (~90 reactions) optimizing the reactant concentrations, the temperature–time program, the solvent ratio, and the addition of benzoic acid as modulating reagent led to the optimized synthesis procedure, which could also be successfully upscaled to larger reactors (Table S1 in the Supporting Information).

**Crystal Structure of CAU-21-BPDC (**1**).** The crystal structure of **1** was determined using single-crystal X-ray diffraction data. Obtaining single crystals of an aluminum-based MOF suitable for in-house acquisition of diffraction data is remarkable. To the best of our knowledge, only a few other examples are currently known.<sup>23,33,34</sup> Most often, Al-MOFs can only be obtained as microcrystalline powders, which hampers a structure determination.<sup>13,27,72,73</sup>

The asymmetric unit of **1** contains two crystallographically independent  $\text{Al}^{3+}$  ions bridged by one  $\mu\text{-OH}$  group and one linker molecule (Figure 4 and Figure S10 in the Supporting Information). Selected bond lengths are summarized in Table S5 in the Supporting Information.

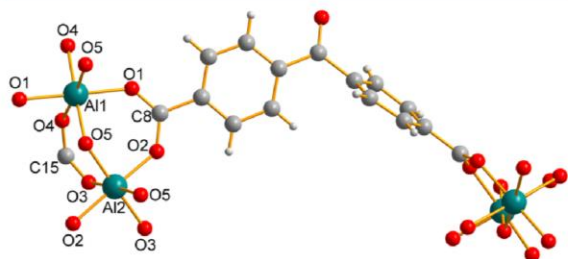


**Figure 4.** Extended representation of the asymmetric unit of CAU-21-BPDC showing the complete coordination sphere of the  $\text{Al}^{3+}$ -ions as well as the bridging nature of the  $\text{BPDC}^{2-}$  ion. Aluminum atoms are shown in teal, oxygen atoms in red, carbon atoms in gray, and hydrogen atoms in light gray.

The IBU of CAU-21-BPDC has already been observed in MOF-519/520<sup>33</sup> and consists of eight  $\text{AlO}_6$  polyhedra which are cis-connected via  $\mu\text{-OH}$  groups to form an eight-membered ring. The coordination sphere of the  $\text{AlO}_6$  polyhedra is completed by 16 carboxylate groups. In the unit cell, the 8-ring IBUs are connected by the linker molecules to a framework with **bcu** topology with octahedral and tetrahedral cavities (Figure 5).

Ringlike IBUs have also been observed in some other Al-MOFs.<sup>20,32–34</sup> A distinct 8-membered-ring-based MOF is CAU-1.<sup>32</sup> The IBUs of CAU-1 consist of corner- and edge-sharing  $\text{AlO}_6$  polyhedra, bridged by hydroxide and methoxide groups and coordinated by 12 carboxylate groups.<sup>32</sup> The 8-

membered rings are interlinked by 12 amino terephthalate ions to 12 other units to form as well a *bcc* packing of clusters. However, in contrast to CAU-1, the connection of the rings in the horizontal plane is missing in CAU-21-BPDC, where a connection to only 8 other IBUs is observed (Figure 6). Thus, for CAU-1 an **fcu** topology is found, while the structure of CAU-21-BPDC represents an example for a doubly connected **bcu** net.

In **1** each connection between the IBUs is established by two  $\text{BPDC}^{2-}$  linker molecules (Figure S11 in the Supporting Information). The connectivity leads to two kinds of pores which correspond to the octahedral and the tetrahedral cavities formed by the packing of the IBUs (Figure 7). The octahedral cavities are accessible through the small opening (3.6 Å), which corresponds to the diameter of the IBU, and their connection leads to the formation of 1D channels along the crystallographic *b* axis. The maximum channel diameter is 6.5 Å, with the van der Waals radii of the atoms lining the walls taken into account.

**Vibrational and  $^1\text{H-NMR}$  Spectroscopy.** The IR and  $^1\text{H-NMR}$  spectra of CAU-21-BPDC (**1**) are displayed in Figures S12 and S13 in the Supporting Information. Bands of high intensity (Figure S12) appear at 1624 and 1437  $\text{cm}^{-1}$ , which correspond to the asymmetric and symmetric stretching vibrations of the carboxylate groups of the  $\text{BPDC}^{2-}$  molecules. The presence of the keto group in the linker molecule is confirmed by its  $\text{C}=\text{O}$  stretching vibration at 1674  $\text{cm}^{-1}$ .<sup>23</sup> At 1566 and 1504  $\text{cm}^{-1}$  the ring stretching vibrations are visible, whereas  $\text{C-H}$  out of plane deformation vibrations of the aromatic ring absorb at 849  $\text{cm}^{-1}$ .<sup>31</sup> In the broad band at 579  $\text{cm}^{-1}$  the  $\text{C-CO-C}$  in-plane and  $\text{C-CO}$  deformation vibrations can be observed. The vibration at 934  $\text{cm}^{-1}$  corresponds to the  $\text{O-H}$  deformation of  $\mu\text{-OH}$  groups connecting the  $\text{Al}^{3+}$  ions, whereas the  $\text{O-H}$  stretching vibration is located at 3741  $\text{cm}^{-1}$ .<sup>75</sup> Additional vibrations at 788 and 735  $\text{cm}^{-1}$  can be observed, which point to the presence of a monosubstituted aromatic ring. This is due to the presence of benzoate ions in **1**. The presence of benzoate ions in CAU-21-BPDC was also confirmed via solution  $^1\text{H-NMR}$  spectroscopy (Figure S13). The sample was dissolved in 5% NaOD in  $\text{D}_2\text{O}$  and measured at 200 MHz. Integration of the signals reveals the presence of ca. 14% benzoate molecules in the sample. On the basis of the IR spectra, which do not show the presence of free carboxylic acid groups, we propose that the benzoate molecules are part of the framework and partially substitute the linker molecules in CAU-21-BPDC.

**Thermal Stability.** According to the results of the TG measurement, the framework of CAU-21-BPDC decomposes at 300 °C (Figure 8). Up to a temperature of approximately 140 °C occluded solvent molecules are removed, which results in a mass loss of 3.7%. This corresponds to a loss of 0.7  $\text{H}_2\text{O}$  molecules per formula unit (calculated 3.8%). At a temperature of approximately 300 °C the framework of CAU-21-BPDC starts to decompose. This decomposition takes place in several steps. In the first step up to approximately 420 °C a loss of 11.0% is observed, which could correspond to the loss of two  $\text{H}_2\text{O}$  molecules per formula unit (calculated 11.1%) possibly due to the dehydration of the IBUs. In the temperature range 420–630 °C the linker molecules ( $\text{BPDC}^{2-}$  and  $\text{BA}^-$ ) are oxidized. For the complete decomposition of the framework a weight loss of 80.6% can be observed, which corresponds well to the calculated weight loss of 82.7%. For these calculations, it

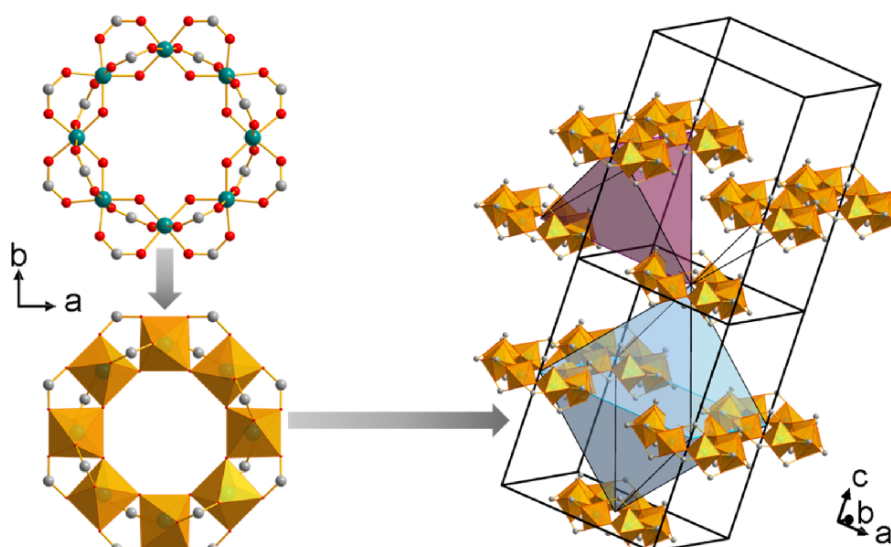


**Figure 5.** Crystal structure of CAU-21-BPDC (**1**): (left) IBU which is formed by eight cis corner-sharing  $\text{AlO}_6$  polyhedra ( $\text{AlO}_6$  polyhedra are shown in orange, aluminum atoms in teal, oxygen atoms in red, and carbon atoms in gray); (right) *bcc* packing of these IBUs and formation of tetrahedral (purple) and octahedral (light blue) cavities.

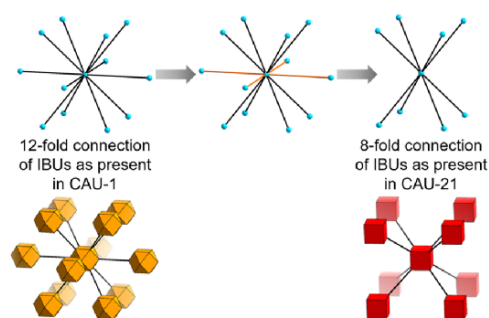


**Figure 6.** Connectivity of the IBUs in CAU-1 and CAU-21-BPDC. IBUs are represented as spheres in the nets (top), while in the augmented representations the IBUs are represented by polyhedra (bottom). The horizontal connection to the other IBUs (marked with orange bonds) is missing in the structure of CAU-21.

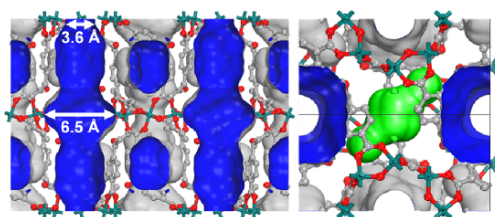


**Figure 7.** (left) Representation of 1D channels in CAU-21-BPDC (**1**) as seen along [010]. (right) Pore shape of the tetrahedral cavities shown in green. Aluminum atoms are shown in teal, oxygen atoms in red, and carbon atoms in gray. The Connolly surface area was calculated with a probe diameter of 3.3 Å (kinetic diameter of  $\text{CO}_2$ ) using Materials Studio and is shown in blue.<sup>74</sup>

was assumed that X-ray amorphous  $\text{Al}_2\text{O}_3$  was formed as the final product.

According to temperature-dependent PXRD studies, CAU-21-BPDC is stable up to 420 °C (Figure 8). The differences in

the thermal stabilities originate from different measurement setups. While the TG measurements are carried out in aluminum oxide crucibles in a continuous air flow, capillaries are used for temperature-dependent PXRD measurements. The PXRD data reveal a shift of reflections with increasing temperature. Parametric Pawley refinements reveal an increase of the crystallographic *a* and *b* axes as well as a shrinkage of the *c* axis (Figure S14 in the Supporting Information).

Taking these results into account, the sum formula for CAU-21-BPDC was deduced to be  $[\text{Al}(\text{OH})(\text{BPDC})_{0.93}(\text{BA})_{0.14}]\cdot 0.7\text{H}_2\text{O}$ . This formula also corresponds well to the results of the elemental analysis (measured/calculated: C, 56.5%/55.6%; H, 3.1%/3.3%; N, 0.4%/0%). The measured percentages of nitrogen result from residual DMF molecules, which could not be removed upon activation. On the basis of the NMR, IR, and TG data, the presence of the benzoate ions in the reaction product was unequivocally demonstrated. The data suggest a partial substitution of one  $\text{BPDC}^{2-}$  by two  $\text{BA}^-$  ions and a statistical disorder of the  $\text{BA}^-$  ions throughout the crystal.

Considering the thermal stability of other aluminum-based MOFs, CAU-21-BPDC is less stable than most of these compounds, for which thermal stabilities above 350 °C are often reported.<sup>11,13,26,31,72</sup> In comparison to MOF-519/520, where the same IBUs are present and which decompose at approximately 280 °C, CAU-21-BPDC exhibits a slightly higher thermal stability.<sup>33</sup>

**Sorption Properties.** Prior to the sorption measurements, CAU-21-BPDC was activated for 48 h at 200 °C under reduced pressure ( $10^{-2}$  kPa). The small pores are not accessible for  $\text{N}_2$  molecules at 77 K, but they are accessible for  $\text{CO}_2$  at 298 K (50 mg/g at 1 bar, Figure 9). This is due to the smaller kinetic diameter (3.3 and 3.64 Å for  $\text{CO}_2$  and  $\text{N}_2$ , respectively), the larger framework flexibility, and improved adsorption kinetics. This observation suggests that the small pore opening of 3.6 Å inside the IBU that gives access to the octahedral cavities prevents the adsorption of  $\text{N}_2$ , while  $\text{CO}_2$  can adsorb. However, we cannot clearly attribute this to a defined gate-opening mechanism or rotational motion of the aromatic rings, but

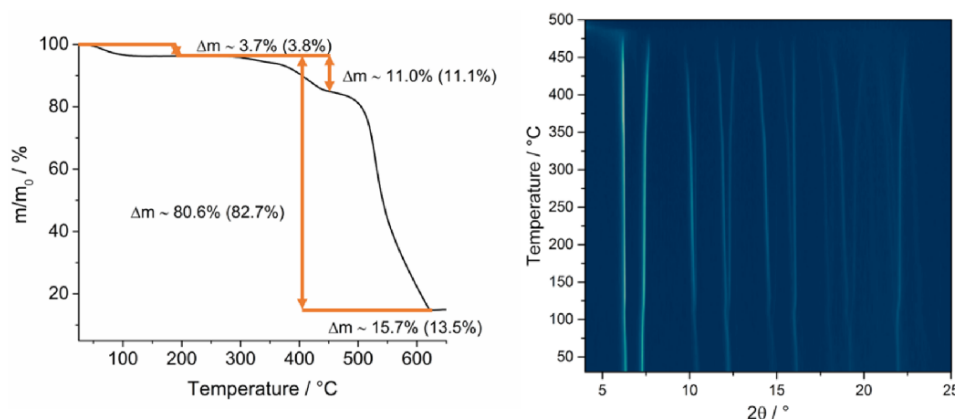


**Figure 8.** Results of the thermogravimetric measurements of CAU-21-BPDC (left) and the temperature-dependent PXRD study (right). The observed and expected weight losses and the residual mass are marked in the graph.

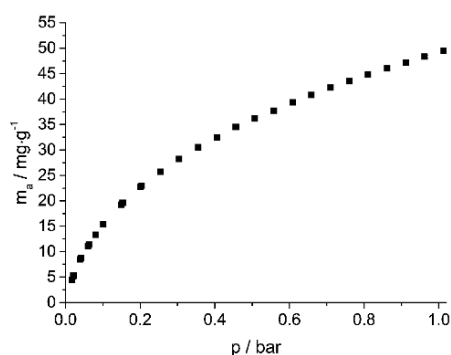


**Figure 9.** CO<sub>2</sub> sorption isotherm of CAU-21-BPDC measured at 298 K.

these processes could well explain the adsorption at higher temperature. Indeed, this material can selectively adsorb CO<sub>2</sub> over N<sub>2</sub> via a molecular sieving effect.

The observed uptake of CO<sub>2</sub> (50 mg/g) in CAU-21-BPDC is comparable with the uptake of MIL-101(Cr), ZIF-8, and MOF-177 (42, 43, and 65 mg/g, respectively) at this pressure (1 bar).<sup>76</sup> Nevertheless, much higher uptakes have been reported: for example, for MOF-5, MIL-53(Al), and HKUST-1 (85, 106, and 198 mg/g, respectively).<sup>76</sup>

#### Synthesis of Isoreticular Compounds Using H<sub>2</sub>ODB.

Using H<sub>2</sub>ODB as a linker molecule, compounds isoreticular with CAU-8-BPDC and CAU-21-BPDC could be obtained. H<sub>2</sub>ODB exhibits the same V-shaped linker geometry as H<sub>2</sub>BPDC. However, in the H<sub>2</sub>ODB molecule the phenyl rings can rotate freely around the oxygen–carbon bond of the ether groups, in comparison with the conjugated and thus more rigid keto groups in H<sub>2</sub>BPDC. This fact could result in a larger torsion angle between the phenyl rings in H<sub>2</sub>ODB. A comparison between both linker molecules, including atom distances and bond angles, is shown in Figure 10.

**HT Investigation To Afford CAU-8-ODB (2) and CAU-21-ODB (3).** The HT investigation of the system Al<sup>3+</sup>/H<sub>2</sub>ODB/DMF/water under solvothermal conditions resulted in the discovery of the title compounds 2 and 3. In the first experiments the volume of DMF was kept at 500 μL and no water was added to the reaction mixture. The Al<sup>3+</sup>: H<sub>2</sub>ODB molar ratio was varied in the first 6 reactors, and their absolute

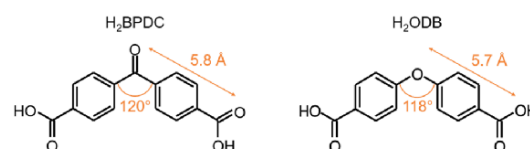


**Figure 10.** Schematic comparison between the linker molecules H<sub>2</sub>BPDC and H<sub>2</sub>ODB. Angles between the phenyl rings and the distance between the center of the molecule and the carbon atom of the carboxylic acid group are displayed. Distances and angles are taken from refs 23 and 77.

concentration was increased in the following 18 syntheses. The exact composition of the reaction mixtures can be found in Table S2 in the Supporting Information (reactions 1–24). The experiment and the results which are based on PXRD measurements are visualized in Figure 11. Employing AlCl<sub>3</sub>,

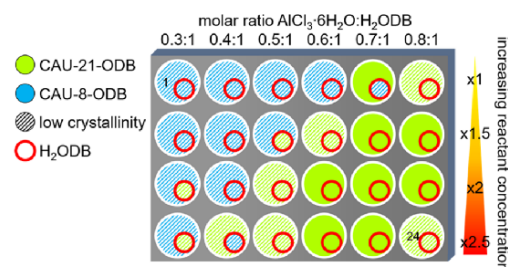


**Figure 11.** Schematic representation of the obtained products and the observed tendencies in the HT investigation that led to the discovery of CAU-8-ODB and CAU-21-ODB. One unit corresponds to an amount of 39 μmol. The results are based on PXRD measurements.

6H<sub>2</sub>O, the formation of CAU-8-ODB (2) and CAU-21-ODB (3) could be observed, but in every reaction vessel an impurity of H<sub>2</sub>ODB is present. In this experiment, 2 could only be obtained as a powder with low crystallinity. For the formation of 2 a high excess of H<sub>2</sub>ODB is necessary, while 3 is formed at Al<sup>3+</sup>:H<sub>2</sub>ODB molar ratios of close to 1. CAU-21-ODB (3) could be obtained as a highly crystalline product, but an impurity of H<sub>2</sub>ODB is present in every sample, which can easily be removed by a consecutive washing step with DMF at 85 °C overnight.

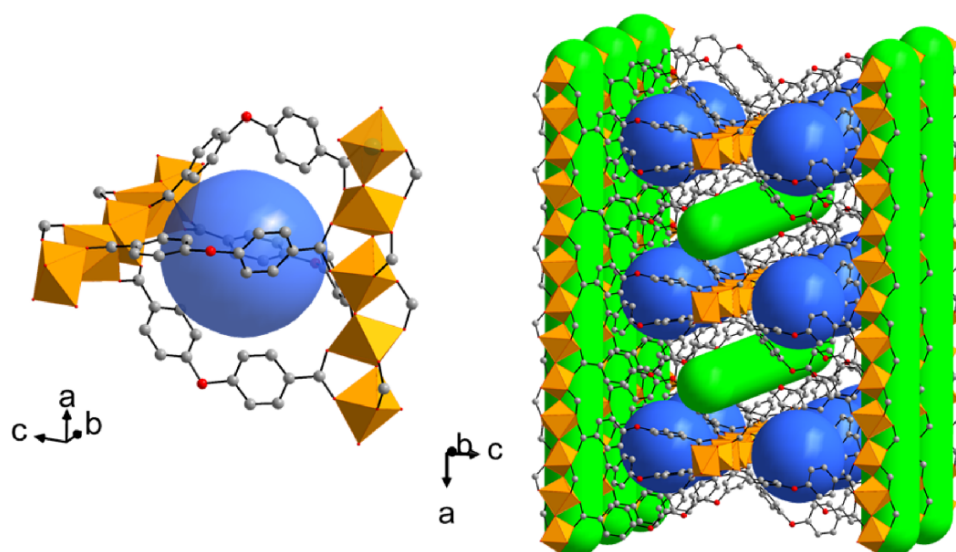


**Figure 12.** Crystal structure of CAU-8-ODB: (left) spherical cavities with a diameter of 6 Å (blue) formed through the connection of perpendicular chains via four linker molecules; (right) 1D channels with a diameter of 4.4 Å (green) located in the perpendicular layers of the IBUs.

Since the crystallinity of compound **2** was not sufficiently good enough to carry out further investigations and because of the presence of residual linker molecules, the reaction conditions of the two compounds had to be optimized. The optimization reactions for CAU-8-ODB were carried out using 23 mL Teflon lined steel autoclaves, whereas for **3** the HT reactor system was used. The optimized synthesis procedures for **2** drastically differ from those found in the HT setup (see the [Experimental Section](#)). Detailed information about the HT reactions is given in [Table S2](#) in the Supporting Information. Although both compounds were obtained as microcrystalline powders, only the structure of CAU-8-ODB could be refined. For CAU-21-ODB a Pawley fit was carried out, which confirmed the phase purity of the product. Nevertheless, a comparison of the PXRD pattern of the structural model obtained by DFT calculations and the measured PXRD pattern gives very good agreement ([Figure S2](#) in the Supporting Information).

**Structure Description of CAU-8-ODB (2).** The crystal structure of **2** is isorecticular with that of CAU-8-BPDC, which was reported previously.<sup>23</sup> The IBU consists of trans-connected corner-sharing  $\text{AlO}_6$  polyhedra which form infinite linear chains. These chains are ordered in parallel to each other to form layers. Neighboring layers are oriented perpendicular to each other ([Figure 12](#), left), and the interconnection of two perpendicular adjacent chains is established via four  $\text{ODB}^{2-}$  molecules ([Figure 12](#), right). Thus, a three-dimensional framework with 1D channels with a diameter of 5.3 Å and spherical cavities with a diameter of 6.4 Å are formed. The final Rietveld plot of the structure refinement using PXRD data is shown in [Figure S15](#) in the Supporting Information.

**Comparison of the Structures.** Each pair of compounds containing the same linker molecule are framework polymorphs. A comparison of the crystallographic framework densities and especially the DFT lattice energies—corresponding to the depth of the potential well at the global minimum—showed that the crystal packing of CAU-21 is energetically more favorable than that of the CAU-8 geometry. For example,

the relative energy difference and the calculated energy difference  $\Delta E$  between the global minimum energy structures of CAU-8 and CAU-21 solids of 0.41 and 0.74 kJ/(mol atom) were obtained for the  $\text{H}_2\text{BPDC}$  and  $\text{H}_2\text{ODB}$  derivatives, respectively. These energy differences are primarily attributed to the specific crystal packing of trans corner-sharing  $\text{AlO}_6$  polyhedra forming infinite chains and cis corner-sharing octanuclear  $\text{AlO}_6$  clusters, while no conformational changes occurred in the organic linkers.

The use of both linker molecules lead to isorecticular compounds. Since the structure refinement of CAU-21-ODB was not successful, only the structures of CAU-8-ODB and CAU-8-BPDC are compared. The connectivity of the one-dimensional IBUs leads to slightly different C–C/O–C angles and torsion angles between the aromatic rings ([Figure S16](#) in the Supporting Information), which in turn results in a shortening of the  $c$  axis in CAU-8-ODB. The distance of the parallel IBUs and the pore diameter is reduced from 5 to 4.4 Å in CAU-8-BPDC and CAU-8-ODB, respectively. The larger torsion angle of  $\text{ODB}^{2-}$  in CAU-8-ODB influences the size of the spherical cavities. The diameter of these spherical cavities shrinks slightly, since the aromatic rings are more strongly protruding into the pores ([Figure S17](#) in the Supporting Information).

**Thermal Stability of CAU-8-ODB (2) and CAU-21-ODB (3).** For the calculations, it was assumed that X-ray amorphous  $\text{Al}_2\text{O}_3$  was formed as the final product. According to the thermogravimetric measurements, compound **2** is stable up to 370 °C in air ([Figure S18](#) in the Supporting Information) and thus is only slightly more thermally stable in comparison to CAU-8-BPDC (350 °C).<sup>23</sup> Up to a temperature of approximately 150 °C occluded solvent molecules are removed from the pores (mass loss 2.2%), and above 370 °C the framework decomposes. The measured weight losses and the residual mass correspond well to the expected values, which were calculated using the composition  $[\text{Al}(\text{OH})\text{ODB}]\cdot 0.4\text{H}_2\text{O}$ . This formula is also confirmed by the results of the elemental analysis ([Table S8](#) in the Supporting Information). The thermal stability also

was confirmed by temperature-dependent PXRD data (Figure S19 in the Supporting Information).

The thermal stability of compound **3** is also in the same range as that observed for the isoreticular compound CAU-21-BPDC. Both compounds start to decompose at approximately 300 °C (Figure S20 in the Supporting Information). First, occluded solvent molecules are removed up to a temperature of 120 °C. Up to 450 °C a second weight loss is observed, and from 450 to 620 °C the linker molecules decompose, which results in a mass loss of 77% (calculated 76%). Taking these results into account, the chemical formula of **3** could be deduced to be  $[\text{Al}(\text{OH})\text{ODB}] \cdot 0.9\text{H}_2\text{O}$ , which corresponds well to the results of the elemental analysis shown in Table S9 in the Supporting Information. The discrepancy ( $\pm 2\%$ ) for CAU-21-ODB as observed by elemental analysis (C and H content too low) could be due to the formation of trace impurities of X-ray amorphous  $\text{Al}_2\text{O}_3$ . The thermal stability was also confirmed by temperature-dependent PXRD data (Figure S21 in the Supporting Information). These measurements show a thermal stability up to 420 °C. The differences in the thermal stabilities originate from different measuring methods.

**Vibrational and  $^1\text{H}$ -NMR Spectroscopy of CAU-8-ODB (2) and CAU-21-ODB (3).** The IR and  $^1\text{H}$ -NMR spectra of **2** and **3** are displayed in Figures S22 and S23 in the Supporting Information. Because of the similarity of the spectra due to the presence of the same linker molecule in both MOFs, only the IR spectrum of CAU-8-ODB is discussed. Intense bands are observed at 1599 and 1431  $\text{cm}^{-1}$  corresponding to the asymmetric and the symmetric stretching vibrations of the carboxylate groups of the  $\text{ODB}^{2-}$  molecules. The ring stretching vibrations are located at 1565 and 1502  $\text{cm}^{-1}$ . The strong vibrations at 1249 and 1164  $\text{cm}^{-1}$  correspond to the C–O–C asymmetric and symmetric stretching vibrations, whereas the C–O–C in-plane deformation vibration is located at 541  $\text{cm}^{-1}$ . The vibration at 784  $\text{cm}^{-1}$  is characteristic for 1,4-substituted aromatic rings, and the C–H out-of-plane vibration can be observed at 881  $\text{cm}^{-1}$ . A deformation vibration corresponding to the  $\mu$ -OH groups connecting the  $\text{Al}^{3+}$  ions is located at 976  $\text{cm}^{-1}$ , whereas the stretching vibrations are observed at 3715  $\text{cm}^{-1}$  (**2**) and at 3650  $\text{cm}^{-1}$  (**3**), respectively.<sup>75</sup> The  $^1\text{H}$ -NMR spectra of dissolved samples of **2** and **3** and that of  $\text{H}_2\text{ODB}$  are displayed in Figure S23.

**Sorption Properties of CAU-8-ODB (2) and CAU-21-ODB (3).** Prior to the sorption measurements, the MOFs were activated for 6 h at 200 °C under reduced pressure ( $10^{-2}$  kPa). The nitrogen sorption experiment of **2** yields a type I isotherm, proving the microporosity of CAU-8-ODB (Figure S24 in the Supporting Information). Results of additional sorption measurements for CAU-8-ODB can be found in Figure S25–S29 in the Supporting Information and are summarized in Tables 2 and Tables S9 and S10 in the Supporting Information.

In contrast, CAU-21-ODB is not porous toward  $\text{N}_2$  but adsorbs 70 mg/g (1.59 mmol/g) of  $\text{CO}_2$  at 298 K and 1 bar (Figure S30 in the Supporting Information). The porosity toward only  $\text{CO}_2$  could be due to the very small pore openings in CAU-21, the smaller kinetic diameter of  $\text{CO}_2$ , and the higher measurement temperature. Due to its inability to adsorb  $\text{N}_2$ , this material is a potential candidate for  $\text{CO}_2/\text{N}_2$  separation via molecular sieving.

## CONCLUSION

Two new isoreticular Al-MOFs containing octanuclear clusters have been discovered employing the V-shaped linker molecules

**Table 2. Results of the Sorption Measurements of the Title Compounds**

material	$a_{\text{BET}}$ ( $\text{m}^2/\text{g}$ ) at 77 K	$V_{\text{mic}}$ ( $\text{cm}^3/\text{g}$ ) at 77 K <sup>a</sup>	theor $V_{\text{mic}}$ ( $\text{cm}^3/\text{g}$ ) <sup>a</sup>	$\text{CO}_2$ (mmol/g) at 298 K
CAU-21-BPDC				1.14
CAU-21-ODB				1.59
CAU-8-BPDC	1078 <sup>c</sup>	0.46	0.48 <sup>b</sup>	1.07
CAU-8-ODB	1004	0.47	0.53 <sup>b</sup>	2.48

<sup>a</sup>Determined at  $p/p_0 = 0.5$ . <sup>b</sup>Calculated with PLATON.<sup>78</sup> <sup>c</sup>The specific surface area and micropore volume are higher than those reported in the ref 23 due to a more thorough washing step using DMF.

$\text{H}_2\text{BPDC}$  and  $\text{H}_2\text{ODB}$  (denoted CAU-21-BPDC and CAU-21-ODB with the framework composition  $[\text{Al}(\text{OH})(\text{linker})]$ ). Using both linker molecules, framework polymorphs, denoted as CAU-8-BPDC and CAU-8-ODB, are obtained by adjustment of the synthesis conditions. The direct interconversion of the polymorphs could not be accomplished; however, analysis of the framework density and DFT calculations lead to the conclusion that the CAU-21 structure is in both cases the thermodynamically stable form. As one of the rare cases in Al-MOFs, the crystal structure of CAU-21-BPDC could be determined from single-crystal X-ray diffraction data. All Al-MOFs were thoroughly characterized. They are thermally stable up to ca. 350 °C, and the CAU-21 compounds exhibit size-selective gas adsorption properties.

## ASSOCIATED CONTENT

### Supporting Information

The Supporting Information is available free of charge on the ACS Publications website at DOI: 10.1021/acs.inorgchem.7b00202.

Exact amounts used for the HT syntheses, PXRD patterns, IR spectra, figures of the asymmetric units and the crystal structures, bond lengths and detailed information about the in situ investigation, and energetics of all the MOFs as predicted by DFT and sorption isotherms and their evaluation (PDF)

The CIF files of the compounds can be found in the CCDC database with the numbers 1529931 (CAU-21-BPDC), 1529928 (CAU-8-ODB), and 1529930 ( $[\text{Al}(\text{HODB})_2(\text{OH})]$ ). The CIF file of the calculated structure of CAU-21-ODB is provided in the Supporting Information.

## AUTHOR INFORMATION

### Corresponding Author

\*N.S.: tel, +49-431-880-1675; fax, +49-431-880-1775; e-mail, stock@ac.uni-kiel.de.

### ORCID

A. Ken Inge: 0000-0001-9118-1342

Helge Reinsch: 0000-0001-5288-1135

Chia-Her Lin: 0000-0002-1360-0828

Norbert Stock: 0000-0002-0339-7352

### Notes

The authors declare no competing financial interest.

## ACKNOWLEDGMENTS

The authors acknowledge support by the group of Prof. Dr. Wolfgang Bensch for the in situ equipment made available and DESY, Hamburg, Germany, for the provided beamtime. M.W. and G.M. thank the ANR CHESDENS (ANR-13-SEED-0001-01). A.K.I. is supported by the Knut and Alice Wallenberg Foundation (KAW) through the MAX IV postdoctoral scholarship under the grant number KAW 2012.0363 and also by the Röntgen-Ångström Cluster (VR) through the MATsynCELL project. This work was financially supported by the Deutsche Forschungsgemeinschaft (DFG) (STO 643/10-1).

## REFERENCES

- (1) Stock, N. In *Encyclopedia of Inorganic and Bioinorganic Chemistry*; Wiley: Chichester, U.K., 2011.
- (2) Loiseau, T.; Volkringer, C.; Haouas, M.; Taulelle, F.; Férey, G. Crystal chemistry of aluminium carboxylates: From molecular species towards porous infinite three-dimensional networks. *C. R. Chim.* **2015**, *18* (12), 1350–1369.
- (3) Schilling, L.-H.; Reinsch, H.; Stock, N. In *The Chemistry of Metal–Organic Frameworks*; Wiley-VCH: Weinheim, Germany, 2016; pp 105–135.
- (4) Cychoz, K. A.; Matzger, A. J. Water Stability of Microporous Coordination Polymers and the Adsorption of Pharmaceuticals from Water. *Langmuir* **2010**, *26* (22), 17198–17202.
- (5) Gaab, M.; Trukhan, N.; Maurer, S.; Gummaraju, R.; Müller, U. The progression of Al-based metal-organic frameworks – From academic research to industrial production and applications. *Microporous Mesoporous Mater.* **2012**, *157*, 131–136.
- (6) Ahnfeldt, T.; Gunzelmann, D.; Loiseau, T.; Hirsemann, D.; Senker, J.; Férey, G.; Stock, N. Synthesis and modification of a functionalized 3D open-framework structure with MIL-53 topology. *Inorg. Chem.* **2009**, *48* (7), 3057–3064.
- (7) Goesten, M. G.; Juan-Alcañiz, J.; Ramos-Fernandez, E. V.; Sai Sankar Gupta, K. B.; Stavitski, E.; van Bekkum, H.; Gascon, J.; Kapteijn, F. Sulfation of metal–organic frameworks: Opportunities for acid catalysis and proton conductivity. *J. Catal.* **2011**, *281* (1), 177–187.
- (8) Ahnfeldt, T.; Gunzelmann, D.; Wack, J.; Senker, J.; Stock, N. Controlled modification of the inorganic and organic bricks in an Al-based MOF by direct and post-synthetic synthesis routes. *CrystEngComm* **2012**, *14* (12), 4126–4136.
- (9) Modrow, A.; Zargarani, D.; Herges, R.; Stock, N. Introducing a photo-switchable azo-functionality inside Cr-MIL-101-NH<sub>2</sub> by covalent post-synthetic modification. *Dalton Trans.* **2012**, *41* (28), 8690–8696.
- (10) Wittmann, T.; Siegel, R.; Reimer, N.; Milius, W.; Stock, N.; Senker, J. Enhancing the Water Stability of Al-MIL-101-NH<sub>2</sub> via Postsynthetic Modification. *Chem. - Eur. J.* **2015**, *21* (1), 314–323.
- (11) Reinsch, H.; van der Veen, M. A.; Gil, B.; Marszalek, B.; Verbiest, T.; de Vos, D.; Stock, N. Structures, Sorption Characteristics, and Nonlinear Optical Properties of a New Series of Highly Stable Aluminum MOFs. *Chem. Mater.* **2013**, *25* (1), 17–26.
- (12) Biswas, S.; Ahnfeldt, T.; Stock, N. New Functionalized Flexible Al-MIL-53-X (X = -Cl, -Br, -CH<sub>3</sub>, -NO<sub>2</sub>, -(OH)<sub>2</sub>) Solids: Syntheses, Characterization, Sorption, and Breathing Behavior. *Inorg. Chem.* **2011**, *50* (19), 9518–9526.
- (13) Halis, S.; Reimer, N.; Klinkebiel, A.; Lüning, U.; Stock, N. Four new Al-based microporous metal-organic framework compounds with MIL-53-type structure containing functionalized extended linker molecules. *Microporous Mesoporous Mater.* **2015**, *216*, 13–19.
- (14) Reimer, N.; Bueken, B.; Leubner, S.; Seidler, C.; Wark, M.; De Vos, D.; Stock, N. Three Series of Sulfo-Functionalized Mixed-Linker CAU-10 Analogues: Sorption Properties, Proton Conductivity, and Catalytic Activity. *Chem. - Eur. J.* **2015**, *21* (35), 12517–12524.
- (15) Casey, W. H. Large Aqueous Aluminum Hydroxide Molecules. *Chem. Rev.* **2006**, *106* (1), 1–16.
- (16) Casey, W. H.; Phillips, B. L.; Furrer, G. Aqueous aluminum polynuclear complexes and nanoclusters: A review. *Rev. Mineral. Geochem.* **2001**, *44*, 167–190.
- (17) Mainicheva, E. A.; Gerasko, O. A.; Sheludyakova, L. A.; Naumov, D. Y.; Naumova, M. I.; Fedin, V. P. Synthesis and crystal structures of supramolecular compounds of polynuclear aluminum-(III) aqua hydroxo complexes with cucurbit[6]uril. *Russ. Chem. Bull.* **2006**, *55* (2), 267–275.
- (18) Reinsch, H.; Marszalek, B.; Wack, J.; Senker, J.; Gil, B.; Stock, N. A new Al-MOF based on a unique column-shaped inorganic building unit exhibiting strongly hydrophilic sorption behaviour. *Chem. Commun.* **2012**, *48* (76), 9486–9488.
- (19) Wang, Z.-W.; Chen, M.; Liu, C.-S.; Wang, X.; Zhao, H.; Du, M. A Versatile Al(III)-Based Metal–Organic Framework with High Physicochemical Stability. *Chem. - Eur. J.* **2015**, *21* (48), 17215–17219.
- (20) Reinsch, H.; Feyand, M.; Ahnfeldt, T.; Stock, N. CAU-3: A new family of porous MOFs with a novel Al-based brick: [Al<sub>2</sub>(OCH<sub>3</sub>)<sub>4</sub>(O<sub>2</sub>C-X-CO<sub>2</sub>)] (X = aryl). *Dalton Trans.* **2012**, *41* (14), 4164–4171.
- (21) Reinsch, H.; Krüger, M.; Wack, J.; Senker, J.; Salles, F.; Maurin, G.; Stock, N. A new aluminium-based microporous metal-organic framework: Al(BTB) (BTB = 1,3,5-benzenetrisbenzoate). *Microporous Mesoporous Mater.* **2012**, *157*, 50–55.
- (22) Loiseau, T.; Serre, C.; Huguenard, C.; Fink, G.; Taulelle, F.; Henry, M.; Bataille, T.; Férey, G. A Rationale for the Large Breathing of the Porous Aluminum Terephthalate (MIL-53) Upon Hydration. *Chem. - Eur. J.* **2004**, *10* (6), 1373–1382.
- (23) Reinsch, H.; Krüger, M.; Marrot, J.; Stock, N. First Keto-Functionalized Microporous Al-Based Metal–Organic Framework: [Al(OH)(O<sub>2</sub>C-C<sub>6</sub>H<sub>4</sub>-CO-C<sub>6</sub>H<sub>4</sub>-CO<sub>2</sub>)]<sub>n</sub>. *Inorg. Chem.* **2013**, *52* (4), 1854–1859.
- (24) Ahnfeldt, T.; Gunzelmann, D.; Loiseau, T.; Hirsemann, D.; Senker, J. r.; Férey, G.; Stock, N. Synthesis and Modification of a Functionalized 3D Open-Framework Structure with MIL-53 Topology. *Inorg. Chem.* **2009**, *48* (7), 3057–3064.
- (25) Reimer, N.; Gil, B.; Marszalek, B.; Stock, N. Thermal post-synthetic modification of Al-MIL-53-COOH: systematic investigation of the decarboxylation and condensation reaction. *CrystEngComm* **2012**, *14* (12), 4119–4125.
- (26) Reinsch, H.; Pillai, R. S.; Siegel, R.; Senker, J.; Lieb, A.; Maurin, G.; Stock, N. Structure and properties of Al-MIL-53-ADP, a breathing MOF based on the aliphatic linker molecule adipic acid. *Dalton Trans.* **2016**, *45* (10), 4179–4186.
- (27) Reimer, N.; Bueken, B.; Leubner, S.; Seidler, C.; Wark, M.; De Vos, D.; Stock, N. Three Series of Sulfo-Functionalized Mixed-Linker CAU-10 Analogues: Sorption Properties, Proton Conductivity, and Catalytic Activity. *Chem. - Eur. J.* **2015**, *21* (35), 12517–24.
- (28) Reinsch, H.; Waitschat, S.; Stock, N. Mixed-linker MOFs with CAU-10 structure: synthesis and gas sorption characteristics. *Dalton Trans.* **2013**, *42* (14), 4840–4847.
- (29) Reinsch, H.; De Vos, D.; Stock, N. Structure and Properties of [Al<sub>4</sub>(OH)<sub>8</sub>(o-C<sub>6</sub>H<sub>4</sub>(CO<sub>2</sub>)<sub>2</sub>)<sub>2</sub>·H<sub>2</sub>O, a Layered Aluminum Phthalate. *Z. Anorg. Allg. Chem.* **2013**, *639* (15), 2785–2789.
- (30) Volkringer, C.; Loiseau, T.; Haouas, M.; Taulelle, F.; Popov, D.; Burghammer, M.; Riekel, C.; Zlotea, C.; Cuevas, F.; Latroche, M.; Phanon, D.; Knöfel, C.; Llewellyn, P. L.; Férey, G. Occurrence of Uncommon Infinite Chains Consisting of Edge-Sharing Octahedra in a Porous Metal Organic Framework-Type Aluminum Pyromellitate Al<sub>4</sub>(OH)<sub>8</sub>[C<sub>10</sub>O<sub>8</sub>H<sub>2</sub>] (MIL-120): Synthesis, Structure, and Gas Sorption Properties. *Chem. Mater.* **2009**, *21* (24), 5783–5791.
- (31) Krüger, M.; Siegel, R.; Dreischarf, A.; Reinsch, H.; Senker, J.; Stock, N. [Al<sub>2</sub>(OH)<sub>2</sub>(TCPB)] – An Al-MOF based on a tetrapropyl linker molecule. *Microporous Mesoporous Mater.* **2015**, *216*, 27–35.
- (32) Ahnfeldt, T.; Guillou, N.; Gunzelmann, D.; Margiolaki, I.; Loiseau, T.; Férey, G.; Senker, J.; Stock, N. [Al<sub>4</sub>(OH)<sub>8</sub>(OCH<sub>3</sub>)<sub>4</sub>(H<sub>2</sub>N-bdc)<sub>3</sub>·x H<sub>2</sub>O: A 12-Connected Porous Metal-Organic Framework

with an Unprecedented Aluminum-Containing Brick. *Angew. Chem.* **2009**, *121* (28), 5265–5268.

(33) Gándara, F.; Furukawa, H.; Lee, S.; Yaghi, O. M. High Methane Storage Capacity in Aluminum Metal–Organic Frameworks. *J. Am. Chem. Soc.* **2014**, *136* (14), 5271–5274.

(34) Loiseau, T.; Lecroq, L.; Volkringer, C.; Marrot, J.; Férey, G.; Haouas, M.; Taulelle, F.; Bourrelly, S.; Llewellyn, P. L.; Latroche, M. MIL-96, a Porous Aluminum Trimesate 3D Structure Constructed from a Hexagonal Network of 18-Membered Rings and  $\mu_3$ -Oxo-Centered Trinuclear Units. *J. Am. Chem. Soc.* **2006**, *128* (31), 10223–10230.

(35) Volkringer, C.; Popov, D.; Loiseau, T.; Férey, G.; Burghammer, M.; Riekel, C.; Haouas, M.; Taulelle, F. Synthesis, Single-Crystal X-ray Microdiffraction, and NMR Characterizations of the Giant Pore Metal–Organic Framework Aluminum Trimesate MIL-100. *Chem. Mater.* **2009**, *21* (24), 5695–5697.

(36) Wittmann, T.; Siegel, R.; Reimer, N.; Milius, W.; Stock, N.; Senker, J. Enhancing the water stability of Al-MIL-101-NH<sub>2</sub> via postsynthetic modification. *Chem. - Eur. J.* **2015**, *21* (1), 314–323.

(37) Haouas, M.; Volkringer, C.; Loiseau, T.; Férey, G.; Taulelle, F. The Extra-Framework Sub-Lattice of the Metal–Organic Framework MIL-110: A Solid-State NMR Investigation. *Chem. - Eur. J.* **2009**, *15* (13), 3139–3146.

(38) Feyand, M.; Nather, C.; Rothkirch, A.; Stock, N. Systematic and In Situ Energy Dispersive X-ray Diffraction Investigations on the Formation of Lanthanide Phosphonatobutanesulfonates: Ln(O<sub>3</sub>P-C<sub>4</sub>H<sub>8</sub>-SO<sub>3</sub>)(H<sub>2</sub>O) (Ln = La–Gd). *Inorg. Chem.* **2010**, *49* (23), 11158–11163.

(39) Schmidt, C.; Stock, N. High-Throughput and in Situ Energy Dispersive X-ray Diffraction Investigation on the Formation of the New Metal Organogermanate Cu(OOCC<sub>2</sub>H<sub>4</sub>Ge)<sub>2</sub>O<sub>3</sub>. *Cryst. Growth Des.* **2011**, *11* (12), 5682–5687.

(40) Ahnfeldt, T.; Moellmer, J.; Guillerme, V.; Staudt, R.; Serre, C.; Stock, N. High-Throughput and Time-Resolved Energy-Dispersive X-Ray Diffraction (EDXRD) Study of the Formation of CAU-1-(OH)<sub>2</sub>: Microwave and Conventional Heating. *Chem. - Eur. J.* **2011**, *17* (23), 6462–6468.

(41) Schmidt, C.; Feyand, M.; Rothkirch, A.; Stock, N. High-throughput and in situ EDXRD investigation on the formation of two new metal aminoethylphosphonates - Ca(O<sub>3</sub>PC<sub>2</sub>H<sub>4</sub>NH<sub>2</sub>) and Ca(OH)(O<sub>3</sub>PC<sub>2</sub>H<sub>4</sub>NH<sub>3</sub>)•2H<sub>2</sub>O. *J. Solid State Chem.* **2012**, *188*, 44–49.

(42) Seidlhofer, B.; Antonova, E.; Wang, J.; Schinkel, D.; Bensch, W. On the Complexity of Crystallization of Thioantimonates: In-situ Energy Dispersive X-ray Diffraction (EDXRD) Studies of the Solvothermal Formation of the Isostructural Thioantimonates [TM-(tren)Sb<sub>4</sub>S<sub>7</sub>] (TM = Fe, Zn). *Z. Anorg. Allg. Chem.* **2012**, *638* (15), 2555–2564.

(43) Feyand, M.; Köppen, M.; Friedrichs, G.; Stock, N. Bismuth Tri- and Tetraarylcarboxylates: Crystal Structures, In Situ X-ray Diffraction, Intermediates and Luminescence. *Chem. - Eur. J.* **2013**, *19* (37), 12537–12546.

(44) Regus, M.; Kuhn, G.; Mankovsky, S.; Ebert, H.; Bensch, W. Investigations of the crystallization mechanism of CrSb and CrSb<sub>2</sub> multilayered films using in-situ X-ray diffraction and in-situ X-ray reflectometry. *J. Solid State Chem.* **2012**, *196*, 100–109.

(45) Antonova, E.; Seidlhofer, B.; Wang, J.; Hinz, M.; Bensch, W. Controlling Nucleation and Crystal Growth of a Distinct Polyoxovanadate Cluster: An In Situ Energy Dispersive X-ray Diffraction Study under Solvothermal Conditions. *Chem. - Eur. J.* **2012**, *18* (48), 15316–15322.

(46) Zhou, Y.; Antonova, E.; Lin, Y.; Grunwaldt, J.-D.; Bensch, W.; Patzke, G. R. In Situ X-ray Absorption Spectroscopy/Energy-Dispersive X-ray Diffraction Studies on the Hydrothermal Formation of Bi<sub>2</sub>W<sub>1-x</sub>Mo<sub>x</sub>O<sub>6</sub> Nanomaterials. *Eur. J. Inorg. Chem.* **2012**, *2012* (5), 783–789.

(47) Bensch, W.; Ophrey, J.; Hain, H.; Gesswein, H.; Chen, D.; Monig, R.; Gruber, P. A.; Indris, S. Chemical and electrochemical insertion of Li into the spinel structure of CuCr<sub>2</sub>Se<sub>4</sub>: ex situ and in situ

observations by X-ray diffraction and scanning electron microscopy. *Phys. Chem. Chem. Phys.* **2012**, *14* (20), 7509–7516.

(48) Pienack, N.; Bensch, W. In-Situ Monitoring of the Formation of Crystalline Solids. *Angew. Chem., Int. Ed.* **2011**, *50* (9), 2014–2034.

(49) Feyand, M.; Hübner, A.; Rothkirch, A.; Wragg, D. S.; Stock, N. Copper Phosphonatoethanesulfonates: Temperature Dependent in Situ Energy Dispersive X-ray Diffraction Study and Influence of the pH on the Crystal Structures. *Inorg. Chem.* **2012**, *51* (22), 12540–12547.

(50) Stock, N.; Bein, T. High-throughput investigation of metal carboxyarylphosphonate hybrid compounds. *J. Mater. Chem.* **2005**, *15* (13), 1384–1391.

(51) Reinsch, H.; Stock, N. High-throughput studies of highly porous Al-based MOFs. *Microporous Mesoporous Mater.* **2013**, *171* (0), 156–165.

(52) Bauer, S.; Stock, N. High performance-methods in solid state chemistry. *Chem. Unserer Zeit* **2007**, *41* (5), 390–398.

(53) Stock, N. High-throughput methods for discovery and optimization of porous crystalline materials. *Chem. Ing. Tech.* **2010**, *82* (7), 1039–1047.

(54) Stock, N. High-throughput investigations employing solvothermal syntheses. *Microporous Mesoporous Mater.* **2010**, *129* (3), 287–295.

(55) Spek, A. Structure validation in chemical crystallography. *Acta Crystallogr., Sect. D: Biol. Crystallogr.* **2009**, *65* (2), 148–155.

(56) *Topas-Academic 4.1 A*; Coelho Software, Brisbane, Australia.

(57) Sheldrick, G. *Acta Crystallogr., Sect. A: Found. Crystallogr.* **2008**, *64*, 112.

(58) VandeVondele, J.; Krack, M.; Mohamed, F.; Parrinello, M.; Chassaing, T.; Hutter, J. Quickstep: Fast and accurate density functional calculations using a mixed Gaussian and plane waves approach. *Comput. Phys. Commun.* **2005**, *167* (2), 103–128.

(59) Hutter, J.; Iannuzzi, M.; Schiffrmann, F.; VandeVondele, J. cp2k: atomistic simulations of condensed matter systems. *WIREs. Comput. Mol. Sci.* **2014**, *4* (1), 15–25.

(60) CP2K; The CP2K Developers Group.

(61) Perdew, J. P.; Burke, K.; Ernzerhof, M. Generalized Gradient Approximation Made Simple. *Phys. Rev. Lett.* **1996**, *77* (18), 3865–3868.

(62) Grimme, S.; Antony, J.; Ehrlich, S.; Krieg, H. A consistent and accurate ab initio parametrization of density functional dispersion correction (DFT-D) for the 94 elements H–Pu. *J. Chem. Phys.* **2010**, *132* (15), 154104.

(63) Grimme, S. Accurate description of van der Waals complexes by density functional theory including empirical corrections. *J. Comput. Chem.* **2004**, *25* (12), 1463–1473.

(64) VandeVondele, J.; Hutter, J. Gaussian basis sets for accurate calculations on molecular systems in gas and condensed phases. *J. Chem. Phys.* **2007**, *127* (11), 114105.

(65) Goedecker, S.; Teter, M.; Hutter, J. Separable dual-space Gaussian pseudopotentials. *Phys. Rev. B: Condens. Matter Mater. Phys.* **1996**, *54* (3), 1703–1710.

(66) Krack, M. Pseudopotentials for H to Kr optimized for gradient-corrected exchange-correlation functionals. *Theor. Chem. Acc.* **2005**, *114* (1), 145–152.

(67) Hartwigsen, C.; Goedecker, S.; Hutter, J. Relativistic separable dual-space Gaussian pseudopotentials from H to Rn. *Phys. Rev. B: Condens. Matter Mater. Phys.* **1998**, *58* (7), 3641–3662.

(68) Gelb, L. D.; Gubbins, K. E. Pore Size Distributions in Porous Glasses: A Computer Simulation Study. *Langmuir* **1999**, *15* (2), 305–308.

(69) Rappe, A. K.; Casewit, C. J.; Colwell, K. S.; Goddard, W. A.; Skiff, W. M. UFF, a full periodic table force field for molecular mechanics and molecular dynamics simulations. *J. Am. Chem. Soc.* **1992**, *114* (25), 10024–10035.

(70) Engelke, L.; Schaefer, M.; Schur, M.; Bensch, W. In Situ X-ray Diffraction Studies of the Crystallization of Layered Manganese Thioantimonates(III) under Hydrothermal Conditions. *Chem. Mater.* **2001**, *13* (4), 1383–1390.

(71) Wharmby, M. T.; Pearce, G. M.; Mowat, J. P. S.; Griffin, J. M.; Ashbrook, S. E.; Wright, P. A.; Schilling, L. H.; Lieb, A.; Stock, N.; Chavan, S.; Bordiga, S.; Garcia, E.; Pirngruber, G. D.; Vreeke, M.; Gora, L. Synthesis and crystal chemistry of the STA-12 family of metal N,N'-piperazinebis(methylenephosphonate)s and applications of STA-12(Ni) in the separation of gases. *Microporous Mesoporous Mater.* **2012**, *157*, 3–17.

(72) Reimer, N.; Reinsch, H.; Inge, A. K.; Stock, N. New Al-MOFs Based on Sulfonyldibenzoate Ions: A Rare Example of Intralayer Porosity. *Inorg. Chem.* **2015**, *54* (2), 492–501.

(73) Halis, S.; Inge, A. K.; Dehning, N.; Weyrich, T.; Reinsch, H.; Stock, N. Dihydroxybenzoquinone as Linker for the Synthesis of Permanently Porous Aluminum Metal–Organic Frameworks. *Inorg. Chem.* **2016**, *55*, 7425–7431.

(74) *Materials Studio v4.1*; Accelrys Software Inc.

(75) Salazar, J. M.; Weber, G.; Simon, J. M.; Bezverkhyy, I.; Bellat, J. P. Characterization of adsorbed water in MIL-53(Al) by FTIR spectroscopy and ab-initio calculations. *J. Chem. Phys.* **2015**, *142* (12), 124702.

(76) Sumida, K.; Rogow, D. L.; Mason, J. A.; McDonald, T. M.; Bloch, E. D.; Herm, Z. R.; Bae, T.-H.; Long, J. R. Carbon Dioxide Capture in Metal–Organic Frameworks. *Chem. Rev.* **2012**, *112* (2), 724–781.

(77) Jin, Z.; Zhao, H.-Y.; Zhao, X.-J.; Fang, Q.-R.; Long, J. R.; Zhu, G.-S. A novel microporous MOF with the capability of selective adsorption of xylenes. *Chem. Commun.* **2010**, *46* (45), 8612.

(78) Kraus, W.; Nolze, G. POWDER CELL - a program for the representation and manipulation of crystal structures and calculation of the resulting X-ray powder patterns. *J. Appl. Crystallogr.* **1996**, *29* (3), 301–303.





## 4.7 Strategien zur Synthese von MOFs mit speziellen optischen Eigenschaften

### 4.7.1 Effect of partial linker fluorination and linker extension on structure and properties of the Al-MOF CAU-10

Der folgende Artikel wurde im Jahre 2017 in der Fachzeitschrift *Microporous and Mesoporous Materials*, ELSEVIER GmbH veröffentlicht. Der Wiederabdruck erfolgte mit freundlicher Genehmigung der ELSEVIER GmbH. Reproduced with permission from:

M. Krüger, H. Reinsch, A. K. Inge, N. Stock, *Micropor. Mesopor. Mat.*, **2017**, *249*, 128-136. DOI: 10.1016/j.micromeso.2017.04.054

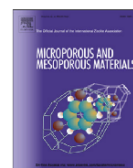
In dieser Arbeit wurde der Effekt der partiellen Fluorierung des MOF-Gerüsts auf dessen Eigenschaften untersucht. Hierfür wurde das System Al<sup>3+</sup>/5-Fluorisophthalsäure (H<sub>2</sub>mBDC-5F)/Isophthalsäure (H<sub>2</sub>mBDC)/DMF/H<sub>2</sub>O im Gemischtlinker-Ansatz analysiert. Dabei konnten drei CAU-10-Derivate erhalten werden, die 11, 28 bzw. 44% fluoridierte Linkermoleküle enthalten (CAU-10-H/F<sub>11</sub>, CAU-10-H/F<sub>28</sub> und CAU-10-H/F<sub>44</sub>). Die Verhältnisse der in den Verbindungen vorliegenden Linkermoleküle wurde mittels <sup>1</sup>H-NMR-Spektroskopie bestimmt. Die Kristallstruktur von CAU-10-H/F<sub>28</sub> wurde mit Hilfe von Rietveld-Methoden aus Röntgenpulverdaten erhalten. CAU-10-H/F<sub>28</sub> kristallisiert in einer tetragonalen Elementarzelle mit den Gitterparametern  $a = b = 21.3075(5)$  und  $c = 10.7101(3)$  Å in der Raumgruppe  $I4_1md$ . Die Kristallstruktur ist aufgebaut aus helikalen Ketten aus *cis*-eckenverknüpften AlO<sub>6</sub>-Oktaedern, die durch die Isophthalationen miteinander verbrückt sind. So werden zugängliche, quadratische, eindimensionale Poren gebildet. Sorptionsmessungen der Verbindungen für N<sub>2</sub>, H<sub>2</sub> und H<sub>2</sub>O zeigten eine starke Abhängigkeit der Menge des adsorbierten Gases vom Grad der Fluorierung. Mit steigendem Fluor-Gehalt sinken die Gesamtaufnahmen der adsorbierten Gase und der hydrophobe Charakter der Verbindung steigt. Zusätzlich konnte mit der Tricarbonsäure 4,4',4''-5-Triazin-2,4,6-triyl-tribenzoesäure (H<sub>3</sub>TATB) ein CAU-10-Derivat, bezeichnet als CAU-10-HTATB, hergestellt werden. Bei der umfangreichen Charakterisierung zeigte sich eine Temperaturstabilität von bis zu 400 °C, jedoch ist die Verbindung unporös gegenüber N<sub>2</sub>. Die Struktur von CAU-10-HTATB konnte ebenfalls erfolgreich mittels Rietveld-Methoden aus Röntgenpulverdaten verfeinert werden (Raumgruppe  $I4_1/a$ ,  $a = b = 36.438(1)$  und  $c = 10.9373(9)$  Å). Zusätzliche Informationen sowie Details zu SHG-Messungen an den fluoridierten Verbindungen befinden sich im Anhang.



Contents lists available at ScienceDirect

## Microporous and Mesoporous Materials

journal homepage: [www.elsevier.com/locate/micromeso](http://www.elsevier.com/locate/micromeso)



### Effect of partial linker fluorination and linker extension on structure and properties of the Al-MOF CAU-10



Martin Krüger<sup>a</sup>, Helge Reinsch<sup>a</sup>, A. Ken Inge<sup>b</sup>, Norbert Stock<sup>a,\*</sup>

<sup>a</sup> Institut für Anorganische Chemie, Christian-Albrechts-Universität, Max-Eyth-Straße 2, 24118 Kiel, Germany

<sup>b</sup> Department of Materials and Environmental Chemistry, Stockholm University, Stockholm S-106 91, Sweden

#### ARTICLE INFO

##### Article history:

Received 14 March 2017

Received in revised form

24 April 2017

Accepted 27 April 2017

Available online 28 April 2017

##### Keywords:

Metal-organic frameworks

Aluminum

Powder X-ray diffraction

CAU-10

Water sorption

#### ABSTRACT

The systematic investigation of the solvothermal system  $\text{Al}^{3+}/5$ -fluoroisophthalic acid ( $\text{H}_2\text{mBDC-5F}$ )/isophthalic acid ( $\text{H}_2\text{mBDC}$ )/DMF/ $\text{H}_2\text{O}$  through a mixed-linker approach led to new mixed-linker CAU-10 derivatives containing 11, 28 and 44% of fluorinated linker molecules (denoted as CAU-10-H/F<sub>11</sub>, CAU-10-H/F<sub>28</sub> and CAU-10-H/F<sub>44</sub>, respectively), as determined by NMR spectroscopy. The crystal structure of CAU-10-H/F<sub>28</sub> was determined using the Rietveld method (space group  $I4_1md$ ,  $a = b = 21.3075(5)$ ,  $c = 10.7101(3)$  Å). The structure is built up by helical chains composed of *cis* corner-sharing  $\text{AlO}_6$  polyhedra. Each of these helices is interconnected to four adjacent helices with alternating rotational orientation through the carboxylate groups of *mBDC*<sup>2-</sup> linker molecules. Thus, accessible, square-shaped channels are formed. Sorption measurements revealed a high dependency of the adsorbed amount of gas on the degree of fluorination. With increasing fluorination, the total uptake decreases in  $\text{N}_2$ ,  $\text{H}_2$  and  $\text{H}_2\text{O}$  sorption experiments and the hydrophobic character of the pores increases.

In addition, an extended CAU-10 derivative, CAU-10-HTATB, was discovered using the tricarboxylic acid 4,4',4''-s-triazine-2,4,6-triyl-tribenzoic acid ( $\text{H}_3\text{TATB}$ ) during the high-throughput investigation of the system  $\text{Al}^{3+}/\text{H}_3\text{TATB}/\text{DMF}/\text{H}_2\text{O}$ . This new MOF, which was denoted CAU-10-HTATB, was thoroughly characterized using IR spectroscopy, thermogravimetric and elemental analysis, temperature dependent powder X-ray diffraction (PXRD) and sorption measurements. Although the compound is thermally stable up to 400 °C according to temperature-dependent PXRD measurements, it is not porous towards  $\text{N}_2$  molecules. The structure of CAU-10-HTATB could be also refined from PXRD data using the Rietveld method (space group  $I4_1/a$ ,  $a = b = 36.438$  (1),  $c = 10.9373$  (9) Å).

© 2017 Published by Elsevier Inc.

#### 1. Introduction

The modular building principle of metal-organic frameworks (MOFs) allows to combine a huge number of inorganic building units (IBUs) with the immense variety of available organic linker molecules [1,2]. Most often linear molecules are investigated as the organic building blocks, leading to famous and well investigated MOF series of which the parent frameworks are known as MIL-53 [ $\text{M}^{\text{III}}(\text{OH})(\text{BDC})$ ] [3–10], MOF-5 [ $\text{ZnO}_4(\text{BDC})_3$ ] [11–13] or HKUST-1 [ $\text{Cu}_3(\text{BTC})_2$ ] [13–15], as a representative for nonlinear linker molecules. The investigation of non-linear, V-shaped linker molecules remained for a long time rather uncommon. Only few examples of MOFs containing V-shaped linker molecules have been reported [16,17]. In previous studies we focused on these rarely employed linker molecules which resulted in Al-MOFs such as CAU-11

[ $\text{Al}(\text{OH})(\text{SDBA})$ ]-0.25DMF [18], CAU-12 [ $\text{Al}_2(\text{OH})_2(\text{DPSTC})(\text{H}_2\text{O})_2$ ]-0.5 $\text{H}_2\text{O}$  [18], based on sulfonyldi- and tetra-benzoic acid as well as CAU-8 [ $\text{Al}(\text{OH})(\text{BPDC})$ ] [19], and CAU-21 [ $\text{Al}(\text{OH})(\text{BPDC})$ ] [20] based on 4,4'-benzophenonedicarboxylic acid as well as the MOF series denoted CAU-10 [ $\text{Al}(\text{OH})(\text{mBDC})$ ] [21], based on isophthalic acid and its derivatives. As an aluminum based MOF, CAU-10 is also interesting for industrial applications due to its high thermal and chemical stability as well as the low price and the low toxicity of aluminum salts [22].

The structure of CAU-10 consist of helical chains of *cis* corner sharing  $\text{AlO}_6$  polyhedra interlinked by isophthalate ions into a 3D framework. Square-shaped channels are formed between four linked helices with diameters up to 7 Å [21]. Several studies reported the use of functionalized linker molecules to modify the pores of the MOF and up to now various functionalized modifications of CAU-10 ( $-\text{H}$  [21],  $-\text{CH}_3$  [21],  $-\text{OCH}_3$  [21],  $-\text{NH}_2$  [21],  $-\text{NO}_2$  [21],  $-\text{OH}$  [21] and  $-\text{Br}$  [23]) have been reported. Furthermore, the mixed-linker approach led to the difunctionalized

\* Corresponding author.

E-mail address: [stock@ac.uni-kiel.de](mailto:stock@ac.uni-kiel.de) (N. Stock).

derivatives CAU-10-H/Br [23], -H/CH<sub>3</sub> [23], -NO<sub>2</sub>/NH<sub>2</sub> [23], -H/SO<sub>3</sub>H [24], -NO<sub>2</sub>/SO<sub>3</sub>H [24] and -OH/SO<sub>3</sub>H [24].

Functionalization of linker molecules can be used to alter the sorption properties of the respective MOF. For example, the parent compound CAU-10-H exhibits extraordinary H<sub>2</sub>O sorption properties which makes it especially interesting for application in heat pumps or as humidity sensors [25–27]. The sulfo-functionalized mixed-linker compounds were applied in proton conductivity, humidity sensing and acid catalysis [24]. An unexpected photo-reactivity was observed for the nitro functionalized CAU-10-NO<sub>2</sub> [28]. Although various functionalized derivatives of CAU-10 have been reported, fluorine modified CAU-10-F is hitherto unknown. Fluorine functionalization of the pores of the MOF could be a valuable tool for the separation of chlorofluorocarbons (CFCs) or to modify the H<sub>2</sub>O sorption properties through hydrophobization of the pores [29].

Herein we present the synthesis and characterization of three mixed-linker compounds with the CAU-10 structure containing different fractions of fluorine incorporated into the framework: [Al(OH)(mBDC)<sub>1-x</sub>(mBDC-5F)<sub>x</sub>] (x = 0.11, 0.28, 0.44). Additional investigations using the tritopic 4,4',4''-s-triazine-2,4,6-triyl-tribenzoic acid (H<sub>3</sub>TATB) as the linker molecule led to the discovery of CAU-10-HTATB. The compounds were characterized by powder X-ray diffraction (PXRD), <sup>1</sup>H-NMR and IR spectroscopy as well as sorption measurements.

## 2. Experimental section

### 2.1. Materials and methods

All chemicals used for the syntheses are commercially available and were employed without further purification. The initial discovery and following subsequent synthesis optimization steps were carried out employing our 24- and 48-high-throughput (HT) reactor system for solvothermal reactions [30–34]. These reactor systems contain custom-made Teflon reaction vessels with a maximum volume of either 2 mL or 250 μL. The high-throughput PXRD measurements were performed in transmission geometry using a STOE HT diffractometer equipped with a  $\chi$ y-stage and an image plate detector system (Cu K<sub>α1</sub> radiation). High-resolution PXRD data were measured on a STOE Stadi-P powder diffractometer equipped with a MYTHEN1K detector (Cu K<sub>α1</sub> radiation). Temperature dependent high-resolution PXRD data were recorded on a STOE Stadi-P diffractometer and equipped with a MYTHEN1K detector using Mo K<sub>α</sub> radiation. These measurements were carried out in air in a 0.5 mm quartz capillary between 1 and 18° in 2θ. <sup>1</sup>H-NMR spectroscopy was carried out on a Bruker DRX 500 at 200 MHz. IR spectra were recorded on an ATI Matheson Genesis spectrometer equipped with an ATR unit in the spectral range of 400–4000 cm<sup>-1</sup>. Thermogravimetric (TG) analyses were performed using a NETZSCH STA 409 CD analyzer. The samples were heated in Al<sub>2</sub>O<sub>3</sub> crucibles at a rate of 4 K min<sup>-1</sup> under a flow of air (75 mL min<sup>-1</sup>). The TG data were corrected for buoyancy and current effects. A HEKAtech Euro EA Elemental Analyzer was used for elemental analysis. Sorption experiments were carried out using a Belsorp-max instrument (BEL JAPAN INC.). Before the sorption experiments, the samples were activated at the specified conditions. Accelrys Materials Studio 4.1 was used for structure optimization by force-field calculations (Universal force-field) [35]. Rietveld refinement of the structural models was carried out with TOPAS Academic v4.1 [36].

### 2.2. Synthesis of 5-fluoroisophthalic acid (H<sub>2</sub>mBDC-5F)

The reaction was carried out by combining the synthesis procedures of Ghosh et al. [37] and Gumbley et al. [38]. A mixture of

1 mL 5-fluoro-*m*-xylene (8.05 mmol, ABCR), 7.11 mL pyridine and 5 mL H<sub>2</sub>O was refluxed under vigorous stirring while slowly adding 7.29 g KMnO<sub>4</sub> (46 mmol) within 90 min. After complete addition the mixture was refluxed for another 7 h affording a brown slurry. After cooling to room temperature 60 mg Na<sub>2</sub>SO<sub>4</sub> and 50 mL of H<sub>2</sub>O were added to the raw product. The solid was filtered off and washed with 25 mL of 1 M HCl. Another 75 mL of 1 M HCl was added to the filtrate until a pH value of pH = 3 was achieved. The filtrate was extracted three times with 75 mL ethylacetate and saturated with NaCl. The aqueous phase was extracted two times with a mixture of 80 mL chloroform, 10 mL methanol and 10 mL H<sub>2</sub>O. The combined organic extracts were dried over Na<sub>2</sub>SO<sub>4</sub> and organic solvents were removed under reduced pressure. The solution was stored in a freezer to obtain crystals, which were filtered off and recrystallized from hot water. A reaction scheme and the <sup>1</sup>H-NMR spectrum of the final product are shown in Figs. S1 and S2 in the Supporting Information. (<sup>1</sup>H-NMR (200 MHz, DMSO, 300 K, TMS): δ = 7.90 [dd, 2H, <sup>4</sup>J = 1.5 Hz, JFH = 8.9 Hz, H4, 4'], 8.30 [t, <sup>4</sup>J = 1.4, 1H, H2] ppm.) Yield: 0.47 g (32%).

### 2.3. Synthesis of 2,4,6-tri-*p*-tolyl-*s*-triazine

The synthesis was carried out following the procedure published by Park et al. [39]. 2.9 mL of *p*-tolunitrile (24.3 mmol, ABCR) were added slowly under stirring to 5.85 mL trifluoromethanesulfonic acid (10 g, 66.6 mmol). The mixture was stirred overnight. Ice cold water was added and neutralized with 25% aqueous ammonia solution. The precipitate was filtered off and subsequently washed with water and acetone. Recrystallization from toluene yielded 2,4,6-tri-*p*-tolyl-*s*-triazine as white needle-shaped crystals. The reaction scheme and the <sup>1</sup>H-NMR spectrum of the final product are shown in Figs. S3 and S4. (<sup>1</sup>H-NMR: (200 MHz, CDCl<sub>3</sub>, 300 K): δ = 8.66 (m, 2H, H-2), 7.37 (m, 2H, H-1), 2.49 (s, 3H, H-3) ppm.) Yield: 2.7 g (94%)

### 2.4. Synthesis of 4,4',4''-*s*-triazine-2,4,6-triyl-tribenzoic acid (H<sub>3</sub>TATB)

The synthesis was carried out following the procedure published by Sun et al. [40]. To a mixture of 66.6 mL conc. acetic acid (1.17 mol) and 4.24 mL conc. H<sub>2</sub>SO<sub>4</sub> (79.4 mmol) in a 500 mL three-necked flask, 2.68 g of 2,4,6-tri-*p*-tolyl-*s*-triazine (7.63 mmol) were added. Subsequently 6.93 g chromium (VI) oxide (69.3 mmol) and 4.73 mL acetic anhydride (49.6 mmol) were added carefully in small amounts (1.5 g and 1 mL, respectively), keeping the temperature below 50 °C (1 h). The resulting black-brown slurry was stirred overnight at room temperature. Subsequently 300 mL of cold water were added, well mixed, and the slurry was filtered. The precipitate was washed with water and dissolved in 300 mL 2 M NaOH solution. Unreacted starting material was removed by filtration and the filtrate was acidified with HCl to yield the crude reaction product, which was again filtered off. Recrystallization from *N,N*-dimethylformamide (DMF) resulted in the pure product, which was washed with methanol and dried under ambient conditions. A reaction scheme and the <sup>1</sup>H-NMR spectrum of the final product are shown in Figs. S5 and S6. (<sup>1</sup>H-NMR: (500 MHz, DMSO, 300 K): δ = 8.84 (m, 2H, H-2), 8.20 (m, 2H, H-1) ppm.) Yield: 3.0 g (89%).

### 2.5. HT experiments to afford CAU-10-H/F<sub>x</sub>

High-throughput investigations under solvothermal reaction conditions were carried out for the system Al<sup>3+</sup>/5-fluoroisophthalic acid (H<sub>2</sub>mBDC-5F)/water/DMF by employing our 24-high-throughput reactor system equipped with Teflon reactors with a volume of 2 mL [32–34]. In this chemical system no CAU-10-F

could be obtained. Therefore, the mixed-linker approach was chosen and the amount of *m*BDC-5F<sup>2-</sup> was increased step wise in the reaction mixture. Thus, a high-throughput investigation was carried out in the system Al<sup>3+</sup>/5-fluoroisophthalic acid (H<sub>2</sub>*m*BDC-5F)/isophthalic acid (H<sub>2</sub>*m*BDC)/water/DMF varying the molar ratios of H<sub>2</sub>*m*BDC-5F: H<sub>2</sub>*m*BDC from 7:1 to 1:7. Using a reaction temperature of 120 °C, a reaction time of 12 h, a constant molar ratio of Al<sup>3+</sup>:linker of 1:1 (one unit corresponds to the amount of 68 μmol) and a solvent mixture of 150 μL DMF and 14.2 μL H<sub>2</sub>O, three partially fluorinated CAU-10 derivatives containing 11, 28 and 44% *m*BDC-5F<sup>2-</sup> could be obtained as microcrystalline powders (Table S1). Amounts of H<sub>2</sub>*m*BDC-5F higher than 44% resulted only in products of low crystallinity.

#### 2.6. Optimized reaction conditions for CAU-10-H/F<sub>x</sub>

The exact amounts of 5-fluoroisophthalic acid (H<sub>2</sub>*m*BDC) and isophthalic acid (H<sub>2</sub>*m*BDC) for the synthesis of CAU-10-H/F<sub>x</sub> (x = 11, 28 and 44%) are provided in Table 1 and in Table S1, numbers 5 to 7. The HT study led to the following optimized synthesis procedure: to a mixture of 135.8 μL 0.5 M Al<sub>2</sub>(SO<sub>4</sub>)<sub>3</sub>·18H<sub>2</sub>O in H<sub>2</sub>O (68 μmol), H<sub>2</sub>*m*BDC-5F and H<sub>2</sub>*m*BDC, 150 μL of DMF (1.93 mmol) and 14.2 μL of deionized water (1.08 mmol) were added. The reactor was sealed and heated to 120 °C within 1 h, held at this temperature for 12 h and then cooled down to room temperature within 1 h. The product was filtered off, stirred in DMF for 2 h and filtered off again. The additional washing step in DMF was necessary due to the presence of recrystallized linker molecules.

#### 2.7. HT experiments to afford CAU-10-HTATB

High-throughput investigations under solvothermal reaction conditions were carried out for the system Al<sup>3+</sup>/4,4',4''-s-triazine-2,4,6-triyl-tribenzoic acid (H<sub>3</sub>TATB)/water/DMF/additive by employing our 24-high-throughput reactor system equipped with Teflon reactors with a volume of 2 mL [32–34]. Using this setup the reaction temperature (135–180 °C), the reaction time (6–72 h) the molar ratio of Al<sup>3+</sup>:H<sub>3</sub>TATB (between 1:1 and 11:4, one unit corresponds to the amount of 11 μmol), the volume ratio DMF:H<sub>2</sub>O (between 0:200 μL and 320:150 μL) and the effect of additives (10–20 μL formic acid, acetic acid, diethyl amine, triethyl amine, as well as 10–50 μL 2 M HNO<sub>3</sub> and 2 M NaOH) were investigated (Table S2). Phase pure CAU-10-HTATB was only obtained as a microcrystalline powder.

#### 2.8. Optimized reaction conditions for CAU-10-HTATB

The HT synthesis optimization led to the following optimized synthesis procedure: to a mixture of 72.5 μL 0.5 M Al(NO<sub>3</sub>)<sub>3</sub>·9H<sub>2</sub>O in DMF (36 μmol) and 20 mg 4,4',4''-s-triazine-2,4,6-triyl-tribenzoic acid (H<sub>3</sub>TATB, 45 μmol), 177.5 μL of *N,N*-dimethylformamide (2.29 mmol, Grüssing) and 50 μL of deionized water (3.81 mmol) were added. The reactor was sealed and heated to 180 °C for 6 h. Yield: 9 mg, 49% based on Al<sup>3+</sup>.

#### 2.9. Structure determination

The crystal structures of CAU-10-H/F<sub>x</sub> and CAU-10-HTATB were determined as follows. Cell parameters were deduced by indexing of the X-ray powder diffraction data using TOPAS Academic [36]. The compounds crystallize in a tetragonal unit cell with extinction conditions matching the space group *I*4<sub>1</sub>*md* and *I*4<sub>1</sub>/*a* for CAU-10-H/F<sub>x</sub> and CAU-10-HTATB, respectively. The structure of CAU-10-Br served as a starting model for CAU-10-H/F<sub>x</sub> and CAU-10-HTATB. Space group transformation from *I*4<sub>1</sub>/*amd* for CAU-10-Br to *I*4<sub>1</sub>*md*

**Table 1**

Exact amounts of 5-fluoroisophthalic acid (H<sub>2</sub>*m*BDC) and isophthalic acid (H<sub>2</sub>*m*BDC) employed for the synthesis of CAU-10-H/F<sub>x</sub> (x = 11, 28 and 44%).

CAU-10-H/F <sub>x</sub>	H <sub>2</sub> <i>m</i> BDC-5F	H <sub>2</sub> <i>m</i> BDC	Yield (based on Al <sup>3+</sup> )
x = 11%	1.6 mg (8.5 μmol)	9.9 mg (65.9 μmol)	6 mg (41%)
x = 28%	3.1 mg (16.5 μmol)	8.5 mg (56.6 μmol)	5 mg (34%)
x = 44%	4.1 mg (21.8 μmol)	7.0 mg (46.6 μmol)	3 mg (19%)

for CAU-10-H/F<sub>x</sub> was carried out using the program Powdercell [41]. Using the program Materials Studio 4.1 [35] the *m*BDC-Br<sup>2-</sup> molecule was exchanged by *m*BDC-F<sup>2-</sup> for CAU-10-H/F<sub>x</sub> and by HTATB<sup>2-</sup> for CAU-10-HTATB. The lattice parameters were fixed to the experimentally determined values and energy minimization calculations were carried out using the universal force field (UFF) as implemented in the Forcite module of Materials Studio 4.1 [35]. This approach led to suitable structural models which could be used in the subsequent Rietveld refinement of CAU-10-H/F<sub>x</sub> and CAU-10-HTATB with TOPAS Academic 4.1 [36]. For the refinement of CAU-1-H/F<sub>28</sub>, the positions of the atoms of the inorganic building unit were freely refined while the linker molecules were treated as rigid bodies and only refined along the *b* and *c* axes. The occupancies of the functional fluorine groups was freely refined and converged to values of 29(1) %, being in excellent agreement with the other analytical methods. Residual electron density was identified by Fourier synthesis and attributed to solvent molecules which were modelled by (partially occupied) oxygen atoms. For refinement of CAU-10-HTATB the positions of atoms in the inorganic building unit were freely refined while the linker was described using a *z*-matrix with the translational and rotational parameters freely refined while allowing the aromatic rings and the carboxylate groups to rotate. Residual electron density was identified by Fourier synthesis and attributed to solvent molecules. Two DMF molecules were positioned in the pores as rigid bodies and their positions were refined. Hydrogen atoms were not included in the model. Detailed information about the results of the refinement of CAU-10-H/F<sub>x</sub> and CAU-10-HTATB are summarized in Table 2. Bond lengths can be found in Tables S3 and S4.

### 3. Results and discussion

#### 3.1. Synthesis of CAU-10-H/F<sub>x</sub> and determination of degree of fluorination

The systematic investigation of the system Al<sup>3+</sup>/H<sub>2</sub>*m*BDC-5F/H<sub>2</sub>*m*BDC/water/DMF was carried out by varying the molar ratio of H<sub>2</sub>*m*BDC to H<sub>2</sub>*m*BDC-5F from 1:7 to 7:1. For the three ratios 1: 7, 2: 6 and 3: 5, highly crystalline products could be obtained (Fig. S7). To determine the ratio of H<sub>2</sub>*m*BDC-5F: H<sub>2</sub>*m*BDC incorporated in the structure, the MOF samples were dissolved in 5% NaOD in D<sub>2</sub>O and <sup>1</sup>H-NMR measurements were carried out. By integrating the signals, the corresponding ratio of *m*BDC<sup>2-</sup> to *m*BDC-5F<sup>2-</sup> in the respective CAU-10-H/F<sub>x</sub> samples could be determined (Fig. S8). A comparison of initially provided amounts and the incorporation of the fluorinated linker is shown in Table S5. In general, the fraction of fluoroisophthalate in the MOF is lower than the employed amount in the synthesis mixture, hence H<sub>2</sub>*m*BDC is predominantly incorporated into the product.

#### 3.2. Crystal structure of CAU-10-H/F<sub>28</sub>

The structure of the CAU-10 framework is built up by helical chains composed of *cis* corner-sharing AlO<sub>6</sub> polyhedra [21]. Each of these helices is interconnected to four adjacent helices with

**Table 2**  
Summary of structure refinement details.

	CAU-10- H/F <sub>28</sub> [Al(OH)(mBDC) <sub>0.72</sub> (mBDC-5F) <sub>0.28</sub> ]	CAU-10-HTATB [Al(OH)(HTATB)]
Structure determination	powder data	powder data
Formula sum	AlC <sub>8</sub> H <sub>4.71</sub> O <sub>5</sub> F <sub>0.29</sub>	AlC <sub>24</sub> H <sub>15</sub> N <sub>3</sub> O <sub>7</sub>
Z	16	16
Crystal system	tetragonal	tetragonal
a = b/Å	21.3075(5)	36.438(1)
c/Å	10.7101(3)	10.9373(9)
V/Å <sup>3</sup>	4862.50(28)	14522(1)
Space group	I4 <sub>1</sub> md	I4 <sub>1</sub> a
R <sub>w</sub> /%	5.69	7.56
R <sub>Bragg</sub> /%	1.92	3.67
GOF	1.45	1.78

alternating rotational orientation through the carboxylate groups of mBDC<sup>2-</sup> linker molecules (Fig. 1).

Thus, square-shaped channels are formed, which can be modulated by the use of functionalized linker molecules. This functionalization can be established by using a mono functionalized linker molecule or by the mixed-linker approach, when linker molecules with different functionality are used [23,24]. Rietveld refinement of CAU-10-H/F<sub>x</sub> was carried out using a PXRD pattern of a sample doped with 28% mBDC-5F<sup>2-</sup>. The final Rietveld plot is shown in Fig. S9.

In comparison to other CAU-10 derivatives which crystallize with different space group symmetry (CAU-10-Br in I4<sub>1</sub>amd or CAU-10-OCH<sub>3</sub> in I4<sub>1</sub>a) the linker molecules in CAU-10-H/F<sub>28</sub> are not arranged pairwise (Fig. 2). The same linker arrangement was also observed in the hydrated form of CAU-10-H [21,25,26]. In CAU-10-H/F<sub>28</sub> square-shaped, sinusoidal channels are formed, which exhibit a maximum diameter of approximately 7 Å, taking the van der Waals radii into account.

### 3.3. Sorption properties of CAU-10-H/F<sub>x</sub>

Prior to the sorption measurements all samples were activated at 200 °C for 16 h under reduced pressure. The Type I N<sub>2</sub> sorption isotherms measured at 77 K confirm the microporosity of the three

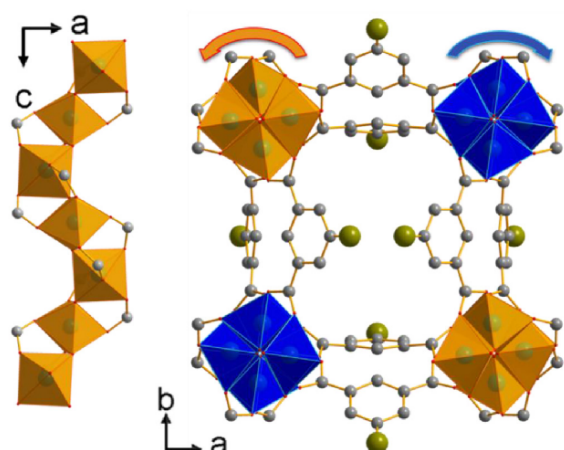


**Fig. 1.** Structure of CAU-10-H/F<sub>28</sub>. Al atoms are displayed in turquoise, O atoms in red, F atoms in green, and C atoms in dark grey. Right-handed and left-handed helices are colored orange and blue, respectively. (For interpretation of the references to colour in this figure legend, the reader is referred to the web version of this article.)

CAU-10-H/F<sub>x</sub> samples (Fig. 3, upper left). In comparison to CAU-10-H (Table 3) the specific surface area, as determined by the BET method, decreases with increasing degree of fluorine doping. This is the expected behavior, which was also observed in CAU-10-H/Br [23]. Strong dependencies of the degree of fluorination can be found in the hydrogen sorption measurements (Fig. 3, upper right). Incorporation of only 11% of fluorinated linker leads to an increase of 11% in capacity compared to CAU-10-H. However, further functionalization results in smaller capacities. Thus, when the degree of fluorination is increased to 28%, the total uptake of H<sub>2</sub> is decreased by 1/3. In water vapor sorption isotherms measured at 298 K (Fig. 3, bottom) a decrease of capacity with increasing degree of fluorination can be observed. Although high capacities are observed, the uptake is decreased by 23–32% (CAU-10-H/F<sub>11</sub> - CAU-10-H/F<sub>44</sub>) in comparison to CAU-10-H. The degree of fluorination also influences the p/p<sub>0</sub> value where a steep increase of water uptake takes place (Fig. 3, bottom left). The S-shaped curves are shifted to slightly higher p/p<sub>0</sub> values with increasing fluorine content, indicating increasing hydrophobicity of the pores (Fig. 3, bottom right). A detailed comparison of the sorption properties (specific surface areas and sorption capacities) of all known CAU-10 derivatives is shown in Table 3.

### 3.4. HT investigation of CAU-10-HTATB

The HT investigation of the system Al<sup>3+</sup>/H<sub>3</sub>TATB/DMF/water under solvothermal conditions resulted in the discovery of CAU-10-HTATB. In the first 15 reactions the volume of H<sub>2</sub>O was kept at 150 μL and the molar ratio of Al<sup>3+</sup>: H<sub>3</sub>TATB was varied. The influence of the solvent ratio of H<sub>2</sub>O: DMF was investigated in the following 9 reactions. The reactor was heated to 145 °C within 1 h, held at this temperature for 12 h and then cooled down to room temperature within 1 h. The exact composition of the reaction mixtures can be found in the Supporting Information Table S2, reactions 1–24. Employing a 0.5 M solution of Al(NO<sub>3</sub>)<sub>3</sub>·9H<sub>2</sub>O in DMF, the formation of CAU-10-HTATB could only be observed in two reaction vessels (Table S2, no. 21 and 22). A yet unidentified product of low crystallinity also formed, but was not stable under ambient conditions. While in the first experiments CAU-10-HTATB could only be obtained as a powder with low crystallinity highly crystalline CAU-10-HTATB was formed with an excess of H<sub>3</sub>TATB using a solvent mixture DMF/water (Table S2, no. 74).

### 3.5. Structure description of CAU-10-HTATB

CAU-10-HTATB was only obtained as microcrystalline powders. Therefore, the crystal structure had to be determined from powder X-ray diffraction data. The final Rietveld plot is shown in Fig. S10.

CAU-10-HTATB exhibits the CAU-10 topology, containing the aforementioned helical IBUs. Thus, the framework is formed by connecting the IBUs through only two of the three carboxylate groups of the linker. The third -COOH group points towards the pores (Fig. 4) which are occupied by DMF molecules. Using the extended linker molecule HTATB<sup>2-</sup> the pore shape of the CAU-10 structure was influenced and pore diameters were increased.

Square shaped channels with a minimum diameter of 4.4 Å and a maximum diameter of 10.8 Å are formed (Fig. 5). Compared to CAU-10-H the diameters are increased (4.0 Å and 7.0 Å, respectively) [21].

### 3.6. Vibrational spectroscopy

The IR spectrum of CAU-10-HTATB is displayed in Fig. 6 and the bands are tentatively assigned based on literature data. Broad

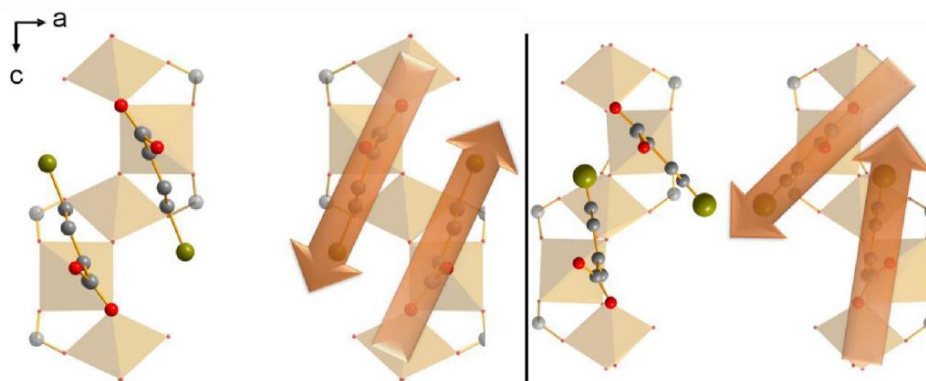


Fig. 2. Parallel ordering of the linker molecules as observed for example in CAU-10-Br (left) in comparison to the non-parallel ordering in CAU-10-H/F<sub>28</sub> (right). The orientation of the linker molecules is indicated by arrows.

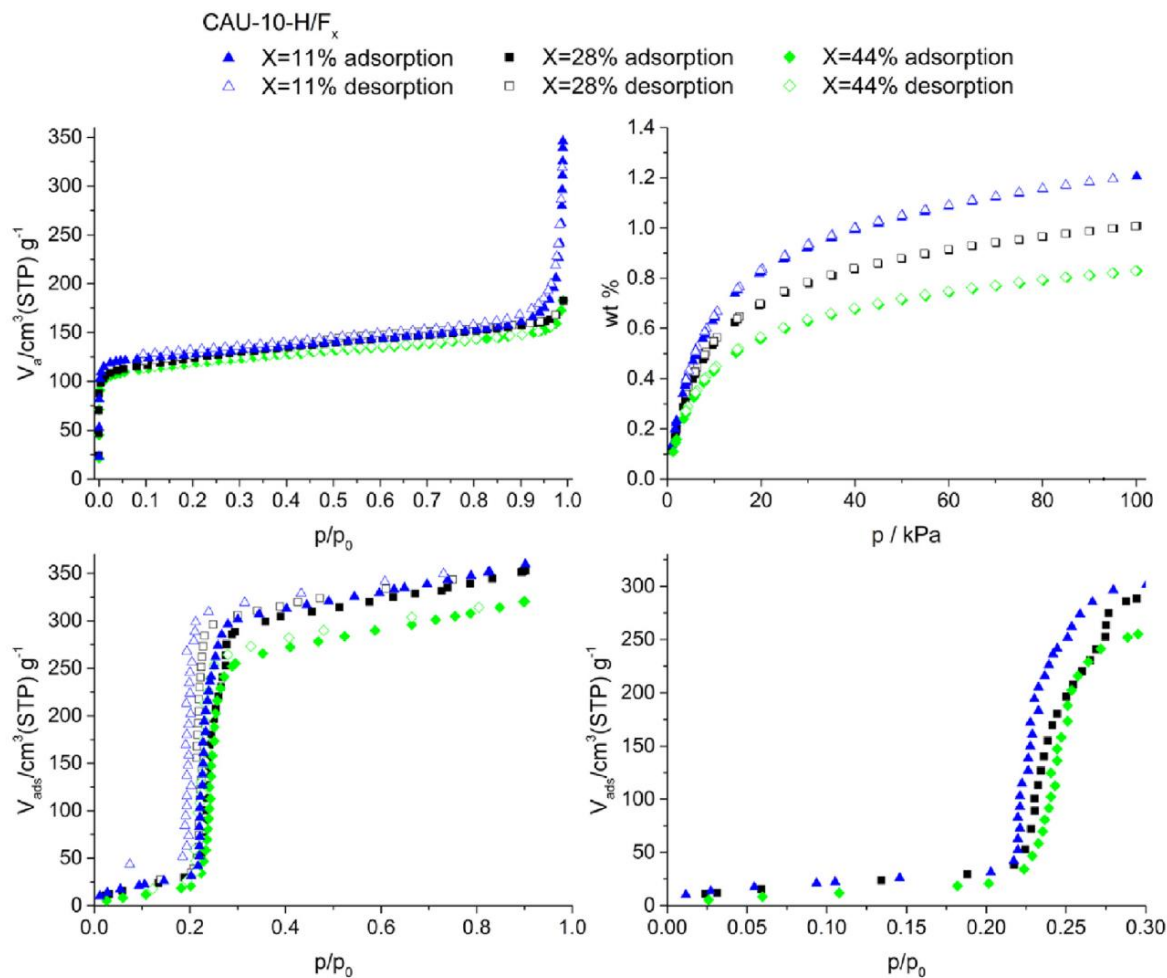


Fig. 3. Sorption isotherms of CAU-10-H/F<sub>x</sub> (X = 11, 28, 44%). The N<sub>2</sub> and H<sub>2</sub> sorption measurements were carried out at 77 K (upper left and right, respectively). H<sub>2</sub>O vapor isotherms were measured at 298 K (bottom). A detailed view of the H<sub>2</sub>O sorption isotherms up to p/p<sub>0</sub> = 0.3 is shown at the bottom right, where the hydrophobic character and the influence of the degree of fluorination can be observed.

**Table 3**

Results of the sorption experiments of the title compounds and detailed comparison to all known CAU-10 derivatives.

CAU-10 Material	N <sub>2</sub> (77 K) a <sub>s,BET</sub> /m <sup>2</sup> g <sup>-1</sup>	N <sub>2</sub> (77 K) V <sub>MIC</sub> /cm <sup>3</sup> g <sup>-1</sup>	H <sub>2</sub> (77 K)/wt%	CO <sub>2</sub> (298 K)/wt%	H <sub>2</sub> O (298 K)/cm <sup>3</sup> g <sup>-1</sup>	Ref.
-H/F <sub>11</sub>	515	0.22	1.21	–	359	
-H/F <sub>28</sub>	466	0.22	1.01	–	351	
-H/F <sub>44</sub>	453	0.20	0.83	–	320	
-H	635	0.25	1.12	10.57	468	[21]
-Br	not porous			3.6	–	[23]
CH <sub>3</sub>	not porous		0.05	6.09	140	[21]
-OCH <sub>3</sub>	+	+	0.82	4.87	92	[21]
-NH <sub>2</sub>	+	+	1.07	8.0	271	[21]
-NO <sub>2</sub>	440	0.18	1.01	8.71	215	[21]
-OH	not porous		0.79	5.57	390	[21]
-H/Br	305	0.14	0.87	8.1	–	[23]
-H/CH <sub>3</sub>	varying, depending on batch					[23]
-NO <sub>2</sub> /NH <sub>2</sub>	+	+	1.01	9.8	–	[23]
-H/SO <sub>3</sub> H <sub>8</sub>	372	0.21	1.03	10.52	407	[24]
-H/SO <sub>3</sub> H <sub>15</sub>	+	+	0.95	9.88	357	[24]
-H/SO <sub>3</sub> H <sub>20.5</sub>	+	+	0.91	9.44	329	[24]
-H/SO <sub>3</sub> H <sub>24</sub>	+	+	0.85	8.87	305	[24]
-NO <sub>2</sub> /SO <sub>3</sub> H <sub>6.5</sub>	324	0.15	0.91	8.61	318	[24]
-NO <sub>2</sub> /SO <sub>3</sub> H <sub>10</sub>	270	0.13	0.81	8.29	351	[24]
-NO <sub>2</sub> /SO <sub>3</sub> H <sub>17.5</sub>	242	0.12	0.69	7.72	332	[24]
-NO <sub>2</sub> /SO <sub>3</sub> H <sub>21.5</sub>	158	0.09	0.64	7.12	382	[24]
-OH/SO <sub>3</sub> H <sub>8</sub>	67	0.04	0.77	6.57	379	[24]
-OH/SO <sub>3</sub> H <sub>12.5</sub>	74	0.05	0.69	8.04	377	[24]

+ no measurement possible due to too long equilibration times.

bands around 3300 cm<sup>-1</sup> point to the presence of H-bonds in the MOF due to solvent-linker interactions. The presence of DMF is confirmed by the bands at 1652 cm<sup>-1</sup>, corresponding to the C–O stretching vibration, at ca. 2900 and 1431 cm<sup>-1</sup>, due to –CH<sub>3</sub> groups and at 1252 cm<sup>-1</sup>, alluding to the C–N stretching vibration [21]. The C–N deformation vibration is located at 699 cm<sup>-1</sup>. A deformation vibration corresponding to the μ–OH groups bridging the Al<sup>3+</sup> ions is located at 981 cm<sup>-1</sup>, whereas the stretching vibration is observed at 3751 cm<sup>-1</sup> [21]. The bands at 1716 and at 1098 cm<sup>-1</sup> can be assigned to the C=O and C–O stretching vibration of the free carboxylic acid group and the bands of the two coordinating carboxylate groups of the HTATB<sup>2-</sup> ion are located at 1652, 1560, 1356 and 1403 cm<sup>-1</sup> corresponding to the asymmetric and symmetric stretching vibrations and the C–O deformation vibration, respectively. The C–H out of plane deformation vibration at 828 cm<sup>-1</sup> proves a 1,4-disubstitution of aromatic benzene rings, whereas the vibrations at 1506 and 1016 cm<sup>-1</sup> can be attributed to the central triazine ring [42]. At 770 cm<sup>-1</sup> the C–H in plane vibrations are located.

### 3.7. Thermal stability

According to thermogravimetric measurements CAU-10-HTATB is stable up to 400 °C. This also corresponds well to the results of the temperature dependent PXRD measurements (Fig. 7). Additionally, a shift of the reflection positions and a change of relative intensities is visible, originating from the removal of occluded solvent molecules. On the other hand the strong differences in the PXRD patterns hint at a structural change upon thermal activation but a structure refinement employing the Rietveld method was not successful. PXRD measurements of the final residue (T = 900 °C) only showed the presence of an X-ray amorphous product. Hence for the evaluation of the TG curve the formation of Al<sub>2</sub>O<sub>3</sub> as the final product was assumed. In the first step, up to 250 °C, occluded solvent molecules are removed from the framework which results in a mass loss of 19.7%. This corresponds to a loss of 1.75 DMF molecules per formula unit (calc. 21.1%). In the next step from 400 to 600 °C the framework decomposes, resulting in a mass loss of 68.1% (calc. 67.6%).

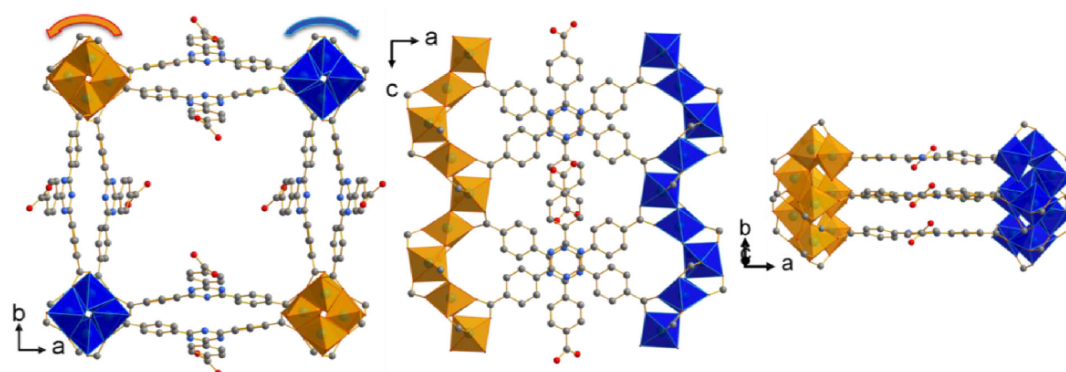


**Fig. 4.** Structure of CAU-10-HTATB. The O atoms are displayed in red, N atoms in blue, and C atoms in dark grey. Occluded solvent molecules located in the pores are not displayed. Right-handed and left-handed helices of corner sharing AlO<sub>6</sub> polyhedra are colored orange and blue, respectively. (For interpretation of the references to colour in this figure legend, the reader is referred to the web version of this article.)



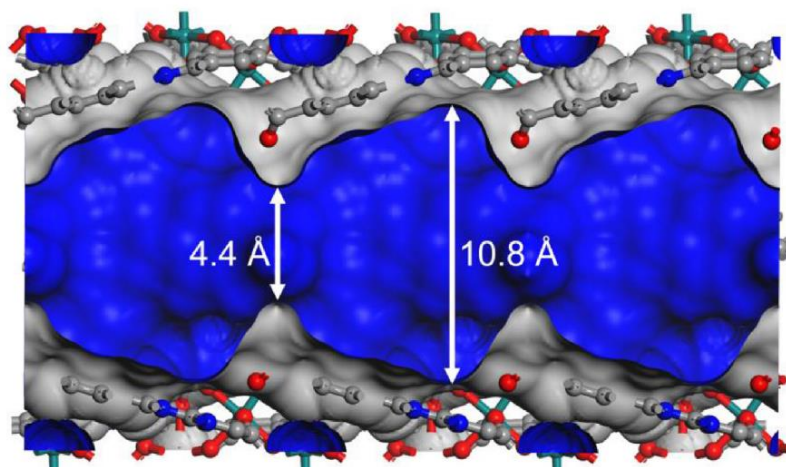


**Fig. 5.** Representation of a channel in CAU-10-HTATB, as seen along [010]. The minimum and maximum pore diameters are provided. The Al atoms are presented in turquoise, C atoms in grey, O atoms in red and N atoms in blue. The accessible solvent surface is shown in blue. (For interpretation of the references to colour in this figure legend, the reader is referred to the web version of this article.)

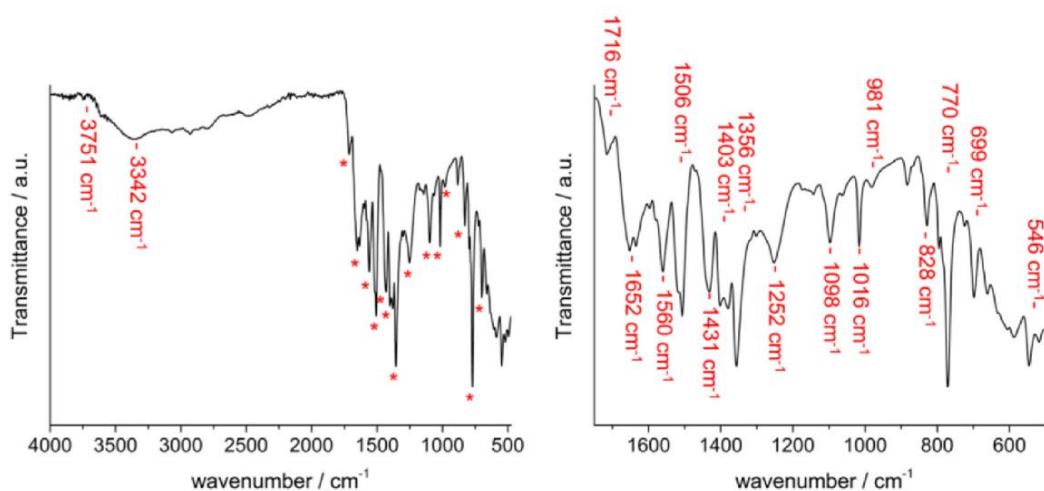


**Fig. 6.** IR spectrum of CAU-10-HTATB. The marked bands are discussed in the manuscript.

Taking these results into account, the formula for CAU-10-HTATB was deduced to be  $[\text{Al}(\text{OH})(\text{HTATB})] \cdot 1.75\text{DMF}$ . This formula also corresponds reasonably well to the results of the elemental analysis (meas./calc. C: 56.3%/55.2%; H: 4.7%/3.9%; N: 11.1%/10.4%).

The thermal stability of CAU-10-HTATB is similar to the ones observed for other CAU-10-X derivatives, ranging from 250 (X = –OH) to 450 °C (X = –NH<sub>2</sub> and –OCH<sub>3</sub>) [21]. The usage of the extended linker molecule H<sub>3</sub>TATB for the CAU-10 MOF synthesis does not seem to have a significant effect on the thermal stability of the framework.

### 3.8. Sorption behavior

The N<sub>2</sub> sorption measurements were carried out at 77 K. Prior to the first sorption measurement the sample was activated for 8 h at 150 °C under reduced pressure (0.1 mbar). CAU-10-HTATB was not porous using this activation temperature (Fig. 8) and PXRD

measurements revealed a decrease of crystallinity (Fig. S11). A shift of the reflection positions is also visible hinting at structural changes upon removal of the guest molecules (Fig. 7, right). Further heating up to 350 °C overnight led only to small additional changes in the PXRD pattern. However, activation of CAU-10-HTATB under milder conditions using a temperature of only 100 °C overnight under reduced pressure resulted in a Type I isotherm. CAU-10-HTATB has a specific surface area of  $a_{\text{s,BET}} = 231 \text{ m}^2\text{g}^{-1}$  and a micropore volume of  $V_{\text{MIC}} = 0.10 \text{ cm}^3\text{g}^{-1}$ , which is much lower than expected for an extended analogue of CAU-10-H and indicates either an incomplete activation, partial decomposition or rearrangement of the framework.

## 4. Conclusion

Three new partially fluorine functionalized CAU-10 derivatives were obtained using the mixed-linker approach. A degree of fluorination of up to 44% was accomplished, which was determined by

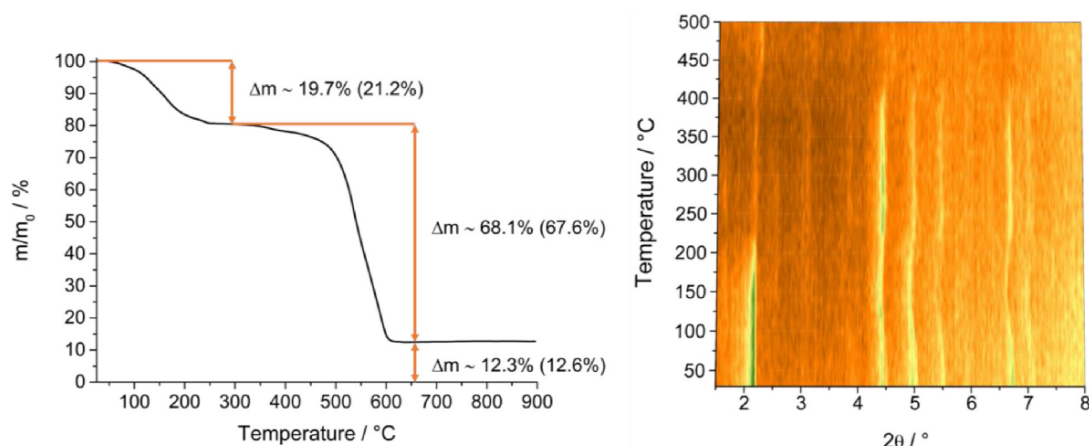


Fig. 7. Results of the thermogravimetric (left) and the temperature dependent PXRD measurement (right) of CAU-10-HTATB, [Al(OH)(HTATB)] · 1.75DMF. The calculated values are given in brackets.

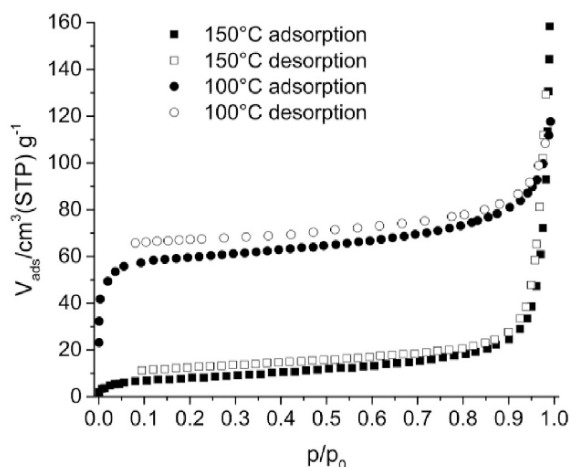


Fig. 8. Results of the N<sub>2</sub> sorption measurements of CAU-10-HTATB carried out at 77 K.

<sup>1</sup>H-NMR spectroscopy. An extensive sorption study was carried out for all three samples including N<sub>2</sub>, H<sub>2</sub> and H<sub>2</sub>O measurements and a strong dependency of the degree of fluorination on the sorption capacity and the host-guest interactions was observed. The structure of CAU-10-H/F<sub>28</sub> was successfully refined using the Rietveld method.

Additionally, a new compound, CAU-10-HTATB with CAU-10 type structure was obtained using the extended linker molecule H<sub>3</sub>TATB. Its crystal structure was successfully refined using the Rietveld method. HTATB<sup>2-</sup> ions connect the IBUs via two carboxylate groups, while the third free carboxylic acid points into the pore. CAU-10-HTATB shows a similar thermal stability compared to other CAU-10 derivatives, but PXRD measurements of samples treated at higher temperatures indicate structural changes which could explain the low uptake of guest molecules.

#### Notes

The authors declare no competing financial interest.

#### Acknowledgment

This work was financially supported by the Deutsche Forschungsgemeinschaft (DFG) (STO 643/10-1). A.K.I. is supported by the Knut and Alice Wallenberg Foundation (KAW) through the MAX IV postdoctoral scholarship under the grant number KAW 2012.0363 and also by the Röntgen-Ångström Cluster (VR) through the MATsynCELL project. We thank Milan Köppen for discussions on Rietveld refinement.

#### Appendix A. Supplementary data

Supplementary data related to this article can be found at <http://dx.doi.org/10.1016/j.micromeso.2017.04.054>.

#### References

- [1] M. O’Keeffe, O.M. Yaghi, *Chem. Rev.* 112 (2011) 675–702.
- [2] T. Loiseau, C. Volkringer, M. Haouas, F. Taulelle, G. Férey, *C. R. Chim.* 18 (2015) 1350–1369.
- [3] C. Serre, F. Millange, C. Thouvenot, M. Nogués, G. Marsolier, D. Louër, G. Férey, *J. Am. Chem. Soc.* 124 (2002) 13519–13526.
- [4] T. Loiseau, C. Serre, C. Huguénard, G. Fink, F. Taulelle, M. Henry, T. Bataille, G. Férey, *Chem. Eur. J.* 10 (2004) 1373–1382.
- [5] T. Ahnfeldt, D. Gunzelmann, T. Loiseau, D. Hirsemann, Jr., Senker, G. Férey, N. Stock, *Inorg. Chem.* 48 (2009) 3057–3064.
- [6] S. Biswas, T. Ahnfeldt, N. Stock, *Inorg. Chem.* 50 (2011) 9518–9526.
- [7] F.-X. Coudert, A.U. Ortiz, V. Haigis, D. Bousquet, A.H. Fuchs, A. Ballandras, G. Weber, I. Bezverkhyy, N. Geoffroy, J.-P. Bellat, G. Ortiz, G. Chaplais, J. Patarin, A. Boutin, *J. Phys. Chem. C* 118 (2014) 5397–5405.
- [8] S. Halis, N. Reimer, A. Klinkebiel, U. Lüning, N. Stock, *Micropor. Mesopor. Mat.* 216 (2015) 13–19.
- [9] J.M. Salazar, G. Weber, J.M. Simon, I. Bezverkhyy, J.P. Bellat, *J. Chem. Phys.* 142 (2015) 124702.
- [10] H. Reinsch, R.S. Pillai, R. Siegel, J. Senker, A. Lieb, G. Maurin, N. Stock, *Dalton Trans.* 45 (2016) 4179–4186.
- [11] M. Eddaoudi, J. Kim, N. Rosi, D. Vodak, J. Wachter, M. O’Keeffe, O.M. Yaghi, *Science* 295 (2002) 469–472.
- [12] J. Hafizovic, M. Bjørgen, U. Olsbye, P.D.C. Dietzel, S. Bordiga, C. Prestipino, C. Lamberti, K.P. Lillerud, *J. Am. Chem. Soc.* 129 (2007) 3612–3620.
- [13] E. Biemmi, S. Christian, N. Stock, T. Bein, *Micropor. Mesopor. Mat.* 117 (2009) 111–117.
- [14] E. Biemmi, A. Darga, N. Stock, T. Bein, *Micropor. Mesopor. Mat.* 114 (2008) 380–386.
- [15] S.R. Bajpe, E. Breynaert, D. Mustafa, M. Jobbagy, A. Maes, J.A. Martens, C.E.A. Kirschhock, *J. Mater. Chem.* 21 (2011) 9768–9771.
- [16] Z. Jin, H.-Y. Zhao, X.-J. Zhao, Q.-R. Fang, J.R. Long, G.-S. Zhu, *Chem. Commun.* 46 (2010).
- [17] H. He, Y. Song, F. Sun, Z. Bian, L. Gao, G. Zhu, *J. Mater. Chem. A* 3 (2015) 16598–16603.

## 4 Synthese und Charakterisierung neuer und funktionalisierter MOFs basierend auf den Elementen der 13. Gruppe und deren spezielle optische Eigenschaften

---

136

M. Krüger et al. / *Microporous and Mesoporous Materials* 249 (2017) 128–136

- [18] N. Reimer, H. Reinsch, A.K. Inge, N. Stock, *Inorg. Chem.* 54 (2014) 492–501.
- [19] H. Reinsch, M. Krüger, J. Marrot, N. Stock, *Inorg. Chem.* 52 (2013) 1854–1859.
- [20] M. Krüger, A.K. Inge, H. Reinsch, Y.-H. Li, M. Wahiduzzaman, C.-H. Lin, S.-L. Wang, G. Maurin, N. Stock, *Inorg. Chem.* (2017), <http://dx.doi.org/10.1021/acs.inorgchem.7b00202>.
- [21] H. Reinsch, M.A. van der Veen, B. Gil, B. Marszalek, T. Verbiest, D. de Vos, N. Stock, *Chem. Mater.* 25 (2012) 17–26.
- [22] M. Gaab, N. Trukhan, S. Maurer, R. Gummaraju, U. Müller, *Micropor. Mesopor. Mat.* 157 (2012) 131–136.
- [23] H. Reinsch, S. Waitschat, N. Stock, *Dalton Trans.* 42 (2013) 4840–4847.
- [24] N. Reimer, B. Bueken, S. Leubner, C. Seidler, M. Wark, D. De Vos, N. Stock, *Chem. Eur. J.* 21 (2015) 12517–12524.
- [25] D. Fröhlich, E. Pantatosaki, P.D. Kolokathis, K. Markey, H. Reinsch, M. Baumgartner, M.A. van der Veen, D.E. De Vos, N. Stock, G.K. Papadopoulos, S.K. Henninger, C. Janiak, *J. Mater. Chem. A* 4 (2016) 11859–11869.
- [26] D. Fröhlich, S.K. Henninger, C. Janiak, *Dalton Trans.* 43 (2014) 15300–15304.
- [27] A. Weiss, N. Reimer, N. Stock, M. Tiemann, T. Wagner, *Micropor. Mesopor. Mat.* 220 (2016) 39–43.
- [28] H. Reinsch, F.M. Hinterholzinger, P. Jäker, F. Hesse, B. Reimer, T. Bein, M. Polozij, D. Nachtigallová, P. Nachtigall, N. Stock, *J. Phys. Chem. C* 119 (2015) 26401–26408.
- [29] S. Biswas, T. Remy, S. Couck, D. Denysenko, G. Rampelberg, J.F.M. Denayer, D. Volkmer, C. Detavernier, P. Van Der Voort, *Phys. Chem. Chem. Phys.* 15 (2013) 3552–3561.
- [30] N. Stock, T. Bein, *J. Mater. Chem.* 15 (2005) 1384–1391.
- [31] H. Reinsch, N. Stock, *Micropor. Mesopor. Mat.* 171 (2013) 156–165.
- [32] S. Bauer, N. Stock, *Chem. Unserer Zeit* 41 (2007) 390–398.
- [33] N. Stock, *Chem. Ing. Tech.* 82 (2010) 1039–1047.
- [34] N. Stock, *Micropor. Mesopor. Mat.* 129 (2010) 287–295.
- [35] *Materials Studio v4.1*, Accelrys Software Inc.
- [36] *Topas Academic 4.1*, A. Coelho.
- [37] A.K. Ghosh, N. Kumaragurubaran, C. Liu, T. Devasamudram, H. Lei, L. Swanson, S. Ankala, J. Tang, G. Bilcer, Compounds which inhibit beta-secretase activity and methods of use thereof, WO2006110668, 2006.
- [38] S.J. Gumbley, R. Stewart, *J. Chem. Soc. Perkin Trans. 2* (1984) 529–531.
- [39] Y.K. Park, S.B. Choi, H. Kim, K. Kim, B.-H. Won, K. Choi, J.-S. Choi, W.-S. Ahn, N. Won, S. Kim, D.H. Jung, S.-H. Choi, G.-H. Kim, S.-S. Cha, Y.H. Jhon, J.K. Yang, J. Kim, *Angew. Chem.* 119 (2007) 8378–8381.
- [40] D. Sun, S. Ma, Y. Ke, D.J. Collins, H.-C. Zhou, *J. Am. Chem. Soc.* 128 (2006) 3896–3897.
- [41] W. Kraus, G. Nolze, *J. Appl. Crystallogr.* 29 (1996) 301–303.
- [42] H.K. Reimschuessel, N.T. McDevitt, *J. Am. Chem. Soc.* 82 (1960) 3756–3762.



#### 4.7.2 Investigation of the Effect of Polar Functional Groups on the Crystal Structures of Indium MOFs

Der folgende Artikel wurde im Jahre 2017 in der Fachzeitschrift *CrystEngComm*, RSC veröffentlicht. Der Wiederabdruck erfolgte mit freundlicher Genehmigung der RSC. Reproduced with permission from:

M. Krüger, M. Albat, A. K. Inge, N. Stock, *CrystEngComm*, **2017**, *19*, 4622-4628. DOI: 10.1039/c7ce01067b

In dieser Arbeit ging es um die gezielte Herstellung von amino- und/oder nitro-funktionalisierten In-MOFs mit potentieller SHG-Aktivität. Hierfür wurden 2-Aminoterephthalsäure (H<sub>2</sub>BDC-NH<sub>2</sub>), 2-Nitroterephthalsäure (H<sub>2</sub>BDC-NO<sub>2</sub>) und 2-Amino-5-nitroterephthalsäure (H<sub>2</sub>BDC-NH<sub>2</sub>/NO<sub>2</sub>) benutzt. Alle Strukturen wurden aus Einkristallröntgenbeugungsdaten ermittelt. Bei der Verwendung von H<sub>2</sub>BDC-NH<sub>2</sub> konnte ein In-MOF der Zusammensetzung [In(BDC-NH<sub>3</sub>)(BDC-NH<sub>2</sub>)]·1.6DMF·1.9H<sub>2</sub>O (In-BDC-NH<sub>2</sub>; Raumgruppe *P*6<sub>2</sub>22, *a* = *b* = 14.738(2), *c* = 12.257(3) Å) erhalten werden, dessen Kristallstruktur zwei interpenetrierende Netze aus InO<sub>8</sub>-Polyedern, verbunden durch BDC-NH<sub>2</sub><sup>2-</sup>-Ionen, mit Quarz-Topologie aufweist. Die Interpenetration reduziert den Porendurchmesser auf 4.4 Å. Außerdem ist der MOF bis zu 300°C stabil. Wird 2-Aminoterephthalsäure durch 2-Nitroterephthalsäure in der Reaktionsmischung ersetzt, entsteht kein MOF mit NO<sub>2</sub>-Funktionalität, sondern eine isoretikuläre Gemischt-Linker-Verbindung, die ausschließlich BDC<sup>2-</sup>- und BDC-NH<sub>2</sub><sup>2-</sup>-Ionen enthält. Somit fand eine Indium-vermittelte Reduzierung der 2-Nitroterephthalsäure während der Synthese statt. Bei der Verwendung des Linkers H<sub>2</sub>BDC-NH<sub>2</sub>/NO<sub>2</sub> unter denselben Reaktionsbedingungen konnte keine zu In-BDC-NH<sub>2</sub> isoretikuläre Verbindung erhalten werden. Erst durch den Austausch des Wassers durch Ethanol im Lösungsmittelgemisch und durch Erhöhung der Reaktionstemperatur auf 150 °C konnte ein bifunktionalisierter In-MOF (In-BDC-NH<sub>2</sub>/NO<sub>2</sub>) mit der Zusammensetzung (DMA)<sub>2</sub>[In<sub>3</sub>(O)(BDC-NH<sub>2</sub>/NO<sub>2</sub>)<sub>4,5</sub>]·DMF (DMA = Dimethylammonium) hergestellt werden. Die Kristallmorphologie ist durch Variation des Volumenverhältnisses von Ethanol zu DMF während der Synthese vom kubischen Kristallen zu gekappten Oktaedern veränderbar. In-BDC-NH<sub>2</sub>/NO<sub>2</sub> kristallisiert in der kubischen Raumgruppe *I*-43*m* mit *a* = 24.8947(1) Å und ist aufgebaut aus trinuclearen {In<sub>3</sub>(μ<sub>3</sub>-O)}-Clustern, die durch die Linker

zu Supertetraedern verknüpft werden. Vier flächenverknüpfte Supertetraeder bilden einen Ultratetraeder, die das finale Netzwerk ausbilden. Zusätzliche Informationen zur Veröffentlichung befinden sich im Anhang.



Cite this: DOI: 10.1039/c7ce01067b

## Investigation of the effect of polar functional groups on the crystal structures of indium MOFs†

Martin Krüger,<sup>a</sup> Martin Albat,<sup>a</sup> A. Ken Inge<sup>b</sup> and Norbert Stock<sup>a\*</sup>

Three new In-MOFs with  $-NH_2$  and/or  $-NO_2$  functionalities are reported using 2-amino- ( $H_2BDC-NH_2$ ), 2-nitro- ( $H_2BDC-NO_2$ ) and 2-amino-5-nitroterephthalic acid ( $H_2BDC-NH_2/NO_2$ ). Their structures were determined from single crystal X-ray diffraction data. The structure of the first In-MOF of composition  $[In(BDC-NH_2)(BDC-NH_2)] \cdot 1.6DMF \cdot 1.9H_2O$  (In-BDC- $NH_2$ ; DMF is dimethylformamide; the space group is  $P6_222$ ,  $a = b = 14.738(2)$  Å and  $c = 12.257(3)$  Å) is built up by two interpenetrating nets of  $InO_8$  polyhedra interconnected by  $BDC-NH_2^{2-}$  ions to form a framework with *qtz* topology. Charge balance is accomplished by partial protonation of the amino group, which was confirmed by IR spectroscopy. The interpenetration leads to a decrease of the pore dimension (4.4 Å in diameter). Thermogravimetric analysis revealed stability up to 300 °C. Replacement of  $H_2BDC-NH_2$  by  $H_2BDC-NO_2$  in the reaction mixture led to the isoreticular MOF containing no  $-NO_2$  groups but exclusively un- and amino-functionalized linkers. Hence an indium mediated reduction of the  $H_2BDC-NO_2$  linker molecule during solvothermal synthesis has occurred. The use of  $H_2BDC-NH_2/NO_2$  under exactly the same reaction conditions did not result in the formation of a MOF, but by changing the synthesis parameters, a new  $-NH_2/-NO_2$  bifunctionalised In-MOF of composition  $(DMA)_2[In_3(\mu_3-O)(BDC-NH_2/NO_2)_{4.5}] \cdot DMF$  (DMA is dimethylammonium), denoted In-BDC- $NH_2/NO_2$ , was obtained. The crystal morphology can be altered from cubic to truncated octahedral crystals by varying the DMF/ethanol volume ratio during synthesis. The compound crystallises in the cubic space group  $I\bar{4}3m$ ,  $a = 24.8947(1)$  Å, and the framework contains trinuclear  $\{In_3(\mu_3-O)\}$  clusters which are interlinked by the  $BDC-NH_2/NO_2^{2-}$  ions to form super-tetrahedra. Four face-sharing super-tetrahedra form ultra-tetrahedra which are connected to form the final cubic framework with an *ncb* topology and isolated inaccessible pores.

Received 7th June 2017,  
Accepted 7th July 2017

DOI: 10.1039/c7ce01067b

rsc.li/crystengcomm

## Introduction

During the past years, the number of metal organic frameworks (MOFs) based on group 13 metal ions has increased steadily.<sup>1–8</sup> In comparison to the solution chemistry of aluminium and gallium, where the formation of complex oxoclusters is very common,<sup>9–14</sup> indium mainly forms isolated  $[In(H_2O)_6]^{3+}$  complexes.<sup>15</sup> The less extensive aqueous solution chemistry of  $In^{3+}$  influences the number of inorganic building units (IBUs) observed with indium. The smaller variety of

IBUs that form with  $In^{3+}$  ions compared to  $Al^{3+}$  and  $Ga^{3+}$  allows for relatively easy design of target structures due to their more predictable nature. In addition, the larger ionic radius of  $In^{3+}$  directly influences the surface charge density, resulting in a higher ligand exchange rate compared to  $Al^{3+}$  and  $Ga^{3+}$ .<sup>16–18</sup> Due to this, Ostwald ripening and reactivity are enhanced. Thus, larger crystals of In-MOFs suitable for structure determination by single crystal X-ray diffraction can usually be obtained. In contrast Al- and Ga-MOFs are often synthesized as microcrystalline powders.<sup>3,4,19–21</sup> In Al- and Ga-MOFs a coordination number (CN) of six is most common<sup>13,14,22–25</sup> but due to the larger ionic radius of the  $In^{3+}$  ion CN = 8 is possible in In-MOFs.<sup>26,27</sup> The formation of isolated  $InO_8$  polyhedra in In-MOFs acting as distorted tetrahedral nodes is hence unique. *Trans* corner-sharing  $InO_6$  octahedra in infinite chains<sup>3</sup> and trimeric IBUs<sup>28</sup> connected by  $\mu_3-O$  are also common in In-MOFs. The type of IBU not only influences the structure, but also the properties of the framework. When an  $InO_8$  IBU is present, the framework is negatively charged.<sup>29,30</sup> Framework properties can also be influenced by exchange of the counter ions<sup>31</sup> or

<sup>a</sup> Institut für Anorganische Chemie, Christian-Albrechts-Universität, Max-Eyth-Straße 2, 24118 Kiel, Germany. E-mail: stock@ac.uni-kiel.de; Fax: +49 4318801775; Tel: +49 4318801675

<sup>b</sup> Department of Materials and Environmental Chemistry, Stockholm University, Stockholm S-106 91, Sweden

† Electronic supplementary information (ESI) available: Details of the linker synthesis, bond length tables, figures of the asymmetric units, <sup>1</sup>H-NMR spectra, TG measurements and PXRD patterns. The CIF files of the compounds can be found in the CCDC database with the numbers 1549126 (In-BDC- $NH_2$ ), 1549127 (In-BDC- $NH_2/NO_2$ ) and 1552697 ( $H_2BDC-NH_2/NO_2$ ). For ESI and crystallographic data in CIF or other electronic format see DOI: 10.1039/c7ce01067b

the introduction of functional groups. The latter mainly influences the sorption behaviour which can result in high storage capacities for H<sub>2</sub> (ref. 28) and CO<sub>2</sub> (ref. 5 and 30) as well as high selectivity for CO<sub>2</sub> over CH<sub>4</sub> (ref. 32) or N<sub>2</sub>.

Herein, we present the synthesis and characterisation of three In-MOFs containing -NH<sub>2</sub> and/or -NO<sub>2</sub> functional groups exhibiting different topologies. In one case an *in situ* reduction of NO<sub>2</sub>-groups is observed.

## Experimental

### Materials

All chemicals used were employed as received from ABCR. Detailed information of the synthesis of 2-amino-5-nitroterephthalic acid (H<sub>2</sub>BDC-NH<sub>2</sub>/NO<sub>2</sub>) can be found in the ESI† (Fig. S1–S7 and Tables S1–S2).

### Synthesis

For the synthesis of In-BDC-NH<sub>2</sub> (1), In-BDC-H/NH<sub>2</sub> (2) and In-BDC-NH<sub>2</sub>/NO<sub>2</sub> (3) our high throughput reactor system for solvothermal reactions containing 24 custom-made Teflon reaction vessels with a maximum volume of 2 mL was employed.<sup>33–37</sup>

[In(BDC-NH<sub>2</sub>)(BDC-NH<sub>2</sub>)] (1, In-BDC-NH<sub>2</sub>). To a mixture of 13.8 μL 2 M In(NO<sub>3</sub>)<sub>3</sub>·H<sub>2</sub>O in DMF (27.6 μmol) and 40 mg 2-aminoterephthalic acid (H<sub>2</sub>BDC-NH<sub>2</sub>, 221 μmol), 61.2 μL of DMF (0.80 mmol) and 75 μL of deionized water (4.17 mmol) were added. The reactor was sealed and heated to 120 °C for 48 h and cooled down to room temperature gradually over 12 h.

H[In(BDC)<sub>0.57</sub>(BDC-NH<sub>2</sub>)<sub>0.43</sub>] (2, In-BDC-H/NH<sub>2</sub>). To a mixture of 23.7 μL 2 M In(NO<sub>3</sub>)<sub>3</sub>·H<sub>2</sub>O in DMF (47.4 μmol) and 100 mg 2-nitroterephthalic acid (H<sub>2</sub>BDC-NO<sub>2</sub>, 474 μmol), 776.3 μL of DMF (10.1 mmol) and 200 μL of deionized water (11.1 mmol) were added. The reactor was sealed and heated to 150 °C for 24 h and cooled down to room temperature gradually over 12 h.

(DMA)<sub>2</sub>[In<sub>3</sub>(μ<sub>3</sub>-O)(BDC-NH<sub>2</sub>/NO<sub>2</sub>)<sub>4.5</sub>] (3, In-BDC-NH<sub>2</sub>/NO<sub>2</sub>) – cubic crystals. To a mixture of 50 μL 2 M In(NO<sub>3</sub>)<sub>3</sub>·H<sub>2</sub>O in DMF (100 μmol) and 22.6 mg 2-amino-5-nitroterephthalic acid (H<sub>2</sub>BDC-NH<sub>2</sub>/NO<sub>2</sub>, 100 μmol), 100 μL of DMF (1.30 mmol) and 350 μL of ethanol (6.01 mmol) were added. The reactor was sealed and heated within 24 h to 150 °C, held at this temperature for 48 h and cooled down to room temperature gradually over 36 h.

(DMA)<sub>2</sub>[In<sub>3</sub>(μ<sub>3</sub>-O)(BDC-NH<sub>2</sub>/NO<sub>2</sub>)<sub>4.5</sub>] (3, In-BDC-NH<sub>2</sub>/NO<sub>2</sub>) – truncated octahedral crystals. To a mixture of 50 μL 2 M In(NO<sub>3</sub>)<sub>3</sub>·H<sub>2</sub>O in DMF (100 μmol) and 22.6 mg 2-amino-5-nitroterephthalic acid (H<sub>2</sub>BDC-NH<sub>2</sub>/NO<sub>2</sub>, 100 μmol), 225 μL of DMF (2.93 mmol) and 225 μL of ethanol (3.86 mmol) were added. The reactor was sealed and heated within 24 h to 150 °C, held at this temperature for 48 h and cooled down to room temperature gradually over 36 h.

Thermal activation under reduced pressure and solvent exchange as well as a combination of these were tested for all three samples. All procedures led to a loss of the structural

integrity and hence no sorption measurements were carried out.

### Characterisation

Powder X-ray diffraction (PXRD) data were collected using a STOE Stadi-P Combi diffractometer equipped with an  $\chi$ -stage and an image plate detector system (Cu K $\alpha$  radiation). SEM images were obtained using a Philips ESEM XL 30 instrument. <sup>1</sup>H-NMR spectroscopy in solution was performed on a Bruker DRX 500 at 200 MHz. Prior to the measurements, the respective MOFs were dissolved in 5% NaOD in D<sub>2</sub>O. IR spectra were recorded on an ATI Matheson Genesis spectrometer equipped with an ATR unit in the spectral range 400–4000 cm<sup>-1</sup>. Thermogravimetric (TG) analyses were carried out using a NETZSCH STA 409 CD analyser. The samples were heated in Al<sub>2</sub>O<sub>3</sub> crucibles at a rate of 4 K min<sup>-1</sup> under a flow of air (75 ml min<sup>-1</sup>). The TG data were corrected for buoyancy and current effects. For elemental analysis, a HEKATECH Euro EA Elemental Analyzer was used. Topological analysis was carried out using Systre<sup>38</sup> within the GAVROG<sup>39</sup> software package in order to achieve the highest symmetry net, and with TOPOSPro.<sup>40</sup> The Connolly surface was simulated using a probe diameter of 3.3 Å (for CO<sub>2</sub>) in the program Materials Studio.<sup>41</sup>

### Structure determination

Crystallographic and refinement details are provided in Table 1, and bond lengths of the compounds described below can be found in Tables S3 and S4 in the ESI† The crystal structure of 1 was determined from single-crystal X-ray diffraction data. X-ray diffraction measurements were performed on a STOE IPDS diffractometer equipped with an image-plate detector with Mo-K $\alpha$  radiation ( $\lambda$  = 0.71073 Å). The crystal structure was solved by direct methods with the program SHELXT-2014 and refined as a racemic twin using

Table 1 Summary of the crystallographic parameters, structure determination and refinement of the title compounds

	In-BDC-NH <sub>2</sub>	In-BDC-NH <sub>2</sub> /NO <sub>2</sub>
Structure determination	Single crystal data	Single crystal data
Formula sum	In <sub>3</sub> C <sub>48</sub> H <sub>33</sub> N <sub>6</sub> O <sub>24</sub>	In <sub>3</sub> C <sub>36</sub> H <sub>12</sub> N <sub>9</sub> O <sub>28</sub>
Z	4	8
Crystal system	Hexagonal	Cubic
a/Å	14.7381(5)	24.8947(1)
b/Å	14.7381(5)	24.8947(1)
c/Å	12.2572(4)	24.8947(1)
V/Å <sup>3</sup>	2305.70(14)	15428.39(19)
Space group	P6 <sub>2</sub> 22	I $\bar{4}$ 3m
Solution method	Direct methods	Direct methods
Range/ $\theta$	1.6–28.1	1.9–25.5
Wavelength/Å	MoK $\alpha$	0.6889
GOF	0.966	1.104
Tot., uniq. data, R <sub>int</sub>	1868, 1868, 0.061	63 530, 2904, 0.070
Observed data [ $I > 2\sigma(I)$ ]	1567	2843
R <sub>1</sub> , wR <sub>2</sub>	0.028, 0.068	0.034, 0.098
$\Delta e$ min/max (e/Å <sup>3</sup> )	-0.62, 0.33	-0.44, 0.84
Calc. density/g cm <sup>-3</sup>	1.02427	1.17352



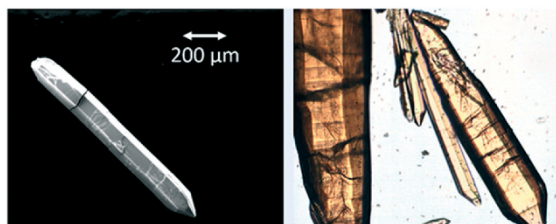


Fig. 1 Single crystals of In-BDC-NH<sub>2</sub> (1) displayed as a SEM micrograph (left) and as an optical image (right).

the program SHELXL-2014.<sup>42,43</sup> Hydrogen atoms were fixed using a riding model. Numerical absorption correction was carried out using XShape and XRed.<sup>44</sup> The electron density inside the pores was eliminated for refinements employing the SQUEEZE command in PLATON.<sup>45,46</sup> A solvent accessible void of 1268 Å<sup>3</sup> per unit cell was found to contain 361 electrons for 1. Single crystal X-ray diffraction data for 3 were collected using a Rigaku Saturn724+ diffractometer at 100 K using synchrotron radiation ( $\lambda = 0.6889$  Å) at the Beamline I19, Diamond Light Source, Didcot, UK. Data reduction and absorption correction were applied using CrysAlisPro, and the structure was solved and refined using SHELXS-2014 and SHELXL-2014, respectively.<sup>42,43</sup> The positions of amino and nitro functional groups were found to be disordered over the aromatic ring. Restraints were applied on the displacement parameters of atoms in the disordered groups. SQUEEZE was used to handle electron density in the pores due to disordered guest species.<sup>45,46</sup> Hydrogen atoms on the aromatic rings were added to parent carbon atoms with constraints using a riding model. Hydrogen atoms of the disordered amino groups were not located in the difference Fourier maps and thus excluded in the refinement.

## Results and discussion

### Structure of [In(BDC-NH<sub>3</sub>)(BDC-NH<sub>2</sub>)] (1)

The structure of In-BDC-NH<sub>2</sub> (1) was solved and refined from single crystal XRD data (Fig. 1 and S8†). An unfunctionalized

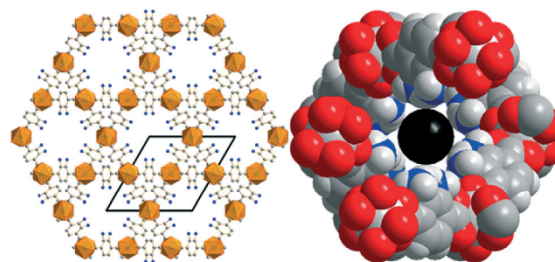


Fig. 3 The structure of In-BDC-NH<sub>2</sub> (1) along [001]. Disordered amino groups (blue) are pointing towards the hexagonal pore (left). H atoms are not displayed. The hexagonal pore (right) exhibits a diameter of 4.4 Å, shown in black, taking the van-der-Waals radii into account.

In-MOF based on terephthalic acid and an analogous Zn-MOF based on isonicotinic acid have been reported previously.<sup>27,47</sup> The structure is based on In<sup>3+</sup> ions, eight-coordinated by four carboxylate groups forming a tetrahedral [In(-CO<sub>2</sub>)<sub>4</sub>]<sup>-</sup> node (Fig. 2). Each indium cation is interconnected to four others by linker molecules to form a distorted quartz-like framework. This framework is interpenetrated by another independent net, resulting in one dimensional hexagonal channels with a diameter of 4.4 Å, taking the van-der-Waals radii into account (Fig. 3). The functional groups are disordered but oriented towards the hexagonal pores along [001]. Charge balance of the framework is accomplished by partial protonation of the amino group of the linker molecule.

### Properties of [In(BDC-NH<sub>3</sub>)(BDC-NH<sub>2</sub>)] (1)

The IR spectrum of In-BDC-NH<sub>2</sub> (1) is displayed in Fig. 4 and an overview is presented in Table S5.† The presence of DMF is visible from the bands at 1661 cm<sup>-1</sup>, corresponding to the C-O stretching vibration, and at 1330 cm<sup>-1</sup>, alluding to C-N stretching vibrations. The C-N deformation vibration is located at 700 cm<sup>-1</sup>.<sup>21</sup> The ammonium ion of the linker molecule, warranting charge balancing, is confirmed by the

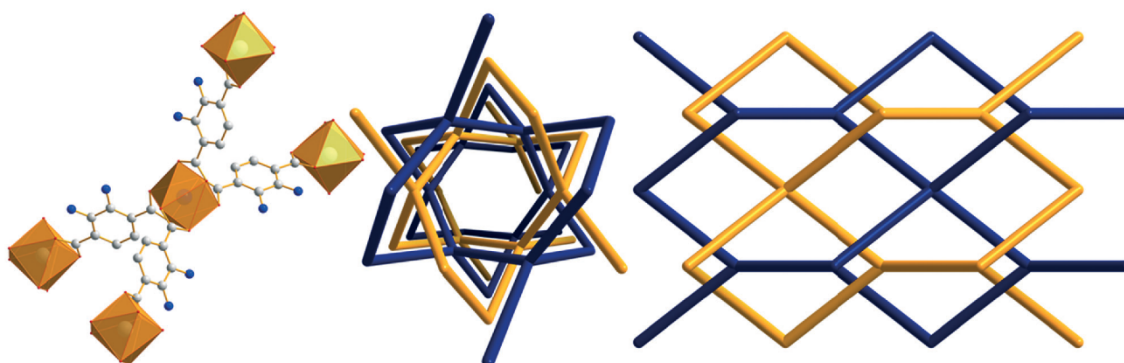


Fig. 2 The IBU of In-BDC-NH<sub>2</sub> (1) and its connection to four adjacent ones are shown (left). The interpenetrating quartz like framework is presented along [001] (middle) and [100] (right). The two independent nets are displayed in orange and blue. H atoms are not displayed.

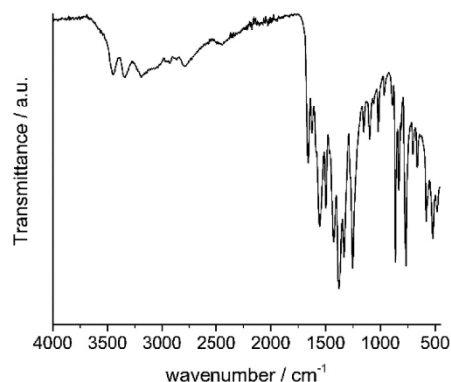


Fig. 4 IR spectrum of In-BDC-NH<sub>2</sub> (1).

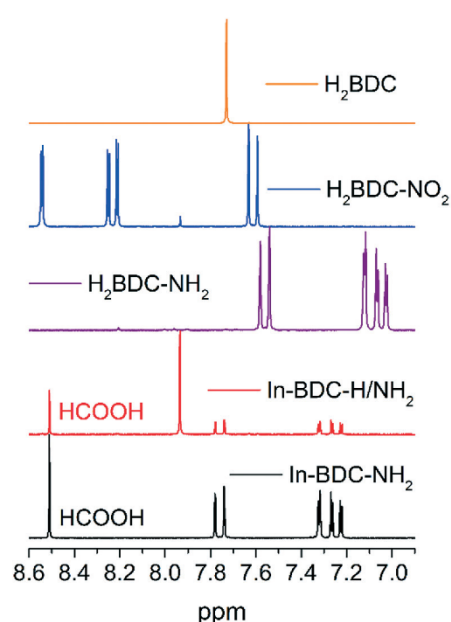


Fig. 5 <sup>1</sup>H-NMR spectra of In-BDC-NH<sub>2</sub> (1), In-BDC-H/NH<sub>2</sub> (2) and the linker used. Additionally, the spectrum of H<sub>2</sub>BDC is displayed. In 1 (black) H<sub>2</sub>BDC-NH<sub>2</sub> (purple) is present. For the synthesis of 2 (red) H<sub>2</sub>BDC-NO<sub>2</sub> (blue) was used, which is *in situ* reduced to H<sub>2</sub>BDC-NH<sub>2</sub> (purple) and H<sub>2</sub>BDC (orange), since no H<sub>2</sub>BDC-NO<sub>2</sub> (blue) is present. HCOOH originates from the hydrolysis of DMF while dissolving the compounds in 5% NaOD in D<sub>2</sub>O.

presence of the bands at 3183 and 2780 cm<sup>-1</sup> corresponding to the asymmetric and the symmetric N-H stretching vibration. The asymmetric and the symmetric deformation vibrations of -NH<sub>3</sub><sup>+</sup> are visible at 1551 and 1498 cm<sup>-1</sup>, respectively. Bands of -NH<sub>3</sub><sup>+</sup> rocking vibrations are present at 1254, 1099 and 1019 cm<sup>-1</sup>.<sup>48</sup> The bands at 1623 cm<sup>-1</sup> and at 1426 cm<sup>-1</sup> can be assigned to the symmetric and the asymmetric stretching vibration of the carboxylate of the linker molecule. The asymmetric and the symmetric NH<sub>2</sub> stretching vibration of unprotonated amino groups can be attributed to the bands

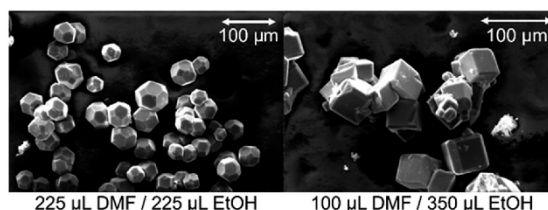


Fig. 6 SEM micrographs of the single crystals obtained as synthesis products of In-BDC-NH<sub>2</sub>/NO<sub>2</sub>. For a volume ratio DMF : EtOH = 225 : 225 μL truncated octahedral crystals are obtained and for a ratio of DMF : EtOH = 100 : 350 μL the crystals exhibit a cubic morphology.

at 3438 and 3336 cm<sup>-1</sup>, respectively, whereas the bands of the N-H out of plane vibration is located at 765 cm<sup>-1</sup> and a band at 1151 cm<sup>-1</sup> corresponds to the C-N stretching vibration. Bands at 861, 832 and 662 cm<sup>-1</sup> can be attributed to one and two neighbouring H atoms of the aromatic ring and its skeletal vibration.<sup>49</sup> Thermogravimetric analysis (Fig. S9†) shows a continuous mass loss starting at 100 °C. First, occluded solvent molecules are removed, resulting in two steps of weight loss. In the first step up to 110 °C, water molecules are removed from the framework, causing a mass loss of 5.8% (calc. 5.4%). The second step up to 200 °C is attributed to the removal of occluded DMF molecules with a mass loss of 19.4% (calc. 18.2%). At a temperature of 200 °C the framework starts to decompose, resulting in a mass loss of 60.3% (calc. 56.5%). Taking these results into account, the composition of In-BDC-NH<sub>2</sub> is deduced to be [In(BDC-NH<sub>3</sub>)(BDC-NH<sub>2</sub>)]·1.6DMF·1.9H<sub>2</sub>O, which is in reasonable agreement with the results of the elemental analysis (meas./calc.: C, 40.7%/39.2%; H, 5.6%/3.9%; N, 8.1%/7.9%). Additionally, the <sup>1</sup>H-NMR spectra confirm the integrity of H<sub>2</sub>BDC-NH<sub>2</sub> (Fig. 5).

#### H[In(BDC)<sub>0.57</sub>(BDC-NH<sub>2</sub>)<sub>0.43</sub>] (2)

The MOF described above was also obtained using 2-nitroterephthalic acid and investigated by PXRD measurements (Fig. S10†) and <sup>1</sup>H-NMR spectroscopy (Fig. 5). The PXRD patterns prove that the very same framework is formed, but the <sup>1</sup>H-NMR spectra reveal that no -NO<sub>2</sub> group is present in the reaction product. According to the results of the <sup>1</sup>H-NMR spectroscopy only BDC<sup>2-</sup> and BDC-NH<sub>2</sub><sup>2-</sup> ions are incorporated into the MOF. Thus, BDC-NO<sub>2</sub><sup>2-</sup> was reduced *in situ*, most probably by In<sup>3+</sup>/DMF to BDC<sup>2-</sup> and BDC-NH<sub>2</sub><sup>2-</sup>. Catalytic reductions in the presence of indium cations have been described previously.<sup>50,51</sup> The synthesis of a nitro functionalized derivative of In-BDC-NH<sub>2</sub> was therefore not successful and instead an *in situ* linker modification of nitroterephthalic acid was observed.

#### Structure of (DMA)<sub>2</sub>[In<sub>3</sub>(μ<sub>3</sub>-O)(BDC-NH<sub>2</sub>/NO<sub>2</sub>)<sub>4.5</sub>] (3)

Based on the results of the synthesis of 2 the formation of a doubly amino-functionalized MOF was anticipated using 2-amino-5-nitroterephthalic acid (H<sub>2</sub>BDC-NH<sub>2</sub>/NO<sub>2</sub>) as the starting material. Employing the same synthesis conditions

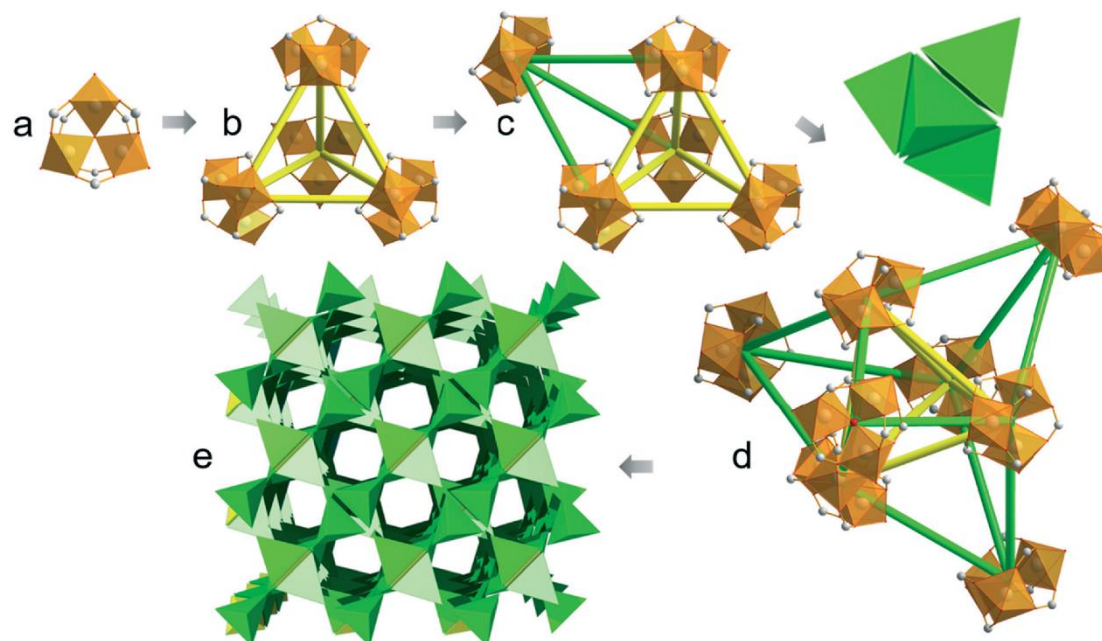


Fig. 7 Explanation of the crystal structure of In-BDC-NH<sub>2</sub>/NO<sub>2</sub> (3) with trinuclear clusters (a) forming super-tetrahedra by connection through tetradentate BDC-NH<sub>2</sub>/NO<sub>2</sub><sup>2-</sup> ions (yellow bars, b). By attaching an additional trinuclear cluster by tridentate BDC-NH<sub>2</sub>/NO<sub>2</sub><sup>2-</sup> ions to each face of a super-tetrahedron (green bars, c) ultra-tetrahedra (d) are formed. These form the final structure (e), symbolized by coloured tetrahedra.

as those used for 2 replacing H<sub>2</sub>BDC-NH<sub>2</sub> by H<sub>2</sub>BDC-NH<sub>2</sub>/NO<sub>2</sub> led to the formation of dimethylammonium 2-amino-5-nitroterephthalate hemihydrate (Fig. S11†).<sup>52</sup> Altering the synthesis conditions resulted in the formation of a new

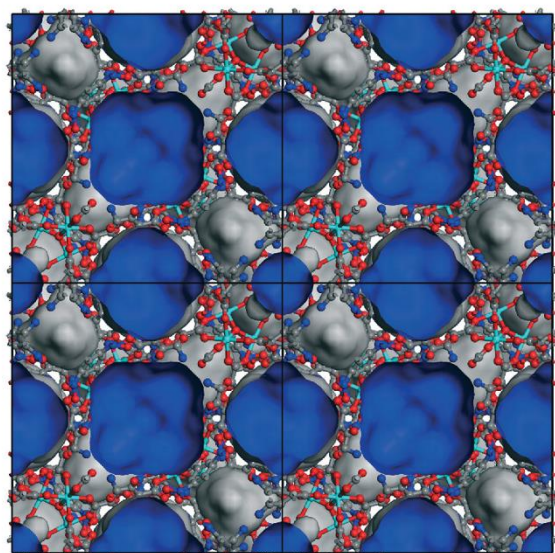


Fig. 8 Representation of non-accessible pores of In-BDC-NH<sub>2</sub>/NO<sub>2</sub> (3) with a diameter of 10.4 Å. The Connolly surface area was calculated with a probe diameter of 3.3 Å (kinetic diameter of CO<sub>2</sub>) using Materials Studio and is shown in blue.<sup>45</sup>

bifunctionalized MOF containing BDC-NH<sub>2</sub>/NO<sub>2</sub><sup>2-</sup> ions. Variation of the solvent volume ratio of DMF : ethanol leads to two different crystal morphologies (Fig. 6). The phase purity of the sample was confirmed by PXRD measurements (Fig. S12†). The framework is based on InO<sub>6</sub> polyhedra connected *via* μ<sub>3</sub>-O to form trinuclear clusters as observed in MIL-100/101 (Fig. 7a and S13†).<sup>53</sup> These clusters are interlinked by disordered tetradentate BDC-NH<sub>2</sub>/NO<sub>2</sub><sup>2-</sup> ions to form super-tetrahedra (Fig. 7b and S14†). An additional trimeric cluster is attached to every face of the super-tetrahedron by tridentate BDC-NH<sub>2</sub>/NO<sub>2</sub><sup>2-</sup> ions. The -COO<sup>-</sup> group binds to the coordination site of the trinuclear cluster, which is usually occupied by a water molecule (Fig. 7c and S15†). Thus, four

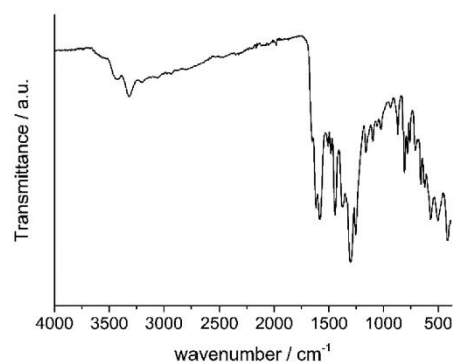


Fig. 9 IR spectrum of In-BDC-NH<sub>2</sub>/NO<sub>2</sub> (3).

additional super-tetrahedra are formed, which are face-sharing with the central super-tetrahedron to form a new ultra-tetrahedron (Fig. 7d). The whole framework is built up by face-to-corner-sharing ultra-tetrahedra (Fig. 7e). Hence, a framework with an underlying **ncb** net is formed if the trinuclear In-clusters are considered as nodes. This topology allows a structure with the presence of non-accessible cavities with a diameter of up to 10.4 Å (Fig. 8). Charge balance of the negative framework is accomplished by the dimethyl ammonium ions located in the pores, which is in good agreement with the electron density removed by the SQUEEZE command (at least 43 electrons per cavity) and also confirmed by NMR spectroscopy (Fig. S16†).

#### Properties of $(\text{DMA})_2[\text{In}_3(\mu_3\text{-O})(\text{BDC-NH}_2/\text{NO}_2)_{4.5}]$ (3)

The IR spectrum of In-BDC-NH<sub>2</sub>/NO<sub>2</sub> (3) is displayed in Fig. 9 and an overview is presented in Table S6.† The presence of DMF is clearly visible with prominent signals at 3193 and 2801 cm<sup>-1</sup> corresponding to the asymmetric and symmetric C–H stretching vibration, and at 1644 cm<sup>-1</sup>, corresponding to the C–O stretching vibration.<sup>21</sup> For charge balance dimethyl ammonium ions are present, originating from the hydrolysis of DMF during synthesis. This is confirmed by the band at 3065 cm<sup>-1</sup> corresponding to the stretching vibrations of ammonium ions. C–H, N–H stretching and N–H deformation vibrations are visible in the bands at 2923, 1096 and 784 cm<sup>-1</sup>, respectively.<sup>54</sup> The bands at 1620 cm<sup>-1</sup> and at 1159 cm<sup>-1</sup> can be assigned to the symmetric and the asymmetric stretching vibration of the carboxylate of the linker molecule. The asymmetric and the symmetric –NH<sub>2</sub> stretching vibrations can be attributed to the bands at 3430 and 3316 cm<sup>-1</sup>, respectively, whereas the N–H out of plane vibrations are located in the bands at 761 and 501 cm<sup>-1</sup>. Bands at 1577, 1023, 871 and 660 cm<sup>-1</sup> can be assigned to C=C stretching vibrations, to C–H in plane vibrations, to one H atom of the aromatic ring and to its skeleton vibration. The functional groups of the linker can be observed in the bands at 1299 and 1254 cm<sup>-1</sup> due to the presence of C–N and the aryl–N stretching vibration.<sup>49</sup> The presence of dimethylammonium was also confirmed by <sup>1</sup>H-NMR spectroscopy (Fig. S16†).

Thermogravimetric analysis (Fig. S17†) shows a continuous mass loss starting at 100 °C. Thus, a clear assignment of steps was not possible. A total mass loss of 79.9% was observed. The composition of In-BDC-NH<sub>2</sub>/NO<sub>2</sub> is deduced to be  $(\text{DMA})_2[\text{In}_3(\mu_3\text{-O})(\text{BDC-NH}_2/\text{NO}_2)_{4.5}]\cdot\text{DMF}$ , which is in good agreement to the results of the elemental analysis (meas./calc.: C, 33.1%/34.0%; H, 3.5%/2.7%; N, 11.0%/11.1%).

## Conclusion

Three new In-MOFs were obtained within this study. The two new functionalised isorecticular In-MOFs, In-BDC-NH<sub>2</sub> (1) and In-BDC-H/NH<sub>2</sub> (2) were obtained from a solvent mixture of DMF and water. The crystal structure of 1 was determined from single crystal XRD data. It contains two interpenetrating nets of InO<sub>8</sub> polyhedra interconnected by BDC-NH<sub>2</sub><sup>2-</sup> ions to

form a framework with a **qtz** topology. One-dimensional, hexagonal pores with a diameter of 4.4 Å are formed and TG measurements indicate a thermal stability up to 300 °C. During the synthesis of In-BDC-H/NH<sub>2</sub> (2) an *in situ* reduction of the employed H<sub>2</sub>BDC-NO<sub>2</sub> linker molecule to H<sub>2</sub>BDC and H<sub>2</sub>BDC-NH<sub>2</sub> was observed, which are exclusively incorporated into the final product.

Additionally, an In-MOF with amino and nitro functionalities, In-BDC-NH<sub>2</sub>/NO<sub>2</sub>, was obtained replacing the water by ethanol in the synthesis. The crystal morphology can be adjusted by varying the DMF to ethanol volume ratio. The crystal structure was also solved and refined using single crystal XRD data. The cubic structure is based on the formation of ultra-tetrahedra which are face-to-corner sharing to form the final framework with an **ncb** topology.

## Acknowledgements

The authors want to thank Helge Reinsch for scientific advice and consultation. This work was financially supported by the Deutsche Forschungsgemeinschaft (DFG) (STO 643/10-1). A. K. I. is supported by the Knut and Alice Wallenberg Foundation (KAW) through the MAX IV postdoctoral scholarship. We acknowledge Beamline I19, Diamond Light Source, UK for access to synchrotron radiation.

## References

- 1 L.-H. Schilling, H. Reinsch and N. Stock, in *The Chemistry of Metal–Organic Frameworks*, Wiley-VCH Verlag GmbH & Co. KGaA, 2016, ch 5, pp. 105–135, DOI: 10.1002/9783527693078.
- 2 T. Loiseau, C. Volkringer, M. Haouas, F. Taulelle and G. Férey, *C. R. Chim.*, 2015, **18**, 1350–1369.
- 3 F. Gándara, B. Gomez-Lor, E. Gutiérrez-Puebla, M. Iglesias, M. A. Monge, D. M. Proserpio and N. Snežko, *Chem. Mater.*, 2008, **20**, 72–76.
- 4 C. Volkringer, T. Loiseau, N. Guillou, G. Férey and E. Elkaïm, *Solid State Sci.*, 2009, **11**, 1507–1512.
- 5 R. Sabouni, H. Kazemian and S. Rohani, *Chem. Eng. Technol.*, 2012, **35**, 1085–1092.
- 6 C. Volkringer, T. Loiseau, N. Guillou, G. Férey, D. Popov, M. Burghammer and C. Riekell, *Solid State Sci.*, 2013, **26**, 38–44.
- 7 M. Mazaj, C. Volkringer, T. Loiseau, V. Kaučič and G. Férey, *Solid State Sci.*, 2011, **13**, 1488–1493.
- 8 X.-L. Chen, Y. Pan and X.-Z. Song, *Polyhedron*, 2016, **117**, 513–517.
- 9 T. Ahnfeldt, N. Guillou, D. Gunzelmann, I. Margiolaki, T. Loiseau, G. Férey, J. Senker and N. Stock, *Angew. Chem.*, 2009, **121**, 5265–5268.
- 10 H. Reinsch, M. Feyand, T. Ahnfeldt and N. Stock, *Dalton Trans.*, 2012, **41**, 4164–4171.
- 11 F. Gándara, H. Furukawa, S. Lee and O. M. Yaghi, *J. Am. Chem. Soc.*, 2014, **136**, 5271–5274.
- 12 T. Loiseau, L. Lecroq, C. Volkringer, J. Marrot, G. Férey, M. Haouas, F. Taulelle, S. Bourrelly, P. L. Llewellyn and M. Latroche, *J. Am. Chem. Soc.*, 2006, **128**, 10223–10230.

- 13 R. Hajjar, C. Volkringer, T. Loiseau, N. Guillou, J. Marrot, G. Férey, I. Margiolaki, G. Fink, C. Morais and F. Taulelle, *Chem. Mater.*, 2011, **23**, 39–47.
- 14 C. Volkringer, T. Loiseau, G. Férey, C. M. Morais, F. Taulelle, V. Montouillout and D. Massiot, *Microporous Mesoporous Mater.*, 2007, **105**, 111–117.
- 15 S. P. Petrosyants and A. B. Ilyukhin, *Russ. J. Inorg. Chem.*, 2011, **56**, 2047–2069.
- 16 R. Shannon, *Acta Crystallogr., Sect. A: Cryst. Phys., Diffraction, Theor. Gen. Crystallogr.*, 1976, **32**, 751–767.
- 17 D. T. Richens, *Chem. Rev.*, 2005, **105**, 1961–2002.
- 18 H. Taube, *Chem. Rev.*, 1952, **50**, 69–126.
- 19 H. Reinsch, R. S. Pillai, R. Siegel, J. Senker, A. Lieb, G. Maurin and N. Stock, *Dalton Trans.*, 2016, **45**, 4179–4186.
- 20 M. Krüger, R. Siegel, A. Dreischarf, H. Reinsch, J. Senker and N. Stock, *Microporous Mesoporous Mater.*, 2015, **216**, 27–35.
- 21 H. Reinsch, M. A. van der Veen, B. Gil, B. Marszalek, T. Verbiest, D. de Vos and N. Stock, *Chem. Mater.*, 2012, **25**, 17–26.
- 22 T. Loiseau, C. Serre, C. Huguénard, G. Fink, F. Taulelle, M. Henry, T. Bataille and G. Férey, *Chem. – Eur. J.*, 2004, **10**, 1373–1382.
- 23 H. Reinsch, M. Krüger, J. Wack, J. Senker, F. Salles, G. Maurin and N. Stock, *Microporous Mesoporous Mater.*, 2012, **157**, 50–55.
- 24 C. Volkringer, D. Popov, T. Loiseau, G. Férey, M. Burghammer, C. Riekel, M. Haouas and F. Taulelle, *Chem. Mater.*, 2009, **21**, 5695–5697.
- 25 T. Loiseau, H. Muguerra, M. Haouas, F. Taulelle and G. Férey, *Solid State Sci.*, 2005, **7**, 603–609.
- 26 S.-T. Zheng, T. Wu, C. Chou, A. Fuhr, P. Feng and X. Bu, *J. Am. Chem. Soc.*, 2012, **134**, 4517–4520.
- 27 W. Ji, H. Hu, W. Zhang, H. Huang, X. He, X. Han, F. Zhao, Y. Liu and Z. Kang, *Dalton Trans.*, 2013, **42**, 10690–10693.
- 28 Y. Liu, J. F. Eubank, A. J. Cairns, J. Eckert, V. C. Kravtsov, R. Luebke and M. Eddaoudi, *Angew. Chem., Int. Ed.*, 2007, **46**, 3278–3283.
- 29 F. Bu, Q. Lin, Q.-G. Zhai, X. Bu and P. Feng, *Dalton Trans.*, 2015, **44**, 16671–16674.
- 30 S.-T. Zheng, J. T. Bu, Y. Li, T. Wu, F. Zuo, P. Feng and X. Bu, *J. Am. Chem. Soc.*, 2010, **132**, 17062–17064.
- 31 C. Volkringer and T. Loiseau, *Mater. Res. Bull.*, 2006, **41**, 948–954.
- 32 B. Yuan, D. Ma, X. Wang, Z. Li, Y. Li, H. Liu and D. He, *Chem. Commun.*, 2012, **48**, 1135–1137.
- 33 N. Stock and T. Bein, *J. Mater. Chem.*, 2005, **15**, 1384–1391.
- 34 H. Reinsch and N. Stock, *Microporous Mesoporous Mater.*, 2013, **171**, 156–165.
- 35 S. Bauer and N. Stock, *Chem. Unserer Zeit*, 2007, **41**, 390–398.
- 36 N. Stock, *Chem. Ing. Tech.*, 2010, **82**, 1039–1047.
- 37 N. Stock, *Microporous Mesoporous Mater.*, 2010, **129**, 287–295.
- 38 O. Delgado-Friedrichs and M. O’Keeffe, *Acta Crystallogr., Sect. A: Found. Crystallogr.*, 2003, **59**, 351–360.
- 39 *Generation, Analysis and Visualization of Reticular Ornaments using Gavrog*, <http://gavrog.org/>.
- 40 V. A. Blatov, A. P. Shevchenko and D. M. Proserpio, *Cryst. Growth Des.*, 2014, **14**, 3576–3586.
- 41 *Materials Studio v4.1*, Accelrys Software Inc.
- 42 G. Sheldrick, *Acta Crystallogr., Sect. A: Found. Adv.*, 2015, **71**, 3–8.
- 43 G. Sheldrick, *Acta Crystallogr., Sect. A: Found. Crystallogr.*, 2008, **64**, 112.
- 44 *XShape and XRed*, Stoe and Cie, Darmstadt, Germany, 1998.
- 45 A. Spek, *Acta Crystallogr., Sect. D: Biol. Crystallogr.*, 2009, **65**, 148–155.
- 46 A. Spek, *J. Appl. Crystallogr.*, 2003, **36**, 7–13.
- 47 J. Sun, L. Weng, Y. Zhou, J. Chen, Z. Chen, Z. Liu and D. Zhao, *Angew. Chem., Int. Ed.*, 2002, **41**, 4471–4473.
- 48 T. Nakanaga, K. Sugawara, K. Kawamata and F. Ito, *Chem. Phys. Lett.*, 1997, **267**, 491–495.
- 49 M. Karabacak, M. Cinar, Z. Unal and M. Kurt, *J. Mol. Struct.*, 2010, **982**, 22–27.
- 50 N. Sakai, S. Asama, S. Anai and T. Konakahara, *Tetrahedron*, 2014, **70**, 2027–2033.
- 51 B. Gomez-Lor, E. Gutiérrez-Puebla, M. Iglesias, M. A. Monge, C. Ruiz-Valero and N. Snejko, *Inorg. Chem.*, 2002, **41**, 2429–2432.
- 52 M. Krueger, M. Albat, F. Pieper and N. Stock, *IUCrData*, 2016, **1**, x160048.
- 53 M. Latroche, S. Surblé, C. Serre, C. Mellot-Draznieks, P. L. Llewellyn, J. H. Lee, J. S. Chang, S. H. Jhung and G. Férey, *Angew. Chem., Int. Ed.*, 2006, **45**, 8227–8231.
- 54 J. J. Fripiat, M. Pennequin, G. Poncelet and P. Cloos, *Clay Miner.*, 1969, **8**, 119–134.



### 4.7.3 Emergence of nonlinear optical activity by incorporation of a linker carrying the *p*-nitroaniline motif in MIL-53 frameworks

Der folgende Artikel wurde im Jahre 2017 in der Fachzeitschrift *Chemistry of Materials*, ACS zur Veröffentlichung eingereicht. Der Wiederabdruck erfolgte mit freundlicher Genehmigung der ACS. Reproduced with permission from:

K. Markey, M. Krüger, T. Seidler, H. Reinsch, T. Verbiest, D. E. De Vos, B. Champagne, N. Stock und M. A. van der Veen, *Chem. Mater.*, **2017**.

Ziel in dieser Veröffentlichung war es, das Donor-Akzeptor-System des *p*-Nitroanilins (PNA) in einen MOF einzubauen. PNA kristallisiert in einer zentrosymmetrischen Struktur und weist daher keinen SHG-Effekt auf. Durch den Einbau in einen MOF sollte eine Ausrichtung der Moleküle erreicht werden, was zu einer SHG-Aktivität führen sollte. Die Dicarbonsäure 2-Amino-5-nitroterephthalsäure (H<sub>2</sub>BDC-NH<sub>2</sub>/NO<sub>2</sub>) besitzt das PNA-Motiv und ist gleichzeitig für die Synthese von Metall-organischen Gerüstverbindungen geeignet. Mit diesem Linker wurden difunktionalisierte MIL-53(M)-Derivate (M = Al, Ga, In) hergestellt und eingehend charakterisiert. Die Strukturen von MIL-53(Al)-BDC-NH<sub>2</sub>/NO<sub>2</sub> [Al(OH)(BDC-NH<sub>2</sub>NO<sub>2</sub>)]·0.92DMF und MIL-53(Ga)-BDC-NH<sub>2</sub>/NO<sub>2</sub> [Ga(OH)(BDC-NH<sub>2</sub>NO<sub>2</sub>)]·0.13EtOH·1.9DMF konnten erfolgreich durch Rietveld-Methoden verfeinert werden. Beide Verbindungen kristallisieren in der orthorhombischen Raumgruppe *Cc*. Die Linkermoleküle der Verbindungen sind in unterschiedlichen Maße fehlgeordnet (Al: 61:39; Ga: 68:32), sodass lokal keine Inversionssymmetrie vorhanden ist. Die Fehlordnung der Linkermoleküle der Verbindungen wurden durch ab initio Berechnungen und durch die Rietveldverfeinerungen der Strukturen bestätigt. Die niedrige Kristallinität von MIL-53(In)-BDC-NH<sub>2</sub>/NO<sub>2</sub> [In(OH)(BDC-NH<sub>2</sub>NO<sub>2</sub>)]·0.86EtOH·0.58DMF·0.43In<sub>2</sub>O<sub>3</sub> verhinderte eine erfolgreiche Strukturverfeinerung. Weiterhin wurden die SHG-Aktivitäten der Verbindungen bestimmt. Bis auf das In-Derivat zeigten alle Verbindungen eine moderate, aber langzeitstabile SHG-Aktivität. Da eine Fehlordnung der Linkermoleküle in der Al- und Ga-Verbindung vorhanden ist, wird die SHG-Aktivität reduziert. Zusätzliche Informationen zur Veröffentlichung befinden sich im Anhang.

## Emergence of nonlinear optical activity by incorporation of a linker carrying the *p*-nitroaniline motif in MIL-53 frameworks

K. Markey,<sup>a,‡</sup> M. Krüger,<sup>b,‡</sup> T. Seidler,<sup>c,d,‡</sup> H. Reinsch,<sup>b</sup> T. Verbiest,<sup>e</sup> D. E. De Vos,<sup>a</sup> B. Champagne,<sup>d\*</sup> N. Stock<sup>b\*</sup> and M. A. van der Veen<sup>f\*</sup>

a. Centre for Surface Chemistry and Catalysis, Faculty of Bioscience Engineering, University of Leuven, 3001 Leuven, Belgium.

b. Institut für Anorganische Chemie, Christian-Albrechts-Universität zu Kiel, Kiel, Germany.

c. K. Gumiński Department of Theoretical Chemistry, Jagiellonian University, Romana Ingardena 3, 30-060 Kraków, Poland.

d. Unité de Chimie Physique Théorique et Structurale, University of Namur, 5000 Namur, Belgium.

e. Molecular Imaging and Photonics, KU Leuven – University of Leuven, 3001 Leuven, Belgium.

f. Catalysis Engineering, Department of Chemical Engineering, Delft University of Technology, 2629 Delft, The Netherlands.

**KEYWORDS.** *Metal-organic frameworks, second harmonic generation microscopy, second order nonlinear optical properties, multiscale ab initio calculations, local field theory calculations.*

---

**ABSTRACT:** *P*-nitroaniline presents the typical motif of a second-order nonlinear optically (NLO) active molecule. However, due to its crystallization in an antiparallel, hence centrosymmetric structure, the NLO activity is lost. In this contribution, the *p*-nitroaniline motif was built successfully into the MIL-53 metal-organic framework. More precisely, MIL-53 was synthesized with 2-amino-5-nitroterephthalate as organic linker, with either Al<sup>3+</sup>, Ga<sup>3+</sup> or In<sup>3+</sup> as inorganic cation. The Al and Ga structures are polar, as confirmed by second-harmonic generation microscopy, yielding stable NLO materials. Indeed, they contain a 22-36% surplus of the dipolar 2-amino-2-nitro benzene oriented in a parallel fashion. The indium compound was shown to be less crystalline and centrosymmetric. Ab initio modelling of the second-order NLO response shows that the Al and Ga materials show a response comparable to typical inorganic commercial NLO materials such as KDP. As a hybrid material, capable of low temperature synthesis and processing and the ultrafast NLO responses associated with organic materials, this material can potentially provide an interesting venue for applications with respect to traditional inorganic NLO materials.

---

### INTRODUCTION

Polar crystalline materials can be used for a wide range of applications as they possess characteristics such as piezoelectricity, pyroelectricity, second-order nonlinear optical (SONLO) activity and, in case of reversible polarity, ferroelectricity.<sup>1-3</sup> SONLO activity specifically can be applied for telecommunication, information storage, optical switching and signal processing.<sup>4</sup> Currently mainly polar inorganic materials are used in commercial applications. However, inorganics have several limitations, with the limitations depending on the envisioned application.<sup>5</sup> A general limitation of inorganic crystals is that their properties can hardly be fine-tuned through chemical synthesis. Organic materials, on the contrary, are tunable and can be processed in more versatile ways.<sup>5,6</sup> However, organic polar molecules have the disadvantage of typically crystallizing in an antiparallel orientation, due to the optimization of dipole-dipole interactions, which cancels the overall dipole moment.<sup>5,7,8</sup> To achieve polar alignment of the or-

ganic entities, methods such as poling of polymers, Langmuir-Blodgett films or self-assembled monolayers are required.<sup>9-14</sup> Crystal engineering methods can also be used to bypass the problem of centrosymmetric organization in organic materials. This is achieved by, for example crystallization of chiral compounds<sup>15</sup> or by co-crystallization with chiral components resulting in non-centrosymmetric polymorphs.<sup>16-18</sup>

Metal-organic frameworks (MOFs) or porous coordination polymers (PCPs) are a promising category of materials which are highly tunable, and which can circumvent the tendency of organic molecules to organize in a non-polar fashion.<sup>5</sup> MOFs are porous hybrid materials composed of metal ions or metal clusters and organic linkers. MOFs are tunable because the metal nodes can be varied, the organic linkers can be chemically engineered and the adsorbates in the pores can be exchanged. Polar organization in MOFs can be attained via several strategies. A first strategy to obtain non-centrosymmetric and potentially polar MOFs is to choose a metal-organic coordination bond geometry



which does not allow centrosymmetric organization. Typical examples of this strategy are diamondoid frameworks<sup>7,19</sup> and MOFs with nicotinate as a linker.<sup>20</sup> As a second strategy polar linkers can potentially organize in a polar fashion due to optimal interactions and steric hindrance keeping the linkers in place. An example of this strategy is the insertion of 2-aminoterephthalate in MIL-53.<sup>21</sup> A third strategy to obtain polarity in MOFs is via polar ordering of guest species in the frameworks' pores, as seen in perovskite structure type MOFs, where nitrogen containing cations are ordered in a polar way in the cavities.<sup>22–25</sup> Also neutral polar species, such as water, can organize in a polar fashion in MOFs.<sup>26,27</sup> A fourth strategy to create polar MOFs is the incorporation of an electronegative ion in the framework structure. An example exploiting this strategy is the fluoride doping of MIL-53 (Fe), which, together with the guest molecules, results in polar organization.<sup>28</sup>

In this research, we want to incorporate the well studied polar *p*-nitroaniline (PNA) motif in a metal-organic framework to potentially organize the linker in a polar organization that can be maintained. The organic PNA molecule is the posterchild polar push-pull molecule for second-order nonlinear optics, generating frequency doubled light. However, crystallization of the molecule leads to the aforementioned antiparallel organization, removing the polarity.<sup>29,30</sup> To obtain a polar material benefitting from the SONLO properties of PNA, researchers successfully adsorbed PNA molecules into zeolites leading to overall polarity.<sup>31–36</sup> However, zeolites have limited chemical modification and processing possibilities. Metal-organic frameworks can alleviate these issues, as they offer tunability, combined with ease of processing and the possibility to obtain polarity. In addition, when a flexible framework such as MIL-53 is chosen, opportunities arise to fine-tune the polarization by variation of the pore openings. In this contribution, for the first time a polar organization of the well-known PNA motif was created via the strategy of creating a linker carrying the PNA motif and incorporating it in several MIL-53 frameworks, yielding highly stable polar and second-order nonlinear optically active materials.

## EXPERIMENTAL SECTION

**Synthesis.** The chemicals used for the synthesis were commercially available and were used without further purification. Gallium and indium salts were purchased at ABCR and used as received. The 2-amino-5-nitroterephthalic acid ( $\text{H}_2\text{BDC-NH}_2/\text{NO}_2$ ) linker was synthesized by a three-step synthesis procedure based on literature published by Skibo et al.<sup>37</sup> Following the literature procedure, starting with the hydrolysis of dimethyl aminoterephthalate to 2-aminoterephthalic acid, the product was reacted with formamide ( $\text{HC(O)NH}_2$ ) to give 2-formamido terephthalic acid. After nitration of this intermediate, the final  $\text{H}_2\text{BDC-NH}_2/\text{NO}_2$  linker was obtained by deprotection. Following the synthesis procedure, single crystals of 2-amino-5-nitroterephthalic acid could be obtained after recrystallization from hot water. The purity of the  $\text{H}_2\text{BDC-NH}_2/\text{NO}_2$  linker was confirmed by <sup>1</sup>H-NMR spectroscopy. More details about the synthesis and characterization can be found in the ESI (Figure S1–S5). A flow chart displaying synthesis pathways, sample treatments

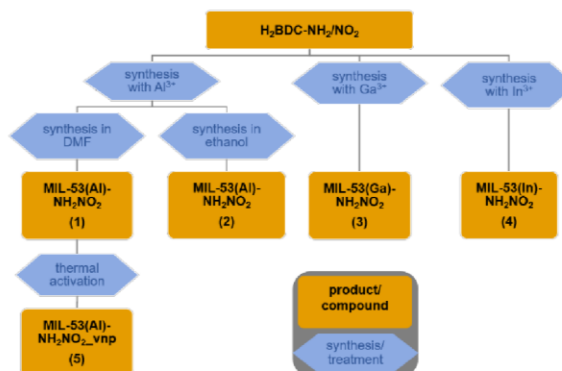


Figure 1. Flow chart of experiments, showing synthesis pathways, sample treatments and corresponding sample names.

and corresponding sample names is shown in Figure 1. Using three different metals (aluminum, gallium, indium), discovery and synthesis optimization of MIL-53 frameworks was carried out employing our 24-high-throughput (HT) reactor system for solvothermal reactions, allowing a fast and efficient determination of optimal reaction parameters.<sup>38–41</sup> The reactor system contains custom-made Teflon reaction vessels with a maximum volume of 2 mL. For our  $\text{M}^{3+}/\text{H}_2\text{BDC-NH}_2/\text{NO}_2/\text{solvent/additive}$  ( $\text{M}=\text{Al}, \text{Ga}, \text{In}$ ) system the following parameters were investigated: the molar ratio  $\text{M}^{3+}:\text{H}_2\text{BDC-NH}_2/\text{NO}_2$ , reaction solvents, volumetric ratio of solvent/water mixture, reaction temperature, reaction time, reaction vessel size and the addition of 2M  $\text{HNO}_3$  or 2M  $\text{NaOH}$  solution. Detailed information of the reactions carried out can be found in Tables S1–S4. MIL-53(Al)- $\text{NH}_2/\text{NO}_2$  was synthesized by two different routes: one using DMF/ $\text{H}_2\text{O}$  as solvent and one with ethanol/ $\text{H}_2\text{O}$  as solvent. MIL-53(Al)- $\text{NH}_2/\text{NO}_2$  in DMF, denoted as **MIL-53(Al)- $\text{NH}_2/\text{NO}_2$  (1)**, was synthesized with the following optimized synthesis conditions: To a mixture of 44.2  $\mu\text{L}$  2M  $\text{AlCl}_3 \cdot 6\text{H}_2\text{O}$  in  $\text{H}_2\text{O}$  (88.4  $\mu\text{mol}$ ) and 20 mg 2-amino-5-nitroterephthalic acid ( $\text{H}_2\text{BDC-NH}_2/\text{NO}_2$ , 88.4  $\mu\text{mol}$ ), 60  $\mu\text{L}$  of DMF (0.78 mmol), 32.5  $\mu\text{L}$   $\text{H}_2\text{O}$  (1.8 mmol) and 13.3  $\mu\text{L}$  1M  $\text{NaOH}$  in  $\text{H}_2\text{O}$  (13.3  $\mu\text{mol}$ ) were added in a 2 mL Teflon reactor. The reactor was sealed carefully and heated to 150 °C within 1 h, held at this temperature for 36 h and then cooled down to room temperature within 1 h. The product was filtered off, washed with *N,N*-dimethylformamide at room temperature for 2 h, filtered off again and dried under ambient conditions. As an alternative route, MIL-53(Al)- $\text{NH}_2/\text{NO}_2$  was prepared in ethanol, denoted as **MIL-53(Al)- $\text{NH}_2/\text{NO}_2$  (2)**, with following optimized synthesis conditions: 21.4 mg of  $\text{AlCl}_3 \cdot 6\text{H}_2\text{O}$  (88.4  $\mu\text{mol}$ ), 20 mg of  $\text{H}_2\text{BDC-NH}_2/\text{NO}_2$ , (88.4  $\mu\text{mol}$ ), 125  $\mu\text{L}$  of ethanol and 25  $\mu\text{L}$  of  $\text{H}_2\text{O}$  were added in a 2 mL Teflon reactor. The reactor was heated to 150 °C within 1 h, held at this temperature for 36 h and cooled down to room temperature within 1 h. Obtained products were filtered off and dried under ambient conditions. Compound **MIL-53(Ga)- $\text{NH}_2/\text{NO}_2$  (3)** was synthesized with the following optimized synthesis conditions: to a mixture of 21.4  $\mu\text{L}$  2M  $\text{Ga}(\text{NO}_3)_3 \cdot \text{H}_2\text{O}$  in  $\text{H}_2\text{O}$  (43  $\mu\text{mol}$ ) and 20 mg 2-amino-5-nitroterephthalic acid ( $\text{H}_2\text{BDC-NH}_2/\text{NO}_2$ , 88.4  $\mu\text{mol}$ ) 60  $\mu\text{L}$  of DMF (0.78 mmol), 25.8  $\mu\text{L}$  ethanol (0.44 mmol) and 20  $\mu\text{L}$  1M  $\text{HNO}_3$  in  $\text{H}_2\text{O}$  (20  $\mu\text{mol}$ ) were

added in a 2 mL Teflon reactor. The reactor was sealed carefully and heated to 150 °C within 1 h, held at this temperature for 16 h and then cooled down to room temperature within 1 h. The product was filtered off and dried under ambient conditions. Compound **MIL-53(In)-NH<sub>2</sub>/NO<sub>2</sub> (4)** was synthesized with the following optimized synthesis conditions: to a mixture of 44.2 µL 2M In(NO<sub>3</sub>)<sub>3</sub>·H<sub>2</sub>O in DMF (88.4 µmol) and 10 mg 2-amino-5-nitrotetraphthalic acid (H<sub>2</sub>BDC-NH<sub>2</sub>/NO<sub>2</sub>, 44.2 µmol) 85.8 µL of DMF (1.12 mmol) and 20 µL ethanol (0.34 mmol) were added in a 2 mL Teflon reactor. The reactor was sealed carefully and heated to 150 °C within 1h, held at this temperature for 16 h and then cooled down to room temperature within 1 h. The product was filtered off and dried under ambient conditions.

**Thermal activation.** Prior to the sorption experiments the samples **1-4** were activated at 200 °C for 16 h under reduced pressure (10<sup>-2</sup> kPa). For MIL-53(Al)-NH<sub>2</sub>/NO<sub>2</sub> (**1**) this activation procedure was carried out twice, ultimately resulting in **MIL-53(Al)-NH<sub>2</sub>/NO<sub>2</sub>\_vnp (5)**, the very narrow pore form of MIL-53(Al)-NH<sub>2</sub>/NO<sub>2</sub> (**1**).

**Structural characterization.** The high-throughput PXRD measurements were performed in transmission geometry using a STOE HT diffractometer equipped with a *xy*-stage and an image plate detector system (Cu K<sub>α1</sub> radiation). Collection of high-resolution powder diffraction data was performed with a STOE Stadi-P powder diffractometer equipped with a MYTHEN1K detector system (Cu K<sub>α1</sub> radiation). Single crystal X-ray diffraction data were collected on a Bruker P4 diffractometer equipped with a IPSPD detector using Mo K<sub>α</sub> radiation. The structural models for the Rietveld refinement for MIL-53(Al)-NH<sub>2</sub>/NO<sub>2</sub> (**1**) and MIL-53(Ga)-NH<sub>2</sub>/NO<sub>2</sub> (**3**) were obtained as follows: The cell parameters were obtained by indexing laboratory high-resolution X-ray powder diffraction data using TOPAS Academic v4.1,<sup>42</sup> indicating strong similarity of the title compound with the hydrated form of Al-MIL-53-np.<sup>43</sup> Using the Accelrys Materials Studio 4.1 software package, the BDC<sup>2-</sup> molecule in MIL-53 was exchanged by BDC-NH<sub>2</sub>/NO<sub>2</sub><sup>2-</sup>.<sup>44</sup> The lattice parameters were fixed to the experimentally determined values and energy minimization calculations were carried out using the universal force-field (UFF) as implemented in the Forcite module of Materials Studio.<sup>44</sup>

**General characterization.** Scanning electron microscopy (SEM) images were recorded on a JSM-6010PLUS/LA instrument from JEOL after sputter coating with palladium-gold. <sup>1</sup>H-NMR spectroscopy was carried out on a Bruker DRX 500 at 200 MHz. Thermogravimetric analyses were performed using a NETZSCH STA 409 CD analyzer. The samples were heated in Al<sub>2</sub>O<sub>3</sub> crucibles at a rate of 4 K min<sup>-1</sup> under a flow of synthetic air (75 ml min<sup>-1</sup>). The TG data were corrected for buoyancy and current effects. A HEKAtech Euro EA Elemental Analyzer was used for elemental analysis. Sorption experiments were carried out using a Belsorp-max instrument (BEL JAPAN INC.). The characterization of the compounds was carried out using as synthesized (for **2** to **4**) or washed samples (for **1**).

**SONLO measurements.** The compounds were always measured in their as synthesized form, unless mentioned otherwise. Second harmonic generation (SHG) scanning

microscopy images were recorded on a multiphoton laser scanning microscope (FV1200MPE, BX61WI frame, Olympus) in transmission mode. The microscope was equipped with a 50x long working distance objective (SLMPlan N, NA = 0.35, Olympus) and a visible light condenser (NA = 0.9, Olympus). To select the 400 nm SHG light a dichroic mirror and band pass filter combination was used (T425lpxr-et405/10bp of Chroma). As the laser source, a femtosecond tunable laser operating at a wavelength of 800 nm was used (~100 fs pulse duration, 80 MHz pulse rate) (Insight DeepSee, Spectra-Physics). The laser light was linearly polarized using a Glan-Taylor polarizer, and the plane of polarization was controlled via a zero-order half-wave plate from Thorlabs. The quantification of the second order NLO activity was done using a customized inverted wide-field SHG microscope (IX71 frame, Olympus) which operates in transmission mode. To be able to consider the incident light as a collimated beam, a long focal length lens (f = 75 mm, NA = 0.013) was used. Images were formed by a 15x long working distance objective (LMU-15x-NUV, NA = 0.32, Thorlabs) and recorded with an EM-CCD camera (Hamamatsu). To select the 400 nm SHG light a filter set consisting of a bandpass filter (BG39, 2 mm, Schott) and an interference filter (F10-100, center wavelength 400 nm, FWHM 10 nm, Melles Griot) was used. As the laser source, a Ti:sapphire laser operating at a wavelength of 800 nm was used (~100 fs pulse duration, 80 MHz pulse rate) (Tsunami, Spectra-Physics) combined with a pump laser (Millenia Pro, Spectra-Physics). The laser light was linearly polarized using a Glan-Taylor polarizer, and the plane of polarization was controlled via a zero-order half-wave plate from Thorlabs. All SHG images were processed with ImageJ and Fiji software.

**Multiscale ab initio/local field theory calculations to determine  $d_{\text{eff}}$ .** For both MIL-53(Al)-NH<sub>2</sub>/NO<sub>2</sub> and MIL-53(Ga)-NH<sub>2</sub>/NO<sub>2</sub> compounds two crystal phases (A and C, see figure 5) were considered in the calculations for  $d_{\text{eff}}$ . These phases (as well as vnp MIL-53(Al)-NH<sub>2</sub>) were first considered as independent pure phases for geometry optimization using periodic boundary conditions (PBC) within the CRYSTAL14 package.<sup>45,46</sup> The optimizations were performed at the density functional theory (DFT) level of theory with the B3LYP exchange-correlation functional and the 6-31G(d,p) basis set. Only the fractional coordinates were optimized with the cell parameters kept fixed at their experimental values. Using these optimized geometries, the calculations of the molecular properties, the polarizability  $\alpha$  and, the first hyperpolarizability  $\beta$  were performed for the individual cations and anions within their embedding crystal field. These fields were simulated with a 100 Å radius sphere of Mulliken point charges obtained from PBC/B3LYP calculations at the optimized crystal geometries.<sup>47</sup> The static ( $\lambda = \infty$ ) responses were computed at the second-order Møller-Plesset (MP2) level of theory with 6-311++G(d,p) basis set. The dynamic MP2 responses were then calculated following a multiplicative approximation that combines static and dynamic B3LYP/6-311++G(d,p) responses to describe frequency dispersion.<sup>48</sup> All the molecular property calculations were performed with Gaussian09 software.<sup>49</sup> Using the molecular properties, the linear susceptibilities,  $\chi^{(1)}$  - and there-

fore the refractive indices,  $n$  - and the second-order nonlinear susceptibilities,  $\chi^{(2)}$ , were then calculated by employing the local field theory (LFT) methodology,<sup>50-55</sup> recently applied to MOFs.<sup>48</sup> Finally, the effective values,  $\langle d_{\text{eff}} \rangle$ , were evaluated after accounting for the weights of the different crystal forms, for phase matching conditions, as well as for the averaging over all light polarization orientations with respect to the crystal grains. The  $d_{\text{eff}}$  values are related to the  $\chi^{(2)}$  tensors by the following equation:

$$d_{\text{eff}} = \frac{1}{2} \underline{e}_i(2\omega) \cdot \underline{\chi}^{(2)} : \underline{e}_j(\omega) \underline{e}_k(\omega) \times \text{sinc}^2\left(\frac{\Delta k r}{2}\right) \quad (1)$$

where  $\underline{e}_i$ ,  $\underline{e}_j$  and  $\underline{e}_k$  are the light waves polarization vectors,  $r$  is the optical path length (symbolizing the grain size in the calculation) and

$$\Delta k = \frac{2\pi}{\lambda} \Delta n; \Delta n = 2n_{\omega}^1 - n_{\omega}^2 - n_{\omega}^3 \quad (2)$$

is the phase mismatch related to the difference of refractive indices. 1, 2, and 3 refer to the crystal axes. Eq. (1) accounts for i) the biaxial nature of the crystal and the fact that non-polarized light beams split into two perpendicularly polarized [called (+) and (-)] beams propagating at different speeds, and for ii) the interaction between the incident light at fundamental frequency [(+) or (-)] and the generated light [also (+) or (-)] at twice its frequency. Finally, all possible orientations of the light wave polarizations with respect to the crystal grains, defined by the polar angles ( $\theta$ ,  $\phi$ ), are taken into account to estimate the average  $\langle d_{\text{eff}} \rangle$  quantities. More details about the whole multiscale method, including the evaluation of the local field, the treatment of the frequency dependence of the linear and nonlinear responses<sup>48,56</sup> and the selection of the charges to describe the in-crystal polarization field<sup>47</sup> are provided in the Supporting Information.

## RESULTS AND DISCUSSION

For our purpose to create functional polar crystals by incorporation of the PNA motif into a metal-organic framework, we started by designing a suitable linker molecule. As the aimed framework structure, we chose MIL-53, since the flexibility of the framework can potentially allow fine-tuning of the polarization, by variation of the pore opening. For the linker molecule to benefit from similar polar and second-order nonlinear optical properties as PNA, the linker was designed containing an extended  $\pi$ -conjugated system with amino and nitro donor- and acceptor-groups. To ensure that the linker can form metal coordination bonds to create a MIL-53 framework, opposing carboxylate ends were added to the aromatic ring. This resulted in the 2-amino-5-nitroterephthalic acid ( $\text{H}_2\text{BDC-NH}_2/\text{NO}_2$ ) molecule (Figure 2). After successful synthesis of the 2-amino-5-nitroterephthalic acid linker (Figure S5), three different metals were used as the nodes to build up the aimed MIL-53 frameworks: aluminum, gallium and indium. All frameworks were synthesized with DMF/ $\text{H}_2\text{O}$  as a solvent, and for the aluminum MOF also a synthesis in ethanol/ $\text{H}_2\text{O}$  was tested. The resulting synthesized compounds are denoted as follows: MIL-53(Al)- $\text{NH}_2/\text{NO}_2$  (**1**) for the aluminum compound synthesized in DMF, MIL-53(Al)- $\text{NH}_2/\text{NO}_2$  (**2**) for the aluminum compound synthesized in ethanol, MIL-53(Ga)- $\text{NH}_2/\text{NO}_2$  (**3**) for the gallium compound synthesized in DMF and MIL-53(In)- $\text{NH}_2/\text{NO}_2$  (**4**) for the

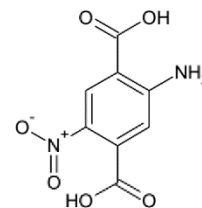


Figure 2. The 2-amino-5-nitroterephthalic acid ( $\text{H}_2\text{BDC-NH}_2/\text{NO}_2$ ) linker molecule.

indium compound synthesized in DMF. The syntheses of the aluminum compounds **1** and **2** both resulted in microcrystalline powders, with the crystals of the DMF synthesis (**1**) having a more or less rectangular shape with lengths around  $10 \mu\text{m}$  and thicknesses around  $2 \mu\text{m}$ , or a cubic shape between  $0.5\text{-}2 \mu\text{m}$  in size (Figure 3.a). The synthesis of the aluminum compound in ethanol (**2**) resulted in longer (between  $10\text{-}50 \mu\text{m}$ ) and thicker (around  $8 \mu\text{m}$ ) crystals than the DMF synthesis (Figure 3.b). The gallium compound **3** was also obtained as a microcrystalline powder, seemingly composed of aggregates of rectangular crystals grown alongside each other, with the larger aggregates having a length between  $20\text{-}30 \mu\text{m}$  and a thickness around  $20 \mu\text{m}$  (Figure 3.c). The indium compound **4** appeared to be less crystalline, as the PXRD pattern did exhibit fewer well resolved reflections (Figure 3.d, S10 PXRD). Additional SEM images can be found in the supporting information (Figure S17-S20).

**Crystal structures.** To determine whether the crystal structures of compounds **1-4** are polar, PXRD measurements were performed to refine the structures using the Rietveld method, since the compounds could only be obtained as microcrystalline powders. MIL-53(Al)- $\text{NH}_2/\text{NO}_2$  (**1**) and MIL-53(Ga)- $\text{NH}_2/\text{NO}_2$  (**3**) were confirmed to crystallize in the polar monoclinic space group  $Cc$  (Figures S6 and S8, containing Rietveld and Pawley refinements). The pattern of MIL-53(Al)- $\text{NH}_2/\text{NO}_2$  (**2**) exhibited fewer well resolved reflections (Figure S7) and therefore a reliable refinement by Rietveld methods was not possible. However, corresponding to the Pawley refinements, the cell parameters of MIL-53(Al)- $\text{NH}_2/\text{NO}_2$  (**2**) hardly differ from those of MIL-53(Al)- $\text{NH}_2/\text{NO}_2$  (**1**) (Table 1). Due to the lower crystallinity of MIL-53(In)- $\text{NH}_2/\text{NO}_2$  (**4**), only the cell parameters could be obtained via indexing the powder pattern and refining them using the Pawley method (Figure S10). Since no structural refinement was possible, the indium compound could not be unambiguously assigned to a centrosymmetric or non-centrosymmetric space group. The crystallographic data of the different MIL-53- $\text{NH}_2/\text{NO}_2$  compounds are summarized in Table 1. According to the results of the Rietveld refinement, structures **1**, **2** and **3** are disordered and hence have multiple linker alignments. Therefore, ab initio calculations were performed to optimize potential framework models. To start, all four possible alternative locations of the amino and nitro groups were considered, as shown in Figure 5, leading to four models, each containing one orientation. Consecutively, PXRD patterns were simulated from these models and compared against the Rietveld refinements of the experimental PXRD data.

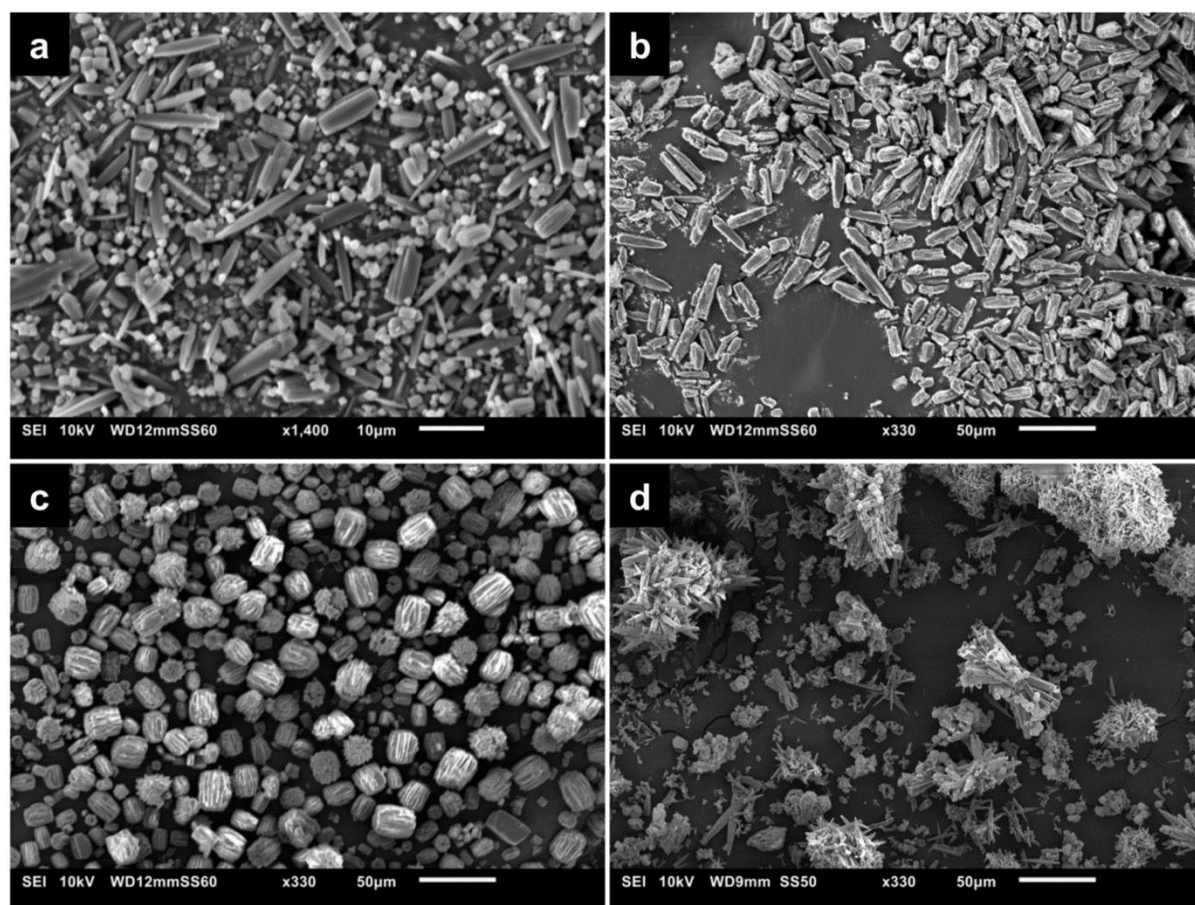


Figure 3. SEM images of  $\text{H}_2\text{BDC-NH}_2/\text{NO}_2$  containing MOFs: **(a)** MIL-53(Al)- $\text{NH}_2/\text{NO}_2$  (**1**), **(b)** MIL-53(Al)- $\text{NH}_2/\text{NO}_2$  (**2**), **(c)** MIL-53(Ga)- $\text{NH}_2/\text{NO}_2$  (**3**) and **(d)** MIL-53(In)- $\text{NH}_2/\text{NO}_2$  (**4**). Note that the first image has a scale bar of 10  $\mu\text{m}$ , whereas the other images have a scale bar of 50  $\mu\text{m}$ .

Table 1. Crystallographic data of the title compounds.

	MIL-53(Al)- $\text{NH}_2/\text{NO}_2$ ( <b>1</b> )	MIL-53(Al)- $\text{NH}_2/\text{NO}_2$ ( <b>2</b> )	MIL-53(Ga)- $\text{NH}_2/\text{NO}_2$ ( <b>3</b> )	MIL-53(In)- $\text{NH}_2/\text{NO}_2$ ( <b>4</b> )
Formula Sum	[Al(OH)(BDC-NH <sub>2</sub> /NO <sub>2</sub> )]	[Al(OH)(BDC-NH <sub>2</sub> /NO <sub>2</sub> )]	[Ga(OH)(BDC-NH <sub>2</sub> /NO <sub>2</sub> )]	[In(OH)(BDC-NH <sub>2</sub> /NO <sub>2</sub> )]
Method	Rietveld	Pawley	Rietveld	Pawley
Wavelength	CuK $\alpha_1$	CuK $\alpha_1$	CuK $\alpha_1$	CuK $\alpha_1$
$a / \text{\AA}$	17.5669(8)	17.565(5)	17.460(1)	16.870(8)
$b / \text{\AA}$	13.3691(7)	13.469(3)	14.1006(7)	13.948(7)
$c / \text{\AA}$	6.6105(2)	6.616(2)	6.7350(2)	7.235(4)
$\beta / ^\circ$	112.125(3)	112.273(8)	112.712(6)	90
Spacegroup	<i>Cc</i>	<i>Cc</i>	<i>Cc</i>	<i>Imam</i> or <i>Ima2</i>
$R_{\text{wp}} / \%$	5.57	3.79	7.41	4.20
$R_{\text{Bragg}} / \%$	1.56	-	2.81	-
GoF	2.11	1.74	2.00	1.54

The comparison revealed that two of these models were reasonably well matching the experimental PXRD data, namely phase A and C. As a last step, the occurrence of combinations of phase A and C was considered. The phase percentages were obtained by using refinable occupancy

and led to the conclusion that the A phase is present in excess over the C phase, which represent its oppositely oriented counterpart, respectively. Optimization of the MIL-53(Al)- $\text{NH}_2/\text{NO}_2$  (**1**) structure resulted in the prediction of a 61:39 ratio of phases A and C (resp.) of linker organiza-

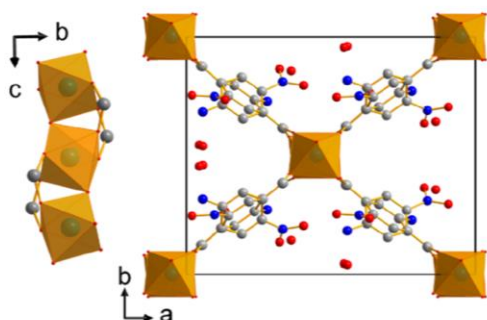


Figure 4. Crystal structure of compound **1** as obtained via Rietveld refinement. The pores contain occluded solvent molecules. Carbon atoms are shown in grey, oxygen in red, nitrogen in blue and  $\text{AlO}_6$  polyhedra in orange.

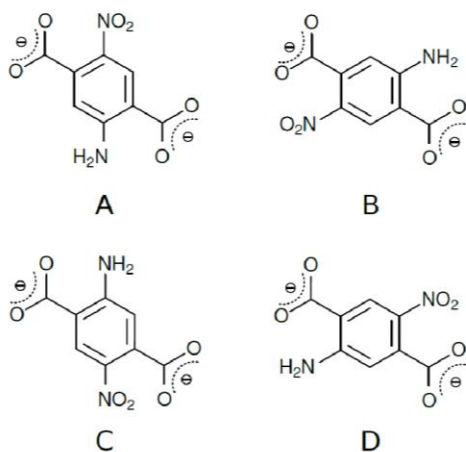


Figure 5. Different positions of the amino and nitro groups in the  $\text{BCD}^{2-}$  anion postulated in the  $\text{MIL-53}(\text{Al})\text{-NH}_2/\text{NO}_2$  structure.

tion (Figure 6). For  $\text{MIL-53}(\text{Al})\text{-NH}_2/\text{NO}_2$  (**2**) the modelling procedure could not be performed, as a reliable Rietveld refinement was not possible for the experimental PXRD pattern. For  $\text{MIL-53}(\text{Ga})\text{-NH}_2/\text{NO}_2$  (**3**) a 68:32 ratio of phases A and C (resp.) of linker organization resulted in the best fit with the experimental PXRD patterns (Figures S8-S9).

**Additional characterization.** To further characterize the new  $\text{MIL-53}\text{-NH}_2/\text{NO}_2$  compounds, the composition and thermal stability of **1-4** were verified by elemental analysis and TG measurements. All samples are stable up to ca. 300 °C, and up to this temperature occluded solvent molecules are removed from the framework (Figures S13-S15). The thermal stability is in the same range as known for other as synthesized functionalized  $\text{MIL-53}$  derivatives (-Cl, -Br,  $\text{CH}_3$ ,  $\text{NO}_2$ ,  $\text{-NH}_2$ ,  $\text{-OH}$ ).<sup>57</sup> The sum formulas of the compounds deduced from the TG measurements are in good agreement with the values obtained by elemental analyses (Table S6). Solution  $^1\text{H-NMR}$ -spectra show that 15% of the amino-groups of **2** were ethylated during synthesis (Figures S21-23).

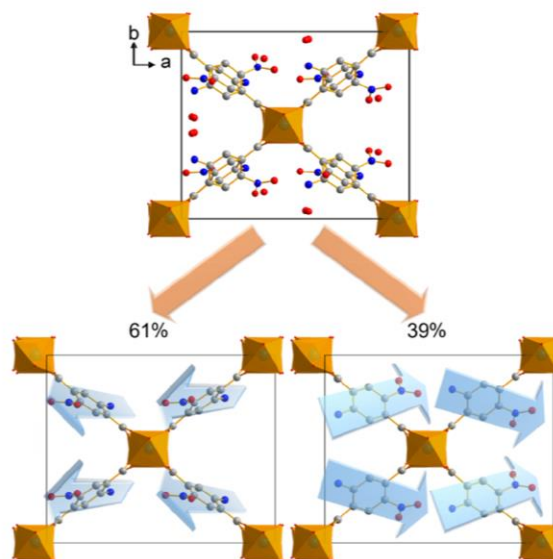


Figure 6. Crystal structure of  $\text{MIL-53}(\text{Al})\text{-NH}_2/\text{NO}_2$  (**1**) along [001]. The disorder (above) of the linker molecules in the structure contains 61% of the  $\text{NO}_2$  groups of the linker molecules showing out of the plane and 39% pointing in plane. Carbon atoms are shown in grey, oxygen in red, nitrogen in blue and  $\text{AlO}_6$  polyhedra in orange.

As there is a large interest for the use of MOFs in sorption applications, the sorption properties of the new  $\text{MIL-53}$  compounds **1-4** were also assessed. Prior to the sorption experiments all samples were activated by means of a temperature treatment to remove the guest molecules. Nitrogen sorption measurements reveal a Type I isotherm for  $\text{MIL-53}(\text{Al})\text{-NH}_2/\text{NO}_2$  (**1**), with a specific surface area (BET) of  $a_{s,\text{BET}} = 287 \text{ m}^2\text{g}^{-1}$  and a micropore volume of  $V_{\text{mic,BET}} = 0.11 \text{ cm}^3\text{g}^{-1}$  (Figure S24). When  $\text{MIL-53}(\text{Al})\text{-NH}_2/\text{NO}_2$  (**1**) was subjected to two consecutive activation treatments instead of one treatment, a very narrow pore form of  $\text{MIL-53}(\text{Al})\text{-NH}_2/\text{NO}_2$  (**1**) was achieved, as shown by the PXRD pattern (Figures 1 and S11; Table S5), denoted as  $\text{MIL-53}(\text{Al})\text{-NH}_2/\text{NO}_2\text{-vnp}$  (**5**).<sup>58</sup> Nitrogen sorption measurements for this very narrow pore form **5** show that the values reduce to  $a_{s,\text{BET}} = 92 \text{ m}^2\text{g}^{-1}$  and  $V_{\text{mic,BET}} = 0.04 \text{ cm}^3\text{g}^{-1}$ . Immersion of the very narrow pore compound **5** in DMF results in a re-establishment of the structure to the as synthesized  $\text{MIL-53}(\text{Al})\text{-NH}_2/\text{NO}_2$  (**1**) structure with the wider pores (Figure S12). Additionally, water,  $\text{CO}_2$  and hydrogen sorption experiments were performed on compound **1** (Figures S25-S27), starting from the sample which received one activation treatment. The measurements reveal a very hydrophilic character of compound **1**, with a total uptake of 12 weight-%  $\text{H}_2\text{O}$  (at 1 bar and 298 K), whereas 9 weight-% of  $\text{CO}_2$  (1 bar, 298 K) and 0.7 weight-% of hydrogen (1 bar, 77 K) can be adsorbed. The uptake of  $\text{CO}_2$  of ca. 90 mg/g in  $\text{MIL-53}(\text{Al})\text{-NH}_2/\text{NO}_2$  (**1**) is comparable with the reported uptake of  $\text{MIL-53}(\text{Al})$  of app. 106 mg/g and  $\text{MIL-53}(\text{Al})\text{-NH}_2$  of app. 98.6 mg/g.<sup>59,60</sup> Compounds **2-4** did not show any uptake of  $\text{N}_2$ , therefore no other types of sorption measurements were carried out for these compounds.

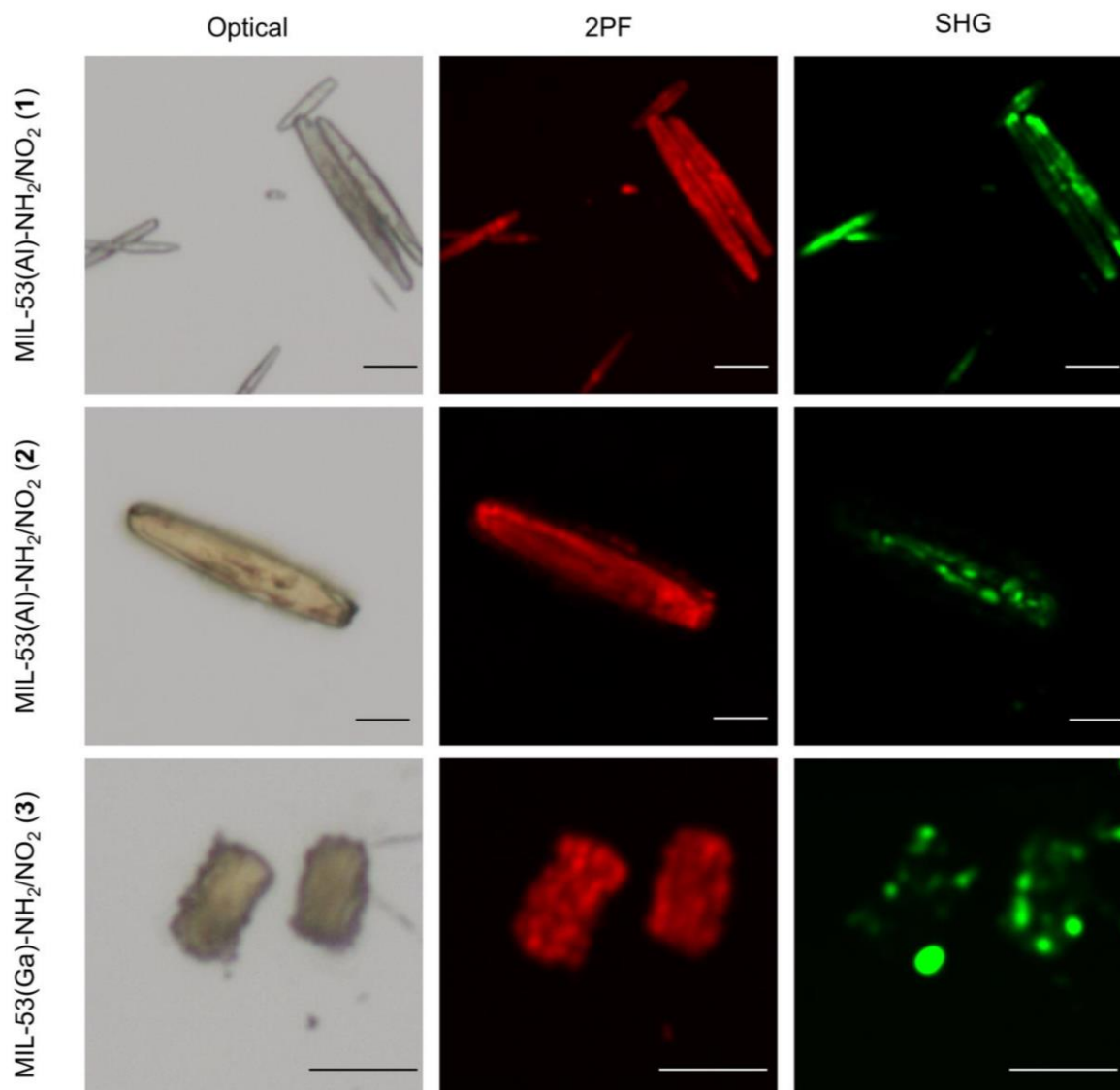


Figure 7. From left to right: optical, two-photon fluorescence and second harmonic generation images. From top to bottom: as synthesized MIL-53(Al)-NH<sub>2</sub>/NO<sub>2</sub> (**1**), MIL-53(Al)-NH<sub>2</sub>/NO<sub>2</sub> (**2**), MIL-53(Ga)-NH<sub>2</sub>/NO<sub>2</sub> (**3**). The SHG images display the average intensity of linearly polarized laser light, calculated over 60 images, each image being 3° apart in polarization direction of the incident polarized beam. The scale bars indicate a distance of 10 μm for each image.

**Second harmonic generation activity.** The PXRD refinements revealed that polar symmetries are achieved due to a net polar organization of the linkers in compounds MIL-53(Al)-NH<sub>2</sub>/NO<sub>2</sub> (**1**), MIL-53(Al)-NH<sub>2</sub>/NO<sub>2</sub> (**2**) and MIL-53(Ga)-NH<sub>2</sub>/NO<sub>2</sub> (**3**). Since polar materials can display interesting second harmonic generation (SHG) activity, the occurrence of SHG was probed locally through SHG microscopy on single crystals of the compounds.

SHG is a nonlinear optical process, taking place when high intensity laser light interacts with materials, possessing a non-centrosymmetric organization.<sup>61</sup> This non-centrosymmetric requirement for second harmonic generation to occur is a consequence of the nature of the process. The SHG process converts the energy and momentum of two photons into one photon with doubled frequency,

by a coherent process, meaning phase relations between the photons are important. By consequence, destructive interference of SHG occurs in centrosymmetric organized materials, as the related third-rank tensor for the second-order nonlinear susceptibility  $\chi^{(2)}$  becomes zero. For non-centrosymmetric organizations, constructive interference of the SHG process occurs, and an SHG signal can be detected. Therefore, SHG microscopy can be used as a tool to distinguish non-centrosymmetric from centrosymmetric organizations. In our case, this allows us to locally probe areas in the crystals where non-centrosymmetric linker alignments are occurring.

Complementary to the SHG images, two-photon fluorescence (2PF) images were recorded. Two-photon fluorescence also is a nonlinear optical process, taking place when

fluorophores are irradiated with high intensity laser light.<sup>61</sup> In 2PF, two photons nearly simultaneously excite a fluorophore, which in turn emits a fluorescence photon. The process is an incoherent process, since the excitation and emission events are separated in time, and phase relations between the emitted versus exciting photons are absent. As there is no symmetry requirement for the process to occur, fluorophores can be visualized regardless of their organization.<sup>62</sup> In our case, the linker with PNA motif acts as the fluorophore. By comparing SHG and 2PF images, areas with non-centrosymmetric linker organizations (visible in both SHG and 2PF images) can be distinguished from areas with random linker organizations (only visible in 2PF images).

From Figure 7 it is clear that compounds MIL-53(Al)-NH<sub>2</sub>/NO<sub>2</sub> (**1**), MIL-53(Al)-NH<sub>2</sub>/NO<sub>2</sub> (**2**) and MIL-53(Ga)-NH<sub>2</sub>/NO<sub>2</sub> (**3**) contain areas displaying SHG activity. Those areas thus contain non-centrosymmetric linker organizations, more specifically polar alignments, as determined by the PXRD refinements. Comparison of SHG and 2PF images clearly show that the two-photon fluorescence signal is more homogeneously distributed than the SHG signal. This means that an overall polar linker organization is not present throughout the entire crystals. In contrast with compounds **1-3**, MIL-53(In)-NH<sub>2</sub>/NO<sub>2</sub> (**4**) does not display SHG activity (Figure S30). Apart from the non-SHG active powder, a single particle shows SHG-activity in the image. This is likely due to an impurity or minority phase. The apolar symmetry of the indium compound can be explained by the larger M-O distances in the MOF in comparison with the Al- and Ga-compounds (Al-O: 1.8-1.9 Å;<sup>43</sup> Ga-O: 1.8-2.0 Å;<sup>63</sup> In-O: 2.1-2.2 Å<sup>64</sup>), which allow a possible rotation, and hence randomization, of the linker molecules.

To quantify the SHG activity of compounds **1-3**, the effective second order nonlinear optical coefficient  $\langle d_{\text{eff}} \rangle$  was determined experimentally for each compound. The  $\langle d_{\text{eff}} \rangle$  value of a material represents the average SHG activity of a collection of crystals of the material, oriented differently in the measurements' coordinate system. Averaging over all orientations allows quantification of the SHG activity of materials for which measurements along a specific crystal axis are not straightforward, as is the case for small crystals. To obtain an absolute value for  $\langle d_{\text{eff}} \rangle$ , the sample crystals are measured against a reference crystal, of which the  $d$  value is known (in our case a BBO crystal was used as the reference). Using the  $\langle d_{\text{eff}} \rangle$  value for the quantification of the SHG activity of a compound, differences in crystal size and refractive index are taken into account.<sup>65</sup> A detailed description of the  $\langle d_{\text{eff}} \rangle$  calculation is given in the supporting information. The experimentally determined  $\langle d_{\text{eff}} \rangle$  values of compounds **1-3** are summarized in Table 2. For the aluminum compound **1** and the

gallium compound **3**, equal  $\langle d_{\text{eff}} \rangle$  values were measured (0.02 pm.V<sup>-1</sup>). The aluminum compound synthesized in ethanol **2** displayed a higher SHG activity, with a  $\langle d_{\text{eff}} \rangle$  value of 0.05 pm.V<sup>-1</sup>. An explanation for the higher SHG activity of this compound could be a higher A/C fraction (Figure 5), which would lead to more non-centrosymmetrically organized linkers. However, as mentioned previously, we could not determine the A/C fraction for compound **2** through structure refinements, as a reliable structure refinement was not possible for this compound.

Comparing the  $\langle d_{\text{eff}} \rangle$  values of the MIL-53-NH<sub>2</sub>/NO<sub>2</sub> MOFs **1-3** with the reported  $\langle d_{\text{eff}} \rangle$  value of MIL-53(Al)-NH<sub>2</sub> (0.05 ± 0.02 pm/V),<sup>21</sup> for which the terephthalic acid linker is functionalized solely with an amino group, it can be concluded that the SHG activities are in the same range, despite their differences in linker functionalization. This seems counterintuitive, as a higher SHG activity for the compounds with the amino/nitro functionalized linkers could be expected, since this linker possesses a more efficient donor-acceptor system, resulting in a higher hyperpolarizability, which could lead to a higher SHG activity. However, an important determining factor of the SHG efficiency is how the linkers are organized in the crystal structure. The occurrence of several phases of linker organization can lead to (partial) cancellation of the SHG activity. Additionally, MIL-53-NH<sub>2</sub>/NO<sub>2</sub> and MIL-53(Al)-NH<sub>2</sub> reabsorb the wavelength at which SHG is generated (400 nm) most likely to a different extent (See fig. S33 and reference<sup>66</sup>). In fact, a rough estimate of the amount of reabsorbed SHG-light is calculated in the SI for a crystal containing the PNA motif, with the same linker density as for MIL-53(Al)-NH<sub>2</sub>/NO<sub>2</sub> (**1**) and a height of 2 μm. This estimation predicts a transmittance of only 2.1 · 10<sup>-4</sup> % of generated 400 nm SHG light through the sample. While the calculation is based on the extinction coefficient of PNA in water, rather than 2-amino-5-nitroterephthalate build into MIL-53, the majority of the generated SH-light can be expected to be reabsorbed by the MIL-53(Al)-NH<sub>2</sub>/NO<sub>2</sub>. To gain more insight in the differences between the MIL-53-NH<sub>2</sub>/NO<sub>2</sub> compounds and the previously reported MIL-53(Al)-NH<sub>2</sub> compound, they need to be investigated off-resonance, which is also directly relevant for NLO-applications. Hence we theoretically determined the  $\langle d_{\text{eff}} \rangle$  values using ab initio calculations on the crystal structures in the next section.

**Analysis of MIL-53(Al)-NH<sub>2</sub>/NO<sub>2</sub> (**1**), MIL-53(Ga)-NH<sub>2</sub>/NO<sub>2</sub> (**3**) and MIL-53(Al)-NH<sub>2</sub> SHG activity by ab initio calculations.** Multiscale numerical simulations were carried out to predict and interpret the  $\langle d_{\text{eff}} \rangle$  values of MIL-53(Al)-NH<sub>2</sub>/NO<sub>2</sub> (**1**), MIL-53(Ga)-NH<sub>2</sub>/NO<sub>2</sub> (**3**), and MIL-53(Al)-NH<sub>2</sub>. To account for the occurrence of a combination of A and C linker phases in compounds MIL-53(Al)-NH<sub>2</sub>/NO<sub>2</sub> (**1**) and MIL-53(Ga)-NH<sub>2</sub>/NO<sub>2</sub> (**3**), first the  $\chi^{(1)}$  and  $\chi^{(2)}$  tensors for the pure phases of linker organization A and C were calculated. Consecutively, the final  $\chi^{(1)}$  and  $\chi^{(2)}$  tensors were obtained by accounting for the A/C phase ratios, as determined from the powder diffraction refinement, *i.e.* 61:39 for MIL-53(Al)-NH<sub>2</sub>/NO<sub>2</sub> (**1**) and 68:32 for MIL-53(Ga)-NH<sub>2</sub>/NO<sub>2</sub> (**3**).

Table 2. Experimental  $\langle d_{\text{eff}} \rangle$  values.

	$\langle d_{\text{eff}} \rangle / \text{pm.V}^{-1}$
MIL-53-(Al)-NH <sub>2</sub> /NO <sub>2</sub> ( <b>1</b> )	0.02 ± 0.01
MIL-53-(Al)-NH <sub>2</sub> /NO <sub>2</sub> ( <b>2</b> )	0.05 ± 0.02
MIL-53-(Ga)-NH <sub>2</sub> /NO <sub>2</sub> ( <b>3</b> )	0.02 ± 0.01

The resulting  $\chi^{(1)}$  and  $\chi^{(2)}$  tensors and  $\langle d_{\text{eff}} \rangle$  values for MIL-53(Al)-NH<sub>2</sub>/NO<sub>2</sub>, MIL-53(Ga)-NH<sub>2</sub>/NO<sub>2</sub>, and MIL-53(Al)-NH<sub>2</sub> are presented in Table 3 (See also Supporting Information for additional data on the refractive indices as well as linear and nonlinear responses for other incident wavelengths, Tables S7-S8). It is clear that the  $\chi_{ijk}^{(2)}$  tensors for the pure A and C phases are almost equal in magnitude but opposite in sign, especially for the aluminum compound MIL-53(Al)-NH<sub>2</sub>/NO<sub>2</sub> (**1**). This means that the SHG-generating part (mostly the organic linker) is practically oriented antiparallel in phase A versus phase C. Moreover, if a material would contain equal amounts of phases A and C, at a scale below the diffraction limit, practically no SHG would be generated, as the phases would cancel each other out. Because MIL-53(Al)-NH<sub>2</sub>/NO<sub>2</sub> (**1**) and MIL-53(Ga)-NH<sub>2</sub>/NO<sub>2</sub> (**3**) were experimentally found to contain respectively 61:39 and 68:32 ratios of phases A:C, the tensor components and therefore also the SHG activity are not completely cancelled out, but the values are lower than those of the pure phases. Considering the largest  $\chi^{(2)}$  tensor components of the pure phases, this reduction attains a factor of 4-5 for M=Al and 2-3 for M=Ga. Still, relatively high maximum  $\chi_{ijk}^{(2)}$  tensor components are found for the compounds containing mixed phases: 29.3 pm/V for  $\chi_{333}^{(2)}$  (M=Al) and 105.0 pm/V for  $\chi_{111}^{(2)}$  (M=Ga).

However, when calculating the  $\langle d_{\text{eff}} \rangle$  values for the mixed compounds, the responses are strongly reduced and this effect is enhanced when combined with the phase mismatch factor. These two effects can be analyzed separately by considering first the results for a hypothetical zero grain size ( $r = 0$  in Table 3) because they include the averaging over the polar angles but not the phase matching effects and then the results for  $r = 3$  and  $10 \mu\text{m}$  where both effects are accounted for.

First, when only averaging  $d_{\text{eff}}$  over the polar angles to get  $\langle d_{\text{eff}} \rangle$ , the SHG response drops by more than one order of magnitude with respect to the dominant  $\chi^{(2)}$  tensor components (see column  $r = 0 \mu\text{m}$  in Table 3). This reduction is supported by the polar maps of  $d_{\text{eff}}(\theta, \phi)$  (Fig. S31 of Supporting Information), which highlight the  $(\theta, \phi)$  domains that result in large  $d_{\text{eff}}(\theta, \phi)$  values and the fact that many  $(\theta, \phi)$  domains are associated with much smaller SHG responses. Then, while accounting for the grain size,  $\langle d_{\text{eff}} \rangle$  drops quite rapidly with  $r$  (Figure 8). For  $r = 3 \mu\text{m}$ , the responses are already reduced by one order of magnitude with respect to the situation without phase mismatch and by another factor of 3-4 when going from  $r = 3 \mu\text{m}$  to  $10 \mu\text{m}$ . Fig. S32 of Supporting Information describes the phase matching effects on the polar maps of  $d_{\text{eff}}(\theta, \phi)$ .

This ultimately leads to relatively low theoretical  $\langle d_{\text{eff}} \rangle$  values for MIL-53(Al)-NH<sub>2</sub>/NO<sub>2</sub> (**1**) and MIL-53(Ga)-NH<sub>2</sub>/NO<sub>2</sub> (**3**), with respect to the potential  $\chi^{(2)}$  or  $d_{\text{eff}}$  values if pure phase compounds could be created. Then, these final  $\langle d_{\text{eff}} \rangle$  results, *i.e.* when incorporating for all effects, show that the pure A and C phases of compound **1/2** and **3** are characterized by larger values of  $\langle d_{\text{eff}} \rangle$  than compound **4** and that the differences between the A and C phases are larger for the Ga derivative. The comparison of these re-

sults to experiment also suggests that compound (**2**) is characterized by a much more ordered structure and thus higher  $\chi^{(2)}$  than compound **1**.

The  $\langle d_{\text{eff}} \rangle$  values for the optical path of  $10 \mu\text{m}$  of the mixed AC phases of compound (**1**)/(**2**) (0.018 pm/V) and (**3**) (0.032 pm/V) and that of vnp structure of MIL-53(Al)-NH<sub>2</sub> (0.064 pm/V) compare quite well with experimental values (0.02 pm/V, 0.02 pm/V, 0.05 pm/V respectively). Although many effects were accounted for in the calculations, yet, several factors need to be taken under consideration. First of all, the polydispersity of the studied materials hinders a direct comparison of the experimental value with single points ( $r$  values) of Figure 8. The second important factor is the absorption of the SH signal and the associated resonance enhancement, larger in the case of MIL-53(Al/Ga)-NH<sub>2</sub>/NO<sub>2</sub> species than in the case of the amino derivative. This could lead to a conclusion that the final results obtained for MIL-53(Al/Ga)-NH<sub>2</sub>/NO<sub>2</sub> are somewhat underestimated and the true structure of these materials do not disfavor the  $\chi^{(2)}$ . Indeed, the overall values of the phase-matched mixed A/C crystals (0.57 pm/V for Al and 1.05 pm/V for Ga compound) are comparable to that of commercial inorganic NLO materials such as KDP (0.38-0.41 pm/V at 1064 nm) and moreover, the calculated  $\chi^{(2)}$  tensors are considerable, which suggests that the investigated materials are of potential interest.

This ultimately leads to relatively low theoretical  $\langle d_{\text{eff}} \rangle$  values for MIL-53(Al)-NH<sub>2</sub>/NO<sub>2</sub> (**1**) and MIL-53(Ga)-NH<sub>2</sub>/NO<sub>2</sub> (**3**), with respect to the potential  $\chi^{(2)}$  or  $d_{\text{eff}}$  values if pure phase compounds could be created. Then, these final  $\langle d_{\text{eff}} \rangle$  results, *i.e.* when incorporating for all effects, show that the pure A and C phases of compound **1/2** and **3** are characterized by larger values of  $\langle d_{\text{eff}} \rangle$  than compound **4** and that the differences between the A and C phases are larger for the Ga derivative. The comparison of these results to experiment also suggests that compound (**2**) is characterized by a much more ordered structure and thus higher  $\chi^{(2)}$  than compound **1**.

The  $\langle d_{\text{eff}} \rangle$  values for the optical path of  $10 \mu\text{m}$  of the mixed AC phases of compound (**1**)/(**2**) (0.018 pm/V) and (**3**) (0.032 pm/V) with that of vnp structure of MIL-53(Al)-NH<sub>2</sub> (0.064 pm/V) compare quite well with experimental values. Although many effects were accounted for in the calculations, yet, several factors need to be taken under consideration. First of all, the polydispersity of the studied materials hinders a direct comparison of the experimental value with single points ( $r$  values) of Figure 8. The second important factor is the absorption of the SH signal and the associated resonance enhancement, larger in the case of the MIL-53(Al/Ga)-NH<sub>2</sub>/NO<sub>2</sub> species than in the case of the amino derivative. This could lead to a conclusion that the final results obtained for MIL-53(Al/Ga)-NH<sub>2</sub>/NO<sub>2</sub> are somewhat underestimated and the true structure of these materials do not disfavor the  $\chi^{(2)}$ . Indeed, the overall value of the phase-matched mixed A/C crystal is comparable to that of commercial inorganic NLO materials such as KDP and moreover, the calculated  $\chi^{(2)}$  tensors are considerable, which suggests that the investigated materials are of potential interest.



Table 3. MP2/LFT results for MIL-53(Al)-NH<sub>2</sub>/NO<sub>2</sub>, MIL-53(Ga)-NH<sub>2</sub>/NO<sub>2</sub> and MIL-53(Al)-NH<sub>2</sub> (in the very narrow pore phase) calculated for an incident wavelength of 1064 nm: selected  $\chi^{(2)}$  tensor components (in pm/V) and  $\langle d_{\text{eff}} \rangle$  (in pm/V). For MIL-53(M)-NH<sub>2</sub>/NO<sub>2</sub>, results are listed for the pure A and C phases as well as for the A:C ratios obtained from PXRD analysis.

Compound/Phase	$\chi_{333}^{(2)}$	$\chi_{111}^{(2)}$	$\chi_{133}^{(2)}$	$\chi_{113}^{(2)}$	$\langle d_{\text{eff}} \rangle$	$\langle d_{\text{eff}} \rangle$	$\langle d_{\text{eff}} \rangle$
					r = 0 $\mu\text{m}$	r = 3 $\mu\text{m}$	r = 10 $\mu\text{m}$
MIL-53(Al)-NH <sub>2</sub> /NO <sub>2</sub> Phase A	133.9	-1.5	-16.3	-2.1	2.56	0.285	0.080
MIL-53(Al)-NH <sub>2</sub> /NO <sub>2</sub> Phase C	-134.2	1.5	16.2	2.1	2.54	0.276	0.079
<b>MIL-53(Al)-NH<sub>2</sub>/NO<sub>2</sub> A/C (61:39)</b>	29.3	-0.3	-3.6	-0.5	<b>0.57</b>	<b>0.066</b>	<b>0.018</b>
MIL-53(Ga)-NH <sub>2</sub> /NO <sub>2</sub> Phase A	-4.4	222.2	-6.9	13.3	2.58	0.198	0.061
MIL-53(Ga)-NH <sub>2</sub> /NO <sub>2</sub> Phase C	4.3	-147.1	7.0	-4.9	2.70	0.354	0.110
<b>MIL-53(Ga)- NH<sub>2</sub>/NO<sub>2</sub> A/C (68:32)</b>	-1.3	105.0	-3.2	1.9	<b>1.05</b>	<b>0.105</b>	<b>0.032</b>
<b>MIL-53(Al)-NH<sub>2</sub> (vnp)</b>	6.2	-15.8	-6.6	-2.6	<b>1.88</b>	<b>0.191</b>	<b>0.064</b>

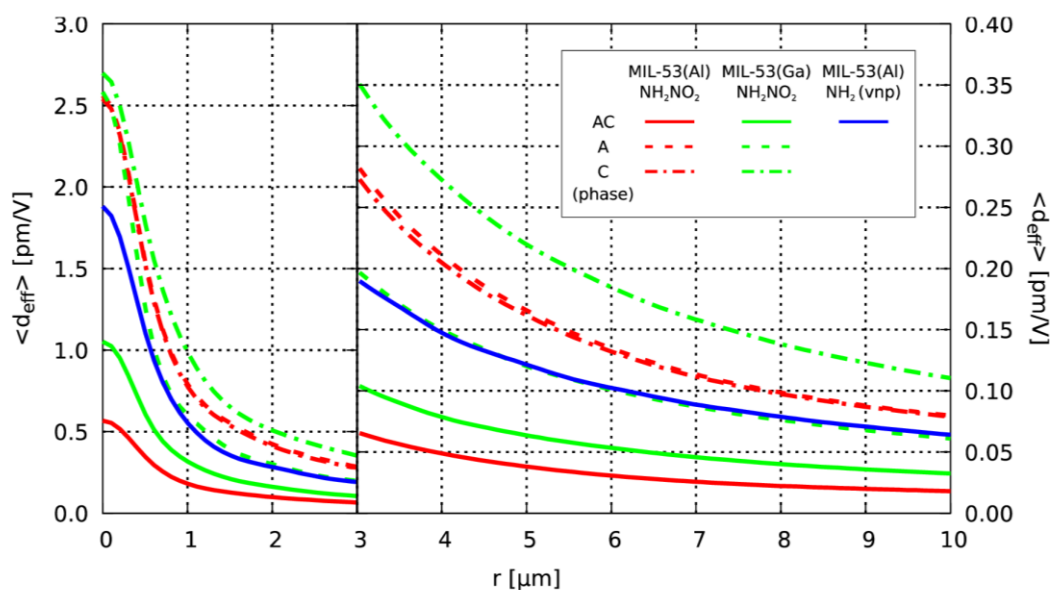


Figure 8. Grain size dependence of the calculated  $\langle d_{\text{eff}} \rangle$  values for MIL-53(Al)-NH<sub>2</sub>/NO<sub>2</sub>, MIL-53(Ga)-NH<sub>2</sub>/NO<sub>2</sub> and MIL-53(Al)-NH<sub>2</sub>(vnp). For MIL-53(M)-NH<sub>2</sub>/NO<sub>2</sub>, results are listed for the pure A and C phases as well as for the A:C ratios obtained from PXRD analysis.

## CONCLUSION

In this contribution, for the first time a polar organization of the well-known *p*-nitroaniline motif was achieved by incorporation of the motif in metal-organic framework structures. To be able to incorporate the motif in several MIL-53 MOFs, a linker was designed possessing an extended pi-conjugated system with amino donor- and nitro ac-

ceptor-groups, as in PNA. Combining this linker with three different cations as nodes (Al, Ga, In), several MIL-53 frameworks were created. MIL-53(Al)-NH<sub>2</sub>/NO<sub>2</sub> and MIL-53(Ga)-NH<sub>2</sub>/NO<sub>2</sub> displayed a net polar and thus SHG active organization of the linkers, whereas the MIL-53(In)-NH<sub>2</sub>/NO<sub>2</sub> compound did not display SHG activity, indicating no polar organization was obtained.

The SHG activity of the aluminum and gallium compounds was experimentally determined to be in the same range as that of the previously reported MIL-53(Al)-NH<sub>2</sub>, where only an amino donor group resides on the terephthalate linker. Ab initio calculations revealed that, while the terephthalate linker with the amino and nitro functionalization is more NLO efficient than the linker with sole amino functionalization, the occurrence of multiple phases of linker organization in MIL-53(M)-NH<sub>2</sub>/NO<sub>2</sub> structures leads to partial cancellation of the SHG activity. Therefore, the SHG activities of MIL-53(Al)-NH<sub>2</sub>/NO<sub>2</sub> and MIL-53(Ga)-NH<sub>2</sub>/NO<sub>2</sub> lie in the same range as that of MIL-53(Al)-NH<sub>2</sub>. Moreover, theoretical calculations revealed that the SHG activity of the MIL-53(M)-NH<sub>2</sub>/NO<sub>2</sub> structures decreases with increasing grain size and that for the smallest grain size, where perfect phase matching occurs, the theoretical SHG activity is comparable to that of commercial inorganic NLO materials, such as KDP. This means that the investigated materials are of potential interest.

This research shows that the creation of metal-organic frameworks containing linkers which mimic interesting SONLO properties of organic molecules in their motif, can be a promising strategy to obtain functional polar crystals.

### AUTHOR INFORMATION

#### Corresponding Author

\*M. A. van der Veen; Tel.: +31-15-2786458. E-mail: m.a.vanderveen@tudelft.nl

\* N. Stock; Tel.: +49-431-8801675. Email: stock@ac.uni-kiel.de

\*B. Champagne; Tel.: +32-81-724554. Email: benoit.champagne@unamur.be

#### Author Contributions

‡ K. Markey, M. Krüger and T. Seidler contributed equally.

#### Funding Sources

M.K. was financially supported by the Deutsche Forschungsgemeinschaft (DFG) (STO 643/10-1). KM and DDV are grateful to Belspo for funding in the IAP project Functional Supramolecular Systems. DDV, TV and MvdV are grateful for the financial support from the Hercules Foundation and to FWO.

#### Notes

The authors do not compete financial interest.

### REFERENCES

- (1) Ye, Z.-G.; Institute of Materials, M. *Handbook of Dielectric, Piezoelectric and Ferroelectric Materials: Synthesis, Properties and Applications*; Woodhead Pub. and Maney Pub. on behalf of The Institute of Materials, Minerals & Mining, 2008.
- (2) Curtin, D. Y.; Paul, I. C. Chemical Consequences of the Polar Axis in Organic Solid-State Chemistry. *Chem. Rev.* **1981**, *81* (6), 525–541.
- (3) Asadi, K.; van der Veen, M. A. Ferroelectricity in Metal-Organic Frameworks: Characterization and Mechanisms. *Eur. J. Inorg. Chem.* **2016**, No. 27, 4332–4344.
- (4) Fainman, Y.; Ma, J.; Lee, S. H. Non-Linear Optical Materials and Applications. *Mater. Sci. Rep.* **1993**, *9* (2–3), 53–139.
- (5) Hollingsworth, M. D. Crystal Engineering: From Structure to Function. *Science* **2002**, *295* (5564), 2410–2413.
- (6) Mingabudinova, L. R.; Vinogradov, V. V.; Milichko, V. A.; Hey-
- (7) Hawkins, E.; Vinogradov, A. V. Metal-organic Frameworks as Competitive Materials for Non-Linear Optics. *Chem. Soc. Rev.* **2016**, *45*, 5408–5431.
- (8) Evans, O. R.; Lin, W. Crystal Engineering of NLO Materials Based on Metal-Organic Coordination Networks. *Accounts Chem. Res.* **2002**, *35* (7), 511–522.
- (9) Shi, Y.; Zhang, C.; Zhang, H.; Bechtel, J. H.; Dalton, L. R.; Robinson, B. H.; Steier, W. H. Low (Sub-1-Volt) Halfwave Voltage Polymeric Electro-Optic Modulators Achieved by Controlling Chromophore Shape. *Science* **2000**, *288* (5463), 119–122.
- (10) Burland, D. M.; Miller, R. D.; Walsh, C. A. Second-Order Nonlinearity in Poled-Polymer Systems. *Chem. Rev.* **1994**, *94* (1), 31–75.
- (11) Marks, T. J.; Ratner, M. A. Design, Synthesis, and Properties of Molecule-Based Assemblies with Large Second-Order Optical Nonlinearities. *Angew. Chem. Int. Edit.* **1995**, *34* (2), 155–173.
- (12) Ashwell, G. J.; Jackson, P. D.; Crossland, W. A. Non-Centrosymmetry and Second-Harmonic Generation in Z-Type Langmuir-Blodgett Films. *Nature* **1994**, *368* (6470), 438–440.
- (13) Penner, T. L.; Motschmann, H. R.; Armstrong, N. J.; Ezenyilimba, M. C.; Williams, D. J. Efficient Phase-Matched Second-Harmonic Generation of Blue Light in an Organic Waveguide. *Nature* **1994**, *367* (6458), 49–51.
- (14) Lin, W. W.; Lin, W. W.; Wong, G. K.; Marks, T. J. Supramolecular Approaches to Second-Order Nonlinear Optical Materials. Self-Assembly and Microstructural Characterization of Intrinsically Acentric [(Aminophenyl)azo]pyridinium Superlattices. *J. Am. Chem. Soc.* **1996**, *118* (34), 8034–8042.
- (15) Katz, H. E.; Wilson, W. L.; Scheller, G. Chromophore Structure, Second Harmonic Generation, and Orientational Order in Zirconium Phosphonate/Phosphate Self-Assembled Multilayers. *J. Am. Chem. Soc.* **1994**, *116* (15), 6636–6640.
- (16) Zyss, J.; Nicoud, J. F.; Coquillay, M. Chirality and Hydrogen Bonding in Molecular Crystals for Phase-Matched Second-Harmonic Generation: N-(4-Nitrophenyl)-(L)-Prolinol (NPP). *J. Chem. Phys.* **1984**, *81* (9), 4160.
- (17) Gryl, M.; Krawczuk, A.; Stadnicka, K. Polymorphism of Urea-barbituric Acid Co-Crystals. *Acta Crystallogr. B* **2008**, *64* (5), 623–632.
- (18) Gryl, M.; Koziel, M.; Stadnicka, K.; Matulková, I.; Němec, I.; Tesařová, N.; Němec, P. Lidocaine Barbiturate: A Promising Material for Second Harmonic Generation. *CrystEngComm* **2013**, *15* (17), 3275.
- (19) Gryl, M.; Seidler, T.; Stadnicka, K.; Matulkova, I.; Nemeč, I.; Tesarova, N.; Nemeč, P. The Crystal Structure and Optical Properties of a Pharmaceutical Co-Crystal - the Case of the Melamine-Barbital Addition Compound. *CrystEngComm* **2014**, *16* (26), 5765–5768.
- (20) Evans, O. R.; Xiong, R.; Wang, Z.; Wong, G. K.; Lin, W. Crystal Engineering of Acentric Diamondoid. *Angew. Chem. Int. Edit.* **1999**, *38* (4), 536–538.
- (21) Mendiratta, S.; Lee, C. H.; Lee, S. Y.; Kao, Y. C.; Chang, B. C.; Lo, Y. H.; Lu, K. L. Structural Characteristics and Non-Linear Optical Behaviour of a 2-Hydroxynicotinate-Containing Zinc-Based Metal-Organic Framework. *Molecules* **2015**, *20* (5), 8941–8951.
- (22) Serra-Crespo, P.; van der Veen, M. A.; Gobechiya, E.; Houthoofd, K.; Filinchuk, Y.; Kirschhock, C. E. A.; Martens, J. A.; Sels, B. F.; De Vos, D. E.; Kapteijn, F.; et al. NH<sub>2</sub>-MIL-53(Al): A High-Contrast Reversible Solid-State Nonlinear Optical Switch. *J. Am. Chem. Soc.* **2012**, *134* (20), 8314–8317.
- (23) Jain, P.; Dalal, N. S.; Toby, B. H.; Kroto, H. W.; Cheetham, A. K. Order-Disorder Antiferroelectric Phase Transition in a Hybrid Inorganic-Organic Framework with the Perovskite Architecture. *J. Am. Chem. Soc.* **2008**, *130* (32), 10450–10451.
- (24) Jain, P.; Ramachandran, V.; Clark, R. J.; Zhou, H. D.; Toby, B. H.; Dalal, N. S.; Kroto, H. W.; Cheetham, A. K. Multiferroic Behavior Associated with an Order-Disorder Hydrogen Bonding Transition in Metal-Organic Frameworks (MOFs) with the Perovskite ABX<sub>3</sub> Architecture. *J. Am. Chem. Soc.* **2009**, *131* (38), 13625–13627.
- (25) Zhang, W.; Cai, Y.; Xiong, R. G.; Yoshikawa, H.; Awaga, K. Exceptional Dielectric Phase Transitions in a Perovskite-Type Cage Compound. *Angew. Chem. Int. Edit.* **2010**, *49* (37), 6608–6610.

## 4 Synthese und Charakterisierung neuer und funktionalisierter MOFs basierend auf den Elementen der 13. Gruppe und deren spezielle optische Eigenschaften

- (25) Xu, G.-C.; Ma, X.-M.; Zhang, L.; Wang, Z.-M.; Gao, S. Disorder-Order Ferroelectric Transition in the Metal Formate Framework of  $[\text{NH}_4][\text{Zn}(\text{HCOO})_3]$ . *J. Am. Chem. Soc.* **2010**, *132* (28), 9588–9590.
- (26) Cui, H.; Zhou, B.; Long, L.-S.; Okano, Y.; Kobayashi, H.; Kobayashi, A. A Porous Coordination-Polymer Crystal Containing One-Dimensional Water Chains Exhibits Guest-Induced Lattice Distortion and a Dielectric Anomaly. *Angew. Chem. Int. Edit.* **2008**, *47* (18), 3376–3380.
- (27) Dong, X.-Y.; Li, B.; Ma, B.-B.; Li, S.-J.; Dong, M.-M.; Zhu, Y.-Y.; Zang, S.-Q.; Song, Y.; Hou, H.-W.; Mak, T. C. W. Ferroelectric Switchable Behavior through Fast Reversible De/adsorption of Water Spirals in a Chiral 3D Metal-Organic Framework. *J. Am. Chem. Soc.* **2013**, *135* (28), 10214–10217.
- (28) Markey, K.; Putzeys, T.; Horcajada, P.; Devic, T.; Guillou, N.; Wübberhorst, M.; Cleuvenbergen, S. Van; Verbiest, T.; De Vos, D. E.; van der Veen, M. A. Second Harmonic Generation Microscopy Reveals Hidden Polar Organization in Fluoride Doped MIL-53(Fe). *Dalton T.* **2016**, *45*, 4401–4406.
- (29) Abrahams, S. C.; Robertson, J. M. The Crystal Structure of P-Nitroaniline. *Acta Crystallogr.* **1948**, *1*, 252–259.
- (30) Donohue, J.; Trueblood, K. The Crystal Structure of P-Nitroaniline. *Acta Crystallogr.* **1956**, *9*, 960–965.
- (31) Wübberhorst, M.; Klap, G. J.; Jansen, J. C.; van Bekkum, H.; van Turnhout, J. Glass Transition of One-Dimensional Molecular Chains of P-Nitroaniline Confined in AlPO4-5 Nanopores Revealed by Dielectric Spectroscopy. *J. Chem. Phys.* **1999**, *111* (Ise 10), 5637–5640.
- (32) van der Veen, M. A.; Van Noyen, J.; Sels, B. F.; Jacobs, P. A.; Verbiest, T.; De Vos, D. E. Mapping of the Organization of P-Nitroaniline in SAPO-5 by Second-Harmonic Generation Microscopy. *Phys. Chem. Chem. Phys.* **2010**, *12* (36), 10688.
- (33) van der Veen, M. A.; Sels, B. F.; De Vos, D. E.; Verbiest, T. Localization of P-Nitroaniline Chains Inside Zeolite ZSM-5 with Second-Harmonic Generation Microscopy. *J. Am. Chem. Soc.* **2010**, *132* (19), 6630–6631.
- (34) Marlow, F.; Wübberhorst, M.; Caro, J. Pyroelectric Effects on Molecular Sieve Crystals Loaded with Dipole Molecules. *J. Phys. Chem.-US* **1994**, *98* (47), 12315–12319.
- (35) Klap, G. J.; van Klooster, S. M.; Wübberhorst, M.; Jansen, J. C.; van Bekkum, H.; van Turnhout, J. Polarization Reversal in AlPO4-5 Crystals Containing Polar or Nonpolar Organic Molecules: A Scanning Pyroelectric Microscopy Study. *J. Phys. Chem. B* **1998**, *102* (47), 9518–9524.
- (36) Klap, G. J.; Wübberhorst, M.; Jansen, J. C.; van Koningsveld, H.; van Bekkum, H.; van Turnhout, J. Polar Growth and Directional Adsorption of Large AlPO4-5 Crystals Determined by Scanning Pyroelectric Microscopy. *Chem. Mater.* **1999**, *11* (9), 3497–3503.
- (37) Skibo, E. B.; Gilchrist, J. H. Synthesis and Electrochemistry of Pyrimidoquinazoline-5,10-Diones. Design of Hydrolytically Stable High Potential Quinones and New Reductive Alkylation Systems. *J. Org. Chem.* **1988**, *53* (18), 4209–4218.
- (38) Stock, N. Hochdurchsatzmethoden Zur Entdeckung Und Optimierung Kristalliner Poröser Materialien. *Chem.-Ing.-Tech.* **2010**, *82* (7), 1039–1047.
- (39) Stock, N. High-Throughput Investigations Employing Solvothermal Syntheses. *Micropor. Mesopor. Mat.* **2010**, *129* (3), 287–295.
- (40) Stock, N.; Biswas, S. Synthesis of Metal-Organic Frameworks (MOFs): Routes to Various MOF Topologies, Morphologies, and Composites. *Chem. Rev.* **2012**, *112* (2), 933–969.
- (41) Bauer, S.; Stock, N. Hochdurchsatz-Methoden in Der Festkörperchemie. Schneller Zum Ziel. *Chem. Unserer Zeit* **2007**, *41* (5), 390–398.
- (42) Coelho Software. Topas Academic 4.2. Topas Academic 2007.
- (43) Loiseau, T.; Serre, C.; Huguénard, C.; Fink, G.; Taulelle, F.; Henry, M.; Bataille, T.; Férey, G. A Rationale for the Large Breathing of the Porous Aluminum Terephthalate (MIL-53) Upon Hydration. *Chem.-Eur. J.* **2004**, *10* (6), 1373–1382.
- (44) Accelrys Software Inc. Materials Studio, Version 5.0. Accelrys Software Inc: San Diego, CA, USA 2009.
- (45) Dovesi, R.; Orlando, R.; Erba, A.; Zicovich-Wilson, C. M.; Civalleri, B.; Casassa, S.; Maschio, L.; Ferrabone, M.; De La Pierre, M.; D'Arco, P.; et al. CRYSTAL14: A Program for the Ab Initio Investigation of Crystalline Solids. *Int. J. Quantum Chem.* **2014**, *114* (19), 1287–1317.
- (46) Dovesi, R.; Saunders, V. R.; Roetti, C.; Orlando, R.; Zicovich-Wilson, C. M.; Pascale, F.; Civalleri, B.; Doll, K.; Harrison, N. M.; Bush, I. J.; et al. *CRYSTAL14 User's Manual*; University of Torino: Torino, 2014.
- (47) Seidler, T.; Champagne, B. Which Charge Definition for Describing the Crystal Polarizing Field and the  $\chi^{(1)}$  and  $\chi^{(2)}$  of Organic Crystals? *Phys. Chem. Chem. Phys.* **2015**, *17* (29), 19546–19556.
- (48) Seidler, T.; Champagne, B. Second-Order Nonlinear Optical Susceptibilities of Metal-Organic Frameworks Using a Combined Local Field Theory/Charge Embedding Electrostatic Scheme. *J. Phys. Chem. C* **2016**, *120* (12), 6741–6749.
- (49) Frisch, M. J.; Trucks, G. W.; Schlegel, H. B.; Scuseria, G. E.; Robb, M. A.; Cheeseman, J. R.; Scalmani, G.; Barone, V.; Mennucci, B.; Petersson, G. A.; et al. Gaussian 09, Revision B.01. *Gaussian 09, Revision B.01, Gaussian, Inc., Wallingford CT*. Wallingford CT 2009.
- (50) MUNN, R. W. A General Microscopic Theory of Bulk Second-Harmonic Generation from Molecular Crystals. *Mol. Phys.* **1996**, *89* (2), 555–569.
- (51) Kirtman, B.; Dykstra, C. E.; Champagne, B. Major Intermolecular Effects on Nonlinear Electrical Response in a Hexatriene Model of Solid State Polyacetylene. *Chem. Phys. Lett.* **1999**, *305* (1–2), 132–138.
- (52) Reis, H.; Papadopoulos, M. G.; Calaminici, P.; Jug, K.; Köster, A. M. Calculation of Macroscopic Linear and Nonlinear Optical Susceptibilities for the Naphthalene, Anthracene and Meta-Nitroaniline Crystals. *Chem. Phys.* **2000**, *261* (3), 359–371.
- (53) Seidler, T.; Stadnicka, K.; Champagne, B. Investigation of the Linear and Second-Order Nonlinear Optical Properties of Molecular Crystals within the Local Field Theory. *J. Chem. Phys.* **2013**, *139* (11), 114105.
- (54) Seidler, T.; Stadnicka, K.; Champagne, B. Second-Order Nonlinear Optical Susceptibilities and Refractive Indices of Organic Crystals from a Multiscale Numerical Simulation Approach. *Adv. Opt. Mater.* **2014**, *2* (10), 1000–1006.
- (55) Seidler, T.; Stadnicka, K.; Champagne, B. Evaluation of the Linear and Second-Order NLO Properties of Molecular Crystals within the Local Field Theory: Electron Correlation Effects, Choice of XC Functional, ZPVA Contributions, and Impact of the Geometry in the Case of 2-Methyl-4-Nitroaniline. *J. Chem. Theory Comput.* **2014**, *10* (5), 2114–2124.
- (56) Seidler, T.; Stadnicka, K.; Champagne, B. Linear and Second-Order Nonlinear Optical Properties of Ionic Organic Crystals. *J. Chem. Phys.* **2014**, *141* (10), 104109.
- (57) Wittmann, T.; Siegel, R.; Reimer, N.; Milius, W.; Stock, N.; Senker, J. Enhancing the Water Stability of Al-MIL-101-NH<sub>2</sub> via Postsynthetic Modification. *Chem.-Eur. J.* **2015**, *21* (1), 314–323.
- (58) Ahnfeldt, T.; Gunzelmann, D.; Loiseau, T.; Hirsemann, D.; Senker, J.; Férey, G.; Stock, N. Synthesis and Modification of a Functionalized 3D Open-Framework Structure with MIL-53 Topology. *Inorg. Chem.* **2009**, *48* (7), 3057–3064.
- (59) Sumida, K.; Rogow, D. L.; Mason, J. A.; McDonald, T. M.; Bloch, E. D.; Herm, Z. R.; Bae, T.; Long, J. R. Carbon Dioxide Capture in Metal-Organic Frameworks. *Chem. Rev.* **2012**, *112* (2), 724–781.
- (60) Serra-Crespo, P.; Gobechiya, E.; Ramos-Fernandez, E. V.; Juan-Alcañiz, J.; Martínez-Joaristi, A.; Stavitski, E.; Kirschhock, C. E. a; Martens, J. a; Kapteijn, F.; Gascon, J. Interplay of Metal Node and Amine Functionality in NH<sub>2</sub>-MIL-53: Modulating Breathing Behavior through Intra-Framework Interactions. *Langmuir* **2012**, *28* (35), 12916–12922.
- (61) Boyd, R. W. *Nonlinear Optics*; Elsevier, 2008.
- (62) Le Floch, V.; Brasselet, S.; Roch, J.-F.; Zyss, J. Monitoring of Orientation in Molecular Ensembles by Polarization Sensitive Nonlinear Microscopy. *J. Phys. Chem. B* **2003**, *107* (45), 12403–12410.
- (63) Loiseau, T.; Muguerra, H.; Haouas, M.; Taulelle, F.; Férey, G. Hydrothermal Synthesis and Structural Characterization of a Gallium Pyromellitate Ga(OH)(btcc)-0.5H<sub>2</sub>O, with Infinite Ga-(μ<sub>2</sub>-OH)-Ga Chains (MIL-61). *Solid State Sci.* **2005**, *7* (5), 603–

- 609.
- (64) Gándara, F.; Gomez-Lor, B.; Gutiérrez-Puebla, E.; Iglesias, M.; Monge, M. A.; Proserpio, D. M.; Snejko, N. An Indium Layered MOF as Recyclable Lewis Acid Catalyst. *Chem. Mater* **2008**, *20* (1), 72–76.
  - (65) Van Der Veen, M. A.; Verbiest, T.; De Vos, D. E. Probing Microporous Materials with Second-Harmonic Generation. *Micropor. Mesopor. Mat.* **2013**, *166*, 102–108.
  - (66) Falaise, C.; Volkringer, C.; Facqueur, J.; Bousquet, T.; Gasnot, L.; Loiseau, T. Capture of Iodine in Highly Stable Metal-organic Frameworks: A Systematic Study. *Chem. Commun.* **2013**, *49* (87), 10320.



## 5 Zusammenfassung

Die Ergebnisse dieser Arbeit lassen sich in zwei Themenbereiche unterteilen:

1. Synthese und Charakterisierung neuer und isoretikulärer MOFs
2. Synthese und Charakterisierung neuer funktionalisierter Derivate einer bekannten Gerüststruktur

In dieser Arbeit wurden 18 neue und funktionalisierter Verbindungen basierend auf verschiedenen Linkermolekülen mittels Hochdurchsatzmethoden hergestellt und deren Synthesen optimiert (Abbildung 5.1). Unter Verwendung von gewinkelten Linkern konnte eine neue Gerüststruktur, CAU-21, erhalten werden. Isoretikuläre Verbindungen zu CAU-8 und CAU-21 wurden unter Einsatz eines anderen gewinkelten Linkermoleküls ähnlicher Geometrie hergestellt. Die Synthese von vier zu MIL-118B [ $\text{Al}_2(\text{OH})_2(\text{BTEC})$ ] ( $\text{BTEC}^{4-} = 1,2,4,5\text{-Benzoltetracarboxylat}$ ) isoretikulären Verbindungen (X-CAU-9) gelang unter Verwendung einer verlängerten Tetracarbonsäure und verschiedenen dreiwertigen Kationen.

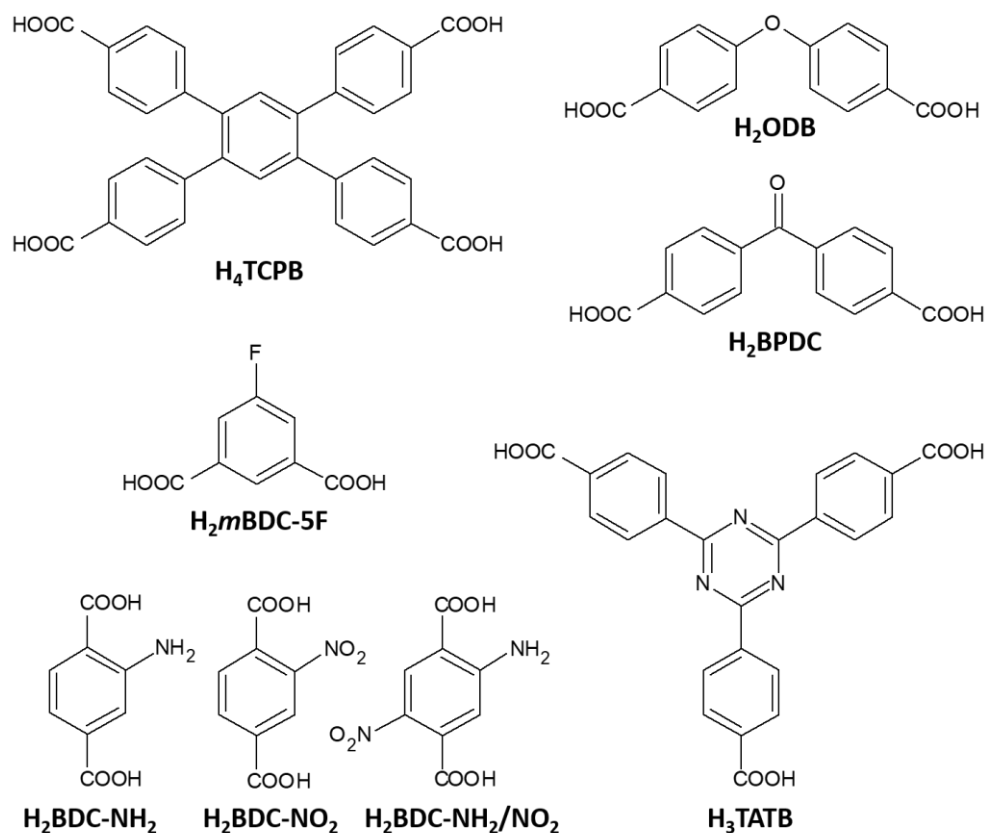


**Abb. 5.1** Übersicht über die in dieser Arbeit verwendeten Linkermoleküle.

Durch die Vergrößerung des Linkers konnte eine isoretikuläre CAU-10-Verbindung (CAU-10-HTATB) erhalten werden. Zusätzlich konnten, ausgehend von Mischungen unterschiedlich funktionalisierter Linkermoleküle, drei fluorierte isoretikuläre CAU-10-Verbindungen hergestellt werden. Außerdem konnten funktionalisierte In-MOFs hergestellt werden, deren Gerüststruktur die Quarz-Topologie besitzen. Durch den Einsatz eines bifunktionalisierten Linkermoleküls konnten drei verschiedene MIL-53-Derivate basierend auf dreiwertigen Kationen hergestellt werden und außerdem wurde ein bifunktionalisierter In-MOF erhalten. Eine Übersicht über in dieser Arbeit untersuchten Verbindungen ist in Tabelle 5.1 gezeigt.

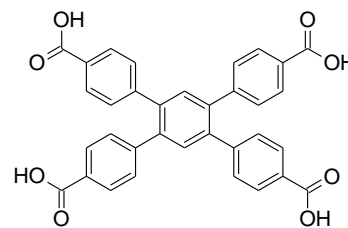
**Tab. 5.1** Übersicht über die in dieser Arbeit hergestellten Verbindungen.

Name	Zusammensetzung des Gerüsts	$a_{s,BET} / \text{m}^2/\text{g}$	$V_{mic,BET} / \text{cm}^3/\text{g}$	thermische Stabilität / °C
Al-CAU-9	[Al <sub>2</sub> (OH) <sub>2</sub> (TCPB)]	1118	0.45	480
Ga-CAU-9	[Ga <sub>2</sub> (OH) <sub>2</sub> (TCPB)]	568	0.28	320
In-CAU-9	[In <sub>2</sub> (OH) <sub>2</sub> (TCPB)]	487	0.21	320
Cr-CAU-9	[Cr <sub>2</sub> (OH) <sub>2</sub> (TCPB)]	510	0.22	300
CAU-21-BPDC	[Al(OH)(BPDC)]	n.p.	n.p.	300
CAU-21-ODB	[Al(OH)(ODB)]	n.p.	n.p.	300
CAU-8-ODB	[Al(OH)(ODB)]	1004	0.47	370
CAU-10-H/F <sub>11</sub>	[Al(OH)( <i>m</i> BDC) <sub>0.89</sub> ( <i>m</i> BDC-5F) <sub>0.11</sub> ]	515	0.22	N/A
CAU-10-H/F <sub>28</sub>	[Al(OH)( <i>m</i> BDC) <sub>0.72</sub> ( <i>m</i> BDC-5F) <sub>0.28</sub> ]	466	0.22	N/A
CAU-10-H/F <sub>44</sub>	[Al(OH)( <i>m</i> BDC) <sub>0.56</sub> ( <i>m</i> BDC-5F) <sub>0.44</sub> ]	453	0.20	N/A
CAU-10-HTATB	[Al(OH)(HTATB)]	231	0.10	400
In-BDC-NH <sub>2</sub>	[In(BDC-NH <sub>3</sub> )(BDC-NH <sub>2</sub> )]	n.a.	n.a.	200
In-BDC-H/NH <sub>2</sub>	H[In(BDC) <sub>0.57</sub> (BDC-NH <sub>2</sub> ) <sub>0.43</sub> ]	n.a.	n.a.	N/A
In-BDC-NH <sub>2</sub> /NO <sub>2</sub>	(DMA) <sub>2</sub> [In <sub>3</sub> (O)(BDC-NH <sub>2</sub> /NO <sub>2</sub> ) <sub>4.5</sub> ]	n.a.	n.a.	100
MIL-53(Al)-NH <sub>2</sub> /NO <sub>2</sub> (DMF)	[Al(OH)(BDC-NH <sub>2</sub> /NO <sub>2</sub> )]	287	0.11	300
MIL-53(Al)-NH <sub>2</sub> /NO <sub>2</sub> (EtOH)	[Al(OH)(BDC-NH <sub>2</sub> /NO <sub>2</sub> )]	n.p.	n.p.	300
MIL-53(Ga)-NH <sub>2</sub> /NO <sub>2</sub>	[Ga(OH)(BDC-NH <sub>2</sub> /NO <sub>2</sub> )]	n.p.	n.p.	300
MIL-53(In)-NH <sub>2</sub> /NO <sub>2</sub>	[In(OH)(BDC-NH <sub>2</sub> /NO <sub>2</sub> )]	n.p.	n.p.	300

n.p. = nicht porös    n.a. = nicht aktivierbar    N/A = nicht gemessen

## 5.1 Synthese und Charakterisierung neuer und isoretikulärer MOFs

Unter Verwendung der Tetracarbonsäure 1,2,4,5-tetrakis-(4-carboxyphenyl)-benzol ( $H_4TCPB$ ) konnte CAU-9, eine zu MIL-118  $[Al_2(OH)_2(BTEC)]$  ( $BTEC^{4-} = 1,2,4,5$ -Benzoltetracarboxylat) isoretikuläre Verbindung mit verlängertem Linker hergestellt und charakterisiert werden. Dabei konnte keine Phasentransformation bei der Aktivierung, wie sie beim MIL-118 beobachtet werden kann, in der neuen Verbindung festgestellt werden. Außerdem wurden die Sorptionseigenschaften von CAU-9 untersucht. Weiterhin stand die Synthese der Verbindung mit anderen dreiwertigen Kationen wie  $Ga^{3+}$ ,  $In^{3+}$  und  $Cr^{3+}$  im Fokus. Hier wurde der Einfluss des Austauschs der zur Synthese verwendeten Kationen auf die Sorptionseigenschaften und die thermische Stabilität untersucht und im Falle von  $Cr^{3+}$  eine postsynthetische Modifizierung durchgeführt. Ein Überblick über die kristallographischen Daten ist in Tabelle 5.1.1 gegeben. Nur die Struktur von Al-CAU-9 konnte erfolgreich mittels der Rietveld-Methode verfeinert werden. Für die anderen Verbindungen wurden die Zellparameter durch Pawley-Fit der Röntgenpulverdiffraktogramme erhalten.



**Tab. 5.1.1** Kristallographische Daten und verfeinerte Zellparameter der verschiedenen CAU-9-Derivate.

Verbindung	Al-CAU-9	Ga-CAU-9	In-CAU-9	Cr-CAU-9
Summenformel	$Al_2C_{34}H_{20}O_{10}$	$Ga_2C_{34}H_{20}O_{10}$	$In_2C_{34}H_{20}O_{10}$	$Cr_2C_{34}H_{20}O_{10}$
Kristallsystem	orthorhombisch	orthorhombisch	monoklin	orthorhombisch
Raumgruppe	<i>Cmmm</i>	<i>Cmmm</i>	<i>P2/m</i>	<i>Cmmm</i>
$a / \text{Å}$	31.562(4)	21.861(2)	11.637(1)	21.654(6)
$b / \text{Å}$	6.642(7)	6.714(3)	15.725(2)	6.829(3)
$c / \text{Å}$	10.6612(7)	15.844(2)	7.204(1)	15.844(6)
$\alpha / ^\circ$	90	90	90	90
$\beta / ^\circ$	90	90	80.97(2)°	90
$\gamma / ^\circ$	90	90	90	90
Methode der Strukturlösung	Strukturmodell			
Methode der Verfeinerung	Rietveld	Pawley	Pawley	Pawley
$R_{\text{Bragg}} / \%$	0.68			
GoF	1.54	1.39	2.19	1.13
$r_{\text{wp}} / \%$	5.28	4.04	6.94	3.37



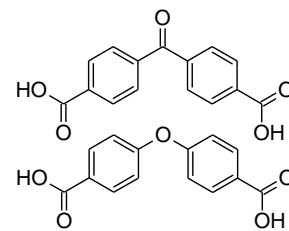
1. Die systematische Untersuchung des Systems  $M^{3+}/H_4TCPB/H_2O/DMF/Additiv$  ( $M = Al, Ga, In, Cr$ ) unter solvothermalen Bedingungen mittels Hochdurchsatzsynthese führte zur Entdeckung einer neuen Verbindung, die CAU-9 genannt wurde. Nach Aufreinigung der Syntheseprodukte mit DMF konnten die Zusammensetzungen der Derivate aus einer Kombination aus Elementaranalyse und thermogravimetrischen Messungen bestimmt werden (Tabelle 5.1.2).

**Tab. 5.1.2** Zusammensetzungen verschiedenen CAU-9-Derivate.

Name	Zusammensetzung des Derivats
Al-CAU-9	$[Al_2(OH)_2(TCPB)] \cdot 2DMF$
Ga-CAU-9	$[Ga_2(OH)_2(TCPB)] \cdot 1.2H_2O \cdot 2.63DMF$
In-CAU-9	$[In_2(OH)_2(TCPB)] \cdot 2DMF$
Cr-CAU-9	$[Cr_2(OH)_2(TCPB)] \cdot 1.4H_2O \cdot 1.9DMF \cdot 2.9Cr_2O_3$

2. Die Struktur von Al-CAU-9 wurde bestimmt, indem auf Basis der Struktur von  $[Al_2(OH)_2(TCPP)]$  (Al-PMOF,  $TCPP^{4-} = \text{meso-tetra(4-carboxylato-phenyl)porphyrin}$ )<sup>[92]</sup> ein Strukturmodell erstellt wurde, welches mit Hilfe der Rietveld-Methode verfeinert werden konnte. Die Kristallstruktur enthält Ketten *trans*-eckenverknüpfter  $AlO_6$ -Oktaeder, die durch die Carboxylatgruppen der  $TCPB^{4-}$ -Ionen miteinander verknüpft werden. Das Netzwerk wird durch die Verbrückung von jeweils vier der IBUs durch ein Linkermolekül aufgebaut und besitzt zwei Arten rautenförmiger Kanälen mit jeweils  $5 \times 9 \text{ \AA}$  und  $10.4 \times 5 \text{ \AA}$  Durchmesser.
3. Die  $N_2$ -Sorptionsmessungen der CAU-9-Derivate bei 77 K ergaben jeweils eine Typ I Sorptionsisotherme, jedoch sind die adsorbierten Mengen an  $N_2$  sehr unterschiedlich. Al-CAU-9 nimmt ebenfalls  $H_2O$ -Dampf auf, jedoch zeigt die Isotherme den charakteristischen Verlauf eines hydrophoben Materials. Auch die thermischen Stabilitäten der Verbindungen sind unterschiedlich. Sie sind zusammen mit den Sorptionseigenschaften in Tabelle 5.1 zusammengefasst.
4. Eine postsynthetische Modifizierung in Form einer Nitrierung wurde an Cr-CAU-9 durchgeführt. Wie Röntgenpulvermessungen bestätigen verliert das Reaktionsprodukt an Kristallinität im Vergleich zum Edukt, jedoch bleibt das MOF-Gerüst intakt.  $^1H$ -NMR-spektroskopische Untersuchungen konnten keine eindeutige Nitrierung des zentralen aromatischen Ringes des  $TCPB^{4-}$  nachweisen, auch eine Oxidation zum Benzochinon ist möglich.

Unter Verwendung des gewinkelten Linkermoleküls 4,4'-Benzophenondicarbonsäure (H<sub>2</sub>BPDC) konnte der Al-MOF CAU-21-BPDC synthetisiert und charakterisiert werden. Diese Verbindung wurde im gleichen chemischen System wie CAU-8-BPDC entdeckt,



konnte aber bis dato nicht phasenrein hergestellt und charakterisiert werden. Mit dem geometrisch ähnlichen Linkermolekül 4,4'-Oxidibenzoessäure (H<sub>2</sub>ODB) konnten CAU-8-ODB und CAU-21-BPDC hergestellt werden, die isoretikulär zu ihren BPDC-Derivaten sind. Die jeweiligen Netzwerke mit gleichem Linkermolekül sind polymorph. Im Fokus der Untersuchungen stand außerdem der Vergleich der vier Verbindungen hinsichtlich Sorptionseigenschaften und der thermischen Stabilität. Ein Überblick über die kristallographischen Daten ist in Tabelle 5.1.3 gegeben.

**Tab. 5.1.3** Kristallographische Daten der verschiedenen CAU-8- und CAU-21-Derivate.

Verbindung	CAU-8-BPDC	CAU-8-ODB	CAU-21-BPDC	CAU-21-ODB	
Summenformel	AlC <sub>15</sub> H <sub>8</sub> O <sub>6</sub>	AlC <sub>14</sub> H <sub>8</sub> O <sub>6</sub>	AlC <sub>15</sub> H <sub>8</sub> O <sub>6</sub>	AlC <sub>14</sub> H <sub>8</sub> O <sub>6</sub>	
Z	16	16	16	16	
Kristallsystem	tetragonal	tetragonal	tetragonal	tetragonal	tetragonal
<i>a</i> / Å	12.984(2)	13.1035(7)	17.2528(7)	16.6220	16.583(6)
<i>b</i> / Å	12.984(2)	13.1035(7)	17.2528(7)	16.6220	16.583(6)
<i>c</i> / Å	52.301(10)	51.757(4)	23.8643(1)	23.5280	23.52(1)
<i>V</i> / Å <sup>3</sup>	8818(3)	8886(1)	7103(7)	6500.57	6467(6)
Raumgruppe	<i>I</i> 4 <sub>1</sub> / <i>a</i>	<i>I</i> 4 <sub>1</sub> / <i>a</i>	<i>I</i> 422	<i>I</i> 422	
Methode der Strukturlösung	Direkte Methoden	Strukturmodell	Direkte Methoden	DFT-Berechnungen	
Methode der Verfeinerung	SHELXS	Rietveld	SHELXS	DFT-Berechnungen	Pawley
Range / °2θ	1.6 - 25.0	4 - 70	2.4 - 26.4	2 - 90	
R <sub>wp</sub> / %		5.81		4.49	
R <sub>Bragg</sub> / %		1.19			
GOF	0.899	2.46	1.015	1.99	
tot., uneq., Reflexe, R <sub>int</sub>	30871, 3851, 0.123		24969, 3655, 0.118		
beobachtete Reflexe [I > 2σ(I)]	1916		2338		
R <sub>1</sub> , wR <sub>2</sub>	0.089, 0.242		0.079, 0.183		
Δe (e/Å <sup>3</sup> )	-0.31, 0.59		-0.30, 0.39		

Die Kristallstrukturen von CAU-21-BPDC und CAU-8-BPDC konnten aus Einkristallröntgenbeugungsdaten ermittelt werden. Für die Strukturen von CAU-8-ODB und CAU-21-ODB wurden Strukturmodelle aufgestellt, von denen ersteres durch Rietveld-Methoden verfeinert werden konnte. Die Struktur von CAU-21-ODB wurde durch DFT-Rechnung ermittelt.

1. Durch systematische Untersuchung des Systems  $\text{Al}^{3+}/\text{H}_2\text{BPDC}/\text{H}_2\text{O}/\text{DMF}/\text{Benzoessäure}$  unter solvothermalen Bedingungen mittels Hochdurchsatzmethoden konnte der neue Al-MOF CAU-21-BPDC phasenrein erhalten werden. Weitere Untersuchungen mit 4,4'-Oxidbenzoessäure ( $\text{H}_2\text{ODB}$ ) führten zur Herstellung von Verbindungen mit CAU-8 und CAU-21-Struktur (CAU-8-ODB bzw. CAU-21-ODB). Die Zusammensetzungen der Produkte konnten aus einer Kombination aus  $^1\text{H-NMR}$ -Spektroskopie, Elementaranalyse und thermogravimetrischen Messungen bestimmt werden (Tabelle 5.1.4). Die als Additiv für die Synthese verwendete Benzoessäure ist teilweise in das Gerüst von CAU-21-BPDC eingebaut.

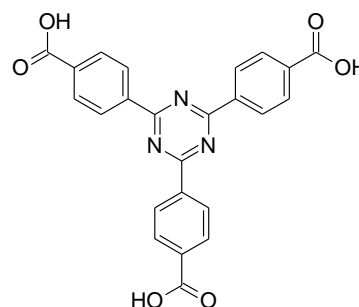
**Tab. 5.1.4** Zusammensetzungen verschiedenen CAU-21- und CAU-8-Derivate.

Name	Zusammensetzung des Derivats
CAU-21-BPDC	$[\text{Al}(\text{OH})(\text{BPDC})_{0.93}(\text{BA})_{0.14}]\cdot 0.7\text{H}_2\text{O}$
CAU-21-ODB	$[\text{Al}(\text{OH})(\text{ODB})]\cdot 0.9\text{H}_2\text{O}$
CAU-8-ODB	$[\text{Al}(\text{OH})(\text{ODB})]\cdot 0.4\text{H}_2\text{O}$

2. In situ Röntgenbeugungsuntersuchungen am DORIS Speicherring, Beamline F3 am DESY Hamburg haben gezeigt, dass die beiden Polymorphe CAU-8 und CAU-21 sich nicht ineinander umwandeln, sondern beide unabhängig voneinander vorliegen. Außerdem tritt bei der Bildung ein Intermediat auf, welches zwar durch Reaktionsabbruchversuche isoliert, dessen Kristallstruktur jedoch nicht bestimmt werden konnte.
3. Die Struktur von CAU-21 wurde mit Hilfe von Einkristallbeugungsdaten bestimmt. Sie basiert auf oktanuclearen Ringen *cis*-eckenverknüpfter  $\text{AlO}_6$ -Oktaeder, die die anorganischen Baueinheit formen. Die IBU ist kubisch innen zentriert gepackt und je zwei IBUs sind durch zwei Linkerionen miteinander verbrückt sind. So entstehen eindimensionale, zugängliche Poren, die einen variablen Durchmesser von 3.6 – 6.5 Å aufweisen. Zusätzlich werden nicht zugängliche Poren durch die Verknüpfung der IBUs mit den  $\text{BPDC}^{2-}$ -Ionen ausgebildet.

4. Die CAU-21-Derivate sind unporös gegenüber  $N_2$ , jedoch kann  $CO_2$  adsorbiert werden. Dabei werden von CAU-21-BPDC 50 mg/g und vom CAU-21-ODB 70 mg/g aufgenommen. Die  $N_2$  Sorptionsisothermen des CAU-8-Derivates weisen einen Typ Ia Verlauf auf. Die thermischen Stabilitäten der Verbindungen sind zusammen mit den Sorptionseigenschaften in Tabelle 5.1 zusammengefasst.

Durch den Einsatz der Tricarbonsäure 4,4',4''-s-Triazin-2,4,6-triyl-tribenzoesäure ( $H_3TATB$ ) konnte ein CAU-10-Derivat hergestellt und charakterisiert werden. Dabei wird das MOF-Gerüst nur durch die Verknüpfung von zwei Carboxylatgruppen mit der anorganischen Baueinheit aufgebaut, die dritte liegt ungebunden in der Struktur vor. Die kristallographischen Parameter sind in Tabelle 5.1.5 zusammengefasst. Obwohl thermogravimetrische Messungen eine Stabilität von ca. 400 °C gezeigt haben, war eine vollständige Aktivierung der Probe unter reduzierten Druck nicht möglich. Temperaturabhängige röntgenpulverdiffraktometrische Messungen deuten auf eine strukturelle Veränderung der Verbindung bei steigender Temperatur hin. Deswegen wird in  $N_2$ -Sorptionsmessungen eine geringe Aufnahme festgestellt (Tabelle 5.1)



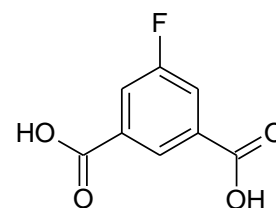
**Tab. 5.1.5** Kristallographische Daten von CAU-10-HTATB.

Verbindung	CAU-10-HTATB
Summenformel	$AlC_{24}H_{15}O_7N_3$
Kristallsystem	tetragonal
Raumgruppe	$I4_1/a$
$a / \text{Å}$	36.438(1)
$b / \text{Å}$	36.438(1)
$c / \text{Å}$	10.9373(9)
$\alpha / ^\circ$	90
$\beta / ^\circ$	90
$\gamma / ^\circ$	90
Methode der Strukturlösung	Strukturmodell
Methode der Verfeinerung	Rietveld
$R_{\text{Bragg}} / \%$	3.67
GoF	1.78
$r_{\text{wp}} / \%$	7.56

## 5.2 Synthese und Charakterisierung neuer funktionalisierter Derivate einer bekannten Gerüststruktur

In dieser Arbeit wurden insgesamt elf funktionalisierte Derivate bekannter Verbindungen hergestellt. Der Hauptteil bezieht sich dabei auf Verbindungen mit CAU-10- und MIL-53-Struktur. Hierfür wurden sowohl die isoretikuläre Synthese ausgenutzt (MIL-53), als auch Mischungen unterschiedlich funktionalisierter Linkermoleküle verwendet (CAU-10).

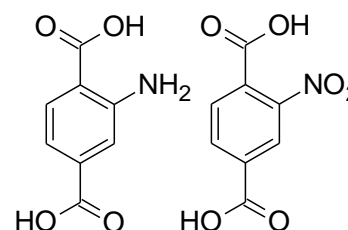
1. Bei der systematischen Untersuchung des Systems  $\text{Al}^{3+}/5$ -Fluorisophthalsäure ( $\text{H}_2\text{mBDC-5F}$ )/Isophthalsäure ( $\text{H}_2\text{mBDC}$ )/DMF/ $\text{H}_2\text{O}$  als Gemischtlinker-Ansatz konnten drei CAU-10-Derivate, CAU-10-H/ $\text{F}_x$  ( $x = 11, 28, 44\%$ ), mit unterschiedlichen Fluorgehalt erhalten werden. Das Strukturmodell von CAU-10-H/ $\text{F}_{28}$ , basierend auf CAU-10-Br, konnte erfolgreich mittels Rietveld-Methode verfeinert werden. Umfangreiche Sorptionsuntersuchungen zeigen eine starke Abhängigkeit der Gesamtkapazität und der Hydrophobizität vom Fluorgehalt. Die Ergebnisse der Sorptionsuntersuchungen sind in Tabelle 5.2.1 zusammengefasst. Bei zusätzlich durchgeführten SHG-Messungen konnte keine Aktivität festgestellt werden.



**Tab. 5.2.1** Zusammenfassung der Sorptionsmessdaten von CAU-10-H/ $\text{F}_x$  ( $x = 11, 28, 44\%$ ).

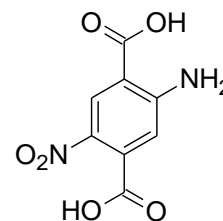
CAU-10-H/ $\text{F}_x$	$\text{N}_2$ (77 K) $a_{s,\text{BET}}$ / $\text{m}^2/\text{g}$	$\text{N}_2$ (77 K) $V_{\text{MIC}}$ / $\text{cm}^3/\text{g}$	$\text{H}_2$ (77 K) / wt%	$\text{H}_2\text{O}$ (298 K) / $\text{cm}^3/\text{g}$
$x = 11$	515	0.22	1.21	359
$x = 28$	466	0.22	1.01	351
$x = 44$	453	0.20	0.83	320

2. Unter Verwendung von 2-Aminoterephthalsäure ( $\text{H}_2\text{BDC-NH}_2$ ) und 2-Nitroterephthalsäure ( $\text{H}_2\text{BDC-NO}_2$ ) konnten zwei In-MOFs (In-BDC- $\text{NH}_2$  und In-BDC-H/ $\text{NH}_2$ ) mit Quarz-Topologie hergestellt werden. Die Struktur von In-BDC- $\text{NH}_2$ ,  $[\text{In}(\text{BDC-NH}_3)(\text{BDC-NH}_2)]$ , konnte aus Einkristallbeugungsdaten ermittelt werden. Diese enthält zwei interpenetrierende Netze aus  $\text{InO}_8$ -Polyedern, verbunden durch BDC- $\text{NH}_2^{2-}$ -Ionen. Die Interpenetration reduziert den Porendurchmesser auf 4.4 Å. Außerdem ist der MOF bis zu einer Temperatur von 300°C in Luft stabil. Die



kristallographischen Daten sind in Tabelle 5.2.2 zusammengefasst. Beim Einsatz von  $\text{H}_2\text{BDC-NO}_2$  findet eine in situ Reduktion der Carbonsäure zum unfunktionalisierten und aminofunktionalisierten Derivat statt. Es entsteht ein Gemischt-Linker-MOF (In-BDC-H/ $\text{NH}_2$ ) der Zusammensetzung  $\text{H}[\text{In}(\text{BDC})_{0.57}(\text{BDC-NH}_2)_{0.43}]$ , der eine zu In-BDC- $\text{NH}_2$  isoretikuläre Struktur aufweist.

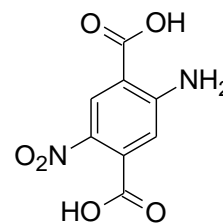
3. Bei der Verwendung der bifunktionalisierten 2-Amino-5-nitroterephthalsäure ( $\text{H}_2\text{BDC-NH}_2/\text{NO}_2$ ) konnte ein kubischer In-MOF (In-BDC- $\text{NH}_2/\text{NO}_2$ ) erhalten werden, dessen Kristallmorphologie durch die Einstellung des DMF/EtOH-Verhältnisses während der Synthese von kubisch zu gekappten Oktaedern variiert werden konnte. Dieser hat die Zusammensetzung  $(\text{DMA})_2[\text{In}_3(\text{O})(\text{BDC-NH}_2/\text{NO}_2)_{4.5}] \cdot \text{DMF}$ . In-BDC- $\text{NH}_2/\text{NO}_2$  ist aufgebaut aus trinuclearen  $\{\text{In}_3(\mu_3\text{-O})\}$ -Clustern, die durch die Linker zu Supertetraedern verknüpft werden. Vier flächenverknüpfte Supertetraeder bilden einen Ultratetraeder, die das finale Netzwerk ausbilden. Die kristallographischen Daten sind in Tabelle 5.2.2 dargestellt.



**Tab. 5.2.2** Kristallographische Daten von In-BDC- $\text{NH}_2$  und In-BDC- $\text{NH}_2/\text{NO}_2$ .

Verbindung	In-BDC- $\text{NH}_2$	In-BDC- $\text{NH}_2/\text{NO}_2$
Summenformel	$\text{In}_3\text{C}_{48}\text{H}_{33}\text{O}_{24}\text{N}_6$	$\text{In}_3\text{C}_{36}\text{H}_{12}\text{O}_{28}\text{N}_9$
Z	4	8
Kristallsystem	hexagonal	kubisch
$a / \text{Å}$	14.7381(5)	24.8947(1)
$b / \text{Å}$	14.7381(5)	24.8947(1)
$c / \text{Å}$	12.2572(4)	24.8947(1)
$V / \text{Å}^3$	2305.70(14)	15428.39(19)
Raumgruppe	$P6_222$	$I-43m$
Methode der Strukturlösung	Direkte Methoden	Direkte Methoden
Methode der Verfeinerung	SHELXS	SHELXS
Range / $^\circ 2\theta$	1.6 – 28.1	1.9 – 25.5
Wellenlänge	$\text{MoK}\alpha$	0.6889
GOF	0.966	1.104
tot., uneq, Reflexe , $R_{\text{int}}$	1868, 1868, 0.061	63530, 2904, 0.070
beobachtete Reflexe [ $I > 2\sigma(I)$ ]	1567	2843
$R_1, wR_2$	0.028, 0.068	0.034, 0.098
$\Delta e$ min/max ( $e/\text{Å}^3$ )	-0.62, 0.33	-0.44, 0.84

4. Ebenfalls unter Verwendung von H<sub>2</sub>BDC-NH<sub>2</sub>/NO<sub>2</sub> konnten vier neue MIL-53-Derivate mit Al<sup>3+</sup>-, In<sup>3+</sup>- und Ga<sup>3+</sup>-Ionen erhalten werden. Die Synthesen von MIL-53(Al)-NH<sub>2</sub>/NO<sub>2</sub> gelangen sowohl im Lösungsmittelgemisch DMF/H<sub>2</sub>O (Namenszusatz DMF), als auch im Gemisch EtOH/H<sub>2</sub>O (Namenszusatz EtOH). Im letzteren Fall konnten die Kristallitgrößen gesteigert werden, jedoch wurde eine Ethylierung von 15% der NH<sub>2</sub>-Gruppen nachgewiesen. Bis auf MIL-53(Al)-NH<sub>2</sub>/NO<sub>2</sub>(DMF) waren alle Verbindungen unporös gegenüber Stickstoff. Diese zeigt eine Abnahme der Sorptionskapazitäten bei wiederholten Messungen der gleichen Probe, da sich die Struktur durch den thermischen Aktivierungsprozess in die *vnp*-Form umwandelt. Außerdem wurden für MIL-53(Al)-NH<sub>2</sub>/NO<sub>2</sub>(DMF) H<sub>2</sub>O Sorptionsmessungen durchgeführt (12 wt-% Aufnahme), die einen stark hydrophilen Charakter der Verbindung zeigen. Außerdem können ca. 90 mg/g CO<sub>2</sub> aufgenommen werden. Die thermischen Stabilitäten der MIL-53-Derivate sind in Tabelle 5.1 dargestellt. Die Strukturen von MIL-53(Al)-NH<sub>2</sub>/NO<sub>2</sub>(DMF) und MIL-53(Ga)-NH<sub>2</sub>/NO<sub>2</sub> konnten erfolgreich mittels Rietveld-Methode verfeinert werden. Die Zellparameter der anderen Verbindungen wurden durch Indizierung der Röntgenpulverdiffraktogramme erhalten und mittels Pawley-Methoden verfeinert. Die kristallographischen Daten der MIL-53-Verbindungen, die über isoretikuläre Synthese erhalten wurden, sind in Tabelle 5.2.3 dargestellt.



**Tab. 5.2.3** Kristallographische Daten der verschiedenen MIL-53-Derivate.

Verbindung	MIL-53(Al)-NH <sub>2</sub> /NO <sub>2</sub> (DMF)	MIL-53(Al)-NH <sub>2</sub> /NO <sub>2</sub> (EtOH)	MIL-53(Ga)-NH <sub>2</sub> /NO <sub>2</sub>	MIL-53(In)-NH <sub>2</sub> /NO <sub>2</sub>
Summenformel	AlC <sub>8</sub> H <sub>5</sub> O <sub>7</sub> N <sub>2</sub>	AlC <sub>8</sub> H <sub>5</sub> O <sub>7</sub> N <sub>2</sub>	GaC <sub>8</sub> H <sub>5</sub> O <sub>7</sub> N <sub>2</sub>	InC <sub>8</sub> H <sub>5</sub> O <sub>7</sub> N <sub>2</sub>
Kristallsystem	monoklin	monoklin	monoklin	orthorhombisch
Spacegroup	<i>Cc</i>	<i>Cc</i>	<i>Cc</i>	<i>Imam</i>
<i>a</i> / Å	17.5669(8)	17.565(5)	17.460(1)	16.870(8)
<i>b</i> / Å	13.3691(7)	13.469(3)	14.1006(7)	13.948(7)
<i>c</i> / Å	6.6105(2)	6.616(2)	6.7350(2)	7.235(4)
$\beta$ / °	112.125(3)	112.273(8)	112.712(6)	90
Methode der Strukturlösung	Strukturmodell		Strukturmodell	
Methode der Verfeinerung	Rietveld	Pawley	Rietveld	Pawley
R <sub>Bragg</sub> / %	1.56	-	2.81	-
GoF	2.11	1.74	2.00	1.54
r <sub>wp</sub> / %	5.57	3.79	7.41	4.20
	(DMF) = Synthese im DMF/H <sub>2</sub> O-Gemisch		(EtOH) = Synthese im EtOH/H <sub>2</sub> O-Gemisch	

Durch eine teilweise Ausordnung der Linkermoleküle in den Strukturen der Al- und Ga-Verbindungen liegt keine Zentrosymmetrie vor. Dies war Ziel der Synthese dieser Verbindungen und ermöglicht die Untersuchung der SHG-Aktivität der Materialien.



## 6 Ausblick

In der Arbeit wurde gezeigt, dass durch Anwendung des Isoretikularitätsprinzips in der MOF-Synthese neue poröse Verbindungen mit veränderten Poreneigenschaften erhalten werden konnten. Die Möglichkeit der postsynthetischen Modifizierung von Cr-CAU-9 eröffnet ein breites Feld an Untersuchungen bezüglich dieser Verbindung. Falls eine Nitrofunktionalität in der Gerüststruktur erhalten werden konnte, könnte als nächster Schritt die Reduzierung zur Aminofunktion durchgeführt werden. Diese funktionelle Gruppe ermöglicht mit Hilfe der Carbonylchemie die weitere Modifizierung der Poreneigenschaften. Auch eine Einführung von Anwendung in der Protonenleitung ist durch Einführung von sauren funktionellen Gruppen denkbar. Allerdings ist der Platz in der Pore begrenzt, sodass sorgsam ausgewählt werden muss, welche postsynthetischen Modifizierungsreaktionen möglich sind.

Dazu ist es allerdings notwendig, das Cr-CAU-9 phasenrein herzustellen und dessen Struktur zu bestimmen. Die Strukturbestimmung muss auch bei den Ga- und In-Derivaten durchgeführt werden. Ansätze wurden hier bereits durchgeführt, allerdings sind noch keine finalen Verfeinerungen verfügbar.

Auch durch Austausch des Linkers in der CAU-8- und CAU-21-Struktur können die Poreneigenschaften weiter modifiziert werden. Vorversuche wurden schon mit 2,2-Bis(4-carboxyphenyl)hexafluoropropan ( $H_2BCHF$ ) durchgeführt. Dabei konnte aber keine zu CAU-8 oder CAU-21 isoretikuläre Verbindung hergestellt werden. Mit der gewinkelten Carbonsäure 4,4'-Sulfonyldibenzoessäure ( $H_2SDBA$ ) konnte schon eine Verbindung erhalten werden (CAU-11)<sup>[94]</sup>, jedoch könnte eine Anpassung der Syntheseparameter zu einer Verbindung mit CAU-8- oder CAU-21-Struktur führen. Bei der Verwendung von  $H_2BCHF$ , 4,4'-Methyldibenzoessäure ( $H_2MDBA$ ) und 4,4'-Iminodibenzoessäure ( $H_2IDBA$ ) sollte beachtet werden, dass deren Struktur keine planare, sondern eine tetraedrische Geometrie aufweist, die auch zu anderen Gerüststrukturen führen kann (Abbildung 6.1). Zumindest für die CAU-8-Struktur sollte der Austausch der  $Al^{3+}$ -Ionen durch  $Ga^{3+}$ - oder  $In^{3+}$ -Ionen in der Synthese möglich sein, da diese ebenfalls die gleichen kettenförmigen eindimensionalen Baueinheiten bilden.

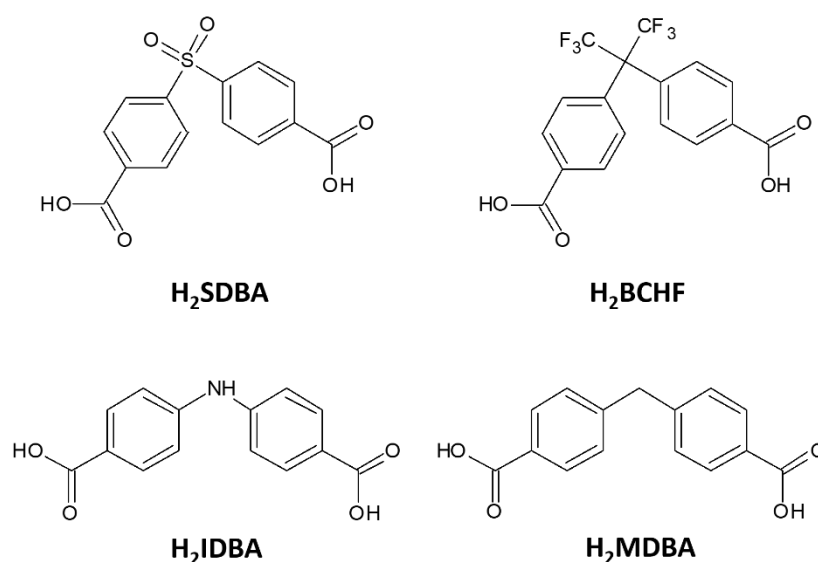


**Abb. 6.1** Potentielle gewinkelte Linkermoleküle für die Synthese von Verbindungen mit CAU-8- und CAU-21-Struktur.

Mit den gezeigten Linkermolekülen könnte es auch möglich sein, ein CAU-10-Derivat mit erweiterten Porenradien herzustellen, wie es in dieser Arbeit mit dem Linker H<sub>3</sub>TATB gezeigt wurde. Hier ist dann eine weitere Modifizierung der Sorptionseigenschaften möglich.

Für die Synthese azentrischer, polarer Metall-Organischer Gerüstverbindungen sollte der Ansatz der gezielten Bildung von Verbindungen mit Quarz-Topologie weiterverfolgt werden. Durch vergrößerte und chirale Linkermoleküle konnte bereits gezeigt werden, dass die SHG-Aktivität gesteigert werden konnte.<sup>[73-75]</sup> Dafür ist es auch vorteilhaft gezielt mehrfach interpenetrierende Netzwerke auszubilden. Durch Synthesen unter Zusatz von HF<sup>[61]</sup> oder durch Einlagerung chiraler Moleküle oder in die Poren der hergestellten MOFs mit Quarz-Topologie oder MIL-53-Struktur könnte ebenfalls die SHG-Aktivität gesteigert werden.

Ein weiterer interessanter Ansatz ist die Synthese von Verbindungen, deren SHG-Aktivität gezielt geschaltet werden kann. Vorversuche wurden mit [Zn<sub>2</sub>(H<sub>2</sub>BDC-NH<sub>2</sub>NO<sub>2</sub>)<sub>2</sub>(DABCO)] (bifunktionalisierter Zn-DMOF) durchgeführt, der aus Schichten aus untereinander durch (funktionalisierte) Terephthalationen verbrückte Zn-Paddle-Wheel-Einheiten besteht, die durch Pyrazin oder 4,4'-Bipyridin verknüpft sind.<sup>[95-97]</sup> Durch ein angelegtes sehr starkes elektrisches Feld könnten sich die polaren Linkermoleküle in den Schichten ausrichten und SHG-Aktivität induzieren. Dies geschieht dadurch, dass durch das Ausrichten der Linkermoleküle ein vorhandenes Inversionszentrum entfernt wird.

## 7 Literaturverzeichnis

- [1] M. E. Davis, *Nature*, **2002**, *417*, 813-821.
- [2] M. Thommes, K. Kaneko, V. Neimark Alexander, P. Olivier James, F. Rodriguez-Reinoso, J. Rouquerol, S. W. Sing Kenneth, in *Pure and Applied Chemistry*, Vol. 87, **2015**, p. 1051.
- [3] L. Puppe, *Chem. Unserer Zeit*, **1986**, *20*, 117-127.
- [4] L.-H. Schilling, H. Reinsch, N. Stock, in *The Chemistry of Metal–Organic Frameworks*, Wiley-VCH Verlag GmbH & Co. KGaA, **2016**, pp. 105-135.
- [5] T. Loiseau, C. Serre, C. Huguenard, G. Fink, F. Taulelle, M. Henry, T. Bataille, G. Férey, *Chem.-Eur. J.*, **2004**, *10*, 1373-1382.
- [6] K. J. Gagnon, H. P. Perry, A. Clearfield, *Chem. Rev.*, **2011**, *112*, 1034-1054.
- [7] G. K. H. Shimizu, R. Vaidhyanathan, J. M. Taylor, *Chem. Soc. Rev.*, **2009**, *38*, 1430-1449.
- [8] S.-T. Zheng, T. Wu, C. Chou, A. Fuhr, P. Feng, X. Bu, *J. Am. Chem. Soc.*, **2012**, *134*, 4517-4520.
- [9] A. Weiss, N. Reimer, N. Stock, M. Tiemann, T. Wagner, *Micropor. Mesopor. Mat.*, **2016**, *220*, 39-43.
- [10] O. M. Yaghi, M. O’Keeffe, N. W. Ockwig, H. K. Chae, M. Eddaoudi, J. Kim, *Nature*, **2003**, *423*, 705.
- [11] H. Furukawa, J. Kim, N. W. Ockwig, M. O’Keeffe, O. M. Yaghi, *J. Am. Chem. Soc.*, **2008**, *130*, 11650-11661.
- [12] I. J. Kang, N. A. Khan, E. Haque, S. H. Jung, *Chem.-Eur. J.*, **2011**, *17*, 6437-6442.
- [13] M. Gaab, N. Trukhan, S. Maurer, R. Gummaraju, U. Müller, *Micropor. Mesopor. Mat.*, **2012**, *157*, 131-136.
- [14] H. Reinsch, S. Waitschat, S. M. Chavan, K. P. Lillerud, N. Stock, *Eur. J. Inorg. Chem.*, **2016**, *2016*, 4490-4498.
- [15] H. Reinsch, *Eur. J. Inorg. Chem.*, **2016**, *2016*, 4290-4299.
- [16] W. H. Casey, *Chem. Rev.*, **2006**, *106*, 1-16.
- [17] W. H. Casey, B. L. Phillips, G. Furrer, *Rev. Mineral Geochem.*, **2001**, *44*, 167-190.
- [18] H. Reinsch, N. Stock, *Micropor. Mesopor. Mat.*, **2013**, *171*, 156-165.
- [19] H. Reinsch, M. Krüger, J. Marrot, N. Stock, *Inorg. Chem.*, **2013**, *52*, 1854-1859.
- [20] H. Reinsch, M. A. van der Veen, B. Gil, B. Marszalek, T. Verbiest, D. de Vos, N. Stock, *Chem. Mater.*, **2012**, *25*, 17-26.
- [21] C. Volkringer, D. Popov, T. Loiseau, N. Guillou, G. Férey, M. Haouas, F. Taulelle, C. Mellot-Draznieks, M. Burghammer, C. Riekkel, *Nat. Mater.*, **2007**, *6*, 760-764.
- [22] P. M. Forster, N. Stock, A. K. Cheetham, *Angew. Chem., Int. Ed.*, **2005**, *44*, 7608-7611.
- [23] N. Stock, S. Biswas, *Chem. Rev.*, **2012**, *112*, 933-969.
- [24] A. Rabenau, *Angew. Chem.*, **1985**, *97*, 1017-1032.
- [25] C. Janiak, H. J. Meyer, D. Gudat, R. Alsfasser, E. Riedel, *Riedel Moderne Anorganische Chemie*, De Gruyter, Berlin/Boston, **2012**.
- [26] S. Bauer, N. Stock, *Chem. Unserer Zeit*, **2007**, *41*, 390-398.
- [27] N. Reimer, *Dissertation*, CAU Kiel, **2015**.
- [28] N. Stock, *Chem. Ing. Tech.*, **2010**, *82*, 1039-1047.

- [29] *Win XPOW 3.3*, **2015**, Stoe & Cie GmbH.
- [30] *Topas Academic 4.1*, A. Coelho.
- [31] A. Altomare, M. Camalli, C. Cuocci, C. Giacovazzo, A. Moliterni, R. Rizzi, *J. Appl. Crystallogr.*, **2009**, *42*, 1197-1202.
- [32] K. Brandenburg, *Diamond 3.2*, **2014**, Crystal Impact.
- [33] Materials Studio v4.1, Accelrys Software Inc.
- [34] V. Favre-Nicolin, R. Cerny, J. Rohlicek, M. Husak, *F.O.X. - Free Objects for Xtallography*, **2000-2011**.
- [35] G. Sheldrick, *Acta Crystallographica Section A*, **2015**, *71*, 3-8.
- [36] Stoe, Cie, *XShape and XRed*, Darmstadt, Germany, **1998**.
- [37] A.L.Spek, *PLATON, A Multipurpose Crystallographic Tool*, Utrecht University, Utrecht, The Netherlands (2010)
- [38] A. Spek, *J. Appl. Crystallogr.*, **2003**, *36*, 7-13.
- [39] A. Spek, *Acta Crystallographica Section D*, **2009**, *65*, 148-155.
- [40] V. A. Blatov, A. P. Shevchenko, D. M. Proserpio, *Cryst. Growth Des.*, **2014**, *14*, 3576-3586.
- [41] O. Delgado-Friedrichs, M. O'Keeffe, *Acta Crystallographica Section A*, **2003**, *59*, 351-360.
- [42] *Generation, Analysis and Visualization of Reticular Ornaments using Gavrog*, <http://gavrog.org/>, abgerufen am: 30.08.2017.
- [43] W. Massa, *Kristallstrukturbestimmung, Vol. 5*, Teubner, Wiesbaden, **2007**.
- [44] A. L. Patterson, *Physical Review*, **1934**, *46*, 372-376.
- [45] J. Karle, H. Hauptman, *Acta Crystallographica*, **1956**, *9*, 635-651.
- [46] L. Spieß, R. Schwarzer, H. Behnken, G. Teichert, *Moderne Röntgenbeugung: Röntgendiffraktometrie für Materialwissenschaftler, Physiker und Chemiker*, Vieweg+Teubner Verlag, **2015**.
- [47] L.-H. Schilling, *Dissertation*, CAU Kiel, **2013**.
- [48] K. D. M. Harris, M. Tremayne, B. M. Kariuki, *Angew. Chem., Int. Ed.*, **2001**, *40*, 1626-1651.
- [49] R. W. Boyd, *Nonlinear Optics*, Elsevier Science, **2008**.
- [50] Weber, Herziger, *Laser. Grundlagen und Anwendung*, Physik Verlag, **1972**.
- [51] K. Betzler, M. Wöhlecke, *Skript zur Vorlesung "Nonlinear Optics"*, Universität Osnabrück, **SS 05**.
- [52] Y. F. Shepelev, R. S. Bubnova, S. K. Filatov, N. A. Sennova, N. A. Pilneva, *J. Solid State Chem.*, **2005**, *178*, 2987-2997.
- [53] D. F. Xue, S. Y. Zhang, *Acta Crystallographica Section B*, **1998**, *54*, 652-656.
- [54] S. Dahaoui, N. K. Hansen, B. Menaert, *Acta Crystallographica Section C*, **1997**, *53*, 1173-1176.
- [55] T. Fukami, *physica status solidi (a)*, **1990**, *117*, K93-K96.
- [56] R. Hsu, E. N. Maslen, D. du Boulay, N. Ishizawa, *Acta Crystallographica Section B*, **1997**, *53*, 420-428.
- [57] C. J. Xiao, C. Q. Jin, X. H. Wang, *Mater. Chem. Phys.*, **2008**, *111*, 209-212.
- [58] C. Wang, T. Zhang, W. Lin, *Chem. Rev.*, **2012**, *112*, 1084-1104.
- [59] M. A. van der Veen, F. Vermoortele, D. E. De Vos, T. Verbiest, *Anal. Chem.*, **2012**, *84*, 6378-6385.

- [60] M. A. van der Veen, F. Vermoortele, D. E. De Vos, T. Verbiest, *Anal. Chem.*, **2012**, *84*, 6386-6390.
- [61] K. Markey, T. Putzeys, P. Horcajada, T. Devic, N. Guillou, M. Wubbenhorst, S. V. Cleuvenbergen, T. Verbiest, D. E. De Vos, M. A. van der Veen, *Dalton Trans.*, **2016**, *45*, 4401-4406.
- [62] G. Nickerl, A. Henschel, R. Grönker, K. Gedrich, S. Kaskel, *Chem. Ing. Tech.*, **2011**, *83*, 90-103.
- [63] S. Ma, J. A. Fillinger, M. W. Ambrogio, J.-L. Zuo, H.-C. Zhou, *Inorg. Chem. Commun.*, **2007**, *10*, 220-222.
- [64] Z. Lin, F. Jiang, L. Chen, D. Yuan, M. Hong, *Inorg. Chem.*, **2005**, *44*, 73-76.
- [65] Z.-Y. Du, Y.-H. Sun, X. Xu, G.-H. Xu, Y.-R. Xie, *Eur. J. Inorg. Chem.*, **2010**, *2010*, 4865-4869.
- [66] S. Du, H. Zhang, in *Metal-Organic Frameworks for Photonics Applications* (Eds.: B. Chen, G. Qian), Springer Berlin Heidelberg, Berlin, Heidelberg, **2014**, pp. 145-165.
- [67] Y.-T. Wang, H.-H. Fan, H.-Z. Wang, X.-M. Chen, *J. Mol. Struct.*, **2005**, *740*, 61-67.
- [68] W. Xu, W. Liu, F.-Y. Yao, Y.-Q. Zheng, *Inorg. Chim. Acta*, **2011**, *365*, 297-301.
- [69] X.-Q. Liang, D.-P. Li, C.-H. Li, X.-H. Zhou, Y.-Z. Li, J.-L. Zuo, X.-Z. You, *Cryst. Growth Des.*, **2010**, *10*, 2596-2605.
- [70] Q. Ye, Y.-H. Li, Q. Wu, Y.-M. Song, J.-X. Wang, H. Zhao, R.-G. Xiong, Z. Xue, *Chem.-Eur. J.*, **2005**, *11*, 988-994.
- [71] W. Lin, Z. Wang, L. Ma, *J. Am. Chem. Soc.*, **1999**, *121*, 11249-11250.
- [72] Y. Liu, G. Li, X. Li, Y. Cui, *Angew. Chem.*, **2007**, *119*, 6417-6420.
- [73] O. R. Evans, R.-G. Xiong, Z. Wang, G. K. Wong, W. Lin, *Angew. Chem., Int. Ed.*, **1999**, *38*, 536-538.
- [74] W. Lin, L. Ma, O. R. Evans, *Chem. Commun.*, **2000**, 2263-2264.
- [75] O. R. Evans, W. Lin, *Chem. Mater.*, **2001**, *13*, 2705-2712.
- [76] T. R. Whitfield, X. Wang, L. Liu, A. J. Jacobson, *Solid State Sci.*, **2005**, *7*, 1096-1103.
- [77] M. N. Timofeeva, V. N. Panchenko, N. A. Khan, Z. Hasan, I. P. Prosvirin, S. V. Tsybulya, S. H. Jhung, *Applied Catalysis A: General*, **2017**, *529*, 167-174.
- [78] J. P. S. Mowat, V. R. Seymour, J. M. Griffin, S. P. Thompson, A. M. Z. Slawin, D. Fairen-Jimenez, T. Duren, S. E. Ashbrook, P. A. Wright, *Dalton Trans.*, **2012**, *41*, 3937-3941.
- [79] C. Serre, F. Millange, C. Thouvenot, M. Noguès, G. Marsolier, D. Louër, G. Férey, *J. Am. Chem. Soc.*, **2002**, *124*, 13519-13526.
- [80] C. Volkringer, T. Loiseau, N. Guillou, G. Férey, E. Elkaim, A. Vimont, *Dalton Trans.*, **2009**, 2241-2249.
- [81] P. Serra-Crespo, E. Stavitski, F. Kapteijn, J. Gascon, *RSC Advances*, **2012**, *2*, 5051-5053.
- [82] S. Biswas, T. Ahnfeldt, N. Stock, *Inorg. Chem.*, **2011**, *50*, 9518-9526.
- [83] A. Comotti, S. Bracco, P. Sozzani, S. Horike, R. Matsuda, J. Chen, M. Takata, Y. Kubota, S. Kitagawa, *J. Am. Chem. Soc.*, **2008**, *130*, 13664-13672.
- [84] T. Ahnfeldt, D. Gunzelmann, T. Loiseau, D. Hirsemann, J. r. Senker, G. Férey, N. Stock, *Inorg. Chem.*, **2009**, *48*, 3057-3064.
- [85] N. Reimer, B. Gil, B. Marszalek, N. Stock, *CrystEngComm*, **2012**, *14*, 4119-4125.
- [86] S. Biswas, T. Remy, S. Couck, D. Denysenko, G. Rampelberg, J. F. M. Denayer, D. Volkmer, C. Detavernier, P. Van Der Voort, *Phys. Chem. Chem. Phys.*, **2013**, *15*, 3552-3561.
- [87] D. Himsl, D. Wallacher, M. Hartmann, *Angew. Chem., Int. Ed.*, **2009**, *48*, 4639-4642.

- [88] P. Serra-Crespo, M. A. van der Veen, E. Gobechiya, K. Houthoofd, Y. Filinchuk, C. E. A. Kirschhock, J. A. Martens, B. F. Sels, D. E. De Vos, F. Kapteijn, J. Gascon, *J. Am. Chem. Soc.*, **2012**, *134*, 8314-8317.
- [89] H. Reinsch, S. Waitschat, N. Stock, *Dalton Trans.*, **2013**, *42*, 4840-4847.
- [90] N. Reimer, B. Bueken, S. Leubner, C. Seidler, M. Wark, D. De Vos, N. Stock, *Chem.-Eur. J.*, **2015**, *21*, 12517-12524.
- [91] C. Volkringer, T. Loiseau, N. Guillou, G. r. Férey, M. Haouas, F. Taulelle, N. Audebrand, I. Margiolaki, D. Popov, M. Burghammer, C. Riekel, *Cryst. Growth Des.*, **2009**, *9*, 2927-2936.
- [92] A. Fateeva, P. A. Chater, C. P. Ireland, A. A. Tahir, Y. Z. Khimyak, P. V. Wiper, J. R. Darwent, M. J. Rosseinsky, *Angew. Chem.*, **2012**, *124*, 7558-7562.
- [93] S. Bernt, V. Guillermin, C. Serre, N. Stock, *Chem. Commun.*, **2011**, *47*, 2838-2840.
- [94] N. Reimer, H. Reinsch, A. K. Inge, N. Stock, *Inorg. Chem.*, **2014**, *54*, 492-501.
- [95] D. N. Dybtsev, H. Chun, K. Kim, *Angew. Chem., Int. Ed.*, **2004**, *43*, 5033-5036.
- [96] J. S. Grosch, F. Paesani, *J. Am. Chem. Soc.*, **2012**, *134*, 4207-4215.
- [97] H. Jasuja, Y. Jiao, N. C. Burtch, Y.-g. Huang, K. S. Walton, *Langmuir*, **2014**, *30*, 14300-14307.



# **TEIL III**

## **ANHANG**





## Supporting Information

### [Al<sub>2</sub>(OH)<sub>2</sub>(TCPB)] – an Al-MOF based on a tetratopic linker molecule

Martin Krüger\*, Renée Siegel\*, Anna Dreischarf\*, Helge Reinsch\*, Jürgen Senker\* and Norbert Stock\*

\* Institut für Anorganische Chemie, Christian Albrechts Universität zu Kiel, Kiel, Germany

× Centre for Materials Science and Nanotechnology Chemistry, University of Oslo, Oslo, Norway

\* Department of Inorganic Chemistry 3, Universität Bayreuth, Bayreuth, Germany

CAU-9 was discovered by investigating the system Al<sup>3+</sup>/H<sub>4</sub>TCPB/H<sub>2</sub>O/DMF/Additive in our 48 high throughput reactor system. For the first investigation a volume ratio H<sub>2</sub>O:DMF of 50:100 µL and a temperature program of 1h heating up to 150 °C, keeping this temperature for 18 h and cooling down to RT within 12 h were used. The molar ratios of Al<sup>3+</sup>:H<sub>4</sub>TCPB were varied from 1:2 to 8:2. Al(NO<sub>3</sub>)<sub>3</sub>·9H<sub>2</sub>O served as the Al source (Tab. S1).

Tab. S1: Exact amounts of starting materials during the HT-experiment that led to the discovery of CAU-9. To demonstrate the reproducibility of the synthesis some reactions were carried out using the same molar ratios.

number	n(Al <sup>3+</sup> ) [µmol]	n(H <sub>4</sub> TCPB) [µmol]	m(Al <sup>3+</sup> ) [mg]	m(H <sub>4</sub> TCPB) [mg]
1	4,476	8,952	1,7	5,0
2	8,952	8,952	3,4	5,0
3	13,428	8,952	5,0	5,0
4	17,904	8,952	6,7	5,0
5	26,856	8,952	10,1	5,0
6	35,808	8,952	13,4	5,0
7	17,904	8,952	6,7	5,0
8	20,142	8,952	7,6	5,0
9	22,380	8,952	8,4	5,0
10	24,618	8,952	9,2	5,0
11	26,856	8,952	10,1	5,0
12	31,332	8,952	11,8	5,0

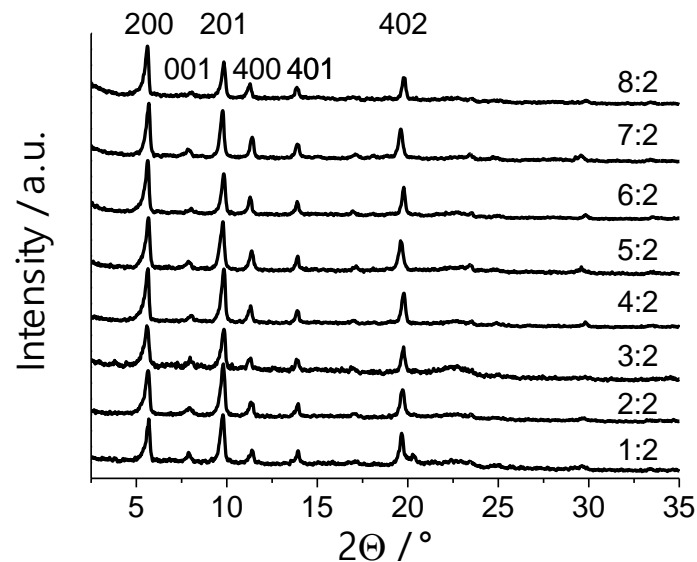


Fig. S1: Results of the high-throughput investigation of the first screening investigations of the system Al<sup>3+</sup>/H<sub>4</sub>TCPB/DMF/H<sub>2</sub>O. The molar ratio Al<sup>3+</sup>:H<sub>4</sub>TCPB in the reaction mixture is shown. The value of 1 corresponds to 4.48 μmol of starting material. The crystallinity of the samples rise up to a molar ratio of Al<sup>3+</sup>:H<sub>4</sub>TCPB of 6:2. Using larger molar ratios, peak broadening is noticeable.

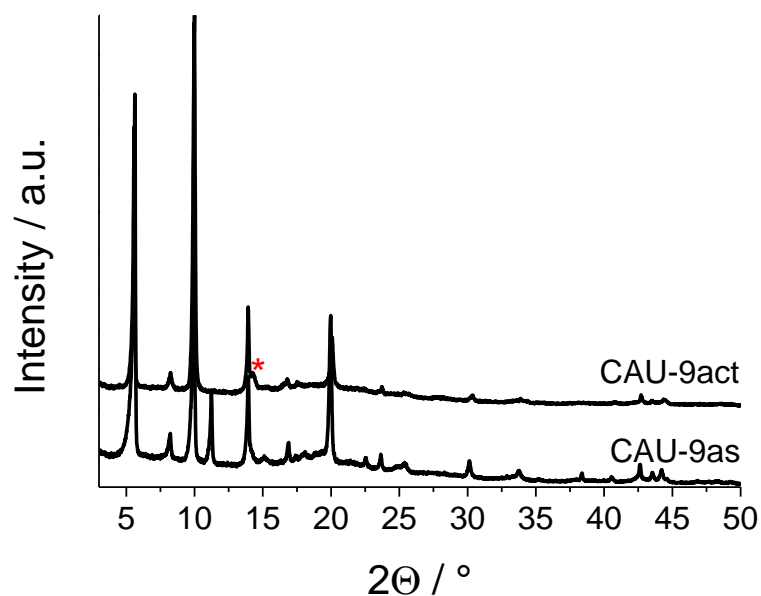


Fig. S2: Comparison of the PXRD patterns of CAU-9as and CAU-9act. The reflection marked by an asterisk can be assigned to boehmite (AlO(OH)).

## Structural data for CAU-9act

```
_chemical_name_mineral CAU-9
_cell_length_a      31.5625(40)
_cell_length_b      6.6422(66)
_cell_length_c      10.66115(69)
_cell_angle_alpha   90
_cell_angle_beta    90
_cell_angle_gamma   90
_cell_volume        2235.1(22)
_symmetry_space_group_name_H-M CMMM
loop_
_symmetry_equiv_pos_as_xyz
'-x, -y, -z'
'-x, -y, z'
'-x, y, -z'
'-x, y, z'
'-x+1/2, -y+1/2, -z'
'-x+1/2, -y+1/2, z'
'-x+1/2, y+1/2, -z'
'-x+1/2, y+1/2, z'
'x, -y, -z'
'x, -y, z'
'x, y, -z'
'x, y, z'
'x+1/2, -y+1/2, -z'
'x+1/2, -y+1/2, z'
'x+1/2, y+1/2, -z'
'x+1/2, y+1/2, z'
loop_
_atom_site_label
_atom_site_type_symbol
_atom_site_symmetry_multiplicity
_atom_site_fract_x
_atom_site_fract_y
_atom_site_fract_z
_atom_site_occupancy
_atom_site_B_iso_or_equiv
Al1 Al  0 0.25 0.25 0 1 2.0(12)
O1 O   0 0.2765(12) 0 0 1 7.1(11)
O2 O   0 0.29312(36) 0.3182(38) 0.12311(85) 1 7.1(11)
C1 C   0 0.30442(38) 0.5 0.1423(12) 1 1.00(60)
C2 C   0 0.34725(38) 0.5 0.2181(10) 1 1.00(60)
C3 C   0 0.36593(25) 0.3181(44) 0.25166(47) 1 1.00(60)
C4 C   0 0.40357(34) 0.3179(52) 0.31772(93) 1 1.00(60)
C5 C   0 0.42269(48) 0.5 0.3510(12) 1 1.00(60)
C6 C   0 0.46111(42) 0.5 0.4357(13) 1 1.00(60)
C7 C   0 0.5 0.5 0.3706(14) 1 1.00(60)
```

The presence of boehmite in the activated sample CAU-9act was deduced from the most intense Bragg reflection (020 at 14.3 °(2theta)). This observation is supported by the NMR-spectroscopic studies. The refinement was carried out by fixing the atomic positions and refining the lattice parameter. The refined values  $a = 3.689(3)$ ;  $b = 12.348(3)$ ;  $c = 2.849(2)$  compare well with the ones reported in the literature (ICSD-100391:  $a = 3.7007(6)$ ,  $b = 12.2344(19)$ ,  $c = 2.8735(4)$ ).<sup>1</sup>

Tab. S2: Bond lengths (Å) in the structure of CAU-9.

Al1	O1	1.823(23)
	O2	1.932(13)
C1	O2	1.300(22)
	C2	1.533(19)
C3	C2	1.398(30)
	C4	1.295(14)
C5	C4	1.401(34)
	C6	1.505(23)
C7	C6	1.437(17)

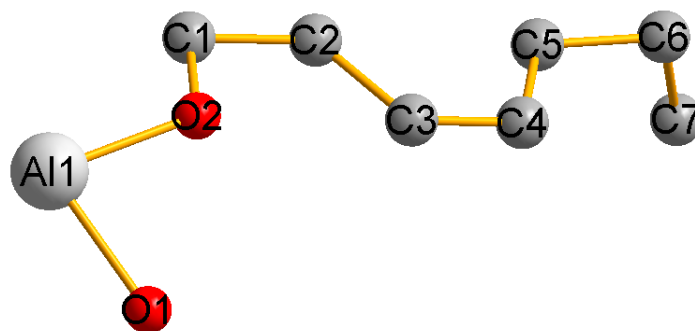


Fig. S3: Asymmetric unit of CAU-9 with numbering scheme used in Tab. S1.

<sup>1</sup> Farkas, L.;Gado, P.;Werner, P.E., Materials Research Bulletin 1977, 12, 1213-1219.

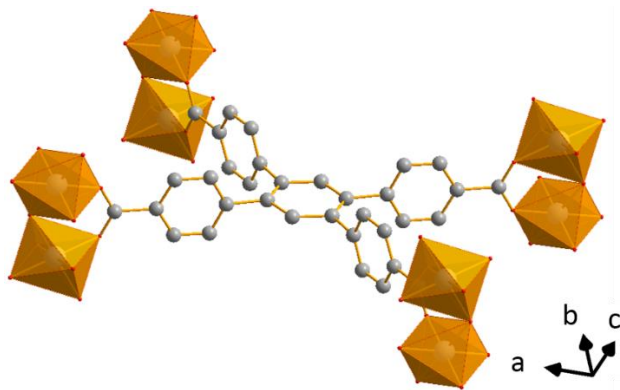


Fig. S4: Coordination environment of the  $\text{TCPB}^{4-}$  ion in CAU-9act.

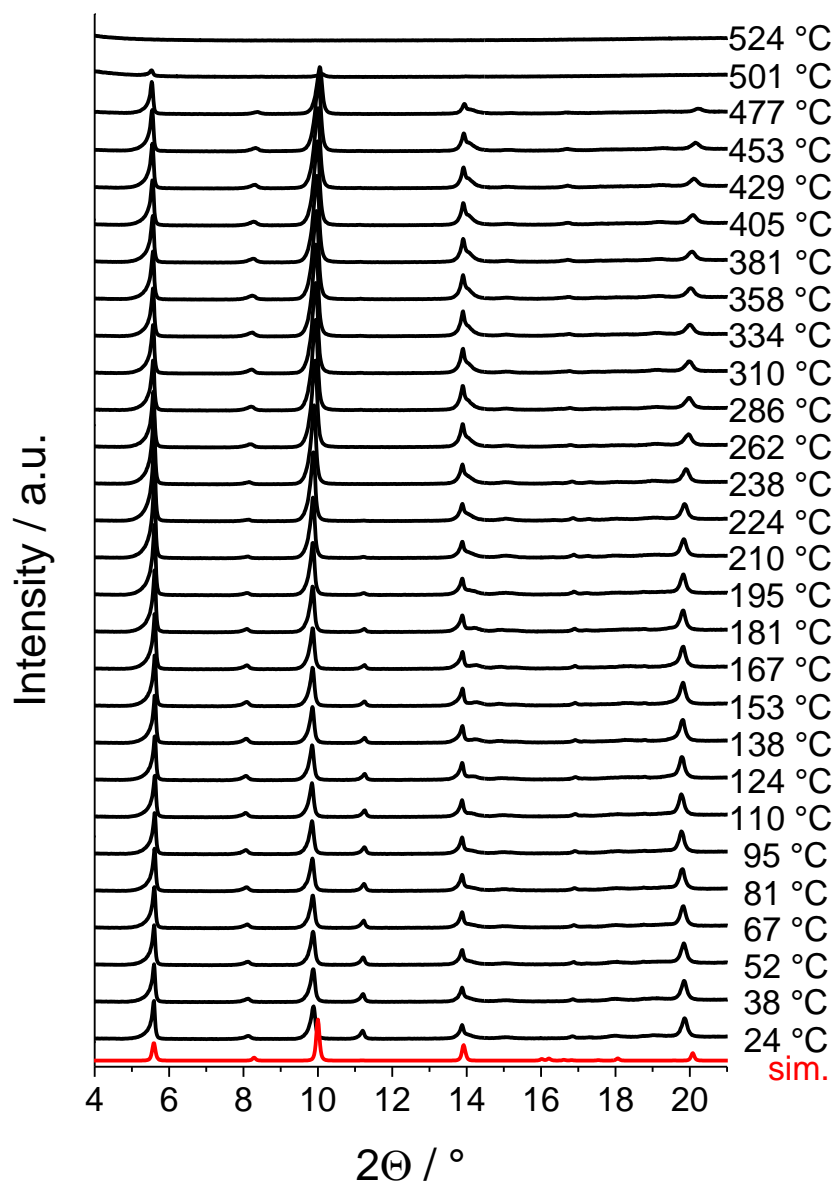


Fig. S5: Results of the temperature dependent X-ray powder diffraction carried out on CAU-9 in a capillary under air. The PXRD pattern in red is the one simulated from the structure determination.

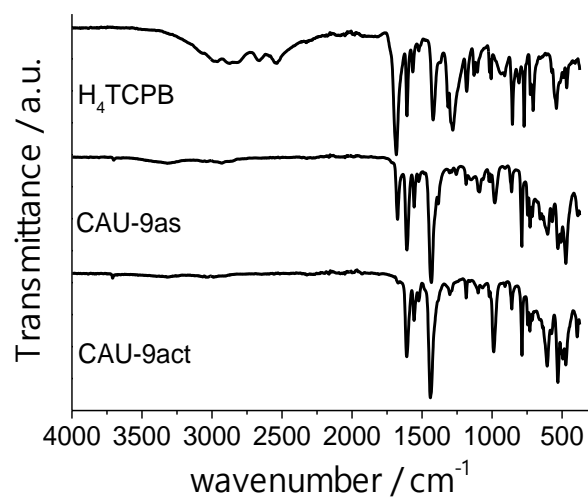


Fig. S6: Full IR-spectra of H<sub>4</sub>TCPB, CAU-9as and CAU-9act.

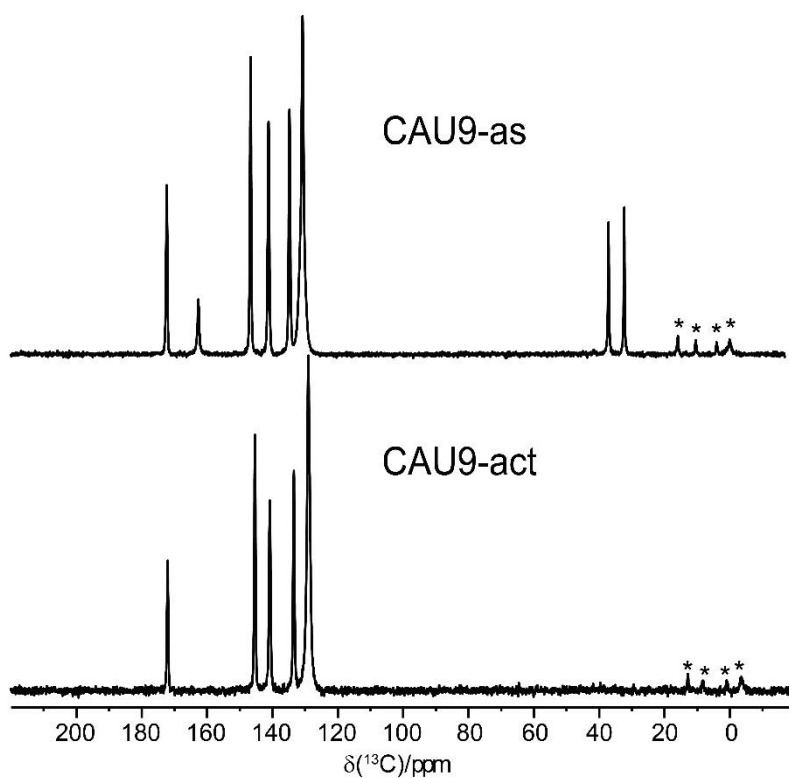


Fig. S7: <sup>13</sup>C CP MAS spectra CAU-9act (bottom) and CAU-9as (top). The signals marked by an asterisk (\*) are due to rotational side bands.

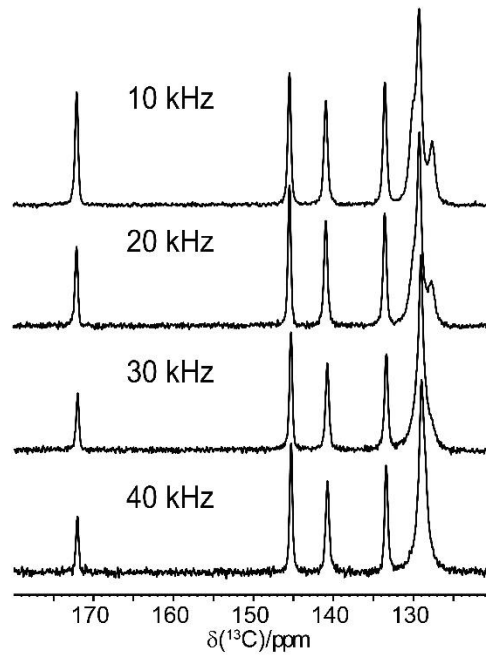


Fig. S8:  $^{13}\text{C}$  CP MAS spectra CAU-9act at different spinning speed.

When comparing the  $^{13}\text{C}$  spectra of the activated sample at different spinning speed, we observe strong changes in the shape (number of overlapping peak) for the peak at 129 ppm. Since the structure of CAU-9 is stable up to  $480^\circ\text{C}$ , the only parameter that changes is the different pressure sustained by the sample while spinning (the faster the spinning, the stronger the pressure). This MOF structure would thus be sensitive to the pressure.

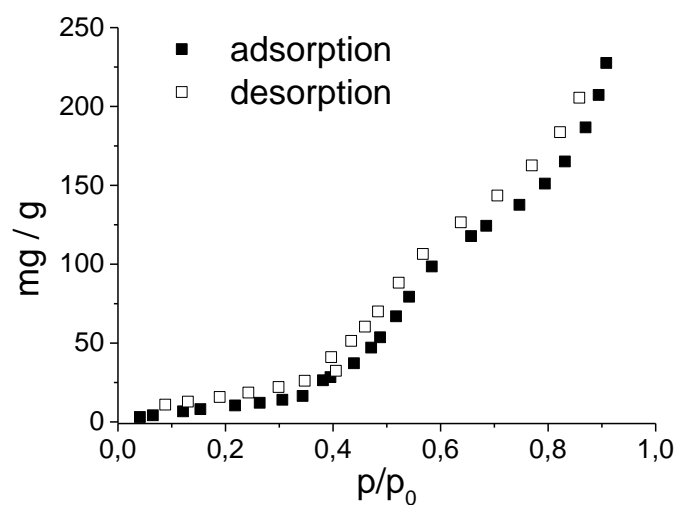


Fig. S9:  $\text{H}_2\text{O}$  sorption isotherm of CAU-9. The measurement was carried out at 298 K.



## Zusätzliche Informationen zu Ga-, In- und Cr-CAU-9

Die Synthese erfolgte analog zu den in der Veröffentlichung verwendeten Verfahren. Die exakten Synthesebedingungen sind in Tabelle A1 dargestellt.

**Tab. A1** Synthesebedingungen der verschiedenen CAU-9-Derivate.

Verbindung	Ga-CAU-9	In-CAU-9	Cr-CAU-9
Metallsalzquelle	Ga(NO <sub>3</sub> ) <sub>3</sub> ·H <sub>2</sub> O, 2M in H <sub>2</sub> O	In(NO <sub>3</sub> ) <sub>3</sub> ·H <sub>2</sub> O, 2M in DMF	Cr(C <sub>5</sub> H <sub>7</sub> O <sub>2</sub> ) <sub>3</sub>
Menge Metallsalzquelle	9.0 µL	9.0 µL	3.1 mg
H <sub>4</sub> TCPB	5.0 mg	5.0 mg	5.0 mg
H <sub>2</sub> O	21 µL	51 µL	140 µL
DMF	120 µL	90 µL	-
2M NaOH			10 µL
Temperaturprogramm	1 h/24 h\12 h, 150 °C	1 h/24 h\12 h, 150 °C	65 h, 190 °C

Die erhaltenen Produkte wurden nach der Isolierung 1 h unter Rühren in DMF bei 25 °C gereinigt um nicht reagierte Linkermoleküle zu entfernen. Anschließend gemessene hochaufgelöste Röntgenpulverdiffraktogramme konnten erfolgreich indiziert werden. Die aus der Indizierung der Röntgenpulverdiffraktogramme erhaltenen Zellparameter wurden durch Pawley-Methoden verfeinert. Die entsprechenden Pawley-Fits sind in Abbildung A1 dargestellt, die verfeinerten Zellparameter können Tabelle A2 entnommen werden.

**Tab. A2** Verfeinerte Zellparameter der verschiedenen CAU-9-Derivate.

Verbindung	Ga-CAU-9	In-CAU-9	Cr-CAU-9
Raumgruppe	<i>Cmmm</i>	<i>P2/m</i>	<i>Cmmm</i>
<i>a</i> / Å	21.861(2)	11.637(1)	21.654(6)
<i>b</i> / Å	6.714(3)	15.725(2)	6.829(3)
<i>c</i> / Å	15.844(2)	7.204(1)	15.844(6)
$\alpha$ / °	90	90	90
$\beta$ / °	90	80.97(2)°	90
$\gamma$ / °	90	90	90
GoF	1.39	2.19	1.13
$r_{wp}$	4.04	6.94	3.37

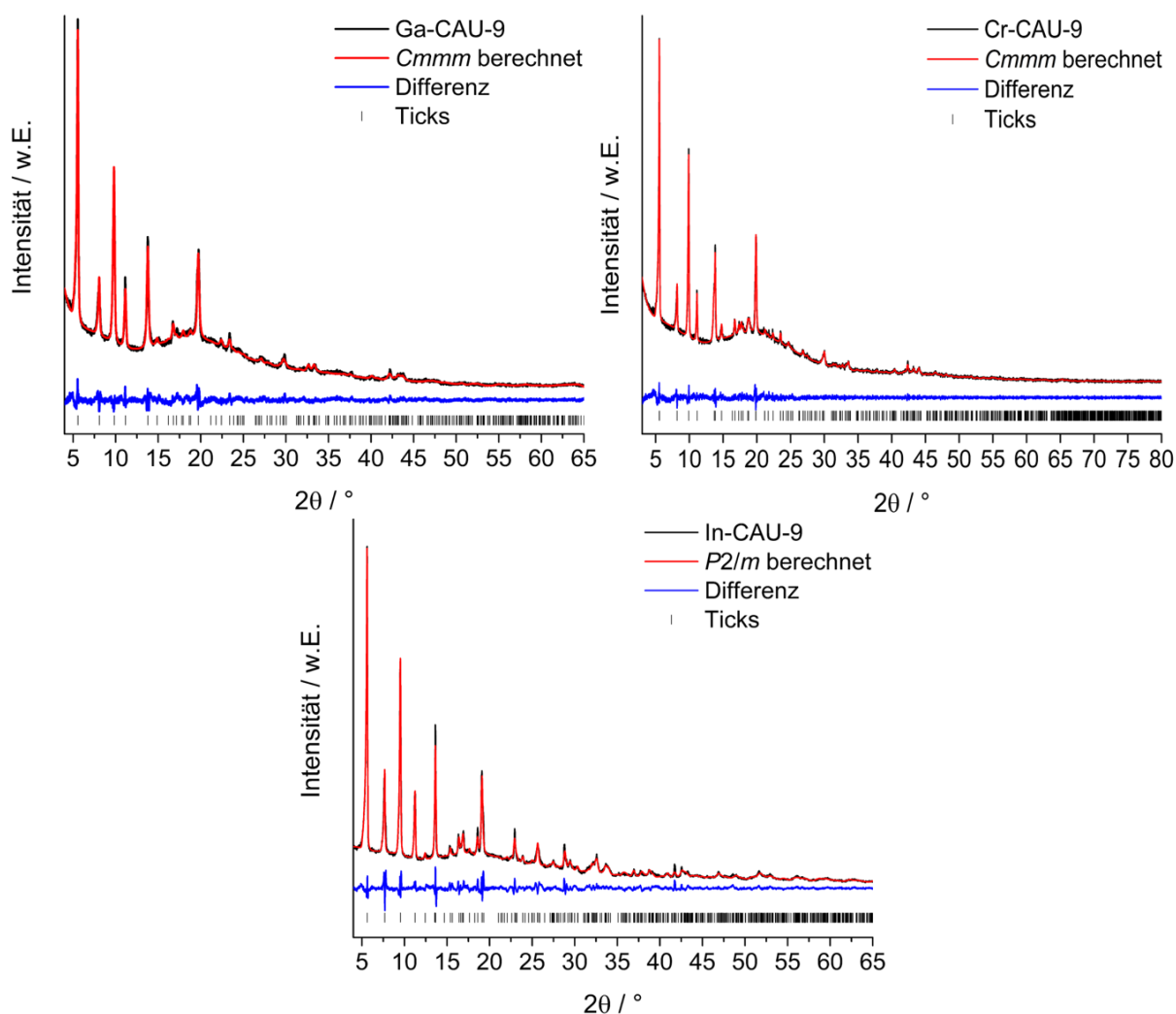


**Abb. A1** Darstellung der Pawley-Verfeinerungen der verschiedenen CAU-9-Derivate.

Die Zusammensetzung der Verbindungen wurden mittels Elementaranalyse und Thermogravimetrie bestimmt. In Cr-CAU-9 ist eine Verunreinigung an  $\text{Cr}_2\text{O}_3$  vorhanden, die auch durch Syntheseoptimierung nicht verhindert werden konnte. Die Summenformeln der Verbindungen und die Ergebnisse der Elementaranalyse sind in Tabelle A3 dargestellt. In Abbildung A2 sind die Thermogravimetriekurven der Verbindungen zu finden.

**Tab. A2** Summenformel und Ergebnisse der Elementaranalyse der verschiedenen CAU-9-Derivate.

Verbindung	Ga-CAU-9			In-CAU-9			Cr-CAU-9		
Summenformel	[Ga <sub>2</sub> (OH) <sub>2</sub> (TCPB)] ·1.2H <sub>2</sub> O·2.63DMF			[In <sub>2</sub> (OH) <sub>2</sub> (TCPB)] ·3DMF			[Cr <sub>2</sub> (OH) <sub>2</sub> (TCPB)] ·1.4H <sub>2</sub> O·1.9DMF·2.9Cr <sub>2</sub> O <sub>3</sub>		
	C / %	H / %	N / %	C / %	H / %	N / %	C / %	H / %	N / %
gemessen	57.3	4.6	3.7	42.2	3.6	3.5	36.9	3.0	2.0
berechnet	56.7	4.2	3.2	49.8	4.0	4.1	36.8	2.8	2.1

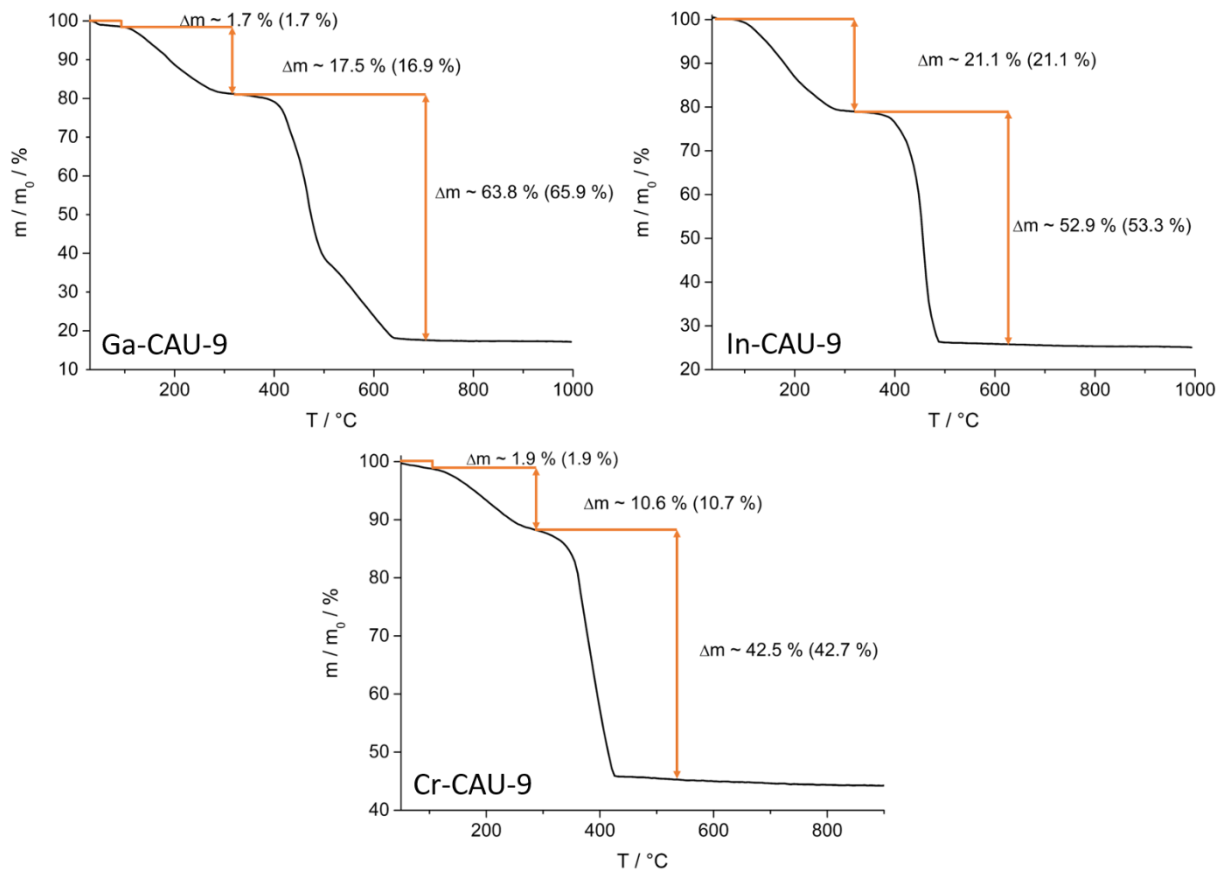


**Abb. A2** TG-Kurven der verschiedenen CAU-9-Derivate.

Alle Verbindungen wurden für  $N_2$ -Sorptionsmessungen für 16 h bei 200 °C aktiviert. Es konnten Typ I Isothermen erhalten werden, die auf eine Mikroporosität der Verbindungen hinweisen. Allerdings sind die nach BET erhaltenen scheinbaren spezifischen Oberflächen und Mikroporenvolumina drastisch geringer als die des Al-CAU-9. Die erhaltenen Werte aus der Auswertung der Sorptionsisothermen nach BET sind in Tabelle A3 zusammengefasst und die  $N_2$ -Sorptionsisothermen bei 77 K der Verbindungen sind in Abbildung A3 gezeigt.

**Tab. A3** Ergebnisse der  $N_2$ -Sorptionsmessungen bei 77 K der verschiedenen CAU-9-Derivate.

Verbindung	Ga-CAU-9	In-CAU-9	Cr-CAU-9
$a_{s,BET} / m^2/g$	568	487	510
$V_{mic,BET} / cm^3/g$	0.28	0.21	0.22

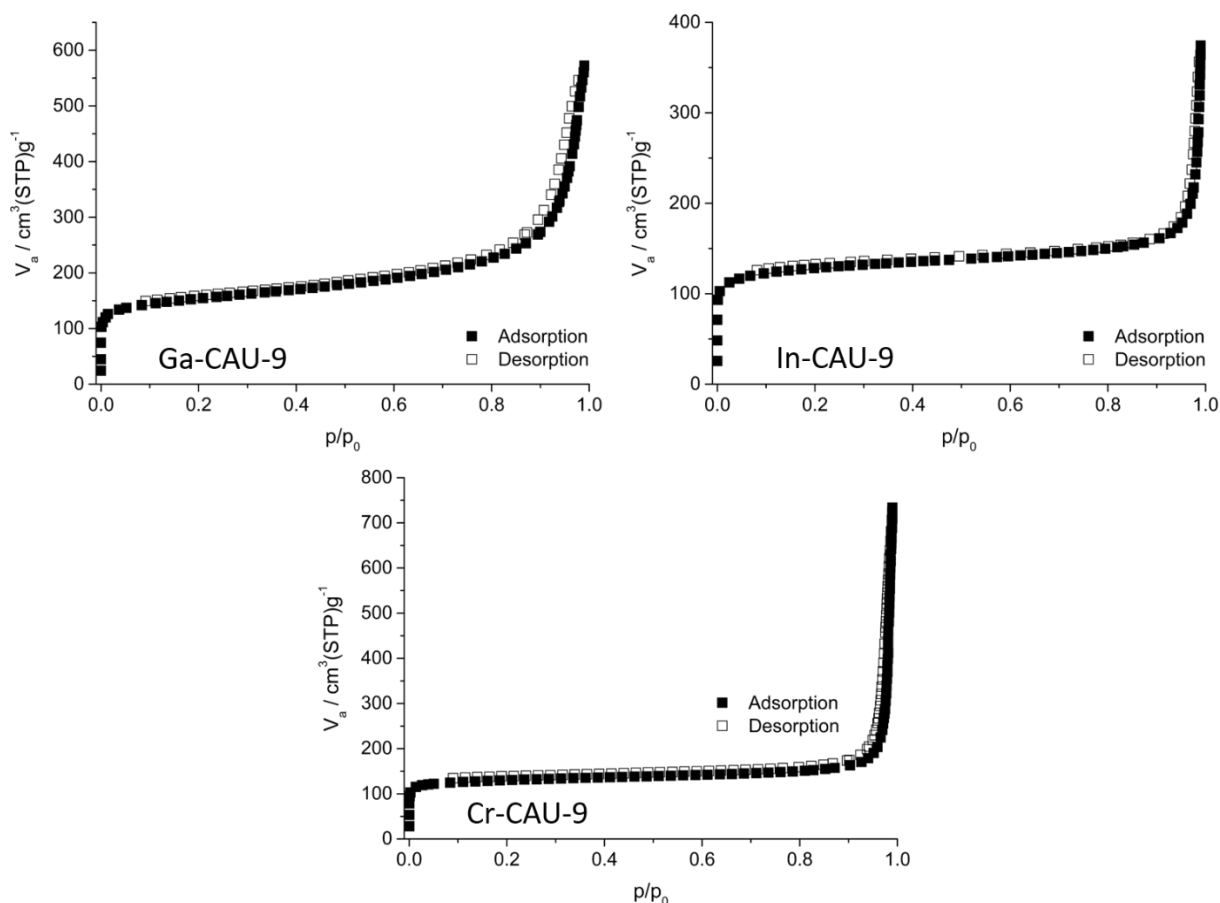


**Abb. A3**  $\text{N}_2$ -Sorptionsisothermen der verschiedenen CAU-9-Derivate (Messtemperatur 77 K).

Mit Cr-CAU-9 wurde eine Nitrierung nach Bernt et al.<sup>2</sup> durchgeführt. Hierfür wurde eine Mischung aus 1.155 mL konz.  $\text{H}_2\text{SO}_4$  und 0.825 mL konz. Salpetersäure in einem Dreihalskolben vorgelegt. Dazu wurden 16.5 mg Cr-CAU-9 zugegeben und 5 h bei 0 °C gerührt. Anschließend wurde die Mischung auf Raumtemperatur erwärmt und auf 8.25 mL Eis gegeben. Das isolierte Produkt wurde je zwei Mal in 15 mL  $\text{H}_2\text{O}$  und in 15 mL Ethanol in der Mikrowelle bei 150 °C gewaschen. Der erhaltene Feststoff wurde an Luft bei 70 °C über Nacht getrocknet. Von dem erhaltenen Feststoff wurde ein Pulverdiffraktogramm aufgenommen (Abbildung A4). Demnach hat die Kristallinität von Cr-CAU-9 stark abgenommen, jedoch ist das MOF-Gerüst erhalten geblieben. Weiterhin wurde das Produkt mittels  $^1\text{H}$ -NMR-Spektroskopie charakterisiert. Dazu wurde die Verbindung durch Zugabe von 2 M NaOH aufgelöst und das ausgefallene  $\text{Cr}(\text{OH})_3$  abfiltriert. Anschließend wurde die Lösung mit 2 M HCl auf pH = 2 angesäuert und das Lösungsmittel bei 70 °C entfernt. Der getrocknete Feststoff konnte in 5 % NaOD/ $\text{D}_2\text{O}$  gelöst und ein  $^1\text{H}$ -NMR-Spektrum gemessen werden (Abbildung A5).

<sup>2</sup> S. Bernt, V. Guillerm, C. Serre, N. Stock, *Chem. Commun.*, **2011**, 47, 2838-2840.

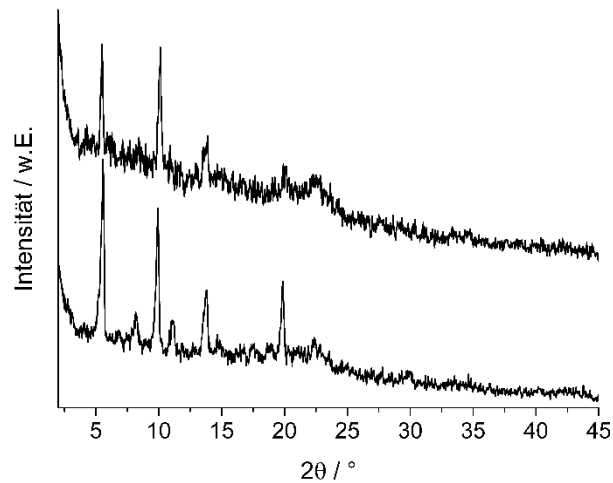


**Abb. A4** Pulverdiffraktogramme von Cr-CAU-9 vor (unten) nach (oben) der Nitrierung.

In dem  $^1\text{H-NMR}$ -Spektrum sind zwei Duplett-Signale im aromatischen Bereich zu erkennen, die den H-Atomen der Benzoessäure-Reste entsprechen. Das Signal des zentralen aromatischen Rings des  $\text{H}_4\text{TCPB}$ , welches bei einer chemischen Verschiebung von 7.6 ppm zu erwarten ist, fehlt, sodass von einer Funktionalisierung an diesem Ring auszugehen ist. Allerdings kann anhand der Verschiebungen der Signale nicht eindeutig geklärt werden, ob eine Nitrierung stattgefunden hat. Auch eine Oxidation zum Benzochinon durch die verwendete Salpetersäure ist möglich (Abbildung A5).

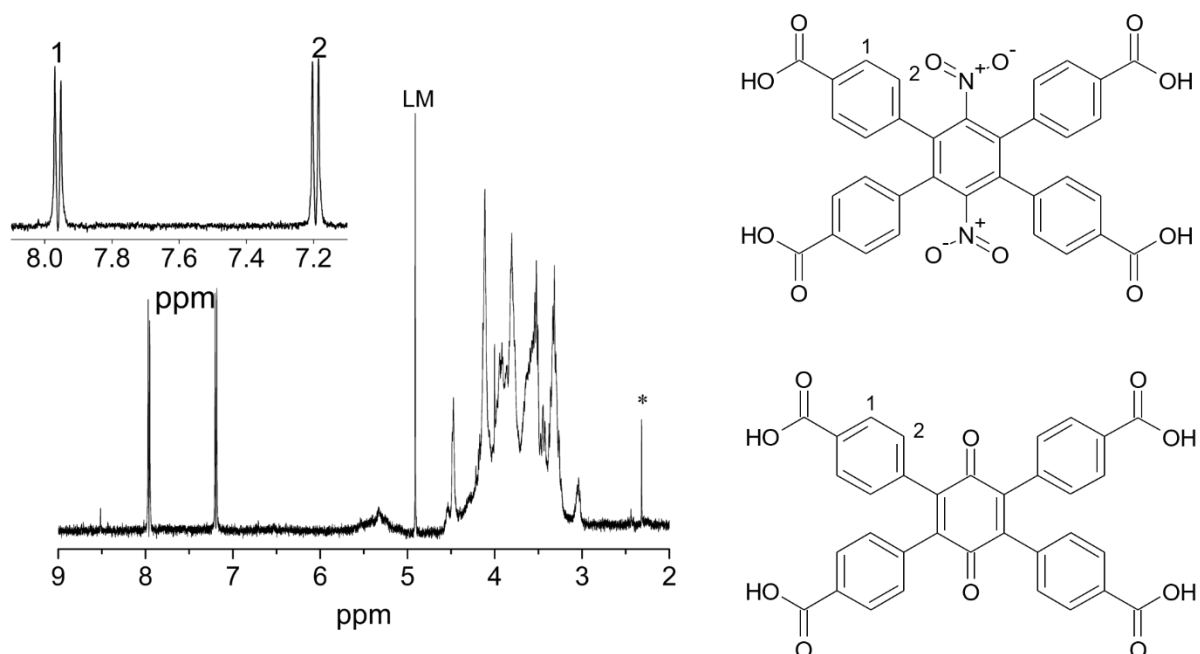


**Abb. A4**  $^1\text{H-NMR}$ -Spektrum vom Produkt der Nitrierung mit zwei möglichen Funktionalisierungen des zentralen aromatischen Ringes des  $\text{H}_4\text{TCPB}$ .

# Polymorphous Al-MOFs based on V-shaped linker molecules: synthesis, properties and *in situ* investigation of their crystallization

*Martin Krüger,<sup>†</sup> A. Ken Inge,<sup>‡</sup> Helge Reinsch,<sup>†</sup> Yuan-Han Li,<sup>\*</sup> Mohammad Wahiduzzaman,<sup>\*</sup>  
Chia-Her Lin,<sup>^</sup> Sue-Lein Wang,<sup>\*\*</sup> Guillaume Maurin,<sup>\*</sup> and Norbert Stock<sup>†\*</sup>*

<sup>†</sup> Institut für Anorganische Chemie, Christian-Albrechts-Universität, Max-Eyth-Straße 2,  
24118 Kiel, Germany

<sup>‡</sup> Berzelii Center EXSELENT on Porous Materials and Department of Materials and  
Environmental Chemistry, Stockholm University, Stockholm S-106 91, Sweden

<sup>\*\*</sup> Department of Chemistry, National Tsing Hua University, Hsinchu 300, Taiwan

<sup>\*</sup> Institut Charles Gerhardt Montpellier, UMR-5253 Université Montpellier CNRS ENSCM,  
Place E. Bataillon 34095, Montpellier cedex 05, France

<sup>^</sup> Department of Chemistry, Chung-Yuan Christian University, 200 Chung Pei Road, Chung-  
Li 32023, Taiwan

**Table of Contents**

Table S1. Molar ratios and exact amounts of the reactants employed in the HT experiments for CAU-21-BPDC. ....	131
Table S2. Molar ratios and exact amounts of the reactants employed in the HT experiments for CAU-8-ODB and CAU-21-ODB. ....	133
Figure S1. Comparison of the measured PXRD pattern of CAU-21-BPDC with the ones calculated from minimum energy structures obtained from DFT calculations. ....	135
Figure S2. Comparison of the measured PXRD pattern of CAU-21-ODB with the ones calculated from minimum energy structures obtained from DFT calculations. ....	135
Figure S3. Comparison of the measured PXRD pattern of CAU-8-ODB with the ones calculated from minimum energy structures obtained from DFT calculations. ....	136
Table S5. Selected bond lengths of CAU-21-BPDC. ....	137
Table S6. Selected bond lengths of CAU-8-ODB. For the parts refined using rigid bodies no standard deviations are given. ....	137
Table S7. Selected bond lengths of the crystal structure of CAU-21-ODB obtained from DFT calculations. ....	138
Figure S4. Plot of the Pawley refinement of CAU-21-ODB. ....	138
Figure S6. PXRD patterns of the ex situ quenching experiments of the intermediate carried out at 130 °C. After 25 mins the intermediate has formed. ....	139
Figure S7. Comparison of high resolution PXRD patterns of the intermediate obtained from the ex situ quenching experiments and PXRD patterns of CAU-8-BPDC and CAU-21-BPDC. The intermediate was washed in DMF at 60 °C for 3h to remove residual linker molecules. ....	140
Figure S8. Results of the in situ time resolved PXRD investigation of CAU-8-BPDC at 140 °C (A) and at 150 °C (B) in top view. Reflections of CAU-8-BPDC are marked with their hkl indices. ....	140
Figure S9. Comparison of the reaction progress ( $\alpha$ ) of CAU-8-BPDC obtained from the normalized intensities of the 013 reflection. The higher the temperature the faster CAU-8-BPDC is formed. ....	141
Figure S10. Asymmetric unit of CAU-21-BPDC with numbering scheme as used in Table S5. ....	141
Figure S11. Crystal structure of CAU-21-BPDC. The connection between two IBUs is established via two linker molecules (left). Each IBU is connected by 16 linker molecules (middle), so that a 3D framework is formed (right). ....	141
Figure S12. Infrared spectrum of CAU-21-BPDC, a detailed view is given on the right. Bands discussed in the manuscript are labeled with asterisks in the full spectrum and with wavenumbers in the detailed view. ....	142

Figure S13. $^1\text{H-NMR}$ spectrum of CAU-21-BPDC (black) in comparison to the spectra of the $\text{H}_2\text{BPDC}$ linker (red) and benzoic acid (blue).....	142
Figure S14. Results of the parametric Pawley refinement of CAU-21-BPDC.....	143
Figure S15. Final Rietveld plot of CAU-8-ODB.....	143
Figure S16. Comparison of the $\text{BPDC}^{2-}$ (left) and the $\text{ODB}^{2-}$ (right) ion in the CAU-8 structure. The angle between the aromatic rings is given in black and the torsion angle between the aromatic rings in green.....	144
Figure S17. Comparison of the spherical cavities in the CAU-8-BPDC (left) and CAU-8-ODB (right).....	144
Figure S18. Results of the thermogravimetric measurements of CAU-8-ODB, measured with a heating rate of 4 K/min under air. The weight losses are marked in the graph, expected values are given in brackets.....	144
Figure S19. Results of the temperature dependent PXRD study of CAU-8-ODB.....	145
Figure S20. Results of the thermogravimetric measurements of CAU-21-ODB, measured with a heating rate of 4 K/min under air. The weight losses are marked in the graph, expected values are given in brackets.....	145
Figure S21. Results of the temperature dependent X-ray diffraction studies of CAU-21-ODB.....	146
Table S8. Results of the elemental analyses for CAU-8-ODB and CAU-21-ODB. Measured percentages of nitrogen result from residual DMF molecules, which couldn't be removed upon activation.....	146
Figure S22. Infrared spectra of CAU-8-ODB (black) and CAU-21-ODB (blue), a detailed view is given on the right. Bands discussed in the manuscript are labeled with asterisks in the full spectrum and with wavenumbers in the detailed view.....	147
Figure S23. $^1\text{H-NMR}$ spectra of CAU-8-ODB (red) and CAU-21-ODB (blue) in comparison to the spectra of the $\text{H}_2\text{ODB}$ (black). .....	147
Figure S24. $\text{N}_2$ sorption isotherms of CAU-8-ODB measured at 77 K. Filled symbols represent the adsorption, empty symbols the desorption branch.....	148
Figure S25. $\text{H}_2$ sorption isotherm of CAU-8-ODB measured at 77 K. Filled symbols represent the adsorption, empty symbols the desorption branch.....	148
Figure S26. $\text{CO}_2$ sorption isotherms of CAU-8-ODB measured at 273 and at 298 K. Filled symbols represent the adsorption, empty symbols the desorption branch.....	149
Figure S27. $\text{CO}_2$ sorption isotherms of CAU-8-ODB measured at 273 and at 298 K. Filled symbols represent the adsorption, empty symbols the desorption branch.....	149
Table S9. Working capacity of CAU-8-ODB for $\text{CO}_2$ . The total volumetric uptake of CAU-8-ODB was calculated by extrapolation of the total uptake isotherm using a dual site Langmuir model at 35 bar and found to be $291.8 \text{ cm}^3(\text{STP})\text{cm}^{-3}$ at 273K and $196.5 \text{ cm}^3(\text{STP})\text{cm}^{-3}$ at 298K.	



---

Using a desorption pressure of 5 bar, the working capacity of CO <sub>2</sub> (desorption pressure is at 5 bar) was obtained for 273 and 298 K. ....	150
Figure S28. CH <sub>4</sub> sorption isotherms of CAU-8-ODB measured at 273 and at 298 K. Filled symbols represent the adsorption, empty symbols the desorption branch. ....	150
Figure S29. CH <sub>4</sub> sorption isotherms of CAU-8-ODB measured at 273 and at 298 K. Filled symbols represent the adsorption, empty symbols the desorption branch. ....	151
Table S10. Working capacity for CAU-8-ODB for CH <sub>4</sub> . The working capacity for a desorption pressure of 5 bar was determined as follows: The total volumetric uptake of CAU-8-ODB was calculated by extrapolation of the total uptake isotherm using a dual site Langmuir model at 35 bar and found to be 314 cm <sup>3</sup> (STP)cm <sup>-3</sup> at 273K and 216 cm <sup>3</sup> (STP)cm <sup>-3</sup> at 298K. ....	151
Figure S30: CO <sub>2</sub> sorption isotherm of CAU-21-ODB measured at 298 K. ....	152
Figure S31. The PXRD refinement result of [Al(HODB) <sub>2</sub> (OH)]. ....	154
Figure S32. SEM micrograph of a crystal of [Al(HODB) <sub>2</sub> (OH)]. ....	154
Table S10. Crystallographic data of [Al(HODB) <sub>2</sub> (OH)] obtained from single crystal data and PXRD data refinement. ....	155
Figure S33. (a) The coordination environment of Al <sup>3+</sup> and ODB <sup>2-</sup> ions in [Al(ODB) <sub>2</sub> (OH)]. (b) and (c) view of the crystal structure along [010] and [100], respectively. ....	156
Table S11. Selected bond lengths of [Al(HODB) <sub>2</sub> (OH)]. ....	156

**Table S1.** Molar ratios and exact amounts of the reactants employed in the HT experiments for CAU-21-BPDC.

metal source	No.	equivalent H <sub>2</sub> BPDC	equivalent Al <sup>3+</sup>	benzoic acid [mg]	H <sub>2</sub> BPDC [mg]	Al <sup>3+</sup> [ $\mu$ L/mg]	V H <sub>2</sub> O [ $\mu$ L]	V DMF [ $\mu$ L]	temperature program
2 M Al(NO <sub>3</sub> ) <sub>3</sub> · 9H <sub>2</sub> O in H <sub>2</sub> O	1	3	4	0	30	74.1	125.9	300	1h/12h\1h 135°C
	2	4	4	0	40	74.1	125.9	300	
	3	5	4	0	50	74.1	125.9	300	
	4	4	5	0	40	92.6	107.4	300	
	5	5	5	0	50	92.6	107.4	300	
	6	6	5	0	60	92.6	107.4	300	
	7	5	6	0	50	111.1	88.9	300	
	8	6	6	0	60	111.1	88.9	300	
	9	7	6	0	70	111.1	88.9	300	
	10	6	7	0	60	129.6	70.4	300	
	11	7	7	0	70	129.6	70.4	300	
	12	8	7	0	80	129.6	70.4	300	
	13	3	4	10	30	74.1	125.9	300	
	14	4	4	10	40	74.1	125.9	300	
	15	5	4	10	50	74.1	125.9	300	
	16	4	5	10	40	92.6	107.4	300	
	17	5	5	10	50	92.6	107.4	300	
	18	6	5	10	60	92.6	107.4	300	
	19	5	6	10	50	111.1	88.9	300	
	20	6	6	10	60	111.1	88.9	300	
	21	7	6	10	70	111.1	88.9	300	
	22	6	7	10	60	129.6	70.4	300	
	23	7	7	10	70	129.6	70.4	300	
	24	8	7	10	80	129.6	70.4	300	
	25	5	4	10	50	74.1	325.9	100	
	26	5	4	10	50	74.1	275.9	150	
	27	5	4	10	50	74.1	225.9	200	
	28	5	4	10	50	74.1	175.9	250	
	29	5	4	10	50	74.1	125.9	300	
	30	5	4	10	50	74.1	75.9	350	
	31	5	4	15	50	74.1	325.9	100	
	32	5	4	15	50	74.1	275.9	150	
	33	5	4	15	50	74.1	225.9	200	
	34	5	4	15	50	74.1	175.9	250	
	35	5	4	15	50	74.1	125.9	300	
	36	5	4	15	50	74.1	75.9	350	
	37	4	4	10	40	74.1	75.9	350	
	38	5	4	10	50	74.1	75.9	350	
	39	6	4	10	60	74.1	75.9	350	
	40	4	4	10	40	74.1	25.9	400	
	41	5	4	10	50	74.1	25.9	400	
	42	6	4	10	60	74.1	25.9	400	
	43	3	4	10	30	74.1	125.9	300	
	44	4	4	10	40	74.1	125.9	300	1h/12h\1h 120°C

45	5	4	10	50	74.1	125.9	300
46	4	5	10	40	92.6	107.4	300
47	5	5	10	50	92.6	107.4	300
48	6	5	10	60	92.6	107.4	300
49	5	6	10	50	111.1	88.9	300
50	6	6	10	60	111.1	88.9	300
51	7	6	10	70	111.1	88.9	300
52	6	7	10	60	129.6	70.4	300
53	7	7	10	70	129.6	70.4	300
54	8	7	10	80	129.6	70.4	300
55	3	4	10	30	74.1	125.9	300
56	4	4	10	40	74.1	125.9	300
57	5	4	10	50	74.1	125.9	300
58	4	5	10	40	92.6	107.4	300
59	5	5	10	50	92.6	107.4	300
60	6	5	10	60	92.6	107.4	300
61	5	6	10	50	111.1	88.9	300
62	6	6	10	60	111.1	88.9	300
63	7	6	10	70	111.1	88.9	300
64	6	7	10	60	129.6	70.4	300
65	7	7	10	70	129.6	70.4	300
66	8	7	10	80	129.6	70.4	300
67	3	4	10	30	74.1	125.9	300
68	4	4	10	40	74.1	125.9	300
69	5	4	10	50	74.1	125.9	300
70	4	5	10	40	92.6	107.4	300
71	5	5	10	50	92.6	107.4	300
72	6	5	10	60	92.6	107.4	300
73	5	6	10	50	111.1	88.9	300
74	6	6	10	60	111.1	88.9	300
75	7	6	10	70	111.1	88.9	300
76	6	7	10	60	129.6	70.4	300
77	7	7	10	70	129.6	70.4	300
78	8	7	10	80	129.6	70.4	300
79	3	4	10	30	74.1	225.9	200
80	4	4	10	40	74.1	225.9	200
81	5	4	10	50	74.1	225.9	200
82	4	5	10	40	92.6	207.4	200
83	5	5	10	50	92.6	207.4	200
84	6	5	10	60	92.6	207.4	200
85	5	6	10	50	111.1	188.9	200
86	6	6	10	60	111.1	188.9	200
87	7	6	10	70	111.1	188.9	200
88	6	7	10	60	129.6	170.4	200
89	7	7	10	70	129.6	170.4	200
90	8	7	10	80	129.6	170.4	200

16h/24h/72h 110°C

**Table S2.** Molar ratios and exact amounts of the reactants employed in the HT experiments for CAU-8-ODB and CAU-21-ODB.

metal source	No.	equivalent H <sub>2</sub> ODB	equivalent Al <sup>3+</sup>	H <sub>2</sub> ODB [mg]	Al <sup>3+</sup> [ $\mu$ L/mg]	V H <sub>2</sub> O [ $\mu$ L]	V DMF [ $\mu$ L]	temperature program
AlCl <sub>3</sub> ·6H <sub>2</sub> O	1	1	0.3	12	3.4	0	500	1h/12h\1h 140°C
	2	1	0.4	12	4.5	0	500	
	3	1	0.5	12	5.6	0	500	
	4	1	0.6	12	6.7	0	500	
	5	1	0.7	12	7.9	0	500	
	6	1	0.8	12	9	0	500	
	7	1.5	0.45	18	5	0	500	
	8	1.5	0.6	18	6.7	0	500	
	9	1.5	0.75	18	8.4	0	500	
	10	1.5	0.9	18	10.1	0	500	
	11	1.5	1.05	18	11.8	0	500	
	12	1.5	1.2	18	13.5	0	500	
	13	2	0.6	24	6.7	0	500	
	14	2	0.8	24	9	0	500	
	15	2	1	24	11.2	0	500	
	16	2	1.2	24	13.5	0	500	
	17	2	1.4	24	15.7	0	500	
	18	2	1.6	24	18	0	500	
	19	2.5	0.75	30	8.4	0	500	
	20	2.5	1	30	11.2	0	500	
	21	2.5	1.25	30	14	0	500	
	22	2.5	1.5	30	16.8	0	500	
	23	2.5	1.75	30	19.6	0	500	
	24	2.5	2	30	22.4	0	500	
2 M Al(NO <sub>3</sub> ) <sub>3</sub> ·9H <sub>2</sub> O in H <sub>2</sub> O	25	1	0.8	12.0	9.0	0.0	500.0	1h/12h\1h 170°C
	26	1	0.8	12.0	9.0	50.0	450.0	
	27	1	0.8	12.0	9.0	100.0	400.0	
	28	1	1	12.0	11.2	0.0	500.0	
	29	1	1	12.0	11.2	50.0	450.0	
	30	1	1	12.0	11.2	100.0	400.0	
	31	2	1.6	24.0	17.9	0.0	500.0	
	32	2	1.6	24.0	17.9	50.0	450.0	
	33	2	1.6	24.0	17.9	100.0	400.0	
	34	2	2	24.0	22.4	0.0	500.0	
	35	2	2	24.0	22.4	50.0	450.0	
	36	2	2	24.0	22.4	100.0	400.0	
Al(SO <sub>4</sub> ) <sub>3</sub> ·19H <sub>2</sub> O	37	5	3	60.0	69.7	180.3	250.0	1h/12h\1h 145°C
	38	5	3.5	60.0	81.3	168.7	250.0	
	39	5	4.5	60.0	104.6	145.4	250.0	
	40	5	5.5	60.0	127.8	122.2	250.0	
	41	5	6.5	60.0	151.0	99.0	250.0	
	42	5	7	60.0	162.6	87.4	250.0	
Al(SO <sub>4</sub> ) <sub>3</sub> ·19H <sub>2</sub> O	43	1	0.3	12.0	9.3	0.0	500.0	1h/12h\1h 125°C
	44	1	0.3	12.0	9.3	50.0	450.0	

	45	1	0.3	12.0	9.3	100.0	400.0	
	46	1	0.5	12.0	15.5	0.0	500.0	
	47	1	0.5	12.0	15.5	50.0	450.0	
	48	1	0.5	12.0	15.5	100.0	400.0	
	49	2	0.6	24.0	18.6	0.0	500.0	
	50	2	0.6	24.0	18.6	50.0	450.0	
	51	2	0.6	24.0	18.6	100.0	400.0	
	52	2	1	24.0	30.9	0.0	500.0	
	53	2	1	24.0	30.9	50.0	450.0	
	54	2	1	24.0	30.9	100.0	400.0	
0.5 M $\text{Al}(\text{NO}_3)_3 \cdot 9\text{H}_2\text{O}$ in DMF	55	2	0.5	20.0	38.7	0.0	961.3	1h/12h/1h 125°C
	56	2	0.75	20.0	58.1	0.0	941.9	
	57	2	1	20.0	77.5	0.0	922.5	
	58	2	1.25	20.0	96.8	0.0	903.2	
	59	2	1.5	20.0	116.2	0.0	883.8	
	60	2	2	20.0	154.9	0.0	845.1	
	61	3	0.5	30.0	38.7	0.0	961.3	
	62	3	1	30.0	77.5	0.0	922.5	
	63	3	1.5	30.0	116.2	0.0	883.8	
	64	3	2	30.0	154.9	0.0	845.1	
	65	3	2.5	30.0	193.6	0.0	806.4	
	66	3	3	30.0	232.4	0.0	767.6	
	67	4	0.5	40.0	38.7	0.0	961.3	
	68	4	1.5	40.0	116.2	0.0	883.8	
	69	4	2	40.0	154.9	0.0	845.1	
	70	4	2.5	40.0	193.6	0.0	806.4	
	71	4	3	40.0	232.4	0.0	767.6	
	72	4	4	40.0	309.8	0.0	690.2	
	73	5	1	50.0	77.5	0.0	922.5	
	74	5	2	50.0	154.9	0.0	845.1	
	75	5	2.5	50.0	193.6	0.0	806.4	
	76	5	3	50.0	232.4	0.0	767.6	
	77	5	4	50.0	309.8	0.0	690.2	
	78	5	5	50.0	387.3	0.0	612.7	

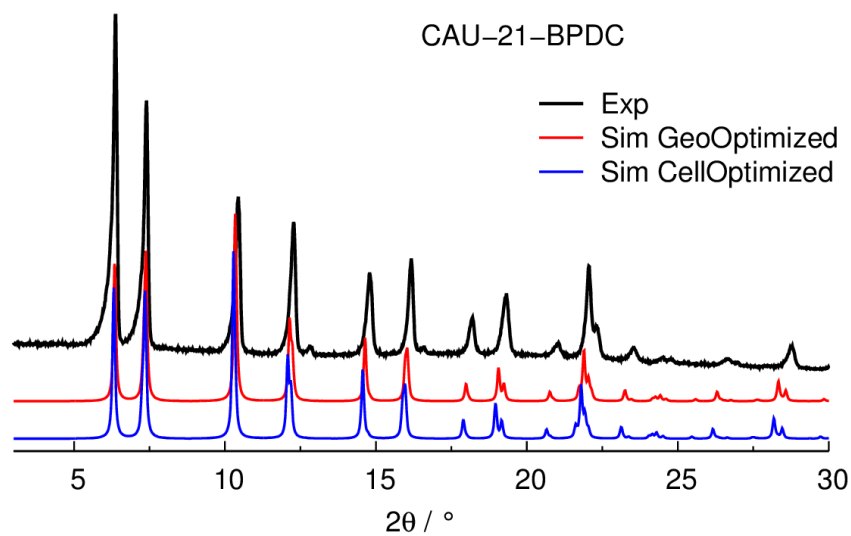


**Figure S1.** Comparison of the measured PXRD pattern of CAU-21-BPDC with the ones calculated from minimum energy structures obtained from DFT calculations.

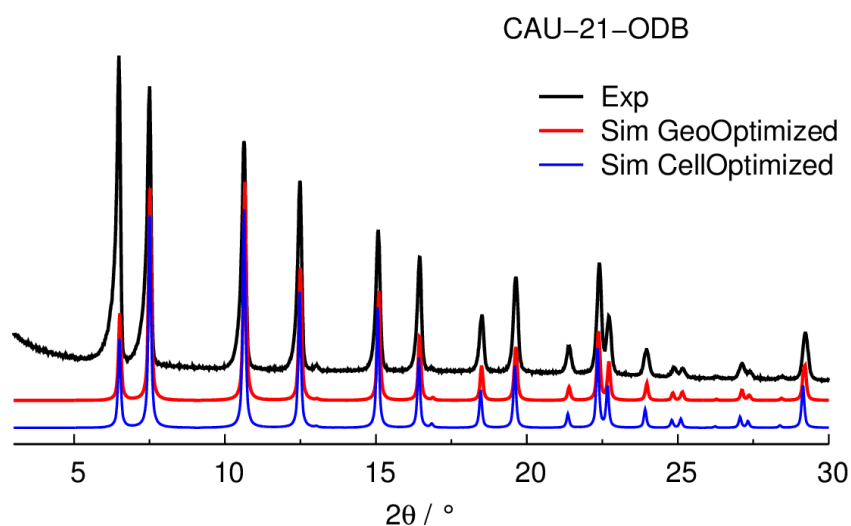


**Figure S2.** Comparison of the measured PXRD pattern of CAU-21-ODB with the ones calculated from minimum energy structures obtained from DFT calculations.

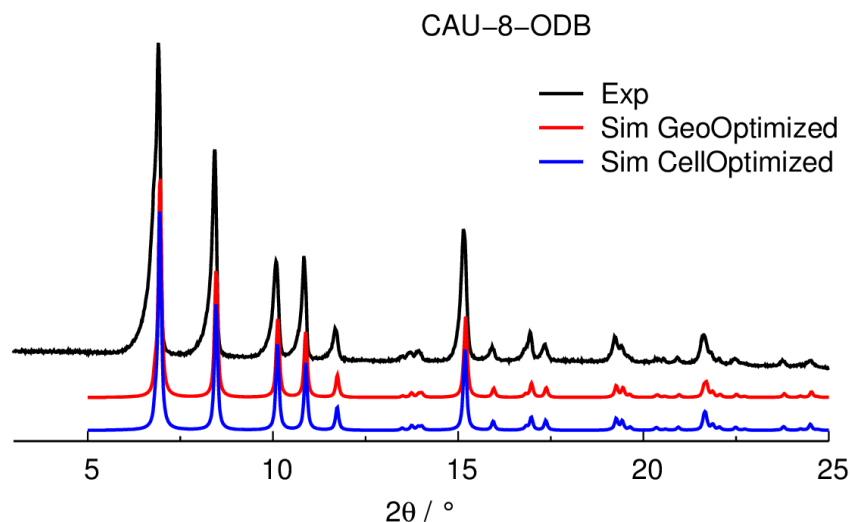


**Figure S3.** Comparison of the measured PXRD pattern of CAU-8-ODB with the ones calculated from minimum energy structures obtained from DFT calculations.

**Table S3.** Structural and energetic comparison of CAU-8-BPDC and CAU-21-BPDC.

	CAU-8-BPDC		CAU-21-BPDC	
	Experiment	Simulation	Experiment	Simulation
SG	ITA-88: $I4_1/a$	ITA-88: $I4_1/a$	ITA-97: $I422$	ITA-97: $I422$
$a=b / \text{Å}$	13.0625	13.059	17.098	17.187
$c / \text{Å}$	52.565	52.795	23.930	24.019
$V / \text{Å}^3$	8969.11	9000.53	6995.73	7095.04
Energy (kcal/mol/atom)	-3829.5911*	-3829.6007	-3829.6748*	-3829.6984

\* atomic positions were optimized

**Table S4.** Structural and energetic comparison of CAU-8-ODB and CAU-21-ODB.

	CAU-8-ODB		CAU-21-ODB	
	Experiment	Simulation	Experiment	Simulation
SG	ITA-88: $I4_1/a$	ITA-88: $I4_1/a$	ITA-97: $I422$	ITA-97: $I422$
$a=b / \text{Å}$	13.1035	13.1190	16.5838	16.6220
$c / \text{Å}$	51.7576	51.708	23.5178	23.5280
$V / \text{Å}^3$	8886.85	8899.37	6467.43	6500.57
Energy (kcal/mol/atom)	-3838.1064*	-3838.1193	-3838.2956*	-3838.2969

\* atomic positions were optimized

**Table S5.** Selected bond lengths of CAU-21-BPDC.

atom 1	atom 2	distance / Å	atom 1	atom 2	distance / Å
Al1	O1	1.923(4)	C3	C4	1.364(9)
	O4	1.897(4)	C4	C5	1.367(9)
	O5	1.864(4)	C5	C6	1.374(9)
Al2	O2	1.899(4)		C8	1.491(8)
	O3	1.892(4)	C6	C7	1.397(10)
	O5	1.856(4)	C9	C10	1.369(10)
O1	C8	1.242(7)		C14	1.400(10)
O2	C8	1.278(7)	C10	C11	1.351(11)
O3	C15	1.251(7)	C11	C12	1.349(11)
O4	C15	1.250(7)	C12	C13	1.376(11)
C1	O6	1.241(10)	C13	C14	1.338(10)
C1	C2	1.462(10)	C14	C15	1.488(9)
	C11	1.513(11)			
C2	C7	1.348(10)			
	C3	1.374(10)			

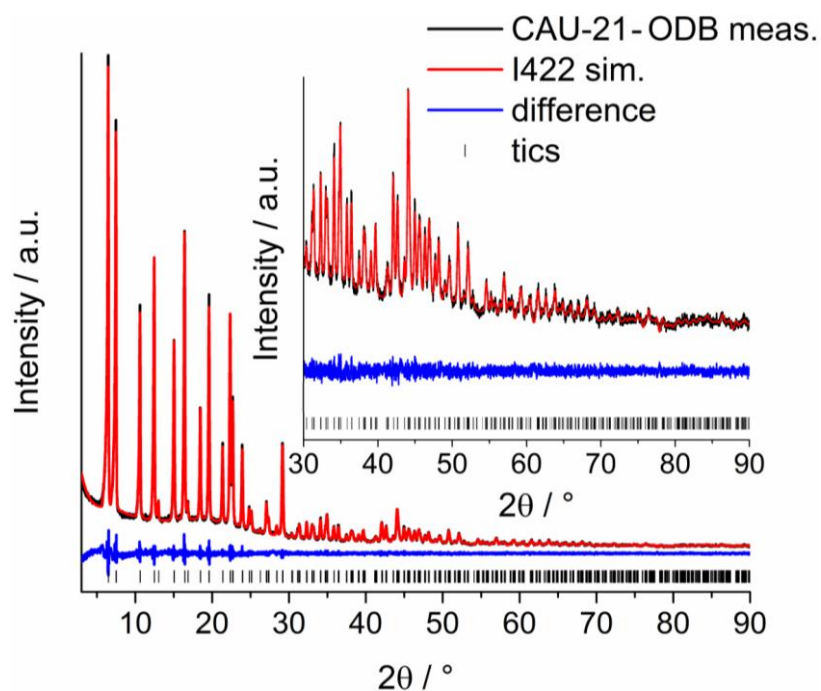
**Table S6.** Selected bond lengths of CAU-8-ODB. For the parts refined using rigid bodies no standard deviations are given.

atom 1	atom 2	distance / Å	atom 1	atom 2	distance / Å
Al1	O1	1.876(21)	C1	C2	1.480
	O2	1.914(18)	C2	C3	1.408
	O5	1.920(20)		C7	1.407
Al2	O4	1.840(20)	C3	C4	1.399
	O3	1.833(17)	C4	C5	1.402
	O1	1.914(21)	C5	C6	1.413
O2	C1	1.275(16)	C6	C7	1.397
O3	C1	1.280(15)	C8	C9	1.398
O4	C14	1.279(18)		C13	1.411
O5	C14	1.300(20)	C9	C10	1.397
O6	C5	1.529(15)	C10	C11	1.411
	C9	1.501(14)	C11	C12	1.410
				C14	1.486
			C12	C13	1.403



**Table S7.** Selected bond lengths of the crystal structure of CAU-21-ODB obtained from DFT calculations.

atom 1	atom 2	distance / Å	atom 1	atom 2	distance / Å	
Al1	O1	1.9035	C1	C2	1.4896	
	O4	1.8958		C2	C3	1.4028
	O5	1.8714		C7	C4	1.4012
Al2	O5	1.8804		C3	C4	1.3910
	O2	1.9392		C4	C5	1.3950
	O3	1.9188		C5	C6	1.3941
O1	C14	1.2759		C6	C7	1.3916
O2	C14	1.2816		C8	C9	1.4032
O3	C1	1.2752		C13	C10	1.4011
O4	C1	1.2708		C9	C11	1.3914
O6	C5	1.3978		C10	C12	1.4007
	C8	1.3769		C11	C14	1.4074
				C12	C13	1.4835
						1.3853

**Figure S4.** Plot of the Pawley refinement of CAU-21-ODB.

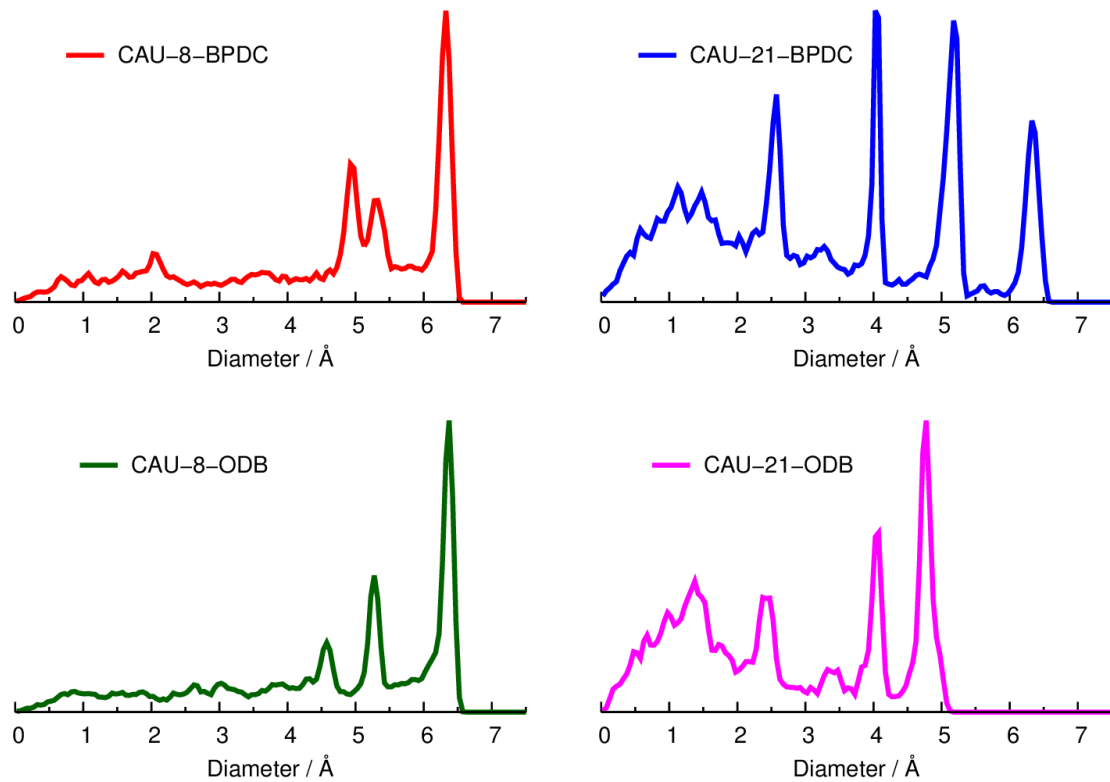


**Figure S5.** Pore size distributions of CAU-8 and CAU-21 (-BPDC and -ODB) calculated from the DFT calculated crystal structures.

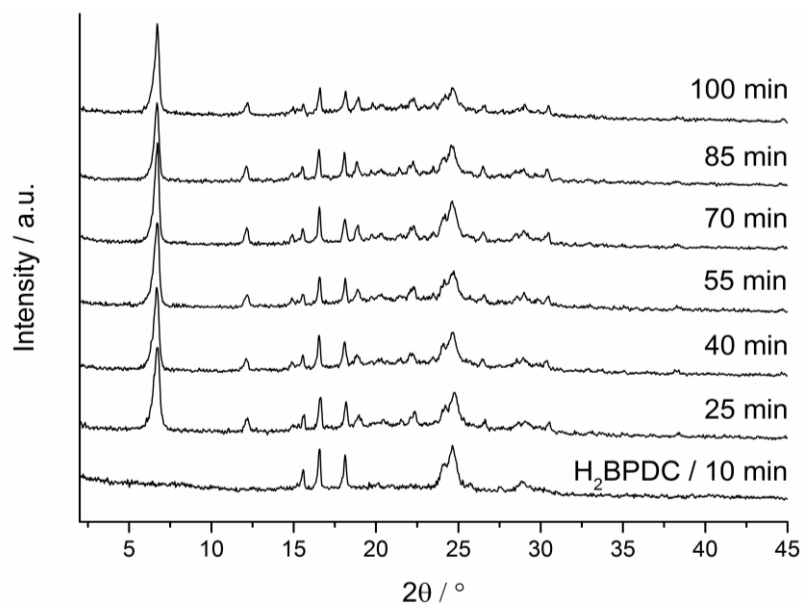


**Figure S6.** PXRD patterns of the *ex situ* quenching experiments of the intermediate carried out at 130 °C. After 25 mins the intermediate has formed.

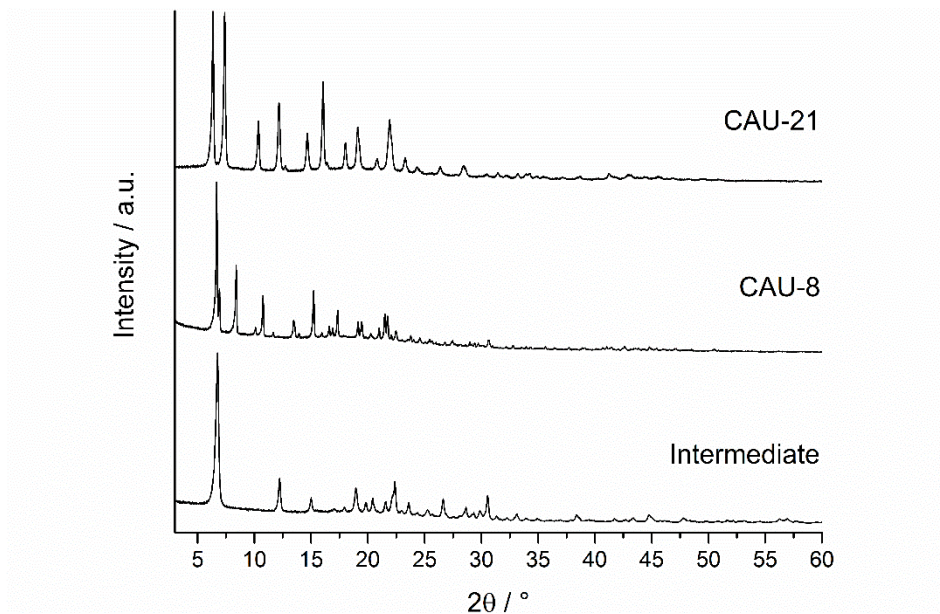


**Figure S7.** Comparison of high resolution PXRD patterns of the intermediate obtained from the *ex situ* quenching experiments and PXRD patterns of CAU-8-BPDC and CAU-21-BPDC. The intermediate was washed in DMF at 60 °C for 3h to remove residual linker molecules.

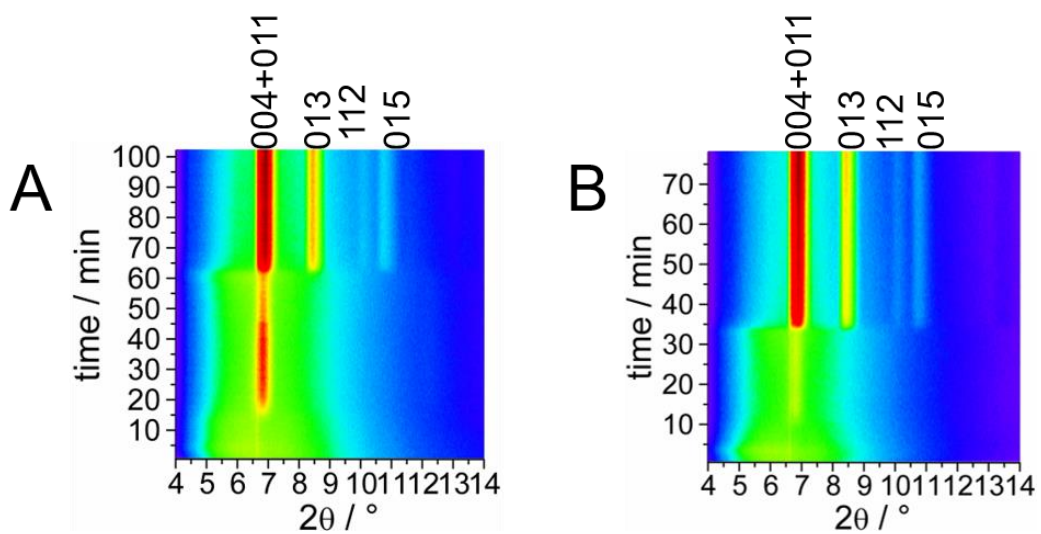


**Figure S8.** Results of the *in situ* time resolved PXRD investigation of CAU-8-BPDC at 140 °C (A) and at 150 °C (B) in top view. Reflections of CAU-8-BPDC are marked with their hkl indices.

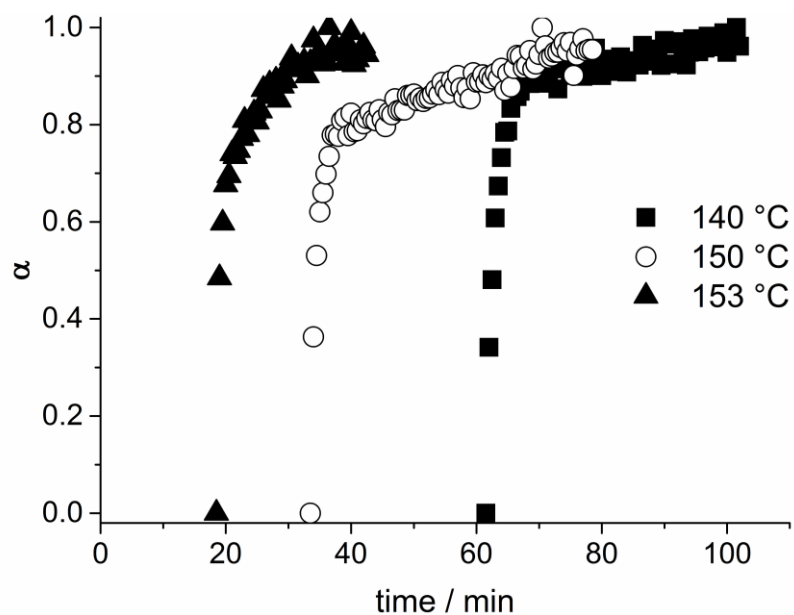


**Figure S9.** Comparison of the reaction progress ( $\alpha$ ) of CAU-8-BPDC obtained from the normalized intensities of the 013 reflection. The higher the temperature the faster CAU-8-BPDC is formed.

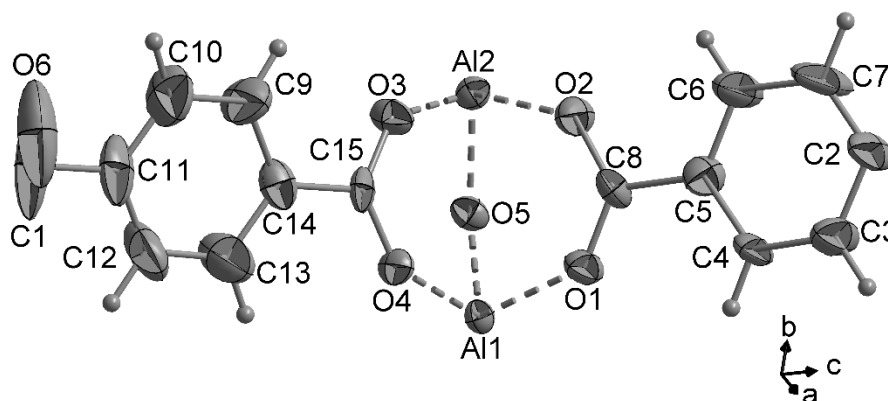


**Figure S10.** Asymmetric unit of CAU-21-BPDC with numbering scheme as used in Table S5.

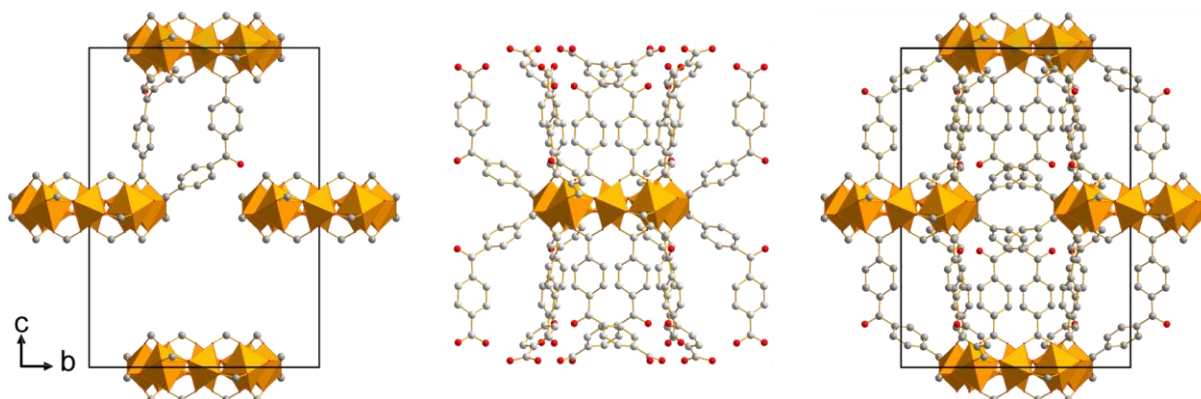


**Figure S11.** Crystal structure of CAU-21-BPDC. The connection between two IBUs is established via two linker molecules (left). Each IBU is connected by 16 linker molecules (middle), so that a 3D framework is formed (right).

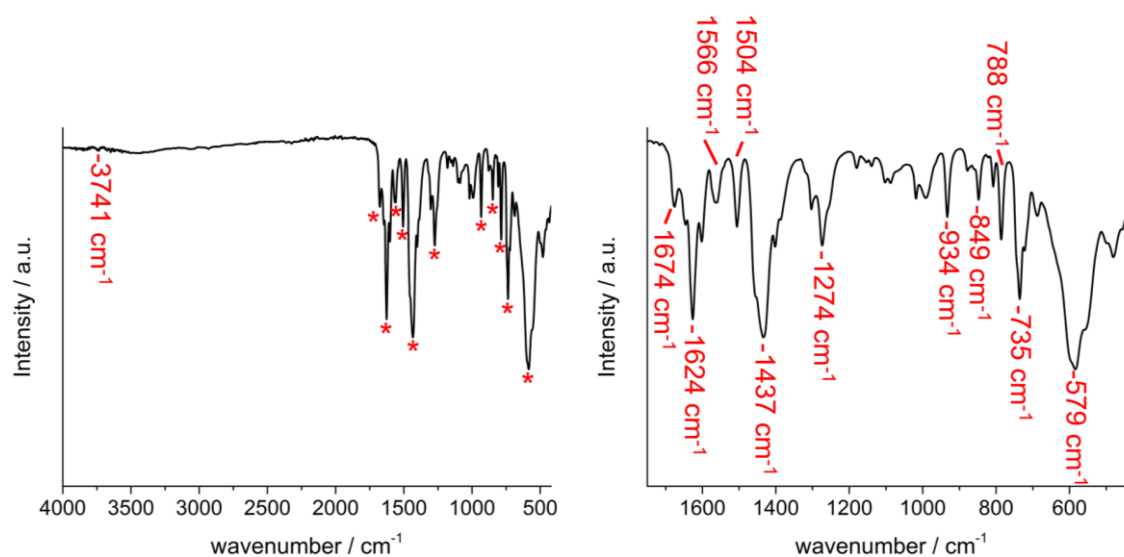


**Figure S12.** Infrared spectrum of CAU-21-BPDC, a detailed view is given on the right. Bands discussed in the manuscript are labeled with asterisks in the full spectrum and with wavenumbers in the detailed view.

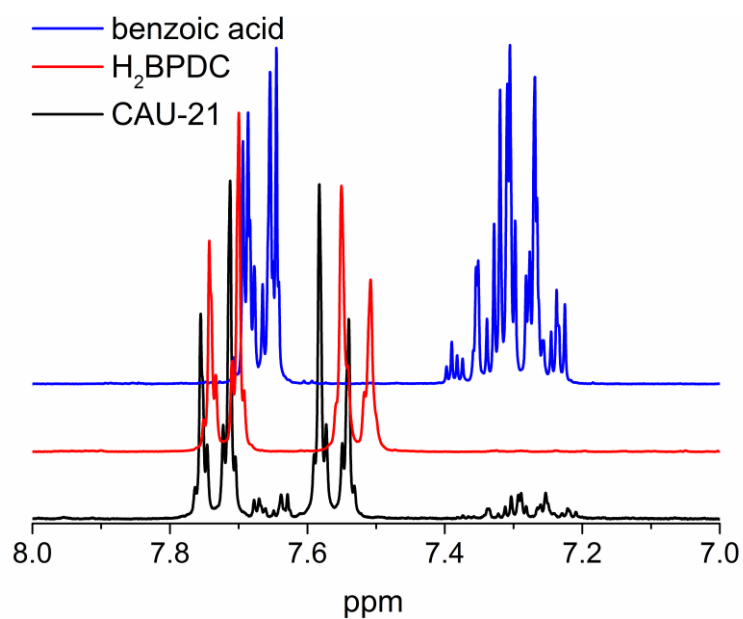


**Figure S13.** <sup>1</sup>H-NMR spectrum of CAU-21-BPDC (black) in comparison to the spectra of the H<sub>2</sub>BPDC linker (red) and benzoic acid (blue).

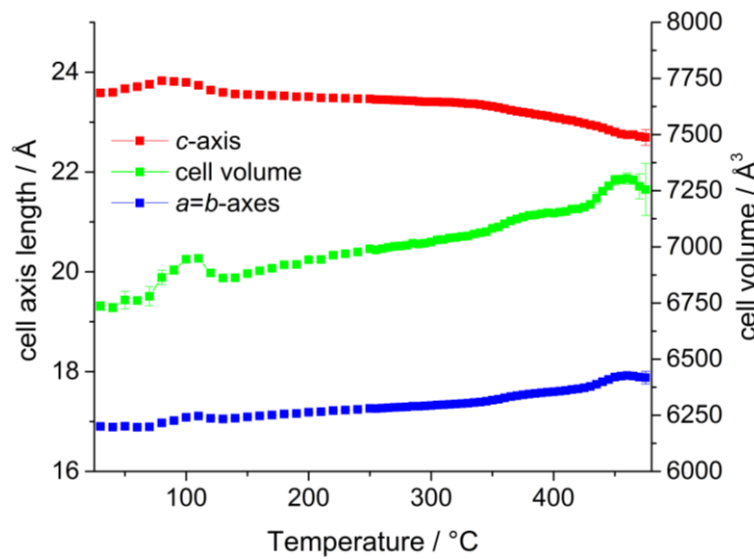


**Figure S14.** Results of the parametric Pawley refinement of CAU-21-BPDC.

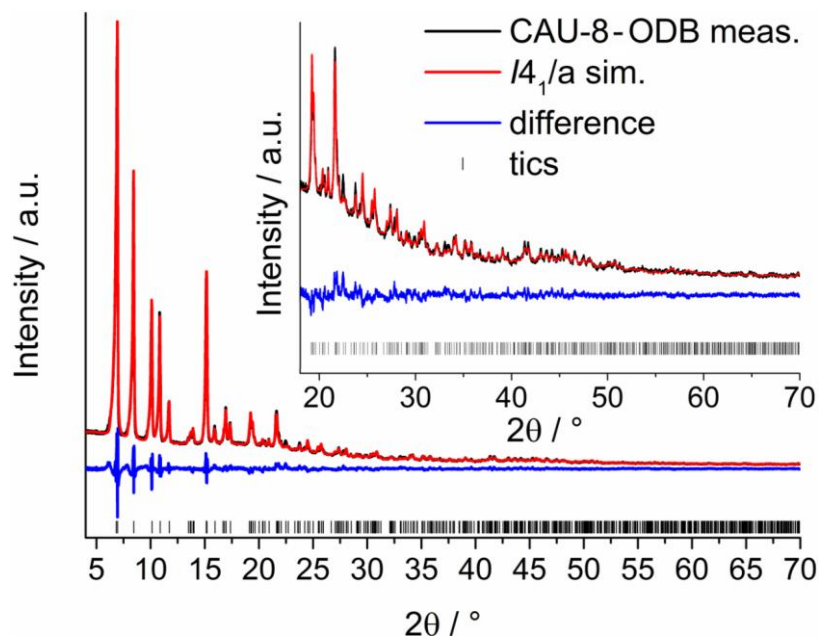


**Figure S15.** Final Rietveld plot of CAU-8-ODB.

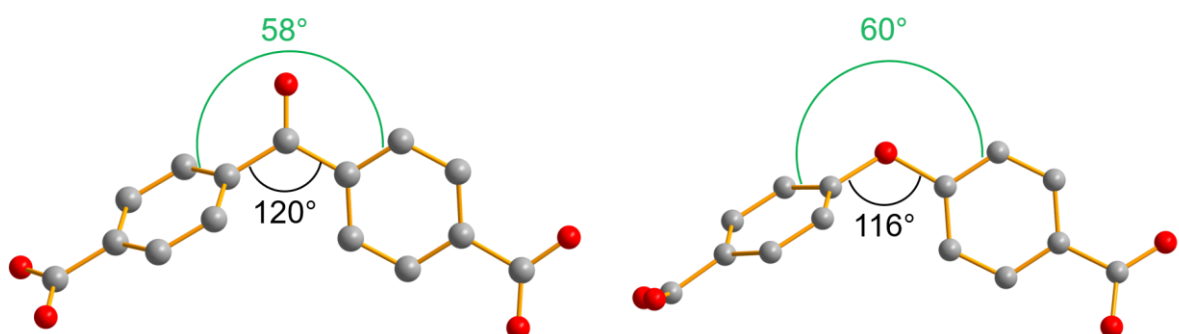


**Figure S16.** Comparison of the BPDC<sup>2-</sup> (left) and the ODB<sup>2-</sup> (right) ion in the CAU-8 structure. The angle between the aromatic rings is given in black and the torsion angle between the aromatic rings in green.

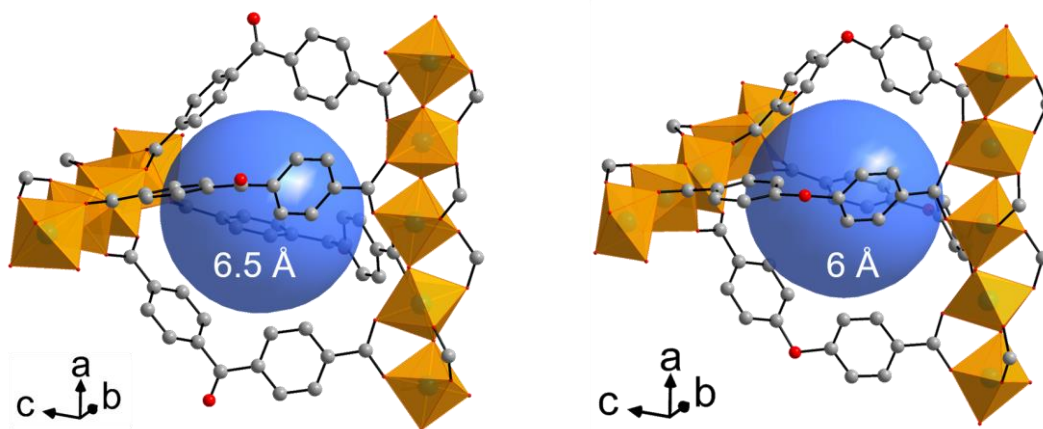


**Figure S17.** Comparison of the spherical cavities in the CAU-8-BPDC (left) and CAU-8-ODB (right).

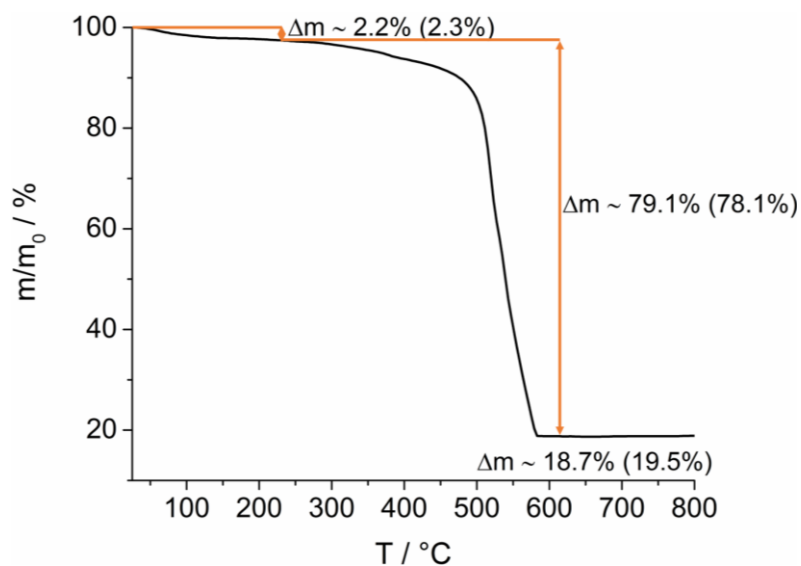


**Figure S18.** Results of the thermogravimetric measurements of CAU-8-ODB, measured with a heating rate of 4 K/min under air. The weight losses are marked in the graph, expected values are given in brackets.

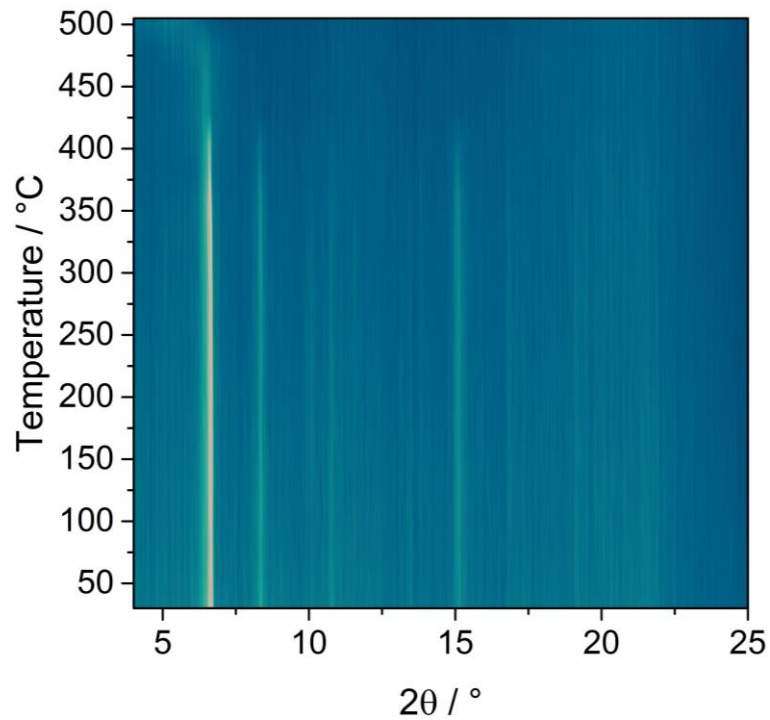


**Figure S19.** Results of the temperature dependent PXRD study of CAU-8-ODB.

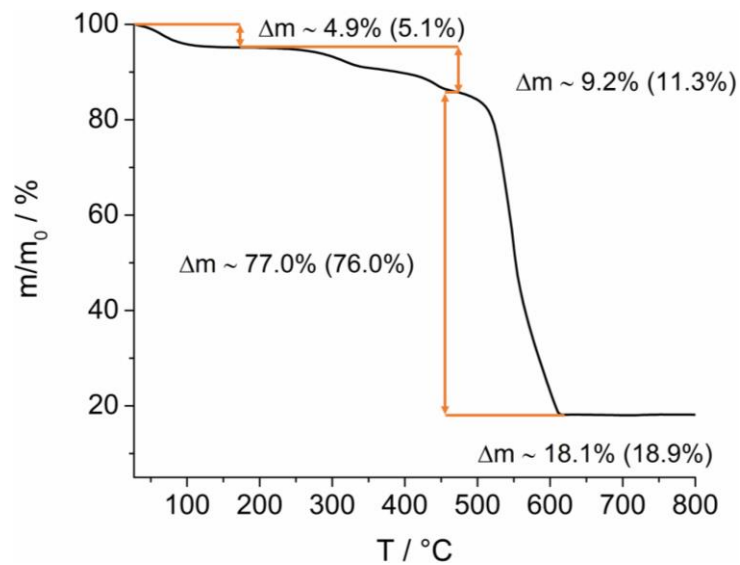


**Figure S20.** Results of the thermogravimetric measurements of CAU-21-ODB, measured with a heating rate of 4 K/min under air. The weight losses are marked in the graph, expected values are given in brackets.



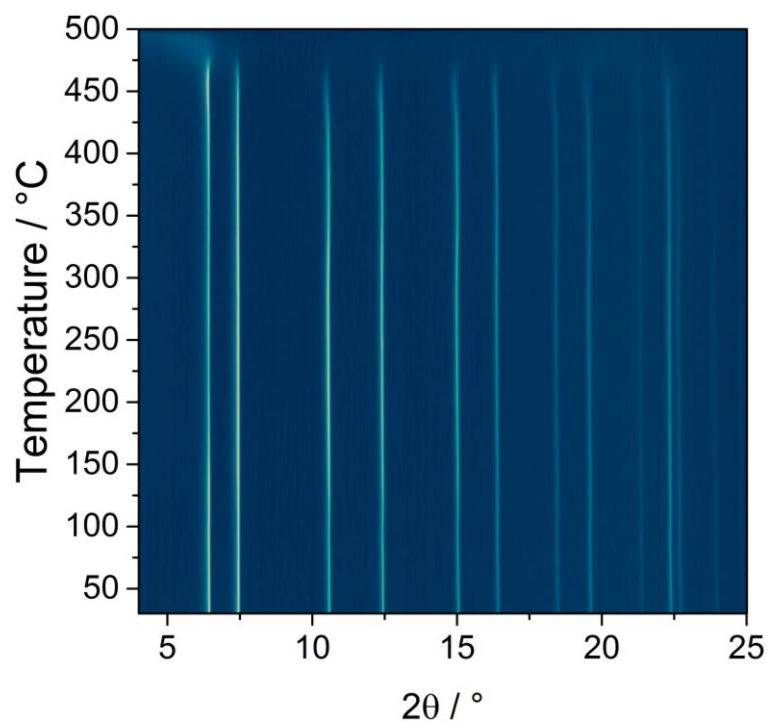


**Figure S21.** Results of the temperature dependent X-ray diffraction studies of CAU-21-ODB.

**Table S8.** Results of the elemental analyses for CAU-8-ODB and CAU-21-ODB. Measured percentages of nitrogen result from residual DMF molecules, which couldn't be removed upon activation.

	<b>[Al(OH)ODB]·0.4H<sub>2</sub>O</b>	<b>C [%]</b>	<b>H [%]</b>	<b>N [%]</b>
<b>CAU-8-ODB</b>	measured	54.8	3.1	0
	calculated	54.7	3.2	0
	<b>[Al(OH)ODB]·0.9H<sub>2</sub>O</b>	<b>C [%]</b>	<b>H [%]</b>	<b>N [%]</b>
<b>CAU-21-ODB</b>	measured	51.3	3.1	0.3
	calculated	53.1	5.1	0

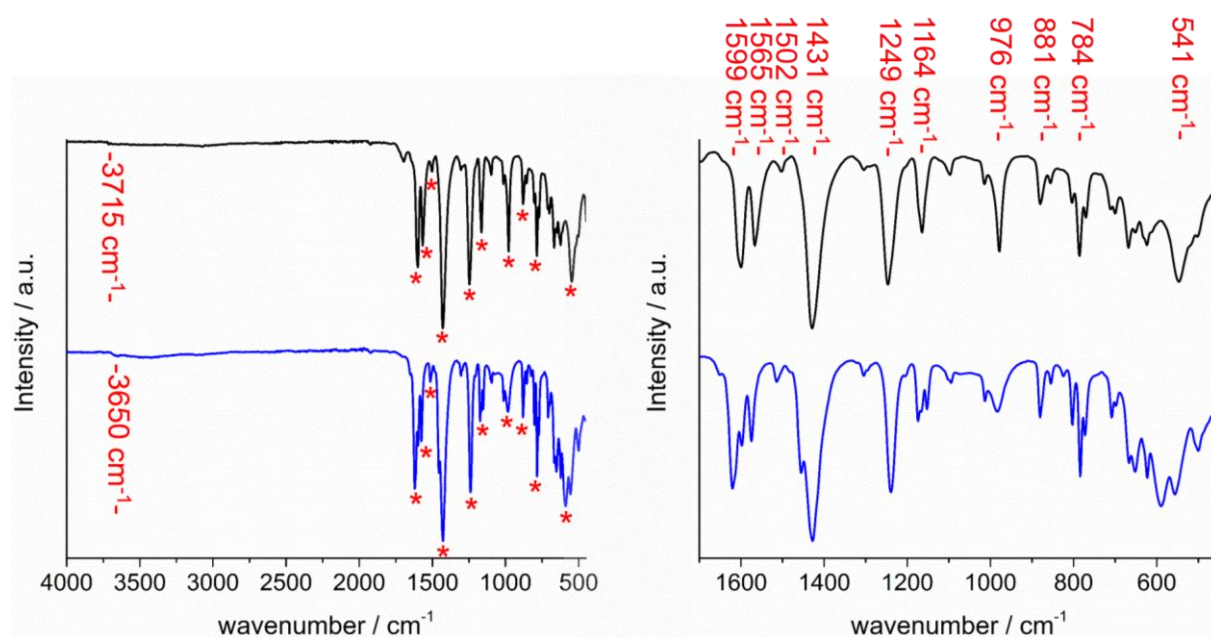


**Figure S22.** Infrared spectra of CAU-8-ODB (black) and CAU-21-ODB (blue), a detailed view is given on the right. Bands discussed in the manuscript are labeled with asterisks in the full spectrum and with wavenumbers in the detailed view.

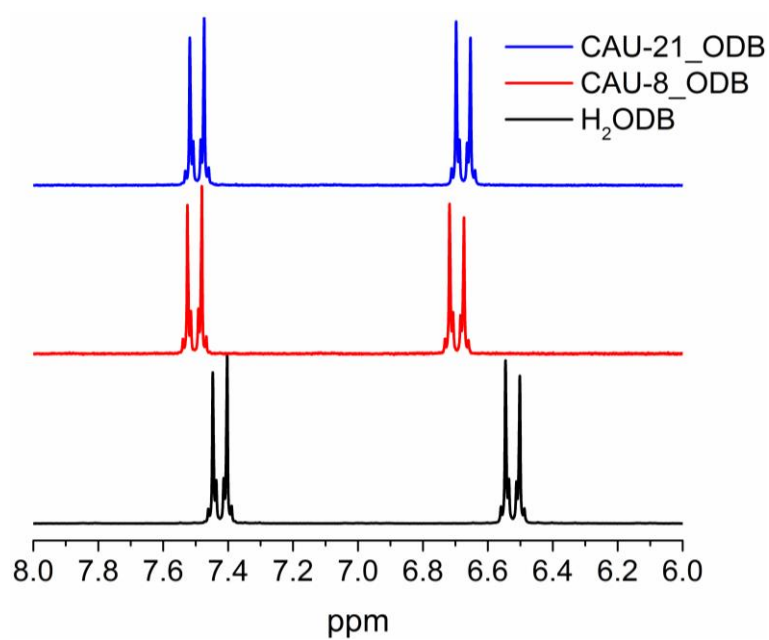


**Figure S23.**  $^1\text{H}$ -NMR spectra of CAU-8-ODB (red) and CAU-21-ODB (blue) in comparison to the spectra of the  $\text{H}_2\text{ODB}$  (black).

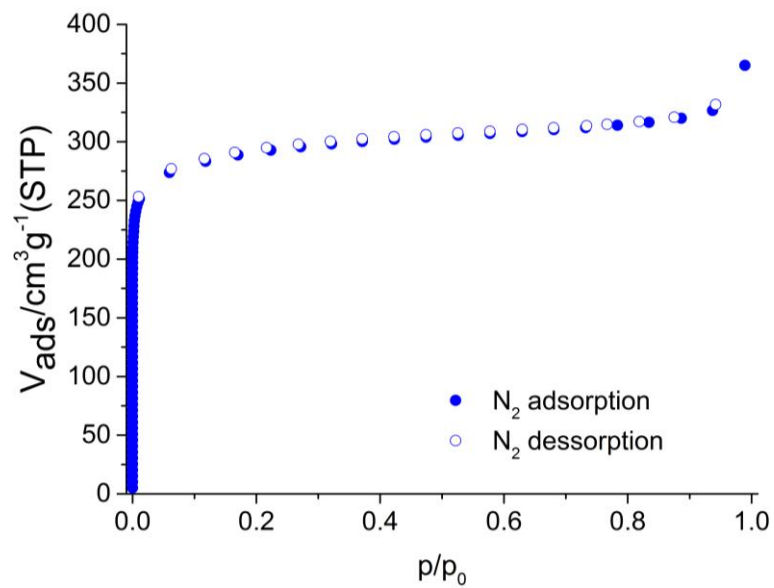


**Figure S24.** N<sub>2</sub> sorption isotherms of CAU-8-ODB measured at 77 K. Filled symbols represent the adsorption, empty symbols the desorption branch.

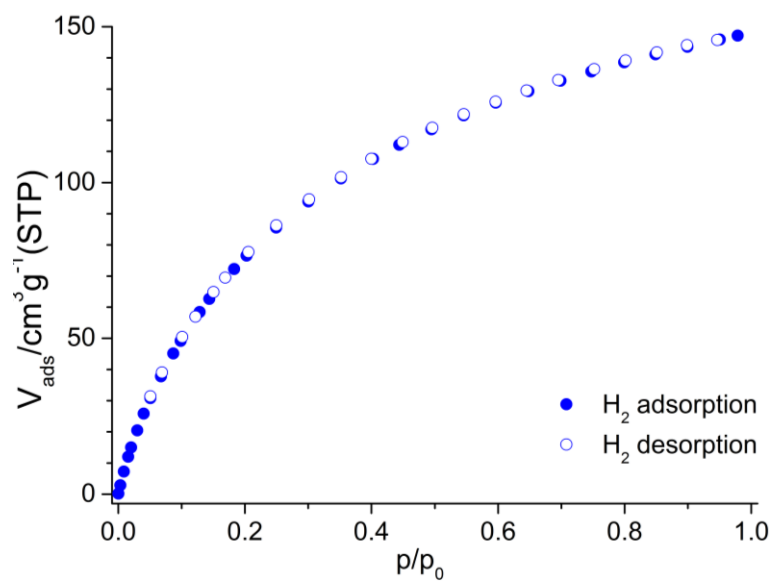


**Figure S25.** H<sub>2</sub> sorption isotherm of CAU-8-ODB measured at 77 K. Filled symbols represent the adsorption, empty symbols the desorption branch.

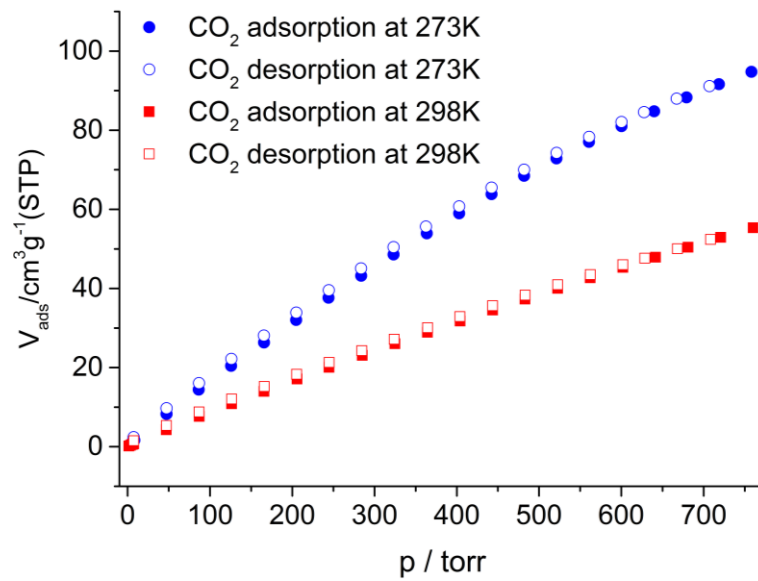


**Figure S26.** CO<sub>2</sub> sorption isotherms of CAU-8-ODB measured at 273 and at 298 K. Filled symbols represent the adsorption, empty symbols the desorption branch.

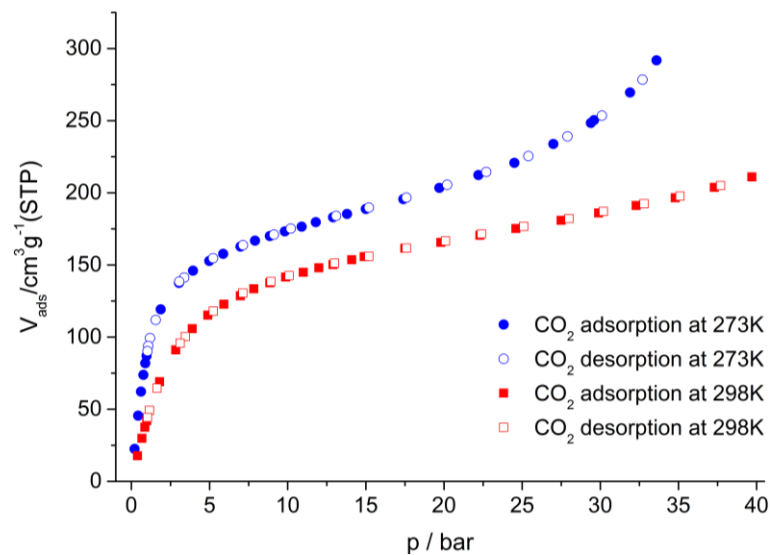


**Figure S27.** CO<sub>2</sub> sorption isotherms of CAU-8-ODB measured at 273 and at 298 K. Filled symbols represent the adsorption, empty symbols the desorption branch.

**Table S9.** Working capacity of CAU-8-ODB for CO<sub>2</sub>. The total volumetric uptake of CAU-8-ODB was calculated by extrapolation of the total uptake isotherm using a dual site Langmuir model at 35 bar and found to be 291.8 cm<sup>3</sup>(STP)cm<sup>-3</sup> at 273K and 196.5 cm<sup>3</sup>(STP)cm<sup>-3</sup> at 298K. Using a desorption pressure of 5 bar, the working capacity of CO<sub>2</sub> (desorption pressure is at 5 bar) was obtained for 273 and 298 K.

	Total CO <sub>2</sub> uptake at 30 bar (cm <sup>3</sup> /cm <sup>3</sup> )	Working capacity at 30 bar (cm <sup>3</sup> /cm <sup>3</sup> )
273K	253.7	100.8
298K	186.2	70.2

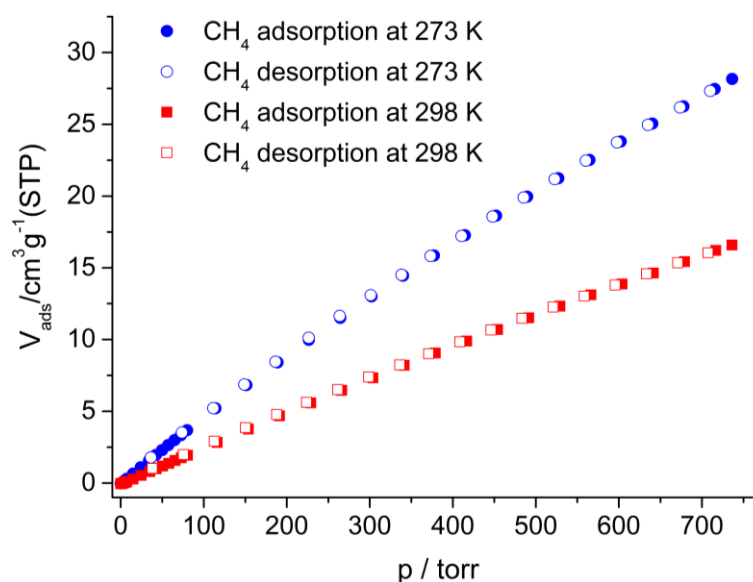


**Figure S28.** CH<sub>4</sub> sorption isotherms of CAU-8-ODB measured at 273 and at 298 K. Filled symbols represent the adsorption, empty symbols the desorption branch.

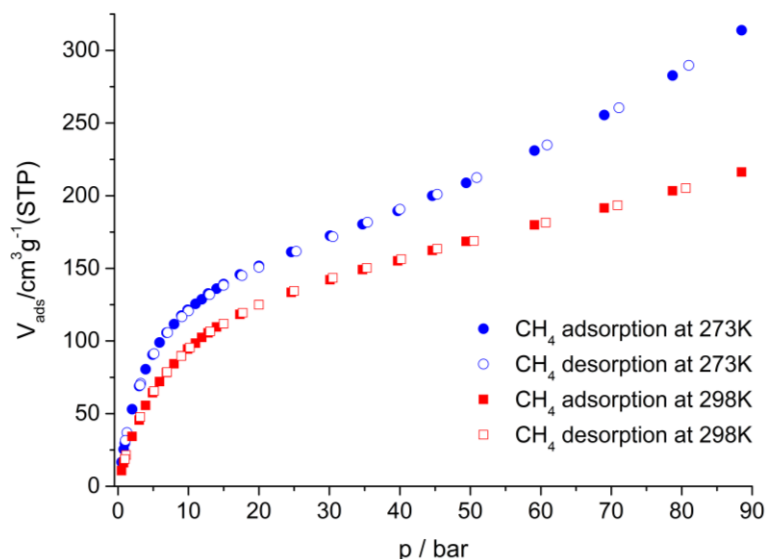


**Figure S29.**  $\text{CH}_4$  sorption isotherms of CAU-8-ODB measured at 273 and at 298 K. Filled symbols represent the adsorption, empty symbols the desorption branch.

**Table S10.** Working capacity for CAU-8-ODB for  $\text{CH}_4$ . The working capacity for a desorption pressure of 5 bar was determined as follows: The total volumetric uptake of CAU-8-ODB was calculated by extrapolation of the total uptake isotherm using a dual site Langmuir model at 35 bar and found to be  $314 \text{ cm}^3(\text{STP})\text{cm}^{-3}$  at 273K and  $216 \text{ cm}^3(\text{STP})\text{cm}^{-3}$  at 298K.

	Total $\text{CH}_4$ uptake at 35 bar ( $\text{cm}^3 / \text{cm}^3$ )	Working capacity at 35 bar ( $\text{cm}^3 / \text{cm}^3$ )	Total $\text{CH}_4$ uptake at 65 bar ( $\text{cm}^3 / \text{cm}^3$ )	Working capacity at 65 bar ( $\text{cm}^3 / \text{cm}^3$ )	Total $\text{CH}_4$ uptake at 80 bar ( $\text{cm}^3 / \text{cm}^3$ )	Working capacity at 80 bar ( $\text{cm}^3 / \text{cm}^3$ )
273K	181	90	246	154	287	196
298K	150	85	187	122	205	140

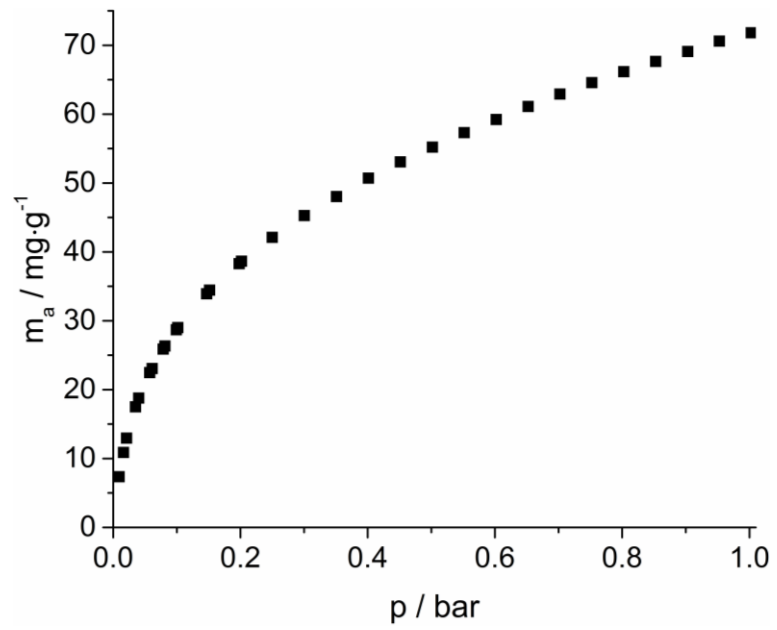


**Figure S30:** CO<sub>2</sub> sorption isotherm of CAU-21-ODB measured at 298 K.

REFINEMENT DETAILS FOR [Al(HODB)<sub>2</sub>(OH)]

**Powder X-Ray Diffraction Analysis of [Al(HODB)<sub>2</sub>(OH)].** The refinement of the single crystal data (not shown) resulted only in high R values ( $R_1 = 0.1295$ ). Therefore the structure of [Al(HODB)<sub>2</sub>(OH)] was determined from PXRD data using the Rietveld method. The structure model of [Al(HODB)<sub>2</sub>(OH)] was obtained from the single crystal data. Initially, only the Al atoms were included using the fractional coordinates. The lattice parameters were adjusted to the values obtained from the lattice parameter refinement of the PXRD data. Subsequently, the atoms of the 4,4'-oxybisdicarboxylate linker without hydrogen atoms were inserted. The geometry optimizations converged to give a plausible crystal structure by adjustments of the bond length of aluminum to oxygen atoms bond angles of O-Al-O. The calculated and measured powder X-ray diffraction patterns were in good agreement. The exported .res file was further examined by PLATON software by the Addsym command. This would produce a new suitable .res file for the further use on the structure analysis. The models were used as a starting point for the Rietveld refinement.

The structure model of [Al(HODB)<sub>2</sub>(OH)] was refined from the PXRD data of an of the activated sample, heated at 150 °C. The Rietveld refinement was carried out with the GSAS program. The structure was refined in the space group *P*-1 and the lattice parameters  $a=6.5149(6)$ ,  $b=12.7760(11)$ ,  $c=15.2145(10)$  Å,  $\alpha=101.9499(35)^\circ$ ,  $\beta=94.313(6)^\circ$ , and  $\gamma=101.579(7)^\circ$  were obtained. The final Rietveld plot and the results of the structure refinement is shown in Figure S31.



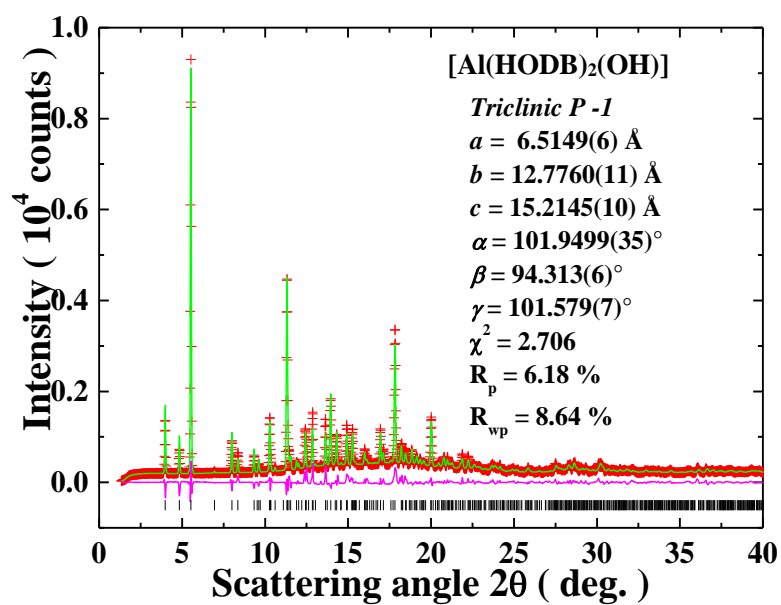


Figure S31. The PXRD refinement result of  $[\text{Al}(\text{HODB})_2(\text{OH})]$ .

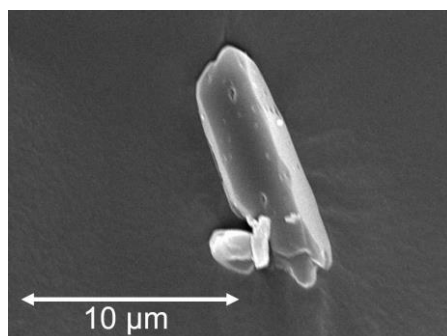
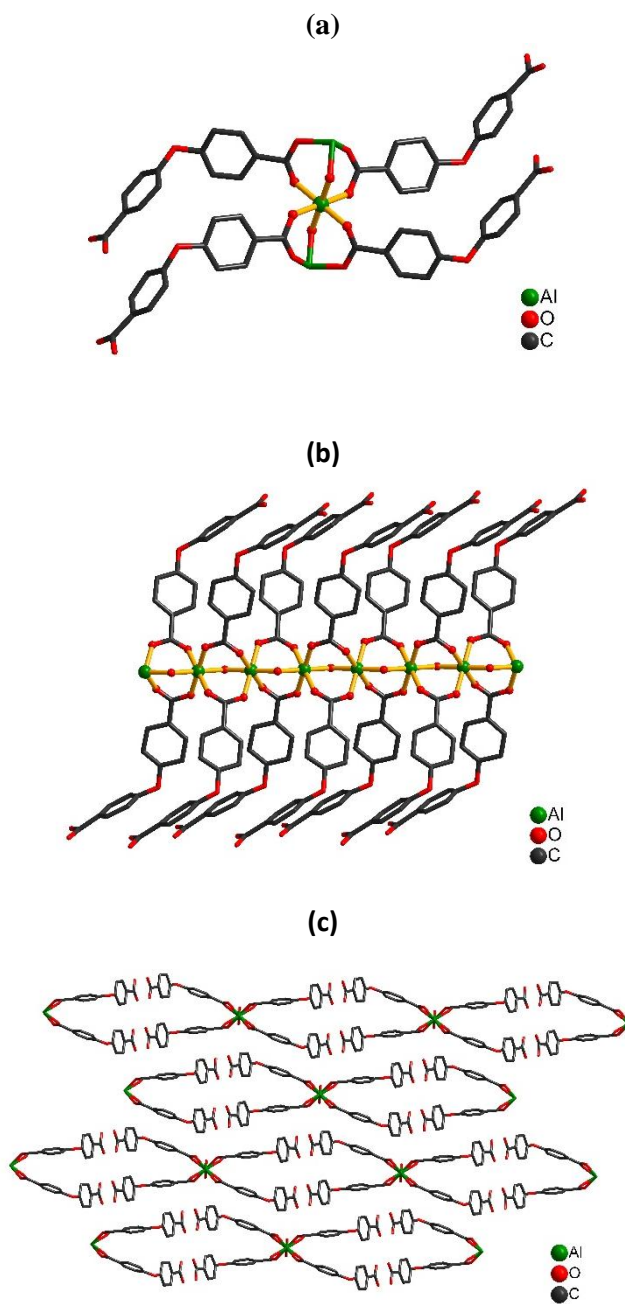


Figure S32. SEM micrograph of a crystal of  $[\text{Al}(\text{HODB})_2(\text{OH})]$ .

**Table S10.** Crystallographic data of [Al(HODB)<sub>2</sub>(OH)] obtained from single crystal data and PXRD data refinement.

	[Al(HODB) <sub>2</sub> (OH)]	[Al(HODB) <sub>2</sub> (OH)]
formula	C <sub>56</sub> H <sub>16</sub> Al <sub>2</sub> O <sub>22</sub>	C <sub>56</sub> Al <sub>2</sub> O <sub>22</sub>
fw	1094.676	1078.566
space group	<i>P</i> -1	<i>P</i> -1
<i>a</i> , Å	6.553 (1)	6.5149(6)
<i>b</i> , Å	12.868(3)	12.7760(11)
<i>c</i> , Å	15.331(3)	15.2145(10)
$\alpha$ , °	102.022(2)	101.9499(35)
$\beta$ , °	94.257(2)	94.313(6)
$\gamma$ , °	101.514(2)	101.579(7)
volume, Å <sup>3</sup>	1229.5(5)	1204.7(2)
<i>Z</i>	2	2
<i>D</i> <sub>calc</sub> , g cm <sup>-3</sup>	1.5	1.49
$\mu$ , mm <sup>-1</sup>	0.821	
<i>T</i> , °C	296(2)	298
$\lambda$ , Å	1.5418	1.0333
reflections collected	13054	
independent reflections	4066	
<i>R</i> (int)	0.0896	
Goodness-of-fit on <i>F</i> <sup>2</sup>	0.902	
<i>R</i> <sub>1</sub> [ <i>I</i> > 2σ( <i>I</i> )]	0.1295	
<i>wR</i> <sub>2</sub> [ <i>I</i> > 2σ( <i>I</i> )]	0.2949	
<i>R</i> <sub>1</sub> [all data]	0.3316	
<i>wR</i> <sub>2</sub> [all data]	0.3959	
$\chi^2$		2.71
<i>R</i> <sub><i>p</i></sub>		0.0618
<i>R</i> <sub><i>wp</i></sub>		0.0864



**Figure S33.** (a) The coordination environment of Al<sup>3+</sup> and ODB<sup>2-</sup> ions in [Al(ODB)<sub>2</sub>(OH)]. (b) and (c) view of the crystal structure along [010] and [100], respectively.

**Table S11.** Selected bond lengths of [Al(HODB)<sub>2</sub>(OH)].

atom 1	atom 2	distance / Å	atom 1	atom 2	distance / Å
Al1	O1	1.9444(4)	C5	C7	1.3479(2)
	O7	1.9167(4)	C6	C7	1.4271(3)
	O10	1.8831(4)	C8	C9	1.3998(4)
Al2	O6	1.9336(4)		C12	1.3384(3)
	O10	1.8681(3)	C9	C10	1.4565(3)
	O11	1.9341(5)	C10	C11	1.3836(3)
O1	C1	1.2285(2)	C11	C13	1.3854(4)
O2	C5	1.4099(3)		C14	1.5926(3)
	C8	1.4203(3)	C12	C13	1.4213(2)
O3	C14	1.1767(3)	C15	C16	1.5550(3)
O4	C14	1.2930(3)	C16	C15	1.5550(3)
O5	C19	1.4016(2)		C17	1.4503(4)
	C22	1.4074(3)		C20	1.3489(3)
O6	C28	1.2952(3)	C17	C18	1.4799(3)
O7	C28	1.1909(2)	C18	C19	1.3078(3)
O8	C15	1.3162(3)	C19	C21	1.4578(4)
O9	C15	1.1894(3)	C20	C21	1.4641(3)
O11	C1	1.2044(2)	C22	C23	1.4203(3)
C1	C2	1.5684(3)		C24	1.3833(3)
C2	C3	1.4078(3)	C23	C25	1.4232(3)
	C6	1.4275(2)	C24	C27	1.4715(3)
C3	C4	1.4322(3)	C25	C26	1.3940(3)
C4	C5	1.3440(2)	C26	C27	1.4051(3)
				C28	1.5003(3)

## Supporting Information

# Effect of partial linker fluorination and linker extension on structure and properties of the Al-MOF CAU-10

*Martin Krüger,<sup>†</sup> Helge Reinsch,<sup>†</sup> A. Ken Inge,<sup>‡</sup> and Norbert Stock<sup>†\*</sup>*

<sup>†</sup> Institut für Anorganische Chemie, Christian-Albrechts-Universität, Max-Eyth-Straße 2,  
24118 Kiel, Germany

<sup>‡</sup> Department of Materials and Environmental Chemistry, Stockholm University, Stockholm  
S-106 91, Sweden

## Table of Content

Figure S1: Reaction path for the synthesis of 5-Fluoro isophthalic acid (H <sub>2</sub> mBDC-5F) by oxidation of 5-Fluoro-m-xylene with KMnO <sub>4</sub> in pyridine. ....	160
Figure S2: <sup>1</sup> HNMR spectrum of H <sub>2</sub> mBDC-5F. Corresponding integrals are marked beneath the spectrum. ....	160
Figure S3: Reaction path for the synthesis of p-Tolunitrile in trifluoromethanesulfonic acid to 2,4,6-tri-p-tolyl-s-triazine. ....	160
Figure S4: <sup>1</sup> HNMR spectrum of 2,4,6-tri-p-tolyl-s-triazine. ....	161
Figure S5: Reaction path for the synthesis of 2,4,6-tri-p-tolyl-s-triazine to 4,4',4''-s-triazine-2,4,6-triyl-tribenzoic acid (H <sub>3</sub> TATB). ....	161
Figure S6: <sup>1</sup> HNMR spectrum of 4,4',4''-s-triazine-2,4,6-triyl-tribenzoic acid (H <sub>3</sub> TATB). ...	162
Table S1: HT investigation of CAU-10-F. Reaction conditions and exact amounts of starting materials are given. ....	162
Table S2: HT investigation of CAU-10-TATB. Reaction conditions and exact amounts of starting materials are given. ....	163
Table S3: Selected bond lengths of CAU-10-F <sub>28%</sub> . ....	165
Table S4: Selected bond lengths of CAU-10-TATB. ....	166
Figure S7: Results of the first HT investigation of CAU-10-F. For the three ratios of H <sub>2</sub> mBDC-5F: H <sub>2</sub> mBDC of 1/8 : 7/8, 2/8 : 6/8 and 3/8 : 5/8 highly crystalline products could be obtained. ....	167
Figure S8: <sup>1</sup> HNMR spectra of CAU-10-F. Integrals are marked red and corresponding H atoms are assigned to the signals. ....	168
Table S5: Initially provided amounts and obtained fluorination of CAU-10-F. ....	168
Figure S9: Final Rietveld plot of CAU-10-F <sub>28%</sub> . ....	169
Figure S10. Final Rietveld plot of CAU-10-HTATB. ....	169
Figure S11: Comparison of PXRD patterns of CAU-10-HTATB_as, a pattern collected after activation at 150°C under reduced pressure and sorption measurement and one of a sample thermally activated at 350 °C. ....	170
CIF file of CAU-10-H-F <sub>28%</sub> . ....	1704
CIF file of CAU-10-HTATB. ....	1706

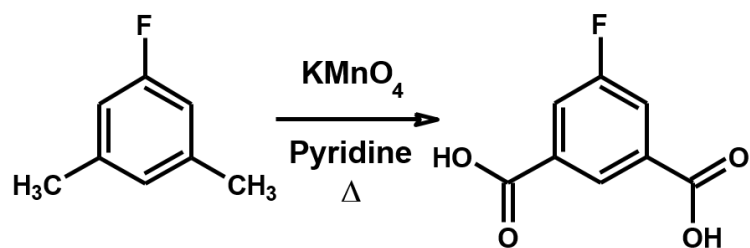


**Figure S1:** Reaction path for the synthesis of 5-fluoroisophthalic acid ( $\text{H}_2\text{mBDC-5F}$ ) by oxidation of 5-fluoro-*m*-xylene with  $\text{KMnO}_4$  in pyridine.

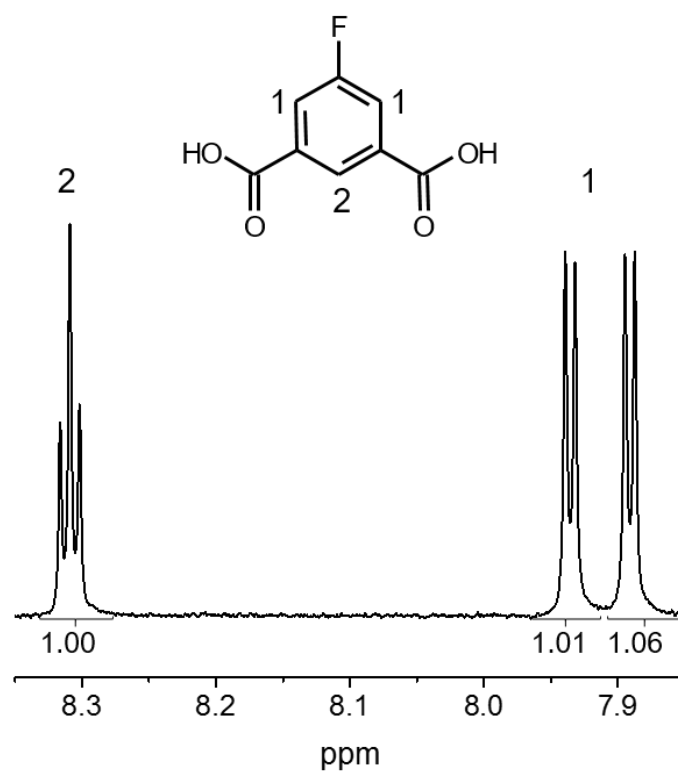


**Figure S2:**  $^1\text{H NMR}$  spectrum of  $\text{H}_2\text{mBDC-5F}$ . Corresponding integrals are also given.

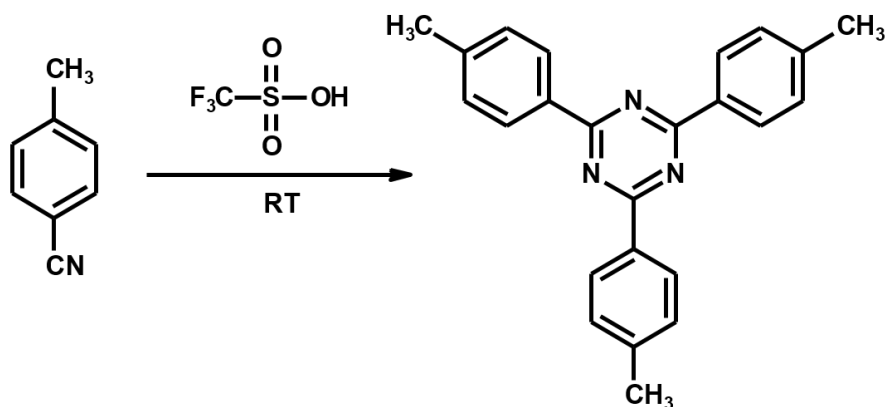


**Figure S3:** Reaction path for the synthesis of *p*-Tolunitrile in trifluoromethanesulfonic acid to 2,4,6-tri-*p*-tolyl-*s*-triazine.

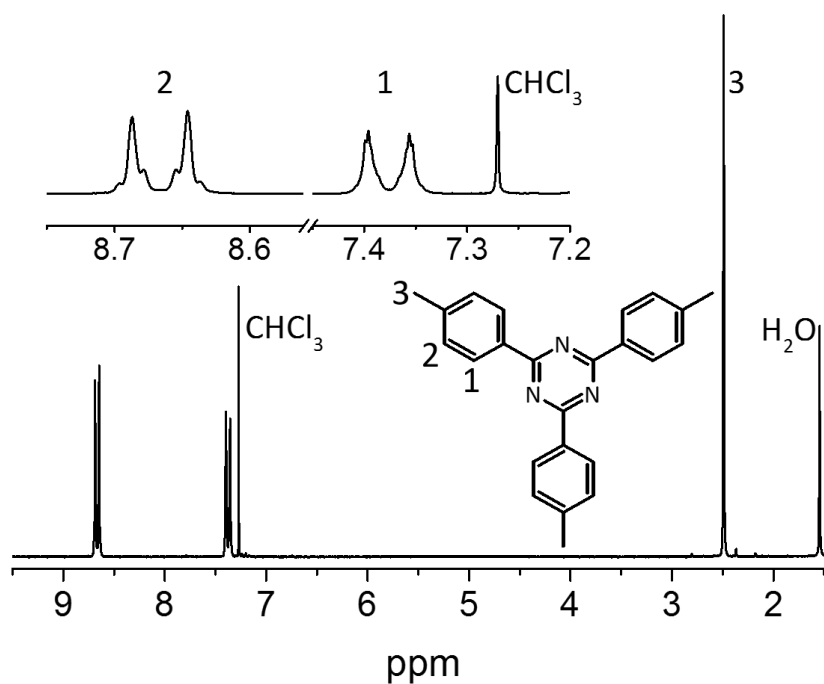


**Figure S4:**  $^1\text{H NMR}$  spectrum of 2,4,6-tri-*p*-tolyl-*s*-triazine.

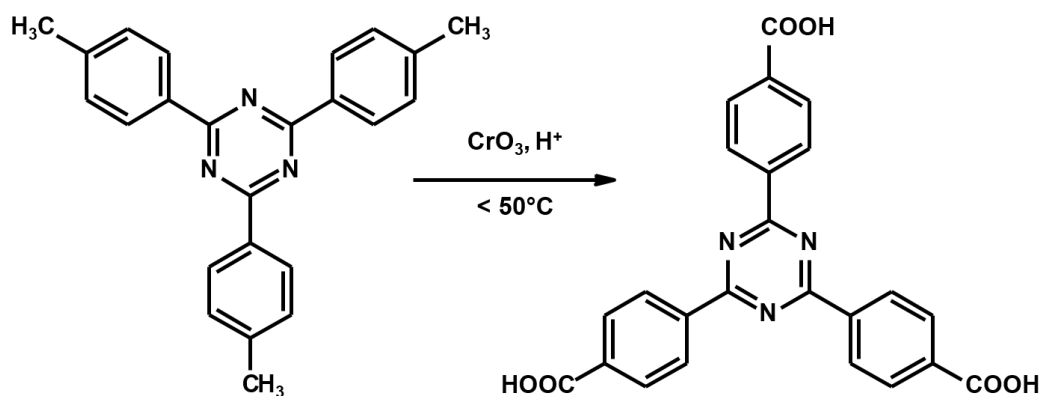


**Figure S5:** Reaction path for the synthesis of 2,4,6-tri-*p*-tolyl-*s*-triazine to 4,4',4''-*s*-triazine-2,4,6-triyl-tribenzoic acid ( $\text{H}_3\text{TATB}$ ).



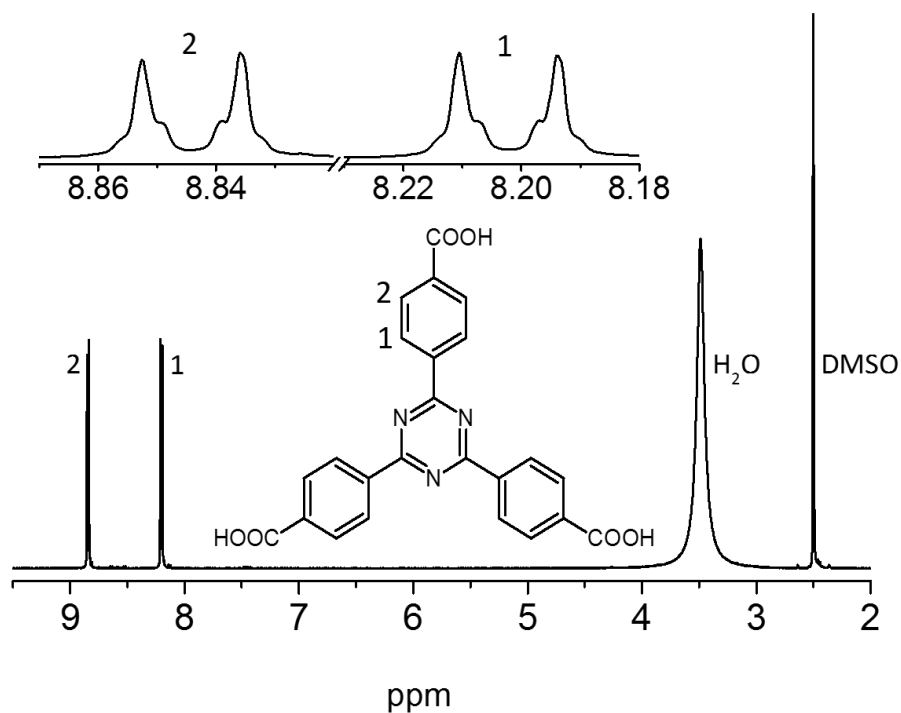


**Figure S6:** <sup>1</sup>H NMR spectrum of 4,4',4''-s-triazine-2,4,6-triyl-tribenzoic acid (H<sub>3</sub>TATB).

**Table S1:** HT investigation of CAU-10-F. Reaction conditions and exact amounts of starting materials are provided.

metal source	No.	equivalent H <sub>2m</sub> BDC	ratio H <sub>2m</sub> BDC	equivalent H <sub>2m</sub> BDC-5F	ratio H <sub>2m</sub> BDC-5F	H <sub>2m</sub> BDC/ H <sub>2m</sub> BDC-5F	equivalent Al <sup>3+</sup>	H <sub>2m</sub> BDC [mg]	H <sub>2m</sub> BDC-5F [mg]	Al <sup>3+</sup> [μL/mg]	V H <sub>2</sub> O [μL]	V DMF [μL]	temperature program
0.5 M Al <sub>2</sub> (SO <sub>4</sub> ) <sub>3</sub> in H <sub>2</sub> O	1	0.125	1	0.875	7	0.14	1	1.4	10.9	135.8	14.2	150	1h/12h\1h 120°C
	2	0.25	2	0.75	6	0.33	1	2.8	9.4	135.8	14.2	150	
	3	0.375	3	0.625	5	0.6	1	4.2	7.8	135.8	14.2	150	
	4	0.5	4	0.5	4	1	1	5.6	6.3	135.8	14.2	150	
	5	0.625	5	0.375	3	1.67	1	7.0	4.1	135.8	14.2	150	
	6	0.75	6	0.25	2	3	1	8.5	3.1	135.8	14.2	150	
	7	0.875	6	0.125	1	7	1	9.9	1.6	135.8	14.2	150	
	8	0	0	1	8	0	1	0.0	12.5	135.8	14.2	150	

**Table S2:** HT investigation of CAU-10-HTATB. Reaction conditions and exact amounts of starting materials are provided. As starting material for Al<sup>3+</sup> 2 M Al(NO<sub>3</sub>)<sub>3</sub> in DMF was used. Optimized reaction conditions are marked in orange.

No.	equivalent H <sub>3</sub> TATB	equivalent Al <sup>3+</sup>	Additive [μL]	H <sub>3</sub> TATB [mg]	Al <sup>3+</sup> [μL]	V H <sub>2</sub> O [μL]	V DMF [μL]	temperature program
1	1	0.5	0	5	11.0	150.0	339	1h/12h\1h 145°C
2	1	1	0	5	30.0	150.0	320	
3	1.5	0.75	0	7.5	17.0	150.0	333	
4	1	2	0	5	45.0	150.0	305	
5	1	3	0	5	60.0	150.0	290	
6	2	1	0	10	23.0	150.0	327	
7	2	3	0	10	60.0	150.0	290	
8	2	4	0	10	90.0	150.0	260	
9	2	5	0	10	120.0	150.0	230	
10	3	4	0	15	90.0	150.0	260	
11	3	6	0	15	135.0	150.0	215	
12	3	8	0	15	180.0	150.0	170	
13	4	5	0	20	120.0	150.0	230	
14	4	8	0	20	180.0	150.0	170	
15	4	11	0	20	240.0	150.0	110	
16	1	1	0	5	23.0	200.0	277	
17	1.5	1.5	0	7.5	34.0	200.0	266	
18	2	2	0	10	45.0	200.0	255	
19	4	3	0	20	68.0	50.0	182.0	
20	4	3	0	20	68.0	75.0	157.0	
21	4	3	0	20	68.0	100.0	132.0	
22	4	3	0	20	68.0	150.0	82.0	
23	4	3	0	20	68.0	175.0	57.0	
24	4	3	0	20	68.0	200.0	32.0	
			HCOOH					
25	4	4	10	20	90.6	125.0	84.4	
26	4	4	15	20	90.6	125.0	84.4	
27	4	4	20	20	90.6	125.0	84.4	
			acetic acid					
28	4	4	10	20	90.6	125.0	84.4	
29	4	4	15	20	90.6	125.0	84.4	
30	4	4	20	20	90.6	125.0	84.4	
			diethyl amine					
31	4	4	10	20	90.6	125.0	84.4	
32	4	4	15	20	90.6	125.0	84.4	
33	4	4	20	20	90.6	125.0	84.4	
			dimethyl amine					
34	4	4	10	20	90.6	125.0	84.4	
35	4	4	15	20	90.6	125.0	84.4	
36	4	4	20	20	90.6	125.0	84.4	

37	4	4	0	20	90.6	125.0	84.4	12h 135°C	
38	4	4	0	20	90.6	125.0	84.4	12h 155°C	
39	4	4	0	20	90.6	125.0	84.4	18h 145°C	
40	4	4	0	20	90.6	125.0	84.4	72h 145°C	
41	4	4	0	20	90.6	125.0	84.4	24h 145°C	
42	3	1	0	15	4.2	125.0	175	1h/12h\1h 160°C	
43	3	2	0	15	8.5	125.0	175		
44	3	3	0	15	12.7	125.0	175		
45	3	4	0	15	17.0	125.0	175		
46	4	1	0	20	4.2	125.0	175		
47	4	2	0	20	8.5	125.0	175		
48	4	3	0	20	12.7	125.0	175		
49	4	4	0	20	17.0	125.0	175		
50	4	2.6	0	20	58.9	191.1	50		1h/6h\1h 180°C
51	4	2.8	0	20	63.4	186.6	50		
52	4	3	0	20	68.0	182.0	50		
53	4	3.2	0	20	72.5	177.5	50		
54	4	3.4	0	20	77.0	173.0	50		
55	4	3.6	0	20	81.6	168.4	50		
			HCOOH						
56	4	3	10	20	12.7	125.0	175	1h/8h\1h 155°C	
57	4	3	10	20	12.7	150.0	150		
58	4	3	10	20	12.7	100.0	200		
59	4	4	10	20	17.0	125.0	175		
60	4	4	10	20	17.0	150.0	150		
61	4	4	10	20	17.0	100.0	200		
			2M HNO <sub>3</sub>					1h/8h\1h 160°C	
62	4	3.2	10	20	72.5	40	177.5		
63	4	3.2	15	20	72.5	35	177.5		
64	4	3.2	20	20	72.5	30	177.5		
65	4	3.2	30	20	72.5	20	177.5		
66	4	3.2	40	20	72.5	10	177.5		
67	4	3.2	50	20	72.5	0	177.5		
			2M NaOH						
68	4	3.2	10	60	111	89	300		
69	4	3.2	15	70	111	89	300		
70	4	3.2	20	60	130	70	300		
71	4	3.2	30	70	130	70	300		
72	4	3.2	40	80	130	70	300		
73	4	3.2	50	30	74	126	300		
			HCOOH						
74	4	3.2	0	20	72.5	50	177.5	1h/6h\1h 180°C	
75	4	3.2	10	20	72.5	50	177.5		
76	4	3.2	25	20	72.5	50	177.5		
77	4	3.2	50	20	72.5	50	177.5		
78	4	3.2	75	20	72.5	50	177.5		
79	4	3.2	100	20	72.5	50	177.5		

**Table S3:** Selected bond lengths of CAU-10-F<sub>28</sub>%. For the parts refined using rigid bodies no standard deviations are given.

atom 1	atom 2	distance / Å
Al1	O1	1.8738(117)
	O2	1.8995(82)
	O3	1.8767(103)
	O4	1.9334(80)
	O5	1.9641(91)
O2	C3	1.2672(82)
O3	C3	1.2669(74)
O4	C8	1.2732(80)
O5	C8	1.3025(72)
C1	C2	1.4120
	C3	1.4652
	C4	1.3997
C2	C5	1.3926
C5	F1	1.3539
C6	C7	1.4123
	C8	1.4770
	C9	1.4073
C7	C10	1.3900
	F2	1.3539

**Table S4:** Selected bond lengths of CAU-10-TATB. For the parts refined using rigid bodies no standard deviations are given.

atom 1	atom 2	distance / Å	atom 1	atom 2	distance / Å	
Al1	O1	1.8898(119)	C4	C5	1.3711	
	O2	2.0323(117)		C9	1.3711	
	O3	1.9877(116)		C5	C6	1.3711
	O4	2.0130(106)		C6	C7	1.3711
	O7	1.9299(352)		C7	C8	1.3711
O1	C10	1.2935		C10	1.5000	
O2	C10	1.2935	C8	C9	1.3711	
O3	C17	1.2935	C11	C12	1.3711	
O4	C17	1.2935		C16	1.3711	
O5	C24	1.2935	C12	C13	1.3711	
O6	C24	1.2935	C13	C14	1.3711	
N1	C1	1.3747	C14	C15	1.3711	
	C2	1.3747		C17	1.5000	
N2	C2	1.3747	C15	C16	1.3711	
	C3	1.3747	C18	C19	1.3711	
N3	C1	1.3747		C23	1.3711	
	C3	1.3747	C19	C20	1.3711	
C1	C4	1.3894	C20	C21	1.3711	
C2	C11	1.3894	C21	C22	1.3711	
C3	C18	1.3894		C24	1.5000	
			C22	C23	1.3711	

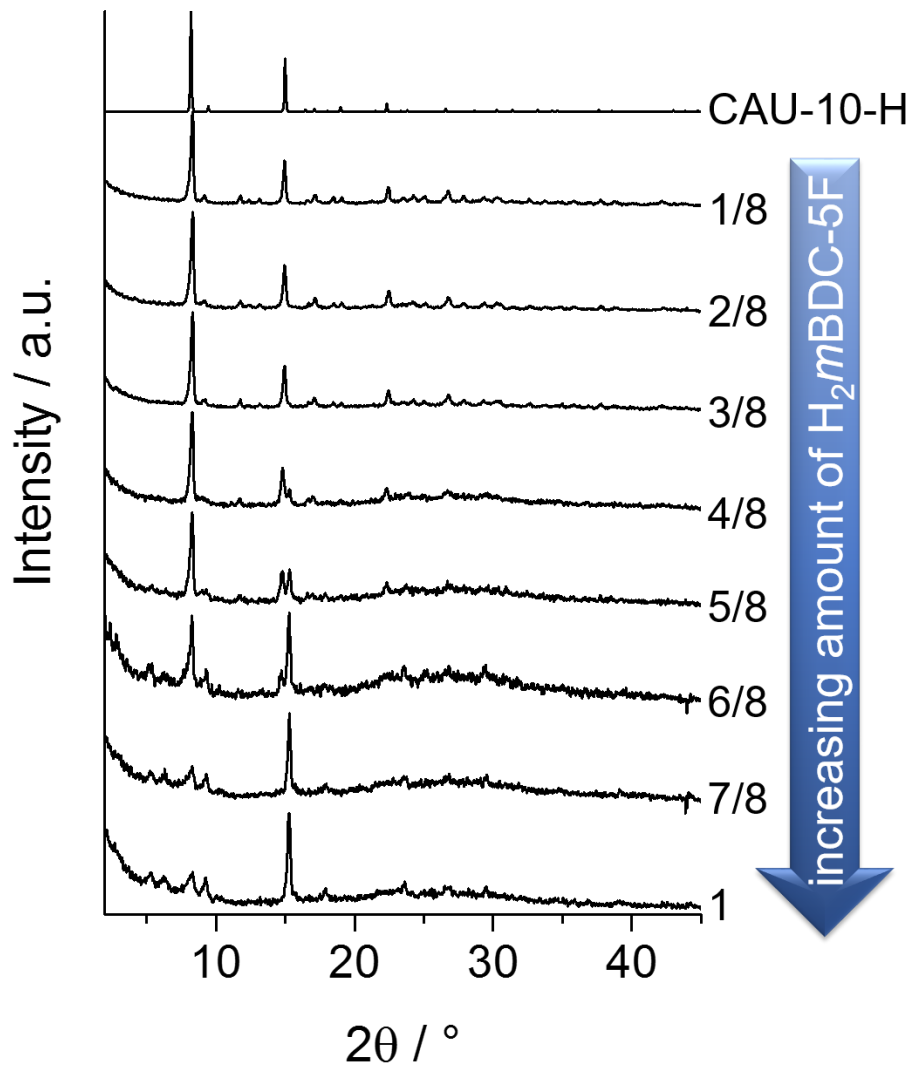


**Figure S7:** Results of the first HT investigation of CAU-10-F. For the three ratios of H<sub>2</sub>mBDC-5F: H<sub>2</sub>mBDC of 1/8 : 7/8, 2/8 : 6/8 and 3/8 : 5/8 highly crystalline products could be obtained.

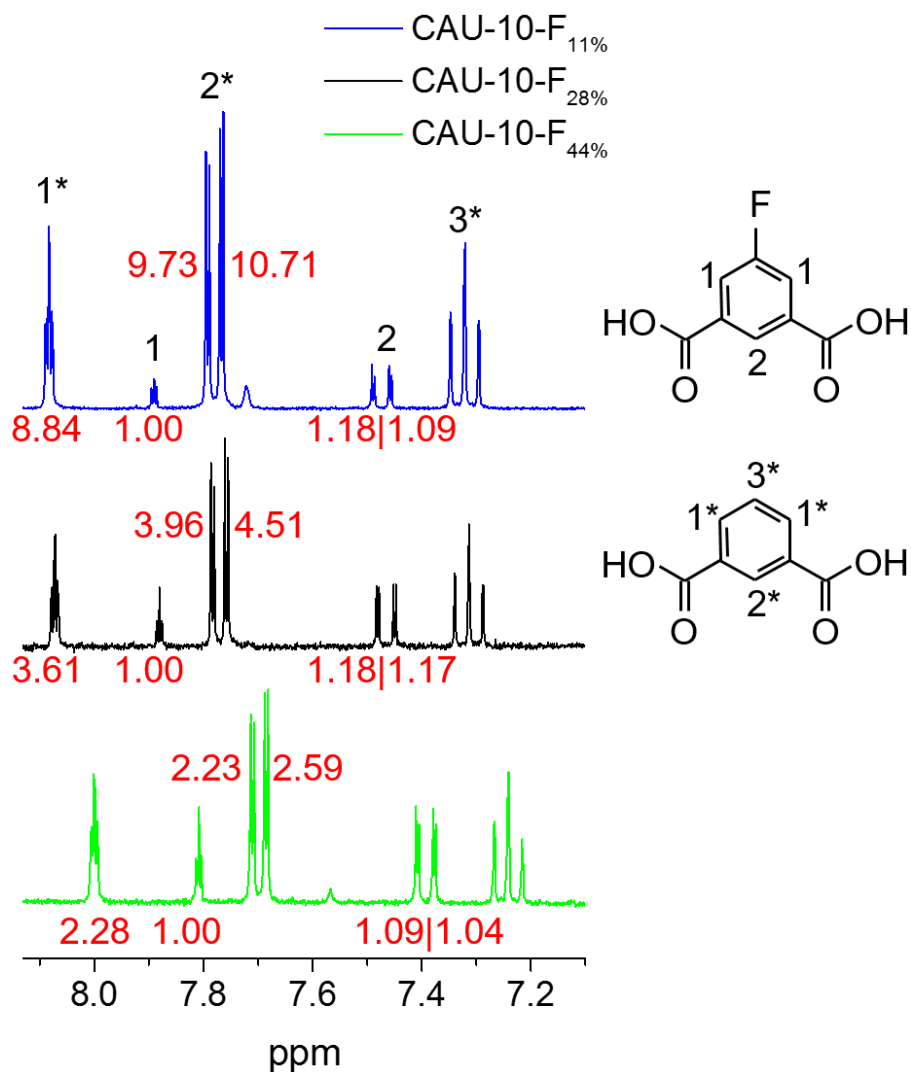


**Figure S8:**  $^1\text{H}$ NMR spectra of CAU-10-F. Integrals are marked red and corresponding H atoms are assigned to the signals.

**Table S5:** Initially provided amounts and obtained fluorination of CAU-10-F.

sample	ratio 5F- <i>m</i> BDC : H <sub>2</sub> <i>m</i> BDC	
	initially provided ratio	obtained ratio after synthesis
CAU-10-F <sub>44%</sub>	1 : 1.7 $\pm$ 59%	1 : 2.27 $\pm$ 44%
CAU-10-F <sub>28%</sub>	1 : 3 $\pm$ 34%	1 : 3.6 $\pm$ 28%
CAU-10-F <sub>11%</sub>	1 : 7 $\pm$ 14%	1 : 8.95 $\pm$ 11%

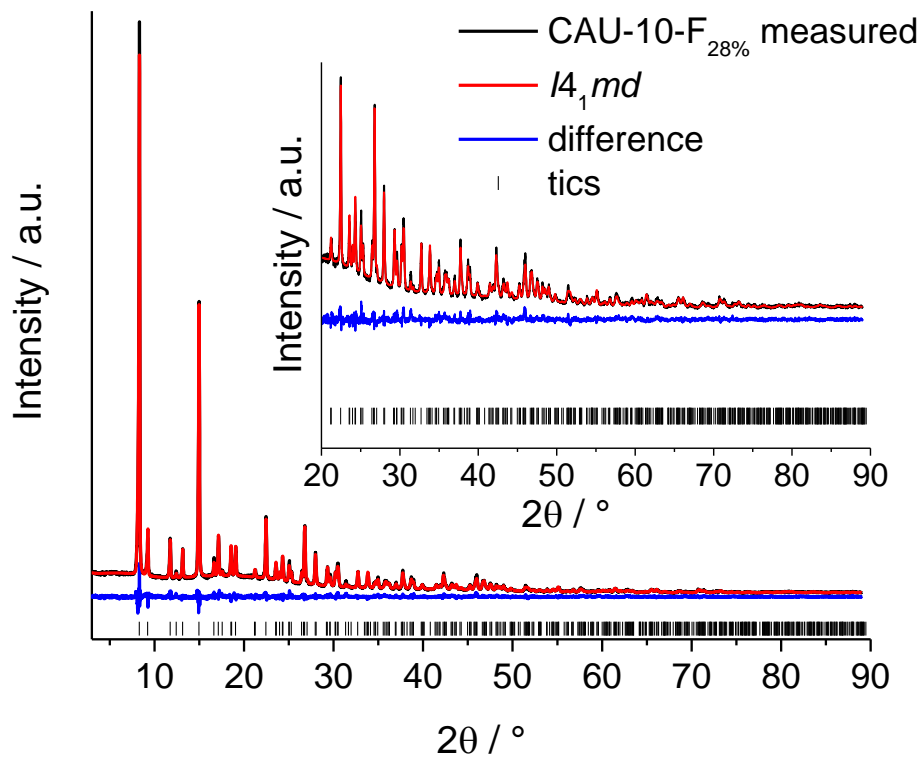


**Figure S9:** Final Rietveld plot of CAU-10-F<sub>28%</sub>.

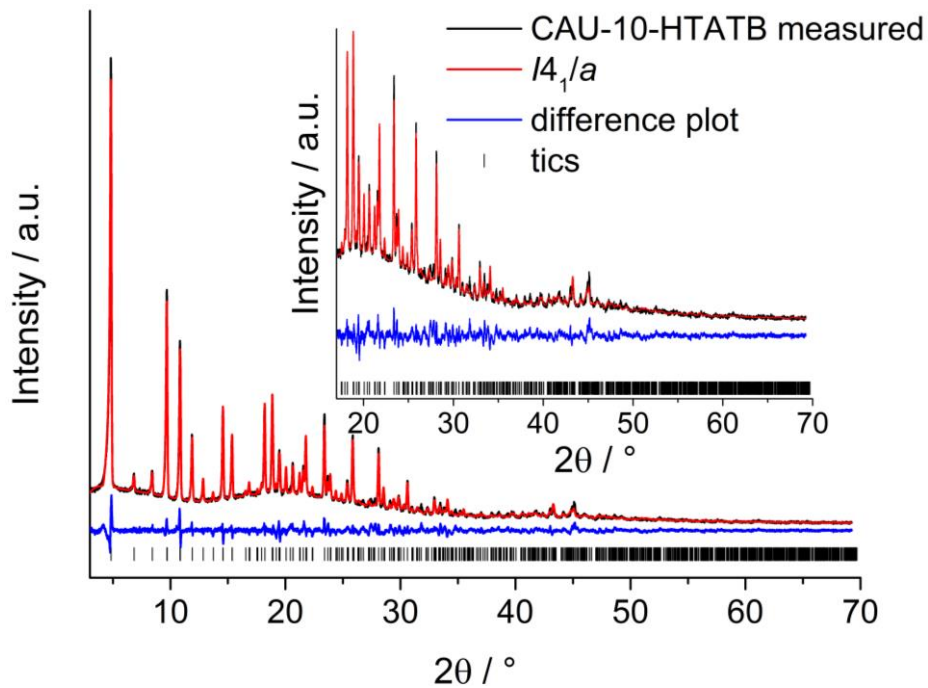


**Figure S10.** Final Rietveld plot of CAU-10-HTATB.



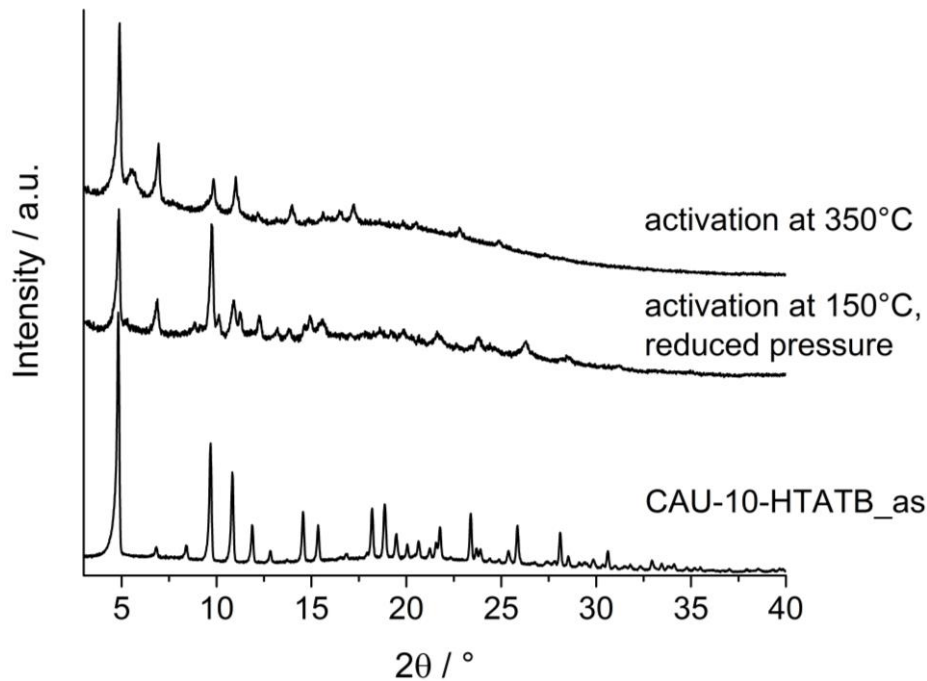


**Figure S11:** Comparison of PXRD patterns of CAU-10-HTATB<sub>as</sub>, a pattern collected after activation at 150°C under reduced pressure and sorption measurement and one of a sample thermally activated at 350 °C.

#### CAU-10-H-F28%

```

data_CAU-10-H-F28%
_chemical_name_mineral ??
_cell_length_a 21.30748(52)
_cell_length_b 21.30748(52)
_cell_length_c 10.71014(34)
_cell_angle_alpha 90
_cell_angle_beta 90
_cell_angle_gamma 90
_cell_volume 4862.50(28)
_symmetry_space_group_name_H-M I41MD
loop_
_symmetry_equiv_pos_as_xyz
'-x+1/2, -y+1/2, z+1/2'
'-x+1/2, y+1/2, z+1/2'
'-y, x+1/2, z+1/4'
'-y+1/2, -x, z-1/4'
'y, x+1/2, z+1/4'
'y+1/2, -x, z-1/4'
'x, -y, z'
'x, y, z'
'-x, -y, z'
'-x, y, z'
'-y+1/2, x, z-1/4'
'-y, -x+1/2, z+1/4'

```

'y+1/2, x, z-1/4'  
'y, -x+1/2, z+1/4'  
'x+1/2, -y+1/2, z+1/2'  
'x+1/2, y+1/2, z+1/2'

loop\_

\_atom\_site\_label

\_atom\_site\_type\_symbol

\_atom\_site\_symmetry\_multiplicity

\_atom\_site\_fract\_x

\_atom\_site\_fract\_y

\_atom\_site\_fract\_z

\_atom\_site\_occupancy

\_atom\_site\_B\_iso\_or\_equiv

Al1 Al 0 0.25450(25) 0.31356(22) 0.24966(59) 1 0.20(16)

O1 O 0 0.24984(43) 0.25685(48) 0.38306(95) 1 0.20(16)

O2 O 0 0.65790(28) 0.30353(41) 0.2235(11) 1 0.20(16)

O3 O 0 0.37621(45) 0.24120(50) 0.37679(56) 1 0.20(16)

O4 O 0 0.33483(27) 0.17664(55) 0.7746(10) 1 0.20(16)

O5 O 0 0.61890(46) 0.23231(35) 0.62167(65) 1 0.20(16)

C1 C 0 0.5568 0.265843 0.2053469 1 0.20(23)

C2 C 0 0.5565 0.2752184 0.07483775 1 0.20(23)

C3 C 0 0.6162 0.2695221 0.273884 1 0.20(23)

C4 C 0 0.5 0.2595322 0.2697854 1 0.20(23)

C5 C 0 0.5 0.2796799 0.01008098 1 0.20(23)

F1 F 0 0.5 0.2920292 -0.1139187 0.292(13) 0.20(23)

C6 C 0 0.4428 0.1682171 0.759457 1 0.20(23)

C7 C 0 0.44355 0.1228256 0.855538 1 0.20(23)

C8 C 0 0.38215 0.1881375 0.7057155 1 0.20(23)

C9 C 0 0.5 0.1913379 0.7125553 1 0.20(23)

C10 C 0 0.5 0.1005883 0.9032186 1 0.20(23)

F2 F 0 0.5 0.05848153 0.9978887 0.289(14) 0.20(23)

Ow0 O 0 0.0203(16) 0.06486(39) 0.8176(21) 0.445(11) 1.98(35)

Ow1 O 0 0.42751(70) 0.56571(67) 0.9234(16) 0.700(16) 1.98(35)

Ow2 O 0 0.59714(55) 0.43787(50) 0.1668(14) 0.961(13) 1.98(35)

Ow3 O 0 0.34864(52) 0.33618(65) 0.8285(14) 1.000(11) 1.98(35)

Ow4 O 0 0.5 0.6200(20) 0.5554(41) 0.406(16) 1.98(35)

### CAU-10-HTATB

data\_topas\_cif\_out

\_chemical\_name\_mineral CAU-10-HTATB

\_cell\_length\_a 36.43783(99)

\_cell\_length\_b 36.43783(99)

\_cell\_length\_c 10.93731(91)

\_cell\_angle\_alpha 90

\_cell\_angle\_beta 90

\_cell\_angle\_gamma 90

\_cell\_volume 14521.6(14)

\_symmetry\_space\_group\_name\_H-M I41/a

loop\_

\_symmetry\_equiv\_pos\_as\_xyz

'-x, -y+1/2, -z+1/4'  
'-x+1/2, -y+1/2, z+1/2'  
'-y, x+1/2, z+1/4'  
'-y+1/2, x+1/2, -z+1/2'  
'y, -x, -z'  
'y+1/2, -x, z-1/4'  
'x, y, z'  
'x+1/2, y, -z-1/4'  
'-x+1/2, -y, -z-1/4'  
'-x, -y, z'  
'-y+1/2, x, z-1/4'  
'-y, x, -z'  
'y+1/2, -x+1/2, -z+1/2'  
'y, -x+1/2, z+1/4'  
'x+1/2, y+1/2, z+1/2'  
'x, y+1/2, -z+1/4'

loop\_

\_atom\_site\_label

\_atom\_site\_type\_symbol

\_atom\_site\_symmetry\_multiplicity

\_atom\_site\_fract\_x

\_atom\_site\_fract\_y

\_atom\_site\_fract\_z

\_atom\_site\_occupancy

\_atom\_site\_B\_iso\_or\_equiv

Al1 Al 0 0.29224(22) 0.75331(32) 0.1359(13) 1 2.00(83)  
O7 O 0 0.25522(90) 0.75872(63) 0.2608(31) 1 5.00(63)  
N1 N 0 0.7859135 -0.4976728 1.480891 1 3.07(42)  
N2 N 0 0.8013831 -0.5316552 1.302225 1 3.07(42)  
N3 N 0 0.8018488 -0.4663264 1.297396 1 3.07(42)  
C1 C 0 0.7913805 -0.4654477 1.418116 1 3.07(42)  
C2 C 0 0.7909147 -0.5307765 1.422945 1 3.07(42)  
C3 C 0 0.8068501 -0.4994301 1.239451 1 3.07(42)  
C4 C 0 0.7863258 -0.4319902 1.47668 1 3.07(42)  
C5 C 0 0.7894604 -0.3998908 1.412108 1 3.07(42)  
C6 C 0 0.7844724 -0.3668745 1.4699 1 3.07(42)  
C7 C 0 0.7763497 -0.3659577 1.592265 1 3.07(42)  
C8 C 0 0.7732151 -0.3980571 1.656838 1 3.07(42)  
C9 C 0 0.7782032 -0.4310734 1.599045 1 3.07(42)  
C10 C 0 0.7708927 -0.3298372 1.655491 1 3.07(42)  
C11 C 0 0.7853893 -0.5633459 1.486391 1 3.07(42)  
C12 C 0 0.783268 -0.5630465 1.611546 1 3.07(42)  
C13 C 0 0.7778154 -0.5951864 1.674155 1 3.07(42)  
C14 C 0 0.774484 -0.6276257 1.611609 1 3.07(42)  
C15 C 0 0.7766053 -0.6279251 1.486453 1 3.07(42)  
C16 C 0 0.782058 -0.5957852 1.423844 1 3.07(42)  
C17 C 0 0.7685188 -0.6627874 1.680104 1 3.07(42)

C18 C 0 0.8174303 -0.5003182 1.117441 1 3.07(42)  
C19 C 0 0.8262347 -0.5330945 1.063302 1 3.07(42)  
C20 C 0 0.8366753 -0.5339709 0.9429009 1 3.07(42)  
C21 C 0 0.8383116 -0.5020709 0.8766384 1 3.07(42)  
C22 C 0 0.8295072 -0.4692947 0.9307769 1 3.07(42)  
C23 C 0 0.8190666 -0.4684183 1.051178 1 3.07(42)  
C24 C 0 0.8497339 -0.5030297 0.744917 1 3.07(42)  
O1 O 0 0.7452587 -0.3262449 1.736419 1 5.00(63)  
O2 O 0 0.791821 -0.3022825 1.629083 1 5.00(63)  
O3 O 0 0.7831143 -0.6929277 1.640879 1 5.00(63)  
O4 O 0 0.7487793 -0.6629674 1.778393 1 5.00(63)  
O5 O 0 0.8699469 -0.5296312 0.7049547 1 5.00(63)  
O6 O 0 0.8393705 -0.4772549 0.6712949 1 5.00(63)  
N4 N 0 -3.437842 -3.463651 0.2910568 1 5.00(73)  
C25 C 0 -3.465407 -3.448757 0.3935484 1 5.00(73)  
C26 C 0 -3.447344 -3.458148 0.1494164 1 5.00(73)  
C27 C 0 -3.400774 -3.484048 0.3302056 1 5.00(73)  
O8 O 0 -3.393648 -3.488175 0.4364359 1 5.00(73)  
N5 N 0 -0.6402463 2.126914 2.54912 1 5.00(73)  
C28 C 0 -0.6010945 2.120391 2.611688 1 5.00(73)  
C29 C 0 -0.6763947 2.129209 2.631817 1 5.00(73)  
C30 C 0 -0.6432498 2.131142 2.403856 1 5.00(73)  
O9 O 0 -0.6161385 2.12942 2.341834 1 5.00(73)

### Zusätzliche Informationen zu SHG-Messungen an CAU-10-H/F<sub>x</sub>

An allen fluorierten CAU-10-Derivaten wurden zusätzlich Messungen zur Bestimmung der SHG-Aktivität durchgeführt (Abbildung A5). Die Verbindungen zeigten jedoch keine SHG-Aktivität, obwohl die Kristallisation in der azentrischen Raumgruppe  $I4_1md$  dies vermuten ließ. Das Fehlen eines Inversionszentrums ist eine notwendige, aber keine hinreichende Bedingung für die SHG-Aktivität einer Verbindung. So kann trotz einer azentrischen Kristallisation keine SHG-Aktivität erkennbar sein, weil z.B. keine eindeutige Polarisationsrichtung vorliegt.

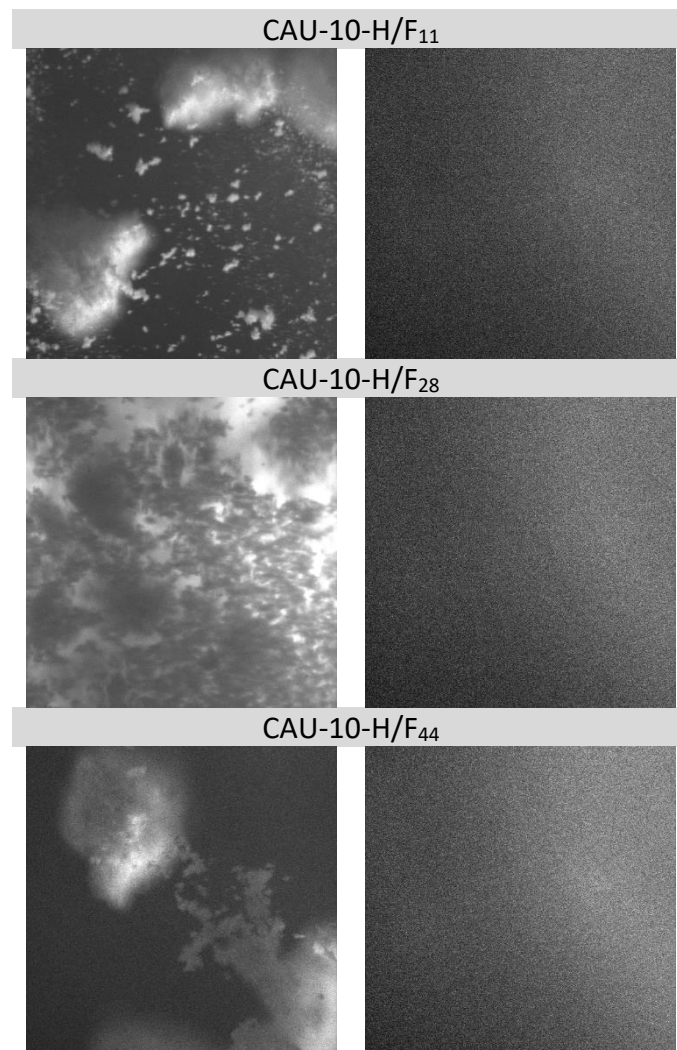


**Abb. A5** Optische Bilder (links) und SHG-Bilder (rechts) der verschiedenen fluorierten CAU-10-Derivate. Es ist keine SHG-Aktivität der Proben erkennbar.

SUPPORTING INFORMATION

## **Investigation of the Effect of polar Functional Groups on the Crystal Structures of Indium MOFs**

Martin Krüger,<sup>a</sup> Martin Albat,<sup>a</sup> A. Ken Inge,<sup>b</sup> and Norbert Stock<sup>a</sup>

<sup>a</sup> Institut für Anorganische Chemie, Christian-Albrechts-Universität, Max-Eyth-Straße 2, 24118 Kiel, Germany.

<sup>b</sup> Department of Materials and Environmental Chemistry, Stockholm University, Stockholm SE-106 91, Sweden.

**Table of Content**

Fig. S1 Reaction scheme for the synthesis of 2-amino-5-nitroterephthalic acid (H <sub>2</sub> BDC-NH <sub>2</sub> /NO <sub>2</sub> ). .....	178
Fig. S2 <sup>1</sup> H-NMR spectrum of 2-aminoterephthalic acid. ....	179
Fig. S3 <sup>1</sup> H-NMR spectrum of 2-formamidoterephthalic acid. ....	179
Fig. S4 <sup>1</sup> H-NMR spectrum of 2-amino-5-nitroterephthalic acid (H <sub>2</sub> BDC-NH <sub>2</sub> /NO <sub>2</sub> ) measured in DMSO-D <sub>6</sub> . ....	180
Fig. S5 <sup>1</sup> H-NMR spectrum of 2-amino-5-nitroterephthalic acid (H <sub>2</sub> BDC-NH <sub>2</sub> /NO <sub>2</sub> ) measured in 5% NaOD/D <sub>2</sub> O. ....	181
Table S1 Crystal structure data of 2-amino-5-nitroterephthalic acid (H <sub>2</sub> BDC-NH <sub>2</sub> /NO <sub>2</sub> ). .....	181
Table S2 Selected bond lengths of H <sub>2</sub> BDC-NH <sub>2</sub> . ....	182
Fig. S6 Asymmetric unit of 2-amino-5-nitroterephthalic acid (H <sub>2</sub> BDC-NH <sub>2</sub> /NO <sub>2</sub> ). ....	182
Fig. S7 Crystal structure of 2-amino-5-nitroterephthalic acid (H <sub>2</sub> BDC-NH <sub>2</sub> /NO <sub>2</sub> ). Above the hydrogen bonding model is shown, whereas the unit cell along [010] is shown below. Carbon atoms are shown in grey, nitrogen in blue and oxygen in red. Hydrogen bonds are marked in dashed lines. ....	183
Table S3 Selected bond lengths of In-BDC-NH <sub>2</sub> (1). ....	184
Table S4 Selected bond lengths of In-BDC-NH <sub>2</sub> /NO <sub>2</sub> (3). ....	184
Fig. S8 Asymmetric unit of In-BDC-NH <sub>2</sub> (1) with numbering scheme as used in Table S3. ....	185
Table S5 Overview of the bands visible in The IR spectrum of In-BDC-NH <sub>2</sub> (1) discussed in the manuscript. ....	185
Fig. S9 Thermogravimetric measurement of In-BDC-NH <sub>2</sub> (1). The calculated values based on the assumed sum formula are given in brackets. ....	186
Fig. S10 Comparison of the PXRD pattern recorded for granulated crystals of In-BDC-H/NH <sub>2</sub> and the simulated pattern of In-BDC-NH <sub>2</sub> . ....	186
Fig. S11 Comparison of the PXRD pattern recorded for the sample using the same synthesis conditions as used for 1 with linker molecule replaced by H <sub>2</sub> BDC-NH <sub>2</sub> /NO <sub>2</sub> and the simulated pattern of dimethylammonium 2-amino-5-nitroterephthalate hemihydrate obtained from single crystal XRD measurements. <sup>2</sup> .....	187
Fig. S12 Comparison of the PXRD pattern recorded for In-BDC-NH <sub>2</sub> /NO <sub>2</sub> and the simulated pattern of In-BDC-NH <sub>2</sub> /NO <sub>2</sub> obtained from single crystal XRD measurements. ....	187
Fig. S13 Asymmetric unit of In-BDC-NH <sub>2</sub> /NO <sub>2</sub> with numbering scheme as used in Table S4. ....	188

Fig. S14 Crystal structure of In-BDC-NH<sub>2</sub>/NO<sub>2</sub>. Trinuclear clusters composed of three InO<sub>6</sub> octahedra bridged by an  $\mu_3$ -O atom (left) are interlinked by a disordered tetradentate BDC-NH<sub>2</sub>/NO<sub>2</sub><sup>2-</sup> ions (middle) to form a super-tetrahedron (right). ..... 188

Fig. S15 Crystal structure of In-BDC-NH<sub>2</sub>/NO<sub>2</sub>. To each super-tetrahedron (left) four additional trinuclear In-O-clusters are attached via tridentate carboxylate ions (middle). Thus, four additional super-tetrahedra are formed (right; only two face-sharing super-tetrahedra are displayed), face-sharing with the central one (left). ..... 189

Fig. S16 <sup>1</sup>H-NMR spectrum of In-BDC-NH<sub>2</sub>/NO<sub>2</sub>. The MOF was dissolved in 5% NaOD/D<sub>2</sub>O. Signals of DMF as well as HCOO<sup>-</sup> and dimethylammonium ions (DMA), the hydrolysis products of DMF, are visible. .... 189

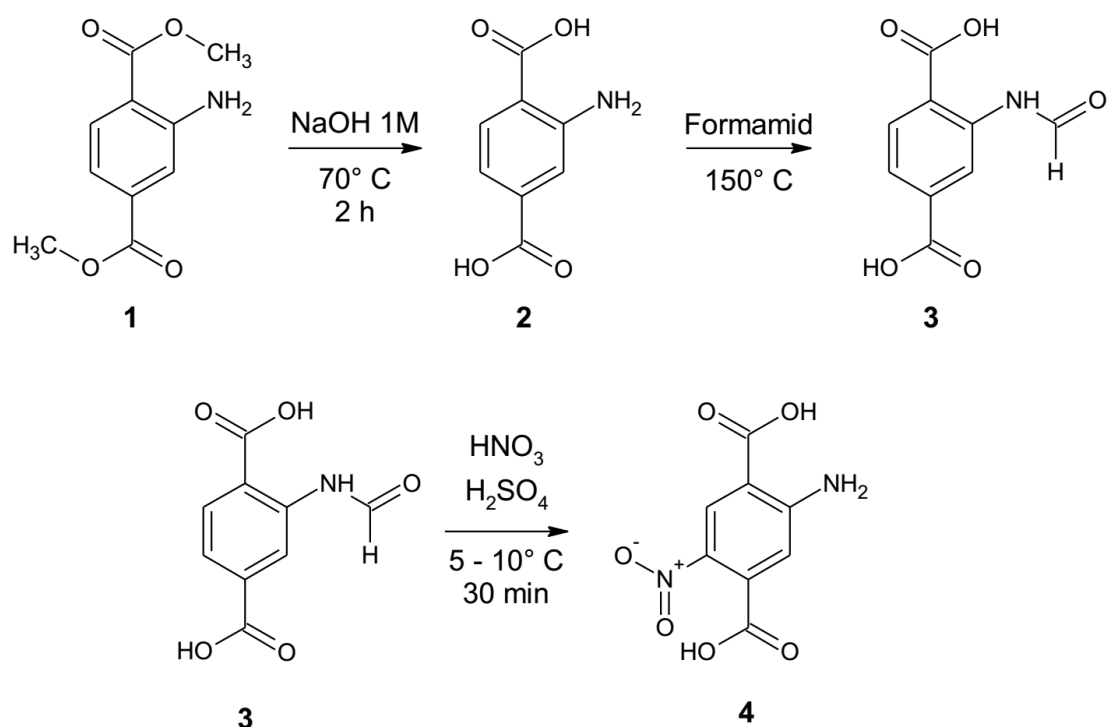
Table S6 Overview of the bands visible in The IR spectrum of In-BDC-NH<sub>2</sub>/NO<sub>2</sub> (3) discussed in the manuscript. .... 190

Fig. S17 Thermogravimetric measurement of In-BDC-NH<sub>2</sub>/NO<sub>2</sub>. A clear assignment of decomposition steps was not possible. .... 190



## Synthesis of 2-amino-5-nitroterephthalic acid

The synthesis was accomplished by following the literature procedure reported by Skibo et al.<sup>[1]</sup> The reaction scheme is shown in Figure 1.



**Fig. S1** Reaction scheme for the synthesis of 2-amino-5-nitroterephthalic acid (H<sub>2</sub>BDC-NH<sub>2</sub>/NO<sub>2</sub>).

**Step 1:** A mixture of 87g (416 mmol) of dimethyl aminoterephthalate and 800 mL of a 1M NaOH solution was heated in a 1 L flask to 70 °C until the solid was solved completely. After cooling down to room temperature conc. HCl was added until a yellow solid precipitated which was filtered and washed with water. The <sup>1</sup>H-NMR spectrum of the final product is displayed in Figure S2.

Yield: 67 g (370 mmol, 89%)

**<sup>1</sup>H-NMR:** (200 MHz, DMSO-D<sub>6</sub>, 300 K): δ [ppm]: 7.77 (1H, d, J = 8.3 Hz, H<sub>3</sub>), 7.39 (1H, d, J = 1.4 Hz, H<sub>1</sub>), 7.02 (1H, dd, J = 8.3 Hz, J = 1.6 Hz, H<sub>2</sub>).

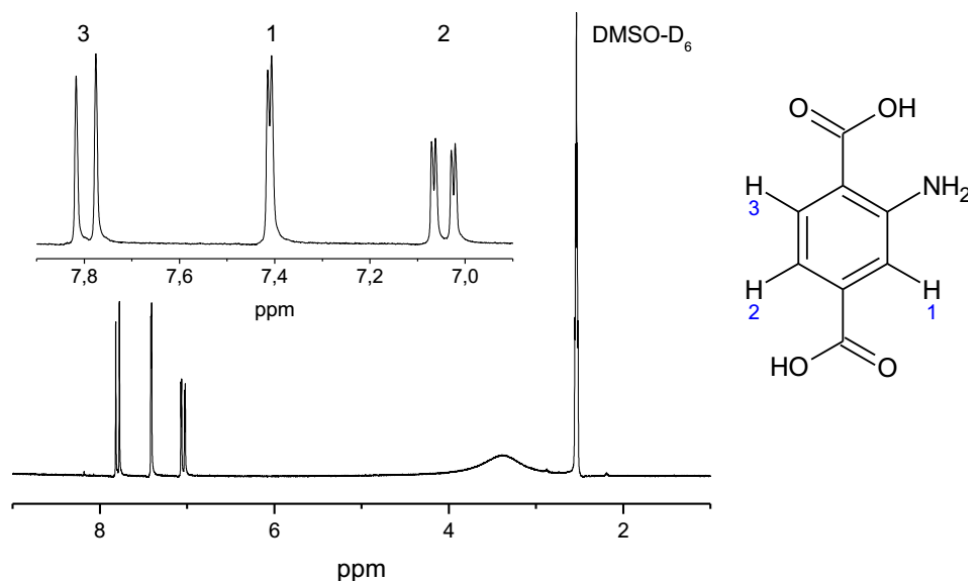


**Fig. S2**  $^1\text{H-NMR}$  spectrum of 2-aminoterephthalic acid.

**Step 2:** A suspension of 20.8 g 2-aminoterephthalic acid (114 mmol) and 100 mL formamide was heated rapidly to 150 °C until the solid was solved. During cooling down to room temperature a brown solid precipitated which was filtered of and dissolved in a saturated aqueous  $\text{Na}(\text{HCO}_3)$  solution. While acidifying this solution with conc. acetic acid a white solid precipitated which was filtered off, washed with water and dried completely. The  $^1\text{H-NMR}$  spectrum of the final product is displayed in Figure S3.

Yield: 9.7 g (53 mmol, 48%)

**$^1\text{H-NMR}$ :** (200 MHz,  $\text{DMSO-D}_6$ , 300 K):  $\delta$  [ppm]: 9.1 (1H, s H1), 8.54 (1H, s H2), 8.07 (1H, d,  $J = 8.2$  Hz, H4), 7.69 (1H dd,  $J = 8.2$  Hz,  $J = 1.7$  Hz, H3)

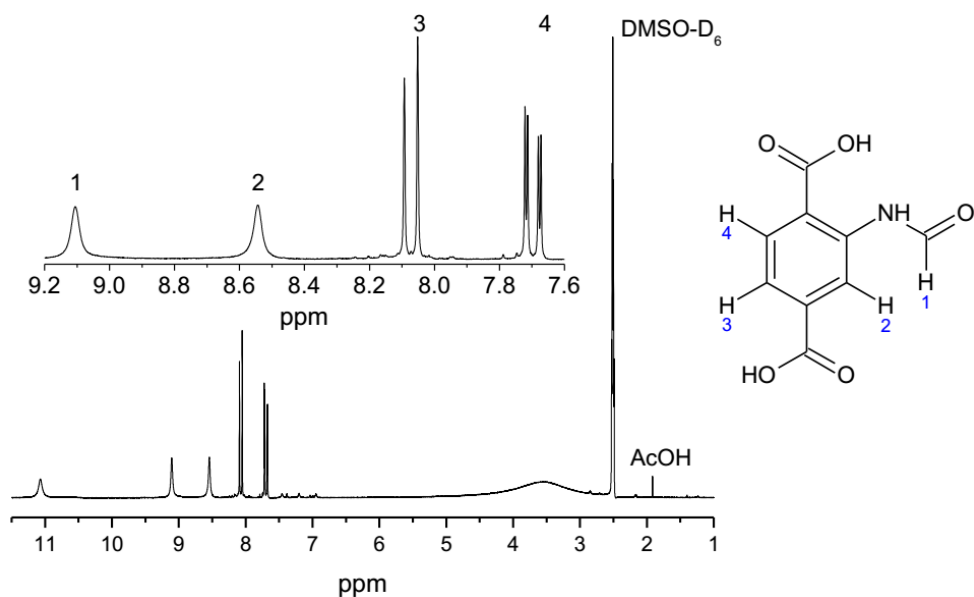


**Fig. S3**  $^1\text{H-NMR}$  spectrum of 2-formamidoterephthalic acid.

**Step 3:** To 20 mL of fuming nitric acid, cooled in an ice bath, 5.1 g (24 mmol) of formamidoterephthalic acid was added under stirring. To this suspension 10 mL of conc. sulfuric acid, which was also cooled in an ice bath, was added slowly within 15-20 minutes keeping the temperature between 5-10°C. After addition, the solid was dissolved and the solution was poured on 100 g of ice and stored in a refrigerator overnight. The precipitated solid was filtered off and recrystallized from hot water. Orange-brown crystals of 2-amino-5-nitroterephthalic acid ( $\text{H}_2\text{BDC-NH}_2/\text{NO}_2$ ) were obtained. The  $^1\text{H-NMR}$  spectrum of the final product is displayed in Figure S4 and S5. Detailed information of the crystal structure of  $\text{H}_2\text{BDC-NH}_2/\text{NO}_2$  can be found in Table S1 and Figures S6 and S7.

Yield: 1.5 g (6.6 mmol, 27%)

$^1\text{H-NMR}$ : (200 MHz,  $\text{DMSO-D}_6$ , 300 K):  $\delta$  [ppm]: 8.49 (1H, s, H1), 6.89 (1H, s, H2).

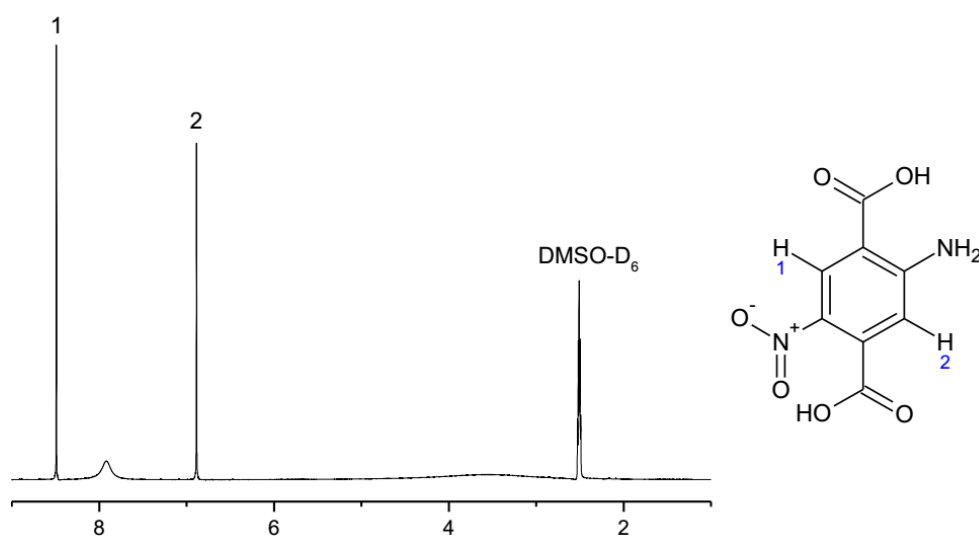


**Fig. S4**  $^1\text{H-NMR}$  spectrum of 2-amino-5-nitroterephthalic acid ( $\text{H}_2\text{BDC-NH}_2/\text{NO}_2$ ) measured in  $\text{DMSO-D}_6$ .

**$^1\text{H-NMR}$ :** (200 MHz, NaOD/D<sub>2</sub>O, 300 K):  $\delta$  [ppm]: 8.36 (1H, s, H1), 6.41 (1H, s, H2).

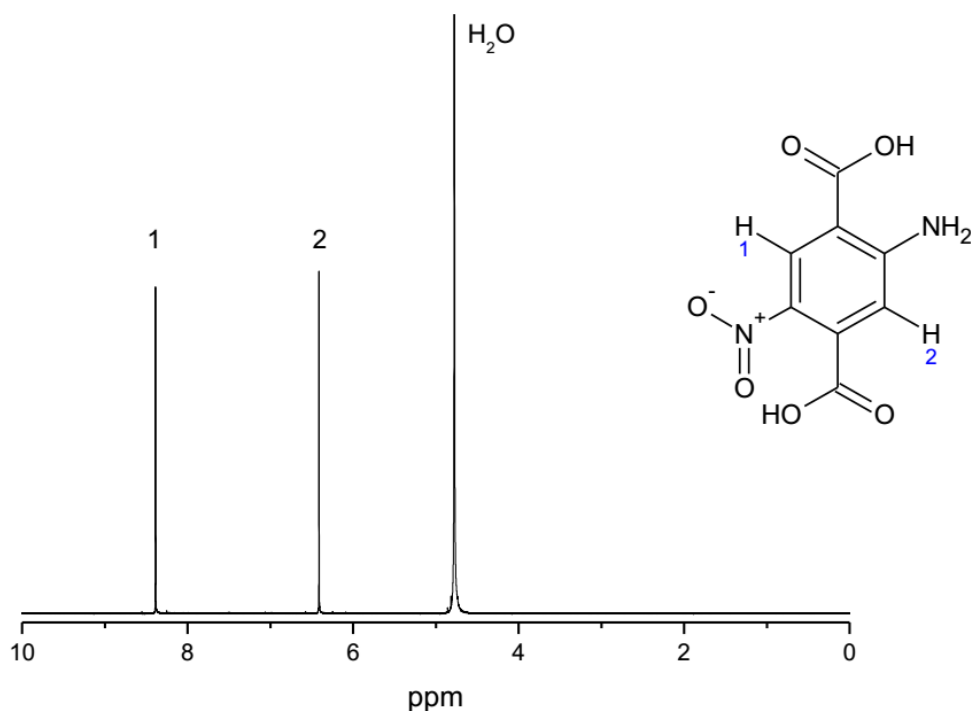


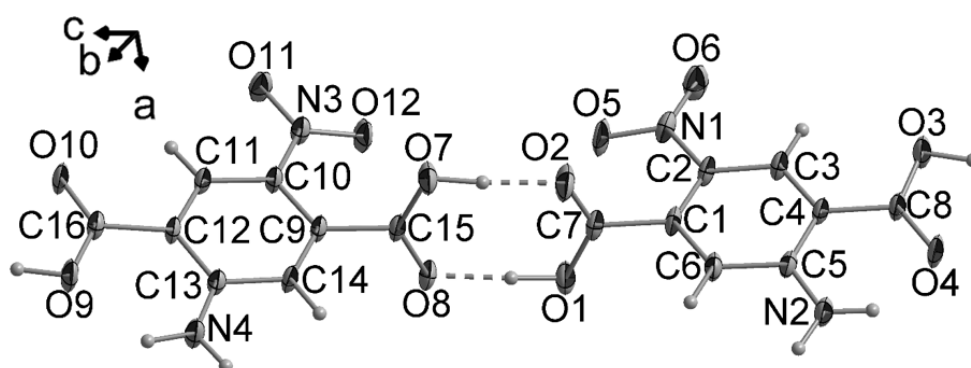
**Fig. S5**  $^1\text{H-NMR}$  spectrum of 2-amino-5-nitroterephthalic acid (H<sub>2</sub>BDC-NH<sub>2</sub>/NO<sub>2</sub>) measured in 5% NaOD/D<sub>2</sub>O.

**Table S1** Crystal structure data of 2-amino-5-nitroterephthalic acid (H<sub>2</sub>BDC-NH<sub>2</sub>/NO<sub>2</sub>).

	H <sub>2</sub> BDC-NH <sub>2</sub> /NO <sub>2</sub>
structure determination	single crystal data
formula sum	C <sub>8</sub> H <sub>6</sub> N <sub>2</sub> O <sub>6</sub>
Z	4
crystal system	triclinic
<i>a</i> / Å	6.7000(13)
<i>b</i> / Å	9.2100(18)
<i>c</i> / Å	15.040(3)
$\alpha$ / °	78.47(3)
$\beta$ / °	78.31(3)
$\gamma$ / °	89.31(3)
<i>V</i> / Å <sup>3</sup>	890.1(3)
space group	P-1
solution method	direct methods
range / °2 $\theta$	2.3 – 28.0
wavelength / Å	MoK $\alpha$
GOF	1.026
tot., uniq. data, R <sub>int</sub>	4159, 4159, 0.0
observed data [ <i>I</i> > 2 $\sigma$ ( <i>I</i> )]	2818
<i>R</i> <sub>1</sub> , <i>wR</i> <sub>2</sub>	0.059, 0.180
$\Delta e$ min./max (e/Å <sup>3</sup> )	-0.53, 0.39
calc. density / g/cm <sup>3</sup>	1.17352

**Table S2** Selected bond lengths of H<sub>2</sub>BDC-NH<sub>2</sub>.

atom 1	atom 2	distance / Å	atom 1	atom 2	distance / Å
C1	C2	1.408(3)	C10	C11	1.386(3)
	C6	1.368(3)	C10	N3	1.438(3)
	C7	1.510(3)	C11	C12	1.387(3)
C2	C3	1.390(3)	C12	C13	1.427(3)
	N1	1.443(3)		C16	1.487(3)
C3	C4	1.395(3)	C13	C14	1.428(3)
C4	C5	1.426(3)		N4	1.341(3)
	C8	1.476(3)	C15	O7	1.293(3)
C5	C6	1.428(3)		O8	1.233(3)
	N2	1.342(3)	C16	O9	1.316(3)
C7	O1	1.293(3)		O10	1.223(3)
	O2	1.228(3)	N1	O5	1.247(3)
C8	O3	1.311(3)		O6	1.230(3)
	O4	1.228(3)	N3	O11	1.228(2)
C9	C10	1.407(3)		O12	1.243(2)
	C14	1.371(3)			
	C15	1.506(3)			

**Fig. S6** Asymmetric unit of 2-amino-5-nitroterephthalic acid (H<sub>2</sub>BDC-NH<sub>2</sub>/NO<sub>2</sub>).

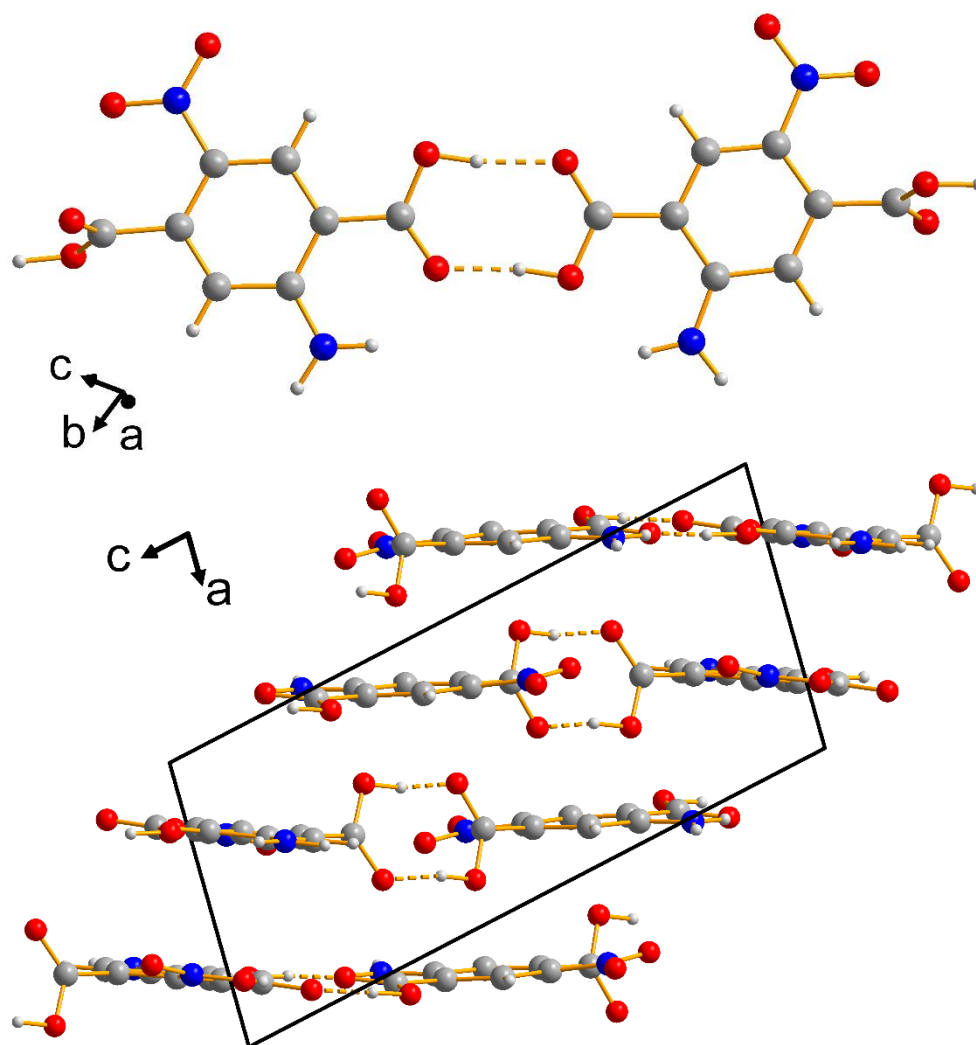


**Fig. S7** Crystal structure of 2-amino-5-nitroterephthalic acid ( $\text{H}_2\text{BDC-NH}_2/\text{NO}_2$ ). Above the hydrogen bonding model is shown, whereas the unit cell along  $[010]$  is shown below. Carbon atoms are shown in grey, nitrogen in blue and oxygen in red. Hydrogen bonds are marked in dashed lines.

**Table S3** Selected bond lengths of In-BDC-NH<sub>2</sub> (1).

atom 1	atom 2	distance / Å
In1	O1	2.261(2)
	O2	2.292(2)
C1	O1	1.266(5)
	O2	1.277(5)
C1	C4	1.491(4)
C2	N1	1.367(10)
C2	C2	1.430(8)
C3	C4	1.386(6)

**Table S4** Selected bond lengths of In-BDC-NH<sub>2</sub>/NO<sub>2</sub> (3).

atom 1	atom 2	distance / Å	atom 1	atom 2	distance / Å	
In1	O1	2.0355(4)	C1	C2	1.511(15)	
	O2	2.087(6)		C2	C3	1.358(13)
	O4	2.152(4)		C3	C4	1.392(18)
	O5	2.168(4)			N1	1.64(3)
O2	C1	1.221(17)	C4	C5	1.325(19)	
O3	C1	1.268(18)		N2	1.36(3)	
O4	C6	1.234(6)	C5	C6	1.509(10)	
O5	C7	1.224(6)	C7	C8	1.499(11)	
O6	N1	1.18(3)	C8	C9A	1.365(16)	
O7	N1	1.39(4)		C9B	1.43(3)	
O8	N3	1.41(3)	C9A	N3	1.51(2)	
O9	N3	1.35(2)	C9B	N4	1.412(14)	

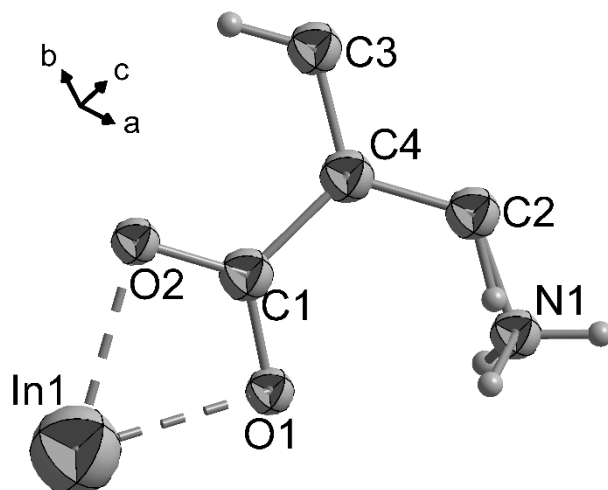
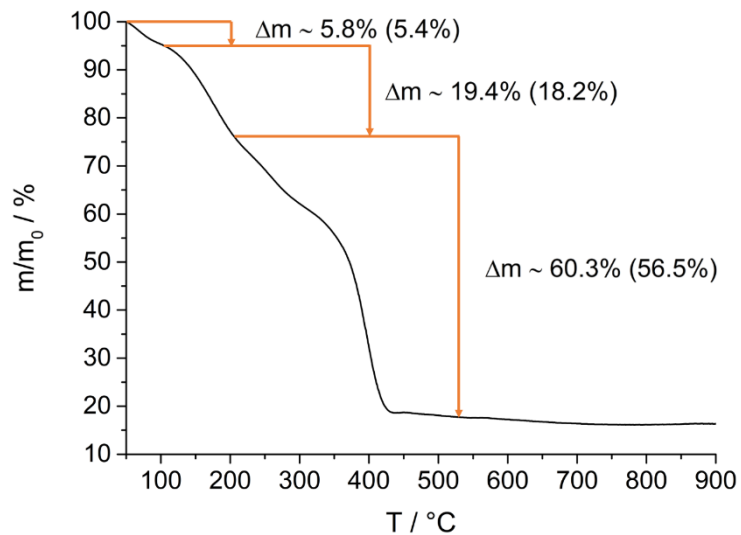


**Fig. S8** Asymmetric unit of In-BDC-NH<sub>2</sub> (**1**) with numbering scheme as used in Table S3.

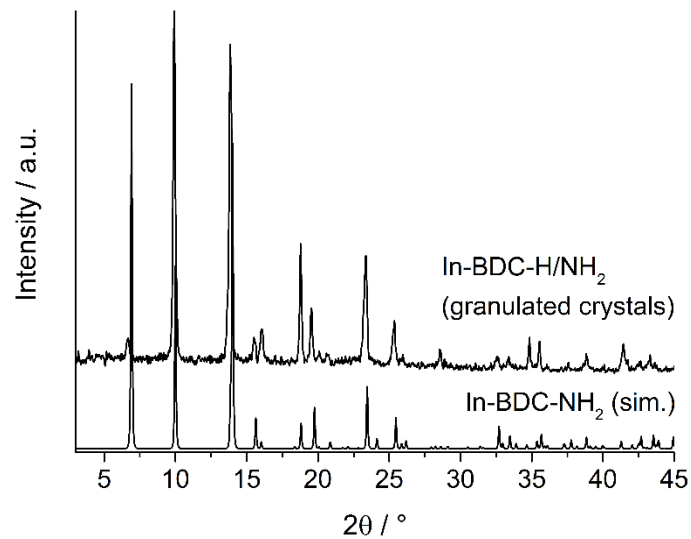
**Table S5** Overview of the bands visible in The IR spectrum of In-BDC-NH<sub>2</sub> (**1**) discussed in the manuscript.

wavenumber / cm <sup>-1</sup>	vibration	wavenumber / cm <sup>-1</sup>	vibration
3438	asym. -NH <sub>2</sub> stretching	1254	-NH <sub>3</sub> <sup>+</sup> rocking
3336	sym. -NH <sub>2</sub> stretching	1151	C-N stretching
3183	asym. N-H stretching	1099	-NH <sub>3</sub> <sup>+</sup> rocking
2780	sym. N-H stretching	1019	-NH <sub>3</sub> <sup>+</sup> rocking
1661	C-O stretching	861	arom. ring
1623	sym. carboxylate stretching	832	arom. ring
1551	asym. -NH <sub>3</sub> <sup>+</sup> deformation	765	N-H out of plane
1498	sym. -NH <sub>3</sub> <sup>+</sup> deformation	700	C-N deformation
1426	asym. carboxylate stretching	662	arom. ring
1330	C-N stretching		

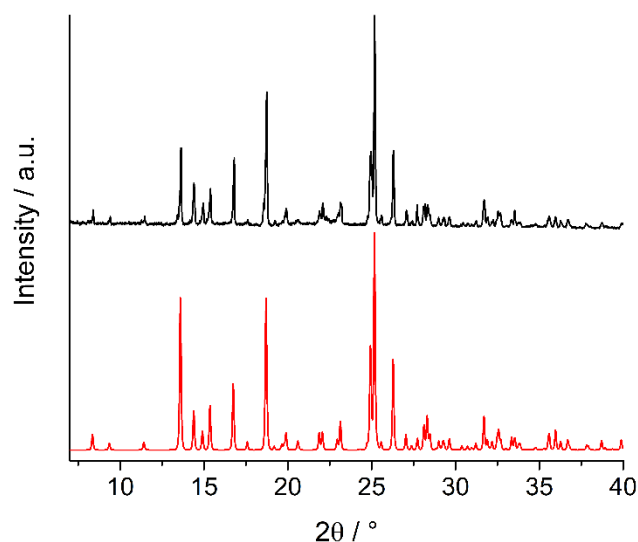




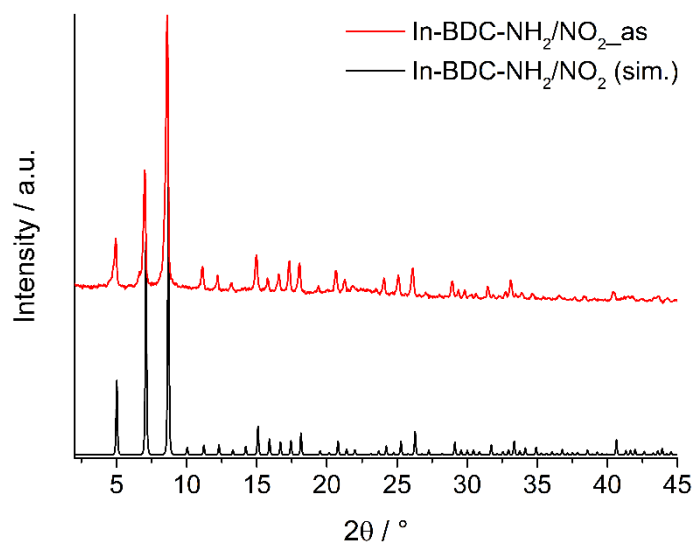
**Fig. S9** Thermogravimetric measurement of In-BDC-NH<sub>2</sub> (**1**). The calculated values based on the assumed sum formula are given in brackets.



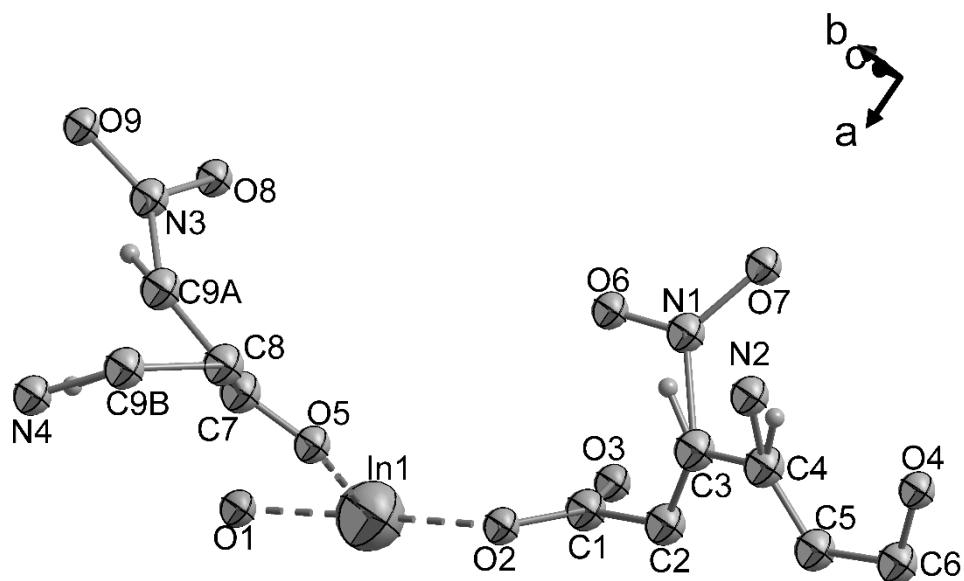
**Fig. S10** Comparison of the PXR D pattern recorded for granulated crystals of In-BDC-H/NH<sub>2</sub> and the simulated pattern of In-BDC-NH<sub>2</sub>.



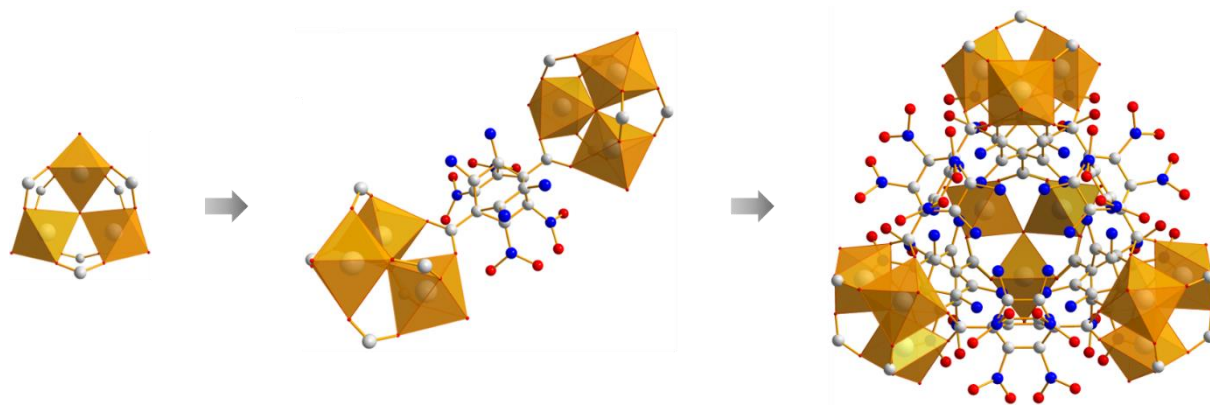
**Fig. S11** Comparison of the PXRD pattern recorded for the sample using the same synthesis conditions as used for **1** with linker molecule replaced by  $\text{H}_2\text{BDC-NH}_2/\text{NO}_2$  and the simulated pattern of dimethylammonium 2-amino-5-nitroterephthalate hemihydrate obtained from single crystal XRD measurements.<sup>[2]</sup>



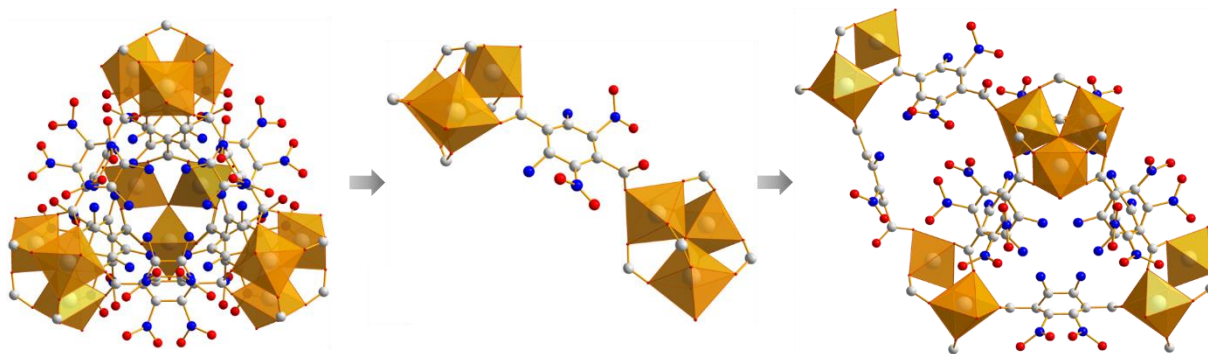
**Fig. S12** Comparison of the PXRD pattern recorded for In-BDC-NH<sub>2</sub>/NO<sub>2</sub> and the simulated pattern of In-BDC-NH<sub>2</sub>/NO<sub>2</sub> obtained from single crystal XRD measurements.



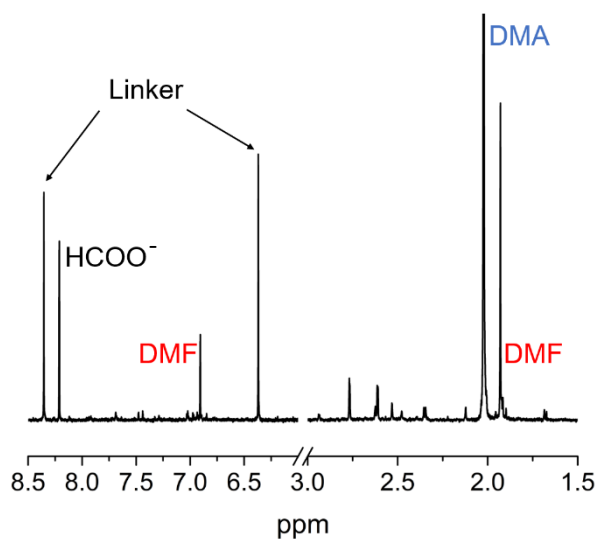
**Fig. S13** Asymmetric unit of In-BDC-NH<sub>2</sub>/NO<sub>2</sub> with numbering scheme as used in Table S4.



**Fig. S14** Crystal structure of In-BDC-NH<sub>2</sub>/NO<sub>2</sub>. Trinuclear clusters composed of three InO<sub>6</sub> octahedra bridged by an  $\mu_3$ -O atom (left) are interlinked by a disordered tetradentate BDC-NH<sub>2</sub>/NO<sub>2</sub><sup>2-</sup> ions (middle) to form a super-tetrahedron (right).



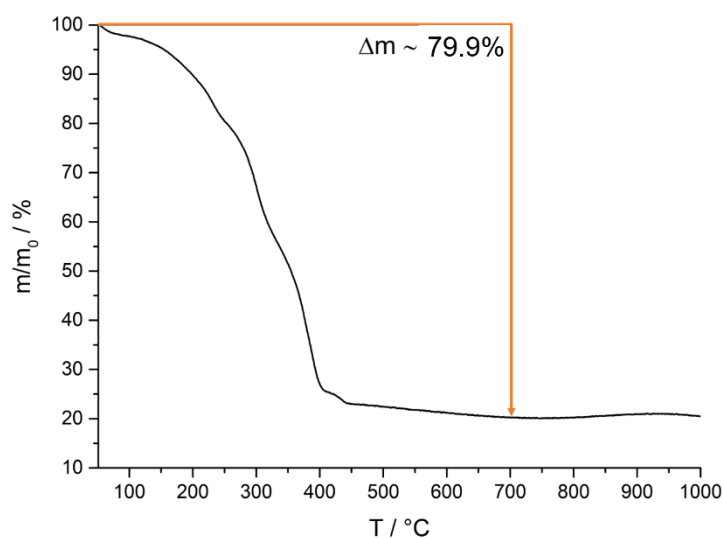
**Fig. S15** Crystal structure of In-BDC-NH<sub>2</sub>/NO<sub>2</sub>. To each super-tetrahedron (left) four additional trinuclear In-O-clusters are attached via tridentate carboxylate ions (middle). Thus, four additional super-tetrahedra are formed (right; only two face-sharing super-tetrahedra are displayed), face-sharing with the central one (left).



**Fig. S16** <sup>1</sup>H-NMR spectrum of In-BDC-NH<sub>2</sub>/NO<sub>2</sub>. The MOF was dissolved in 5% NaOD/D<sub>2</sub>O. Signals of DMF as well as HCOO<sup>-</sup> and dimethylammonium ions (DMA), the hydrolysis products of DMF, are visible.

**Table S6** Overview of the bands visible in The IR spectrum of In-BDC-NH<sub>2</sub>/NO<sub>2</sub> (**3**) discussed in the manuscript.

wavenumber / cm <sup>-1</sup>	vibration	wavenumber / cm <sup>-1</sup>	vibration
3430	asym. -NH <sub>2</sub> stretching	1254	Ar-N stretching
3316	sym. -NH <sub>2</sub> stretching	1159	asym. carboxylate stretching
3193	asym. C-H stretching	1096	N-H stretching
3065	ammonium stretching vibration	1023	C-H stretching
2923	C-H stretching	871	arom. ring
2801	sym. C-H stretching	784	N-H deformation
1644	C-O stretching	761	N-H out of plane
1620	sym. carboxylate stretching	660	arom. ring
1577	C=C stretching	501	N-H out of plane
1299	C-N stretching		

**Fig. S17** Thermogravimetric measurement of In-BDC-NH<sub>2</sub>/NO<sub>2</sub>. A clear assignment of decomposition steps was not possible.

## References

- [1] E. B. Skibo and J. H. Gilchrist, *The Journal of Organic Chemistry*, 1988, **53**, 4209-4218.
- [2] M. Krueger, M. Albat, F. Pieper and N. Stock, *IUCrData*, 2016, **1**, x160048.

## Supplementary Information

### Emergence of nonlinear optical activity by incorporation of a linker carrying the *p*-nitroaniline motif in MIL-53 frameworks

K. Markey,<sup>a†</sup> M. Krüger,<sup>b†</sup> T. Seidler,<sup>c,d†</sup> H. Reinsch,<sup>b</sup> T. Verbiest,<sup>e</sup> D. E. De Vos,<sup>a</sup> B. Champagne,<sup>d</sup> N. Stock<sup>b</sup> and M. A. van der Veen<sup>f</sup>

- a. Centre for Surface Chemistry and Catalysis, Faculty of Bioscience Engineering, University of Leuven, Leuven, Belgium.
  - b. Institut für Anorganische Chemie, Christian-Albrechts-Universität zu Kiel, Kiel, Germany.
  - c. K. Gumiński Department of Theoretical Chemistry, Jagiellonian University, Romana Ingardena 3, 30-060 Kraków, Poland.
  - d. Unité de Chimie Physique Théorique et Structurale, University of Namur, 5000 Namur, Belgium.
  - e. Molecular Imaging and Photonics, KU Leuven – University of Leuven, 3001 Leuven, Belgium.
  - f. Catalysis Engineering, TU Delft, 2628 Delft, The Netherlands.
- † K. Markey, M. Krüger and T. Seidler contributed equally.

### Contents

Linker synthesis.....	192
MOF Synthesis .....	195
XRD patterns and refinements .....	202
TG curves and elementary analysis .....	208
SEM images .....	211
NMR spectra.....	215
Sorption experiments.....	217
SHG microscopy.....	219
Calculation of $\langle d_{\text{eff}} \rangle$ values.....	221
Ab initio calculations .....	222
Estimation of the transmittance of 400 nm light through MIL-53(Al)-NH <sub>2</sub> -NO <sub>2</sub> crystals .....	228
UV-vis spectrum .....	229
SHG of MIL-53(Al)-NH <sub>2</sub> /NO <sub>2</sub> (1) as a function of temperature .....	229
Bibliography .....	230

## Linker synthesis

2-Amino-5-nitroterephthalic acid ( $H_2BDC-NH_2/NO_2$ ): The synthesis was accomplished by following the literature procedure published by Skibo et al. The reaction scheme is shown in **Figure S1**.

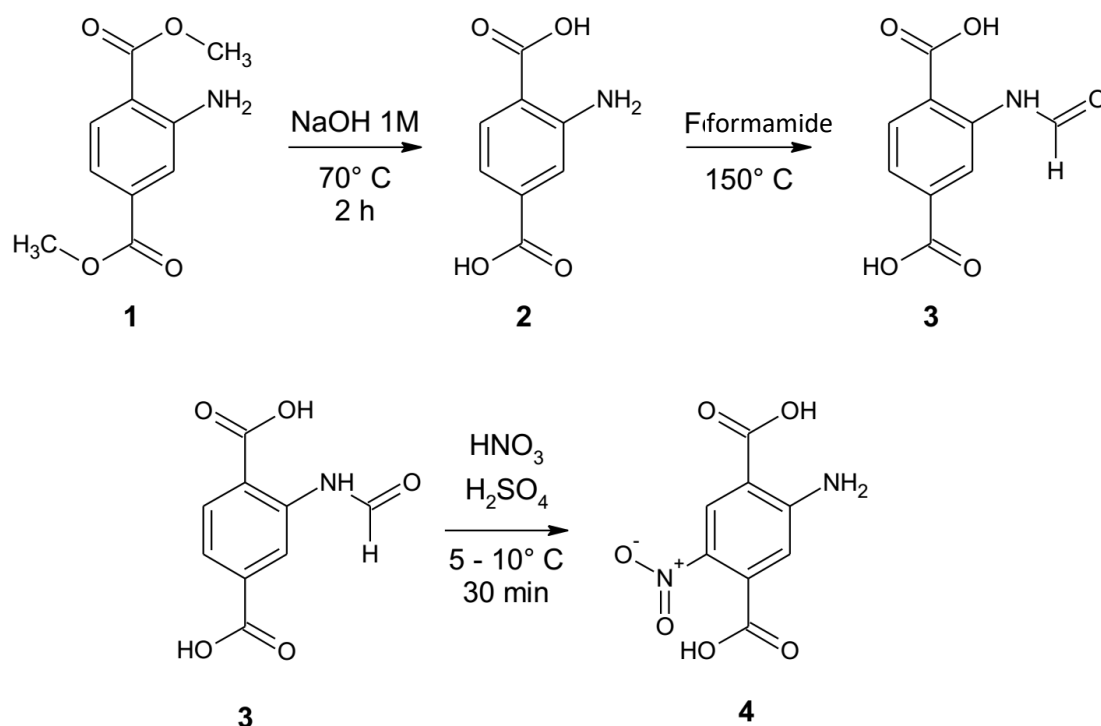


**Figure S1.** Reaction scheme for the synthesis of 2-amino-5-nitroterephthalic acid ( $H_2BDC-NH_2/NO_2$ ).

**Step 1:** A mixture of 87g (416 mmol) of dimethyl aminoterephthalate and 800 mL of a 1M NaOH solution was heated in a 1 L flask to 70 °C until the solid was dissolved completely. After cooling down to room temperature conc. HCl was added until a yellow solid precipitated which was filtered and washed with water.

Yield: 67 g (370 mmol, 89%)

**<sup>1</sup>H-NMR:** (200 MHz, DMSO-D<sub>6</sub>, 300 K):  $\delta$  [ppm]: 7.77 (1H, d, J = 8.3 Hz, H3), 7.39 (1H, d, J = 1.4 Hz, H1), 7.02 (1H, dd, J = 8.3 Hz, J = 1.6 Hz, H2).

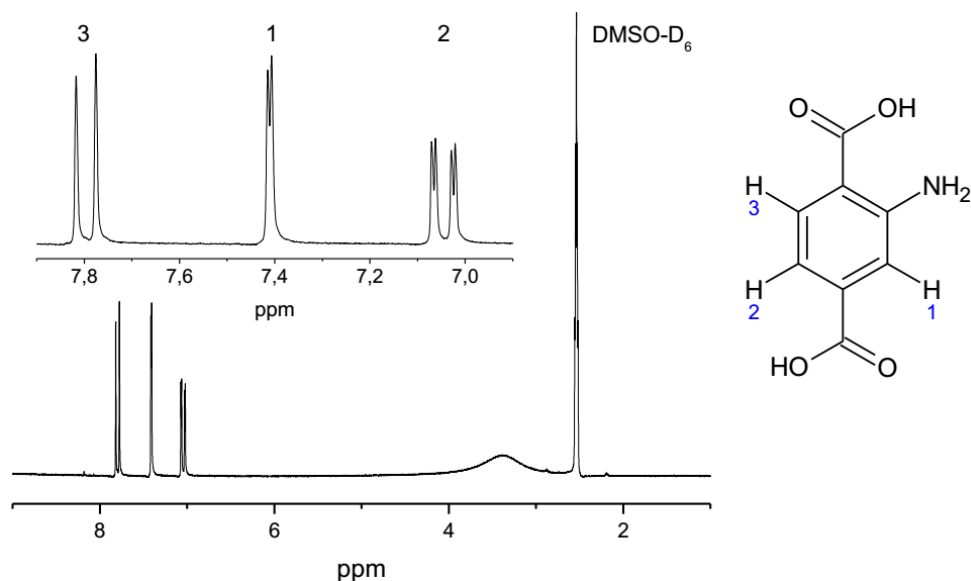


**Figure S2.**  $^1\text{H-NMR}$  spectrum of aminoterephthalic acid.

**Step 2:** A suspension of 20.8 g aminoterephthalic acid (114 mmol) and 100 mL formamide was heated rapidly to 150 °C until the solid was dissolved. During cooling down to room temperature a brown solid precipitated which was filtered off and dissolved in a saturated aqueous  $\text{Na}(\text{HCO}_3)$  solution. While acidifying this solution with conc. acetic acid a white solid precipitated which was filtered off, washed with water and dried completely.

Yield: 9.7 g (53 mmol, 48%)

**$^1\text{H-NMR}$ :** (200 MHz,  $\text{DMSO-D}_6$ , 300 K):  $\delta$  [ppm]: 9.1 (1H, s H1), 8.54 (1H, s H2), 8.07 (1H, d,  $J = 8.2$  Hz, H4), 7.69 (1H dd,  $J = 8.2$  Hz,  $J = 1.7$  Hz, H3)

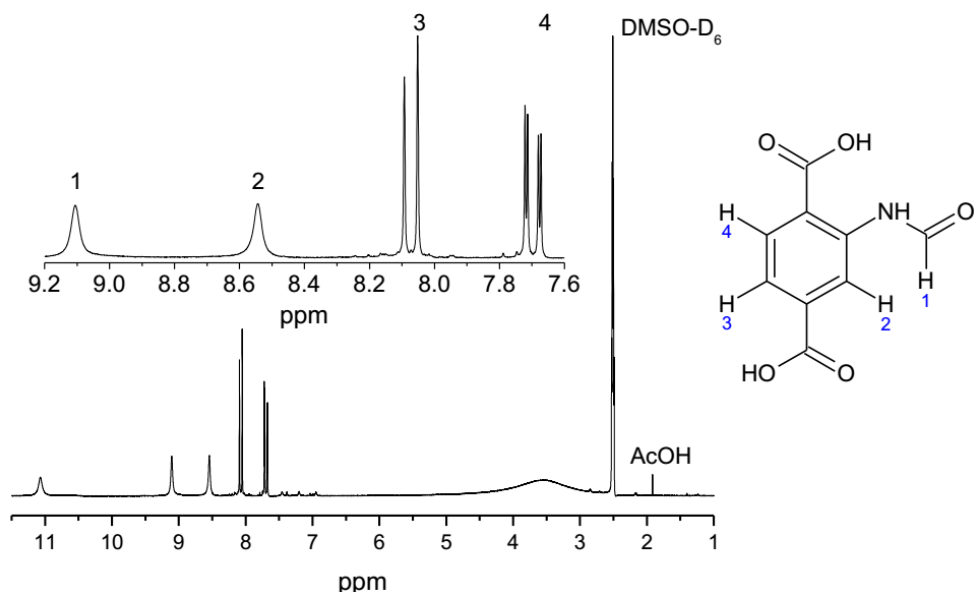


**Figure S3.**  $^1\text{H-NMR}$  spectrum of formamidoterephthalic acid.

**Step 3:** To 20 mL of fuming nitric acid, cooled in an ice bath, 5.1 g (24 mmol) of formamidoterephthalic acid was added under stirring. To this suspension 10 mL of conc. sulfuric acid, which was also cooled in an ice bath, was added slowly within 15-20 minutes keeping the temperature between 5-10°C. After addition, the solid was dissolved and the solution was poured on 100 g of ice and stored in a refrigerator



overnight. The precipitated solid was filtered off and recrystallized from hot water. Orange-brown crystals were obtained.

Yield: 1.5 g (6.6 mmol, 27%)

**<sup>1</sup>H-NMR:** (200 MHz, DMSO-D<sub>6</sub>, 300 K): δ [ppm]: 8.49 (1H, s, H1), 6.89 (1H, s, H2).

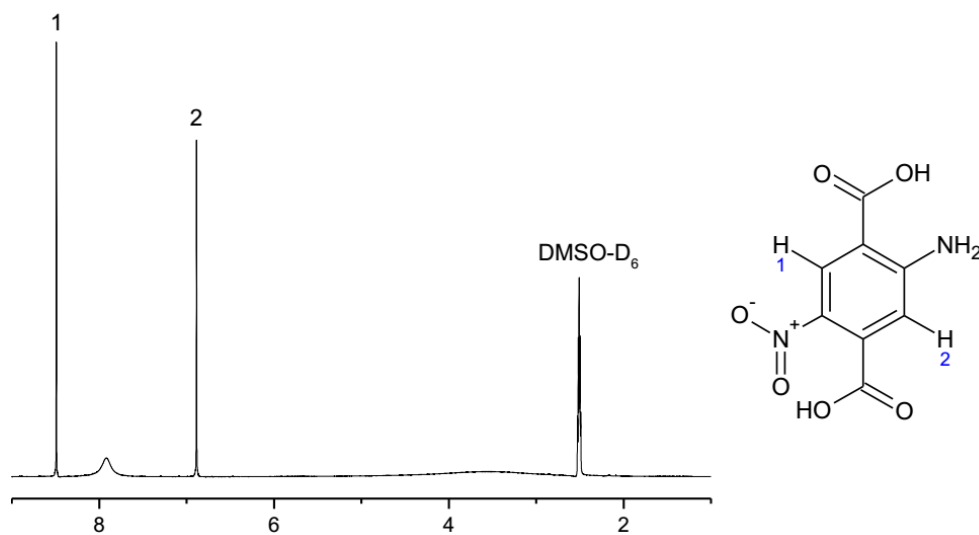


**Figure S4.** <sup>1</sup>H-NMR spectrum of 2-amino-5-nitroterephthalic acid (H<sub>2</sub>BDC-NH<sub>2</sub>/NO<sub>2</sub>) measured in DMSO-D<sub>6</sub>.

**<sup>1</sup>H-NMR:** (200 MHz, NaOD/D<sub>2</sub>O, 300 K): δ [ppm]: 8.36 (1H, s, H1), 6.41 (1H, s, H2).

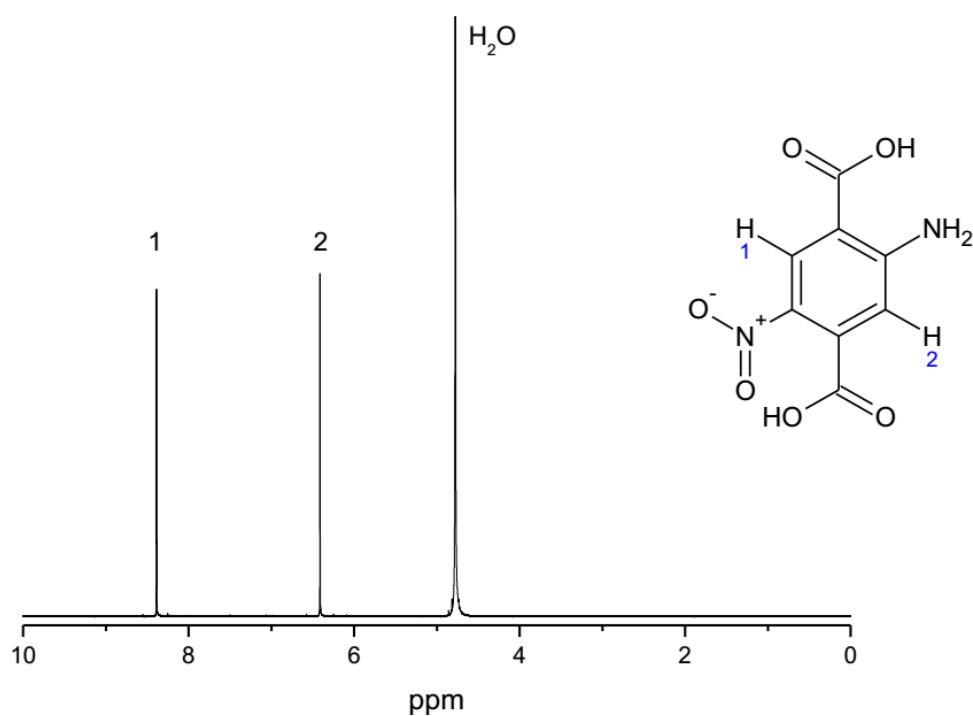


**Figure S5.** <sup>1</sup>H-NMR spectrum of 2-amino-5-nitroterephthalic acid (H<sub>2</sub>BDC-NH<sub>2</sub>/NO<sub>2</sub>) measured in 5% NaOD/D<sub>2</sub>O.

## MOF Synthesis

Table S1. Molar ratios and exact amounts of the reactants employed in the HT experiments for MIL-53(Al)-NH<sub>2</sub>/NO<sub>2</sub>.

metal source	No.	equivalent linker	equivalent Al <sup>3+</sup>	additive [μL/mg]	linker [mg]	Al <sup>3+</sup> [μL/mg]	V H <sub>2</sub> O [μL]	V DMF [μL]	temperature program
2 M AlCl <sub>3</sub> ·6H <sub>2</sub> O in H <sub>2</sub> O	1	2	1	0	20.0	22.1	477.9	0.0	1h/12h\1h 160°C
	2	2	2	0	20.0	44.2	455.8	0.0	
	3	2	3	0	20.0	66.4	433.6	0.0	
	4	3	2	0	30.0	44.2	455.8	0.0	
	5	3	3	0	30.0	66.4	433.6	0.0	
	6	3	4	0	30.0	88.5	411.5	0.0	
2 M Al(NO <sub>3</sub> ) <sub>3</sub> ·9H <sub>2</sub> O in H <sub>2</sub> O	7	2	1	0	20.0	22.1	477.9	0.0	
	8	2	2	0	20.0	44.2	455.8	0.0	
	9	2	3	0	20.0	66.4	433.6	0.0	
	10	3	2	0	30.0	44.2	455.8	0.0	
	11	3	3	0	30.0	66.4	433.6	0.0	
	12	3	4	0	30.0	88.5	411.5	0.0	
2 M AlCl <sub>3</sub> ·6H <sub>2</sub> O in H <sub>2</sub> O	13	1	1	0	10.0	22.1	127.9	0.0	1h/12h\1h 180°C
	14	1	2	0	10.0	44.2	105.8	0.0	
	15	1	4	0	10.0	88.5	61.5	0.0	
	16	2	0.5	0	20.0	11.1	138.9	0.0	
	17	2	1	0	20.0	22.1	127.9	0.0	
	18	2	2	0	20.0	44.2	105.8	0.0	
	19	2	2	0	20.0	44.2	105.8	0.0	
	20	2	2	0	20.0	44.2	85.8	20.0	
	21	2	2	0	20.0	44.2	65.8	40.0	
	22	2	2	0	20.0	44.2	45.8	60.0	
	23	2	2	0	20.0	44.2	25.8	80.0	
	24	2	2	0	20.0	44.2	5.8	100.0	
	25	1	1	0	10.0	22.1	277.9	200.0	
	26	1	2	0	10.0	44.2	255.8	200.0	
27	1	3	0	10.0	66.4	233.6	200.0		
28	2	0.5	0	20.0	11.1	288.9	200.0		
29	2	1	0	20.0	22.1	277.9	200.0		
30	2	2	0	20.0	44.2	255.8	200.0		
AlCl <sub>3</sub> ·6H <sub>2</sub> O	31	1	1	0	10.0	10.7	300.0	200.0	
	32	1	2	0	10.0	21.4	300.0	200.0	
	33	1	3	0	10.0	32.0	300.0	200.0	
	34	2	0.5	0	20.0	5.3	300.0	200.0	
	35	2	1	0	20.0	10.7	300.0	200.0	
	36	2	2	0	20.0	21.4	300.0	200.0	
					2M NaOH [μL]				
	37	2	2	4.4	20.0	21.4	295.6	200.0	
38	2	2	8.8	20.0	21.4	291.2	200.0		

	39	2	2	13.3	20.0	21.4	286.7	200.0	
	40	2	2	17.7	20.0	21.4	282.3	200.0	
	41	2	2	22.1	20.0	21.4	277.9	200.0	
	42	2	2	26.5	20.0	21.4	273.5	200.0	
2 M $\text{AlCl}_3 \cdot 6\text{H}_2\text{O}$ in $\text{H}_2\text{O}$	43	1	1	0	10.0	22.1	67.9	60.0	
	44	1	2	0	10.0	44.2	45.8	60.0	
	45	1	3	0	10.0	66.4	23.6	60.0	
	46	2	0.5	0	20.0	11.1	78.9	60.0	
	47	2	1	0	20.0	22.1	67.9	60.0	
	48	2	2	0	20.0	44.2	45.8	60.0	
$\text{AlCl}_3 \cdot 6\text{H}_2\text{O}$	49	1	1	10	10.0	10.7	90.0	60.0	
	50	1	2	10	10.0	21.4	90.0	60.0	
	51	1	3	10	10.0	32.0	90.0	60.0	
	52	2	0.5	10	20.0	5.3	90.0	60.0	
	53	2	1	10	20.0	10.7	90.0	60.0	
	54	2	2	10	20.0	21.4	90.0	60.0	
	55	2	2	8.8	20.0	21.4	81.2	60.0	
	56	2	2	17.7	20.0	21.4	72.3	60.0	
	57	2	2	26.5	20.0	21.4	63.5	60.0	
	58	2	2	35.4	20.0	21.4	54.6	60.0	
	59	2	2	44.2	20.0	21.4	45.8	60.0	
	60	2	2	53.1	20.0	21.4	36.9	60.0	
2 M $\text{AlCl}_3 \cdot 6\text{H}_2\text{O}$ in $\text{CH}_2\text{Cl}_2$	61	2	2	13.3	20.0	44.2	32.5	60.0	
	62	2	2	22.1	20.0	44.2	23.6	60.0	
	63	3	3	0.0	30.0	66.4	23.6	60.0	
	64	3	3	17.7	30.0	66.4	5.9	60.0	
$\text{AlCl}_3 \cdot 6\text{H}_2\text{O}$	65	3	3	26.5	30.0	32.0	63.5	60.0	
	66	3	3	35.4	30.0	32.0	54.6	60.0	
2 M $\text{AlCl}_3 \cdot 6\text{H}_2\text{O}$ in $\text{CH}_2\text{Cl}_2$	67	2	2	13.3	20.0	44.2	32.5	60.0	
	68	2	2	22.1	20.0	44.2	23.6	60.0	
	69	3	3	0.0	30.0	66.4	23.6	60.0	
	70	3	3	17.7	30.0	66.4	5.9	60.0	
$\text{AlCl}_3 \cdot 6\text{H}_2\text{O}$	71	3	3	26.5	30.0	32.0	63.5	60.0	
	72	3	3	35.4	30.0	32.0	54.6	60.0	

**Table S2.** Molar ratios and exact amounts of the reactants employed in the HT experiments for MIL-53(Al)-NH<sub>2</sub>/NO<sub>2</sub> (2).

metal source	No.	equivalent linker	equivalent Al <sup>3+</sup>	additive [μL/mg]	linker [mg]	Al <sup>3+</sup> [μL/mg]	V H <sub>2</sub> O [μL]	V EtOH [μL]	temperature program
AlCl <sub>3</sub> ·6H <sub>2</sub> O	1	2	2	0	20.0	21.4	125.0	25.0	1h/36h\1h 150°C
	2	2	2	0	20.0	21.4	100.0	50.0	
	3	2	2	0	20.0	21.4	75.0	75.0	
	4	2	2	0	20.0	21.4	50.0	100.0	
	5	2	2	0	20.0	21.4	25.0	125.0	
	6	2	2	0	20.0	21.4	0.0	150.0	
	7	2	2	0	20.0	21.4	10.0	140.0	
	8	2	2	0	20.0	21.4	15.0	135.0	
	9	2	2	0	20.0	21.4	20.0	130.0	
	10	2	2	0	20.0	21.4	25.0	125.0	
	11	2	2	0	20.0	21.4	30.0	120.0	
	12	2	2	0	20.0	21.4	35.0	115.0	

**Table S3.** Molar ratios and exact amounts of the reactants employed in the HT experiments for MIL-53(Ga)-NH<sub>2</sub>/NO<sub>2</sub>.

metal source	No.	equivalent linker	equivalent Ga <sup>3+</sup>	additive [μL/mg]	linker [mg]	Ga <sup>3+</sup> [μL/mg]	V EtOH [μL]	V H <sub>2</sub> O [μL]	temperature program	
2M Ga(NO <sub>3</sub> ) <sub>3</sub> ·H <sub>2</sub> O in H <sub>2</sub> O	1	1	0.5	0	10.0	11.1	10.0	128.9	1h/36h\1h 150°C	
	2	1	1	0	10.0	22.1	10.0	117.9		
	3	1	2	0	10.0	44.2	10.0	95.8		
	4	2	1	0	20.0	22.1	10.0	117.9		
	5	2	2	0	20.0	44.2	10.0	95.8		
	6	2	4	0	20.0	88.5	10.0	51.5		
	7	1	0.5	0	10.0	11.1	20.0	118.9		
	8	1	1	0	10.0	22.1	20.0	107.9		
	9	1	2	0	10.0	44.2	20.0	85.8		
	10	2	1	0	20.0	22.1	20.0	107.9		
	11	2	2	0	20.0	44.2	20.0	85.8		
	12	2	4	0	20.0	88.5	20.0	41.5		
	13	1	0.5	0	10.0	11.1	40.0	98.9	8h/16h\4h 150°C	
	14	1	1	0	10.0	22.1	40.0	87.9		
	15	1	2	0	10.0	44.2	40.0	65.8		
	16	2	1	0	20.0	22.1	40.0	87.9		
	17	2	2	0	20.0	44.2	40.0	65.8		
	18	2	4	0	20.0	88.5	40.0	21.5		
	19	1	0.5	0	10.0	11.1	60.0	78.9		
	20	1	1	0	10.0	22.1	60.0	67.9		
	21	1	2	0	10.0	44.2	60.0	45.8		
	22	2	1	0	20.0	22.1	60.0	67.9		
	23	2	2	0	20.0	44.2	60.0	45.8		
	24	2	4	0	20.0	88.5	60.0	1.5		
	25	2	2	0	20.0	44.2	10.0	95.8		24h/2 4h\12 h 150°C
	26	2	2	0	20.0	44.2	20.0	85.8		
	27	2	2	0	20.0	44.2	50.0	55.8		

28	2	2	0	20.0	44.2	60.0	45.8	4h/16h\8h 150°C
29	2	2	0	20.0	44.2	85.0	20.8	
30	2	2	0	20.0	44.2	100.0	5.8	
31	2	2	0	20.0	44.2	10.0	95.8	
32	2	2	0	20.0	44.2	20.0	85.8	
33	2	2	0	20.0	44.2	50.0	55.8	
34	2	2	0	20.0	44.2	60.0	45.8	
35	2	2	0	20.0	44.2	85.0	20.8	
36	2	2	0	20.0	44.2	100.0	5.8	
37	2	2	0	20.0	44.2	10.0	95.8	
38	2	2	0	20.0	44.2	60.0	45.8	
39	2	2	0	20.0	44.2	100.0	5.8	
40	2	1	0	20.0	22.1	20.0	107.9	
41	2	2	0	20.0	44.2	20.0	85.8	
42	2	4	0	20.0	88.5	20.0	41.5	
43	2	2	0	20.0	44.2	30.0	225.8	
44	2	2	0	20.0	44.2	150.0	105.8	
45	2	2	0	20.0	44.2	250.0	5.8	
46	2	1	0	20.0	22.1	50.0	227.9	
47	2	2	0	20.0	44.2	50.0	205.8	
48	2	4	0	20.0	88.5	50.0	161.5	
							V DMF [μL]	
49	2	2	0	20.0	44.2	10.0	95.8	
50	2	2	0	20.0	44.2	60.0	45.8	
51	2	2	0	20.0	44.2	100.0	5.8	
52	2	1	0	20.0	22.1	20.0	107.9	
53	2	2	0	20.0	44.2	20.0	85.8	
54	2	4	0	20.0	88.5	20.0	41.5	
55	2	2	0	20.0	44.2	30.0	225.8	
56	2	2	0	20.0	44.2	150.0	105.8	
57	2	2	0	20.0	44.2	250.0	5.8	
58	2	1	0	20.0	22.1	50.0	227.9	
59	2	2	0	20.0	44.2	50.0	205.8	
60	2	4	0	20.0	88.5	50.0	161.5	
			2M NaOH [μL]				V H <sub>2</sub> O [μL]	
61	2	2	0.0	21.4	20.0	60.0	35.8	
62	2	2	0.0	21.4	20.0	60.0	25.8	
63	2	2	0.0	21.4	20.0	60.0	15.8	
64	2	2	10.0	21.4	20.0	60.0	35.8	
65	2	2	20.0	21.4	20.0	60.0	25.8	
66	2	2	30.0	21.4	20.0	60.0	15.8	
67	2	2	0.0	21.4	20.0	60.0	35.8	
68	2	2	0.0	21.4	20.0	60.0	25.8	
69	2	2	0.0	21.4	20.0	60.0	15.8	
70	2	2	10.0	21.4	20.0	60.0	35.8	
71	2	2	20.0	21.4	20.0	60.0	25.8	
72	2	2	30.0	21.4	20.0	60.0	15.8	

			1M HNO <sub>3</sub> [μL]			V DMF [μL]	V EtOH [μL]
73	2	2	10.0	21.4	20.0	60.0	35.8
74	2	2	20.0	21.4	20.0	60.0	25.8
75	2	2	30.0	21.4	20.0	60.0	15.8
						V H <sub>2</sub> O [μL]	V EtOH [μL]
76	2	2	10.0	21.4	20.0	60.0	35.8
77	2	2	20.0	21.4	20.0	60.0	25.8
78	2	2	30.0	21.4	20.0	60.0	15.8

1h/16h\1h 150°C

**Table S4.** Molar ratios and exact amounts of the reactants employed in the HT experiments for MIL-53(Ga)-NH<sub>2</sub>/NO<sub>2</sub>.

metal source	No.	equivalent linker	equivalent In <sup>3+</sup>	additive [μL/mg]	linker [mg]	In <sup>3+</sup> [μL/mg]	V EtOH [μL]	V H <sub>2</sub> O [μL]	temperature program
2M In(NO <sub>3</sub> ) <sub>3</sub> · H <sub>2</sub> O in H <sub>2</sub> O	1	1	0.5	0	10.0	11.1	10.0	128.9	1h/36h\1h 150°C
	2	1	1	0	10.0	22.1	10.0	117.9	
	3	1	2	0	10.0	44.2	10.0	95.8	
	4	2	1	0	20.0	22.1	10.0	117.9	
	5	2	2	0	20.0	44.2	10.0	95.8	
	6	2	4	0	20.0	88.5	10.0	51.5	
	7	1	0.5	0	10.0	11.1	20.0	118.9	
	8	1	1	0	10.0	22.1	20.0	107.9	
	9	1	2	0	10.0	44.2	20.0	85.8	
	10	2	1	0	20.0	22.1	20.0	107.9	
	11	2	2	0	20.0	44.2	20.0	85.8	
	12	2	4	0	20.0	88.5	20.0	41.5	
	13	1	0.5	0	10.0	11.1	40.0	98.9	8h/16h\4h 150°C
	14	1	1	0	10.0	22.1	40.0	87.9	
	15	1	2	0	10.0	44.2	40.0	65.8	
	16	2	1	0	20.0	22.1	40.0	87.9	
	17	2	2	0	20.0	44.2	40.0	65.8	
	18	2	4	0	20.0	88.5	40.0	21.5	
	19	1	0.5	0	10.0	11.1	60.0	78.9	
	20	1	1	0	10.0	22.1	60.0	67.9	
	21	1	2	0	10.0	44.2	60.0	45.8	
	22	2	1	0	20.0	22.1	60.0	67.9	
	23	2	2	0	20.0	44.2	60.0	45.8	
	24	2	4	0	20.0	88.5	60.0	1.5	
	25	2	2	0	20.0	44.2	10.0	95.8	24h/24h\12h 150°C
	26	2	2	0	20.0	44.2	20.0	85.8	
	27	2	2	0	20.0	44.2	50.0	55.8	
	28	2	2	0	20.0	44.2	60.0	45.8	
	29	2	2	0	20.0	44.2	85.0	20.8	
	30	2	2	0	20.0	44.2	100.0	5.8	
	31	2	2	0	20.0	44.2	10.0	95.8	
	32	2	2	0	20.0	44.2	20.0	85.8	

4h/  
16  
h\8  
h

33	2	2	0	20.0	44.2	50.0	55.8	12h/36h\12h 130°C
34	2	2	0	20.0	44.2	60.0	45.8	
35	2	2	0	20.0	44.2	85.0	20.8	
36	2	2	0	20.0	44.2	100.0	5.8	
37	2	2	0	20.0	44.2	10.0	95.8	
38	2	2	0	20.0	44.2	60.0	45.8	
39	2	2	0	20.0	44.2	100.0	5.8	
40	2	1	0	20.0	22.1	20.0	107.9	
41	2	2	0	20.0	44.2	20.0	85.8	
42	2	4	0	20.0	88.5	20.0	41.5	
43	2	2	0	20.0	44.2	30.0	225.8	
44	2	2	0	20.0	44.2	150.0	105.8	
45	2	2	0	20.0	44.2	250.0	5.8	
46	2	1	0	20.0	22.1	50.0	227.9	
47	2	2	0	20.0	44.2	50.0	205.8	
48	2	4	0	20.0	88.5	50.0	161.5	
							V DMF [μL]	
49	2	2	0	20.0	44.2	10.0	95.8	
50	2	2	0	20.0	44.2	60.0	45.8	
51	2	2	0	20.0	44.2	100.0	5.8	
52	2	1	0	20.0	22.1	20.0	107.9	
53	2	2	0	20.0	44.2	20.0	85.8	
54	2	4	0	20.0	88.5	20.0	41.5	
55	2	2	0	20.0	44.2	30.0	225.8	
56	2	2	0	20.0	44.2	150.0	105.8	
57	2	2	0	20.0	44.2	250.0	5.8	
58	2	1	0	20.0	22.1	50.0	227.9	
59	2	2	0	20.0	44.2	50.0	205.8	
60	2	4	0	20.0	88.5	50.0	161.5	
			2M NaOH [μL]			V H <sub>2</sub> O [μL]		
61	2	2	0.0	21.4	20.0	60.0	35.8	
62	2	2	0.0	21.4	20.0	60.0	25.8	
63	2	2	0.0	21.4	20.0	60.0	15.8	
64	2	2	10.0	21.4	20.0	60.0	35.8	
65	2	2	20.0	21.4	20.0	60.0	25.8	
66	2	2	30.0	21.4	20.0	60.0	15.8	
67	2	2	0.0	21.4	20.0	60.0	35.8	
68	2	2	0.0	21.4	20.0	60.0	25.8	
69	2	2	0.0	21.4	20.0	60.0	15.8	
70	2	2	10.0	21.4	20.0	60.0	35.8	
71	2	2	20.0	21.4	20.0	60.0	25.8	
72	2	2	30.0	21.4	20.0	60.0	15.8	
			1M HNO <sub>3</sub> [μL]			V DMF [μL]	V EtOH [μL]	
73	2	2	10.0	21.4	20.0	60.0	35.8	
74	2	2	20.0	21.4	20.0	60.0	25.8	
75	2	2	30.0	21.4	20.0	60.0	15.8	

							V H <sub>2</sub> O [μL]	V EtOH [μL]
	76	2	2	10.0	21.4	20.0	60.0	35.8
	77	2	2	20.0	21.4	20.0	60.0	25.8
	78	2	2	30.0	21.4	20.0	60.0	15.8
							V EtOH [μL]	V DMF [μL]
2M In(NO <sub>3</sub> ) <sub>3</sub> · H <sub>2</sub> O in DMF		2	2	0	20.0	44.2	10.0	95.8
		2	2	0	20.0	44.2	60.0	45.8
		2	2	0	20.0	44.2	100.0	5.8
		2	1	0	20.0	22.1	20.0	107.9
		2	2	0	20.0	44.2	20.0	85.8
		2	4	0	20.0	88.5	20.0	41.5
		2	2	0	20.0	44.2	30.0	225.8
		2	2	0	20.0	44.2	150.0	105.8
		2	2	0	20.0	44.2	250.0	5.8
		2	1	0	20.0	22.1	50.0	227.9
		2	2	0	20.0	44.2	50.0	205.8
		2	4	0	20.0	88.5	50.0	161.5
		1	0.5	0	10.0	11.1	10.0	128.9
		1	1	0	10.0	22.1	10.0	117.9
		1	2	0	10.0	44.2	10.0	95.8
		2	1	0	20.0	22.1	10.0	117.9
		2	2	0	20.0	44.2	10.0	95.8
		2	4	0	20.0	88.5	10.0	51.5
		1	0.5	0	10.0	11.1	20.0	118.9
		1	1	0	10.0	22.1	20.0	107.9
		1	2	0	10.0	44.2	20.0	85.8
		2	1	0	20.0	22.1	20.0	107.9
		2	2	0	20.0	44.2	20.0	85.8
		2	4	0	20.0	88.5	20.0	41.5
		1	0.5	0	10.0	11.1	40.0	98.9
		1	1	0	10.0	22.1	40.0	87.9
		1	2	0	10.0	44.2	40.0	65.8
		2	1	0	20.0	22.1	40.0	87.9
		2	2	0	20.0	44.2	40.0	65.8
		2	4	0	20.0	88.5	40.0	21.5
		1	0.5	0	10.0	11.1	60.0	78.9
		1	1	0	10.0	22.1	60.0	67.9
		1	2	0	10.0	44.2	60.0	45.8
		2	1	0	20.0	22.1	60.0	67.9
		2	2	0	20.0	44.2	60.0	45.8
		2	4	0	20.0	88.5	60.0	1.5

12h/36h/12h 130°C

1h/6h/1h 150°C



## XRD patterns and refinements

MIL-53(Al)-NH<sub>2</sub>/NO<sub>2</sub> (1) synthesized in DMF

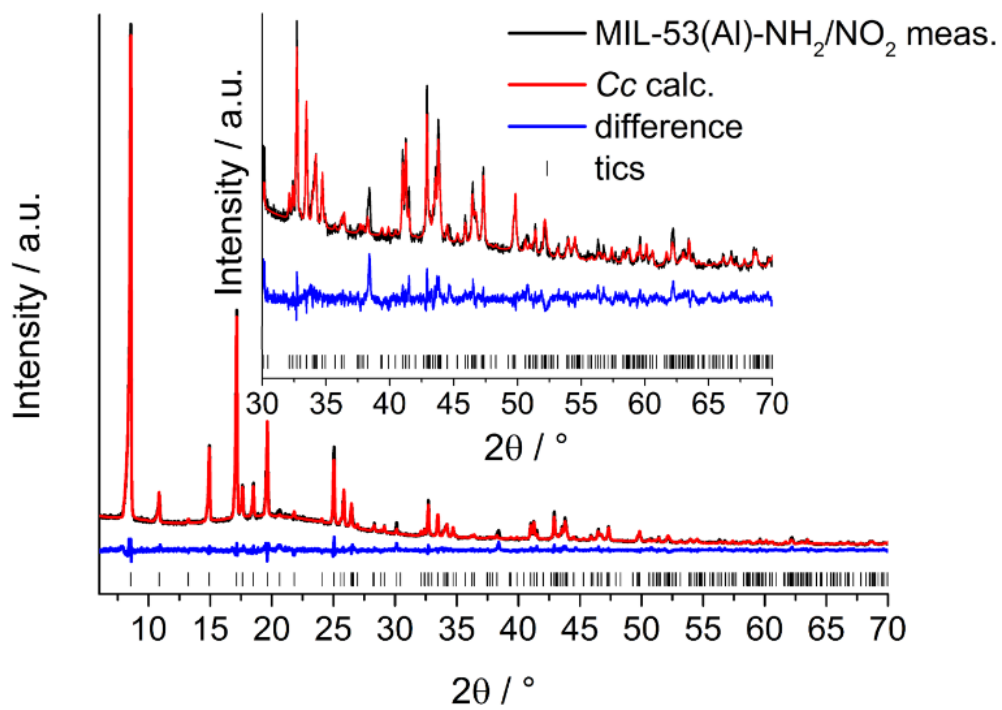


**Figure S6.** Final Rietveld plot of MIL-53(Al)-NH<sub>2</sub>/NO<sub>2</sub> synthesized in DMF (1).

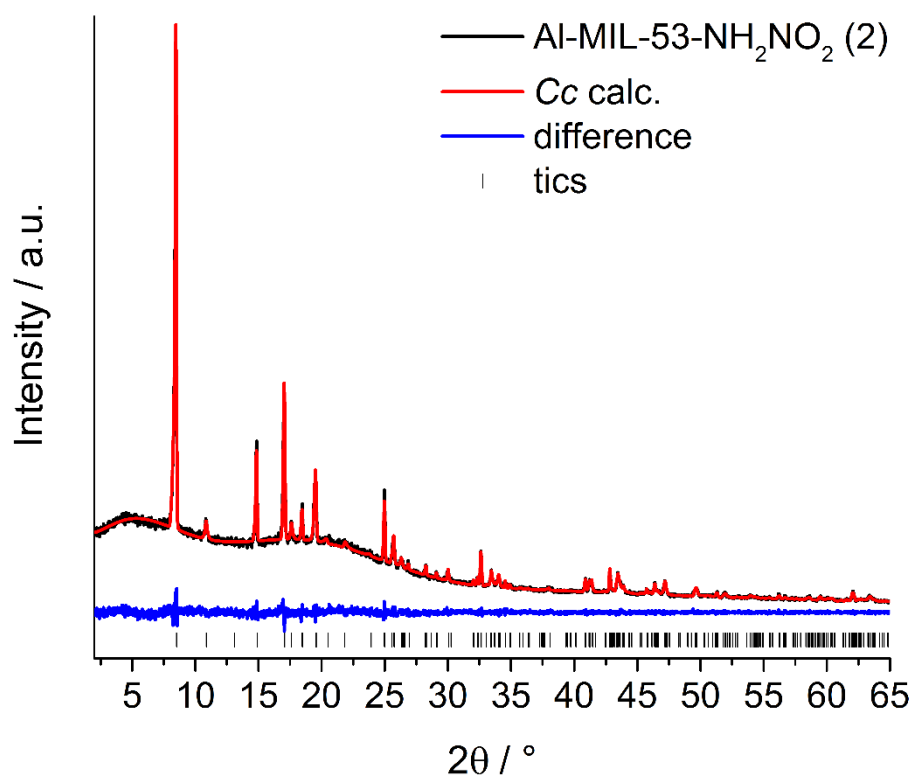
MIL-53(Al)-NH<sub>2</sub>/NO<sub>2</sub> (2) synthesized in EtOH

Figure S7. Pawley refinement of MIL-53(Al)-NH<sub>2</sub>/NO<sub>2</sub> (2) synthesized in EtOH (2).

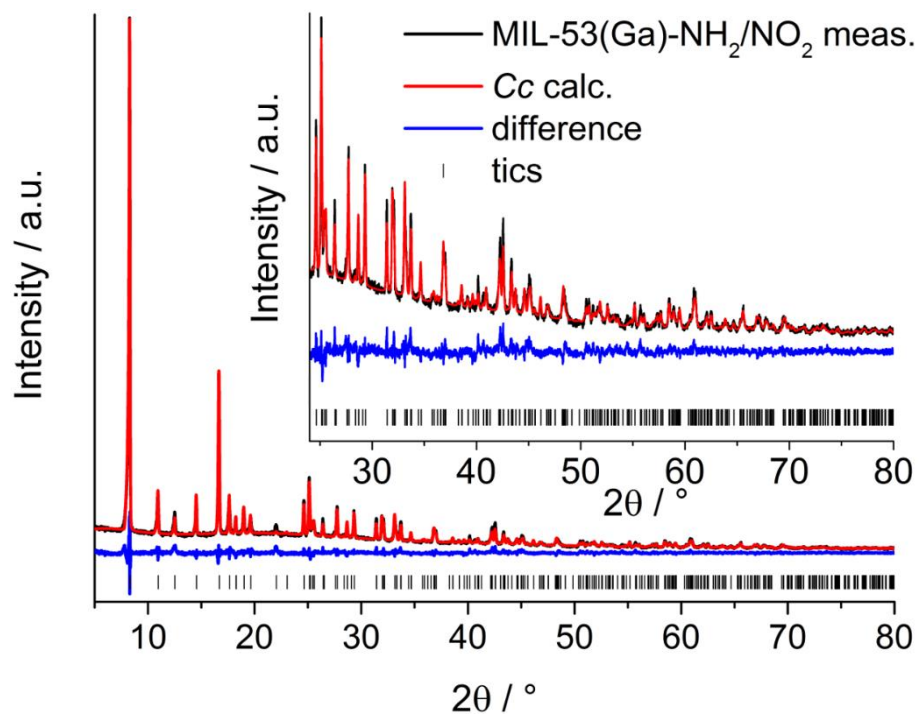
MIL-53(Ga)-NH<sub>2</sub>/NO<sub>2</sub> (3)

Figure S8. Final Rietveld plot of MIL-53(Ga)-NH<sub>2</sub>/NO<sub>2</sub>(3).

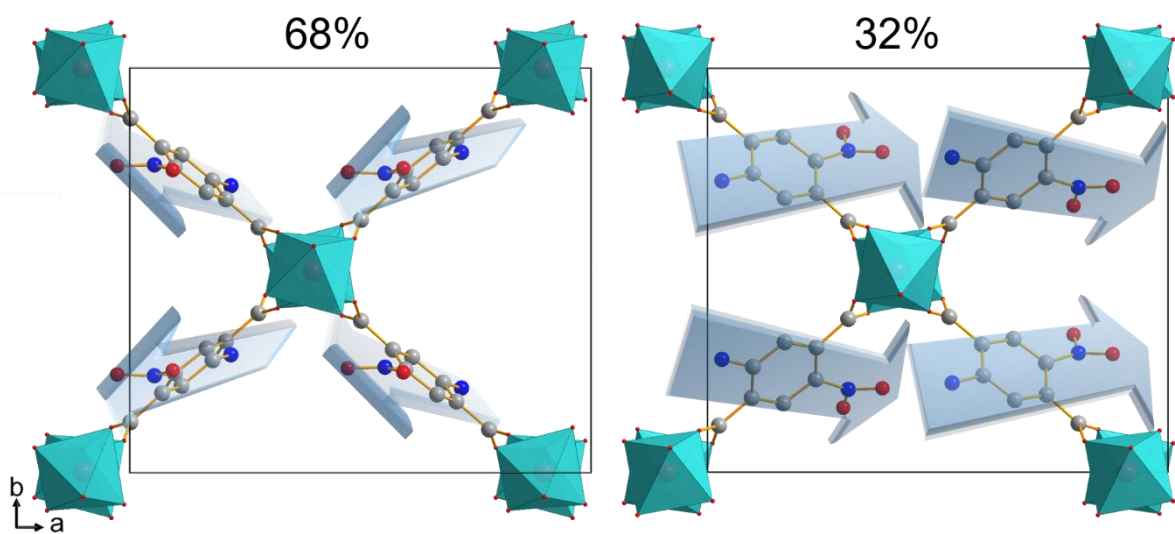
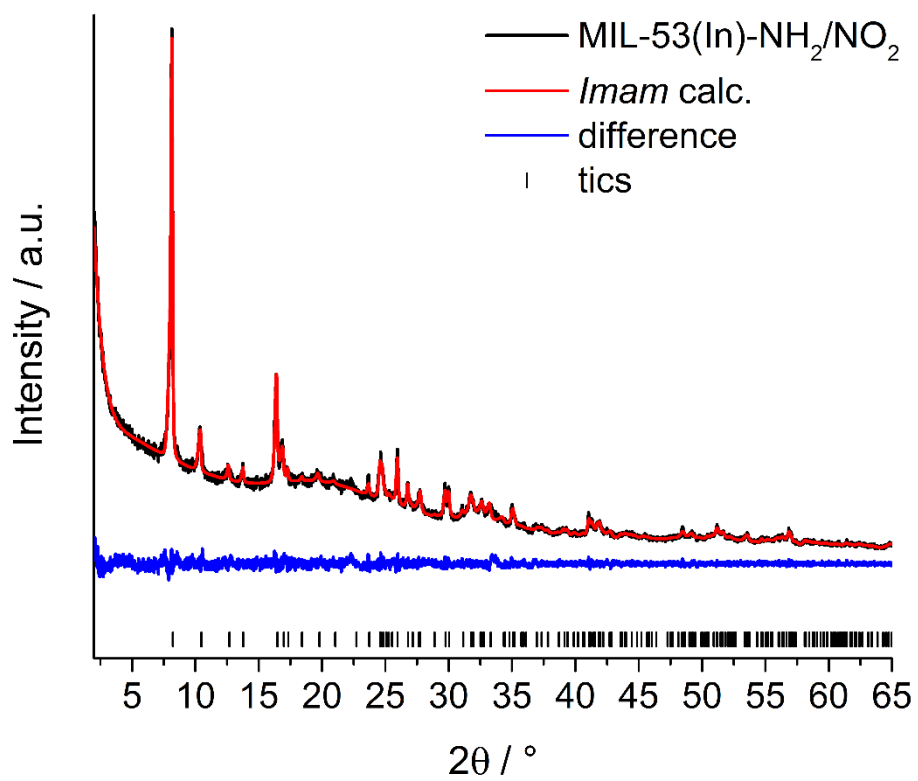


Figure S9. Crystal structure of MIL-53(Ga) along [001]. The disordering (above) of the structure contains 68% of the NO<sub>2</sub> groups of the linker molecules showing out of the plane and 39% pointing in plane. Carbon atoms are shown in grey, oxygen in red, nitrogen in blue and GaO<sub>6</sub> polyhedra in turquoise.

MIL-53(In)-NH<sub>2</sub>/NO<sub>2</sub> (4)

**Figure S10.** Plot of the Pawley refinement of MIL-53(In)-NH<sub>2</sub>/NO<sub>2</sub> (4).

MIL-53(Al)-NH<sub>2</sub>/NO<sub>2</sub>\_vnp (5), the XRD pattern of the as synthesized material is shown in the manuscript

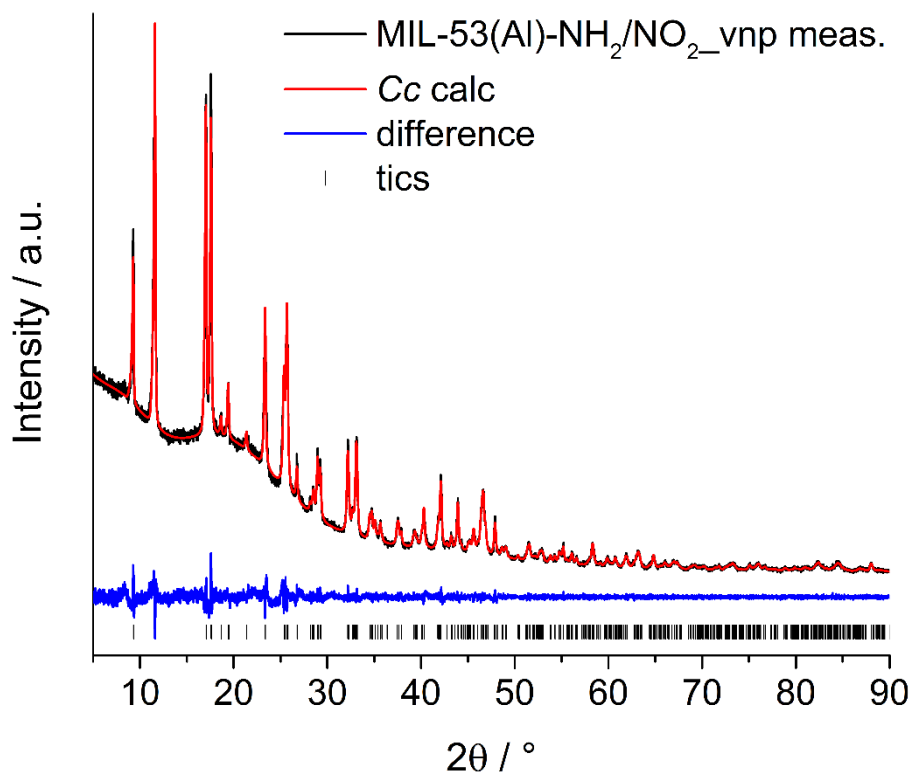
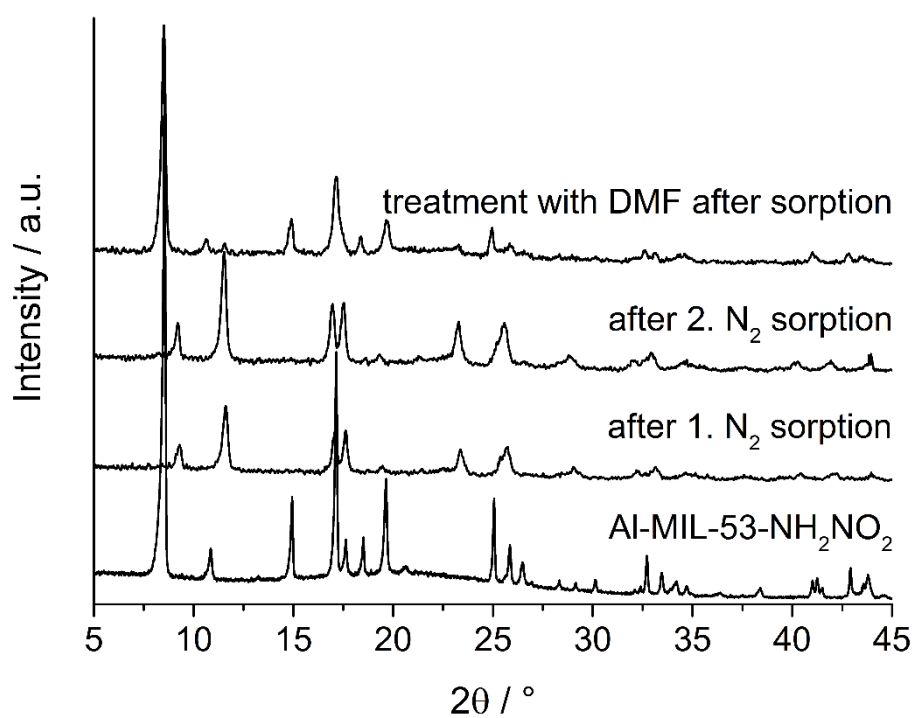


Figure S11. Pawley refinement of MIL-53(Al)-NH<sub>2</sub>/NO<sub>2</sub>\_vnp (5).

Table S5. Results of the Pawley refinement of MIL-53(Al)-NH<sub>2</sub>/NO<sub>2</sub>\_vnp.

MIL-53(Al)-NH <sub>2</sub> /NO <sub>2</sub> _vnp	
$a / \text{Å}$	20.125(1)
$b / \text{Å}$	8.2940(6)
$c / \text{Å}$	6.6506(4)
$\beta / ^\circ$	109.531(5)
space group	Cc
$R_{wp} / \%$	3.04
GoF	1.86



**Figure S12.** The vnp form of MIL-53(Al)-NH<sub>2</sub>/NO<sub>2</sub> (5) obtained after N<sub>2</sub> sorption experiments (PXRDs shown in the middle) can be transformed to the as synthesized form (1, bottom) by immersion with DMF (top).

## TG curves and elementary analysis

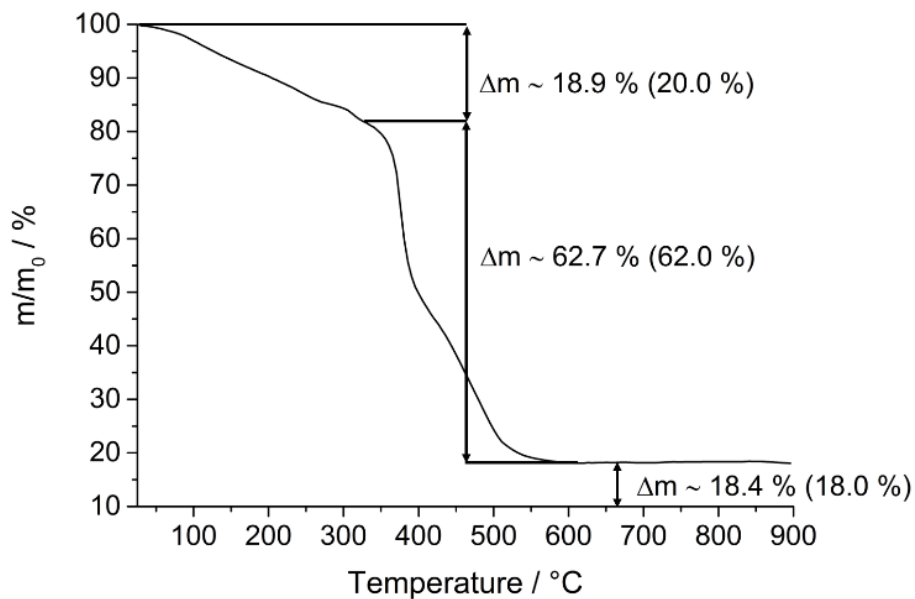


**Figure S13.** Thermogravimetric measurement for MIL-53(Al)-NH<sub>2</sub>/NO<sub>2</sub> synthesized in DMF (1). Calculated values for the assumed sum formula are given in brackets.

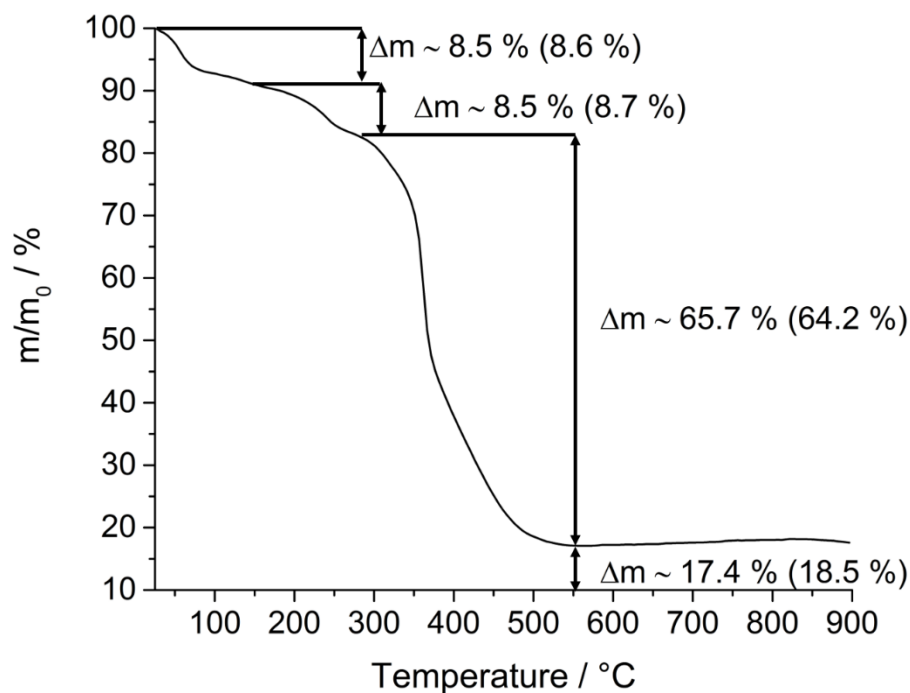


**Figure S14.** Thermogravimetric measurement for MIL-53(Al)-NH<sub>2</sub>/NO<sub>2</sub> synthesized in EtOH (2). Calculated values for the assumed sum formula are given in brackets.

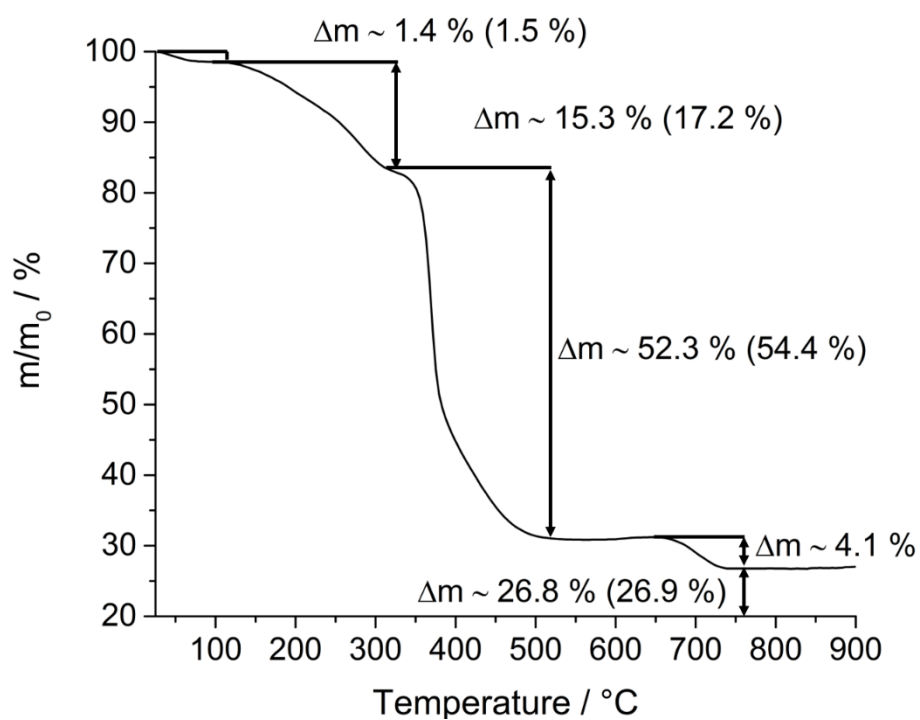


**Figure S15.** Thermogravimetric measurement for MIL-53(Ga)-NH<sub>2</sub>/NO<sub>2</sub> (3). Calculated values for the assumed sum formula are given in brackets. The step at 700 °C is originating from the decomposition of Ga species like Ga(NO<sub>3</sub>)O, Ga(OH)<sub>3</sub> and Ga(OH)O to Ga<sub>2</sub>O<sub>3</sub>.<sup>[1]</sup>



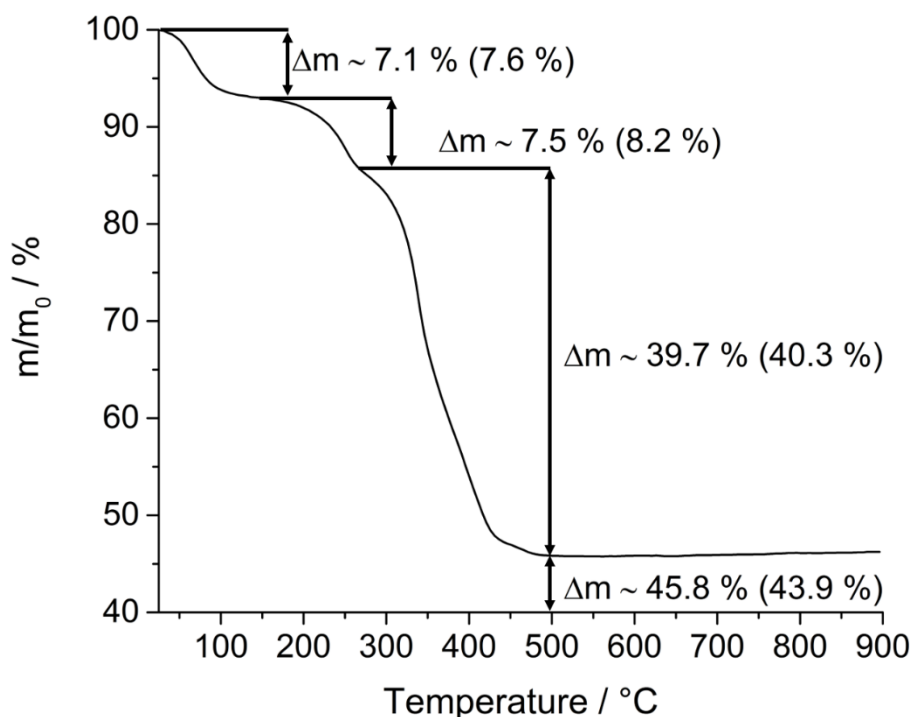


**Figure S16.** Thermogravimetric measurement for MIL-53(In)-NH<sub>2</sub>/NO<sub>2</sub> (4). Calculated values for the assumed sum formula are given in brackets.

**Table S6.** Elementary analysis for the MIL-53 compounds. Sum formulas were obtained from thermogravimetric measurements.

compound		C / %	H / %	N / %
MIL-53(Al)-NH <sub>2</sub> NO <sub>2</sub>	calc.	38.5	3.4	12.2
[Al(OH)(BDC-NH <sub>2</sub> NO <sub>2</sub> )]·0.92DMF	meas.	38.0	3.2	11.8
MIL-53(Al)-NH <sub>2</sub> NO <sub>2</sub> (2)	calc.	34.1	3.6	8.6
[Al(OH)(BDC-NH <sub>2</sub> NO <sub>2</sub> )]·0.61EtOH·1.57H <sub>2</sub> O	meas.	37.1	2.8	9.2
MIL-53(Ga)-NH <sub>2</sub> NO <sub>2</sub>	calc.	34.4	3.2	10.6
[Ga(OH)(BDC-NH <sub>2</sub> NO <sub>2</sub> )]·0.13EtOH·1.9DMF	meas.	33.3	2.9	10.1
MIL-53(In)-NH <sub>2</sub> NO <sub>2</sub>	calc.	26.7	2.4	7.0
[In(OH)(BDC-NH <sub>2</sub> NO <sub>2</sub> )]·0.86EtOH·0.58DMF·0.43In <sub>2</sub> O <sub>3</sub>	meas.	23.4	2.0	5.9

## SEM images

MIL-53(Al)-NH<sub>2</sub>/NO<sub>2</sub> (1) synthesis in DMF

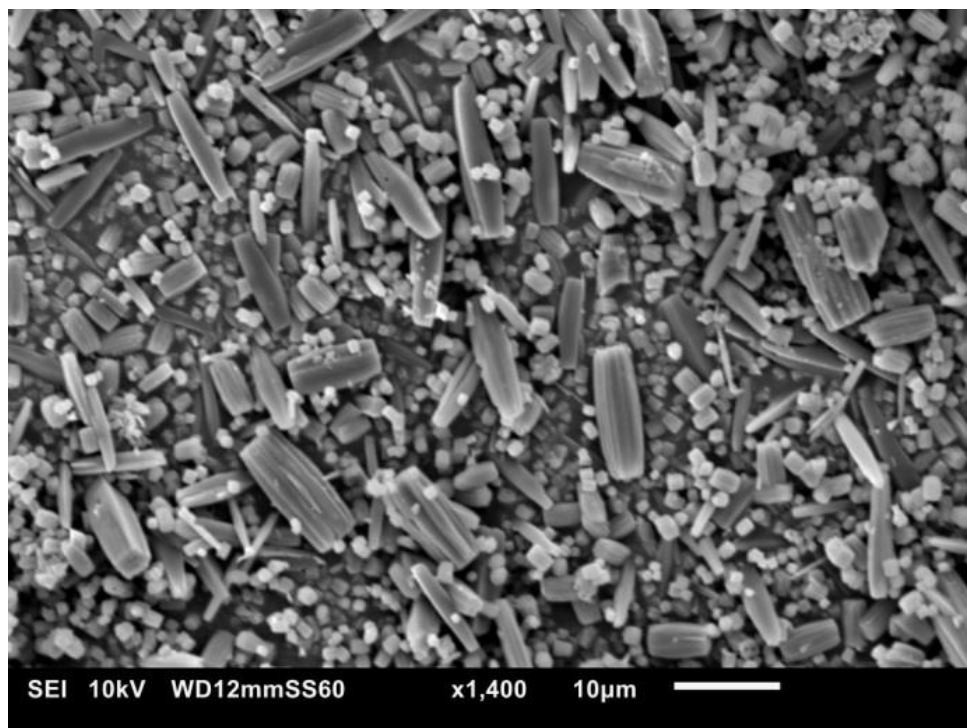


**Figure S17.** For MIL-53(Al)-NH<sub>2</sub>/NO<sub>2</sub> (1) elongated rectangular crystals with a size around 10 μm were obtained, along with small cubic crystals between 0.5-2 μm in size.

**MIL-53(Al)-NH<sub>2</sub>/NO<sub>2</sub> (2) synthesis in ethanol**

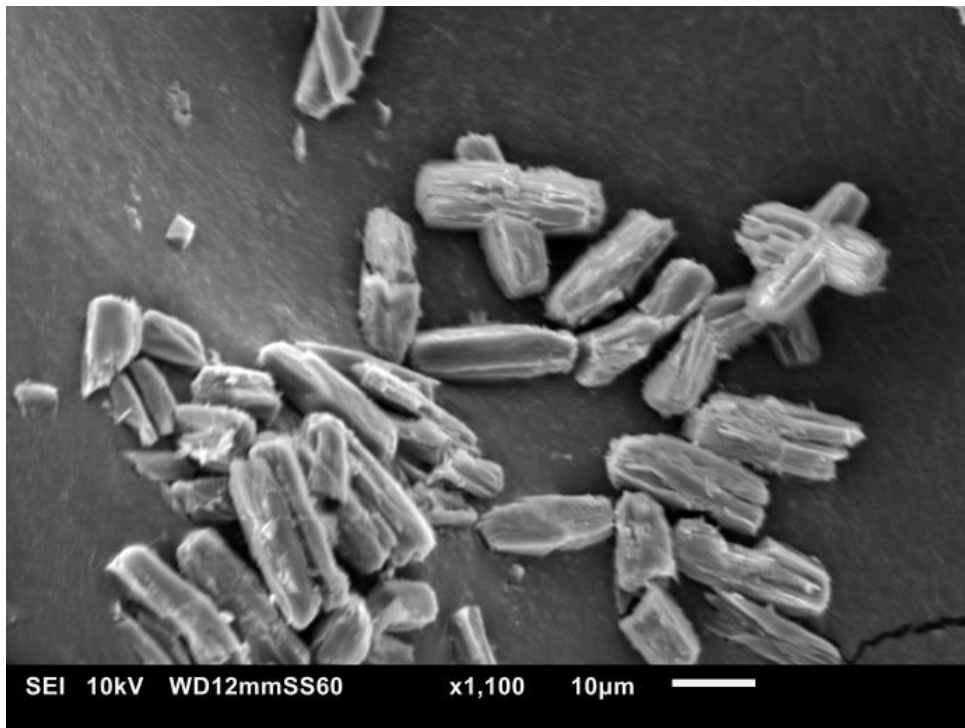


**Figure S18.** For MIL-53(Al)-NH<sub>2</sub>/NO<sub>2</sub> (2) synthesized in ethanol, thicker crystals than for synthesis in DMF were obtained.

**MIL-53(Ga)-NH<sub>2</sub>/NO<sub>2</sub> (3)**

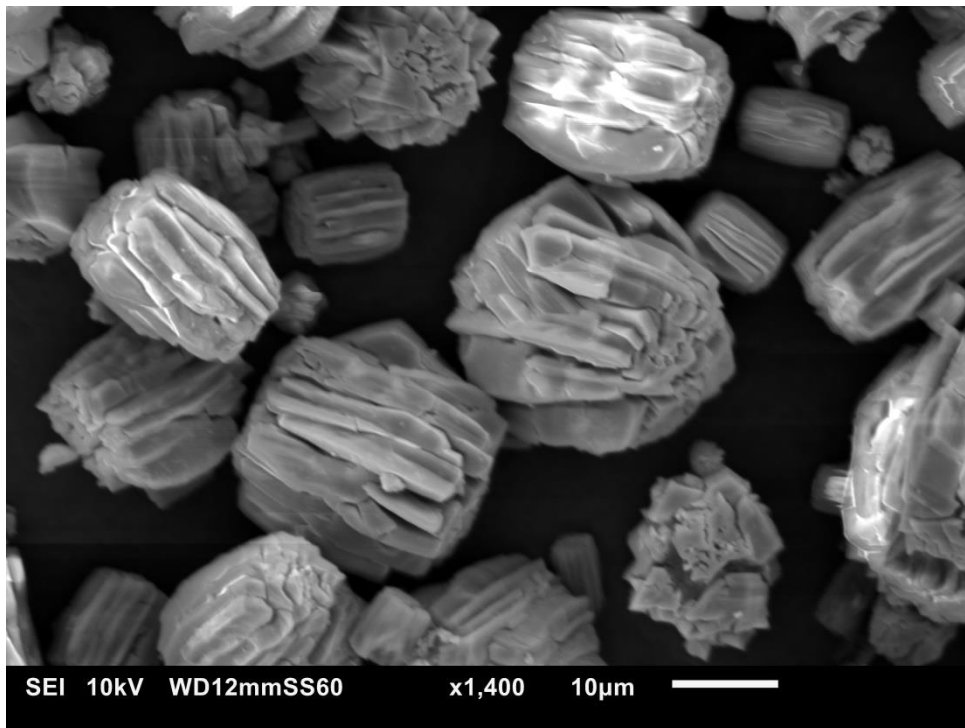


**Figure S19.** For MIL-53(Ga)-NH<sub>2</sub>/NO<sub>2</sub> (3) aggregated crystals were obtained that seem to consist out of elongated rectangular crystals grown alongside each other.

MIL-53(In)-NH<sub>2</sub>/NO<sub>2</sub> (4)

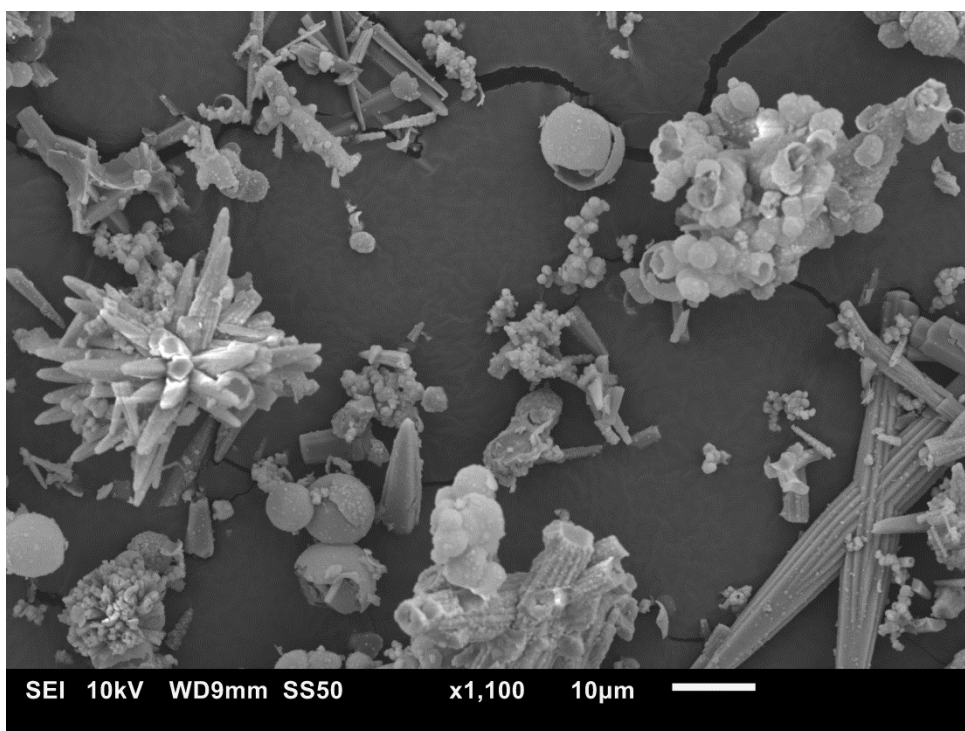
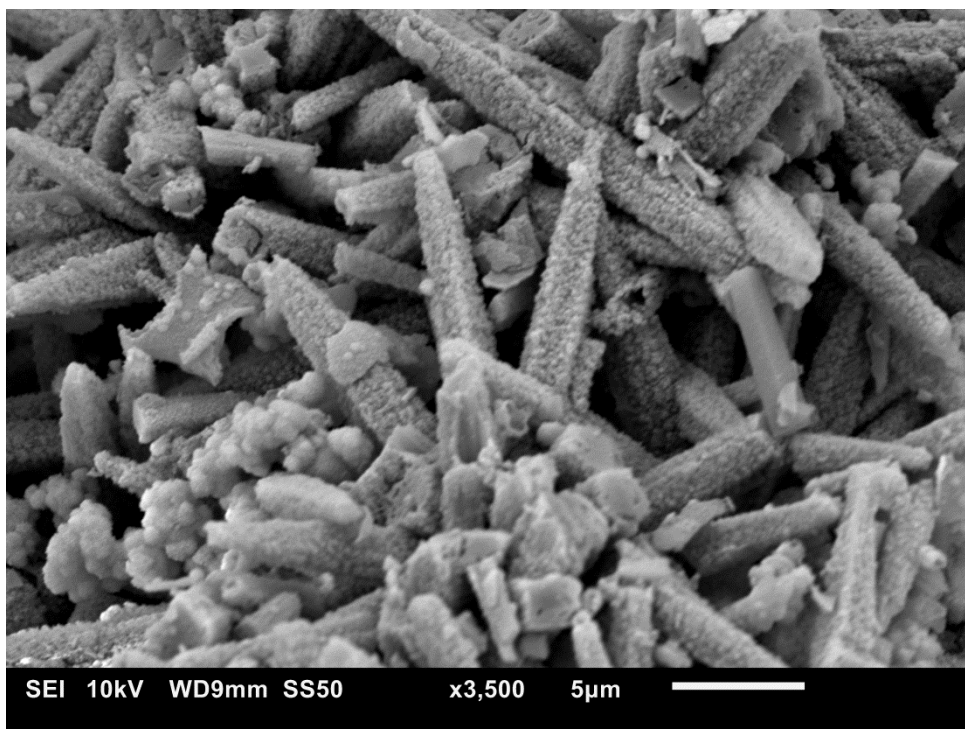


**Figure S20.** For MIL-53(In)-NH<sub>2</sub>/NO<sub>2</sub> (4) only limited crystallinity was achieved, with crystals being very polycrystalline and aggregated.

## NMR spectra

During the synthesis of MIL-53(Al)-NH<sub>2</sub>/NO<sub>2</sub> (**2**) in ethanol, 15% of the amino groups were ethylated. **Figure S21** shows the numbering scheme of the linker molecule for the discussion in the NMR spectra. The allocation of the signals was confirmed by 2D NMR spectroscopy.

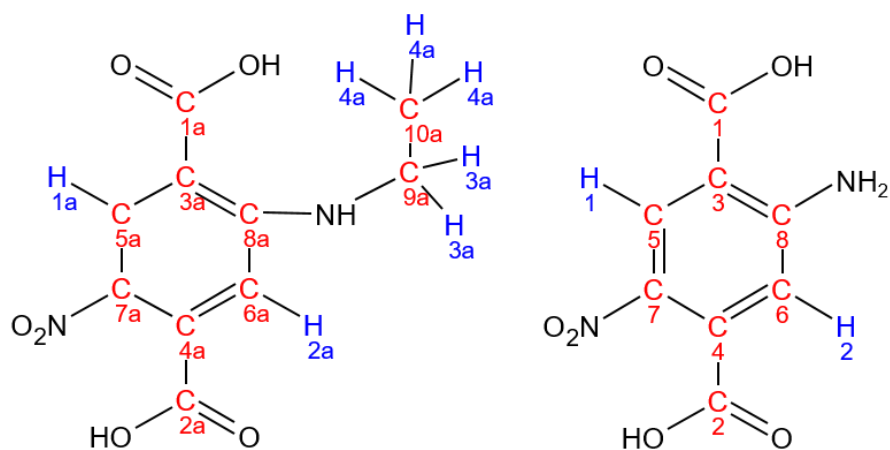


**Figure S21.** Numbering scheme of H<sub>2</sub>BDC-NH<sub>2</sub>/NO<sub>2</sub> (right) and the ethylated linker molecule (left) as it is used in the NMR spectra displayed.

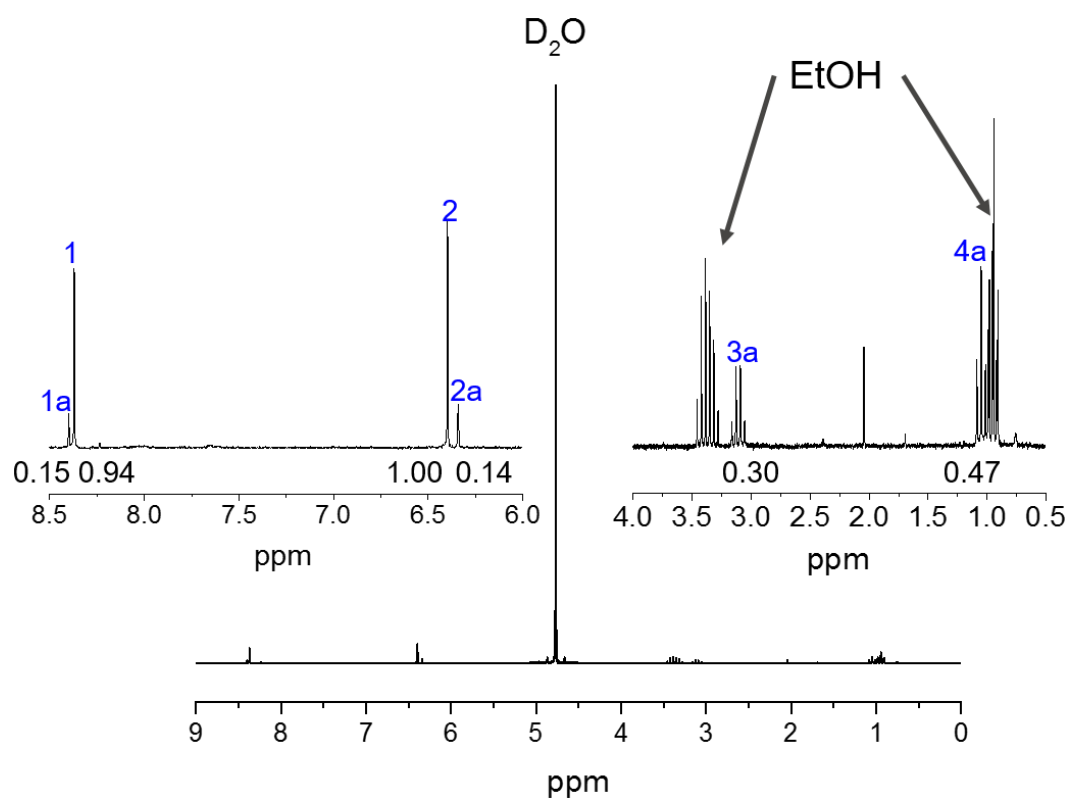


**Figure S22.**  $^1\text{H-NMR}$  spectrum of MIL-53(Al)-NH<sub>2</sub>/NO<sub>2</sub> (2) dissolved in 5% NaOD in D<sub>2</sub>O. The integrals are displayed beneath the corresponding signals.

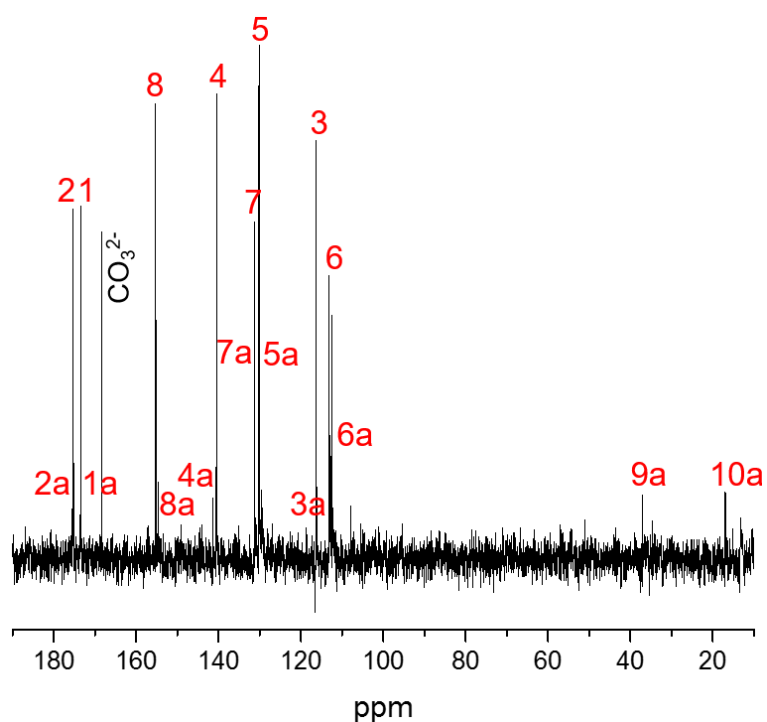


**Figure S23.**  $^{13}\text{C-NMR}$  spectrum of MIL-53(Al)-NH<sub>2</sub>/NO<sub>2</sub> (2) dissolved in 5% NaOD in D<sub>2</sub>O. The carbonate peak is due to the solution of CO<sub>2</sub> in the solvent used.

## Sorption experiments

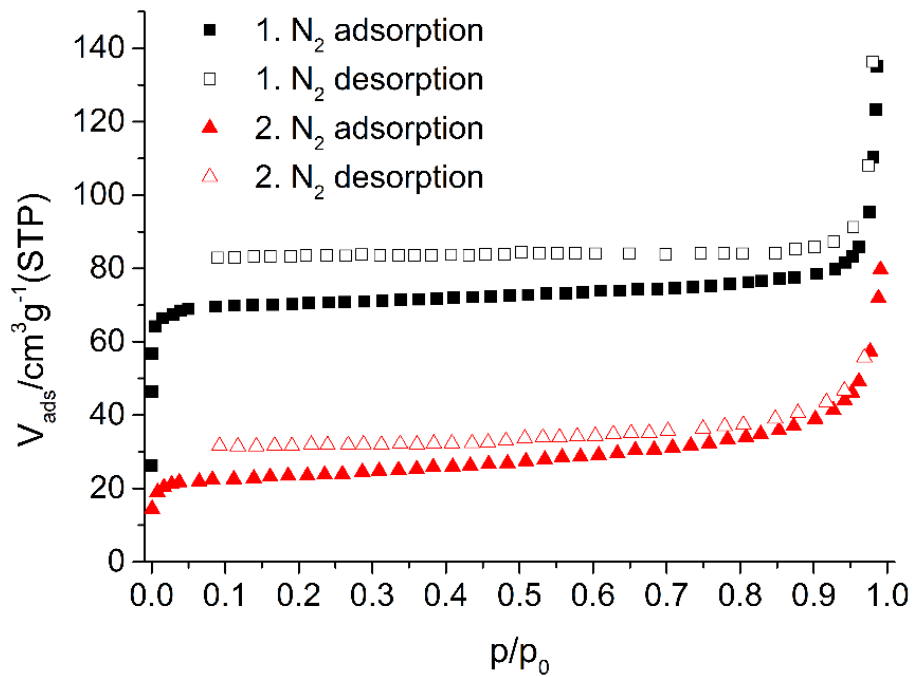


Figure S24. N<sub>2</sub> sorption isotherms of MIL-53(Al)-NH<sub>2</sub>/NO<sub>2</sub> synthesized in DMF (1).

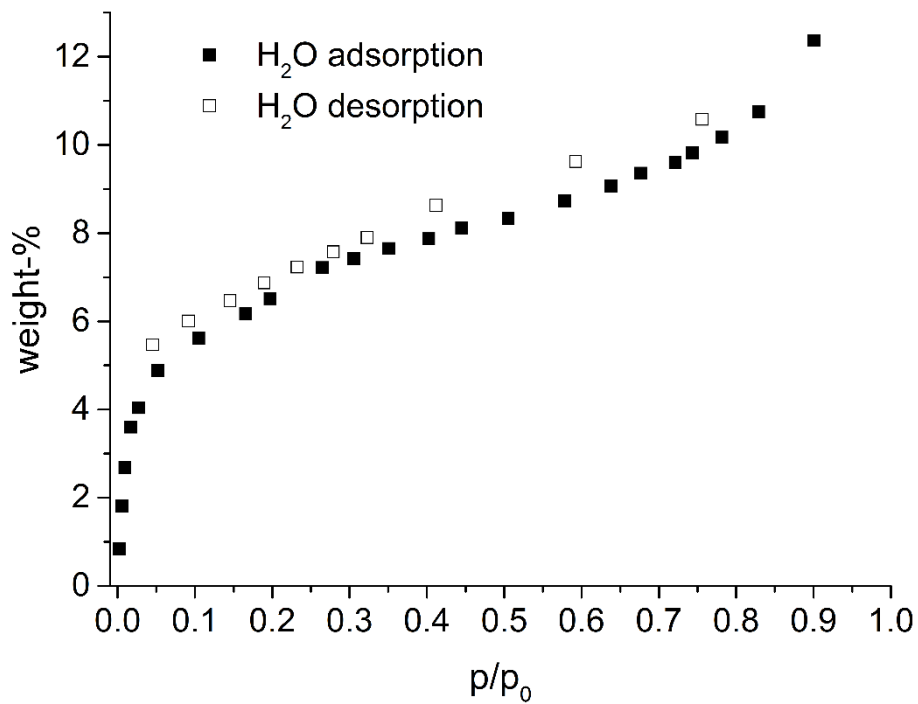


Figure S25. H<sub>2</sub>O sorption isotherms of MIL-53(Al)-NH<sub>2</sub>/NO<sub>2</sub> (1).



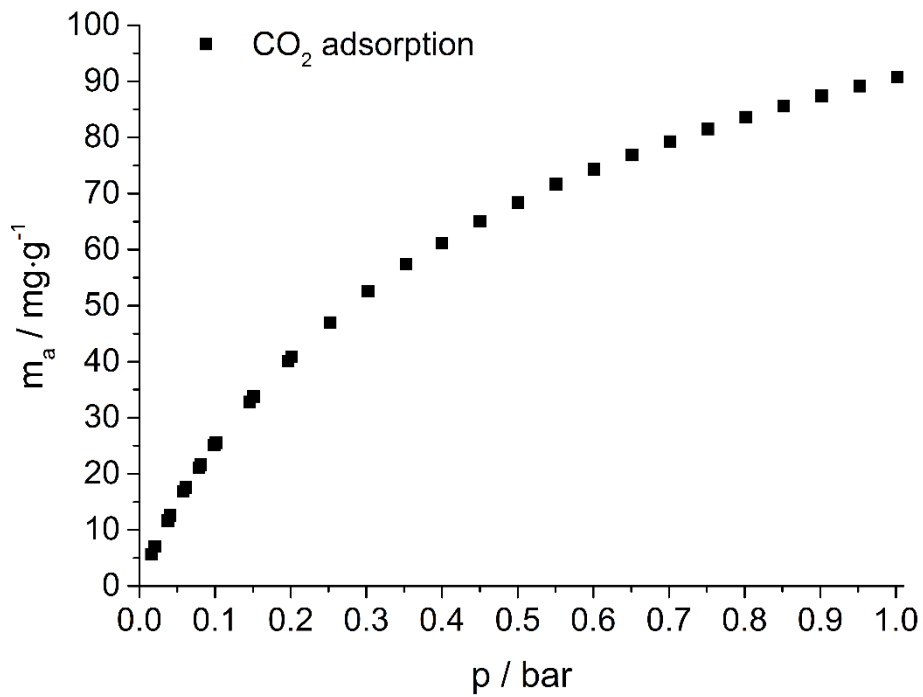


Figure S26. CO<sub>2</sub> sorption isotherm of MIL-53(Al)-NH<sub>2</sub>/NO<sub>2</sub> (1).

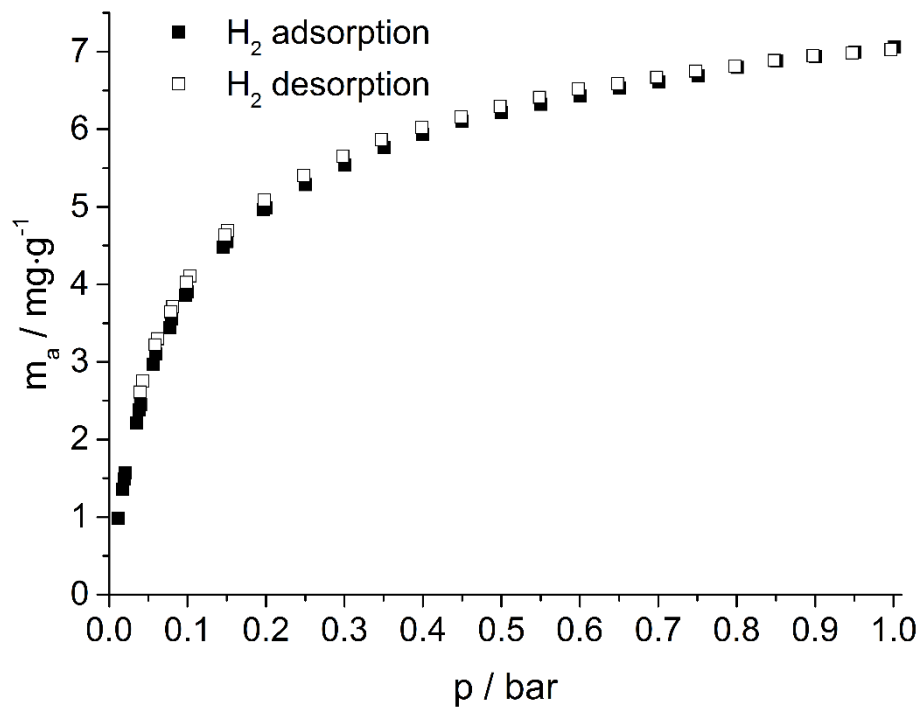
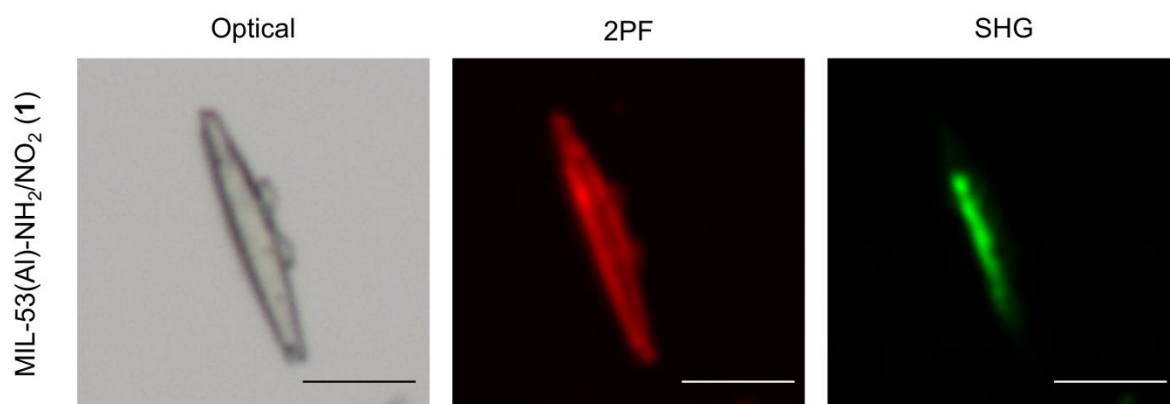


Figure S27. H<sub>2</sub> sorption isotherms of MIL-53(Al)-NH<sub>2</sub>/NO<sub>2</sub> (1).

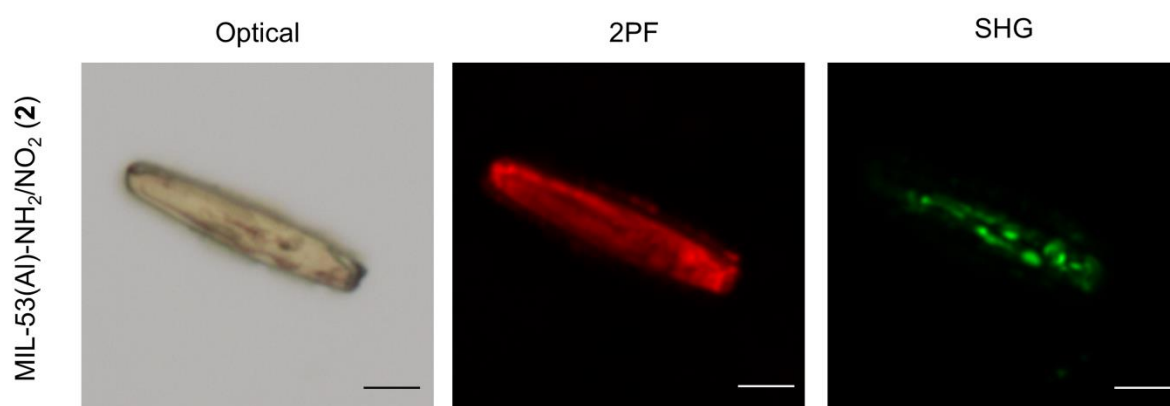
## SHG microscopy

### MIL-53(Al)-NH<sub>2</sub>/NO<sub>2</sub> (1) as synthesized in DMF

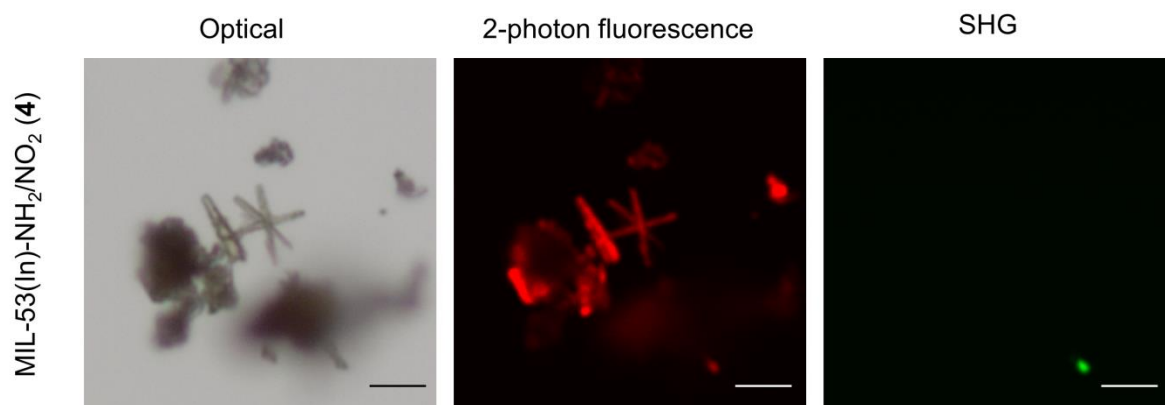


**Figure S28.** From left to right: optical, two-photon fluorescence and second harmonic generation images of MIL-53(Al)-NH<sub>2</sub>/NO<sub>2</sub> (1). The SHG image displays the average intensity calculated over 60 images, each image being 3° apart in polarization direction of the incident polarized laser beam. The scale bars indicate a distance of 10 μm for each image.

### MIL-53(Al)-NH<sub>2</sub>/NO<sub>2</sub> (2) as synthesized in ethanol



**Figure S29.** From left to right: optical, two-photon fluorescence and second harmonic generation images of MIL-53(Al)-NH<sub>2</sub>/NO<sub>2</sub> (2). The SHG image displays the average intensity calculated over 60 images, each image being 3° apart in polarization direction of the incident polarized laser beam. The scale bars indicate a distance of 10 μm for each image.

**MIL-53(In)-NH<sub>2</sub>/NO<sub>2</sub> (4) as synthesized in DMF**

**Figure S30.** From left to right: optical, two-photon fluorescence and second harmonic generation images of MIL-53(In)-NH<sub>2</sub>/NO<sub>2</sub> (4). The SHG image displays the average intensity calculated over 60 images, each image being 3° apart in polarization direction of the incident polarized laser beam. The scale bars indicate a distance of 10 μm for each image.

## Calculation of $\langle d_{\text{eff}} \rangle$ values

To obtain the value for  $d_{\text{eff}}$ , the procedure as previously used by van der Veen *et al.* was followed.<sup>2,3</sup> Firstly, the SHG intensity of the sample was measured ( $I_{2\omega,x}$ ) in an SHG wide field microscopy setup; next the SHG intensity of a reference sample was measured ( $I_{2\omega,BBO}$ ). Beta barium borate (BBO) was used as a reference, 100  $\mu\text{m}$  thick, cut to achieve type I phase matching and to optimize the quadratic nonlinear response ( $\theta = 29.2^\circ$ ,  $\varphi = 90^\circ$ ; Eksma optics, BBO-601H). The formula for the second-order nonlinear coefficient  $\langle d_{\text{eff}} \rangle$  was derived as follows:

$$I_{2\omega,x} = A \frac{\langle d_{\text{eff}} \rangle^2 r^2 I_{\omega,x}^2}{n_{2\omega,x} n_{\omega,x}^2}$$

$$I_{2\omega,BBO} = A \frac{d_{00e}^2 L^2 I_{\omega,BBO}^2}{n_{\theta,2\omega,BBO} n_{\omega,BBO}^2}$$

$$\Rightarrow \langle d_{\text{eff}} \rangle = \sqrt{\frac{I_{2\omega,x}}{I_{2\omega,BBO}} \cdot d_{00e}^2 \cdot \frac{L^2}{r^2} \cdot \frac{I_{\omega,BBO}^2}{I_{\omega,x}^2} \cdot \frac{n_{2\omega,x} n_{\omega,x}^2}{n_{\theta,2\omega,BBO} n_{\omega,BBO}^2}}$$

With:

$A$  = all the variables that are identical for both the sample and the BBO crystal

$I_{2\omega,x}$  = the SHG intensity of the sample

$I_{2\omega,BBO}$  = intensity of the SHG light of the BBO reference, measured with a plane of polarization of linearly polarized laser light for which the SHG intensity reaches a maximum

$I_{\omega}$  = the intensity of the incident laser light, linearly polarized

$r$  = the height of the crystallites

$n_{2\omega}$  = the refractive index at the frequency of the second-harmonic light

$n_{\omega}$  = the refractive index at the frequency of the incident laser light

The values of the refractive indices of metal-organic frameworks vary between 1.2 and 1.65 in the VIS to NIR spectral region.<sup>4-6</sup> We used a value of 1.5 for both  $n_{2\omega}$  and  $n_{\omega}$ , as this was the value determined for the related material MIL-53(Al)-NH<sub>2</sub>.<sup>2</sup>

$d_{00e} = 2.01 \text{ pm/V}$  = effective nonlinearity coefficient for type I phase-matched interaction for BBO

$L$  = the thickness of the BBO crystal, 100  $\mu\text{m}$

$n_{\theta,2\omega,BBO}$  = extraordinary refractive index at the frequency of the SHG light, propagating at an angle  $\theta$  with the optical axis of the crystal

$n_{\omega,BBO}^2$  = ordinary refractive index of BBO at the frequency of the incident light  $\omega$

Linearly polarized laser light was used to irradiate the sample and all the SHG signal was collected (no analyzer was positioned between the sample and the detector). To calculate the  $d_{\text{eff}}$  value for one crystal, the average over nine different orientations of linearly polarized laser light (all  $10^\circ$  apart) was calculated. To obtain the final  $\langle d_{\text{eff}} \rangle$  value, the results were averaged over approximately 20 different crystals.

## Ab initio calculations

Additional details about the multi-scale approach to calculate the macroscopic electric properties ( $\chi^{(1)}$  and  $\chi^{(2)}$  tensors). This method combines first principles calculations of the molecular properties with a classical electrostatic interactions scheme, known as the local field theory (LFT), to account for the crystal environment effects.<sup>7-11</sup> In LFT methodology, the  $\chi^{(1)}$  and  $\chi^{(2)}$  tensors read:

$$\begin{aligned}\underline{\underline{\chi}}^{(1)}(-\omega; \omega) &= \frac{1}{\varepsilon_0 V} \sum_k \underline{\underline{d}}_k^T(\omega) \cdot \underline{\underline{\alpha}}_k(-\omega; \omega) \\ \underline{\underline{\chi}}^{(2)}(-2\omega; \omega, \omega) &= \frac{1}{2\varepsilon_0 V} \sum_k \underline{\underline{d}}_k^T(2\omega) \cdot \underline{\underline{\beta}}_k(-2\omega; \omega, \omega): \underline{\underline{d}}_k^T(\omega) \underline{\underline{d}}_k^T(\omega)\end{aligned}$$

where the k-sum runs over all (sub)molecules of the unit cell,  $\alpha_k$  and  $\beta_k$  are the k-th (sub)molecule (hyper)polarizability tensors obtained by distributing evenly the ions (hyper)polarizabilities on the heavy atoms with the hydrogen atoms attached to them,  $\varepsilon_0$  is the dielectric permittivity of vacuum, V is the unit cell volume and

$$\begin{aligned}\underline{\underline{d}}_k(\omega) &= \sum_k \underline{\underline{D}}_{kk'}(\omega) \\ \underline{\underline{D}}^{-1}(\omega) &= \left[ \underline{\underline{1}} - \frac{1}{V\varepsilon_0} \underline{\underline{L}} \cdot \underline{\underline{\alpha}}(-\omega; \omega) \right]\end{aligned}$$

where  $\underline{\underline{L}}$  is the Lorentz factor tensor,  $\underline{\underline{\alpha}}$  is the supermatrix of (sub)molecular polarizabilities. Therefore,  $\underline{\underline{d}}_k$  interrelates the local electric field  $\underline{F}_k$  (on the k-th (sub)molecule) with the macroscopic electric field  $\underline{E}$ :

$$\underline{F}_k = \underline{\underline{d}}_k \cdot \underline{E}$$

The  $\chi^{(1)}$  tensor components were calculated in the abc\* orthogonal reference frame and the  $\chi^{(2)}$  tensor components are reported in the eigenbasis of the calculated dielectric tensor  $\underline{\underline{\varepsilon}}(\omega) = \underline{\underline{1}} + \underline{\underline{\chi}}^{(1)}(\omega)$  whose eigenvectors are the squares of the refractive indices. The final  $\chi^{(1)}$  and  $\chi^{(2)}$  tensors of the investigated material (combining A and C phases) were obtained as weighted averages, first in the abc\* frame, then the resulting  $\chi^{(2)}$  was transformed to the optical indicatrix axes of the averaged  $\underline{\underline{\varepsilon}}(\omega) = \underline{\underline{1}} + \underline{\underline{\chi}}^{(1)}(\omega)$  tensor (using the weights from the powder diffraction refinement).

The calculations of molecular properties,  $\alpha$  and  $\beta$ , were performed for the individual cations (+2 charge) and anions (-2 charge) within their embedding electric field. Beforehand, starting from the X-ray diffraction data the geometry of the different crystals were optimized using periodic boundary conditions, the B3LYP exchange-correlation potential and the 6-31G(d,p) basis set. Only the fractional coordinates were optimized with the cell parameters kept fixed at their experimental values. The Crystal14 package<sup>12</sup> was employed. This in-crystal electric field was simulated by a 100 Å radius sphere of Mulliken point charges, calculated using the PBC/B3LYP/6-31G(d,p) method on the optimized crystal. The adequacy of this choice of charge definition has recently been discussed.<sup>13</sup> First, the static ( $\lambda = \infty$ ) responses were evaluated at the second-order Møller-Plesset method (MP2) level. The dynamic MP2 (Møller-Plesset second-order perturbation theory) molecular properties were evaluated by employing a modified multiplicative scheme,<sup>14</sup> where the static MP2 values are combined with the static coupled-perturbed Kohn-Sham (CPKS) and dynamic time-dependent DFT (TDDFT) tensors evaluated using the B3LYP XC functional, following the scheme described in Ref. 15. At both levels, the selected basis set is the 6-311++G(d,p) basis and it contains both diffuse and polarization functions for an accurate prediction of the linear and nonlinear molecular properties. All the molecular property calculations were performed with Gaussian09.<sup>16</sup> Performing calculations at the experimental incident wavelength of 800 nm was not possible since the  $\lambda/2$  wavelength (400 nm) is already in the resonant regime of the anions, which leads to qualitatively wrong hyperpolarizability values. Additional TDDFT/B3LYP/6-311++G(d,p) calculations of the excitation energies of the anions in the crystal field confirmed that the first excitation energies correspond to a wavelength of 393 nm, 422 nm, and 325 nm for compounds **1**, **3**, and **4**, respectively, in close agreement with experiment. Nevertheless, the computational results at an incident wavelength of 1064 nm (SHG at 532 nm) are expected to be sufficiently close for analyzing the experimental results. Frequency/wavelength dependence of the macroscopic responses is further described in Tables S7-S8.

Using the  $\chi^{(1)}$  and  $\chi^{(2)}$  tensor components the  $d_{eff}$  values were calculated for types I and type II phase matchings (PM) conditions. The (non-polarized or polarized one when not aligned on the natural o or e polarization vectors, which is the general case) light beam traveling through anisotropic medium (biaxial crystal in our case) splits into two perpendicularly polarized beams [(+) and (-)] traveling at different speeds inversely proportional to the refractive indices associated to those polarizations: with  $n_+ > n_-$  ( $v_+ < v_-$ , where  $v$  is the phase velocity). The second-order process involves interaction between three beams: two at fundamental frequency ( $\omega$ ) and one at the double frequency ( $2\omega$ ). The effectiveness of the SHG interaction is governed by the extent of the (+) and (-) index surfaces overlap for the two frequencies. Two possibilities are usually considered: i) interaction of the fundamental rays having (+) polarization with the SHG beam at (-) polarization (type I PM) and ii) fundamental rays having opposite polarizations (+ and -) with SHG at (-) polarization (type II PM). Then, having defined the polarization directions of the light waves using the polar angles ( $\theta, \phi$ ) (with  $0 \leq \theta \leq \pi$  and  $0 \leq \phi \leq 2\pi$ ) the  $d_{eff}$  values are evaluated using:

$$d_{eff} = \frac{1}{2} \underline{e}_i(2\omega) \cdot \underline{\chi}^{(2)} : \underline{e}_j(\omega) \underline{e}_k(\omega) \times \text{sinc}^2\left(\frac{\Delta k r}{2}\right)$$

where  $\underline{e}_i, \underline{e}_j$  and  $\underline{e}_k$  are the light waves polarization vectors,  $r$  is the optical path length (symbolizing the grain size in the calculation) and

$$\Delta k = \frac{2\pi}{\lambda} \Delta n; \Delta n = 2n_{2\omega}^1 - n_{\omega}^2 - n_{\omega}^3$$

is the phase mismatch related to the difference of refractive indices. 1, 2, and 3 refer to the crystal axes. Finally, all possible orientations of the light wave polarization with respect to the crystal grains, defined by the polar angles ( $\theta, \phi$ ), are taken into account to provide the average  $\langle d_{eff} \rangle$  quantities.

**Table S7.** MP2/LFT results for MIL-53(Al)-NH<sub>2</sub>/NO<sub>2</sub> and MIL-53(Al)-NH<sub>2</sub> (in the very narrow pore phase): refractive indices, selected  $\chi^{(2)}$  tensor components (pm/V), and  $\langle d_{eff} \rangle$  (pm/V) for different grain sizes at different wavelengths (nm). For MIL-53(Al)-NH<sub>2</sub>/NO<sub>2</sub>, results are listed for the pure A and C phases as well as for the A/C mixture (A:C = 61:39 as obtained from XRD analysis).

Compound and phase	$\lambda$	$n_1$	$n_2$	$n_3$	$\chi_{333}^{(2)}$	$\chi_{111}^{(2)}$	$\chi_{133}^{(2)}$	$\langle d_{eff} \rangle$ r = 0 $\mu\text{m}$	$\langle d_{eff} \rangle$ r = 3 $\mu\text{m}$	$\langle d_{eff} \rangle$ r = 10 $\mu\text{m}$
MIL-53(Al)-NH <sub>2</sub> /NO <sub>2</sub> Phase A	$\infty$	1.539	1.416	1.721	51.2	-1.1	-7.7	1.460	0.049	0.006
	1064	1.553	1.427	1.762	133.9	-1.5	-16.3	<b>2.559</b>	0.285	0.080
	532	1.611	1.469	1.974						
MIL-53(Al)-NH <sub>2</sub> /NO <sub>2</sub> Phase C	$\infty$	1.539	1.416	1.722	-51.3	1.1	7.6	1.463	0.049	0.006
	1064	1.553	1.427	1.762	-134.2	1.5	16.2	<b>2.540</b>	0.276	0.079
	532	1.611	1.469	1.975						
MIL-53(Al)-NH <sub>2</sub> /NO <sub>2</sub> A/C (61:39)	$\infty$	1.539	1.416	1.721	11.2	-0.2	-1.7	0.319	0.011	0.001
	1064	1.553	1.427	1.762	29.3	-0.3	-3.6	<b>0.567</b>	0.066	0.018
	532	1.611	1.469	1.974						
MIL-53(Al)-NH <sub>2</sub> (vnp)	$\infty$	1.759	1.445	1.912	3.9	-8.1	-5.6	1.073	0.019	0.002
	1064	1.780	1.454	1.949	6.2	-15.8	-6.6	<b>1.881</b>	0.191	0.064
	532	1.862	1.496	2.116						

**Table S8.** MP2/LFT results for MIL-53(Ga)-NH<sub>2</sub>/NO<sub>2</sub>: refractive indices, selected  $\chi^{(2)}$  tensor components (pm/V), and  $\langle d_{eff} \rangle$  (pm/V) for different grain sizes at different wavelengths (nm). The results are listed for the pure A and C phases as well as for the A/C mixture (A:C = 68:32 as obtained from XRD analysis).

Compound and phase	$\lambda$	$n_1$	$n_2$	$n_3$	$\chi_{333}^{(2)}$	$\chi_{111}^{(2)}$	$\chi_{133}^{(2)}$	$\chi_{113}^{(2)}$	$\langle d_{eff} \rangle$ r = 0 $\mu\text{m}$	$\langle d_{eff} \rangle$ r = 3 $\mu\text{m}$	$\langle d_{eff} \rangle$ r = 10 $\mu\text{m}$
MIL-53(Ga)-NH <sub>2</sub> /NO <sub>2</sub> Phase A	$\infty$	1.708	1.380	1.480	-1.9	69.0	-2.2	4.5	1.637	0.030	0.004
	1064	1.757	1.389	1.494	-4.4	222.2	-6.9	13.3	<b>2.582</b>	0.198	0.061
	532	2.062	1.436	1.560							
MIL-53(Ga)-NH <sub>2</sub> /NO <sub>2</sub> Phase C	$\infty$	1.668	1.373	1.469	2.0	-47.7	2.1	-3.2	1.325	0.032	0.004
	1064	1.703	1.383	1.488	4.3	-147.1	7.0	-4.9	<b>2.698</b>	0.354	0.110
	532	1.922	1.436	1.582							
MIL-53(Ga)-NH <sub>2</sub> /NO <sub>2</sub> A/C (68:32)	$\infty$	1.695	1.378	1.477	-0.5	31.8	-1.0	1.0	0.673	0.014	0.002
	1064	1.740	1.387	1.493	-1.3	105.0	-3.2	1.9	<b>1.053</b>	0.105	0.032
	532	2.014	1.436	1.574							

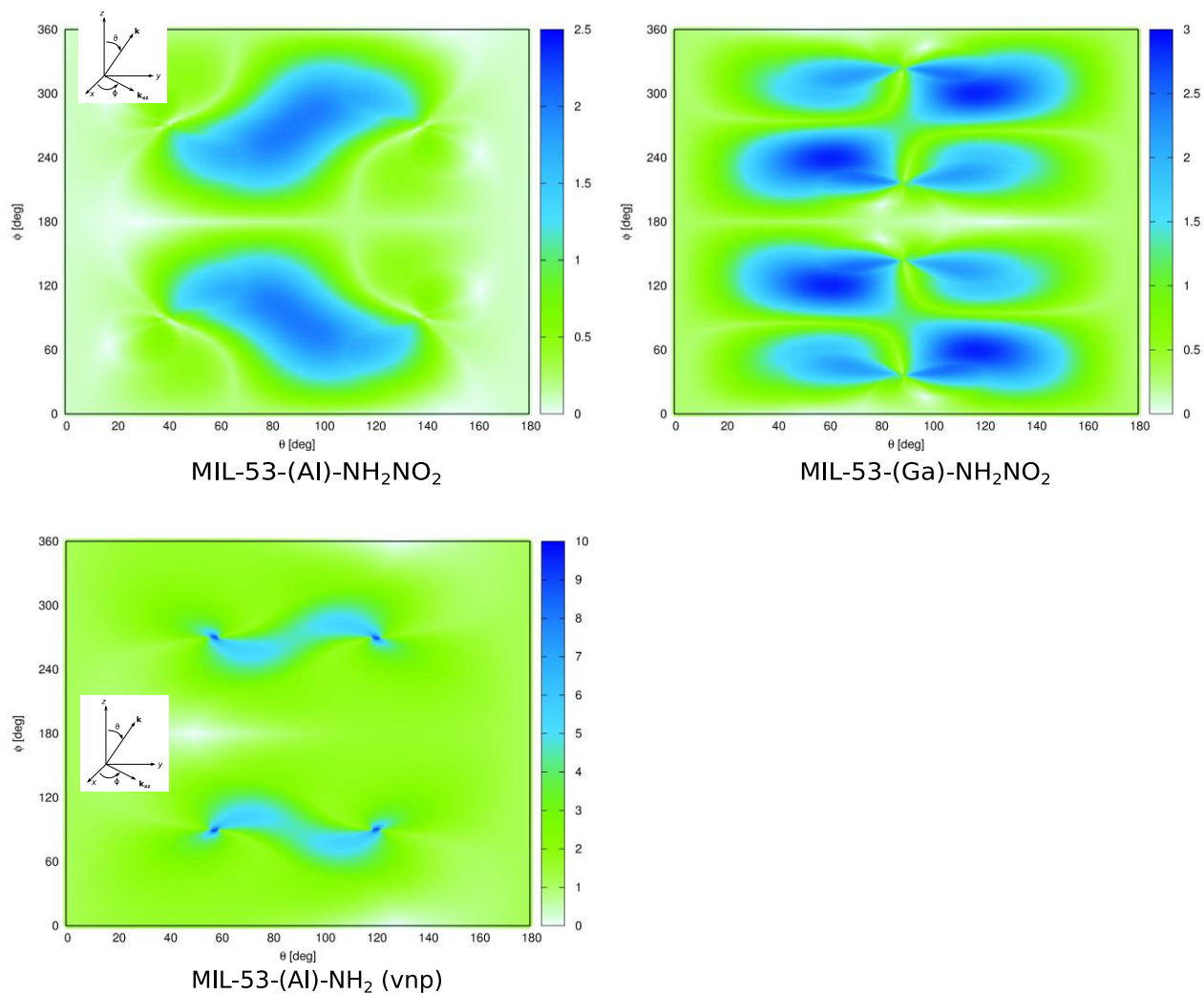
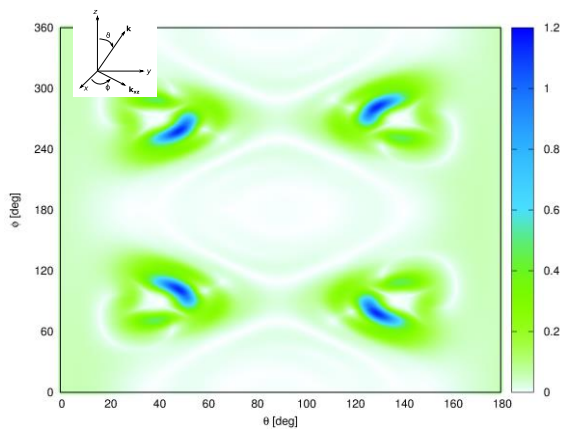


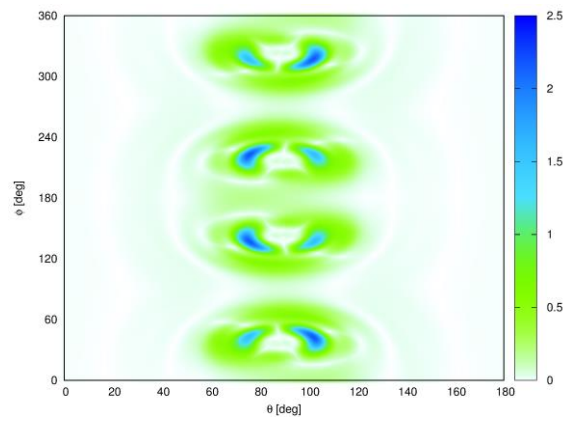
**Figure S31.** Angular dependence of the calculated  $d_{\text{eff}}$  (in pm/V) for MIL-53-(Al)-NH<sub>2</sub>/NO<sub>2</sub>, MIL-53(Ga)-NH<sub>2</sub>/NO<sub>2</sub>, and MIL-53(Al)-NH<sub>2</sub> (vnp) at  $\lambda=1064$  nm for  $r = 0$   $\mu\text{m}$  (the inset gives the definition of the polar angles  $(\theta, \phi)$ ,  $k$  being the wave vector of light, corresponding to the direction of propagation).



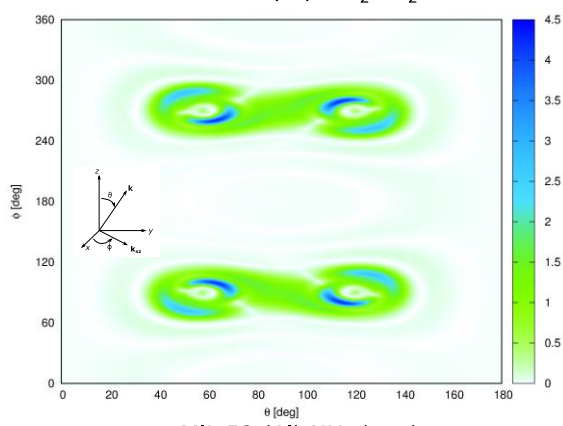
**3  $\mu\text{m}$**



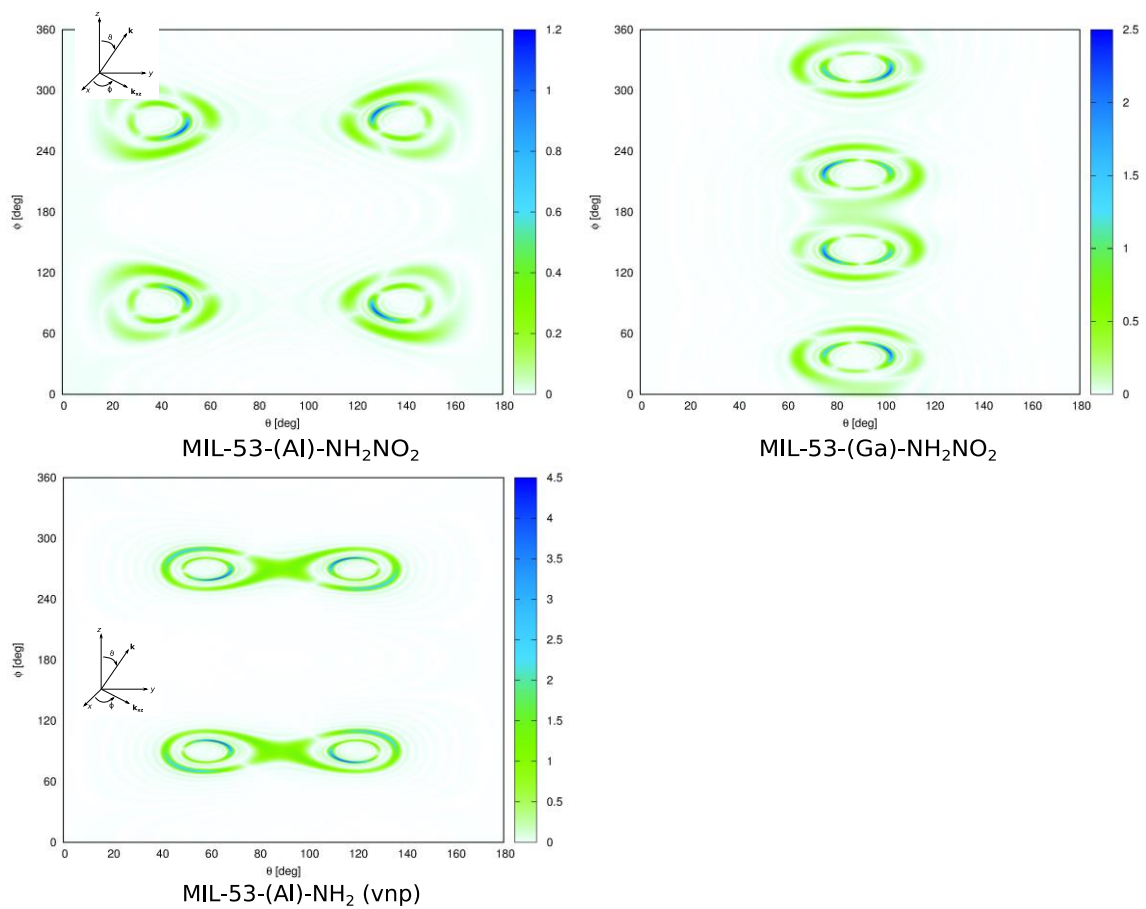
MIL-53-(Al)-NH<sub>2</sub>NO<sub>2</sub>



MIL-53-(Ga)-NH<sub>2</sub>NO<sub>2</sub>



MIL-53-(Al)-NH<sub>2</sub> (vnp)

$10\ \mu\text{m}$ 

**Figure S32.** Angular dependence of the calculated  $d_{\text{eff}}$  (in pm/V) for MIL-53-(Al)-NH<sub>2</sub>/NO<sub>2</sub>, MIL-53(Ga)-NH<sub>2</sub>/NO<sub>2</sub>, and MIL-53(Al)-NH<sub>2</sub> (vnp) at  $\lambda=1064\ \text{nm}$  for  $r = 3\ \mu\text{m}$  (top) and  $10\ \mu\text{m}$  (bottom) (the inset gives the definition of the polar angles  $(\theta, \phi)$ ,  $k$  being the wave vector of light, corresponding to the direction of propagation).

## Estimation of the transmittance of 400 nm light through MIL-53(Al)-NH<sub>2</sub>-NO<sub>2</sub> crystals

To estimate the transmittance of the generated 400 nm SHG light through the MIL-53(Al)-NH<sub>2</sub>-NO<sub>2</sub> crystals we can use the law of Lambert Beer:

$$A = \epsilon lc = \log \frac{I_0}{I} = \log \frac{1}{T} \quad [1]$$

With:  $A$  the absorbance

$T$  the transmittance

$\epsilon$  the molar extinction coefficient

$l$  the path length of the beam of light through the material sample

$c$  the amount concentration of the attenuating species in the material sample

$I_0$  the incident intensity

$I$  the transmitted intensity

To calculate the transmittance  $T$ , we can convert formula [1] to:

$$T = 10^{-\epsilon lc} \quad [2]$$

For MIL-53(Al)-NH<sub>2</sub>-NO<sub>2</sub> crystals, the transmittance  $T$  can be estimated using the following values:

- For the molar extinction coefficient, we use the molar extinction coefficient of PNA:  
 $\epsilon_{400 \text{ nm}}(\text{PNA}) = 12300 \frac{\text{L}}{\text{mol.cm}}$  determined by Bru et al. for free PNA in water<sup>17</sup>
- The average path length of generated 400 nm SHG light in MIL-53(Al)-NH<sub>2</sub>-NO<sub>2</sub> crystals with an average height of 2  $\mu\text{m}$  is:  $l = 1 \mu\text{m}$
- The concentration relates to the number density through the following equation:

$$c = \frac{n}{N_A} \quad [3]$$

With:  $n$  the number density of the attenuating species in the material sample  
 $N_A$  the Avogadro constant =  $6.022 \times 10^{23} \text{ mol}^{-1}$

- The number density of the linker with PNA motif in MIL-53(Al)-NH<sub>2</sub>-NO<sub>2</sub> can be derived from the crystal structure:  $n = \frac{4 \text{ molecules}}{1438,18 \text{ \AA}^3}$

With these values we can estimate the transmittance of generated 400 nm SHG light through MIL-53(Al)-NH<sub>2</sub>-NO<sub>2</sub> crystals with a thickness of 2  $\mu\text{m}$  to be  $2,1 \cdot 10^{-4} \%$ :

$$T = 10^{-\epsilon lc}$$

$$T = 10^{-\left[12300 \frac{\text{L}}{\text{mol cm}} \cdot 1 \mu\text{m} \cdot \frac{4 \text{ molecules}}{1438,18 \text{ \AA}^3} \cdot \frac{1 \text{ mol}}{6,022 \cdot 10^{23} \text{ molecules}}\right]}$$

$$T = 10^{-\left[12300 \frac{\text{L}}{\text{mol cm}} \cdot \frac{1 \text{ dm}^3}{1 \text{ L}} \cdot 1 \mu\text{m} \cdot \frac{10^{-4} \text{ cm}}{1 \mu\text{m}} \cdot \frac{4 \text{ molecules}}{1438,18 \text{ \AA}^3} \cdot \frac{1 \text{ \AA}^3}{10^{-27} \text{ dm}^3} \cdot \frac{1 \text{ mol}}{6,022 \cdot 10^{23} \text{ molecules}}\right]}$$

$$T = 2,1 \cdot 10^{-6}$$

## UV-vis spectrum

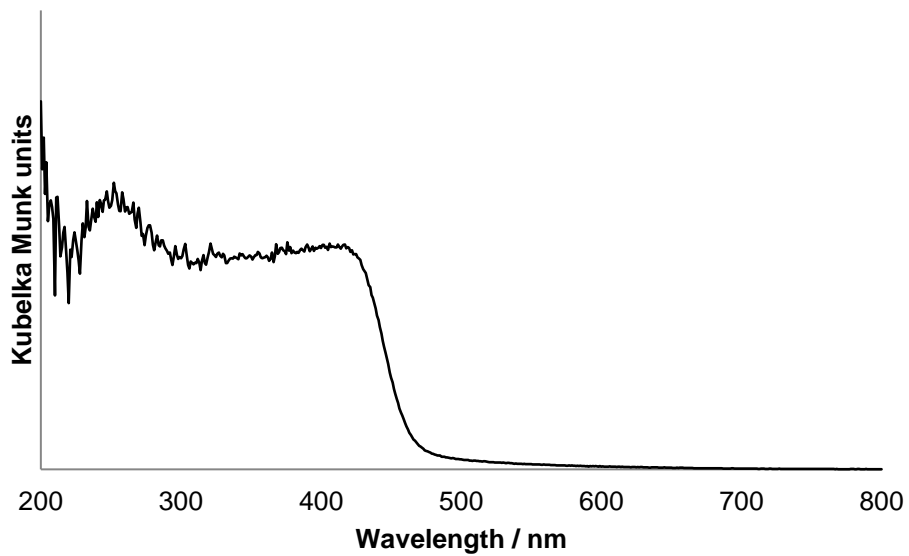


**Figure S33.** UV-vis spectrum of MIL-53-NH<sub>2</sub>/NO<sub>2</sub> (1). For the measurement, 5wt% of MIL-53-NH<sub>2</sub>/NO<sub>2</sub> in BaSO<sub>4</sub> was used. Reflectance data were converted with the Kubelka Munk equation:  $F(R) = (1-R)^2 / 2R$ .

## SHG of MIL-53(Al)-NH<sub>2</sub>/NO<sub>2</sub> (1) as a function of temperature

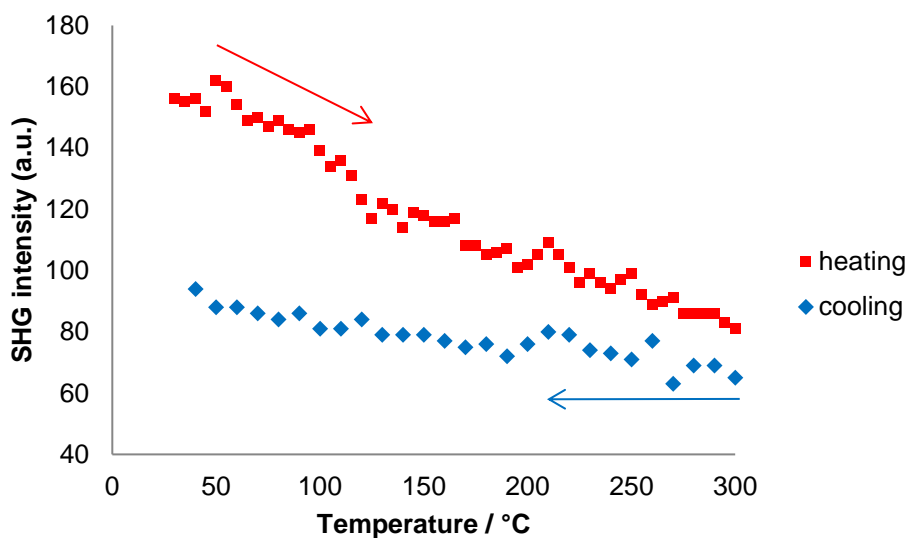


**Figure S34.** SHG intensity of MIL-53(Al)-NH<sub>2</sub>/NO<sub>2</sub> (1) during heating and cooling at a rate of 1 °C.min<sup>-1</sup> under N<sub>2</sub> flow. Between heating and cooling, the temperature was held constant at 300 °C overnight.

## Bibliography

- (1) Berbenni, V.; Milanese, C.; Bruni, G.; Marini, A. *Journal of Thermal Analysis and Calorimetry* **2005**, *82*, 401–407.
- (2) Serra-Crespo, P.; van der Veen, M. A.; Gobechiya, E.; Houthoofd, K.; Filinchuk, Y.; Kirschhock, C. E. A.; Martens, J. A.; Sels, B. F.; De Vos, D. E.; Kapteijn, F.; Gascon, J. *Journal of the American Chemical Society* **2012**, *134*, 8314–7.
- (3) Reinsch, H.; van der Veen, M. A.; Gil, B.; Marszalek, B.; Verbiest, T.; De Vos, D. E.; Stock, N. *Chemistry of Materials* **2013**, *25*, 17–26.
- (4) Horcajada, P.; Serre, C.; Grosso, D.; Boissière, C.; Perruchas, S.; Sanchez, C.; Férey, G. *Advanced Materials* **2009**, *21*, 1931–1935.
- (5) Yang, L.-M.; Vajeeston, P.; Ravindran, P.; Fjellvåg, H.; Tilset, M. *Inorganic chemistry* **2010**, *49*, 10283–90.
- (6) Yang, L.-M.; Ravindran, P.; Vajeeston, P.; Tilset, M. *Physical chemistry chemical physics : PCCP* **2012**, *14*, 4713–23.
- (7) MUNN, R. W. *Molecular Physics* **1996**, *89*, 555–569.
- (8) Kirtman, B.; Dykstra, C. E.; Champagne, B. *Chemical Physics Letters* **1999**, *305*, 132–138.
- (9) Reis, H.; Papadopoulos, M. G.; Calaminici, P.; Jug, K.; Köster, A. M. *Chemical Physics* **2000**, *261*, 359–371.
- (10) Seidler, T.; Stadnicka, K.; Champagne, B. *The Journal of Chemical Physics* **2013**, *139*, 114105.
- (11) Seidler, T.; Stadnicka, K.; Champagne, B. *Advanced Optical Materials* **2014**, *2*, 1000–1006.
- (12) Dovesi, R.; Orlando, R.; Erba, A.; Zicovich-Wilson, C. M.; Civalleri, B.; Casassa, S.; Maschio, L.; Ferrabone, M.; De La Pierre, M.; D'Arco, P.; Noël, Y.; Causà, M.; Rérat, M.; Kirtman, B. *International Journal of Quantum Chemistry* **2014**, *114*, 1287–1317.
- (13) Seidler, T.; Champagne, B. *Phys. Chem. Chem. Phys.* **2015**, *17*, 19546–19556.
- (14) Sekino, H.; Bartlett, R. J. *International Journal of Quantum Chemistry* **1984**, *26*, 255–265.
- (15) Seidler, T.; Champagne, B. *The Journal of Physical Chemistry C* **2016**, *120*, 6741–6749.
- (16) Frisch, M. J.; Trucks, G. W.; Schlegel, H. B.; Scuseria, G. E.; Robb, M. A.; Cheeseman, J. R.; Scalmani, G.; Barone, V.; Mennucci, B.; Petersson, G. A.; Nakatsuji, H.; Caricato, M.; Li, X.; Hratchian, H. P.; Izmaylov, A. F.; Bloino, J.; Zheng, G.; Sonnenberg, J. L.; Hada, M.; Ehara, M.; Toyota, K.; Fukuda, R.; Hasegawa, J.; Ishida, M.; Nakajima, T.; Honda, Y.; Kitao, O.; Nakai, H.; Vreven, T.; Montgomery, J. A.; Peralta, J. E.; Ogliaro, F.; Bearpark, M.; Heyd, J. J.; Brothers, E.; Kudin, K. N.; Staroverov, V. N.; Kobayashi, R.; Normand, J.; Raghavachari, K.; Rendell, A.; Burant, J. C.; Iyengar, S. S.; Tomasi, J.; Cossi, M.; Rega, N.; Millam, J. M.; Klene, M.; Knox, J. E.; Cross, J. B.; Bakken, V.; Adamo, C.; Jaramillo, J.; Gomperts, R.; Stratmann, R. E.; Yazyev, O.; Austin, A. J.; Cammi, R.; Pomelli, C.; Ochterski, J. W.; Martin, R. L.; Morokuma, K.; Zakrzewski, V. G.; Voth, G. A.; Salvador, P.; Dannenberg, J. J.; Dapprich, S.; Daniels, A. D.; Farkas, Foresman, J. B.; Ortiz, J. V.; Cioslowski, J.; Fox, D. J. *Gaussian 09, Revision B.01, Gaussian, Inc., Wallingford CT* **2009**.
- (17) Bru, R.; Walde, P. *European Journal of Biochemistry* **1991**, *199*, 95–103.



---

## Liste der Publikationen und Beiträge

---

### Vorträge

05. Juli 2016 AC Kolloquium Christian-Albrechts-Universität zu Kiel  
*Funktionale Koordinationspolymere der Gruppe 13 Elemente*

### Poster

06.-08. März 2013 Deutsche Zeolith-Tagung Hamburg  
*New Al-MOFs containing tricarboxylate linker molecules*

26.-28. Februar 2014 Deutsche Zeolith-Tagung Paderborn  
*In situ investigation of the formation of CAU-8 –  
[Al(OH)(O<sub>2</sub>C-C<sub>6</sub>H<sub>4</sub>-C(O)-C<sub>6</sub>H<sub>4</sub>-CO<sub>2</sub>)]*

25.-27. Februar 2015 Deutsche Zeolith-Tagung Oldenburg  
*[Al<sub>2</sub>(OH)<sub>2</sub>(TCPB)] – a new, thermally stable Al-MOF*

### Publikationen

H. Reinsch, M. Krüger, J. Wack, J. Senker, F. Salles, G. Maurin und N. Stock  
A new aluminium-based microporous metal–organic framework: Al(BTB)  
(BTB = 1,3,5-benzenetrisbenzoate), *Micropor. Mesopor. Mater.*, 2012, **157**, 50-55.

H. Reinsch, M. Krüger, J. Marrot und N. Stock  
First Keto-Functionalized Microporous Al-Based Metal–Organic Framework:  
[Al(OH)(O<sub>2</sub>C-C<sub>6</sub>H<sub>4</sub>-CO-C<sub>6</sub>H<sub>4</sub>-CO<sub>2</sub>)], *Inorg. Chem.*, 2013, **52**, 1854--1859.

H. G. Baldovi, M. Krüger, H. Reinsch, M. Alvaro, N. Stock und H. Garcia  
Transient absorption spectroscopy and photochemical reactivity of CAU-8, *J. Mater. Chem. C.*,  
2015, **3**, 3607–3613.

M. Krüger, R. Siegel, A. Dreischarf, H. Reinsch, J. Senker und N. Stock  
[Al<sub>2</sub>(OH)<sub>2</sub>(TCPB)] - an Al-MOF based on a tetratopic linker molecule, *Micropor. Mesopor. Mat.*,  
**2015**, *216*, 27-35.

M. Krüger, M. Albat, F. Pieper und N. Stock  
Dimethylammonium 2-amino-5-nitroterephthalate hemihydrate, *IUCrData*, 2016, **1**,  
x160048.

M.-C. Schlegel, D. Töbrens, R. Svetogorov, M. Krüger, N. Stock, H. Reinsch, D. Wallacher, R.  
Stewart und M. Russina  
Conformation-controlled hydrogen storage in the CAU-1 metal–organic framework, *Chem.  
Chem. Phys.*, **2016**, *18*, 29258-29267.

M. Krüger, H. Reinsch, A. K. Inge und N. Stock  
Effect of partial linker fluorination and linker extension on structure and properties of the Al-  
MOF CAU-10, *Micropor. Mesopor. Mat.*, **2017**, *249*, 128-136.

M. Krüger, A. K. Inge, H. Reinsch, Y.-H. Li, M. Wahiduzzaman, C.-H. Lin, S.-L. Wang, G. Maurin  
und N. Stock  
Polymorphous Al-MOFs based on V-shaped Linker molecules: Synthesis, Properties, and In-  
Situ investigation of their crystallization, *Inorg. Chem.*, 2017, **56**, 5851-5862.

M. Krüger, M. Albat, A. K. Inge und N. Stock  
Investigation of the Effect of Polar Functional Groups on the Crystal Structures of Indium  
MOFs, *CrystEngComm.*, 2017, **19**, 4622-4628.

K. Markey, M. Krüger, T. Seidler, F. Pieper, H. Reinsch, T. Verbiest, M. Albat, D. E. De Vos, B.  
Champagne, N. Stock und M. A. van der Veen  
Emergence of nonlinear optical activity by incorporation of a linker carrying the *p*-nitroaniline  
motif in MIL-53 frameworks, *Chem. Mater.*, 2017, eingereicht.



---

# Curriculum Vitae

---

## Persönliche Details

Geburtsdatum	13. Oktober 1987
Geburtsort	Schwerin
Staatsangehörigkeit	deutsch

## Ausbildung

Februar 2013 – September 2017	<b>Promotion im Fachbereich Anorganische Chemie bei Prof. Dr. N. Stock</b>  Thema der Dissertation: „ <i>Synthese und Charakterisierung neuer und funktionalisierter MOFs basierend auf den Elementen der 13. Gruppe und deren spezielle optische Eigenschaften</i> “
Oktober 2010 – Januar 2013	<b>Master of Science im Fachbereich Anorganische Chemie</b>  Thema der Masterarbeit: „ <i>Einsatz von Al<sub>13</sub>-Keggin-Ionen zur Synthese von Anorganisch-Organischen Hybridverbindungen</i> “
Oktober 2007 – April 2011	<b>Bachelor of Science im Fachbereich Chemie</b>  Thema der Bachelorarbeit: „ <i>Synthese und Charakterisierung von CAU-4, [Al((O<sub>2</sub>C-C<sub>6</sub>H<sub>4</sub>)<sub>3</sub>C<sub>6</sub>H<sub>3</sub>)]</i> “
Bis Juni 2007	<b>Elbe-Gymnasium Boizenburg</b>  Erwerb der allgemeinen Hochschulreife

## **Eidesstattliche Erklärung**

Hiermit versichere ich an Eides statt, dass ich die vorliegende Arbeit selbstständig - mit Ausnahme der wissenschaftlichen Beratung durch meinen Betreuer Herrn Prof. Stock - und nur unter Verwendung der angegebenen Hilfsmittel angefertigt habe. Sie hat nur im Rahmen dieses Prüfungsverfahrens vorgelegen. Teile der Arbeit wurden in den genannten Journalen als wissenschaftliche Beiträge veröffentlicht oder wurden eingereicht. Zusätzlich erkläre ich, dass ich noch keinen Promotionsversuch unternommen habe und dass die Arbeit unter Einhaltung der Regeln guter wissenschaftlicher Praxis der Deutschen Forschungsgesellschaft entstanden ist.

Kiel, im September 2017 \_\_\_\_\_

*Martin Krüger*